AFRL-AFOSR-VA-TR-2020-0095

ENABLING THE STRUCTURAL DESIGN OF HIGH-MACH, HIGH-ALTITUDE VEHICLES THROUGH A HOLISTIC APPROACH TO UNCERTAINTY MODELING

Marc Mignolet
ARIZONA STATE UNIVERSITY

05/01/2020
Final Report

Air Force Research Laboratory
AF Office Of Scientific Research (AFOSR)/ RTA1
Arlington, Virginia 22203
Air Force Materiel Command

DISTRIBUTION A: Distribution approved for public release.

REPORT DOCUMENTATION PAGE

Form Approved
OMB No. 0704-0188

1. REPORT DATE *(DD-MM-YYYY)*	2. REPORT TYPE	3. DATES COVERED *(From - To)*
15-07-2020	Final Performance	01 Feb 2016 to 31 Jan 2020

4. TITLE AND SUBTITLE
ENABLING THE STRUCTURAL DESIGN OF HIGH-MACH, HIGH-ALTITUDE VEHICLES THROUGH A HOLISTIC APPROACH TO UNCERTAINTY MODELING

5a. CONTRACT NUMBER

5b. GRANT NUMBER
FA9550-16-1-0021

5c. PROGRAM ELEMENT NUMBER
61102F

6. AUTHOR(S)
Marc Mignolet

5d. PROJECT NUMBER

5e. TASK NUMBER

5f. WORK UNIT NUMBER

7. PERFORMING ORGANIZATION NAME(S) AND ADDRESS(ES)
ARIZONA STATE UNIVERSITY
660 S MILL AVE STE 312
TEMPE, AZ 85281 US

8. PERFORMING ORGANIZATION REPORT NUMBER

9. SPONSORING/MONITORING AGENCY NAME(S) AND ADDRESS(ES)
AF Office of Scientific Research
875 N. Randolph St. Room 3112
Arlington, VA 22203

10. SPONSOR/MONITOR'S ACRONYM(S)
AFRL/AFOSR RTA1

11. SPONSOR/MONITOR'S REPORT NUMBER(S)
AFRL-AFOSR-VA-TR-2020-0095

12. DISTRIBUTION/AVAILABILITY STATEMENT
A DISTRIBUTION UNLIMITED: PB Public Release

13. SUPPLEMENTARY NOTES

14. ABSTRACT

The overall focus of this investigation was on the modeling and management of uncertainties, both epistemic and aleatoric, in structural-thermal reduced order models for the nonlinear geometric response of heated structures. This effort was motivated by and in strong support of the design and operation of the future hypersonic vehicles envisioned by the Air Force. Following the proposal, this investigation was divided into the three thrusts stated below and the work carried out under each thrust is summarized below.

Research Thrust #1: Modeling of Aleatoric and Epistemic Uncertainties within Multi-Physics ROMs

The focus of this first thrust was on developing the necessary modeling of epistemic and aleatoric uncertainties directly on the reduced order models. This effort built upon an earlier paper by the PI which proposed an approach applicable to simple structural model but exhibiting indeterminacy and significant numerical issues for more complex ones. The first key contribution to the Thrust #1 was then to resolve both the indeterminacy and the numerical issues and successfully applying the approach to several ROMs of complex structures.

15. SUBJECT TERMS
uncertainty modeling, reduced order model, combined loading

16. SECURITY CLASSIFICATION OF:			17. LIMITATION OF ABSTRACT	18. NUMBER OF PAGES	19a. NAME OF RESPONSIBLE PERSON
a. REPORT	b. ABSTRACT	c. THIS PAGE			TILEY, JAIMIE
Unclassified	Unclassified	Unclassified	UU		

Standard Form 298 (Rev. 8/98)
Prescribed by ANSI Std. Z39.18

				19b. TELEPHONE NUMBER *(Include area code)* 703-588-8316

ENABLING THE STRUCTURAL DESIGN OF HIGH-MACH, HIGH-ALTITUDE VEHICLES THROUGH A HOLISTIC APPROACH TO UNCERTAINTY MODELING
CONTRACT FA9550-16-1-0021

FINAL REPORT

Marc P. Mignolet
SEMTE, Faculties of Mechanical and Aerospace Engineering
Arizona State University, Tempe, AZ 85287

JOURNAL PUBLICATIONS AND CONFERENCE PAPERS

Journal Publications:

[J1]: Wang, X.Q., Mignolet, M.P., and Soize, C., "Structural Uncertainty Modeling for Nonlinear Geometric Response using Nonintrusive Reduced Order Models," *Probabilistic Engineering Mechanics*, Vol. 60, 103033, pp. 1-9, 2020.

This paper is an extension of [C8].

[J2]: Song, P., Wang, X.Q., Murthy, R., Matney, A.K., and Mignolet, M.P., "Nonlinear Geometric Thermoelastic Response of Structures with Uncertain Thermal and Structural Properties," *AIAA Journal*, In Press.

[J3]: Wang, X.Q., Liao, Y., and Mignolet, M.P., "Uncertainty Analysis of Piezoelectric Vibration Energy Harvesters Using a Finite Element Level-Based Maximum Entropy Approach," *ASCE-ASME Journal of Risk and Uncertainty in Engineering Systems Part B: Mechanical Engineering*, In Press.

Journal Papers in Preparation:

[P1]: Wang, X.Q., Lin, J., and Mignolet, M.P., "Improved Deterministic and Stochastic Identification of Stiffness Parameters of Nonlinear Reduced Order Model," To be Submitted to *Computational Mechanics*.

This paper includes the work of [C1], [C6] and work carried out under another contract

[P2]: Perez, R., Song, P., Wang, X.Q., and Mignolet, M.P., " Uncertainty Management in Reduced Order Models of Nonlinear Geometric Response – Part I: Sparsity," To be Submitted to *International Journal for Uncertainty Quantification*.

[P3]: Song, P., Wang, X.Q., and Mignolet, M.P., " Uncertainty Management in Reduced Order Models of Nonlinear Geometric Response – Part II: Incomplete Bases," To be Submitted to *International Journal for Uncertainty Quantification*.

This sequence of 2 papers will include the work of [C3], [A1] as well as additional work carried out under another contract.

[P4]: Wang, X.Q., and Mignolet, M.P., "Basis Selection for Reduced Order Modeling of Structures in the Nonlinear Geometric Regime- Part I: Isothermal Structures," To be Submitted to *Journal of Sound and Vibration.*

[P5]: Wang, X.Q., and Mignolet, M.P., "Basis Selection for Reduced Order Modeling of Structures in the Nonlinear Geometric Regime- Part I: Heated Structures," To be Submitted to *Journal of Sound and Vibration.*

This sequence of 2 papers will include the work of [C2], [C5], [C7] as well as additional work carried out under another contract.

Conference Papers:

[C1]: Wang, X.Q., and Mignolet, M.P., "Uncertainty Quantification of Nonlinear Stiffness Coefficients in Non-Intrusive Reduced Order Models," *Proceedings of the International Modal Analysis Conference, IMAC XXXVIII*, Houston, Texas, Feb. 10-13, 2020.

[C2]: Wang, X.Q., and Mignolet, M.P., "Enrichments of Structural Bases for the Reduced Order Modeling of Heated Structures Undergoing Nonlinear Geometric Response," *Proceedings of the International Modal Analysis Conference, IMAC XXXVIII*, Houston, Texas, Feb. 10-13, 2020.

[C3]: Song, P., Wang, X.Q., and Mignolet, M.P., "Uncertainty Management for the Stochastic Response of Uncertain Structures," *Proceedings of the AIAA Science and Technology Forum and Exposition (SciTech2020)*, Orlando, Florida, Jan.6-10, 2020. AIAA Paper AIAA-2020-1419.

[C4]: Sharma, P., Wang, X.Q., and Mignolet, M.P., "Toward an Uncertain Modeling of Hypersonic Aerodynamic Forces," *Proceedings of the AIAA Science and Technology Forum and Exposition (SciTech2020)*, Orlando, Florida, Jan.6-10, 2020. AIAA-2020-1878.

[C5]: Lin, J., Wang, X.Q., and Mignolet, M.P., "Nonlinear Reduced Order Modeling of a Cylindrical Shell Exhibiting Mode Veering and Symmetry Breaking," *Proceedings of the International Modal Analysis Conference, IMAC XXXVII*, Orlando, Florida, Jan. 28-31, 2019.

[C6]: Wang, X.Q., Lin, J., Wainwright, B.A., and Mignolet, M.P., "Multiple-Level Identification of Stiffness Coefficients in Nonlinear Reduced Order Modeling," *Proceedings of the International Modal Analysis Conference, IMAC XXXVII*, Orlando, Florida, Jan. 28-31, 2019.

[C7]: Lin, J., Wang, X.Q., and Mignolet, M.P., "Nonlinear Reduced Order Modeling of Strongly Nonlinear Behavior: A Revisit of a Curved Beam Example," *Proceedings of the International Modal Analysis Conference, IMAC XXXVI*, Orlando, Florida, Feb. 12- 15, 2018.

[C8]: Wang, X.Q., Mignolet, M.P., and Soize, C., "Nonlinear Geometric Modeling of Uncertain Structures through Nonintrusive Reduced Order Modeling," *Proceedings of the Eighth International Conference On Computational Stochastic Mechanics*, Paros, Greece, Jun. 10-13, 2018.

Theses

[T1] : Sharma, P., "Toward an Uncertain Modeling of Hypersonic Aerodynamic Forces," M.S., May 2017.

[T2]: Lin, J., "Nonlinear Reduced Order Modeling of Structures Exhibiting a Strong Nonlinearity, Ph.D., May 2020 (Chapters 4 and 6).

Recent Work Currently Unpublished

[A1]: Extension of the concepts of [C3] to include the epistemic uncertainty associated with incomplete bases

EXECUTIVE SUMMARY

The overall focus of this investigation was on the modeling and management of uncertainties, both epistemic and aleatoric, in reduced order models for the nonlinear geometric response of heated structures. This effort was motivated by and in strong support of the design and operation of the future hypersonic vehicles envisioned by the Air Force.

The prediction of the structural response, temperature distribution, and aeroelastic behavior of these vehicles will require fully coupled structural-thermal-aerodynamic analyses, at least, with the possible addition of material and servo/control analyses. The high temperature and large aerodynamic loads that are expected on these vehicles will induce "large" structural deformations that require the inclusion of nonlinear geometric effects so that all 3 fields (structural, thermal, aerodynamic) will involve nonlinear solutions. While the combination of finite element and computational fluid dynamic (CFD) solution methods can be used to tackle this multi-physics problem, the expected computational effort will be very large and will be unsuitable at the design phase and/or for the large time span computations that are required for mission analyses and fatigue life prediction. Accordingly, it is well expected that reduced order and surrogate models will play an important role for these more demanding situations. Of particular interest here are the structural-thermal reduced order models that the PI's group has spearheaded over the last 17 years.

Uncertainties will also be present when analyzing hypersonic vehicles and should be accounted for in the design and thus in the reduced order modeling strategy. The uncertainties will certainly originate from variations from vehicle to vehicle and also over time for the same vehicle, owing to the appearance and progression of damage and material changes. Besides these aleatoric uncertainties, there will also be epistemic ones originating from aerodynamic/structural modeling assumptions as well as from the approximation of the corresponding full order models by reduced order ones.

In the context of the present effort, uncertainty management is the recognition that it is not efficient to carry out all computations with minimal epistemic uncertainty (i.e., the most accurate computational models) when aleatoric uncertainty is present (e.g., vehicle-to-vehicle variability). Rather, it is computationally advantageous to reduce somewhat the model complexity, i.e., allow epistemic uncertainty to increase until it becomes measurable with respect to its aleatoric counterpart.

Following the proposal, this investigation was divided into the three thrusts stated below and the work carried out under each thrust will be summarized. The technical details of the work are presented in the Appendices which contain the work of [J1]-[J3], [C1]-[C8], [T1]-[T2], and [A1]. A brief summary of the reduced order modeling strategy is first included to clarify the issues and contributions of the various thrusts.

Reduced Order Modeling Background

The reduced order models used in this research are based on a representation of the vectors of structural displacements $\underline{u}$ and temperature $\underline{T}$ on underlying finite element meshes as expansions – one for displacements and one for temperature - on fixed basis functions but with time/loading varying generalized coordinates. That is,

$$\underline{u}(t) = \sum_{n=1}^{M} q_n(t)\, \underline{\psi}^{(n)} \qquad\qquad \underline{T}(t) = \sum_{n=1}^{\mu} \tau_n(t)\, \underline{\phi}^{(n)} \tag{1}$$

where $\underline{\phi}^{(n)}$ and $\underline{\psi}^{(n)}$ are the time-independent thermal and structural basis functions, or modes, while $\tau_n(t)$ and $q_n(t)$ are the time-dependent thermal and structural generalized coordinates.

The governing equations for these coordinates can be derived from finite deformation thermoelasticity as

$$M_{ij}\ddot{q}_j + D_{ij}\dot{q}_j + K_{ij}^{(1)}(\tau_l)\,q_j + K_{ijl}^{(2)}(\tau_l)q_j q_l + K_{ijlp}^{(3)}(\tau_l)q_j q_l q_p = F_i(\tau_l) \tag{2}$$

and

$$B_{ij}\,\dot{\tau}_j + \widetilde{K}_{ij}\tau_j = P_i \tag{3}$$

In Eq. (2), M_{ij} and D_{ij} denote mass and damping terms while $K_{ij}^{(1)}$, $K_{ijl}^{(2)}$, $K_{ijlp}^{(3)}$ are temperature-dependent linear, quadratic, and cubic stiffness coefficients and F_i are the modal forces involving both purely mechanical/aerodynamic loads and thermally induced ones. In Eq. (3), B_{ij} and $\widetilde{K}_{ij}$ are capacitance and conductance coefficients, which are generally dependent on temperature. Finally, the source term P_i represents the combined effects of an applied flux, non-zero homogenous boundary conditions, radiation, latency, etc., as applicable.

When the material properties are independent of temperature, all parameters in Eqs (2) and (3) are constant except for the linear stiffnesses $K_{ij}^{(1)}$ and modal forces F_i which are linearly dependent on the thermal generalized coordinates $\tau_n(t)$. If the Young's modulus and coefficient of thermal expansion are linearly dependent on temperature, then the linear stiffness and modal forces become cubic polynomial of the $\tau_n(t)$ while the quadratic and cubic stiffnesses depend linearly on them.

The reduced order modeling strategy used here is based on underlying finite element models developed in commercial software and thus all components of it, i.e., basis functions and parameters, must determined from them through standard outputs of these codes. In this light, one key aspect of the structural reduced order model of Eqs (1) and (2) is the number of stiffness parameters that it involves which is of order $M^4/6$ in the absence of thermal effects but rises to $(\mu+1)\,M^4/6 + \mu^3\,M^2/6$ when linear variations of the properties with temperature are included.

The best approach currently available to identify these parameters from the underlying finite element model is through the outputting of the tangent stiffness matrix of static solutions. Thus, for each finite element static solution, a maximum of $M(M+1)/2$ equations can be derived. The number of such static solutions is then at best $M^2/3$ in the absence of thermal effects but rises to $(\mu+1)\,M^2/3 + \mu^3/3$ with linear dependence on temperature.

To provide perspective for this identification effort, note that the largest model considered to date involved $M = 85$ modes for a structural-only problem (i.e. $\mu=0$) leading to approximately $8.7\ 10^6$ coefficients and requiring 3655 static solutions for the identification of the linear and nonlinear stiffnesses. With temperature effects, the largest model considered is $M = 44$ and $\mu = 42$ leading to $5.08\ 10^7$ coefficients and requiring over 50,000 static solutions for the identification of the linear and nonlinear stiffnesses. It is concluded that the stiffness coefficients identification is a computationally important effort for ROMs with large bases.

A final important point regarding the stiffness coefficients is that Eq. (2) is exact under a particular constitutive law, i.e., for a Kirchhoff – St Venant material. However, this is typically not the stress-strain relation adopted in most commercial finite element codes for beam and plate models in large deformations (details are not available as proprietary). In that sense, Eq. (2) is only an approximation of the finite element results and thus the identification of the stiffness coefficients exhibits computational inaccuracies.

Research Thrust #1: Modeling of Aleatoric and Epistemic Uncertainties within Multi-Physics ROMs

Since the present reduced order modeling formulation is based on underlying finite element models, it could be envisioned that the uncertainty would be modeled directly at the finite element level using standard approaches. Then, finite element samples would be generated and the corresponding samples of the reduced order model would be obtained one at a time using the identification procedure developed for the mean model. This approach may be acceptable for ROMs with small bases corresponding to simple structures but not for the realistic structures/large bases considered here as the identification effort of all ROM samples would be daunting. It was thus critical to develop a strategy to model the uncertainty directly at the ROM level, i.e., in which the ROM samples would be directly generated from the mean ROM.

Such a strategy was proposed by the PI and a co-author several years ago [1] and was successfully validated but only for a simple straight clamped-clamped beam. More complex validations were later found to be very difficult to achieve owing to (i) an indeterminacy and (ii) numerical issues induced by the inaccuracies of the stiffness coefficients discussed above. These issues led to the key matrix not being positive definite as expected using the ROM formulation. For the beam example of [1], the indeterminacy could be resolved and the numerical issues were mild and the matrix could be made positive semi definite without affecting the ROM accuracy.

In this light, the first key contribution to the Thrust #1 is the paper [J1] and [C8], see Appendix A, in which we resolved both the indeterminacy – through an optimization process – and the numerical issues – through various small modifications of the methodology - and successfully applied the approach to several ROMs of complex structures.

Relying on the success of [J1], the introduction of uncertainty in structural *and thermal* ROMs was next investigated and resolved, see journal paper [J2] and Appendix B. These two efforts provided the core methodology for the uncertainty modeling and management used in the rest of the project.

In parallel to the above efforts, two aspects of the mean model ROM construction were also addressed to prepare for the Thrust #2 work. The first of these aspects focused on better defining a set of "enrichments", i.e., structural basis functions the role of which is to allow a good prediction of the structural response under thermal loading. These enrichments are necessary because the rest of the structural basis relies on low frequency linear modes and related nonlinear deformations (referred to as dual modes) which capture well the response to transverse mechanical loads. However, heating of the structure induces different, mostly in plane displacements and thus a separate set of basis functions is necessary. This study, published in [C2] (see Appendix C), clarified several construction procedures of these enrichments. Among the structures considered to exemplify these concepts is a beam subjected to a uniform temperature over a limited spatial domain of the beam. Interestingly, this structure is mathematically equivalent to a simple model of an energy harvester demonstrating that the current work has far ranging applications, well beyond hypersonic vehicles panels.

The second aspect of the mean ROM construction considered under Thrust #1 is the identification of the stiffness coefficients. As discussed in the ROM background section, these coefficients may be subject to inaccuracies due to constitutive law differences between the finite element formulation and the one of the ROM. To address this issue, a novel identification approach was defined in [C6], see Appendix D, that relies on multiple static solutions at different response levels to obtain improved estimates of the coefficients. This approach was accordingly referred to as "multi level" and has since been used very successfully in connection with other structures considered here and in two other contracts.

The inaccuracies of the stiffness coefficients which can be quantified in the multi level identification approach were considered as uncertainties in the ensuing study [C1], see Appendix E, and it was demonstrated there that the uncertainty model of [J1] is fully applicable to this situation. This study provides, to the PI's knowledge, the first assessment of epistemic uncertainty and its modeling in nonlinear ROMs.

The final effort carried out under Thrust #1 focused on extending the energy harvester application of the current ROMs which came to light in [C2]. More specifically, it was desired to assess the effects of uncertainty, modeled as in [J2], on the benefits of the harvester. That effort was initiated by considering first the linear regime which had received only scant consideration. This preliminary work was published as [J3], See Appendix F. It is hoped that this study will be continued in the near future with the application of the methodology of [J2] in the nonlinear regime.

Research Thrust 2: Uncertainty Management in Structural/Thermal ROM Governing Equations – Sparse Uncertain ROMs

This second research thrust relied heavily on the first one and more specifically on the uncertainty modeling approaches of [J1] and [J2] to address the epistemic uncertainty that results from (i) incomplete bases and (ii) "sparse" sets of stiffnesses.

The construction of the structural and thermal bases are key steps of the mean ROM but are not always straightforward. Two of the challenges that may be encountered are that:

(i) the basis necessary to achieve a specific error level in the predicted displacements/temperatures is large with many of the basis functions contributing little to the improvement in prediction, and/or

(ii) the processes in place for the basis construction do not lead to predictions that satisfy the desired error levels.

Note that the first case can in fact reduce to the second one if it is decided, for computational efficiency, to not take all the basis functions but rather only those that provide significant error reduction. In such cases, the basis is incomplete and there exists an epistemic uncertainty. The work carried out in [A1], see Appendix G, addresses this issue and demonstrates that this epistemic uncertainty can be modeled as done in [J1] and [J2] whether the basis is incomplete in enrichments, thermal basis functions, or dual modes.

The second component of Thrust #2 focused on addressing the computational challenge associated with the very large number of stiffness coefficients, especially when temperature variations exist, as discussed in the ROM background section. One approach to resolve this issue is to optimize the basis functions so that the corresponding ROM achieves a specific accuracy with a minimum number of basis functions. This issue has been successfully investigated in [C5], [C7], and [T2], see Appendix H.

Another approach to address the above computational challenge is to use "sparse" ROMs, i.e., ROMs in which a series of stiffness coefficients are neglected. As discussed in [C3] and [2], this strategy can be extremely efficient as a very large number of nonlinear stiffness coefficients have very little effect on the response. Formally though, this approach induces epistemic uncertainty and it was thus desired to be able to quantify and model this uncertainty. This was achieved successfully using once again the modeling of [J1] and [J2], see [C3] and Appendix I.

Research Thrust 3: Uncertain Aero-Structure Interface Modeling

While the research thrusts 1 and 2 are structure-focused, the aerodynamics is nevertheless strongly present providing both forces and heat flux. What is really needed from

aerodynamics is to relate the surface displacements, velocities, and temperatures to the aerodynamic forces and heat flux. Such relations can be obtained analytically assuming a linear aerodynamic model, either using piston theory or a linearized solver. At the opposite end of the computational complexity spectrum are full Navier-Stokes CFD computations which require very fine grids and much smaller time steps than those used for the structural response and temperature computations, thereby rendering the aerodynamic solution as the computational bottleneck. The high relative cost of the aerodynamic computations is especially true when using the thermo-structural ROM from Eqs. (2)-(3) which are notably less computationally intensive than their finite elements counterparts.

To address the aerodynamic computational bottleneck, it was proposed here to investigate the modeling of the epistemic uncertainty on the structural loads that is induced by the adoption of a lower fidelity aerodynamic model. The availability of such a representation would permit the designer to adapt the choice of the aerodynamic model to the level of structural uncertainty present.

This effort was achieved in [C4] and [T1] by starting from piston theory aerodynamics and enriching it with terms that model the downstream propagation of upstream structural deformations. The surrogates formed in this process provided a good approximation of the pressure distributions obtained by CFD on a simple deforming panel. Then, the epistemic uncertainty was modeled within the surrogates leading to a stochastic model of the aerodynamic forces that can be used in conjunction with uncertain ROMs to obtain, in a computationally very efficient way, the fully coupled structural-thermal-aerodynamic response.

Additional References

[1] Mignolet, M.P., A. Przekop, S.A. Rizzi, and S.M. Spottswood, *A review of indirect/non-intrusive reduced order modeling of nonlinear geometric structure*, Journal of Sound and Vibration, 2013, **332**(10): p. 2437-2460.

[2] Perez, R.A., Smarslok, B.P., and Mignolet, M.P., "Deterministic and Stochastic Partial Linearization Approach for Nonlinear Reduced Order Models of Structures," *Proceedings of the AIAA Science and Technology Forum and Exposition (SciTech2015)*, Orlando, Florida, Jan. 5-9, 2015, AIAA Paper AIAA 2015-2052.

APPENDIX A:

[J1]: Wang, X.Q., Mignolet, M.P., and Soize, C., "Structural Uncertainty Modeling for Nonlinear Geometric Response using Nonintrusive Reduced Order Models," *Probabilistic Engineering Mechanics*, Vol. 60, 103033, pp. 1-9, 2020.
[C8]: Wang, X.Q., Mignolet, M.P., and Soize, C., "Nonlinear Geometric Modeling of Uncertain Structures through Nonintrusive Reduced Order Modeling," *Proceedings of the Eighth International Conference On Computational Stochastic Mechanics*, Paros, Greece, Jun. 10-13, 2018.

Probabilistic Engineering Mechanics 60 (2020) 103033

Contents lists available at ScienceDirect

Probabilistic Engineering Mechanics

journal homepage: www.elsevier.com/locate/probengmech

Structural uncertainty modeling for nonlinear geometric response using nonintrusive reduced order models

X.Q. Wang [a], Marc P. Mignolet [a,*], Christian Soize [b]

[a] SEMTE Faculties of Mechanical and Aerospace Engineering, Arizona State University, Tempe, AZ 85048, USA
[b] Laboratoire Modélisation et Simulation Multi Echelle, Université Gustave Eiffel, 77454 Marne-la-Vallee, France

ARTICLE INFO

Keywords:
Uncertainty modeling
Maximum entropy
Uncertain structure
Nonlinear geometric structural response
Reduced order modeling

ABSTRACT

The focus of the present investigation is on the introduction of uncertainty directly in reduced order models of the nonlinear geometric response of structures following maximum entropy concepts. While the approach was formulated and preliminary validated in an earlier paper, its broad application to a variety of structures based on their finite element models from commercial software was impeded by two key challenges. The first of these involves an indeterminacy in the mapping of the nonlinear stiffness coefficients identified from the finite element model to those of the reduced order model form that is suitable for the uncertainty analysis. The second challenge is that a key matrix in the uncertainty modeling was expected to be positive definite but was numerically observed not to be. This latter issue is shown here to be rooted in differences in nonlinear finite element modeling between the commercial software and the theoretical developments. Both of these challenges are successfully resolved and applications examples are presented that confirm the broad applicability of the methodology.

1. Introduction

Over the last two decades, maximum entropy concepts have been broadly and very successfully used to model uncertainties in structures directly at the level of reduced order models (ROMs) constructed from the finite element model of the mean structure, see [1,2] for reviews. In addition to its capability to account for some epistemic uncertainty, this approach is computationally much more expedient than its alternative, which is to first introduce uncertainty in the finite element model then construct a ROM for each sample of the random structure. The computational saving is particularly significant for large size linear finite element models but also for nonlinear geometric problems where the ROMs include a large number of linear, quadratic, and cubic stiffness coefficients, see [3] for an overview. These coefficients must either be identified from a standard (e.g., commercial) finite element model using nonintrusive techniques [3–5] or computed using a dedicated finite element formulation [6–9] based on the reduced order modeling results of [10]. The latter of these two approaches lends itself naturally to the introduction of uncertainty at the ROM level using the maximum entropy concepts as originally discussed in [10]. The application of this strategy to the ROMs identified nonintrusively [3–5] from a commercial finite element code has been exemplified in [10] on a simple flat beam structure. More complex applications of this approach have been impeded by two key challenges, of decomposition and non-positive definiteness, in transforming the identified ROM into one that is suitable for the uncertainty analysis. The focus of the present investigation is on efficiently resolving these two challenges and applying them to a representative set of structures in the nonlinear geometric regime.

2. Reduced order models of nonlinear geometric structural response

The reduced order models considered in the present study are based on a representation of the nonlinear geometric response of the structure in the form

$$\boldsymbol{u}(t) = \sum_{n=1}^{M} q_n(t)\, \boldsymbol{U}^{(n)} \tag{1}$$

where $\boldsymbol{u}(t)$ denotes the vector of displacements of the finite element degrees of freedom, $\boldsymbol{U}^{(n)}$ are basis functions (modes) of the ROM specified in the spatial domain of the finite element mesh, and $q_n(t)$ are the time dependent generalized coordinates.

To obtain a set of nonlinear ordinary differential equations for the generalized coordinates $q_n(t)$, it is convenient to consider the continuum equivalent of Eq. (1), i.e.,

$$u_i(\boldsymbol{X},t) = \sum_{n=1}^{M} q_n(t)\; U_i^{(n)}(\boldsymbol{X}),\; i = 1,2,3, \tag{2}$$

* Corresponding author.
E-mail addresses: xiaoquan.wang.1@asu.edu (X.Q. Wang), marc.mignolet@asu.edu (M.P. Mignolet), christian.soize@univ-eiffel.fr (C. Soize).

https://doi.org/10.1016/j.probengmech.2020.103033
Received 16 January 2020; Accepted 29 January 2020
Available online 4 February 2020

where $\boldsymbol{X}$ denotes an arbitrary point of the structure in its undeformed configuration. Then, introducing Eq. (2) in the equations of finite deformation elasticity and proceeding with a Galerkin approach provides the desired equations. This process was accomplished in [10] considering a Kirchhoff–Saint Venant type material in which the 2nd Piola–Kirchhoff stress tensor S is linearly related to the Green strain tensor E by

$$S_{ij} = C_{ijkl}\, E_{kl} \tag{3}$$

where C denotes the deformation independent 4th order elasticity tensor. Under this material assumption, it was shown in [10] that the generalized coordinates $q_n(t)$ satisfy the equations

$$M_{ij}\,\ddot{q}_j + D_{ij}\,\dot{q}_j + K^{(1)}_{ij} q_j + K^{(2)}_{ijl} q_j\, q_l + K^{(3)}_{ijlp} q_j\, q_l\, q_p = F_i, \tag{4}$$

where summation over repeated indices is implied. In the above equation, M_{ij} denote the elements of the mass matrix, $K^{(1)}_{ij}$, $K^{(2)}_{ijl}$, $K^{(3)}_{ijlp}$ are the linear, quadratic, and cubic stiffness coefficients and F_i are the modal forces. Note that a damping matrix D was also introduced in Eq. (4) to model dissipation.

Note in Eq. (4) that a series of terms involve the same monomials of the generalized coordinates, e.g. $K^{(2)}_{ijl}$ and $K^{(2)}_{ilj}$, and thus these terms may naturally be regrouped leading to

$$M_{ij}\,\ddot{q}_j + D_{ij}\,\dot{q}_j + K^{(1)}_{ij} q_j + \overline{K}^{(2)}_{ijl} q_j\, q_l + \overline{K}^{(3)}_{ijlp} q_j\, q_l\, q_p = F_i, \tag{5}$$

which is very similar to Eq. (4) except that there is no repetition in the monomials because $\overline{K}^{(2)}_{ijl}$ and $\overline{K}^{(3)}_{ijlp}$ are nonzero only for $j \le l$ and $j \le l \le p$. Then, comparing Eqs. (4) and (5) yields

$$\overline{K}^{(2)}_{mnl} = \begin{cases} 0 & \text{for } l < n \\ K^{(2)}_{mnn} & \text{for } l = n \\ K^{(2)}_{mnl} + K^{(2)}_{mln} & \text{for } l > n \end{cases} \tag{6a}$$

and

$$\overline{K}^{(3)}_{mnlp} = \begin{cases} 0 & \text{unless } p \ge l \ge n \\ K^{(3)}_{mnnn} & \text{for } p = l = n \\ K^{(3)}_{mnll} + K^{(3)}_{mlnl} + K^{(3)}_{mlln} & \text{for } p = l > n \\ K^{(3)}_{mpll} + K^{(3)}_{mlpl} + K^{(3)}_{mllp} & \text{for } p > l = n \\ 2K^{(3)}_{mnlp} + 2K^{(3)}_{mpln} + 2K^{(3)}_{mlpn} & \text{for } p > l > n \end{cases} \tag{6b}$$

As discussed in [10], the symmetry properties of the elasticity tensor also imply that

$$K^{(3)}_{mnlp} = K^{(3)}_{nmlp} = K^{(3)}_{mnpl} = K^{(3)}_{lpmn}. \tag{7}$$

While Eqs. (4) and (5) were derived based on the continuum representation of Eq. (2), they are assumed here to be valid as well for a discrete, finite element model. In fact, the identification of the coefficients $\overline{K}^{(2)}_{ijl}$ and $\overline{K}^{(3)}_{ijlp}$ from nonintrusive outputs of commercial finite element software (e.g., Nastran) has been studied and can be achieved in different ways, see discussions in [3–5], given the basis functions $\boldsymbol{U}^{(n)}$. The selection of these vectors is discussed in details in [3,5] and references therein and is not repeated here for brevity.

3. Maximum entropy uncertainty modeling at the ROM level

The modeling of uncertainty at a ROM level has been developed, see [1,2], as a constrained optimization problem in which the entropy of the random parameters of the ROM is maximized under constraints which correspond to (i) physical requirements that these parameters must satisfy and (ii) conditions imposed by the user. To exemplify this strategy, consider the important case in which the ROM involves one or multiple positive definite symmetric matrices as occurs for example in linear structural dynamics. Let $\boldsymbol{A}$ be that random matrix and denote by $p_A(a)$ its probability density function which is defined over the domain of support $\overline{\Omega}$ such that A is positive definite and symmetric, i.e., with

$$A_{ij} = A_{ji}. \tag{8}$$

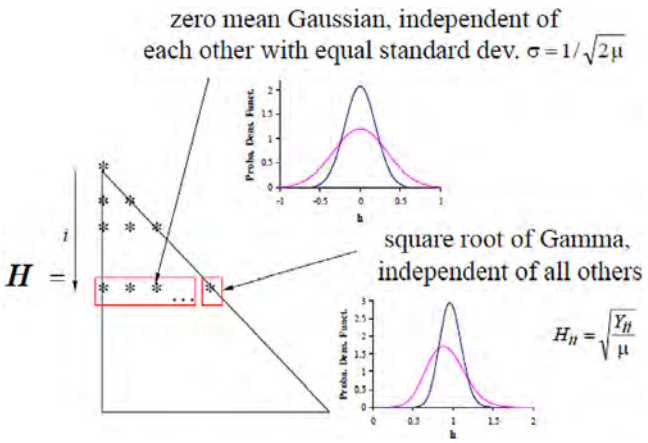

Fig. 1. Structure of the random $\boldsymbol{H}$ matrices with $n = 8$, $i = 2$, and $\lambda_0 = 1$ and 10.

Then, the entropy is

$$S = -\int_{\overline{\Omega}} p_A(a)\, \ln\, p_A(a)\, da \tag{9}$$

where $p_A(a)$ must satisfy

$$\int_{\overline{\Omega}} p_A(a)\, da = 1. \tag{10}$$

In addition to the physical requirements of symmetry and positive definiteness, it is also required that the mean of $\boldsymbol{A}$, denoted as $\overline{\boldsymbol{A}}$ is known, that is,

$$\int_{\overline{\Omega}} a\, p_A(a)\, da = \overline{A} \tag{11}$$

and moreover that

$$\int_{\overline{\Omega}} \ln\left[\det(a)\right] p_A(a)\, da = \nu \text{ finite} \tag{12}$$

which guaranties that the inverse matrix $\boldsymbol{A}^{-1}$ of $\boldsymbol{A}$, which exists almost surely, is a second-order random variable (mean-square integrable).

The probability density function $p_A(a)$ maximizing S given the constraints of Eqs. (8), (10)–(12) can be derived by calculus of variation and is found to be

$$p_A(a) = \widetilde{C}\left[\det(a)\right]^{\lambda_0 - 1} \exp\left[-\mathrm{tr}\left(\widetilde{\mu}^T a\right)\right] \tag{13}$$

where $\widetilde{C}$ is the appropriate constant to satisfy the normalization condition, Eq. (10) and μ and λ_0 are the Lagrange multipliers associated with the constraints of Eqs. (11) and (12), respectively. After a change of random variables, it is found that the matrices A of joint probability density function $p_A(a)$, Eq. (13), can be generated as

$$\boldsymbol{A} = \overline{\boldsymbol{L}}\boldsymbol{H}\,\boldsymbol{H}^T\,\overline{\boldsymbol{L}}^T \tag{14}$$

where $\overline{\boldsymbol{L}}$ is any decomposition, e.g., Cholesky, of $\overline{\boldsymbol{A}}$, i.e.,

$$\overline{\boldsymbol{A}} = \overline{\boldsymbol{L}}\,\overline{\boldsymbol{L}}^T. \tag{15}$$

Moreover, $\boldsymbol{H}$ is a lower triangular matrix such that (see also Fig. 1)

(1) all of its non-zero elements H_{il} are independent random variables,
(2) its off-diagonal elements H_{il}, $i \ne l$, are normally distributed (Gaussian) random variables with standard deviation $\sigma = 1/\sqrt{2\mu}$, and
(3) its diagonal elements H_{ii} are obtained as $H_{ii} = \sqrt{Y_{ii}/\mu}$ where Y_{ii} is Gamma distributed with parameter $(p(i) - 1)/2$ where

$$p(i) = n - i + 2\lambda_0 - 1 \text{ and } \mu = \left(n + 2\lambda_0 - 1\right)/2 \tag{16}$$

In the above equations, n is the size of the matrices and the parameter $\lambda_0 > 0$ is the free parameter of the statistical distribution of the random matrices $\boldsymbol{A}$. An alternative parametrization is through the dispersion parameter δ defined as

$$\delta^2 = \frac{n+1}{n+2\lambda_0-1}. \tag{17}$$

As stated above, a key component of the maximum entropy formulation is the satisfaction of the physical constraints that the ROM parameters must satisfy. While this issue is well understood for the stiffness matrix of linear structural dynamics, it is not as obvious for the combination of linear, quadratic, and cubic stiffness coefficients of the ROM of Eq. (4). The derivation of such a condition was achieved in [10] based on integral expressions of the stiffness coefficients of Eq. (4) obtained as a by-product of the derivation of this governing equation. Specifically, it was found that

$$K^{(1)}_{mn} = \int_{\Omega_0} \frac{\partial U^{(m)}_i}{\partial X_k} C_{iklp} \frac{\partial U^{(n)}_l}{\partial X_p} d\mathbf{X} \tag{18}$$

$$K^{(2)}_{mnp} = \frac{1}{2}\left[\hat{K}^{(2)}_{mnp} + \hat{K}^{(2)}_{pmn} + \hat{K}^{(2)}_{npm}\right] \tag{19}$$

where

$$\hat{K}^{(2)}_{mnp} = \int_{\Omega_0} \frac{\partial U^{(m)}_i}{\partial X_j} C_{ijkl} \frac{\partial U^{(n)}_r}{\partial X_k} \frac{\partial U^{(p)}_r}{\partial X_l} d\mathbf{X} \tag{20}$$

and

$$K^{(3)}_{msnp} = \frac{1}{2}\int_{\Omega_0} \frac{\partial U^{(m)}_i}{\partial X_j} \frac{\partial U^{(s)}_i}{\partial X_k} C_{jklw} \frac{\partial U^{(n)}_r}{\partial X_l} \frac{\partial U^{(p)}_r}{\partial X_w} d\mathbf{X}. \tag{21}$$

In these equations, Ω_0 denotes the domain of the structure in the undeformed configuration, $\boldsymbol{X} \in \Omega_0$.

Next, a reshaping was performed to transform the $M \times M \times M$ third order tensor $\hat{\boldsymbol{K}}^{(2)}$ into a $M \times M^2$ rectangular array $\widetilde{\boldsymbol{K}}^{(2)}$ and the $M \times M \times M \times M$ fourth order tensor $\boldsymbol{K}^{(3)}$ into a $M^2 \times M^2$ square matrix $\widetilde{\boldsymbol{K}}^{(3)}$. These operations are achieved as follows:

$$\widetilde{K}^{(2)}_{mJ} = \hat{K}^{(2)}_{mnp} \quad \text{with} \quad J = (n-1)M + p \tag{22}$$

and

$$\widetilde{K}^{(3)}_{IJ} = K^{(3)}_{msnp} \quad \text{with} \quad I = (m-1)M + s \text{ and } J = (n-1)M + p. \tag{23}$$

With these operations, it was shown that the matrix $\overline{\boldsymbol{K}}_B$ defined as

$$\overline{\boldsymbol{K}}_B = \begin{bmatrix} \boldsymbol{K}^{(1)} & \tilde{\boldsymbol{K}}^{(2)} \\ \tilde{\boldsymbol{K}}^{(2)T} & 2\tilde{\boldsymbol{K}}^{(3)} \end{bmatrix} \tag{24}$$

is positive definite.

Having established the above property, it seems that the modeling of uncertainty of the ROM level for nonlinear geometric structure is now well defined. Specifically [10],

(1) from a finite element model of the structure, identify the parameters $K^{(1)}_{ij}$, $\overline{K}^{(2)}_{ijl}$ and $\overline{K}^{(3)}_{ijlp}$
(2) determine the coefficients $K^{(2)}_{ijl}$ and $K^{(3)}_{ijlp}$ by "inverting" the Eqs. (6a) and (6b) with Eq. (7)
(3) determine the coefficients $\hat{K}^{(2)}_{mnp}$ from Eq. (19)
(4) form the matrices $\widetilde{\boldsymbol{K}}^{(2)}$ and $\widetilde{\boldsymbol{K}}^{(3)}$ from Eqs. (22) and (23), then $\overline{\boldsymbol{K}}_B$ from Eq. (24)
(5) set $\overline{\boldsymbol{A}} = \overline{\boldsymbol{K}}_B$ and follow Eqs. (14)–(16) and Fig. 1 to generate random samples of the matrix $\boldsymbol{A} = \boldsymbol{K}_B$
(6) proceed with steps (4), (3), (2) and (1) in reverse with each sample of $\boldsymbol{K}_B$ to obtain realizations of the uncertain linear, quadratic, and cubic stiffnesses $K^{(1)}_{ij}$, $\overline{K}^{(2)}_{ijl}$ and $\overline{K}^{(3)}_{ijlp}$ denoted as $\breve{K}^{(1)}_{ij}$, $\breve{K}^{(2)}_{ijl}$ and $\breve{K}^{(3)}_{ijlp}$ from which the samples of the uncertain response can be determined.

4. The challenges

The process defined by steps (1)–(6) above seems well characterized but after a closer inspection and trials, two key challenges were encountered:

(I) the determination of the parameters $\hat{K}^{(2)}_{mnp}$ and $K^{(3)}_{ijlp}$ cannot be uniquely performed from Eqs. (6a), (6b), (7), and (19) as there are more unknowns than equations.
(II) when the above determination can be carried out, the resulting mean model matrix $\overline{\boldsymbol{K}}_B$ may not be positive definite when the ROM parameters $K^{(1)}_{ij}$, $\overline{K}^{(2)}_{ijl}$ and $\overline{K}^{(3)}_{ijlp}$ are identified from some finite element codes, e.g., from Nastran.

The positive definiteness of $\overline{\boldsymbol{K}}_B$ stems, see [10], from the positive definiteness of the potential energy in the structure, it is thus an essential property and its violation may lead to unphysical behavior.

An example of this situation has been encountered with a flat cantilevered beam, see [11] and details below, for which a 2-basis function model was derived. The first of these basis function was selected as the first linear mode of the beam and the second as its associated dual (see definition/discussion in [3,5,12]) which exhibits only inplane motions. Performing the identification of this model nonintrusively from a Nastran finite element model using the approaches of [4,5] led to stiffness parameters that were very robust with respect to the identification details. Among these parameters, it was found that $\overline{K}^{(3)}_{1122}$ was rather large and negative [12]. However, from Eqs. (6b) and (7) this parameter should equal $K^{(3)}_{1122}+2K^{(3)}_{1212}$ where $K^{(3)}_{1212}$ must be positive (it is a diagonal term of $\overline{\boldsymbol{K}}_B$) and $K^{(3)}_{1122}$ should be positive according to Eq. (21). Interestingly, the parameter $\overline{K}^{(3)}_{1122}$ identified using the finite element formulation of [13] is positive.

This example clearly demonstrates that there may be an inconsistency between the expressions of Eqs. (6), (7), (18)–(21) and the ROM parameters identified from the finite element software that may affect the positive definiteness of $\overline{\boldsymbol{K}}_B$ but can also have significant implications regarding the accuracy of the ROM. For example, shown in Fig. 2 are the modal force along mode 1 vs. tip displacement predictions from Nastran and two identified ROMs for the cantilevered beam subjected to a uniform transverse load along its span. The Nastran nonlinear static predictions (from SOL 106) show an almost perfectly linear relation. However, the ROM identified from this software, with the negative $\overline{K}^{(3)}_{1122}$ exhibits an unphysical behavior: there exists a peak of the force at a certain displacement level and thus, for sufficiently large load down, the tip of the beam is predicted to move up! This situation does not happen with the nonlinear finite element code Bobtran implementing the formulation of [13] and for which $\overline{K}^{(3)}_{1122}$ is slightly positive. Those prediction lead to a slight stiffening of the beam in the load range considered.

5. Resolution of the challenges

5.1. Overall perspective

The two challenges (I) and (II) above were addressed jointly as follows.

(a) Stiffness parameters for which the "inversion" of Eqs. (6a), (6b), (7), and (19) could not be accomplished uniquely were optimized to render the matrix $\overline{\boldsymbol{K}}_B$ as positive definite as possible.
(b) If the resulting matrix $\overline{\boldsymbol{K}}_B$ was not positive definite, its "least important" elements were modified as little as possible to make it positive definite. After the matrix $\overline{\boldsymbol{K}}_B$ has been modified, the modified mean model predictions were determined and compared with the ones resulting from the originally identified parameters. The modified matrix $\overline{\boldsymbol{K}}_B$ was accepted if the difference in predictions was found small enough. The introduction of uncertainty then followed as in Eqs. (14)–(16) and Fig. 1.

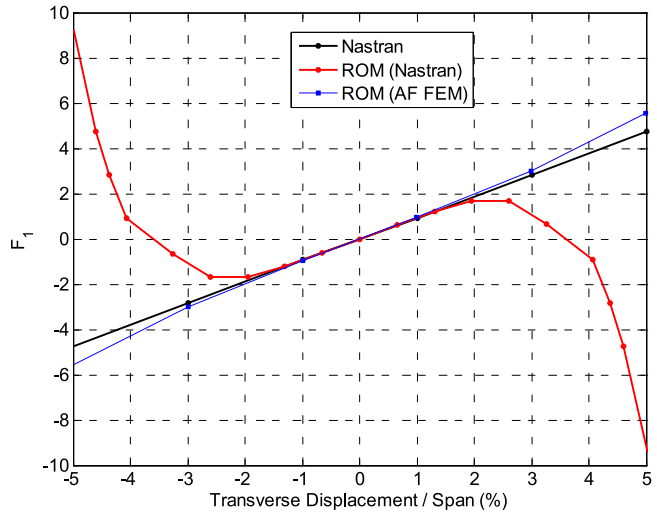

Fig. 2. Modal force along mode 1 vs. tip transverse displacement for a flat cantilevered beam. Results from Nastran nonlinear static (SOL 106), the ROM identified from the Nastran model ("ROM(Nastran)") and from the Air Force code Bobtran ("ROM(AF FEM)") implementing [13].

(c) If the predictions obtained from the modified mean model differed too significantly from those obtained with the originally identified parameters, a modified simulation approach was defined that relies on the $\overline{\boldsymbol{K}}_B$ matrix resulting from step (a) above.

5.2. Optimized decomposition

The first step, (a), of the above process focused on the extraction of the parameters $\hat{K}^{(2)}_{ijl}$ and $K^{(3)}_{ijlp}$ from the identified ones $\overline{K}^{(2)}_{ijl}$ and $\overline{K}^{(3)}_{ijlp}$ *as to render the matrix* $\overline{\boldsymbol{K}}_B$ *as positive definite as possible.*

Consider first the parameters for which all indices are equal, i.e., $\hat{K}^{(2)}_{iii}$ and $K^{(3)}_{iiii}$. For these, no indeterminacy exists and

$$\hat{K}^{(2)}_{iii} = \frac{2}{3}\overline{K}^{(2)}_{iii} \quad \text{and} \quad K^{(3)}_{iiii} = \overline{K}^{(3)}_{iiii}. \tag{25}$$

For coefficients depending on two mode indices i and $j > i$, the indeterminacy exists as there are 4 new quadratic coefficients, $\hat{K}^{(2)}_{ijj}$, $\hat{K}^{(2)}_{iij}$, $\hat{K}^{(2)}_{jij}$, $\hat{K}^{(2)}_{jii}$, and 4 new cubic ones, $K^{(3)}_{iiij}$, $K^{(3)}_{ijjj}$, $K^{(3)}_{ijij}$, $K^{(3)}_{ijij}$, considering the symmetry of Eq. (7) as well as the property $\hat{K}^{(2)}_{ijl} = \hat{K}^{(2)}_{ilj}$ resulting from Eq. (19). There are however only 5 independent equations relating them:

$$\overline{K}^{(2)}_{iij} = 2\hat{K}^{(2)}_{iij} + \hat{K}^{(2)}_{jii} \quad \text{and} \quad \overline{K}^{(2)}_{ijj} = \frac{1}{2}\hat{K}^{(2)}_{ijj} + \hat{K}^{(2)}_{jij}$$

$$\overline{K}^{(3)}_{iiij} = 3K^{(3)}_{iiij} \qquad \overline{K}^{(3)}_{iijj} = K^{(3)}_{iijj} + 2K^{(3)}_{ijij} \quad \text{and} \quad \overline{K}^{(3)}_{ijjj} = K^{(3)}_{ijjj}. \tag{26}$$

To resolve the indeterminacy, it is desired that the matrix $\overline{\boldsymbol{K}}_B$ be made as positive definite as possible given the constraints of Eqs. (26). Since the split of say $\overline{K}^{(2)}_{iij}$ into $\hat{K}^{(2)}_{iij}$ and $\hat{K}^{(2)}_{jii}$ should not be dependent on the coefficients of other modes than i and j, it is more specifically imposed that *the unknown coefficients maximize the lowest eigenvalue of* $\overline{\boldsymbol{K}}^{(2)}_{B,ij}$ which is the 6×6 $\overline{\boldsymbol{K}}_B$ matrix built using the coefficients relevant to modes i and j only. This optimization is performed for all distinct combinations of i and $j > i$ modes which then leads to all parameters $\hat{K}^{(2)}_{ijl}$ and $K^{(3)}_{ijlp}$ with 2 different indices.

For the coefficients involving 3 different indices, i, $j > i$ and $k > j$, a similar effort is carried out: 3 new quadratic coefficients related by 1 independent equation, and 2 new cubic ones related by 1 independent equation and the indeterminacy is resolved by maximizing the lowest eigenvalue of $\overline{\boldsymbol{K}}^{(3)}_{B,ijk}$ which is the 12×12 $\overline{\boldsymbol{K}}_B$ matrix built using the coefficients relevant to modes i, j, and k only. This effort is then repeated for all distinct combinations of $k > j > i$ modes which then leads to all parameters $\hat{K}^{(2)}_{ijl}$ and $K^{(3)}_{ijlp}$ with 3 different indices.

It remains to address the determination of the parameters $K^{(3)}_{ijlp}$ with all 4 indices different. For each set of the 4 indices, there are only 3 such distinct parameters taking into account Eq. (7), i.e., $K^{(3)}_{ijlp}$, $K^{(3)}_{iljp}$, $K^{(3)}_{ipjl}$ assuming $p > l > j > i$ but only 1 independent equation

$$\overline{K}^{(3)}_{ijlp} = 2K^{(3)}_{ijlp} + 2K^{(3)}_{iljp} + 2K^{(3)}_{ipjl}. \tag{27}$$

As before, the indeterminacy is resolved by maximizing the lowest eigenvalue of $\overline{\boldsymbol{K}}^{(4)}_{B,ijlp}$ which is the 20×20 $\overline{\boldsymbol{K}}_B$ matrix built using the coefficients relevant to modes i, j, l and p only. This effort is then repeated for all distinct combinations of $p > l > j > i$ modes to yield the remaining cubic parameters $K^{(3)}_{ijlp}$.

5.3. Rendering $\overline{\boldsymbol{K}}_B$ positive definite

After the series of optimization efforts carried out in the previous section, the resulting matrix $\overline{\boldsymbol{K}}_B$ may be positive definite in which case the uncertainty modeling can proceed as in Eqs. (14)–(16) and Fig. 1. If this matrix is not positive definite, it will be modified in this second step to become positive definite. This modification will be accomplished:

(a) without affecting the part of $\overline{\boldsymbol{K}}_B$ that is positive definite, e.g., the linear stiffness matrix $\boldsymbol{K}^{(1)}$, and

(b) inducing the smallest changes possible to this matrix.

The task (a) has been achieved iteratively by constructing the biggest block of the original matrix $\overline{\boldsymbol{K}}_B$ that is positive definite. This block is at least of size N since the linear stiffness matrix $\boldsymbol{K}^{(1)}$ is positive definite. Accordingly, the top left block of $\overline{\boldsymbol{K}}_B$ of size $N+1$ is first considered and it is checked for positive definiteness (e.g., by constructing its Cholesky decomposition). If it is positive definite, the algorithm moves to the top left block of size $N+2$ and the process is repeated.

Otherwise, a permutation of the rows and columns $N+1$ and $N+2$ is performed. If the top left block of size $N+1$ is now positive definite, the algorithm accepts the permutation and moves forward to the top left block of size $N+2$. On the contrary, the permutation between rows $N+1$ and $N+2$ is reversed and a permutation of rows $N+1$ and $N+3$ is performed followed by a positive definiteness check. This process concludes when no permutation of rows and columns achieves an increase in the size of the top left block of $\overline{\boldsymbol{K}}_B$ which is positive definite.

At that point, the matrix $\overline{\boldsymbol{K}}_B$ has been transformed in a symmetric matrix $\tilde{\boldsymbol{K}}_B$ which has the form

$$\tilde{\boldsymbol{K}}_B = \begin{bmatrix} \boldsymbol{K}_{11} & \boldsymbol{K}_{12} \\ \boldsymbol{K}_{12}^T & \boldsymbol{K}_{22} \end{bmatrix} \tag{28}$$

where $\boldsymbol{K}_{11}$ is positive definite and of size $N_p \times N_p$, $\boldsymbol{K}_{12}$ is of size $N_p \times N_r$, and $\boldsymbol{K}_{22}$ is of size $N_r \times N_r$ where $N_r = N^2 + N - N_p$.

The task (b) above then proceeds with replacing the matrix $\tilde{\boldsymbol{K}}_B$ by

$$\hat{\boldsymbol{K}}_B = \begin{bmatrix} \boldsymbol{K}_{11} & \boldsymbol{K}_{12} \\ \boldsymbol{K}_{12}^T & \boldsymbol{K}_{22} \end{bmatrix} + \begin{bmatrix} 0 & \boldsymbol{\Delta}_1 \\ \boldsymbol{\Delta}_1^T & \boldsymbol{\Delta}_2 \end{bmatrix} = \tilde{\boldsymbol{K}}_B + \boldsymbol{\Delta} \tag{29}$$

where the matrix $\boldsymbol{\Delta}$ will be selected to have the minimum Frobenius norm under the constraint that $\hat{\boldsymbol{K}}_B$ is at least positive semidefinite. The solution of this nonlinear optimization problem will be obtained iteratively through a sequence of linear optimization problems in which the positive definiteness constraint is enforced linearly. To this end, note that a symmetric perturbation $\boldsymbol{\delta A}$ of a symmetric matrix $\boldsymbol{A}$ leads to a first order perturbation of any of its non repeated eigenvalues λ by [14]

$$\delta\lambda = \boldsymbol{\psi}^T \boldsymbol{\delta A} \boldsymbol{\psi} \tag{30}$$

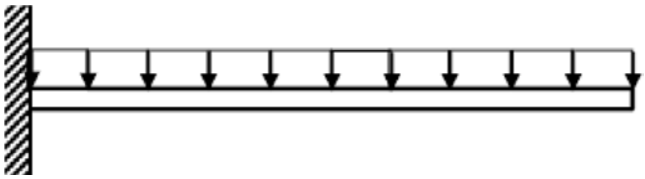

Fig. 3. Cantilevered straight beam with uniform loading.

where $\boldsymbol{\psi}$ is the normalized, $\boldsymbol{\psi}^T\boldsymbol{\psi} = 1$, eigenvector of $\boldsymbol{A}$ corresponding to the eigenvalue λ. Then, assuming that $\boldsymbol{\Delta}$ is small enough for Eq. (30) to apply, the eigenvalues $\hat{\lambda}_i$ of $\hat{\boldsymbol{K}}_B$ can be expressed as

$$\hat{\lambda}_i = \tilde{\lambda}_i + \tilde{\boldsymbol{\psi}}_i^T \boldsymbol{\Delta}\, \tilde{\boldsymbol{\psi}}_i \tag{31}$$

where $\tilde{\lambda}_i$ and $\tilde{\boldsymbol{\psi}}_i$ are the eigenvalues and corresponding normalized eigenvectors of $\tilde{\boldsymbol{K}}_B$. Then, the positive semidefinite requirement can be approximately written as

$$\tilde{\boldsymbol{\psi}}_i^T \boldsymbol{\Delta}\, \tilde{\boldsymbol{\psi}}_i \geq -\tilde{\lambda}_i \text{ for all } i \text{ such that } \tilde{\lambda}_i \leq 0. \tag{32}$$

Adopting these linearized constraints, the determination of $\boldsymbol{\Delta}$ can be rewritten as the minimization of

$$\|\boldsymbol{\Delta}\|_F^2 - 2 \sum_{\tilde{\lambda}_i<0} \mu_i \left[\tilde{\boldsymbol{\psi}}_i^T \boldsymbol{\Delta}\, \tilde{\boldsymbol{\psi}}_i + \tilde{\lambda}_i\right] \tag{33}$$

where $\|\cdot\|_F$ denotes the Frobenius norm and μ_i are the Lagrange multiplier associated to the equality constraints of Eq. (32).

Differentiating the objective function of Eq. (33) yields the linear system of equations

$$\boldsymbol{\Delta}_1 = \sum_{\tilde{\lambda}_i<0} \mu_i\, \tilde{\boldsymbol{\psi}}_i^{(1)} \left[\tilde{\boldsymbol{\psi}}_i^{(2)}\right]^T \tag{34}$$

and

$$\boldsymbol{\Delta}_2 = \sum_{\tilde{\lambda}_i<0} \mu_i\, \tilde{\boldsymbol{\psi}}_i^{(2)} \left[\tilde{\boldsymbol{\psi}}_i^{(2)}\right]^T \tag{35}$$

where the eigenvectors $\tilde{\boldsymbol{\psi}}_i$ are partitioned into vectors $\tilde{\boldsymbol{\psi}}_i^{(1)}$ and $\tilde{\boldsymbol{\psi}}_i^{(2)}$ of N_p and N_r components, respectively. That is, $\tilde{\boldsymbol{\psi}}_i^T = \left[\left[\tilde{\boldsymbol{\psi}}_i^{(1)}\right]^T \left[\tilde{\boldsymbol{\psi}}_i^{(2)}\right]^T\right]$. Finally, the constraints of Eq. (32) yield

$$\sum_{\tilde{\lambda}_r<0} \left(2a_{ri}\, b_{ri} + b_{ri}^2\right) \mu_r = -\tilde{\lambda}_i \text{ with } a_{rs} = \left[\tilde{\boldsymbol{\psi}}_r^{(1)}\right]^T \tilde{\boldsymbol{\psi}}_s^{(1)} \text{ and } b_{rs} = \left[\tilde{\boldsymbol{\psi}}_r^{(2)}\right]^T \tilde{\boldsymbol{\psi}}_s^{(2)} \tag{36}$$

Solving the linear system of Eqs. (36) yields the values of the Lagrange multipliers μ_i which can then be reintroduced in Eqs. (34) and (35) to yield the unknown partitions $\boldsymbol{\Delta}_1$ and $\boldsymbol{\Delta}_2$ of $\boldsymbol{\Delta}$.

The resulting matrix $\hat{\boldsymbol{K}}_B$ will then in general not be positive definite but the process can be repeated with a new $\tilde{\boldsymbol{K}}_B = \hat{\boldsymbol{K}}_B$ until a matrix $\hat{\boldsymbol{K}}_B$ positive definite/semidefinite is finally obtained. At that point, the rows/columns permutations performed to obtain the largest block positive definite are reversed leading to a matrix $\boldsymbol{K}'_B$ which is positive definite and thus could serve as the basis for the uncertainty modeling according to Eqs. (14)–(16) and Fig. 1.

It remains however to assess if rendering the matrix positive definite has changed "significantly" the mean model to the point that the uncertainty analysis may not be relevant to the original mean model. To this end, the quadratic and cubic stiffness coefficients $\hat{K}'^{(2)}_{ijl}$ and $K'^{(3)}_{ijlp}$ are extracted from $\boldsymbol{K}'_B$ and used, with the linear coefficients $K^{(1)}_{ij}$, which have not been modified by the modification of the matrix $\tilde{\boldsymbol{K}}_B$, to compute a set of representative responses of this modified mean model. These responses can then be compared with those from the identified model to assess whether the matrix $\boldsymbol{K}'_B$ is appropriate to carry out the uncertainty analysis.

5.4. $\overline{\boldsymbol{K}}_B$ cannot be made positive definite without affecting the model

For most of the structural models investigated so far, see the application section for details, the procedure described in the previous section yielded a matrix $\boldsymbol{K}'_B$ that closely represents the originally identified mean model and thus can be used to carry out the uncertainty analysis. When this is not the case, however, it is proposed here to modify the modeling approach of Eqs. (14) and (15) using a $L\,D\,L^T$ decomposition [15] in place of the Cholesky one so that it can be applied to the matrix $\overline{\boldsymbol{K}}_B$ resulting from the optimized decomposition. Specifically, this matrix is first rewritten as

$$\overline{\boldsymbol{K}}_B = \overline{\boldsymbol{L}}_{\boldsymbol{K}}\, \boldsymbol{D}\, \overline{\boldsymbol{L}}_{\boldsymbol{K}}^T \tag{37}$$

then, the uncertain matrices are obtained as

$$\boldsymbol{K}_B = \overline{\boldsymbol{L}}_{\boldsymbol{K}}\, \boldsymbol{H}\, \boldsymbol{D}\, \boldsymbol{H}^T \overline{\boldsymbol{L}}_{\boldsymbol{K}}^T \tag{38}$$

where $\boldsymbol{H}$ is the same matrix as in Eq. (14) and Fig. 1. Note in Eq. (37) that the diagonal matrix $\boldsymbol{D}$ will be selected to only carry a sign, i.e., its elements are either +1 or −1 only.

5.5. Uncertainty modeling of the largest positive block only

An alternative to the modifications of Sections 5.3 and 5.4 is to proceed with the modeling of uncertainty only on the largest part of the model that is consistent with the theory of Eqs. (18)–(24) leaving the rest of it equal to the mean model. That is, uncertainty is introduced on the positive definite block $\boldsymbol{K}_{11}$ of Eq. (28) while leaving the corresponding matrices $\boldsymbol{K}_{12}$ and $\boldsymbol{K}_{22}$ unchanged, equal to their

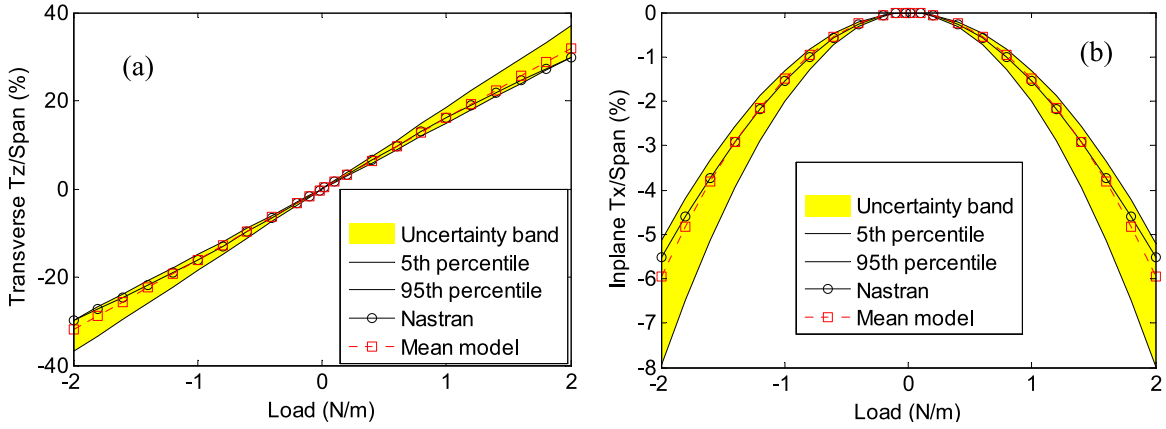

Fig. 4. Static displacement of the cantilevered straight beam tip under a uniform loading. (a) Transverse and (b) inplane displacements (percent of span) vs. load. Mean and uncertain models.

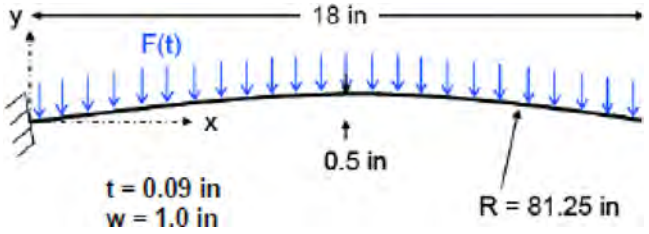

Fig. 5. Cantilevered curved beam with uniform loading.

values resulting for example from the optimization of Eqs. (29)–(36) or as the initial conditions of this process. When the eigenvalues of the matrices $\tilde{\boldsymbol{K}}_B$ and $\hat{\boldsymbol{K}}_B$ differ from those of $\boldsymbol{K}_{11}$ only mostly by the addition of small, positive or negative, eigenvalues, this process could be viewed as similar to the approach of [9] in focusing the uncertainty on the dominant component of the model only.

6. Applications

The above developments were applied to a series of structures for which mean NLROM were obtained in prior investigations. While all of these applications focus on static responses, uncertain dynamic responses could be computed with the same set of uncertain stiffness coefficients as those used for the static problems.

The first example considered is the cantilevered straight beam of Fig. 3 discussed earlier, see Fig. 2, in the context of the positive definiteness of $\overline{\boldsymbol{K}}_B$ and the existence of inconsistencies between the stiffness coefficients obtained from commercial finite element software (Nastran here) and Eqs. (18)–(21). The mean model selected here includes 8 basis functions — the first 4 linear modes and 4 duals as constructed in [16]. The matrix $\overline{\boldsymbol{K}}_B$ obtained after the optimized decomposition was not positive definite. The application of the procedure of Eqs. (28)–(36) did render it positive definite and the predictions obtained from that modified mean model were found to be very close to those from the originally identified model. The uncertainty analysis was then performed using Eqs. (14) and (15) with an overall uncertainty level selected to be $\delta = 0.30$ and shown in Fig. 4 are the transverse and inplane displacements at the tip vs. load level for the mean model as well as 5th–95th percentile uncertainty band.

The process was next repeated with the curved cantilevered beam of Fig. 5 the response of which was modeled using 9 basis functions — the first 3 linear modes and 6 duals. As for the straight cantilevered beam, the matrix $\overline{\boldsymbol{K}}_B$ obtained after the optimized decomposition was not positive definite. Again, the application of the procedure of Eqs. (28)–(36) did render it positive definite and the predictions obtained from that modified mean model were found to be very close to those from the originally identified model. The uncertainty analysis was then performed using Eqs. (14) and (15) with an overall uncertainty level selected to be $\delta = 0.15$ and shown in Fig. 6 are the transverse (vertical) and inplane (horizontal) displacements at the tip vs. load level for the mean model as well as 5th–95th percentile uncertainty band. Comparing these results with those of Fig. 4, it is concluded that the response of the curved beam is much less sensitive to uncertainty than its straight counterpart.

The above process was also repeated for the orthogrid panel of Fig. 7 [17] modeled using 17 basis functions — the first 8 linear modes and 9 duals. The uncertainty analysis was carried out as for the two previous examples with a value $\delta = 0.31$. Then, shown in Fig. 8 are the displacements at a quarter point along the three directions for the mean and uncertain models. It is interesting to observe that the inplane displacements are much more sensitive to the uncertainty than the transverse ones.

The application of the above concepts was also performed on the clamped-clamped curved beam of Fig. 9 in a range of displacements

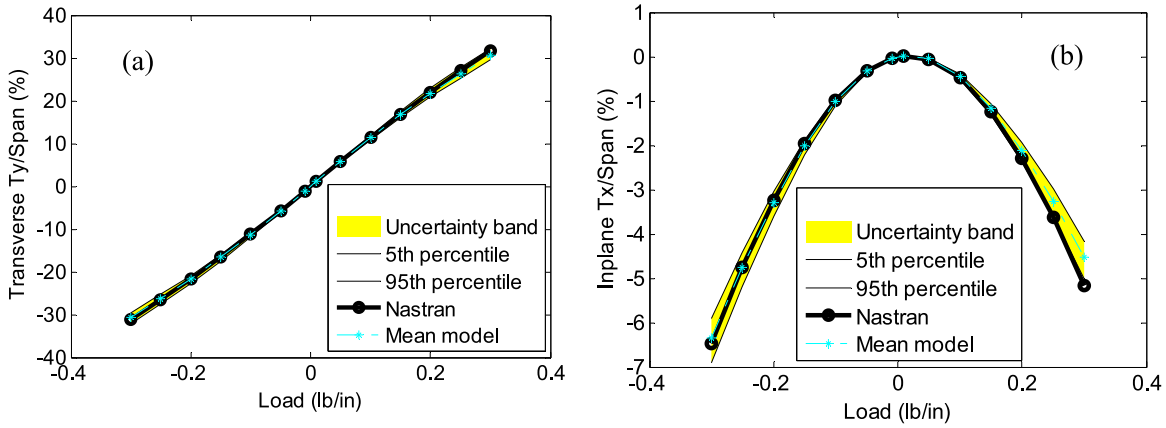

Fig. 6. Static displacement of the cantilevered curved beam tip under uniform loading. (a) Transverse and (b) inplane displacements (percent of span) vs. load. Mean and uncertain models.

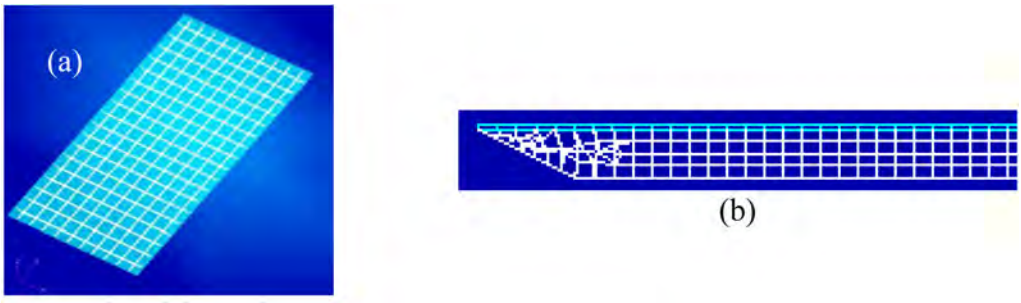

Fig. 7. Orthogrid panel considered in [16] (a) Perspective view and (b) cross-section.

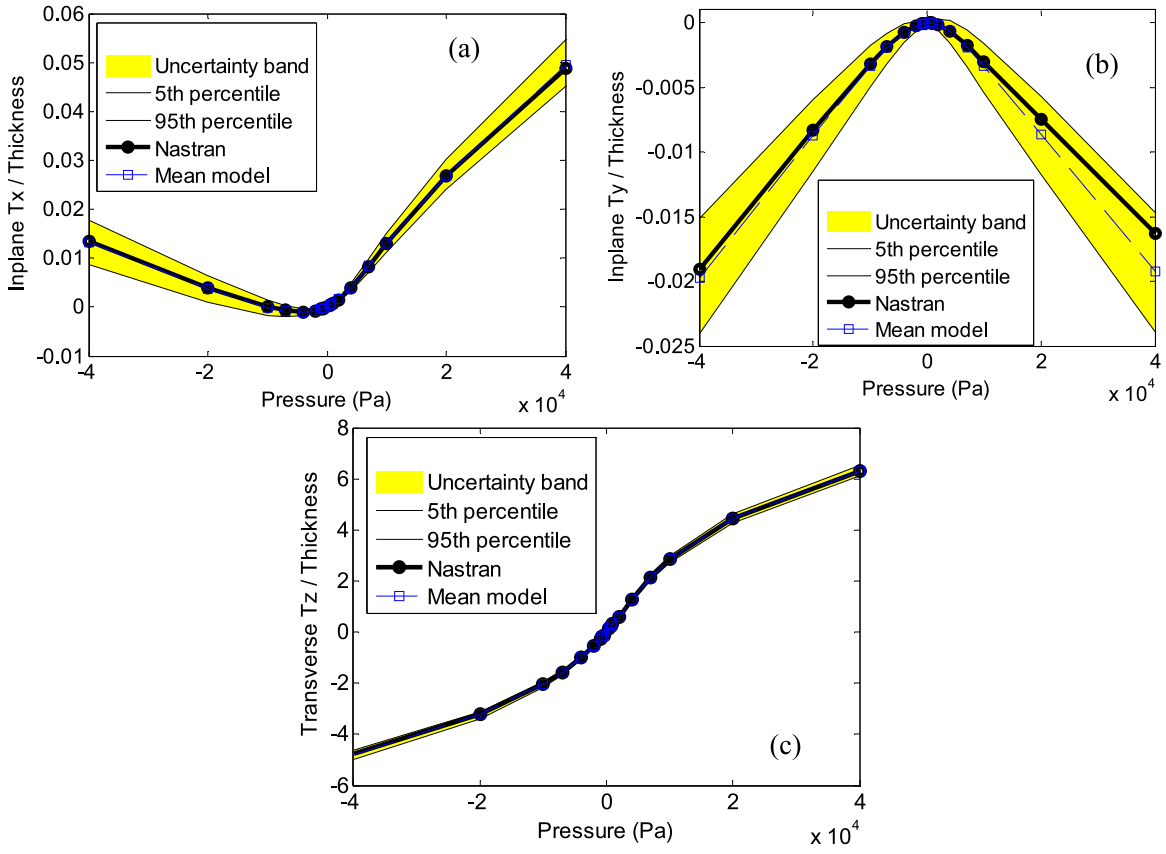

Fig. 8. Static displacement of the orthogrid panel under a uniform loading. (a) Inplane x, (b) inplane y, and (c) transverse z displacements at a quarter point divided by the panel thickness vs. load. Mean and uncertain models.

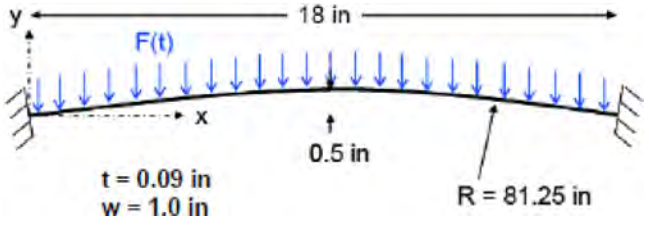

Fig. 9. Clamped-clamped curved beam with uniform loading.

that includes its snap-through. Proceeding as before, the matrix $\overline{\boldsymbol{K}}_B$ obtained after the optimized decomposition was not positive definite but the application of the procedure of Eqs. (28)–(36) did render it positive definite. However, the predictions obtained from that modified mean model were found to be too different from those from the originally identified model, in particular that modified model did not snap through as predicted by either the original NLROM or the finite element model. In this light, the revised uncertainty modeling of Eqs. (37) and (38) was applied with $\delta = 0.026$. Then, shown in Fig. 10 are the transverse (vertical) and inplane (horizontal) displacements at a beam quarter point vs. load level for the mean model as well as 5th–95th percentile uncertainty band. As already observed in connection with the two previous examples, the inplane response of the curved beam

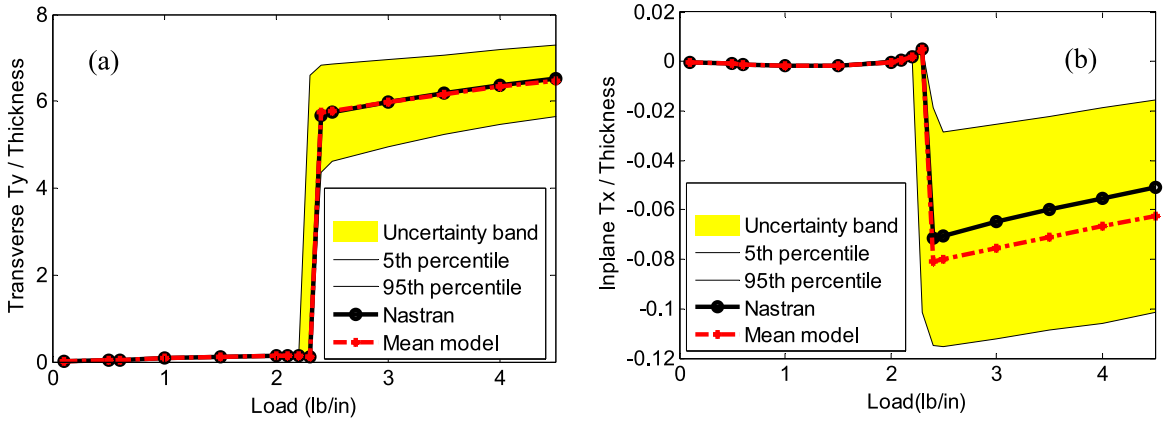

Fig. 10. Static displacement of the clamped-clamped curved beam under a uniform loading. (a) Transverse and (b) inplane displacements (in percent of span) of a beam quarter point vs. load. Mean and uncertain models.

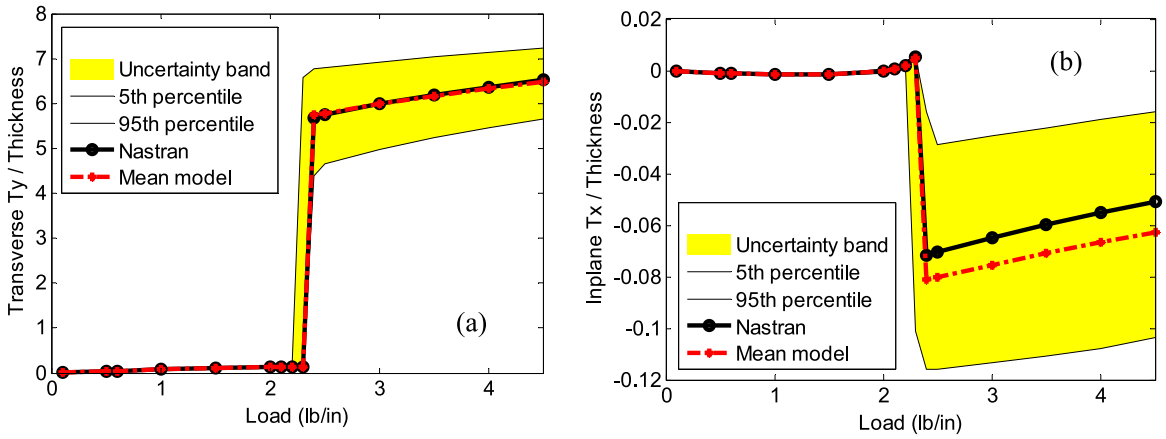

Fig. 11. Static displacement of the clamped-clamped curved beam under a uniform loading. (a) Transverse and (b) inplane displacements (in percent of span) of a beam quarter point vs. load. Mean and uncertain models, approach of Section 5.5.

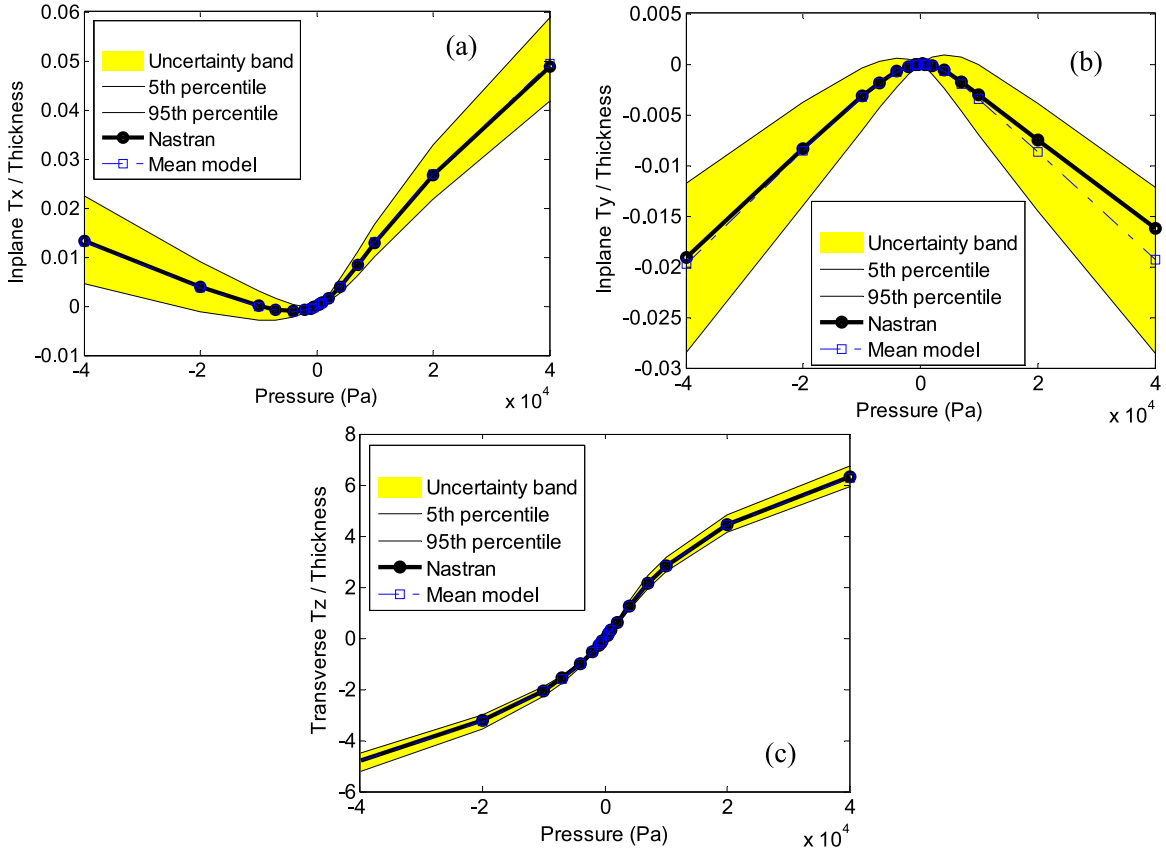

Fig. 12. Static displacement of the orthogrid panel under a uniform loading. (a) Inplane x, (b) inplane y, and (c) transverse z displacements at a quarter point divided by the panel thickness vs. load. Mean and uncertain models, approach of Section 5.5.

appears more sensitive to uncertainty than its transverse counterpart. Note as well the large increase in the uncertainty band post snap through, in both directions, with much smaller variations of the snap through load which are nevertheless much larger than the variability of the response prior to snap through.

The above results were all obtained using the modifications of Sections 5.3 and 5.4 but an assessment of the approach of Section 5.5, i.e., the uncertainty modeling of the matrix $\boldsymbol{K}_{11}$ of Eq. (28), was also performed for the clamped-clamped curved beam of Fig. 9, see Fig. 11 with the same value of $\delta = 0.026$ as in Fig. 10. The strong similarity of the uncertainty bands shown in Figs. 10 and 11 suggests that the introduction of uncertainty on the largest positive definite block $\boldsymbol{K}_{11}$ is an appropriate strategy that is additionally simpler. Another validation was performed on the orthogrid panel of Fig. 7, see Fig. 12 for the results corresponding to $\delta = 0.28$. While the uncertainty band is visibly wider than in Fig. 8, it exhibits the same features again supporting the applicability of the approach of Section 5.5.

7. Summary

The focus of the present investigation was on resolving two key challenges encountered in the introduction of uncertainty in reduced order

models of the nonlinear geometric response following an approach proposed earlier by the authors. The first of these challenges was the indeterminacy of the mapping of the nonlinear stiffness coefficients identified from the finite element model, $\overline{K}^{(2)}_{ijl}$ and $\overline{K}^{(3)}_{ijlp}$, to those suitable for the uncertainty analysis, i.e., $\hat{K}^{(2)}_{mnp}$ and $K^{(3)}_{ijlp}$, see Eqs. (6), (7), and (19). The second challenge was that the matrix $\overline{\boldsymbol{K}}_B$ constructed with these coefficients (and the linear stiffness ones) is not positive definite as showed in the original paper because of differences in nonlinear finite element modeling between the commercial software and the theoretical developments. These challenges were jointly addressed. First, the indeterminacy was resolved by selecting the coefficients to maximize $\overline{\boldsymbol{K}}_B$ while satisfying the constraints of Eqs. (6), (7), and (19). In general, the resulting matrix $\overline{\boldsymbol{K}}_B$ was found not positive definite but a strategy was devised to modify it in a minimal manner to achieve this property. In most of the cases investigated, this modification did not significantly change the predictions of the mean response and thus the uncertainty modeling could proceed from it. In one example, a clamped-clamped curved beam undergoing snap throughs, the changes of mean were large enough. For such situations, a modification of the uncertainty modeling was proposed that handles the non positive definite matrix $\overline{\boldsymbol{K}}_B$ with a $\boldsymbol{LDL^T}$ decomposition vs. a Cholesky one. A final alternative to the above modifications was also proposed in which the uncertainty is only introduced on the largest block of the $\overline{\boldsymbol{K}}_B$ that is positive definite.

The above methods were applied to 4 different structural models of various complexity and the uncertain response to static loading was determined. These efforts first demonstrated the broad applicability of the above methodology but they also suggested that strong nonlinear features of the response, such as inplane displacements due to transverse loading and post-snap through behavior, are particularly sensitive to uncertainty.

Acknowledgments

The financial support of this investigation by the Air Force Office of Scientific Research, USA grant FA9550-16-1-0021 with Dr. Jaimie Tiley as monitor is gratefully acknowledged. The authors wish to thank the Structural Science Center and specifically Drs R. Gordon and J.J. Hollkamp for the use of the code Bobtran which was used for some of the results in Fig. 2.

References

[1] C. Soize, Stochastic models of uncertainties in computational mechanics, Amer. Soc. Civ. Eng. (2012).
[2] C. Soize, Uncertainty Quantification: An Accelerated Course with Advanced Applications in Computational Engineering, Springer-Verlag, 2017.
[3] M.P. Mignolet, A. Przekop, S.A. Rizzi, S.M. Spottswood, A review of indirect/non-intrusive reduced order modeling of nonlinear geometric structures, J. Sound Vib. 332 (2013) 2437–2460.
[4] A.A. Muravyov, S.A. Rizzi, Determination of nonlinear stiffness with application to random vibration of geometrically nonlinear structures, Comput. Struct. 81 (2003) 1513–1523.
[5] R.A. Perez, X.Q. Wang, M.P. Mignolet, Non-intrusive structural dynamic reduced order modeling for large deformations: Enhancements for complex structures, J. Comput. Nonlinear Dyn. 9 (2014) 031008.
[6] E. Capiez-Lernout, C. Soize, M.P. Mignolet, Post-buckling nonlinear static and dynamical analyses of uncertain cylindrical shells and experimental validation, Comput. Methods Appl. Mech. Engrg. 271 (2014) 210–230.
[7] E. Capiez-Lernout, C. Soize, M.P. Mignolet, Computational stochastic statics of an uncertain curved structure with geometrical nonlinearity in three-dimensional elasticity, Comput. Mech. 49 (2012) 87–97.
[8] E. Capiez-Lernout, C. Soize, Uncertainty quantification for an industrial mistuned bladed disk with geometrical nonlinearities, in: Proceeding of the ASME Turbo Expo 2015, Montreal, Quebec, Canada, June 15–19. Paper No. GT2015-42471, 2015.
[9] E. Capiez-Lernout, C. Soize, An improvement of the uncertainty quantification in computational structural dynamics with nonlinear geometrical effects, Int. J. Uncertain. Quantif. 7 (2017) 83–98.
[10] M.P. Mignolet, C. Soize, Stochastic reduced order models for uncertain geometrically nonlinear dynamical systems, Comput. Methods Appl. Mech. Engrg. 197 (2008) 3951–3963.
[11] X.Q. Wang, R. Perez, M.P. Mignolet, R. Capillon, C. Soize, Nonlinear reduced order modeling of complex wing models, in: Proceedings of the 54th Structures, Structural Dynamics and Materials Conference, Boston, Massachusetts, Apr. 8-11, AIAA Paper AIAA-2013-1520, 2013.
[12] K. Kim, A.G. Radu, X.Q. Wang, M.P. Mignolet, Nonlinear reduced order modeling of isotropic and functionally graded plates, Int. J. Non-Linear Mech. 49 (2013) 100–110.
[13] P.C. Dumir, A. Bhaskar, Some erroneous finite element formulations of non-linear vibrations of beams and plates, J. Sound Vib. 123 (3) (1988) 517–527.
[14] H. Morse, P.M. Feshbach, Methods of Theoretical Physics, McGraw-Hill, 1953.
[15] G.H. Golub, C.F. van Loan, Matrix Computations, third ed., Johns Hopkins University Press, 1996.
[16] K. Kim, V. Khanna, X.Q. Wang, M.P. Mignolet, Nonlinear reduced order modeling of flat cantilevered structures, in: Proceedings of the 50th Structures, Structural Dynamics, and Materials Conference, AIAA Paper AIAA-2009-2492, Palm Springs, California, 2009.
[17] A. Gogulapati, K. Brouwer, X.Q. Wang, R. Murthy, J.J. MacNamara, M.P. Mignolet, Full and reduced order aerothermoelastic modeling of built-up aerospace panels in high-speed flows, in: Proceedings of the 58th Structures, Structural Dynamics, and Materials Conference, AIAA Paper AIAA 2017-0180, AIAA SciTech, Grapevine, Texas, 2017.

Proceedings of the Eighth Conference on Computational Stochastic Mechanics
Paros, Greece, June 10--13, 2018

NONLINEAR GEOMETRIC MODELING OF UNCERTAIN STRUCTURES THROUGH NONINTRUSIVE REDUCED ORDER MODELING

X.Q. WANG[1], MARC P. MIGNOLET[1] and CHRISTIAN SOIZE[2]

[1] *SEMTE Faculties of Mechanical and Aerospace Engineering,*
Arizona State University, Tempe, AZ 85048, USA
E-mail: xiaoquan.wang.1@asu.edu, marc.mignolet@asu.edu
[2]*Laboratoire Modélisation et Simulation Multi Echelle,*
Université Paris-Est Marne-la-Vallée, 77454 Marne-la-Vallee, France
E-mail: christian.soize@u-pem.fr

The focus of the present investigation is on the introduction of uncertainty directly in reduced order models of the nonlinear geometric response of structures following maximum entropy concepts. While the approach was formulated and preliminary validated in an earlier paper, its broad application to a variety of structures based on their finite element models from commercial software was impeded by two key challenges. The first of these involves an indeterminacy in the mapping of the nonlinear stiffness coefficients identified from the finite element model to those of the reduced order model form that is suitable for the uncertainty analysis. The second challenge is that a key matrix in the uncertainty modeling was expected to be positive definite but was numerically observed not to be. This latter issue is shown here to be rooted in differences in nonlinear finite element modeling between the commercial software and the theoretical developments. Both of these challenges are successfully resolved and applications examples are presented that confirm the broad applicability of the methodology.

Keywords: Uncertainty modeling, maximum entropy, uncertain structure, nonlinear geometric structural response, reduced order modeling.

1 Introduction

Over the last two decades, maximum entropy concepts have been broadly and very successfully used to model uncertainties in structures directly at the level of reduced order models (ROMs) constructed from the finite element model of the mean structure, see Soize (2016, 2017) for reviews. In addition to its capability to account for some epistemic uncertainty, this approach is computationally much more expedient than its alternative, which is to first introduce uncertainty in the finite element model then construct a ROM for each sample of the random structure. The computational saving is particularly significant for large size linear finite element models but also for nonlinear geometric problems where the ROMs include a large number of linear, quadratic, and cubic stiffness coefficients, see Mignolet et al. (2013) for an overview. These coefficients must either be identified from a standard (e.g., commercial) finite element model using nonintrusive techniques (Mignolet et al. 2013, Muravyov and Rizzi 2003, Perez et al. 2014) or computed using a dedicated finite element formulation (Capiez-Lernout et al. 2012, 2014, Capiez-Lernout and Soize 2015, 2017) based on the reduced order modeling results of Mignolet and Soize (2008)]. The latter of these two approaches lends itself naturally to

the introduction of uncertainty at the ROM level using the maximum entropy concepts as originally discussed in Mignolet and Soize (2008). The application of this strategy to the ROMs identified nonintrusively (Mignolet et al. 2013, Muravyov and Rizzi 2003, Perez et al. 2014) from a commercial finite element code has been exemplified in Mignolet and Soize (2008) on a simple flat beam structure. More complex applications of this approach have been impeded by two key challenges, of decomposition and non-positive definiteness, in transforming the identified ROM into one that is suitable for the uncertainty analysis. The focus of the present investigation is on efficiently resolving these two challenges and applying them to a representative set of structures in the nonlinear geometric regimes.

2 Reduced Order Models of Nonlinear Geometric Structural Response

The reduced order models considered in the present study are based on a representation of the nonlinear geometric response of the structure in the form

$$\boldsymbol{u}(t) = \sum_{n=1}^{M} q_n(t)\, \boldsymbol{U}^{(n)} \tag{1}$$

where $\boldsymbol{u}(t)$ denotes the vector of displacements of the finite element degrees of freedom, $\boldsymbol{U}^{(n)}$ are basis functions (modes) of the ROM specified in the spatial domain of the finite element mesh, and $q_n(t)$ are the time dependent generalized coordinates.

To obtaining a set of nonlinear ordinary differential equations for the generalized coordinates $q_n(t)$, it is convenient to consider the continuum equivalent of Eq. (1), i.e.,

$$u_i(\boldsymbol{X},t) = \sum_{n=1}^{M} q_n(t)\, U_i^{(n)}(\boldsymbol{X}) \tag{2}$$

for i = 1, 2, 3, where $\boldsymbol{X}$ denotes an arbitrary point of the structure in its undeformed configuration. Then, introducing Eq. (2) in the equations of finite deformations elasticity and proceeding with a Galerkin approach provides the desired equations. This process was accomplished in Mignolet and Soize (2008) considering a Kirchhoff-Saint Venant type material in which the second Piola-Kirchhoff stress tensor S is linearly related to the Green strain tensor E by

$$S_{ij} = C_{ijkl}\, E_{kl} \tag{3}$$

where $\boldsymbol{C}$ denotes the deformation independent 4th order elasticity tensor. Under this material assumption, it was shown in Mignolet and Soize (2008) that the generalized coordinates $q_n(t)$ satisfy the equations

$$\begin{aligned} M_{ij}\, \ddot{q}_j + D_{ij}\, \dot{q}_j + K_{ij}^{(1)}\, q_j \\ + K_{ijl}^{(2)}\, q_j\, q_l + K_{ijlp}^{(3)}\, q_j\, q_l\, q_p = F_i \end{aligned} \tag{4}$$

where summation over repeated indices is implied. In the above equation, M_{ij} denote the elements of the mass matrix, $K_{ij}^{(1)}$, $K_{ijl}^{(2)}$, $K_{ijlp}^{(3)}$ are the linear, quadratic, and cubic stiffness coefficients and F_i are the modal forces. Note that a damping matrix $\boldsymbol{D}$ was also introduced in Eq. (4) to model dissipation.

Note in Eq. (4) that a series of terms involve the same monomials of the generalized coordinates, e.g. $K_{ijl}^{(2)}$ and $K_{ilj}^{(2)}$, and thus these terms may naturally be regrouped leading to

$$\begin{aligned} M_{ij}\, \ddot{q}_j + D_{ij}\, \dot{q}_j + K_{ij}^{(1)}\, q_j \\ + \bar{K}_{ijl}^{(2)}\, q_j\, q_l + \bar{K}_{ijlp}^{(3)}\, q_j\, q_l\, q_p = F_i \end{aligned} \tag{5}$$

which is very similar to Eq. (4) except that there is no repetition in the monomials because $\bar{K}_{ijl}^{(2)}$ and $\bar{K}_{ijlp}^{(3)}$ are nonzero only for $j \le l$ and $j \le l \le p$. Then, comparing Eqs (4) and (5) yields

$$\bar{K}^{(2)}_{mnl} = \begin{cases} 0 & \text{for } l < n \\ K^{(2)}_{mnn} & \text{for } l = n \\ K^{(2)}_{mnl} + K^{(2)}_{mln} & \text{for } l > n \end{cases}$$

$$\bar{K}^{(3)}_{mnlp} = \begin{cases} 0 & \text{unless } p \geq l \geq n \\ K^{(3)}_{mnnn} & \text{for } p = l = n \\ K^{(3)}_{mnll} + K^{(3)}_{m\ln l} + K^{(3)}_{mlln} & \text{for } p = l > n \\ K^{(3)}_{mpll} + K^{(3)}_{mlpl} + K^{(3)}_{mllp} & \text{for } p > l = n \\ 2K^{(3)}_{mnlp} + 2K^{(3)}_{mpln} + 2K^{(3)}_{mlpn} & \text{for } p > l > n \end{cases} \quad (6)$$

As discussed in Mignolet and Soize (2008), the symmetry properties of the elasticity tensor also imply that

$$K^{(3)}_{mnlp} = K^{(3)}_{nmlp} = K^{(3)}_{mnpl} = K^{(3)}_{lpmn}. \quad (7)$$

While Eqs (4) and (5) were derived based on the continuum representation of Eq. (2), they are assumed here to be valid as well for a discrete, finite element model. In fact, the identification of the coefficients $\bar{K}^{(2)}_{ijl}$ and $\bar{K}^{(3)}_{ijlp}$ from nonintrusive outputs of commercial finite element software (e.g., Nastran) has been studied and can be achieved in different ways, see discussions in (Mignolet et al. 2013, Muravyov and Rizzi 2003, Perez et al. 2014), given the basis functions $\boldsymbol{U}^{(n)}$. The selection of these vectors is discussed in details in (Capiez-Lernout et al. 2012, Capiez-Lernout and Soize 2015, 2017) and references therein and is not repeated here for brevity.

3 Maximum Entropy Uncertainty Modeling at the ROM Level

The modeling of uncertainty at a ROM level has been developed, see Soize (2012, 2017), as a constrained optimization problem in which the entropy of the random parameters of the ROM is maximized under constraints which correspond to (i) physical requirements that these parameters must satisfy and (ii) conditions imposed by the user. To exemplify this strategy, consider the important case in which the ROM involves one or multiple positive definite symmetric matrices as occurs for example in linear structural dynamics. Let $\boldsymbol{A}$ be that random matrix and denote by $p_A(a)$ its probability density function which is defined over the domain of support $\bar{\Omega}$ such that A is positive definite and symmetric. Then, the entropy is

$$S = -\int_{\bar{\Omega}} p_A(a) \ln p_A(a) da \quad (8)$$

In addition to the physical requirements of symmetry and positive definiteness, it is also required that the total probability equal 1 and that the mean of $\boldsymbol{A}$, denoted as $\bar{\boldsymbol{A}}$ is known, that is,

$$\int_{\bar{\Omega}} p_A(a)\, da = 1 \quad \int_{\bar{\Omega}} a\; p_A(a)\, da = \bar{A} \quad (9), (10)$$

and moreover that

$$\int_{\bar{\Omega}} \ln\left[\det(a)\right] p_A(a)\, da = \nu \text{ finite} \quad (11)$$

which guaranties that the inverse matrix $\boldsymbol{A}^{-1}$ of $\boldsymbol{A}$, which exists almost surely, is a second-order random variable (mean-square integrable).

The probability density function $p_A(a)$ maximizing S given the constraints symmetry and of Eqs (9)-(11) can be derived by calculus of variation and is found to be

$$p_A(a) = \tilde{C}\left[\det(a)\right]^{\lambda_0 - 1} \exp\left[-\mathrm{tr}\left(\tilde{\mu}^T a\right)\right] \quad (12)$$

where $\tilde{C}$ is the appropriate constant to satisfy the normalization condition, Eq. (9) and μ and λ_0 are the Lagrange multipliers associated with the constraints of Eqs (10) and (11), respectively. After a change of random variables, it is found that the matrices A of joint probability density function $p_A(a)$, Eq. (12), can be generated as

$$\boldsymbol{A} = \bar{\boldsymbol{L}}\,\boldsymbol{H}\,\boldsymbol{H}^T\,\bar{\boldsymbol{L}}^T \tag{13}$$

where $\bar{\boldsymbol{L}}$ is any decomposition, e.g., Cholesky, of $\bar{\boldsymbol{A}}$, i.e.,

$$\bar{\boldsymbol{A}} = \bar{\boldsymbol{L}}\,\bar{\boldsymbol{L}}^T\,. \tag{14}$$

Moreover, $\boldsymbol{H}$ is a lower triangular matrix such that (see also Fig. 1)

(1) all of its non-zero elements H_{il} are independent random variables,

(2) its off-diagonal elements H_{il}, $i \neq l$, are normally distributed (Gaussian) random variables with standard deviation $\sigma = 1/\sqrt{2\mu}$, and

(3) its diagonal elements H_{ii} are obtained as $H_{ii} = \sqrt{Y_{ii}/\mu}$ where Y_{ii} is Gamma distributed with parameter $\left(p(i)-1\right)/2$ where

$$p(i) = n - i + 2\lambda_0 - 1 \quad \mu = \left(n + 2\lambda_0 - 1\right)/2 \tag{15}$$

In the above equations, n is the size of the matrices and the parameter $\lambda_0 > 0$ is the free parameter of the statistical distribution of the random matrices A. An alternative parametrization is through the dispersion parameter δ defined as

$$\delta^2 = \frac{n+1}{n+2\lambda_0 - 1}\,. \tag{16}$$

As stated above, a key component of the maximum entropy formulation is the satisfaction of the physical constraints that the ROM parameters must satisfy. While this issue is well understood for the stiffness matrix of linear structural dynamics, it is not as obvious for the combination of linear, quadratic, and cubic stiffness coefficients of the ROM of Eq. (4). The derivation of such a condition was achieved in Mignolet and Soize (2008) based on integral expressions off the stiffness coefficients of Eq. (4) obtained as a by-product of the derivation of this governing equation. Specifically, it was found that

$$K^{(1)}_{mn} = \int_{\Omega_0} \frac{\partial U^{(m)}_i}{\partial X_k} C_{iklp} \frac{\partial U^{(n)}_l}{\partial X_p}\, d\boldsymbol{X} \tag{17}$$

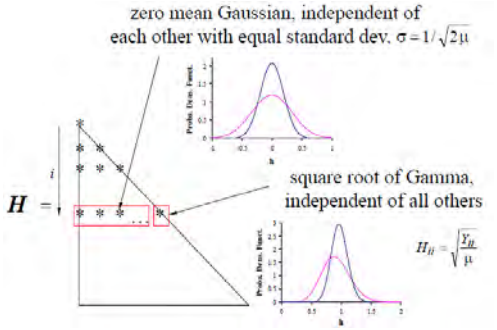

Figure 1. Structure of the random $\boldsymbol{H}$ matrices with $n = 8$, $i = 2$, and $\lambda_0 = 1$ and 10.

$$K^{(2)}_{mnp} = \frac{1}{2}\left[\hat{K}^{(2)}_{mnp} + \hat{K}^{(2)}_{pmn} + \hat{K}^{(2)}_{npm}\right] \tag{18}$$

where

$$\hat{K}^{(2)}_{mnp} = \int_{\Omega_0} \frac{\partial U^{(m)}_i}{\partial X_j} C_{ijkl} \frac{\partial U^{(n)}_r}{\partial X_k} \frac{\partial U^{(p)}_r}{\partial X_l}\, d\boldsymbol{X} \tag{19}$$

and

$$K^{(3)}_{msnp} = \frac{1}{2}\int_{\Omega_0} \frac{\partial U^{(m)}_i}{\partial X_j} \frac{\partial U^{(s)}_i}{\partial X_k} C_{jklw} \frac{\partial U^{(n)}_r}{\partial X_l} \frac{\partial U^{(p)}_r}{\partial X_w}\, d\boldsymbol{X} \tag{20}$$

In these equations, Ω_0 denotes the domain of the structure in the undeformed configuration, $\boldsymbol{X} \in \Omega_0$.

Next, a reshaping was first performed to transforms the MxMxM third order tensor $\hat{\boldsymbol{K}}^{(2)}$ into a MxM^2 rectangular array $\tilde{\boldsymbol{K}}^{(2)}$ and the MxMxMxM fourth order tensor $\boldsymbol{K}^{(3)}$ into a M^2xM^2 square matrix $\tilde{\boldsymbol{K}}^{(3)}$. These operations are achieved as follows:

$$\tilde{K}^{(2)}_{mJ} = \hat{K}^{(2)}_{mnp} \quad \text{with} \quad J=(n\text{-}1)M+p \tag{21}$$

$$\tilde{K}^{(3)}_{IJ} = K^{(3)}_{msnp}\,;\; I=(m\text{-}1)M+s \;\; J=(n\text{-}1)M+p \tag{22}$$

With these operations, it was shown that the matrix $\bar{\boldsymbol{K}}_B$ defined as

$$\bar{\boldsymbol{K}}_B = \begin{bmatrix} \boldsymbol{K}^{(1)} & \tilde{\boldsymbol{K}}^{(2)} \\ \tilde{\boldsymbol{K}}^{(2)T} & 2\tilde{\boldsymbol{K}}^{(3)} \end{bmatrix} \tag{23}$$

is positive definite.

Having established the above property, it seems that the modeling of uncertainty of the

ROM level for nonlinear geometric structure is now well defined. Specifically, (Mignolet and Soize, 2008),

(1) from a finite element model of the structure, identify the parameters $K_{ij}^{(1)}$, $\bar{K}_{ijl}^{(2)}$ and $\bar{K}_{ijlp}^{(3)}$

(2) determine the coefficients $K_{ijl}^{(2)}$ and $K_{ijlp}^{(3)}$ by "inverting" the Eqs (6) with Eq. (7)

(3) determine the coefficients $\hat{K}_{mnp}^{(2)}$ from Eq. (18)

(4) form the matrices $\tilde{\boldsymbol{K}}^{(2)}$ and $\tilde{\boldsymbol{K}}^{(3)}$ from Eqs (21) and (22), then $\bar{\boldsymbol{K}}_B$ from Eq. (23)

(5) set $\bar{\boldsymbol{A}} = \bar{\boldsymbol{K}}_B$ and follow Eqs (13)-(15) and Fig. 1 to generate random samples of the matrix $\boldsymbol{A} = \boldsymbol{K}_B$

(6) proceed with steps (4), (3), (2) and (1) in reverse with each sample of $\boldsymbol{K}_B$ to obtain realizations of the uncertain linear, quadratic, and cubic stiffnesses $K_{ij}^{(1)}$, $\bar{K}_{ijl}^{(2)}$ and $\bar{K}_{ijlp}^{(3)}$ denoted as $\check{K}_{ij}^{(1)}$, $\check{K}_{ijl}^{(2)}$ and $\check{K}_{ijlp}^{(3)}$ from which the sample of the uncertain response can be determined.

4 The Challenges

The process defined by steps (1)-(6) above seems well defined but after a closer inspection and trials, two key challenges were encountered:

(I) the determination of the parameters $\hat{K}_{mnp}^{(2)}$ and $K_{ijlp}^{(3)}$ cannot be uniquely performed from Eqs (6), (7), and (18) as there are more unknowns than equations.

(II) when the above determination can be carried out, the resulting mean model matrix $\bar{\boldsymbol{K}}_B$ may not be positive definite when the ROM parameters $K_{ij}^{(1)}$, $\bar{K}_{ijl}^{(2)}$ and $\bar{K}_{ijlp}^{(3)}$ are identified from some finite element codes, e.g., from Nastran.

The positiveness of $\bar{\boldsymbol{K}}_B$ stems (Mignolet and Soize, 2008) from the positiveness of the potential energy in the structure, it is thus an essential property and its violation may lead to unphysical behavior. An example of this situation has been encountered with a flat cantilevered beam, see Wang et al. (2013).

5 Resolution of the Challenges

5.1 *Overall perspective*

The two challenges (I) and (II) above were addressed jointly as follows.

(a) Stiffness parameters for which the "inversion" of Eqs (6), (7), and (18) could not be accomplished uniquely were optimized to render the matrix $\bar{\boldsymbol{K}}_B$ as positive definite as possible.

(b) If the resulting matrix $\bar{\boldsymbol{K}}_B$ is not positive definite, its "least important" elements were modified as little as possible to make it positive definite. After the matrix $\bar{\boldsymbol{K}}_B$ has been modified, the modified mean model predictions were determined and compared with the ones resulting from the originally identified parameters. The modified matrix $\bar{\boldsymbol{K}}_B$ was accepted if the difference in predictions was found small enough. The introduction of uncertainty then followed as in Eqs (13)-(15) and Fig. 1.

(c) If the predictions obtained from the modified mean model differed too significantly from those obtained with the originally identified parameters, a modified simulation approach was defined that relies on the $\bar{\boldsymbol{K}}_B$ matrix resulting from step (a) above.

5.2 *Optimized decomposition*

The first step, (a), of the above process focused on the extraction of the parameters

$\hat{K}^{(2)}_{ijl}$ and $K^{(3)}_{ijlp}$ from the identified ones $\bar{K}^{(2)}_{ijl}$ and $\bar{K}^{(3)}_{ijlp}$ *as to render the matrix* $\bar{\boldsymbol{K}}_B$ *as positive definite as possible*. Consider first the parameters for which all indices are equal, i.e., $\hat{K}^{(2)}_{iii}$ and $K^{(3)}_{iiii}$. For these, no indeterminacy exists and

$$\hat{K}^{(2)}_{iii} = \frac{2}{3}\bar{K}^{(2)}_{iii} \quad \text{and} \quad K^{(3)}_{iiii} = \bar{K}^{(3)}_{iiii}. \qquad (24)$$

For coefficients depending on two mode indices i and $j > i$, the indeterminacy exists as there are 4 new quadratic coefficients, $\hat{K}^{(2)}_{ij}$, $\hat{K}^{(2)}_{iij}$, $\hat{K}^{(2)}_{jij}$, $\hat{K}^{(2)}_{jii}$, and 4 new cubic ones, $K^{(3)}_{iiij}$, $K^{(3)}_{iijj}$, $K^{(3)}_{ijij}$, $K^{(3)}_{ijjj}$, considering the symmetry of Eq. (7) as well as the property $\hat{K}^{(2)}_{ijl} = \hat{K}^{(2)}_{ilj}$ resulting from Eq. (18). There are however only 5 independent equations relating them:

$$\bar{K}^{(2)}_{iij} = 2\hat{K}^{(2)}_{iij} + \hat{K}^{(2)}_{jii} \qquad \bar{K}^{(2)}_{ijj} = \frac{1}{2}\hat{K}^{(2)}_{ijj} + \hat{K}^{(2)}_{jij}$$

$$\bar{K}^{(3)}_{iiij} = 3K^{(3)}_{iiij} \qquad \bar{K}^{(3)}_{iijj} = K^{(3)}_{iijj} + 2K^{(3)}_{ijij}$$

$$\text{and} \qquad \bar{K}^{(3)}_{ijjj} = K^{(3)}_{ijjj}. \qquad (25)$$

To resolve the indeterminacy, it is desired that the matrix $\bar{\boldsymbol{K}}_B$ be made as positive definite as possible given the constraints of Eqs (25). Since the split of say $\bar{K}^{(2)}_{ij}$ into $\hat{K}^{(2)}_{iij}$ and $\hat{K}^{(2)}_{jii}$ should not be dependent on the coefficients of other modes than i and j, it is more specifically imposed that *the unknown coefficients maximize the lowest eigenvalue of* $\bar{\boldsymbol{K}}^{(2)}_{B,ij}$ which is the 6×6 $\bar{\boldsymbol{K}}_B$ matrix built using the coefficients relevant to modes i and j only. This optimization is performed for all distinct combinations of i and $j > i$ modes leading to all parameters $\hat{K}^{(2)}_{ijl}$ and $K^{(3)}_{ijlp}$ with 2 different indices.

For the coefficients involving 3 different indices, i, $j > i$ and $k > j$, a similar effort is carried out: 3 new quadratic coefficients related by 1 independent equation, and 2 new cubic ones related by 1 independent equation and the indeterminacy is resolved by maximizing the lowest eigenvalue of $\bar{\boldsymbol{K}}^{(3)}_{B,ijk}$ which is the 12×12 $\bar{\boldsymbol{K}}_B$ matrix built using the coefficients relevant to modes i, j, and k only. This effort is then repeated for all distinct combinations of $k > j > i$ modes which then leads to all parameters $\hat{K}^{(2)}_{ijl}$ and $K^{(3)}_{ijlp}$ with 3 different indices.

It remains to address the determination of the parameters $K^{(3)}_{ijlp}$ with all 4 indices different. For each set of the 4 indices, there are only 3 such distinct parameters taking into account Eq. (7), i.e., $K^{(3)}_{ijlp}$, $K^{(3)}_{iljp}$, $K^{(3)}_{ipjl}$ assuming $p > l > j > i$ but only 1 independent equation

$$\bar{K}^{(3)}_{ijlp} = 2K^{(3)}_{ijlp} + 2K^{(3)}_{iljp} + 2K^{(3)}_{ipjl}. \qquad (26)$$

As before, the indeterminacy is resolved by maximizing the lowest eigenvalue of $\bar{\boldsymbol{K}}^{(4)}_{B,ijlp}$ which is the 20×20 $\bar{\boldsymbol{K}}_B$ matrix built using the coefficients relevant to modes i, j, l and p only. This effort is then repeated for all distinct combinations of $p > l > j > i$ modes to yield the remaining cubic parameters $K^{(3)}_{ijlp}$.

5.3 *Rendering* $\bar{\boldsymbol{K}}_B$ *positive definite*

After the series of optimization efforts carried out in the previous section, the resulting matrix $\bar{\boldsymbol{K}}_B$ may be positive definite in which case the uncertainty modeling can proceed as in Eqs (13)-(15) and Fig. 1. If this matrix is not positive definite, it will be modified in this second step to become positive definite. This modification will be accomplished:

(a) without affecting the part of $\bar{\boldsymbol{K}}_B$ that is positive definite, e.g., the linear stiffness

matrix $\boldsymbol{K}^{(1)}$, and

(b) inducing the smallest changes possible to this matrix.

The task (a) has been achieved iteratively by constructing the biggest block of the original matrix $\bar{\boldsymbol{K}}_B$ that is positive definite. This block is at least of size *N* since the linear stiffness matrix $\boldsymbol{K}^{(1)}$ is positive definite. Accordingly, the top left block of $\bar{\boldsymbol{K}}_B$ of size *N*+1 is first considered and it is checked for positive definiteness (e.g., by constructing its Cholesky decomposition). If it is positive definite, the algorithm moves to the top left block of size *N*+2 and the process is repeated.

Otherwise, a permutation of the rows and columns *N*+1 and *N*+2 is performed. If the top left block of size *N*+1 is now positive definite, the algorithm accepts the permutation and moves forward to the top left block of size *N*+2. On the contrary, the permutation between rows *N*+1 and *N*+2 is reversed and a permutation of rows *N*+1 and *N*+3 is performed followed by a positive definiteness check. This process concludes when no permutation of rows and columns achieves an increase in the size of the top left block of $\bar{\boldsymbol{K}}_B$ which is positive definite.

At that point, the matrix $\bar{\boldsymbol{K}}_B$ has been transformed in a symmetric matrix $\tilde{\boldsymbol{K}}_B$ which has the form

$$\tilde{\boldsymbol{K}}_B = \begin{bmatrix} \boldsymbol{K}_{11} & \boldsymbol{K}_{12} \\ \boldsymbol{K}_{12}^T & \boldsymbol{K}_{22} \end{bmatrix} \tag{27}$$

where $\boldsymbol{K}_{11}$ is positive definite and of size N_p, $\boldsymbol{K}_{12}$ is of size $N_p \times N_r$, and $\boldsymbol{K}_{22}$ is of size $N_r \times N_r$, $N_r = N^2 + N - N_p$.

The task (b) above then proceeds with replacing the matrix $\tilde{\boldsymbol{K}}_B$ by

$$\hat{\boldsymbol{K}}_B = \begin{bmatrix} \boldsymbol{K}_{11} & \boldsymbol{K}_{12} \\ \boldsymbol{K}_{12}^T & \boldsymbol{K}_{22} \end{bmatrix} + \begin{bmatrix} \boldsymbol{0} & \boldsymbol{\Delta}_1 \\ \boldsymbol{\Delta}_1^T & \boldsymbol{\Delta}_2 \end{bmatrix} = \tilde{\boldsymbol{K}}_B + \boldsymbol{\Delta} \tag{28}$$

where the matrix $\boldsymbol{\Delta}$ will be selected to have the minimum Frobenius norm under the constraint that $\hat{\boldsymbol{K}}_B$ is at least positive semidefinite. The solution of this nonlinear optimization problem will be obtained iteratively through a sequence of linear optimization problems in which the positive definiteness constraint is enforced linearly. To this end, note that a symmetric perturbation $\boldsymbol{\delta A}$ of a symmetric matrix $\boldsymbol{A}$ leads to a first order perturbation of any of its non repeated eigenvalues λ by

$$\delta\lambda = \boldsymbol{\psi}^T \boldsymbol{\delta A} \boldsymbol{\psi} \tag{29}$$

where $\boldsymbol{\psi}$ is the normalized, $\boldsymbol{\psi}^T\boldsymbol{\psi} = 1$, eigenvector of $\boldsymbol{A}$ corresponding to the eigenvalue λ. Then, assuming that $\boldsymbol{\Delta}$ is small enough for Eq. (29) to apply, the positive semidefinite requirement can be approximately written as

$$\tilde{\boldsymbol{\psi}}_i^T \Delta \tilde{\boldsymbol{\psi}}_i \geq -\tilde{\lambda}_i \text{ for all } i \text{ such that } \tilde{\lambda}_i \leq 0 \,. \tag{30}$$

Adopting these linearized constraints, the determination of $\boldsymbol{\Delta}$ can be rewritten as the minimization of

$$\|\boldsymbol{\Delta}\|_F^2 - 2 \sum_{\tilde{\lambda}_i < 0} \mu_i \left[\tilde{\boldsymbol{\psi}}_i^T \Delta \tilde{\boldsymbol{\psi}}_i + \tilde{\lambda}_i \right] \tag{31}$$

where $\|\cdot\|_F$ denotes the Frobenius norm and μ_i are the Lagrange multiplier associated to the equality constraints of Eq. (30).

Differentiating the objective function of Eq. (31) yields the linear system of equations

$$\boldsymbol{\Delta}_1 = \sum_{\tilde{\lambda}_i < 0} \mu_i \, \tilde{\boldsymbol{\psi}}_i^{(1)} \left[\tilde{\boldsymbol{\psi}}_i^{(2)} \right]^T \tag{32}$$

$$\boldsymbol{\Delta}_2 = \sum_{\tilde{\lambda}_i < 0} \mu_i \, \tilde{\boldsymbol{\psi}}_i^{(2)} \left[\tilde{\boldsymbol{\psi}}_i^{(2)} \right]^T \tag{33}$$

where the eigenvectors $\tilde{\boldsymbol{\psi}}_i$ are partitioned into vectors $\tilde{\boldsymbol{\psi}}_i^{(1)}$ and $\tilde{\boldsymbol{\psi}}_i^{(2)}$ of N_p and N_r components, respectively. That is,

$\tilde{\boldsymbol{\psi}}_i^T = \left[\left[\tilde{\boldsymbol{\psi}}_i^{(1)} \right]^T \left[\tilde{\boldsymbol{\psi}}_i^{(2)} \right]^T \right]$. Finally, the constraints of Eq. (30) yield

$$\sum_{\tilde{\lambda}_r < 0} \left(2\, a_{ri}\, b_{ri} + b_{ri}^2 \right) \mu_r = -\tilde{\lambda}_i \qquad (34)$$

with

$$a_{rs} = \left[\tilde{\boldsymbol{\psi}}_r^{(1)} \right]^T \tilde{\boldsymbol{\psi}}_s^{(1)} \qquad b_{rs} = \left[\tilde{\boldsymbol{\psi}}_r^{(2)} \right]^T \tilde{\boldsymbol{\psi}}_s^{(2)}$$

Solving the linear system of equations (34) yields the values of the Lagrange multipliers μ_i which can then be reintroduced in Eq. (32) and (33) to yield the unknown partitions $\boldsymbol{\Delta}_1$ and $\boldsymbol{\Delta}_2$ of $\boldsymbol{\Delta}$.

The resulting matrix $\hat{\boldsymbol{K}}_B$ will then in general not be positive definite but the process can be repeated with a new $\tilde{\boldsymbol{K}}_B = \hat{\boldsymbol{K}}_B$ until a matrix $\hat{\boldsymbol{K}}_B$ positive definite/semidefinite is finally obtained. At that point, the rows/columns permutations performed to obtain the largest block positive definite are reversed leading to a matrix $\boldsymbol{K}'_B$ which is positive definite and thus could serve as the basis for the uncertainty modeling according to Eqs (13)-(15) and Fig. 1.

It remains however to assess if rendering the matrix positive definite has changed "significantly" the mean model to the point that the uncertainty analysis may not be relevant to the original mean model. To this end, the quadratic and cubic stiffness coefficients $\hat{K}'^{(2)}_{ijl}$ and $K'^{(3)}_{ijlp}$ are extracted from $\boldsymbol{K}'_B$ and used, with the linear coefficients $K^{(1)}_{ij}$, which have not been modified by the modification of the matrix $\tilde{\boldsymbol{K}}_B$, to compute a set of representative responses of this modified mean model. These responses can then be compared with those from the identified model to assess whether the matrix $\boldsymbol{K}'_B$ is appropriate to carry out the uncertainty analysis.

5.4 $\bar{\boldsymbol{K}}_B$ *cannot be made positive definite without affecting the model*

For most of the structural models investigated so far, see the application section for details, the procedure described in the previous section yielded a matrix $\boldsymbol{K}'_B$ that closely represents the originally identified mean model and thus can be used to carry out the uncertainty analysis. When this is not the case, however, it is proposed here to modify the modeling approach of Eqs (13) and (14) using a $L\,D\,L^T$ decomposition (Golub and van Loan 1966) in place of the Cholesky one so that it can be applied to the matrix $\bar{\boldsymbol{K}}_B$ resulting from the optimized decomposition. Specifically, this matrix is first rewritten as

$$\bar{\boldsymbol{K}}_B = \bar{\boldsymbol{L}}_{\boldsymbol{K}}\, \boldsymbol{D}\, \bar{\boldsymbol{L}}_{\boldsymbol{K}}^{\boldsymbol{T}} \qquad (35)$$

then, the uncertain matrices are obtained as

$$\boldsymbol{K}_B = \bar{\boldsymbol{L}}_{\boldsymbol{K}}\, \boldsymbol{H}\, \boldsymbol{D}\, \boldsymbol{H}^T\, \bar{\boldsymbol{L}}_{\boldsymbol{K}}^{T} \qquad (36)$$

where $\boldsymbol{H}$ is the same matrix as in Eq. (14) and Fig. 1. Note in Eq. (35) that the diagonal matrix $\boldsymbol{D}$ will be selected to only carry a sign, i.e., its elements are either +1 or -1 only.

6 Applications

The above developments were applied to a series of structures for which mean NLROM were obtained in prior investigations two of which are presented. While these two applications focus on static responses, uncertain dynamic responses could be computed with the same set of uncertain stiffness coefficients as those used for the static problems.

The first example considered is the orthogrid panel of Fig. 2 (Gogulapati et al. 2017) modeled using 17 basis function – the first 8 linear modes and 9 duals. The matrix $\bar{\boldsymbol{K}}_B$ obtained after the optimized decomposition was not positive definite. The application of the procedure of Eqs (27)-(34) did render it positive definite and the predictions obtained from that modified mean model were found to be very close to those

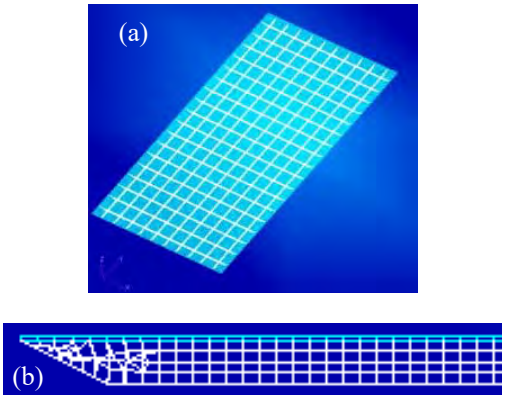

Figure 2. Orthogrid panel considered in (Gogulapati et al. 2017) (a) Perspective view and (b) cross-section.

from the originally identified model. The uncertainty analysis was then performed using Eqs (13) and (14) with an overall uncertainty level selected to be δ=0.31. Then, shown in Fig. 3 are the displacements at a quarter point along the three directions for the mean and uncertain models. It is interesting to observe that the inplane displacements are much more sensitive to the uncertainty than the transverse ones.

A second application of the above concepts focused on the clamped-clamped curved beam of Fig. 4 in a range of displacements that includes its snap-through. Proceeding as before, the matrix $\bar{\boldsymbol{K}}_B$ obtained after the optimized decomposition was not positive definite but the application of the procedure of Eqs (27)-(34) did render it positive definite. However, the predictions obtained from that modified mean model were found to be too different from those from the originally identified model, in particular that modified model did not snap through as predicted by either the original NLROM or the finite element model. In this light, the revised uncertainty modeling of Eqs. (35) and (36) was applied with δ=0.026. Then, shown in Fig. 5 are the transverse (vertical) and inplane

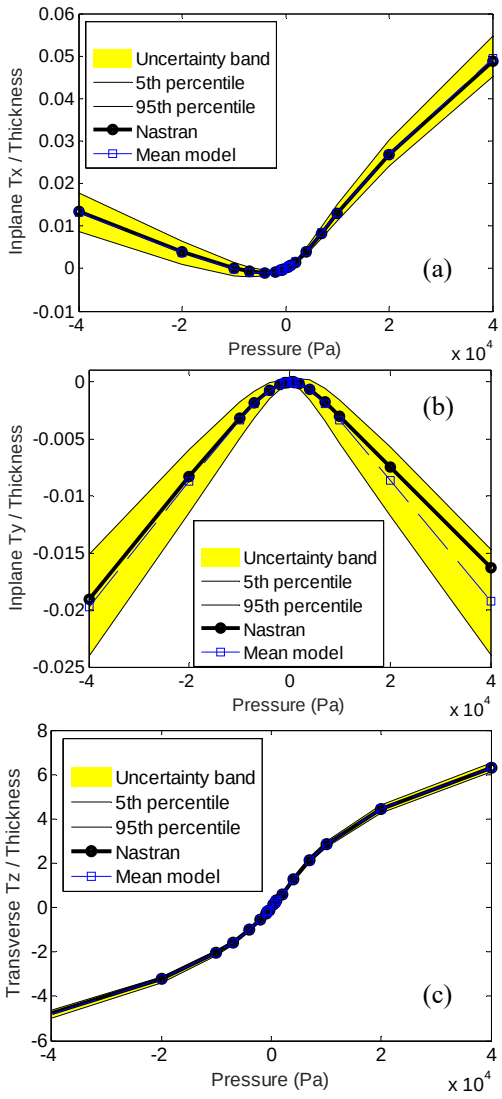

Figure 3. Static displacement of the orthogrid panel under a uniform loading. (a) Inplane *x*, (b) inplane *y*, and (c) transverse *z* displacements at a quarter point, divided by the panel thickness vs. load. Mean and uncertain models.

(horizontal) displacements at a beam quarter point vs. load level for the mean model as well as 5th-95th percentile uncertainty band.

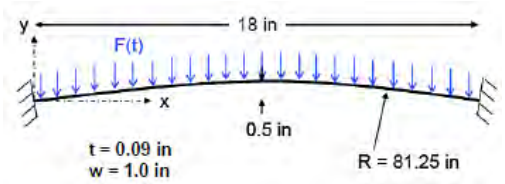

Figure 4. Clamped-clamped curved beam with uniform loading.

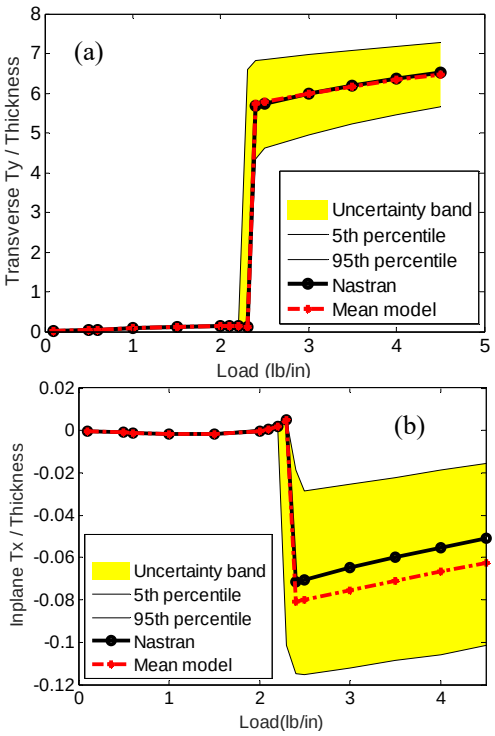

Figure 5. Static displacement of the clamped-clamped curved beam under uniform loading. (a) Transverse and (b) inplane displacements (in percent of span) at beam quarter point vs. load. Mean and uncertain models.

As already observed in connection with the two previous examples, the inplane response of the curved beam appears more sensitive to uncertainty than its transverse counterpart. Note as well the large increase in the uncertainty band post snap through, in both directions, with much smaller variations of the snap through load which are nevertheless much larger than the variability of the response prior to snap through.

7 Summary

The focus of the present investigation was on resolving two key challenges encountered in the introduction of uncertainty in reduced order models of the nonlinear geometric response following an approach proposed earlier by the authors. The first of these challenges was the indeterminacy of the mapping of the nonlinear stiffness coefficients identified from the finite element model, $\bar{K}_{ijl}^{(2)}$ and $\bar{K}_{ijlp}^{(3)}$, to those suitable for the uncertainty analysis, i.e., $\hat{K}_{mnp}^{(2)}$ and $K_{ijlp}^{(3)}$, see Eqs (6),(7), and (18). The second challenge was that the matrix $\bar{\boldsymbol{K}}_B$ constructed with these coefficients (and the linear stiffness ones) is not positive definite as showed in the original paper because of differences in nonlinear finite element modeling between the commercial software and the theoretical developments. These challenges were jointly addressed. First, the indeterminacy was resolved by selecting the coefficients to maximize $\bar{\boldsymbol{K}}_B$ while satisfying the constraints of Eqs (6), (7), and (18). In general, the resulting matrix $\bar{\boldsymbol{K}}_B$ was found not positive definite but a strategy was devised to modify it in a minimal manner to achieve this property. In most of the cases investigated, this modification did not significantly change the predictions of the mean response and thus the uncertainty modeling could proceed from it. In one example, a clamped-clamped curved beam undergoing snap throughs, the changes of mean were large enough. For such situations, a modification of the uncertainty modeling was proposed that handles the non positive definite matrix $\bar{\boldsymbol{K}}_B$ with a $\boldsymbol{LDL}^{\boldsymbol{T}}$ decomposition vs. a Cholesky one.

The above methods were applied to two different structural models of various complexity and the uncertain response to static loading was determined. These efforts first demonstrated the broad applicability of the above methodology but they also

suggested that strong nonlinear features of the response, such as inplane displacements due to transverse loading and post-snap through behavior, are particularly sensitive to uncertainty.

Acknowledgments

The financial support of this investigation by the Air Force Office of Scientific Research grant FA9550-16-1-0021 with Dr. Jaimie Tiley as monitor is gratefully acknowledged.

References

Capiez-Lernout, E. and Soize, C., Uncertainty Quantification for an Industrial Mistuned Bladed Disk with Geometrical Nonlinearities, *Proc. ASME Turbo Expo 2015*, Montreal, Quebec, Canada, June 15–19, 2015, GT2015-42471.

Capiez-Lernout, E. and Soize, C., An Improvement of the Uncertainty Quantification in Computational Structural Dynamics with Nonlinear Geometrical Effects, *International J. Uncertain. Quantification*, 7, 83-98, 2017.

Capiez-Lernout, E., Soize, C. and Mignolet, M. P., Computational Stochastic Statics of an Uncertain Curved Structure with Geometrical Nonlinearity in Three-Dimensional Elasticity, *Computational Mechanics*, 49, 87-97, 2012.

Capiez-Lernout, E., Soize, C. and Mignolet, M. P., Post-Buckling Nonlinear Static and Dynamical Analyses of Uncertain Cylindrical Shells and Experimental Validation, *Computer Methods Appl. Mechanics Engineering*, 271, 210-230, 2014.

Gogulapati, A., Brouwer, K., Wang, X. Q., Murthy, R., MacNamara, J. J. and Mignolet, M. P., Full and Reduced Order Aerothermoelastic Modeling of Built-Up Aerospace Panels in High-Speed Flows, *Proc. 58th Structures, Structural Dynamics, and Materials Conference*, AIAA SciTech, Grapevine, Texas, Jan. 9-13, 2017, AIAA 2017-0180.

Golub, G. H. and van Loan, C. F., *Matrix Computations*, 3rd ed., Johns Hopkins University Press, 1966.

Kim, K., Radu, A. G., Wang, X. Q. and Mignolet, M.P., Nonlinear Reduced Order Modeling of Isotropic and Functionally Graded Plates, *International J.Non-Linear Mechanics*, 49, 100-110, 2013.

Mignolet, M. P., Przekop, A., Rizzi, S. A. and Spottswood, S. M., A Review of Indirect/Non-Intrusive Reduced Order Modeling of Nonlinear Geometric Structures, *J. Sound Vib.* 332, 2437-2460, 2013.

Mignolet, M.P. and Soize, C., Stochastic Reduced Order Models for Uncertain Geometrically Nonlinear Dynamical Systems, *Computer Methods Appl. Mechanics Engineering*, 197, 3951-3963, 2008.

Muravyov, A.A. and Rizzi, S.A., Determination of Nonlinear Stiffness with Application to Random Vibration of Geometrically Nonlinear Structures, *Computers and Structures*, 81, 1513-1523, 2003.

Perez, R. A., Wang, X. Q., Mignolet, M. P., Non-Intrusive Structural Dynamic Reduced Order Modeling for Large Deformations: Enhancements For Complex Structures, *J. Comput. Nonlinear Dynam*,. 9(3), 031008, 2014.

Soize, C., *Stochastic Models of Uncertainties in Computational Mechanics*, American Society of Civil Engineers, Reston, VA, 2012.

Soize, C. *Uncertainty Quantification: An Accelerated Course with Advanced Applications in Computational Engineering*, Springer-Verlag, 2017.

Wang, X. Q., Perez, R., Mignolet, M. P., Capillon, R. and Soize, C., Nonlinear Reduced Order Modeling of Complex Wing Models, *Proc. 54th Structures, Structural Dynamics and Materials Conference*, Boston, MA, Apr. 8-11, 2013, AIAA-2013-1520

APPENDIX B:

[J2]: Song, P., Wang, X.Q., Murthy, R., Matney, A.K., and Mignolet, M.P., "Nonlinear Geometric Thermoelastic Response of Structures with Uncertain Thermal and Structural Properties," *AIAA Journal*, In Press.

NONLINEAR GEOMETRIC THERMOELASTIC RESPONSE OF STRUCTURES WITH UNCERTAIN THERMAL AND STRUCTURAL PROPERTIES

Pengchao Song, X.Q. Wang, Andrew K. Matney,

Raghavendra Murthy, and Marc P. Mignolet

SEMTE, Faculties of Mechanical and Aerospace Engineering, Arizona State University,
501 E. Tyler Mall, Tempe, Arizona, 85287-6106

ABSTRACT

The focus of this investigation is on modeling uncertainties on the structural and thermal properties of heated structures and assessing their effects on the resulting temperature distributions and structural response. This effort is accomplished within the framework of reduced order models (ROMs) of both the thermal (heat conduction) and structural (nonlinear geometric response) problems relying on the maximum entropy nonparametric approach. Uncertainties are introduced on both the heat conduction and the structural response problems. In the latter, it is in particular shown that the purely structural terms of the ROM governing equations and those associated with the structural-thermal coupling should be randomized jointly. Moreover, this can be done through the construction of a large matrix that includes all of them and is shown to be symmetric and positive definite. Several challenges in applying this approach are identified and resolved. Finally, the applicability of the methodology is demonstrated on the response of a simple panel subjected to an oscillating heating flux as an example of strongly coupled thermal-structural problems.

NOMENCLATURE

$\overline{\boldsymbol{A}}$: mean of a random matrix $\boldsymbol{A}$

B_{ij} : element of modal capacitance matrix

$\boldsymbol{C}$: 4th order elasticity tensor

D_{ij} : element of modal damping matrix

F_i : modal mechanical forces.

$F_{il}^{(th)}$: modal force induced by thermal mode l

$\boldsymbol{H}, \boldsymbol{H}_{\boldsymbol{K}}$, $\boldsymbol{H}_T$, $\boldsymbol{H}_S$: triangular random matrices

$K_{ij}^{(1)}$, $K_{ijl}^{(2)}$, $K_{ijlp}^{(3)}$: linear, quadratic, and cubic stiffness coefficients

$K_{ijl}^{(th)}$: linear stiffness coefficients induced by thermal mode l

$\widetilde{K}_{ij}$: element of modal conductance matrix

$\boldsymbol{K}_B$, $\boldsymbol{K}_C$: random matrices composed of structural coefficients and structural and coupling coefficients

M_{ij} : element of modal mass matrix

P_i : modal heat flux

$p_{\boldsymbol{A}}(\boldsymbol{a})$: joint probability density functions of the elements of a random matrix $\boldsymbol{A}$

$q_n(t)$: generalized structural coordinates

$\boldsymbol{T}^{(n)}$: thermal basis functions

$\boldsymbol{\alpha}$: coefficient of thermal expansion tensor

δ: uncertainty level

$\tau_n(t)$: generalized thermal coordinates

Ω_0 : structural domain in the undeformed configuration

$\boldsymbol{\psi}^{(n)}$: structural basis functions

INTRODUCTION

A significant challenge in the prediction of the response of real structures is the lack of precise information on their geometry and/or material properties. If they were accurately known, then standard analysis tools such as finite elements could in principle be used to determine the structural response under specified loads. These observations have led in particular to the modeling of the uncertainty in the geometry and/or material properties through probabilistic concepts, i.e. by treating them as random variables, stochastic processes and fields. This approach permits the consideration of the variability in geometry and/or material properties from one nominally identical structure to another which is referred to as aleatoric uncertainty.

Invariably, computational models approximate or ignore particular features of the problem, e.g. grain structure, anisotropy, curvature of a nominally straight structure, three-dimensionality modeled through plates and beams models, etc. These approximations lead in the predicted response to another form of uncertainty, i.e., epistemic uncertainty, which is typically challenging to model.

A particularly elegant strategy to incorporate both aleatoric and epistemic uncertainties is the maximum entropy based nonparametric method, e.g. see [1-3]. This approach relies on the modeling of the fields of interest, e.g. structural displacements, in a reduced order model format in which the basis is fixed, determined from the mean model. The uncertainty in the structural model is then entirely regrouped into the parameters (stiffness matrix, mass matrix, ...) of the governing equations for the generalized coordinates of this reduced order model. To complete the uncertainty modeling process, it remains to postulate or derive the joint

probability density function of these parameters and a way to simulate them. The approach proposed in [1-3] and adopted here is to derive this joint probability density function to maximize the corresponding entropy under the physical constraints that these parameters must satisfy, such as symmetry, positive definiteness, etc. Moreover, simulating the random parameters/matrices according to this distribution was shown [1-3] to be fast and straightforward. Then, Monte Carlo analyses can be carried out to obtain any desired statistics of the response and they are performed in a particular efficient manner since they only involve the reduced order model. It should be noted that the maximum entropy based nonparametric method does account for aleatoric but also some epistemic uncertainty. It has been used in a variety of different contexts within structural dynamics, e.g., linear structural dynamics [1,4-7], vibro-acoustics [8,9], rotor dynamics [10-12], nonlinear structural dynamics [13,14], linear viscoelastic structures [15], etc., but also in rigid body dynamics [16,17] and micromechanics and multiscale modeling, see [3] for extensive review.

The present investigation focuses on effects of uncertainty on the response of heated structures. In such multidisciplinary problems, the uncertainty may be associated with each discipline and/or with their coupling. Since the consideration of uncertainty on the structural properties alone has been discussed extensively before, this investigation will focus on the novel aspects of the uncertainty on the thermal properties (capacitance, conductance) and the thermal-structural coupling induced by the coefficient of thermal expansion. The propagation of these uncertainties to both temperature distribution and structural response will be determined. In this regard, note that thermal-structural coupling is effectively a one-way interaction. Indeed, the temperature distribution induces stresses in the structure that result in thermal loads and changes in its natural frequencies and mode shapes. In reverse however, the structural deformations directly affect the temperature distribution only through the very weak

latency term which is ignored here. A stronger coupling between the structural deformations and the temperature distribution may however exist in aero-structural-thermal problems since the structural motion will affect the aerodynamics and especially the aeroheating which drives the temperature distribution. This situation is not considered here. Moreover, it will mostly be assumed that all properties are independent of temperature. However, the extension of the proposed formulation to the case where the coefficient of thermal expansion is linearly dependent on temperature is presented in [18] to highlight the process of such extensions.

Owing to the potential or actual occurrence of thermal buckling, it is highly desirable to carry out the structural analysis in a nonlinear geometric format which, unfortunately, leads to a significant increase in computational effort especially when considering dynamic situations. These conflicting requirements have led to the formulation and development of nonlinear thermal-structural reduced order modeling strategies for the temperature and displacements, see [19,20], which are based on similar developments for structural only models, see [21-23]. This reduced order modeling strategy is adopted here and briefly reviewed below.

OVERALL CHALLEGES AND PLAN

The above discussion has motivated the use of reduced order models for the consideration of uncertainties in heated structures because of (i) their computational efficiency but also (ii) of the capability of such models to include both aleatoric and epistemic uncertainties. To benefit from these advantages, it is key that the uncertain reduced order models be constructed directly from their equivalent for the mean model without returning to the underlying finite element model, in particular to avoid the computational cost of constructing the reduced order model for each finite element sample. Modeling uncertainties directly within reduced order models has been done for several problems in the past, including nonlinear reduced order models but of non heated structures. Heated structures however include additional terms in

the governing equations that reflect the coupling of the displacements with the temperature field. A key question addressed here is then how these coupling terms should be randomized to account for the uncertainties. That is, can they be considered separate of the purely structural terms or should they all be randomized together and, either way, how should one proceed?

It is demonstrated in the sequel that the purely structural and structural-thermal coupling terms should be randomized *jointly* through their grouping in a large matrix $\boldsymbol{K}_C$ that is symmetric and theoretically positive definite. Then, the randomization of this matrix can be achieved using the maximum entropy nonparametric approach.

Several challenges are however encountered in the implementation of this overall strategy. First, as formed, the matrix $\boldsymbol{K}_C$ involves a smaller size matrix that does not exist in the reduced order model and which has been found to be difficult to determine accurately from the underlying finite element model. This issue is resolved here by appealing to the maximum entropy principle from which it is found that the matrix can be selected as proportional to the identity matrix. A second novel challenge arises from the desire to control separately the levels of uncertainties on the purely structural terms and on the structural-thermal terms. To this end, a multiplicative decomposition of the uncertainty is proposed. Finally, it is observed that the present formulation shares with its counterpart for non heated structures the potential for the matrix $\boldsymbol{K}_C$ to not be positive definite owing to differences in nonlinear formulation between finite element and reduced order modeling. Fortunately, strategies developed very recently to mitigate this issue are shown to be applicable. With all theoretical and implementation issues resolved, the methodology is demonstrated on an example.

The plan of this paper is as follows. The next two sections provide reviews of (a) the reduced order modeling methods on which uncertainty is introduced and (b) the maximum entropy nonparametric approach. In fact, two versions of this approach are described which are used

for different aspects of the uncertainty modeling. The construction of the matrix $\boldsymbol{K}_C$ is achieved next followed by the detailed strategies proposed for the resolution of the implementation challenges described above. Finally, the applicability of the methodology is demonstrated.

COUPLED STRUCTURAL-THERMAL REDUCED ORDER MODEL (ROM)

The coupled structural-thermal reduced order models employed here are the extension to geometrically nonlinear problems of the modal models used in linear analysis. They are based on the representation of the temperature and displacements of the finite element nodes, stacked in the time varying vectors $\boldsymbol{T}(t)$ and $\boldsymbol{u}(t)$, in expansion forms, i.e.

$$\boldsymbol{T}(t) = \sum_{n=1}^{\mu} \tau_n(t)\, \boldsymbol{T}^{(n)} \tag{1}$$

$$\boldsymbol{u}(t) = \sum_{n=1}^{M} q_n(t)\, \boldsymbol{\psi}^{(n)} \tag{2}$$

In these equations, $\boldsymbol{T}^{(n)}$ and $\boldsymbol{\psi}^{(n)}$ are the thermal and structural basis functions, or modes, while $\tau_n(t)$ and $q_n(t)$ are the time-dependent thermal and structural generalized coordinates. Assuming that the material properties (elasticity tensor, coefficient of thermal expansion) do not vary with temperature, it is found, e.g. [19], for the structural generalized coordinates that (summation over repeated indices assumed)

$$M_{ij}\ddot{q}_j + D_{ij}\dot{q}_j + \left[K_{ij}^{(1)} + K_{ijl}^{(th)}\, \tau_l \right] q_j + K_{ijl}^{(2)} q_j q_l + K_{ijlp}^{(3)} q_j q_l q_p = F_i + F_{il}^{(th)}\, \tau_l \quad . \tag{3}$$

In this equation, M_{ij} denotes the elements of the mass matrix, $K_{ij}^{(1)}$, $K_{ijl}^{(2)}$, $K_{ijlp}^{(3)}$ are linear, quadratic, and cubic stiffness coefficients and F_i are the modal mechanical forces. The parameters $K_{ijl}^{(th)}$ and $F_{il}^{(th)}$ represent the sole coupling terms with the temperature field which is described by the governing equations [19,20]

$$B_{ij}\ \dot{\tau}_j + \widetilde{K}_{ij}\tau_j = P_i \tag{4}$$

where B_{ij} and $\widetilde{K}_{ij}$ are the capacitance and conductance matrices of the finite element model, which are assumed here not to depend on temperature. The source term P_i represents the combined effects of an applied flux, nonzero homogenous boundary conditions, radiation, latency, etc., as applicable.

Having established the forms of the governing equations, i.e., Eqs (3) and (4), it remains to address (i) the selection of the basis functions $\boldsymbol{T}^{(n)}$ and $\boldsymbol{\psi}^{(n)}$ and (ii) the identification of all stiffness, mass, conductance, and capacitance parameters from commercial finite element software. The latter effort is detailed in [19,21-23] for temperature independent structural properties and has been extended in [20] when they vary linearly with the local temperature. The former issue has also been addressed, in [22] for the structural problem, see also [21,23] for the linear + dual modes basis selected here. The construction of the thermal basis has been investigated in a series of papers [19,24-27] and can be achieved from a series snapshots of the temperature distribution, e.g., [24], a priori from the conductance and capacitance matrices [19], or using a combination of a priori information and a few snapshots [25-27].

The above discussion demonstrates that coupled nonlinear structural-thermal reduced order models can be constructed from well characterized finite element models. Given this state of the art, it is then timely to consider the introduction of uncertainty in these models to bridge the gap between designed and realized structures and assess the effects of the differences between them.

UNCERTAINTY MODELING

Basis: Random or Deterministic

When introducing uncertainty in an analysis carried out in a reduced order modeling

framework, as in Eqs (1)-(4), the first question to address is whether the basis functions $\boldsymbol{T}^{(n)}$ and $\boldsymbol{\psi}^{(n)}$ can be kept the same as in the mean model (i.e., the model without uncertainty) or whether they need to be modified. The latter strategy is necessary when the uncertainty triggers a new physical behavior (e.g., buckling not anticipated in the mean model) that is not appropriately captured with the mean model basis. This issue can be prevented by adopting at the onset a basis that addresses not just the mean model behavior but also a broader physics. This is the approach selected here so that the basis functions will remain constant through the uncertainty analysis.

Maximum Entropy Nonparametric Modeling

As described in the introduction, the maximum entropy-based nonparametric stochastic modeling approach initially proposed by Soize [1], see [2,3] for recent comprehensive reviews, is an elegant alternative to the randomization of several parameters/properties of the computational model. It proceeds directly from the mean model matrices, randomizing them so that they always satisfy physical requirements (positive definiteness, symmetry, etc.) and that the joint distribution of their elements achieves the maximum of the entropy. Moreover, as discussed in [1-3], this approach not only permits the modeling of aleatoric (or parameter/data) uncertainty but also some epistemic (or model) uncertainty.

The original formulation of this method [1] focuses on symmetric positive definite $N \times N$ matrices $\boldsymbol{A}$ for which it assumes that the mean $\overline{\boldsymbol{A}}$ is known. This limited information is not sufficient to uniquely define the joint probability density function of the elements of $\boldsymbol{A}$, denoted as $p_{\boldsymbol{A}}(\boldsymbol{a})$. Faced with this issue, Soize proposed in [1] that this joint probability density function be selected as the one that maximizes the entropy S given the available information. That is, $p_{\boldsymbol{A}}(\boldsymbol{a})$ should maximize

$$S = -\int_{\Omega} p_{\boldsymbol{A}}(\boldsymbol{a}) \ln p_{\boldsymbol{A}}(\boldsymbol{a}) d\boldsymbol{a} \tag{5}$$

under the constraints of

Unit total probability: $$\int_{\Omega} p_{\boldsymbol{A}}(\boldsymbol{a})\, d\boldsymbol{a} = 1 \tag{6}$$

Given mean: $$\int_{\Omega} \boldsymbol{a}\, p_{\boldsymbol{A}}(\boldsymbol{a})\, d\boldsymbol{a} = \overline{\boldsymbol{A}}. \tag{7}$$

In addition to the above constraints, it is also imposed that (see discussion in the sequel)

$$\int_{\Omega} \ln\left[\det(\boldsymbol{a})\right] p_{\boldsymbol{A}}(\boldsymbol{a})\, d\boldsymbol{a} = \nu \text{ finite}. \tag{8}$$

In the above equations, the support Ω of the probability density function is then such that the matrix A is positive definite, or equivalently that it admits a Cholesky decomposition, i.e.,

$$\Omega = \left\{ \boldsymbol{a} = \tilde{\boldsymbol{L}}\tilde{\boldsymbol{L}}^T ; \tilde{L}_{ij}, i, j = 1, ..., N : \left[\tilde{L}_{ij} \in (-\infty, +\infty), i > j\right] \cap \left[\tilde{L}_{ii} \in [0, +\infty)\right] \right\}. \tag{9}$$

The probability density function $p_{\boldsymbol{A}}(\boldsymbol{a})$ maximizing S given the constraints of Eqs (6)-(8) can be derived by calculus of variations and is found to be

$$p_{\boldsymbol{A}}(\boldsymbol{a}) = \tilde{C}\left[\det(\boldsymbol{a})\right]^{\lambda_0 - 1} \exp\left[-\mathrm{tr}\left(\tilde{\boldsymbol{\mu}}^T \boldsymbol{a}\right)\right] \tag{10}$$

where $\widetilde{C}$ is the appropriate constant to satisfy the normalization condition, Eq. (6) and $\boldsymbol{\mu}$ and λ_0 are the Lagrange multipliers associated with the constraints of Eqs (7) and (8), respectively. After a change of random variables, it is found that the matrices $\boldsymbol{A}$ of joint probability density function $p_{\boldsymbol{A}}(\boldsymbol{a})$, Eq. (10), can be generated as follows. First, the mean matrix $\overline{\boldsymbol{A}}$ is decomposed as

$$\overline{\boldsymbol{A}} = \overline{\boldsymbol{L}}\, \overline{\boldsymbol{L}}^T \tag{11}$$

e.g., by Cholesky factorization. Then, random matrices A are generated as

$$\boldsymbol{A} = \overline{\boldsymbol{L}}\, \boldsymbol{H}\, \boldsymbol{H}^T\, \overline{\boldsymbol{L}}^T \tag{12}$$

where $\boldsymbol{H}$ is a lower triangular matrix such that (see also Fig. 1)

(1) its off-diagonal elements H_{il}, $i \neq l$, are normally distributed (Gaussian) random

variables with standard deviation $\sigma = 1/\sqrt{2\mu}$, and

(2) its diagonal elements H_{ii} are obtained as $H_{ii} = \sqrt{Y_{ii}/\mu}$ where Y_{ii} is Gamma distributed with parameter $(p(i)-1)/2$ where

$$p(i) = n - i + 2\lambda_0 - 1 \text{ and } \quad \mu = (n + 2\lambda_0 - 1)/2 \tag{13}$$

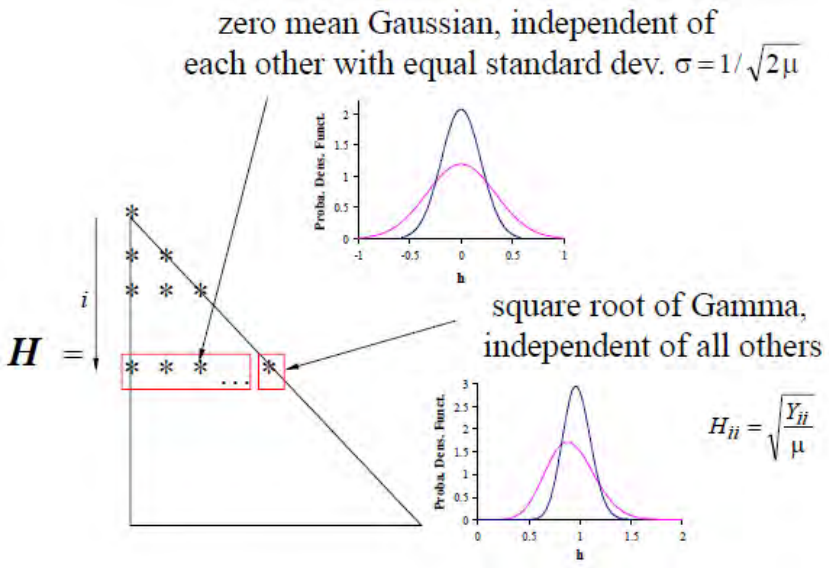

Figure 1. Structure of the random ***H*** matrices with $N = 8$, $i = 2$, and $\lambda_0 = 1$ and 10.

In the above equations, the parameter $\lambda_0 > 0$ is the free parameter of the statistical distribution of the random matrices ***A***. An alternative parametrization is through the dispersion parameter δ defined as

$$\delta^2 = \frac{N+1}{N + 2\lambda_0 - 1}. \tag{14}$$

Maximum Entropy Nonparametric Modeling for Localized Responses

A modification of the nonparametric approach has recently [28] been proposed which is applicable to problems that exhibit a localized response and will be used in the sequel. For such problems, the approach described in the previous section may lead, as part of its epistemic uncertainty modeling, to a more extended response that can be expected. The

recapture of the local behavior can be achieved by first splitting the matrices $\boldsymbol{A}$ and their mean $\overline{\boldsymbol{A}}$ into components that promote the local response and global components of the response, modeling them separately to maintain their characters, and finally reassembling the two components. Specifically, see [28] for details, let

$$\overline{\boldsymbol{A}}_{\boldsymbol{L}} = \overline{\lambda} \sum_i \overline{\phi}_i \, \overline{\phi}_i^T \tag{15}$$

where $\overline{\lambda}$ is the smallest eigenvalue of $\overline{\boldsymbol{A}}$ and $\overline{\phi}_i$ the ith eigenvector of that matrix. Then, the global matrix $\overline{\boldsymbol{A}}_{\boldsymbol{G}}$ is obtained as

$$\overline{\boldsymbol{A}}_{\boldsymbol{G}} = \overline{\boldsymbol{A}} - \overline{\boldsymbol{A}}_{\boldsymbol{L}} \quad . \tag{16}$$

Random matrices A are then generated as

$$\boldsymbol{A} = \boldsymbol{A}_{\boldsymbol{G}} + \boldsymbol{A}_{\boldsymbol{L}} \, . \tag{17}$$

where, given its global character, $\boldsymbol{A}_{\boldsymbol{G}}$ is modeled using the nonparametric approach described in the previous section, i.e., following Eqs (5)-(8) and Fig. 1, and with a specified value of δ. Moreover, to maintain its local character, the matrix $\boldsymbol{A}_{\boldsymbol{L}}$ is expressed as

$$\boldsymbol{A}_{\boldsymbol{L}} = \Lambda \sum_i \overline{\phi}_i \, \overline{\phi}_i^T \tag{18}$$

where the random variable Λ is

$$\Lambda = \alpha \, Y_L \tag{19}$$

with Y_L is a Gamma random variable with coefficient of variation δ_L and α is a deterministic coefficient such that

$$E[\Lambda] = \overline{\lambda} \, . \tag{20}$$

Modeling of Conductance and Capacitance Matrices

Uncertainty in the conductance and capacitance properties of the structure can be included in the reduced order model by modeling the corresponding ROM matrices (conductance and/or capacitance) using the above nonparametric approaches as these matrices are

symmetric and positive definite.

Modeling of the Structural and Coupling Properties

The next task is the modeling of uncertainties in the material properties that affect the structural ROM, e.g., the tensor of elasticity, coefficient of thermal expansion. The intent here is on generating random values of the parameters $K_{ij}^{(1)}$, $K_{ijl}^{(2)}$, $K_{ijlp}^{(3)}$, $K_{ijl}^{(th)}$, and $F_{il}^{(th)}$ *directly*, as opposed to simulating the material properties in the finite element then mapping them to the ROM. To proceed in this manner, it is necessary to first establish the mathematical/physical properties that those parameters must satisfy, then construct simulation algorithms that maintain these properties for every sample.

Such an effort was carried out in [13] for the structural alone problem, i.e., the simulation of the parameters $K_{ij}^{(1)}$, $K_{ijl}^{(2)}$, and $K_{ijlp}^{(3)}$. More specifically, it was shown that a matrix $\boldsymbol{K}_B$ composed of these stiffnesses is positive definite. This property was derived from the following expressions (see [13,21])

$$K_{mn}^{(1)} = \int_{\Omega_0} \frac{\partial U_i^{(m)}}{\partial X_k} C_{iklp} \frac{\partial U_l^{(n)}}{\partial X_p} d\boldsymbol{X} \tag{21}$$

$$K_{mnp}^{(2)} = \frac{1}{2}\left[\hat{K}_{mnp}^{(2)} + \hat{K}_{pmn}^{(2)} + \hat{K}_{npm}^{(2)}\right] \tag{22}$$

where

$$\hat{K}_{mnp}^{(2)} = \int_{\Omega_0} \frac{\partial U_i^{(m)}}{\partial X_j} C_{ijkl} \frac{\partial U_r^{(n)}}{\partial X_k} \frac{\partial U_r^{(p)}}{\partial X_l} d\boldsymbol{X} \tag{23}$$

and

$$K_{msnp}^{(3)} = \frac{1}{2} \int_{\Omega_0} \frac{\partial U_i^{(m)}}{\partial X_j} \frac{\partial U_i^{(s)}}{\partial X_k} C_{jklw} \frac{\partial U_r^{(n)}}{\partial X_l} \frac{\partial U_r^{(p)}}{\partial X_w} d\boldsymbol{X} \,. \tag{24}$$

In these equations, Ω_0 denotes the domain of the structure in the undeformed configuration, $U_i^{(m)}(\boldsymbol{X})$ is the *m*th basis function for the representation of the *i*th component of the

displacement vector over the continuous domain $\boldsymbol{X} \in \Omega_0$. Moreover, C_{iklp} is the elasticity tensor.

Next, a reshaping was first performed to transforms the *M*x*M*x*M* third order tensor $\hat{\boldsymbol{K}}^{(2)}$ into a *M*x*M* ^{2} rectangular array $\widetilde{\boldsymbol{K}}^{(2)}$ and the *M*x*M*x*M*x*M* fourth order tensor $\boldsymbol{K}^{(3)}$ into a *M* ^{2}x*M* ^{2} square matrix $\widetilde{\boldsymbol{K}}^{(3)}$. These operations are achieved as follows:

$$\widetilde{K}^{(2)}_{mJ} = \hat{K}^{(2)}_{mnp} \qquad \text{with} \qquad J=(n\text{-}1)M+p \tag{25}$$

and

$$\widetilde{K}^{(3)}_{IJ} = K^{(3)}_{msnp} \qquad \text{with} \quad I=(m\text{-}1)M+s \quad \text{and} \quad J=(n\text{-}1)M+p. \tag{26}$$

Construct next the expression

$$E_S = K^{(1)}_{mn}\, w_m\, w_n + 2\widetilde{K}^{(2)}_{mJ}\, w_m\, v_J + 2\widetilde{K}^{(3)}_{IJ}\, v_I\, v_J \tag{27}$$

where w_m and v_I are the components *m* and *I* of arbitrary vectors $\boldsymbol{w}$ and v. Then, from Eqs (21)-(24) one finds

$$\begin{aligned} E_S &= \int_{\Omega_0} \left\{ \left(w_m \frac{\partial U^{(m)}_i}{\partial X_k} \right) C_{iklp} \left(w_n \frac{\partial U^{(n)}_l}{\partial X_p} \right) + 2 \left(w_m \frac{\partial U^{(m)}_i}{\partial X_j} \right) C_{ijkl} \left(v_J\, Z^{(J)}_{kl} \right) + \left(v_I\, Z^{(I)}_{jk} \right) C_{jklw} \left(v_J\, Z^{(J)}_{lw} \right) \right\} d\boldsymbol{X} \\ &= \int_{\Omega_0} \left(w_m \frac{\partial U^{(m)}_i}{\partial X_j} + v_I\, Z^{(I)}_{ij} \right) C_{ijkl} \left(w_n \frac{\partial U^{(n)}_k}{\partial X_l} + v_J\, Z^{(J)}_{kl} \right) d\boldsymbol{X} = \int_{\Omega_0} B_{ij}\, C_{ijkl}\, B_{kl}\, d\boldsymbol{X} \end{aligned} \tag{28}$$

where for notational convenience

$$Z^{(J)}_{kl} = \frac{\partial U^{(n)}_r}{\partial X_k} \frac{\partial U^{(p)}_r}{\partial X_l} \qquad \text{and} \qquad B_{ij} = w_m \frac{\partial U^{(m)}_i}{\partial X_j} + v_I\, Z^{(I)}_{ij} \tag{29}$$

Since the elasticity tensor C_{iklp} is positive definite, it is seen from the last equality of Eq. (28) that E_S is positive for any vectors $\boldsymbol{w}$ and v. Rewriting this quantity as

$$E_S = \begin{bmatrix} \boldsymbol{w}^T & \boldsymbol{v}^T \end{bmatrix} \begin{bmatrix} \boldsymbol{K}^{(1)} & \widetilde{\boldsymbol{K}}^{(2)} \\ \widetilde{\boldsymbol{K}}^{(2)T} & 2\widetilde{\boldsymbol{K}}^{(3)} \end{bmatrix} \begin{bmatrix} \boldsymbol{w} \\ \boldsymbol{v} \end{bmatrix} \tag{30}$$

it is seen that the *P*x*P* ($P = M + M^2$) symmetric matrix $\boldsymbol{K}_B$ defined as

$$\boldsymbol{K}_B = \begin{bmatrix} \boldsymbol{K}^{(1)} & \widetilde{\boldsymbol{K}}^{(2)} \\ \widetilde{\boldsymbol{K}}^{(2)T} & 2\widetilde{\boldsymbol{K}}^{(3)} \end{bmatrix} \tag{31}$$

is positive definite.

To extend this discussion to include the structural-thermal coupling terms $K_{ijl}^{(th)}$, and $F_{il}^{(th)}$, note first that these parameters can be expressed as [19]

$$K_{mnp}^{(th)} = \int_{\Omega_0} \frac{\partial U_i^{(m)}}{\partial X_k} \frac{\partial U_i^{(n)}}{\partial X_j} C_{jklr}\, \alpha_{lr}\, T^{(p)}\, d\boldsymbol{X} \tag{32}$$

and

$$F_{mn}^{(th)} = \int_{\Omega_0} \frac{\partial U_i^{(m)}}{\partial X_k} C_{iklr}\, \alpha_{lr}\, T^{(n)}\, d\boldsymbol{X}\,. \tag{33}$$

which are of the same form as Eqs (21)-(24) but involve the strain term $\alpha_{lr}\, T^{(n)}$ where $\boldsymbol{\alpha}$ is the coefficient of thermal expansion tensor and $T^{(n)}(\boldsymbol{X})$ is the *n*th basis function for the temperature in the continuous domain $\boldsymbol{X} \in \Omega_0$.

Next, proceed in reverse of Eqs (27)-(28) and define

$$E_C = \int_{\Omega_0} \left(w_m \frac{\partial U_i^{(m)}}{\partial X_j} + v_I\, Z_{ij}^{(I)} + z_m\, \alpha_{ij}\, T^{(m)} \right) C_{ijkl} \left(w_n \frac{\partial U_k^{(n)}}{\partial X_l} + v_J\, Z_{kl}^{(J)} + z_n\, \alpha_{kl}\, T^{(n)} \right) d\boldsymbol{X} \tag{34}$$

which is positive for all w_m, v_I, and z_m. Expanding the products in the integrand leads to

$$E_C = \begin{bmatrix} \boldsymbol{w}^T & \boldsymbol{v}^T & \boldsymbol{z}^T \end{bmatrix} \begin{bmatrix} \boldsymbol{K}^{(1)} & \widetilde{\boldsymbol{K}}^{(2)} & \boldsymbol{F}^{(th)} \\ \widetilde{\boldsymbol{K}}^{(2)T} & 2\widetilde{\boldsymbol{K}}^{(3)} & \widetilde{\boldsymbol{K}}^{(th)} \\ \boldsymbol{F}^{(th)T} & \widetilde{\boldsymbol{K}}^{(th)T} & \boldsymbol{K}^{(tt)} \end{bmatrix} \begin{bmatrix} \boldsymbol{w} \\ \boldsymbol{v} \\ \boldsymbol{z} \end{bmatrix} \tag{35}$$

where $\widetilde{\boldsymbol{K}}^{(th)}$ is the M^2xμ rectangular array obtained by reshaping the third order tensor $\boldsymbol{K}^{(th)}$ according to

$$\widetilde{K}_{Ip}^{(th)} = \hat{K}_{ijp}^{(th)} \qquad \text{with} \qquad I=(i\text{-}1)M+j \tag{36}$$

and $\boldsymbol{K}^{(tt)}$ is the μxμ symmetric, positive definite matrix of components

$$K_{mn}^{(tt)} = \int_{\Omega_0} \alpha_{jk}\, T^{(m)}\, C_{jklr}\, \alpha_{lr}\, T^{(n)}\, d\boldsymbol{X} \tag{37}$$

Since the expression E_C of Eq. (34) is positive for all w_m, v_I, and z_m, it is concluded that the QxQ ($Q = M + \mu + M^2$) symmetric matrix $\boldsymbol{K}_C$

$$\boldsymbol{K}_C = \begin{bmatrix} \boldsymbol{K}^{(1)} & \widetilde{\boldsymbol{K}}^{(2)} & \boldsymbol{F}^{(th)} \\ \widetilde{\boldsymbol{K}}^{(2)T} & 2\widetilde{\boldsymbol{K}}^{(3)} & \widetilde{\boldsymbol{K}}^{(th)} \\ \boldsymbol{F}^{(th)T} & \widetilde{\boldsymbol{K}}^{(th)T} & \boldsymbol{K}^{(tt)} \end{bmatrix} \tag{38}$$

is positive definite.

The above property provides a clear path for the simulation of parameters $K_{ij}^{(1)}$, $K_{ijl}^{(2)}$, $K_{ijlp}^{(3)}$, $K_{ijl}^{(th)}$, and $F_{il}^{(th)}$ within the maximum entropy nonparametric approach. Specifically, form first the matrix $\overline{\boldsymbol{K}}_C$ of the mean model from the parameters $K_{ij}^{(1)}$, $K_{ijl}^{(2)}$, $K_{ijlp}^{(3)}$, $K_{ijl}^{(th)}$, $F_{il}^{(th)}$, and $K_{mn}^{(tt)}$ of the finite element model of the mean structure. Then, proceed with the simulation of random matrices $\boldsymbol{K}_C$ according to Eqs (11)-(14) and Fig. 1, i.e.,

$$\overline{\boldsymbol{K}}_C = \overline{\boldsymbol{L}}_{\boldsymbol{K}}\, \overline{\boldsymbol{L}}_{\boldsymbol{K}}^T \qquad \text{and} \qquad \boldsymbol{K}_C = \overline{\boldsymbol{L}}_{\boldsymbol{K}}\, \boldsymbol{H}_{\boldsymbol{K}}\, \boldsymbol{H}_{\boldsymbol{K}}^T\, \overline{\boldsymbol{L}}_{\boldsymbol{K}}^T \tag{39),(40}$$

where (assuming a Cholesky decomposition of $\overline{\boldsymbol{K}}_C$)

$$\overline{\boldsymbol{L}}_{\boldsymbol{K}} = \begin{pmatrix} \overline{\boldsymbol{L}}_{SS}^{(1)} & \boldsymbol{0} & \boldsymbol{0} \\ \overline{\boldsymbol{L}}_{SS}^{(2)} & \overline{\boldsymbol{L}}_{SS}^{(3)} & \boldsymbol{0} \\ \overline{\boldsymbol{L}}_{TS}^{(1)} & \overline{\boldsymbol{L}}_{TS}^{(2)} & \overline{\boldsymbol{L}}_{TT} \end{pmatrix} \qquad \text{and} \qquad \boldsymbol{H}_{\boldsymbol{K}} = \begin{pmatrix} \boldsymbol{H}_{SS}^{(1)} & \boldsymbol{0} & \boldsymbol{0} \\ \boldsymbol{H}_{SS}^{(2)} & \boldsymbol{H}_{SS}^{(3)} & \boldsymbol{0} \\ \boldsymbol{H}_{TS}^{(1)} & \boldsymbol{H}_{TS}^{(2)} & \boldsymbol{H}_{TT} \end{pmatrix} \tag{41),(42}$$

where the subscripts *S* and *T* refer to the structural and thermal part of the model.

Finally, decompose the random matrices $\boldsymbol{K}_C$ of Eq. (40) according to the partition of Eq. (38) and identify the random parameters $K_{ij}^{(1)}$, $K_{ijl}^{(2)}$, $K_{ijlp}^{(3)}$, $K_{ijl}^{(th)}$, and $F_{il}^{(th)}$. It is interesting to note in the above format that the simulation of the thermal-structural coupling

properties $K_{ijl}^{(th)}$ and $F_{il}^{(th)}$ is achieved in conjunction with the structural only model but independently of the thermal properties, e.g., capacitance, conductance.

In the context of unheated linear structures, the constraint of Eq. (8) guarantees that the mean squared response is finite, see [1-3]. Since these structures are a subset of the nonlinear geometric ones subjected to temperature considered here, i.e., the matrix $\boldsymbol{K}_C$ reduces to $\boldsymbol{K}^{(1)}$, Eq. (8) will once again be imposed. Note however that no theoretical result regarding the finiteness of the mean square response in the nonlinear heated case is currently available.

While the above developments assumed that the elasticity tensor and thermal expansion were independent of temperature, linear variations of these properties can also be considered in a deterministic ROM formulation, see [20], and in an uncertain one, see [19] for the extension of Eqs (3), (32)-(38) to the case of the thermal expansion varying with temperature as an example of the process.

IMPLEMENTATION CHALLENGES

The above process seems clear and well defined but after a closer inspection and trials, three key challenges were encountered. They are described below separately and their solutions briefly discussed, see Appendix A and B for details.

(A) Identified coefficients vs. symmetric coefficients

The first challenge in applying the above methodology is that the stiffness coefficients present in the mean matrix $\overline{\boldsymbol{K}}_C$ are neither directly not fully identifiable by the standard methods discussed in [19-23]. To clarify this issue, it should first be recognized that a series of terms in Eq. (3) involve the same monomials of the generalized coordinates, e.g. $K_{ijl}^{(2)}$ and

$K_{ilj}^{(2)}$, and thus these terms may naturally be regrouped leading to the ROM governing equations

$$M_{ij}\ddot{q}_j + D_{ij}\dot{q}_j + \left[K_{ij}^{(1)} + K_{ijl}^{(th)}\tau_l \right] q_j + \bar{K}_{ijl}^{(2)} q_j q_l + \bar{K}_{ijlp}^{(3)} q_j q_l q_p = F_i + F_{il}^{(th)}\tau_l \,. \quad (43)$$

This equation is very similar to Eq. (3) except that there is no repetition in the monomials because $\bar{K}_{ijl}^{(2)}$ and $\bar{K}_{ijlp}^{(3)}$ are nonzero only for $j \le l$ and $j \le l \le p$. Note further that the identification methods discussed in [19-23] yield the coefficients $\bar{K}_{ijl}^{(2)}$ and $\bar{K}_{ijlp}^{(3)}$ not $K_{ijl}^{(2)}$ and $K_{ijlp}^{(3)}$ but it is these latter ones which are necessary in Eq. (38). Accordingly, an intermediate step in the simulation process is to transform one set of quadratic and cubic coefficients ($\bar{K}_{ijl}^{(2)}$ and $\bar{K}_{ijlp}^{(3)}$, referred to as "identified") into another ($K_{ijl}^{(2)}$ and $K_{ijlp}^{(3)}$, referred to as "symmetric"). To this end, comparing Eqs (3) and (43) it is found that

$$\bar{K}_{mnl}^{(2)} = \begin{cases} 0 & \text{for } l < n \\ K_{mnn}^{(2)} & \text{for } l = n \\ K_{mnl}^{(2)} + K_{mln}^{(2)} & \text{for } l > n \end{cases} \quad \bar{K}_{mnlp}^{(3)} = \begin{cases} 0 & \text{unless } p \ge l \ge n \\ K_{mnnn}^{(3)} & \text{for } p = l = n \\ K_{mnll}^{(3)} + K_{m\ln l}^{(3)} + K_{mlln}^{(3)} & \text{for } p = l > n \\ K_{mpll}^{(3)} + K_{mlpl}^{(3)} + K_{mllp}^{(3)} & \text{for } p > l = n \\ 2K_{mnlp}^{(3)} + 2K_{mpln}^{(3)} + 2K_{mlpn}^{(3)} & \text{for } p > l > n \end{cases} \quad (44)$$

Moreover, as discussed in [13], the symmetry properties of the elasticity tensor and the form of Eqs (23) and (24) also imply that

$$\hat{K}_{ijl}^{(2)} = \hat{K}_{ilj}^{(2)} \quad (45)$$

and

$$K_{mnlp}^{(3)} = K_{nmlp}^{(3)} = K_{mnpl}^{(3)} = K_{lpmn}^{(3)} \,. \quad (46)$$

Unfortunately, Eqs (44) and (45) are not sufficient to yield a unique set of values of $K_{ijl}^{(2)}$ and $K_{ijlp}^{(3)}$ from given values of $\bar{K}_{ijl}^{(2)}$ and $\bar{K}_{ijlp}^{(3)}$ except for the one mode situation, i.e., all

indices equal. The problem is further compounded by a similar issue in the transformation of the quadratic parameters $K_{ijl}^{(2)}$ to their related coefficients $\hat{K}_{ijl}^{(2)}$ using Eq. (22). It is thus not possible to uniquely map the identified coefficients $\bar{K}_{ijl}^{(2)}$ and $\bar{K}_{ijlp}^{(3)}$ to the corresponding blocks of the matrix $\boldsymbol{K}_C$.

This problem is not specific to the matrix $\boldsymbol{K}_C$, it is also encountered in the purely structural situation, i.e., when constructing the matrix $\boldsymbol{K}_B$, and it has recently been addressed [29] based on the following observations:

(a) the decomposition of the identified coefficients $\bar{K}_{ijl}^{(2)}$ and $\bar{K}_{ijlp}^{(3)}$ into the parameters $\hat{K}_{ijl}^{(2)}$ and $K_{ijlp}^{(3)}$ should only be a function of the modes *i*, *j*, *l* and *i*, *j*, *l*, *p*, respectively.

(b) the decomposition should ensure that the matrix $\boldsymbol{K}_B$ corresponding to the *M* selected modes or any subset of these modes, is positive definite, or as close as possible to it.

Accordingly, it was proposed in [29] to proceed in steps, resolving the indeterminacy on all distinct two-mode coefficients, i.e., $\hat{K}_{ijj}^{(2)}$, $\hat{K}_{iij}^{(2)}$, $\hat{K}_{jij}^{(2)}$, $\hat{K}_{jii}^{(2)}$, $K_{iiij}^{(3)}$, $K_{iijj}^{(3)}$, $K_{ijij}^{(3)}$, and $K_{ijjj}^{(3)}$, by enforcing that they satisfy Eqs (22) and (44) and lead to a maximum of the lowest eigenvalue of the matrix $\boldsymbol{K}_B$ corresponding to the two modes *i* and $j > i$.

Next, the indeterminacy on all distinct three-mode coefficients, i.e., $\hat{K}_{ijl}^{(2)}$, $\hat{K}_{jil}^{(2)}$, $\hat{K}_{lij}^{(2)}$, $K_{iilp}^{(3)}$, and $K_{ilip}^{(3)}$, was similarly resolved by enforcing that they satisfy Eqs (22) and (44) and lead to a maximum of the lowest eigenvalue of the matrix $\boldsymbol{K}_B$ corresponding to the three modes $p > l > j > i$.

Finally, the indeterminacy on all distinct four-mode coefficients, i.e., $K^{(3)}_{ijlp}$, $K^{(3)}_{iljp}$, and $K^{(3)}_{ipjl}$, was again resolved by enforcing that they satisfy Eqs (22) and (44) and lead to a maximum of the lowest eigenvalue of the matrix $\boldsymbol{K}_B$ corresponding to the four modes *i* and *j* > *i* and *l* > *j* > *i*. Note that the above operations do not alter the mean model, they are only necessary to introduce the uncertainty.

(B) Lack of positive definiteness of the matrix $\boldsymbol{K}_B$

After the series of optimization efforts carried out in the previous section, it was found that the resulting matrix $\boldsymbol{K}_B$ may not be positive definite, see [29] for justification and examples. In such cases, it was proposed that this matrix either be modified to become positive definite or that only its positive definite part be randomized. These options proposed in [29] are summarized here in Appendix A and their applicability to the matrix $\boldsymbol{K}_C$ discussed. In performing this operation, it is important that the response of the mean model not be altered visibly, see discussion of Appendix A and [29] for options.

(C) The matrix $\boldsymbol{K}^{(tt)}$ is not well identifiable

An unusual feature of the matrix $\boldsymbol{K}_C$ is that it involves the matrix $\boldsymbol{K}^{(tt)}$ which does not appear in the reduced order model equations, Eqs (3) or (43), and thus its identification/selection requires further discussions.

At first, it was intended to identify the mean value of this matrix. An indirect approach was devised in which the terms $\alpha_{lr}\, T^{(n)}$ and $C_{jklr}\, \alpha_{lr}\, T^{(n)}$ were recognized as components *lr* and *jk* of the thermal only strain tensor $\boldsymbol{\varepsilon}^{(th)}_n$ and the corresponding stress tensor $\boldsymbol{\sigma}^{(th)}_n$ both induced by the thermal mode *n*. Then, the coefficient $K^{(tt)}_{mn}$ corresponds to the integral

(summation over all nodes/elements) of the product $\boldsymbol{\varepsilon}_m^{(th)} : \boldsymbol{\sigma}_n^{(th)}$. It remained then to determine the thermal strain and stresses. This was accomplished by applying temperature along mode *n* on the structure with all of its nodes restrained, the resulting stress distribution would then equal $\boldsymbol{\sigma}_n^{(th)}$ and the corresponding strains $\boldsymbol{\varepsilon}_n^{(th)}$ could then be obtained using the tensor of elasticity.

The implementation of this identification approach within Nastran was not successful, leading, even for very small reduced order models, to matrices $\boldsymbol{K}_C$ that were not positive definite. Accordingly, another strategy was devised. Specifically, since $\boldsymbol{K}^{(tt)}$ is only present in $\boldsymbol{K}_C$, not in Eqs (3) and (43), its determination is effectively part of the stochastic modeling effort. Then, its value being unclear, it was argued that $\boldsymbol{K}^{(tt)}$ should be determined by the entropy optimization effort. It is shown in Appendix B that this condition leads to $\bar{\boldsymbol{L}}_{TT}$, in Eq. (41), is equal to the identity matrix.

This result completes the determination of the lower triangular matrix $\bar{\boldsymbol{L}}_{\boldsymbol{K}}$, its structural only blocks $\bar{\boldsymbol{L}}_{SS}^{(1)}$, $\bar{\boldsymbol{L}}_{SS}^{(2)}$, and $\bar{\boldsymbol{L}}_{SS}^{(3)}$ are determined by the Cholesky decomposition of the positive definite $\boldsymbol{K}_B$ resulting of the steps (A) and (B) above. Moreover, from Eqs (38) and (39),

$$\bar{\boldsymbol{L}}_{TS}^{(1)} = \boldsymbol{F}^{(th)T} \left[\bar{\boldsymbol{L}}_{SS}^{(1)} \right]^{-T} \qquad \text{and} \qquad \bar{\boldsymbol{L}}_{TS}^{(2)} = \left[\tilde{\boldsymbol{K}}^{(th)T} - \bar{\boldsymbol{L}}_{TS}^{(1)} \bar{\boldsymbol{L}}_{SS}^{(2)T} \right] \left[\bar{\boldsymbol{L}}_{SS}^{(3)} \right]^{-T} . \quad (47),(48)$$

IMPLEMENTATION OF SEPARATE UNCERTAINTY LEVELS

The matrix $\boldsymbol{K}_C$ involves two different properties of the structure: its elasticity tensor and its coefficient of thermal expansion the level of variability of which may be different. This situation is somewhat similar to the maximum entropy modeling of uncertainties achieved in

[12] (for a rotordynamics application) and [30] (for an implementation focused on material properties). In these investigations, it was proposed to *compound* the effects, i.e., $\boldsymbol{H}$ matrices, induced by the two types of uncertainties present, i.e., those who maintain a high level symmetry and those who do not.

In the present context, the compounding of the uncertainties in the elasticity and thermal expansion tensors can be achieved by expressing $\boldsymbol{H}_{\boldsymbol{K}}$ as

$$\boldsymbol{H}_{\boldsymbol{K}} = \boldsymbol{H}_T \, \boldsymbol{H}_S \tag{49}$$

where

$$\boldsymbol{H}_T = \begin{pmatrix} \boldsymbol{I} & \boldsymbol{0} & \boldsymbol{0} \\ \boldsymbol{0} & \boldsymbol{I} & \boldsymbol{0} \\ \boldsymbol{H}_{TS}^{(1)} & \boldsymbol{H}_{TS}^{(2)} & * \end{pmatrix} \quad \text{and} \quad \boldsymbol{H}_S = \begin{pmatrix} \boldsymbol{H}_{SS}^{(1)} & \boldsymbol{0} & \boldsymbol{0} \\ \boldsymbol{H}_{SS}^{(2)} & \boldsymbol{H}_{SS}^{(3)} & \boldsymbol{0} \\ \boldsymbol{0} & \boldsymbol{0} & \boldsymbol{I} \end{pmatrix}. \tag{50), (51}$$

In the above equations, $\boldsymbol{I}$ denotes the identity matrix of appropriate dimensions and the * designates a matrix partition which is irrelevant as it does not arise further in the computations, affecting only the matrix $\boldsymbol{K}^{(tt)}$ of the random structures. Rewriting Eq. (40) with (49) yields

$$\boldsymbol{K}_C = \bar{\boldsymbol{L}}_{\boldsymbol{K}} \, \boldsymbol{H}_T \, \boldsymbol{H}_S \, \boldsymbol{H}_S^T \, \boldsymbol{H}_T^T \, \bar{\boldsymbol{L}}_{\boldsymbol{K}}^T = \left(\bar{\boldsymbol{L}}_{\boldsymbol{K}} \, \boldsymbol{H}_T \right) \boldsymbol{H}_S \, \boldsymbol{H}_S^T \left(\bar{\boldsymbol{L}}_{\boldsymbol{K}} \, \boldsymbol{H}_T \right)^T \tag{52}$$

it is seen that the randomization of the structural properties is a two-step process. First, is the randomization by $\boldsymbol{H}_T$ transforming the mean model matrix $\overline{\boldsymbol{K}}_C$ into the random one

$$\boldsymbol{K}_C = \bar{\boldsymbol{L}}_{\boldsymbol{K}} \, \boldsymbol{H}_T \, \boldsymbol{H}_T^T \, \bar{\boldsymbol{L}}_{\boldsymbol{K}}^T = \left(\bar{\boldsymbol{L}}_{\boldsymbol{K}} \, \boldsymbol{H}_T \right) \left(\bar{\boldsymbol{L}}_{\boldsymbol{K}} \, \boldsymbol{H}_T \right)^T \tag{53}$$

which serves as a mean model for the further randomization by $\boldsymbol{H}_S$.

Note in the above process that the random matrix $\boldsymbol{H}_T$ only affects the *ST* blocks of $\boldsymbol{K}_C$, i.e., $K_{ijl}^{(th)}$ and $F_{il}^{(th)}$, and thus it models the uncertainty associated with the thermal expansion which is present only in those terms. On the contrary, the components of the random matrix $\boldsymbol{H}_S$ will affect all blocks of the $\boldsymbol{K}_C$ matrix and thus is appropriate for the

modeling of the uncertainty in the elasticity tensor which is present in all elements of $\boldsymbol{K}_C$.

The selection of blocks of the $\boldsymbol{H}_S$ and $\boldsymbol{H}_T$ matrices as the identity or the zero matrix does not conform with the discussion of Eqs (5)-(14) and Fig. 1 but it is consistent with the extended nonparametric formulation developed in [4] in which the uncertainty associated with the corresponding eigenvalues is set to zero while no constraint is imposed on the variability of the other eigenvalues. Accordingly, the block $\boldsymbol{H}_{TS}^{(1)}$ and $\boldsymbol{H}_{TS}^{(2)}$ are simulated as off-diagonal elements of the matrix $\boldsymbol{H}$ of Fig. 1, i.e., as independent identically distributed zero mean Gaussian random variables with standard deviation σ related to a uncertainty level δ_T. Finally, the 2x2 top left block of $\boldsymbol{H}_S$ is simulated as in Eqs (5)-(14) and Fig. 1 with the appropriate matrix size, i.e., $M + M^2$, and uncertainty level δ_S.

EXAMPLE OF APPLICATION

Mean Model

The panel of [20] was considered to demonstrate the application of the above uncertainty modeling strategies and provide a first assessment of the effects of on the structural-thermal response uncertainty on the thermal properties and/or on the coefficient of thermal expansion.

Following [20], the panel was modeled as an isotropic clamped-clamped beam with properties given in Table 1 and was modeled by finite elements in MSC.Nastran. Structurally, the beam was considered as one-dimensional and was discretized using 40 beam elements ("CBEAM" within Nastran). Thermally, the structure was considered as a two-dimensional object discretized with 40 4-node elements ("CQUAD4" within Nastran) along its length and 6 through the thickness thereby allowing the capture of the temperature distribution along the beam and across its thickness.

Table 1. Clamped-Clamped Beam Mean Properties

Beam Length (L)	0.2286 m
Cross-section Width (w)	0.0127 m
Cross-section Thickness (h)	$7.88\ 10^{-4}$ m
Density	2700 kg/m^3
Young's Modulus	73,000 MPa
Shear Modulus	27,730 MPa
Coeff. Thermal Expansion	$2.5\ 10^{-5}$ /°C
Mesh (CBEAM)	40

The beam was subjected to a triangular flux of width $2\Delta=0.4\ L$, see Fig. 2, oscillating about the middle of the beam ($a_0 = L/2$) with a frequency Ω and an amplitude $\bar{\delta}=0.075\ L$. The peak heat flux was selected so that the peak temperature on the upper surface of the beam would be 10°C for the steady problem ($\Omega = 0$) while the bottom surface was maintained at 0°C. The ends of the beam were also maintained at 0°C. This thermal loading led to a tip static deflection of 0.65 thickness and thus to a nonlinear geometric behavior.

A reduced order model of the panel was constructed using 17 structural modes and 12 thermal basis functions, see [20] for details, which led to an excellent prediction of the full Nastran results. Of particular interest here is the peak response vs. frequency Ω which displays a peak for Ω approximately equal to 1/2 of the first linear natural frequency of the beam, see Fig. 3.

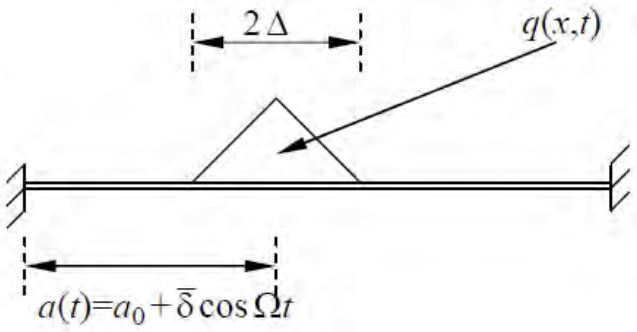

Figure 2. Beam panel subjected to an oscillating flux.

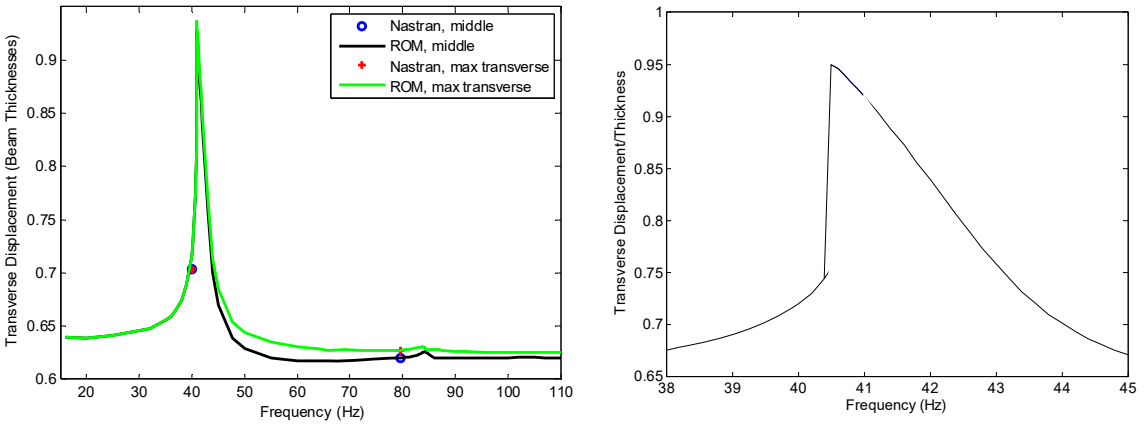

Figure 3. Maximum transverse deflection on the beam and at the beam middle as a function of the flux oscillation frequency Ω as determined from the ROM and Nastran computations.

Uncertainty Modeling and Analysis

The consideration of uncertainty on the conductance properties was first carried out. In selecting the simulation strategy, Eqs (5)-(14) or Eqs (15)-(20), it was first noted in the results presented in [20] that the temperature distribution rapidly decayed to zero away from the zone heated by the triangular flux. This observation suggested that the temperature distribution exhibited a localized behavior. To confirm this expectation, a concentrated flux was applied to the beam and the resulting steady temperature was determined using a full finite element analysis, see Fig. 4(a). It is clearly seen that the temperature is strongly localized. In fact, this behavior results from the fixed temperature boundary condition on the bottom. If this condition was replaced by an adiabatic one, the temperature distribution would be the one shown in Fig. 4(b) which is extended to the entire panel, i.e., exhibits a global behavior.

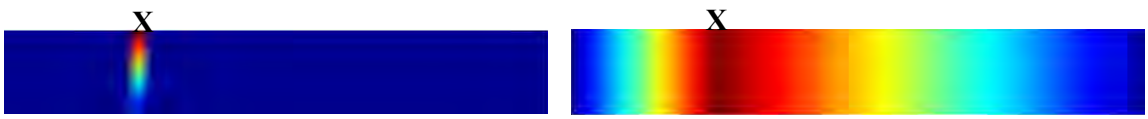

(a) (b)

Figure 4. Distribution of temperature in a beam due to a single heat flux at the location marked by X. (a) Adiabatic boundary condition on beam top but zero temperature on bottom. (b) Adiabatic boundary conditions throughout.

The localized vs. global character of the temperature distribution can also be assessed from the eigenvalues of the conductance-capacitance problem as shown in Fig. 5. A localized character is associated with a series of close eigenvalues occurring at a nonzero value, see Fig. 5(a), while a global problem results when these values are spread in relative values. The existence of these two opposite behaviors for the mean model suggests that the uncertainty modeling strategy of the conductance and capacitance matrices should similarly be able to induce mostly global or mostly local variations. On this basis, the maximum entropy approach for localized responses, Eqs (15)-(20), is proposed here to model these uncertain matrices regardless of the thermal boundary conditions.

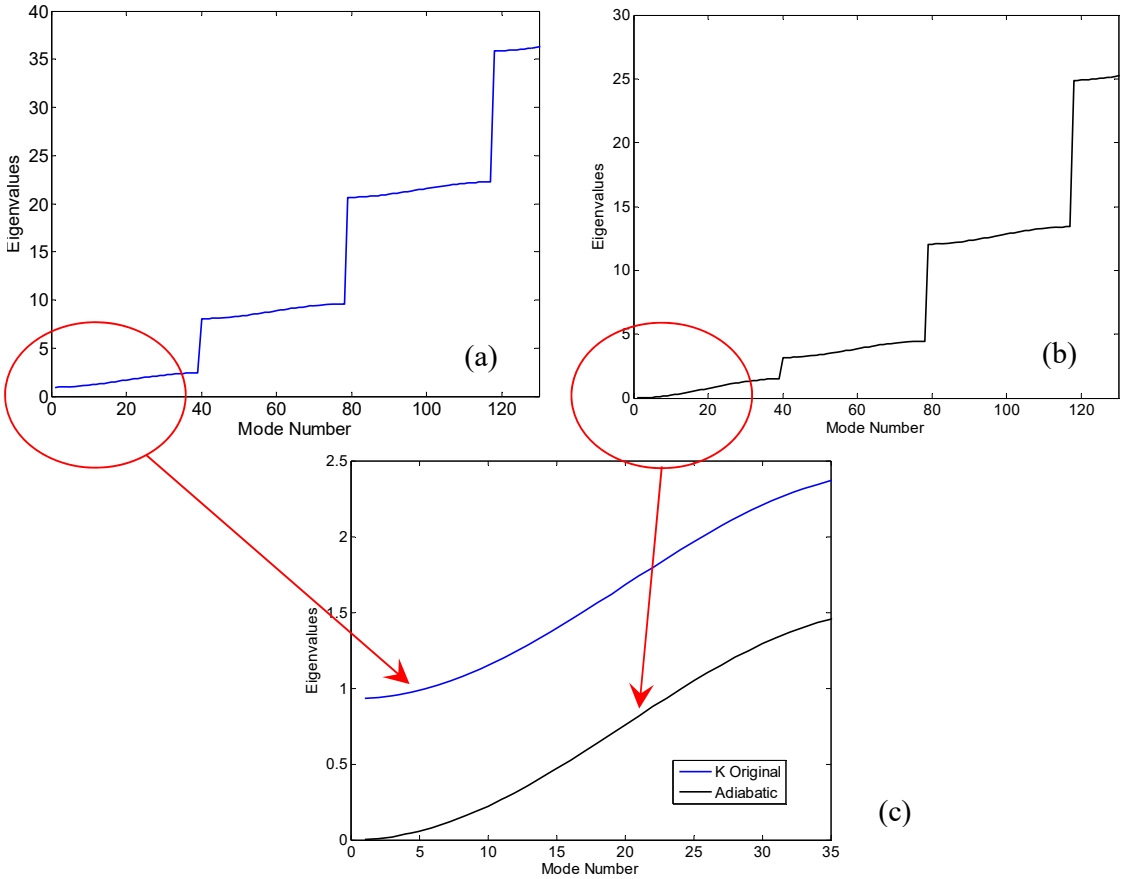

Figure 5. Comparisons of eigenvalues of the conductance-capacitance problem. (a) Case (a) of Fig. 4, (b) Case (b) of Fig. 4. (c) Comparison.

Given the localized behavior of the current example problem (with the fixed temperature boundary conditions), see Fig. 4(a) or 5(a), it was expected that the uncertainty would mostly be introduced on the local component of the model, i.e., $\widetilde{K}_L$. Nevertheless, the effects of introducing the uncertainty on $\widetilde{K}_G$ and $\widetilde{K}_L$ were separately assessed first then jointly. The overall uncertainty level was quantified as in [2] by the dispersion parameter δ of Eq. (14).

Then, shown in Fig. 6 is the temperature distribution on the beam at a representative time induced by the flux oscillating at $\Omega = 2\pi \times 40$ rad/sec (or 40Hz). The yellow band represents the range of values between the 5th and 95th percentile of the temperature obtained at each node point for a value of δ=0.05 on the global component of the conductance matrix, $\widetilde{K}_G$, and no uncertainty on its local counterpart, $\widetilde{K}_L$. Note that the uncertainty band extends very far reaching the boundaries as expected from a global behavior. On the contrary, the temperature induced by a similar uncertainty in $\widetilde{K}_L$ remains very localized to the middle of the beam where the flux is defined, see Fig. 7. Combining these two uncertainties leads to the results of Fig. 8 which exhibit a broad band near the flux and only a very small band away from it as would be physically expected.

Having successfully produced random samples of the temperature distribution, it was next desired to propagate this uncertainty to the structural response. Each sample of the temperature was input to the structural ROM to determine the response over the range of oscillation frequencies Ω corresponding to the peak in Fig. 3(b). The resulting uncertainty band corresponding to the 5th-95th percentile was then evaluated for each frequency and is shown in Fig. 9. Note the broad range of frequencies over which the peak is observed and that the width of the (yellow) uncertainty band in the response at peak is wider than the one on the temperature, i.e., about ± 10% of the mean value vs. ± 5% in Fig. 8.

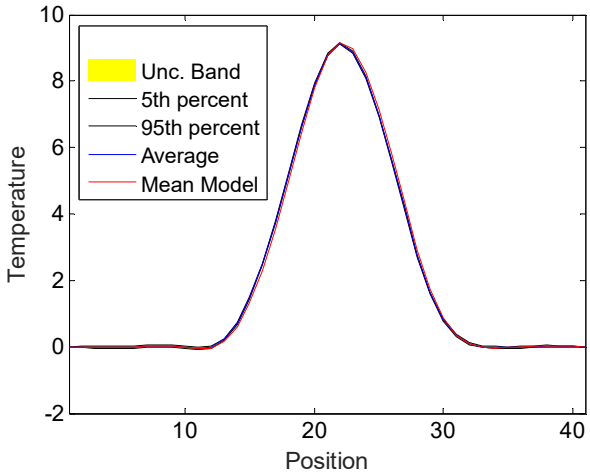

Figure 6. Uncertainty band induced by introducing uncertainty only in the global component of the ROM conductance matrix. 40Hz oscillating triangular heat flux.

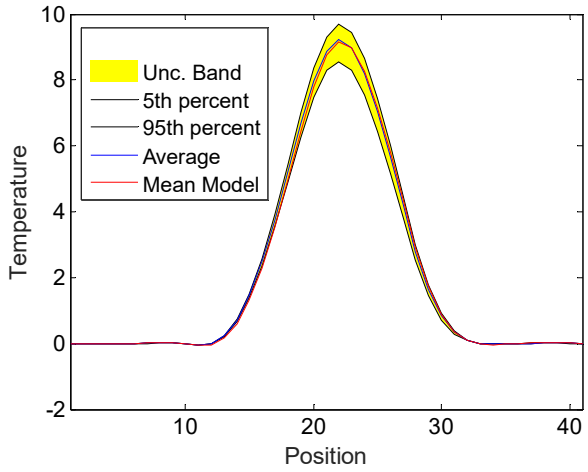

Figure 7. Uncertainty band induced by introducing uncertainty only in the local component of the ROM conductance matrix. 40Hz oscillating triangular heat flux.

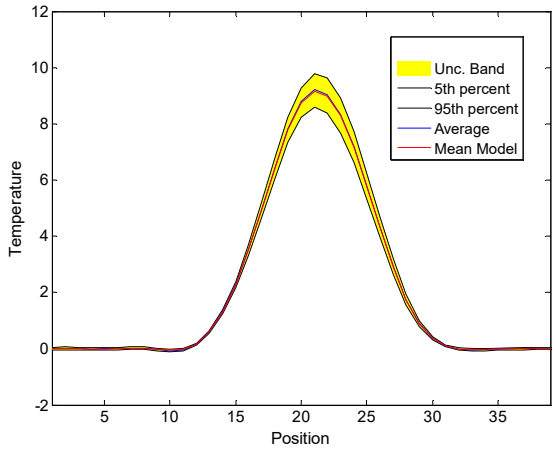

Figure 8. Uncertainty band induced by introducing uncertainty on both local and global components of the ROM conductance matrix. 40Hz oscillating triangular heat flux.

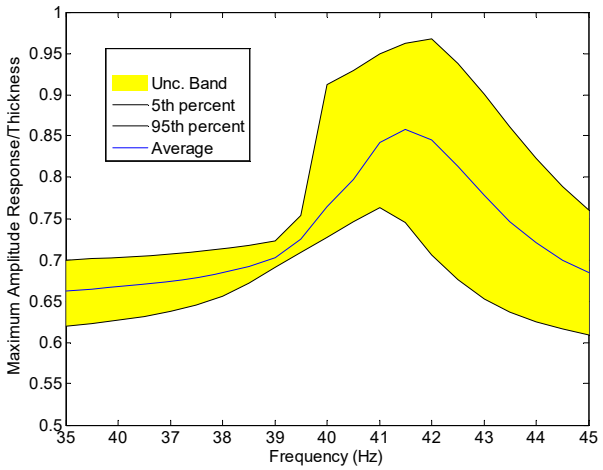

Figure 9. Uncertainty band on peak structural (transverse) response as a function of the flux oscillating frequency. Uncertainty on conductance.

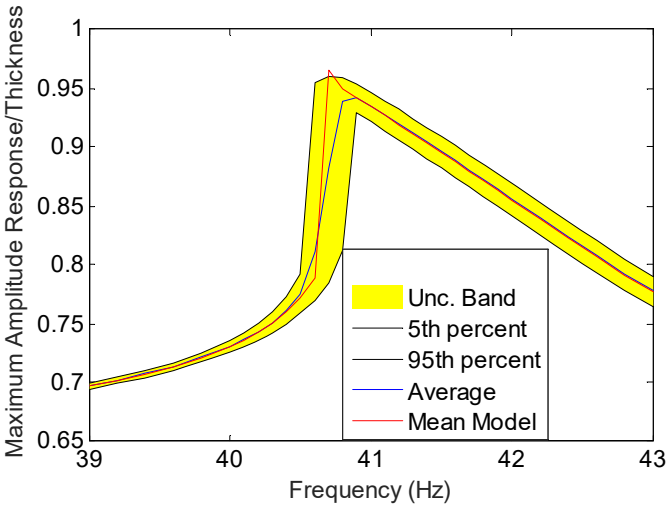

Figure 10. Uncertainty band on peak structural (transverse) response as a function of the flux oscillating frequency. Uncertainty on thermal-structural coupling parameters only.

Uncertainty in the structural model was considered next and it was first observed that the mean model matrix $\bar{\boldsymbol{K}}_B$ was found to be not positive definite. This observation triggered the application of one of the remedies described in Appendix A. More specifically, the uncertainty analysis was carried out according to Eq. (A.11)-(A.13) with the matrix $\boldsymbol{K}_{11}$ of size $N_p = 20$. This approach guarantees that the mean model predictions are not modified. Uncertainty in the thermal expansion, i.e., on the thermal-structural coupling, was introduced

first through the matrix $\boldsymbol{H}_T$ with $\boldsymbol{H}_S$ set to the identity matrix. This effort was carried out with a value of $\delta = 2\times10^{-4}$. This value seems very small but it gives rise to coefficients of variation of 0.51% (l =1), 0.29% (l =3), 0.73% (l =5) on the parameters $K_{11l}^{(th)}$ and 0.48% (l =1), 2.53% (l =3), 7.09% (l =5) on $F_{1l}^{(th)}$ which are the key driving terms to the first and dominant structural mode. Then, shown in Fig. 10 is the uncertainty band and mean model prediction of the peak beam (transverse) response as a function of frequency. Note that the width of the band is larger than the above coefficients of variation of the parameters demonstrating a definite sensitivity of the response with respect to the coefficient of thermal expansion and thus the importance of carrying such uncertainty analyses.

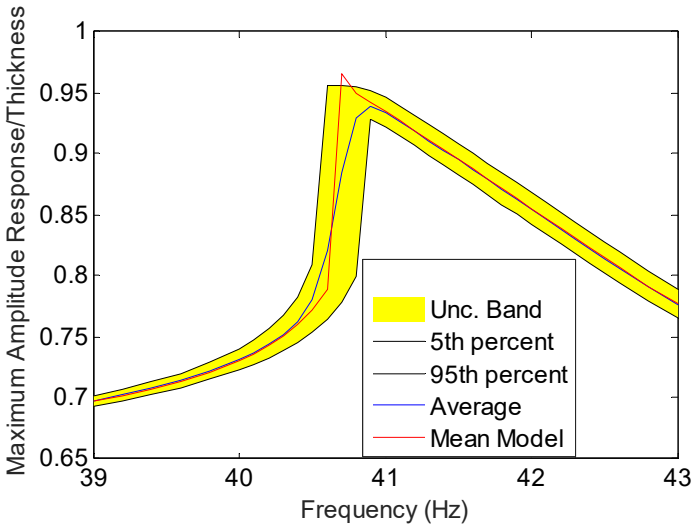

Figure 11. Uncertainty band on peak structural (transverse) response as a function of the flux oscillating frequency. Uncertainty on structural parameters only.

The uncertainty on the structural part only was also considered and implemented through the matrix $\boldsymbol{H}_S$ with $\boldsymbol{H}_T$ set to the identity matrix. This effort was carried out with a value of $\delta = 0.03$ which corresponds to a coefficient of variation of the first natural frequency of 0.34%. Then, shown in Fig. 11 are the uncertainty band and mean model prediction of the

peak beam (transverse) response as a function of frequency. Once again, it is seen that the uncertainty level on the response is much larger than it is for the model coefficients, confirming the sensitivity of the response. Finally, shown in Fig. 12 is uncertainty band induced by both structural and thermal expansion uncertainties. As expected, this band is wider than the ones seen in Figs. 10 and 11 and corresponding to each uncertainty separately.

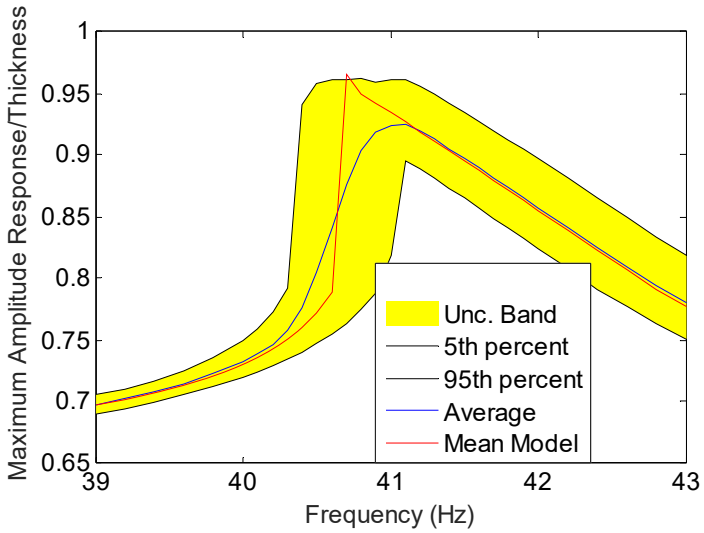

Figure 12. Uncertainty band on peak structural (transverse) response as a function of the flux oscillating frequency. Uncertainty on structural and thermal-structural coupling parameters.

SUMMARY

The focus of this investigation has been on the comprehensive modeling and assessment of uncertainty on thermal and structural properties on the temperature and response of heated structures. This study was conducted directly on coupled thermal-structural reduced order models using maximum entropy concepts to randomize the associated matrices. Moreover, nonlinear geometric effects were included in the structural ROM. The resulting analysis is thus carried out very efficiently as compared to a similar effort involving a modeling of uncertainty at the finite element model level.

The uncertainty on the conductance properties was considered first. Using a particular

beam example, it was shown that the behavior of the temperature distribution may be strongly dependent on the boundary conditions, i.e., being localized near the applied flux or very global. Then, the simulation strategy chosen for the uncertain ROM conductance matrices is a recent extension of the nonparametric approach in which the local and global characters of the uncertainty on the temperature can be separately controlled. Accordingly, this approach is applicable to the various types of thermal boundary conditions. This uncertainty on the thermal properties was propagated to the nonlinear structural response by imposing the random temperature distributions on the panel. The results demonstrate a level of variability of the response that is similar to that of the temperature distributions.

The uncertainties on the structural, i.e., structural and thermal-structural coupling (thermal expansion) properties was considered next. It was shown that these uncertainties may indeed be modeled directly at the ROM level and both appear through the positive definite matrix $\boldsymbol{K}_C$ of Eq. (38). Yet, the formulation permits the imposition of uncertainties on either properties separately or together through their compounding in Eq. (49). Further, practical implementation details that appear when the mean ROM is identified from a black box finite element code were pointed out and resolved in a general setting. The application of these concepts to the beam example was finally performed and it was observed that a coefficient of variation around 0.5% of the key structural-thermal coupling terms led to an increased variability, of the order of ±2%, of the structural response near its peak demonstrating a significant sensitivity of this response with respect to the coefficient of thermal expansion uncertainty. A similar sensitivity was also observed with respect to the structural only parameters of the model.

ACKNOWLEDGEMENTS

The financial support of this work by the Air Force Multi University Research Initiative contract FA9550-15-1-0038 with Dr. Jean-Luc Cambier as Technical Monitor and the Air Force Office of Scientific Research grant FA9550-16-1-0021 with Dr. Jaimie Tiley as Technical Monitor are gratefully acknowledged.

APPENDIX A

As stated in the main text, the process to render the matrix $\boldsymbol{K}_B$ positive definite was achieved in [29]

(a) without affecting the part of $\boldsymbol{K}_B$ that is positive definite, e.g., the linear stiffness matrix $\boldsymbol{K}^{(1)}$, and

(b) inducing the smallest changes possible to this matrix.

The condition (a) has been achieved iteratively by constructing the biggest block of the original matrix $\boldsymbol{K}_B$ that is positive definite. This block is at least of size M since the linear stiffness matrix $\boldsymbol{K}^{(1)}$ is positive definite. Accordingly, the top left block of $\boldsymbol{K}_B$ of size M+1 is first considered and it is checked for positive definiteness (e.g., by constructing its Cholesky decomposition). If it is positive definite, the algorithm moves to the top left block of size M+2 and the process is repeated.

Otherwise, a permutation of the rows and columns M+1 and M+2 is performed. If the top left block of size M+1 is now positive definite, the algorithm accepts the permutation and moves forward to the top left block of size M+2. On the contrary, the permutation between rows M+1 and M+2 is reversed and a permutation of rows M+1 and M+3 is performed followed by a positive definiteness check. This process concludes when no permutation of

rows and columns achieves an increase in the size of the top left block of $\boldsymbol{K}_B$ which is positive definite.

At that point, the matrix $\boldsymbol{K}_B$ has been transformed in a symmetric matrix $\tilde{\boldsymbol{K}}_B$ which has the form

$$\tilde{\boldsymbol{K}}_B = \begin{bmatrix} \boldsymbol{K}_{11} & \boldsymbol{K}_{12} \\ \boldsymbol{K}_{12}^T & \boldsymbol{K}_{22} \end{bmatrix} \tag{A.1}$$

where $\boldsymbol{K}_{11}$ is positive definite and of size N_p, $\boldsymbol{K}_{12}$ is of size $N_p \times N_r$, and $\boldsymbol{K}_{22}$ is of size $N_r \times N_r$ where $N_r = M^2 + M - N_p$.

The task (b) above then proceeds with replacing the matrix $\tilde{\boldsymbol{K}}_B$ by

$$\hat{\boldsymbol{K}}_B = \begin{bmatrix} \boldsymbol{K}_{11} & \boldsymbol{K}_{12} \\ \boldsymbol{K}_{12}^T & \boldsymbol{K}_{22} \end{bmatrix} + \begin{bmatrix} \boldsymbol{0} & \boldsymbol{\Delta}_1 \\ \boldsymbol{\Delta}_1^T & \boldsymbol{\Delta}_2 \end{bmatrix} = \tilde{\boldsymbol{K}}_B + \boldsymbol{\Delta} \tag{A.2}$$

where the matrix $\boldsymbol{\Delta}$ will be selected to have the minimum Frobenius norm under the constraint that $\hat{\boldsymbol{K}}_B$ is at least positive semidefinite. The solution of this nonlinear optimization problem will be obtained iteratively through a sequence of linear optimization problems in which the positive definiteness constraint is enforced linearly. This process leads at iteration *m* to [29]

$$\boldsymbol{\Delta}_1 = \sum_{\tilde{\lambda}_i < 0} \mu_i \, \tilde{\boldsymbol{\psi}}_i^{(1)} \left[\tilde{\boldsymbol{\psi}}_i^{(2)} \right]^T \qquad \boldsymbol{\Delta}_2 = \sum_{\tilde{\lambda}_i < 0} \mu_i \, \tilde{\boldsymbol{\psi}}_i^{(2)} \left[\tilde{\boldsymbol{\psi}}_i^{(2)} \right]^T \tag{A.3),(A.4}$$

where $\tilde{\boldsymbol{\psi}}_i$ and $\tilde{\lambda}_i$ are the eigenvalues of the matrix $\hat{\boldsymbol{K}}_B$ at iteration *m*. Moreover, the eigenvectors are partitioned into vectors $\tilde{\boldsymbol{\psi}}_i^{(1)}$ and $\tilde{\boldsymbol{\psi}}_i^{(2)}$ of N_p and N_r components, respectively. That is, $\tilde{\boldsymbol{\psi}}_i^T = \left[\left[\tilde{\boldsymbol{\psi}}_i^{(1)} \right]^T \left[\tilde{\boldsymbol{\psi}}_i^{(2)} \right]^T \right]$. Finally, the coefficients μ_i are solutions of the linear system of equations

$$\sum_{\tilde{\lambda}_r < 0} \left(2\, a_{ri}\, b_{ri} + b_{ri}^2 \right) \mu_r = -\tilde{\lambda}_i \text{ with } a_{rs} = \left[\tilde{\boldsymbol{\psi}}_r^{(1)} \right]^T \tilde{\boldsymbol{\psi}}_s^{(1)} \text{ and } b_{rs} = \left[\tilde{\boldsymbol{\psi}}_r^{(2)} \right]^T \tilde{\boldsymbol{\psi}}_s^{(2)} \tag{A.5}$$

Solving the linear system of equations (A.5) yields the values of the coefficients μ_i which can then be reintroduced in Eq. (A.3) and (A.4) to yield the unknown partitions Δ_1 and Δ_2 of Δ.

The resulting matrix $\hat{\boldsymbol{K}}_B$ will then in general not be positive definite but the process can be repeated with a new $\tilde{\boldsymbol{K}}_B = \hat{\boldsymbol{K}}_B$ until a matrix $\hat{\boldsymbol{K}}_B$ positive definite/semidefinite is finally obtained. At that point, the rows/columns permutations performed to obtain the largest block positive definite are reversed leading to a matrix $\boldsymbol{K}'_B$ which is positive definite and thus could serve as the basis for the structural uncertainty modeling.

A second option was investigated in [29] in which the uncertainty is introduced only on the largest part of the model that is consistent with the theory of Eqs (21)-(31) leaving the rest of it equal to the mean model. That is, uncertainty is introduced on the positive definite block $\boldsymbol{K}_{11}$ of Eq. (A.1) while leaving the corresponding matrices $\boldsymbol{K}_{12}$ and $\boldsymbol{K}_{22}$ unchanged, equal to their values resulting for example from the above optimization of Eqs (A.13)-(A.5) or as the initial conditions of this process.

In principle, achieving the positive definiteness of the structural only component of the matrix $\boldsymbol{K}_C$ (i.e., $\boldsymbol{K}_B$) is sufficient to enable the stochastic modeling process as defined in Eqs (39)-(42). Unfortunately, barely achieving positive definiteness or semidefiniteness induces ill conditioning in the propagation of the uncertainty to the structural-thermal matrices of the model. Indeed, if $\boldsymbol{K}_B$ is singular, then so is $\bar{\boldsymbol{L}}_{SS}^{(3)}$ (see Eq. (41) and it is not possible to determine $\bar{\boldsymbol{L}}_{TS}^{(2)}$ which should satisfy (see Eq. (39) and (41))

$$\bar{\boldsymbol{L}}_{SS}^{(2)}\,\bar{\boldsymbol{L}}_{TS}^{(1)T} + \bar{\boldsymbol{L}}_{SS}^{(3)}\,\bar{\boldsymbol{L}}_{TS}^{(2)T} = \tilde{\boldsymbol{K}}^{(th)}. \tag{A.6}$$

If the matrix $\boldsymbol{K}_B$ is not singular but has very small eigenvalues, $\bar{\boldsymbol{L}}_{TS}^{(2)}$ will have large terms that depend strongly on these small eigenvalues. Considering further that they probably result from the introduction of the matrix $\boldsymbol{\Delta}_1$ and $\boldsymbol{\Delta}_2$, not from an actual property of the structure, it is concluded that the values of $\bar{\boldsymbol{L}}_{TS}^{(2)}$ will be large and unphysical.

Another perspective on the same issue is that the existence of a nonzero difference $\tilde{\boldsymbol{K}}^{(th)} - \bar{\boldsymbol{L}}_{SS}^{(2)}\,\bar{\boldsymbol{L}}_{TS}^{(1)T}$ is inconsistent with the theory of Eqs (32)-(35). Then, proceeding as done in [29], it is proposed here to introduce the uncertainty only on the part of the model consistent with the theory leaving any inconsistencies as in the mean model.

To formalize this perspective, note first that if $\tilde{\boldsymbol{K}}^{(th)} - \bar{\boldsymbol{L}}_{SS}^{(2)}\,\bar{\boldsymbol{L}}_{TS}^{(1)T}$ is imposed to vanish then $\bar{\boldsymbol{L}}_{TS}^{(2)}$ can be selected as zero to satisfy Eq. (A.6). Next, rewriting the matrix $\boldsymbol{K}_C$ in a partition consistent with Eq. (A.1) leads to

$$\boldsymbol{K}_C = \begin{bmatrix} \boldsymbol{K}_{11} & \boldsymbol{K}_{12}+\boldsymbol{\Delta}_1 & \boldsymbol{K}_{13} \\ \boldsymbol{K}_{12}^T+\boldsymbol{\Delta}_1^T & \boldsymbol{K}_{22}+\boldsymbol{\Delta}_2 & \boldsymbol{K}_{23} \\ \boldsymbol{K}_{13}^T & \boldsymbol{K}_{23}^T & \boldsymbol{K}^{(tt)} \end{bmatrix} = \boldsymbol{K}_C^{(1)} + \boldsymbol{K}_C^{(2)}. \tag{A.7}$$

In this equation,

$$\boldsymbol{K}_C^{(1)} = \begin{bmatrix} \boldsymbol{K}_{11} & \boldsymbol{K}_{12}+\boldsymbol{\Delta}_1 & \boldsymbol{K}_{13} \\ \boldsymbol{K}_{12}^T+\boldsymbol{\Delta}_1^T & \boldsymbol{K}_{22}+\boldsymbol{\Delta}_2 & \boldsymbol{R} \\ \boldsymbol{K}_{13}^T & \boldsymbol{R}^T & \boldsymbol{K}^{(tt)} \end{bmatrix} \quad \text{and} \quad \boldsymbol{K}_C^{(2)} = \begin{bmatrix} \boldsymbol{0} & \boldsymbol{0} & \boldsymbol{0} \\ \boldsymbol{0} & \boldsymbol{0} & \boldsymbol{K}_{23}-\boldsymbol{R} \\ \boldsymbol{0} & \boldsymbol{K}_{23}^T-\boldsymbol{R}^T & \boldsymbol{0} \end{bmatrix} \tag{A.8}$$

where $\boldsymbol{R}$ is a matrix such that the Cholesky decomposition of $\boldsymbol{K}_C^{(1)}$ is of the form

$$\bar{\boldsymbol{L}}_{\boldsymbol{K}}^{(1)} = \begin{pmatrix} \bar{\boldsymbol{L}}_{11} & \boldsymbol{0} & \boldsymbol{0} \\ \bar{\boldsymbol{L}}_{21} & \bar{\boldsymbol{L}}_{22} & \boldsymbol{0} \\ \bar{\boldsymbol{L}}_{31} & \boldsymbol{0} & \boldsymbol{I} \end{pmatrix} \tag{A.9}$$

in which the presence of the identity matrix in the 33 block results from the discussion of Appendix B. Moreover, the null matrix in the 32 block is the vanishing block $\bar{\boldsymbol{L}}_{TS}^{(2)}$. Performing the product of Eq. (39) leads to

$$\bar{\boldsymbol{L}}_{11}\bar{\boldsymbol{L}}_{11}^T=\boldsymbol{K}_{11};\ \ \bar{\boldsymbol{L}}_{21}^T=\bar{\boldsymbol{L}}_{11}^{-1}\left[\boldsymbol{K}_{12}+\Delta_1\right];\ \ \bar{\boldsymbol{L}}_{31}^T=\bar{\boldsymbol{L}}_{11}^{-1}\boldsymbol{K}_{13}\text{; and finally }\boldsymbol{R}=\bar{\boldsymbol{L}}_{21}\bar{\boldsymbol{L}}_{31}^T\ . \tag{A.10}$$

which fully defines $\bar{\boldsymbol{L}}_{\boldsymbol{K}}^{(1)}$. Uncertainty can then be introduced by randomizing the matrix $\boldsymbol{K}_C^{(1)}$ only, keeping $\boldsymbol{K}_C^{(2)}$ as a deterministic addition to each random sample.

Note in the above discussion that the matrix $\bar{\boldsymbol{L}}_{22}$ is typically very small as a result of the modification process of Eq. (A.2)-(A.5) which aims at only reaching positive definiteness for the matrix $\boldsymbol{K}_B$. A simplification of the approach of Eqs (A.7)-(A.10) can then be conceived that simply assumes $\bar{\boldsymbol{L}}_{22}=\boldsymbol{0}$ leading to the matrix

$$\bar{\boldsymbol{L}}_{\boldsymbol{K}}^{(1)}=\begin{pmatrix}\bar{\boldsymbol{L}}_{11} & \boldsymbol{0} & \boldsymbol{0}\\ \bar{\boldsymbol{L}}_{21} & \boldsymbol{0} & \boldsymbol{0}\\ \bar{\boldsymbol{L}}_{31} & \boldsymbol{0} & \boldsymbol{I}\end{pmatrix}\ . \tag{A.11}$$

Since the matrix $\bar{\boldsymbol{L}}_{22}$ is no longer of concern, the modification process of Eq. (A.2)-(A.5) can be further sidestepped and the blocks $\bar{\boldsymbol{L}}_{21}$ and $\bar{\boldsymbol{L}}_{31}$ evaluated directly from their counterparts $\boldsymbol{K}_{12}$ and $\boldsymbol{K}_{13}$ before Eqs (A.2)-(A.5). That is,

$$\bar{\boldsymbol{L}}_{11}\bar{\boldsymbol{L}}_{11}^T=\boldsymbol{K}_{11};\ \ \bar{\boldsymbol{L}}_{21}^T=\bar{\boldsymbol{L}}_{11}^{-1}\boldsymbol{K}_{12};\ \ \bar{\boldsymbol{L}}_{31}^T=\bar{\boldsymbol{L}}_{11}^{-1}\boldsymbol{K}_{13}\text{; and finally }\boldsymbol{R}=\bar{\boldsymbol{L}}_{21}\bar{\boldsymbol{L}}_{31}^T\ . \tag{A.12}$$

To avoid a change of the mean model, the matrix $\boldsymbol{K}_C^{(2)}$ is then selected as

$$\boldsymbol{K}_C^{(2)}=\begin{bmatrix}\boldsymbol{0} & \boldsymbol{0} & \boldsymbol{0}\\ \boldsymbol{0} & \boldsymbol{K}_{22}-\bar{\boldsymbol{L}}_{21}\bar{\boldsymbol{L}}_{21}^T & \boldsymbol{K}_{23}-\boldsymbol{R}\\ \boldsymbol{0} & \boldsymbol{K}_{23}^T-\boldsymbol{R}^T & \boldsymbol{0}\end{bmatrix} \tag{A.13}$$

and is not randomized.

A further modification of this approach can be conceived that combines the above discussion with the alternative approach of [29]. That is, the structural uncertainty modeling is limited to the block $\boldsymbol{K}_{11}$ leaving the corresponding matrices $\boldsymbol{K}_{12}$ and $\boldsymbol{K}_{22}$ unchanged. In this

final framework, only the blocks $\boldsymbol{K}_{11}$, $\boldsymbol{K}_{13}$, and $\boldsymbol{K}^{(tt)}$ are affected by the uncertainty. Then, the matrix $\boldsymbol{K}_C$ can be reduced, for the uncertainty modeling, to

$$\boldsymbol{K}_C^{(s)} = \begin{bmatrix} \boldsymbol{K}_{11} & \boldsymbol{K}_{13} \\ \boldsymbol{K}_{13}^T & \boldsymbol{K}^{(tt)} \end{bmatrix} \tag{A.14}$$

all other terms in $\boldsymbol{K}_C$ remaining equal to their tuned counterparts. The random samples of $\boldsymbol{K}_C^{(s)}$ can then be obtained as

$$\boldsymbol{K}_C^{(s)} = \bar{\boldsymbol{L}}_{\boldsymbol{K}}^{(s)}\, \boldsymbol{H}_T^{(s)}\, \boldsymbol{H}_S^{(s)}\, \boldsymbol{H}_S^{(s)T}\, \boldsymbol{H}_T^{(s)T}\, \bar{\boldsymbol{L}}_{\boldsymbol{K}}^{(s)T} \tag{A.15}$$

where

$$\bar{\boldsymbol{L}}_{\boldsymbol{K}}^{(s)} = \begin{pmatrix} \bar{\boldsymbol{L}}_{11} & \boldsymbol{0} \\ \bar{\boldsymbol{L}}_{31} & \boldsymbol{I} \end{pmatrix};\quad \boldsymbol{H}_T^{(s)} = \begin{pmatrix} \boldsymbol{I} & \boldsymbol{0} \\ \boldsymbol{H}_{TS}^{(s)} & * \end{pmatrix} \text{ and } \boldsymbol{H}_S^{(s)} = \begin{pmatrix} \boldsymbol{H}_{SS}^{(s)} & \boldsymbol{0} \\ \boldsymbol{0} & \boldsymbol{I} \end{pmatrix} \tag{A.16), (A.17), (A.18}$$

consistently with Eqs (A.9), (50), and (51).

APPENDIX B

This appendix focuses on the determination of the deterministic matrix $\bar{\boldsymbol{L}}_{TT}$ yielding a maximum entropy of the random matrices $\boldsymbol{K}_C$ as defined by

$$S_{\boldsymbol{K}} = -\int_{\Omega} p_{\boldsymbol{K}_C}(\boldsymbol{k}) \ln p_{\boldsymbol{K}_C}(\boldsymbol{k})\, d\boldsymbol{k}\,. \tag{A.16}$$

To this end, rewrite first Eq. (40) as

$$\boldsymbol{K}_C = \bar{\boldsymbol{L}}_{\boldsymbol{K}}\, \boldsymbol{G}\, \bar{\boldsymbol{L}}_{\boldsymbol{K}}^T \quad \text{where} \quad \boldsymbol{G} = \boldsymbol{H}_{\boldsymbol{K}}\, \boldsymbol{H}_{\boldsymbol{K}}^T \tag{A.17),(A.18}$$

and note that Eq. (A.17) can be viewed as a linear transformation of the random elements of the matrix $\boldsymbol{G}$ into the random components of $\boldsymbol{K}_C$. Accordingly, the joint probability density functions of the elements of these two matrices are related by the equation

$$p_{\boldsymbol{K}_C}(\boldsymbol{k}) = p_{\boldsymbol{G}}(\boldsymbol{g}) / \left|\det(\boldsymbol{J})\right| \text{ and } \quad d\boldsymbol{k} = \left|\det(\boldsymbol{J})\right| d\boldsymbol{g} \tag{A.19),(A.20}$$

where $\boldsymbol{J}$ is the Jacobian of the transformation. To evaluate this matrix from Eq. (A.7), it is convenient to rewrite it first stacking the columns of the matrix $\boldsymbol{K}_C$ below each other and proceeding similarly with the matrix $\boldsymbol{G}$ consistently with the ***vec*** operation. Then, one obtains

$$\boldsymbol{vec}\left(\boldsymbol{K}_C\right) = \boldsymbol{vec}\left(\bar{\boldsymbol{L}}_{\boldsymbol{K}}\, \boldsymbol{G}\, \bar{\boldsymbol{L}}_{\boldsymbol{K}}^T\right) = \left(\bar{\boldsymbol{L}}_{\boldsymbol{K}} \otimes \bar{\boldsymbol{L}}_{\boldsymbol{K}}\right)\boldsymbol{vec}\left(\boldsymbol{G}\right) \tag{A.21}$$

where $\otimes$ denotes the Kronecker product owing to the property

$$\boldsymbol{vec}\left(\boldsymbol{A}\,\boldsymbol{B}\,\boldsymbol{C}\right) = \left(\boldsymbol{C}^T \otimes \boldsymbol{A}\right)\boldsymbol{vec}\left(\boldsymbol{B}\right) \tag{A.22}$$

for any matrices $\boldsymbol{A}$, $\boldsymbol{B}$, and $\boldsymbol{C}$ with consistent dimensions.

From Eq. (A.21), it is found that

$$\boldsymbol{J} = \bar{\boldsymbol{L}}_{\boldsymbol{K}} \otimes \bar{\boldsymbol{L}}_{\boldsymbol{K}} \qquad \text{so that} \qquad \det\left(\boldsymbol{J}\right) = \det\left(\bar{\boldsymbol{L}}_{\boldsymbol{K}}\right)^2 = \prod_i \bar{L}_{K,ii}^2 \tag{A.23), (A.24}$$

where the last equality holds owing to the triangular structure of $\bar{\boldsymbol{L}}_{\boldsymbol{K}}$.

Next, combining Eq. (A.16), (A.19), and (A.20), it is found that

$$S_{\boldsymbol{K}} = -\int_{\Omega_{\boldsymbol{G}}} p_{\boldsymbol{G}}\left(\boldsymbol{g}\right) \ln\left[\, p_{\boldsymbol{G}}\left(\boldsymbol{g}\right) / \left|\det\left(\boldsymbol{J}\right)\right|\right] d\boldsymbol{g}\,. \tag{A.25}$$

where $\Omega_{\boldsymbol{G}}$ is the appropriate domain of variations of the matrices $\boldsymbol{g}$. Since $\boldsymbol{J}$ is a constant matrix (independent of $\boldsymbol{g}$), Eq. (A.25) reduces to

$$S_{\boldsymbol{K}} = \ln\left[\left|\det\left(\boldsymbol{J}\right)\right|\right] \int_{\Omega_{\boldsymbol{G}}} p_{\boldsymbol{G}}\left(\boldsymbol{g}\right) d\boldsymbol{g} - \int_{\Omega_{\boldsymbol{G}}} p_{\boldsymbol{G}}\left(\boldsymbol{g}\right) \ln\left[\, p_{\boldsymbol{G}}\left(\boldsymbol{g}\right)\right] d\boldsymbol{g} = \ln\left[\left|\det\left(\boldsymbol{J}\right)\right|\right] + S_{\boldsymbol{G}} \tag{A.26}$$

where $S_{\boldsymbol{G}}$ is the entropy of the matrices $\boldsymbol{G}$ and is independent of $\bar{\boldsymbol{L}}_{\boldsymbol{K}}$. Recognizing that

$$\det\left(\boldsymbol{J}\right) = \left[\det\left(\bar{\boldsymbol{L}}_{\boldsymbol{K}}\right)\right]^2 = \left[\det\left(\bar{\boldsymbol{L}}_{SS}^{(1)}\right)\det\left(\bar{\boldsymbol{L}}_{SS}^{(3)}\right)\det\left(\bar{\boldsymbol{L}}_{TT}\right)\right]^2 \tag{A.27}$$

it is concluded that maximizing the entropy $S_{\boldsymbol{K}}$ is achieved when the determinant of $\bar{\boldsymbol{L}}_{TT}$ is as large as possible, implying that some scaling constraint should be added to the problem.

In this regard, consider the effect of $\bar{\boldsymbol{L}}_{TT}$ on the simulated reduced order model coefficients. This matrix affects only the random coefficients $K_{ijl}^{(th)}$ and $F_{il}^{(th)}$ through the

products $\bar{\boldsymbol{L}}_{TT}\,\boldsymbol{H}_{TS}^{(1)}$ and $\bar{\boldsymbol{L}}_{TT}\,\boldsymbol{H}_{TS}^{(2)}$, i.e., $\bar{\boldsymbol{L}}_{TT}$ provides a scaling of the effects of $\boldsymbol{H}_T$ which are all proportional to the standard deviation σ. So, increasing uniformly $\bar{\boldsymbol{L}}_{TT}$ is equivalent to increasing σ. Accordingly, it is not possible to specify or identify both a uniform scaling of $\bar{\boldsymbol{L}}_{TT}$ and the standard deviation σ. The approach chosen here is then to constraint the uniform scaling so that σ can be a true parameter of the model. Thus, to the maximization of the entropy is now added the scaling constraint

$$\left\|\bar{\boldsymbol{L}}_{TT}\right\|_F = \sqrt{\mu}\,. \tag{A.28}$$

The lower triangular matrix $\bar{\boldsymbol{L}}_{TT}$ sought leads to a maximum value of its determinant while satisfying Eq. (A.28). Proceeding with a Lagrange multiplier, it is desired to find the elements $\bar{L}_{ij}$, $i \geq j$, of $\bar{\boldsymbol{L}}_{TT}$ such that $\bar{L}_{ii} > 0$ and

$$\Upsilon = \prod_{i=1}^{\mu} \bar{L}_{ii} + \gamma\left[\sum_{i=1}^{\mu}\sum_{j\leq i} \bar{L}_{ij}^2 - \mu\right] \tag{A.29}$$

is maximum where γ is the Lagrange multiplier. Differentiating Eq. (A.29) with respect to $\bar{L}_{ij}$ $i \neq j$ demonstrates first that these components must all be zero and thus the matrix $\bar{\boldsymbol{L}}_{TT}$ is diagonal. Then, differentiating Eq. (A.29) with respect to $\bar{L}_{jj}$ yields

$$\prod_{i=1, i\neq j}^{\mu} \bar{L}_{ii} + 2\gamma\,\bar{L}_{jj} = 0 \qquad \text{or} \qquad \prod_{i=1}^{\mu} \bar{L}_{ii} + 2\gamma\,\bar{L}_{jj}^2 = 0 \tag{A.30),(A.31}$$

where Eq. (A.31) results from (A.30) by multiplication by $\bar{L}_{jj} \neq 0$. Since the product term in Eq. (A.31) is independent of $\bar{L}_{jj}$, it is concluded that $\bar{L}_{jj}^2$ is independent of the index j and thus, from Eq. (A.28), $\bar{L}_{jj}^2 = 1$. Since the diagonal terms $\bar{L}_{jj}$ must be positive, one obtains $\bar{L}_{jj}$ = 1 for all j and thus the lower triangular matrix $\bar{\boldsymbol{L}}_{TT}$ sought equals the identity matrix.

REFERENCES

[1] Soize, C., "A nonparametric Model of Random Uncertainties for Reduced Matrix Models in Structural Dynamics," *Probabilistic Engineering Mechanics*, Vol. 15, 2000, pp. 277-294. doi: 10.1016/S0266-8920(99)00028-4

[2] Soize, C., *Stochastic Models of Uncertainties in Computational Mechanics,* American Society of Civil Engineers (ASCE), 2012. doi: 10.1061/9780784412237

[3] Soize, C., *Uncertainty Quantification: An Accelerated Course with Advanced Applications in Computational Engineering*, Springer-Verlag, 2017. doi: 10.1007/978-3-319-54339-0.

[4] Mignolet, M.P., and Soize, C., "Nonparametric Stochastic Modeling of Linear Systems with Prescribed Variance of Several Natural Frequencies," *Probabilistic Engineering Mechanics*, Vol. 23, 2008, pp. 267-278. doi: 10.1016/j.probengmech.2007.12.027

[5] Mignolet, M.P., and Soize, C., and Avalos, J., "Nonparametric Stochastic Modeling of Structures with Uncertain Boundary Conditions/Coupling Between Substructures," *AIAA Journal*, Vol. 51, 2013, pp. 1296-1308. doi: 10.2514/1.J051555

[6] Avalos, J., Swenson, E.D., Mignolet, M.P., and Lindsley, N.J., "Stochastic Modeling of Structural Uncertainty/Variability from Ground Vibration Modal Test Data," *Journal of Aircraft*, Vol. 49, 2012, pp. 870-884. doi: 10.2514/1.C031546

[7] Mignolet, M.P., and Chen, P.C., "Aeroelastic Analyses with Uncertainty in Structural Properties," *Proceeding of the AVT-147 Symposium: Computational Uncertainty in Military Vehicle Design*, 2007.

[8] Durand, J.-F., Soize, C., and Gagliardini, L. "Structural-Acoustic Modeling of Automotive Vehicles in Presence of Uncertainties and Experimental Identification and Validation," *The Journal of the Acoustical Society of America*, Vol. 124, No. 3, 2008, pp. 1513-1525. doi: 10.1121/1.2953316

[9] Ohayon, R., and Soize, C., *Advanced Computational Vibroacoustics: Reduced-Order Models and Uncertainty Quantification*, Cambridge University Press, Cambridge, U.K., 2014. doi: 10.1017/CBO9781107785328

[10] Murthy, R., Mignolet, M.P., and El-Shafei, A. "Nonparametric Stochastic Modeling of Uncertainty In Rotordynamics - Part I: Formulation," *Journal of Engineering for Gas Turbines and Power*, Vol. 132, No. 9, 2010, 092501. doi: 10.1115/1.3204645

[11] Murthy, R., Mignolet, M.P., and El-Shafei, A. "Nonparametric Stochastic Modeling of Uncertainty In Rotordynamics - Part II: Applications," " *Journal of Engineering for Gas Turbines and Power*, Vol. 132, No. 9, 2010, 092502. doi: 10.1115/1.3204650

[12] Murthy, R., Tomei, J.C., Wang, X.Q., Mignolet, M.P., and El-Shafei, A.. "Nonparametric Stochastic Modeling Of Structural Uncertainty In Rotordynamics: Unbalance And Balancing Aspects," *Journal of Engineering for Gas Turbines and Power*, Vol. 136, No. 6, 2014, 062506. doi: 10.1115/GT2013-95779.

[13] Mignolet, M.P., and Soize, C. "Stochastic Reduced Order Models for Uncertain Geometrically Nonlinear Dynamical Systems," *Computer Methods in Applied Mechanics and Engineering*, Vol. 197, No. 45, 2008, pp. 3951-3963. doi: 10.1016/j.cma.2008.03.032.

[14] Capiez-Lernout, E., Soize, C., and Mignolet, M.P.. "Post-Buckling Nonlinear Static and Dynamical Analyses of Uncertain Cylindrical Shells and Experimental Validation," *Computer Methods in Applied Mechanics and Engineering*, Vol. 271, 2014, pp. 210-230. doi: 10.1016/j.cma.2013.12.011.

[15] Soize, C., and Poloskov, I.E.. "Time-Domain Formulation In Computational Dynamics

for Linear Viscoelastic Media with Model Uncertainties and Stochastic Excitation," *Computers & Mathematics with Applications*, Vol. 64, No. 11, 2012, pp. 3594-3612. doi: 10.1016/j.camwa.2012.09.010.

[16] Batou, A., and Soize, C.. "Rigid Multibody System Dynamics with Uncertain Rigid Bodies," *Multibody System Dynamics*, Vol. 27, No. 3, 2012, pp. 285-319. doi: 10.1007/s11044-011-9279-2.

[17] Richter, L.A., and Mignolet, M.P.. "Stochastic Modeling of Uncertain Mass Characteristics in Rigid Body Dynamics," *Mechanical Systems and Signal Processing*, Vol. 87, 2017, pp. 43-53. doi: 10.1016/j.ymssp.2016.09.017

[18] Song, P., *Uncertainty Modeling for Nonlinear and Linear Heated Structures*, Ph.D., May 2019.

[19] Perez, R., Wang, X.Q., and Mignolet, M.P., "Nonlinear Reduced Order Models for Thermoelastodynamic Response of Isotropic and FGM Panels," *AIAA Journal*, Vol. 49, 2011, pp. 630-641. doi: 10.2514/6.2009-2309

[20] Matney, A.K., Perez, R.A., and Mignolet, M.P., "Nonlinear Unsteady Thermoelastodynamic Response of a Panel Subjected to an Oscillating Flux by Reduced Order Models," *Proceedings of the 52nd Structures, Structural Dynamics and Materials Conference*, Denver, Colorado, Apr. 4-7, 2011, AIAA 2011-2016. doi: 10.2514/6.2011-2016.

[21] Kim, K., Radu, A.G., Wang, X.Q., and Mignolet, M.P., "Nonlinear Reduced Order Modeling of Isotropic and Functionally Graded Plates," *International Journal of Non-Linear Mechanics*, Vol. 49, pp. 100-110, 2013. doi: 10.1016/j.ijnonlinmec.2012.07.008.

[22] Mignolet, M.P., Przekop, A., Rizzi, S.A., and Spottswood, S.M., "A Review of Indirect/Non-Intrusive Reduced Order Modeling of Nonlinear Geometric Structures," *Journal of Sound and Vibration*. Vol. 332, pp. 2437-2460, 2013. doi: 10.1016/j.jsv.2012.10.017.

[23] Perez, R.A., Wang, X.Q., and Mignolet, M.P., "Non-Intrusive Structural Dynamic Reduced Order Modeling for Large Deformations: Enhancements for Complex Structures," *Journal of Computational and Nonlinear Dynamics*, Vol. 9, No. 3, pp. 031008-1 - 031008-12, 2014. doi: 10.1115/1.4026155

[24] Falkiewicz, N.J., and Cesnik, C.E.S., "Proper Orthogonal Decomposition for Reduced-Order Thermal Solution in Hypersonic Aerothermoelastic Simulations," *AIAA Journal*, Vol. 49, No. 5, 2011, pp. 994-1009. doi: 10.2514/1.J050701

[25] Matney, A.K., Mignolet, M.P., Spottswood, S.M., Culler, A.J., and McNamara, J.J., "Thermal Reduced Order Model Adaptation to Aero-Thermo-Structural Interactions," *Proceedings of the AIAA Science and Technology Forum and Exposition (SciTech2014)*, National Harbor, Maryland, Jan. 13-17, 2014, Paper AIAA 2014-0493. doi: 10.2514/6.2014-0493

[26] Matney, A., Mignolet, M.P., Culler, A.J., McNamara, J.J., and Spottswood, S.M., "Panel Response Prediction through Reduced Order Models with Application to Hypersonic Aircraft," *Proceedings of the AIAA Science and Technology Forum and Exposition (SciTech2015)*, Orlando, Florida, Jan. 5-9, 2015, AIAA Paper AIAA 2015-1630. doi: 10.2514/6.2015-1630

[27] Murthy, R., Wang, X.Q., Matney, A., and Mignolet, M.P., "Optimum Thermal Modes for Coupled Structural - Thermal Reduced Order Models," *Proceedings of the AIAA Science and Technology Forum and Exposition (SciTech2016)*, San Diego, California, Jan. 4-8, 2016, AIAA Paper AIAA 2016-1709. doi: 10.2514/6.2016-1709

[28] Song, P., and Mignolet, M.P., "Reduced Order Model-Based Uncertainty Modeling of Structures with Localized Response," *Probabilistic Engineering Mechanics*, Vol. 51, 2018, pp. 42-55. doi: 10.1016/j.probengmech.2017.12.002

[29] Wang, X.Q., Mignolet, M.P., and Soize, C., "Structural Uncertainty Modeling For Nonlinear Geometric Response Using Nonintrusive Reduced Order Models," *Probabilistic Engineering Mechanics*, To Appear. Available online. doi: 10.1016/j.probengmech.2020.103033.

[30] Guilleminot, J., and Soize, C., "Stochastic Model and Generator for Random Fields with Symmetry Properties: Application to the Mesoscopic Modeling of Elastic Random Media," *Multiscale Modeling and Simulation*, Vol. 11, No. 3, 2013, pp. 840-870. doi: 10.1137/120898346

APPENDIX C:

[C2]: Wang, X.Q., and Mignolet, M.P., "Enrichments of Structural Bases for the Reduced Order Modeling of Heated Structures Undergoing Nonlinear Geometric Response," *Proceedings of the International Modal Analysis Conference, IMAC XXXVIII*, Houston, Texas, Feb. 10-13, 2020.

Enrichments of Structural Bases for the Reduced Order Modeling of Heated Structures Undergoing Nonlinear Geometric Response

X.Q. Wang and Marc P. Mignolet

SEMTE, Faculties of Mechanical and Aerospace Engineering,
Arizona State University, Tempe, AZ 85287-6106

ABSTRACT
The non-intrusive construction of reduced order models (ROMs) for the prediction of the response of structures undergoing large deformations has received significant attention, and new challenges are arising when it is extended to the coupled structural-thermal or structural-thermal-aerodynamic problems. One such challenge is the construction of the basis functions. In the present investigation, a detailed analysis of possible enrichments that could be used and their performance is carried out. This study is first on a piezoelectric beam which exhibits a thermal-piezoelectric analogy. The potential enrichments can be differentiated based on which effects they include of:
(i) the equivalent forces (right-hand-side of governing equations),
(ii) the change in structural behavior due to induced thermal stresses (left-hand-side of governing equations), and
(iii) nonlinear geometric effects (left-hand-side of governing equations).
Enrichments that include 1, 2, or all 3 of the above effects are constructed and their usefulness to capture the response of the beam is studied. It is found that the enrichment has to include all the three effects, and the one derived from the nonlinear response data corresponding to the applied temperature field as a single thermal mode, has the optimal performance. A similar study is repeated in connection with a curved panel subjected to local heating, and similar behavior is observed.
Keywords: heated structures, nonlinear reduced order modeling, enrichment for thermal effects

INTRODUCTION

The non-intrusive construction of reduced order models (ROMs) for the prediction of the response of structures undergoing large deformations, i.e., with nonlinear geometric effects, due to mechanical loading has received significant attention in the last two decades. The key components of this modeling, i.e., (i) the form of the ROM governing equations, (ii) the selection of the basis functions to approximate the response, and (iii) identification strategies of the ROM coefficients from commercial finite element software have all been well developed and are still progressing.

In recent years, this non-intrusive ROM has been extended to the coupled structural-thermal or structural-thermal-aerodynamic problems, especially in the context of hypersonic vehicles [1-5]. The high-temperature thermal loading arising from the hypersonic environment brings new challenges to the development of the ROM, particularly for the construction of the basis functions. Appropriate bases have been devised by adding enrichments that capture the effects of the thermal loading to the basis constructed for mechanical loads only. However, the form of these enrichments has varied with the particular application.

In this light, the focus of the present investigation is on a detailed analysis of the possible enrichments that could be used and their potential benefits. A beam with a piezoelectric actuating patch [6] is studied first since the piezoelectric effect shows similar behavior as the thermal effect. Potential effects are identified for the enrichment to take into account, and possible enrichment options including part or all of these effects are constructed and their usefulness to capture the structural response is studied. A similar investigation is repeated for the curved panel of [7] subjected to local heating.

COUPLED STRUCTURAL-THERMAL NLROM

In the coupled structural-thermal nonlinear reduced order model (NLROM), structural displacement field $\underline{u}$ and the temperature field $\underline{T}$ are expressed as

$$\underline{u}(\underline{X},t)=\sum_{n=1}^{N_S} q_n(t)\,\underline{\phi}^{(n)}(\underline{X}), \tag{1}$$

and

$$\underline{T}(\underline{X},t)=\sum_{n=1}^{N_T} \tau_n(t)\underline{T}^{(n)}(\underline{X}), \tag{2}$$

where the functions $\underline{\phi}^{(n)}(\underline{X})$ and $\underline{T}^{(n)}(\underline{X})$ are structural and thermal basis functions (modes) defined in the undeformed configuration, respectively. They satisfy the corresponding boundary conditions.

Using the Galerkin approach, the governing equations of the coupled structural-thermal NLROM have been derived based on the thermoelasticity theory. The detail of the formulation can be found in [3]. When the structural properties are independent of the temperature and the effects of the latency and the change of geometry are small hence ignored, the governing equation for the structural part is expressed as

$$M_{ij}\,\ddot{q}_j + D_{ij}\,\dot{q}_j + \left[K_{ij}^{(1)} - K_{ijl}^{(th)}\tau_l\right] q_j + K_{ijl}^{(2)}\,q_j\,q_l + K_{ijlp}^{(3)}\,q_j\,q_l\,q_p = F_i + F_{il}^{(th)}\tau_l \tag{3}$$

The thermal effects on the structural deformation are two-folds: one is the term $K_{ijl}^{(th)}\tau_l$ on the left hand side (LHS) of the equation, which alters the linear stiffness of the structure, usually inducing a softening effect responsible for thermal buckling; the other is the term $F_{il}^{(th)}\tau_l$ on the right hand side (RHS) of the equation, which gives rise to an applied force inducing inplane deformation. This inplane deformation is different from the membrane stretching effect due to the geometric nonlinear effect of large deformation as shown later.

The current investigation is focused on the construction of the structural basis, $\underline{\phi}^{(n)}(\underline{X})$, in the coupled structural-thermal ROM. It can be seen from Eq.(3) that the structural basis has to capture the LHS and the RHS thermal effects, in addition to the nonlinear geometric effect due to large structural deformation.

The general construction strategy for the structural basis is an "enrichment" approach, that is, some enrichment modes will be sought as the addition to an isothermal (cold) structural basis which is assumed to be available. In the current investigation, various enrichment options are studied to see whether a nonlinear enrichment could be successful without the need of the data having all three effects. To help classify these enrichment options, a triplet of 1's or 0's will be attached to them. The first number in the triplet refers to whether the RHS thermal effect is included, 1 if it is, 0 otherwise. The second number refers to whether the LHS thermal effect is included, 1 if it is, 0 otherwise. Finally, the third number of the triplet refers to the presence of geometric nonlinearity, it is a 1 if the enrichment is computed with nonlinearity, 0 otherwise.

To assess the quality of the enriched basis, the representation error is employed, defined as:

$$\varepsilon_{re} = \frac{\left\|\underline{u}_{basis} - \underline{u}_{Nastran}\right\|}{\left\|\underline{u}_{Nastran}\right\|}\times 100\%, \tag{4}$$

where $\underline{u}_{Nastran}$ is the vector of structural response (i.e., Nastran displacement), and $\underline{u}_{basis}$ is its best approximation for a given basis Φ, expressed as

$$\underline{u}_{basis} = \Phi \cdot \underline{q}_{proj}, \tag{5}$$

where $\underline{q}_{proj}$ is the vector of projection coefficients, which is obtained by the least squares method. The displacement vector $\underline{u}$ could be the vector of displacements in all six DOFs or in a single DOF (usually a translation DOF, transverse or inplane).

INVESTIGATION OF ENRICHMENT OPTIONS

Beam with piezoelectric actuating patch

The first structure to study is a beam with a piezoelectric actuating patch as shown in Fig. 1. The properties of the beam are listed in Table 1.

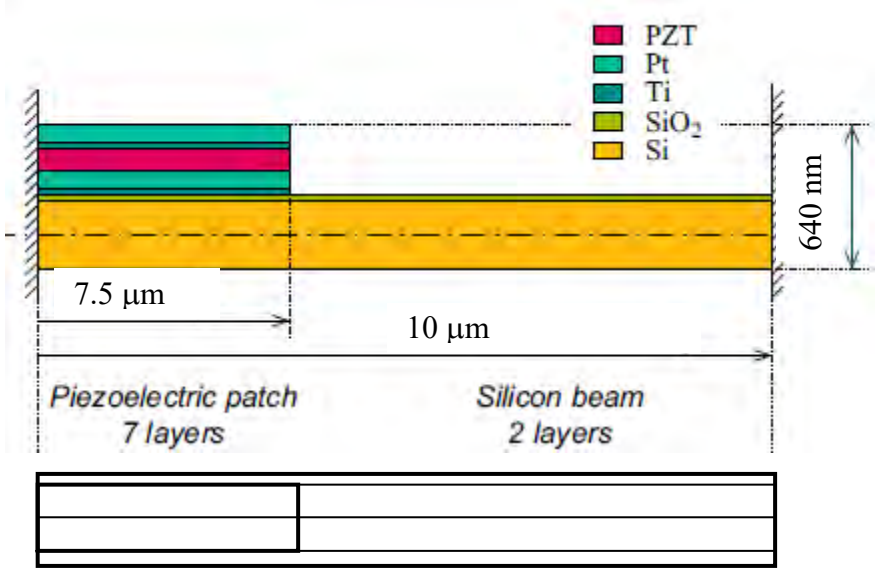

Figure 1. Beam with a piezoelectric patch [6].

The width of the beam for the built-up components (layers 3-7) is slightly less than that for the bottom two layers. Each layer is assumed to be made of a linearly elastic material of Young's modulus (E), Poisson's ratio (ν), and density (ρ) as listed in Table 1. Also given in the table are the piezoelectric properties e_{311} and ε_{33} of the PZT layer. The beam is fully clamped on both sides.

Table 1. Properties of the layers of the beam (bottom to top) [6]

Layer	Material	Width μm	Thick. nm	E GPa	ν	ρ kg/m^3	e_{311} C/m^2	$\hat{\varepsilon}_{33}$ F/m
1	Si	1	340	169	0.3	2500	-	-
2	SiO_2	1	10	70	0.17	2150	-	-
3	Ti	0.9	10	110	0.32	4510	-	-
4	Pt	0.9	80	145	0.35	21450	-	-
5	PZT	0.9	110	96	0.45	7800	17.16	$2.12\ 10^{-8}$
6	Ti	0.9	10	145	0.32	4510	-	-
7	Pt	0.9	80	96	0.35	21450	-	-

A finite element model of the beam was created in Nastran with 40 (along length) x 4 (across width) standard shell elements (CQUAD4). To model the layup of the composite cross-section across the beam, PCOMP cards were used. Since Nastran does not include piezoelectric elements in its library, the thermal analogy was employed with a coefficient of thermal expansion nonzero along the beam axis only. This anisotropy was implemented within NASTRAN through a MAT8 card. Further details can be found in [6].

With the thermal analogy used for the piezoelectric effect, assuming the electric field is expressed as

$$\underline{E}(\underline{X},t) = \sum_{n=1}^{N_T} \hat{\tau}_n(t)\hat{\underline{T}}^{(n)}(\underline{X}), \tag{6}$$

the governing equation of the ROM for the beam is the same as Eq.(3), except that the terms $K_{ijl}^{(th)}\tau_l$ and $F_{il}^{(th)}\tau_l$ now represent the piezoelectric effects on the structural deformation.

In order to study various enrichment options, an isothermal basis of the beam is firstly constructed. This basis has 18 structural modes including 5 linear modes and 13 duals (Basis5L13D). Before proceeding with any enrichment, it is instructive to first assess how well (or badly) the isothermal basis represents the structural responses to the thermal load.

For this beam structure, the thermal load is actually a static voltage applied on the piezoelectric layer, and the nonlinear structural deformation is computed by Nastran. In Fig. 2(a) is shown the maximum transverse displacement of the beam as function of the applied voltage. For the nonlinear static deformation with the highest

applied voltage (150 V), the representation error of the 18-mode isothermal basis is computed by Eq. (4) and shown in Fig. 2(b). It can be seen that the error in the transverse direction is close to 1% while the error in the inplane direction is a few percent. It should be noted that the NLROM with this isothermal basis does not predict the response in Fig. 2(a) well. Therefore, the enrichment is necessary.

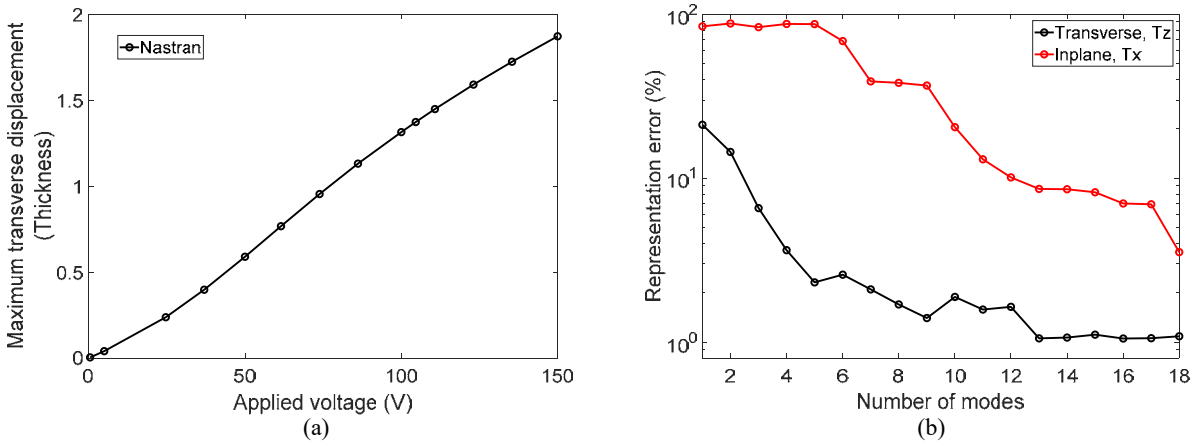

(a) (b)

Figure 2. Beam subjected to the applied voltage on the piezoelectric layer. (a) Nonlinear static response by Nastran; (b) Representation error of the isothermal basis for the highest applied voltage.

In a previous work [6], the linear static response of the beam to the applied voltage was used as the linear enrichment. The representation error was reduced but the prediction is still not good even at smaller applied voltage. In the current study, this linear enrichment is retained to give a 19-mode basis (Basis5L13D1EL), and the additional nonlinear enrichment options are implemented, summarized as follows:

(i) *Hot duals from thermal modes* (1,1,1): dominant POD eigenvectors out of nonlinear displacements due to temperature loads related to thermal modes. Here the voltage load is taken as the single thermal mode, and the displacements are computed by Nastran.

(ii) *Semi-hot duals from RHS effect of thermal modes* (1,0,1): dominant POD eigenvectors out of nonlinear displacements due to the RHS effect of temperature loads related to thermal modes. The RHS effect is not included. Same as (1), the voltage load is taken as the single thermal mode, and the displacements are computed by Nastran.

(iii) *Hot Linear-Cold duals* (1,0,1): duals from the combination of cold linear modes and linear enrichment modes

(iv) *Hot linear modes from thermal modes* (1,1,1): linear structural modes around the deformed positions induced by the temperature loads related to thermal modes. The computation starts as in (1) but the data contains the linear modes around the deformation position as opposed to the displacements themselves.

(v) *Hot linear responses* (1,1,0): dominant POD eigenvectors out of linear structural responses due to temperature loads related to thermal modes. These responses are computed out of the finite element solver using the finite element linear stiffness matrix of the heated structure and the equivalent forces as computed in (2). Geometric nonlinearity is not included.

(vi) *Buckling modes from thermal modes* (0,1,0): buckling modes of the heated structure. These modes include the LHS effect of temperature loads related to thermal modes when nonlinear geometric deformation is taken into account.

These enrichment options are implemented and the nonlinear enrichment modes derived from each option are added to the 19-mode basis (Basis5L13D1EL, common to all options) to obtain the final enriched basis. Once the basis is obtained, its representation error is computed by Eq. (4). The representation errors of all these options are plotted in Fig. 3 for comparison.

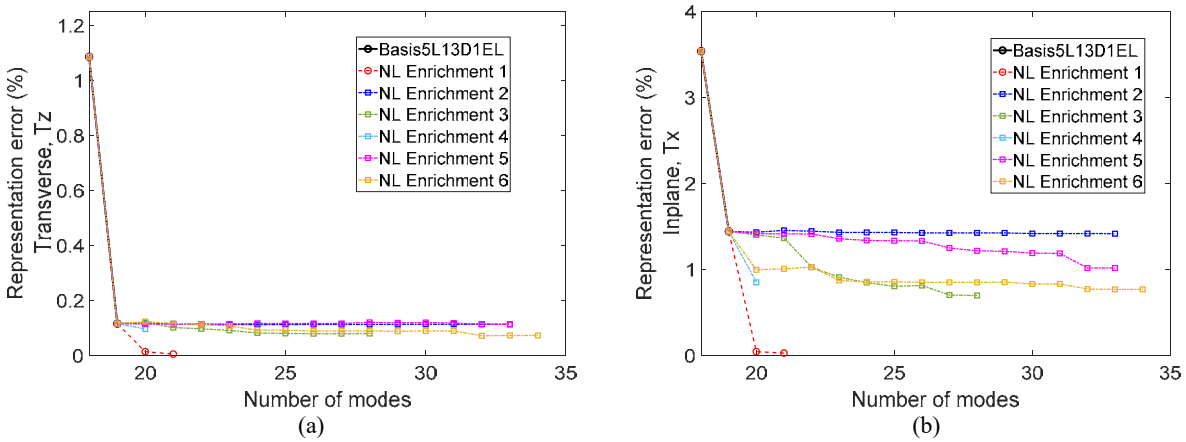

Figure 3. Representation error by various enriched structural bases of the nonlinear static response to the highest applied voltage. (a) Transverse, Tz; and (b) In-plane, Tx.

The error in the transverse direction can be reduced by the linear enrichment further to very small, but the error in the inplane direction is still a little large. Among all the nonlinear enrichment options, four options could reduce the inplane error to be smaller than 1%, and option 1 has the most significant reduction. This is not surprising since the enrichment of option (i) includes all the three effects and is obtained from the same temperature field as resulted from the applied voltage but at different load levels.

Noting that the first enrichment mode of option (i) has reduced the error to a very small level, only that mode is taken as the nonlinear enrichment, leading to the 20-mode enriched basis (Basis5L13D1EL1ENL). The NLROM with this basis is constructed by identifying the stiffness coefficients and the structural-thermal coupling coefficients in Eq.(3). Validations of the NLROM are carried out for the range of applied voltages in Fig. 2(a). The comparison between the Nastran results and the NLROM predictions is shown in Fig. 4, and the matching is quite good.

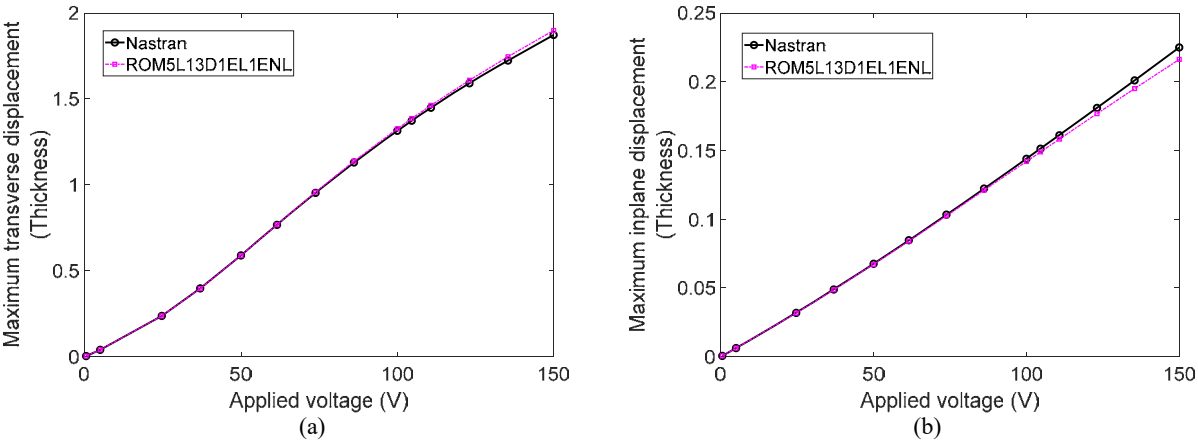

Figure 4. Validation of the 20-mode enriched ROM of the beam for the applied voltage load. (a) Transverse, Tz; and (b) Inplane, Tx.

Curved panel

The second structure to study is a curved panel as shown by its FE model in Fig. 5. It was originally studied by the AFRL researchers for geometric nonlinear response to large aero-acoustic loading with temperature [7]. The curved panel is a part of a cylindrical shell with radius of curvature of 100 inch. A finite element model of the curved panel is constructed using 2457 CQUAD4 shell elements (a 64-by-40 mesh) in Nastran, as shown in Fig. 5. The panel is curved along the *x*-axis while straight along the *z*-axis. When projected on the *x*-*z* plane, its dimensions are 9.75 inch by 15.75 inch, and its thickness is 0.048 in. The panel material is stainless steel with elastic modulus of 2.85×10^6 psi, Poisson's ratio of 0.3, and density of 7.48×10^{-4} lb-sec^2/in^4. The panel is clamped along all the edges.

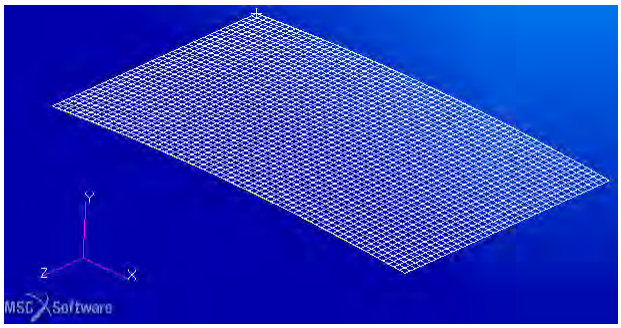

Figure 5. Finite element model of the curved panel.

Similar to the beam model, an isothermal structural basis of the curved panel is firstly constructed for further enrichment study. The basis has 19 modes including 4 linear modes and 15 duals (Basis4L15D). For the curved panel, the thermal load is the temperature field due to a local heating shown in Fig. 6(a). The nonlinear static response of the panel to this temperature load is computed by Nastran and shown in Fig. 6(b).

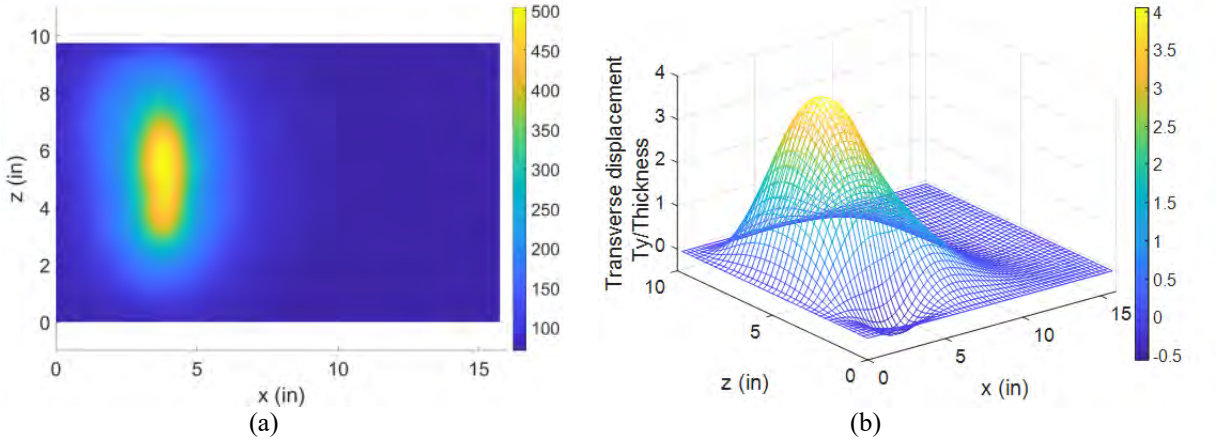

(a) (b)

Figure 6. Temperature field due to a local heating and structural response. (a) Temperature distribution. (b) Nonlinear static response by Nastran.

For this local heating scaled at a set of load levels, the nonlinear static responses are computed by Nastran, and the representation error of the 19-mode isothermal basis with respect to the displacements are checked as shown in Fig. 7. The isothermal basis does not represent the response to the thermal load well, hence the enrichment is necessary.

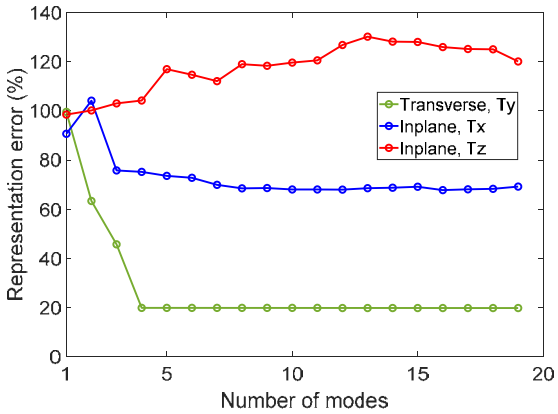

Figure 7. Representation error of the isothermal basis.

The linear static response to this local heating is computed and added to the isothermal basis as the linear enrichment, then various nonlinear enrichment options are constructed and assessed in terms of the representation error. A summary of all the options studied is as follows:

(1) Hot duals from thermal modes (1,1,1): dominant POD eigenvectors out of nonlinear displacements due to temperature loads related to thermal modes including LHS effects. The displacements are determined from nonlinear finite element computations with temperature field from each thermal mode applied.

(2) Semi-hot duals from RHS effect of thermal modes (1,0,1): dominant POD eigenvectors out of nonlinear displacements due to the RHS effect of temperature loads related to thermal modes. The temperature effect on the change of structural properties (LHS) is not included. To determine the displacements, the equivalent forces from the RHS are fist evaluated. This is achieved by blocking all nodes of the finite element model and applying the temperature fields. The corresponding reaction forces at the nodes are then equal to the forces on the right hand side of Eq. (1) at these nodes (changed sign). In a second step, these forces are then applied to the cold finite element model and scaled to mimic the temperature effect.

(3) Semi-hot linear modes from LHS effect of thermal modes (0,1,0): linear structural modes of the heated structure. These modes include the LHS effect of temperature loads related to thermal modes taken into account

(4) Hot linear modes from thermal modes (1,1,1): linear structural modes around the deformed positions induced by the temperature loads related to thermal modes. The computation starts as in (1) but the data contains the linear modes around the deformation position as opposed to the displacements themselves.

(5) Hot Linear-Cold duals (1,0,1): duals from the combination of cold linear modes and linear enrichment modes

(6) Hot linear responses (1,1,0): dominant POD eigenvectors out of linear structural responses due to temperature loads related to thermal modes. These responses are computed out of the finite element solver using the finite element linear stiffness matrix of the heated structure and the equivalent forces as computed in (2). Geometric nonlinearity is not included.

(7) Hot duals from linear responses (1,1,1): *Hot duals from linear responses* (1,1,1): these enrichments are obtained from the nonlinear structural response of the unheated structure to a combination of (i) the force which is the product of the temperature dependent part of the linear stiffness matrix (i.e., the one inducing the LHS effect) and the linear response to the thermal load and (ii) the linear response to the RHS force. The logic for considering such a loading arises from a transfer of the temperature dependent on the left-hand-side of the equations of motion for the generalized coordinates to their right-hand-side.

Moreover, as a variation of option (3),

(3a) Buckling modes from LHS effect of thermal modes (0,1,0): buckling modes with temperature loads related to thermal modes taken into account.

For completeness, the linear enrichment corresponds to the triplet (1,0,0) and the cold duals would be cataloged as (0,0,1).

The above enrichment options are implemented with the quarter-heating temperature field, and the nonlinear enrichment modes derived from each option are added to the basis of 4 linear modes, 15 (cold) duals, and 1 linear enrichment mode (4L15D1EL, common to all options) to obtain the final enriched basis. Once the basis is obtained, its representation error is computed by Eq. (4). The representation errors of all these options are plotted in Fig. 8 for assessment.

Similar to the beam example, option *(1)* is significantly better than the other options, since it includes all the three effects and is obtained from the same temperature field as the local heating but at different load levels within the same range. This can be considered as the scenario that the temperature load is taken as a single and the only thermal mode in the thermal basis, so that the temperature field is perfectly represented by this single-mode thermal basis. In practice, the temperature field is usually complex and varying with time, and a number of thermal modes are needed for the thermal basis. For such a scenario, it would be expected that the enrichment option *(1)* is still the optimal one, but might be used with each thermal mode and/or their combinations and the enrichment modes are assembled to obtain a good structural basis.

Having obtained the enriched basis, that is, 5 nonlinear enrichment modes from option *(1)* added to the 4L15D1EL basis, leading to the final 25-mode basis (4L15D1EL5ENL), the NLROM is constructed by identifying the stiffness coefficients and the structural-thermal coupling coefficients in Eq.(3). Validations of the NLROM are carried out for the local heating at a set of load scales so that the maximum structural displacement is up to about 4 thicknesses. Shown in Fig. 9 is the comparison between the Nastran results and the NLROM predictions. It can be seen that excellent matching is achieved.

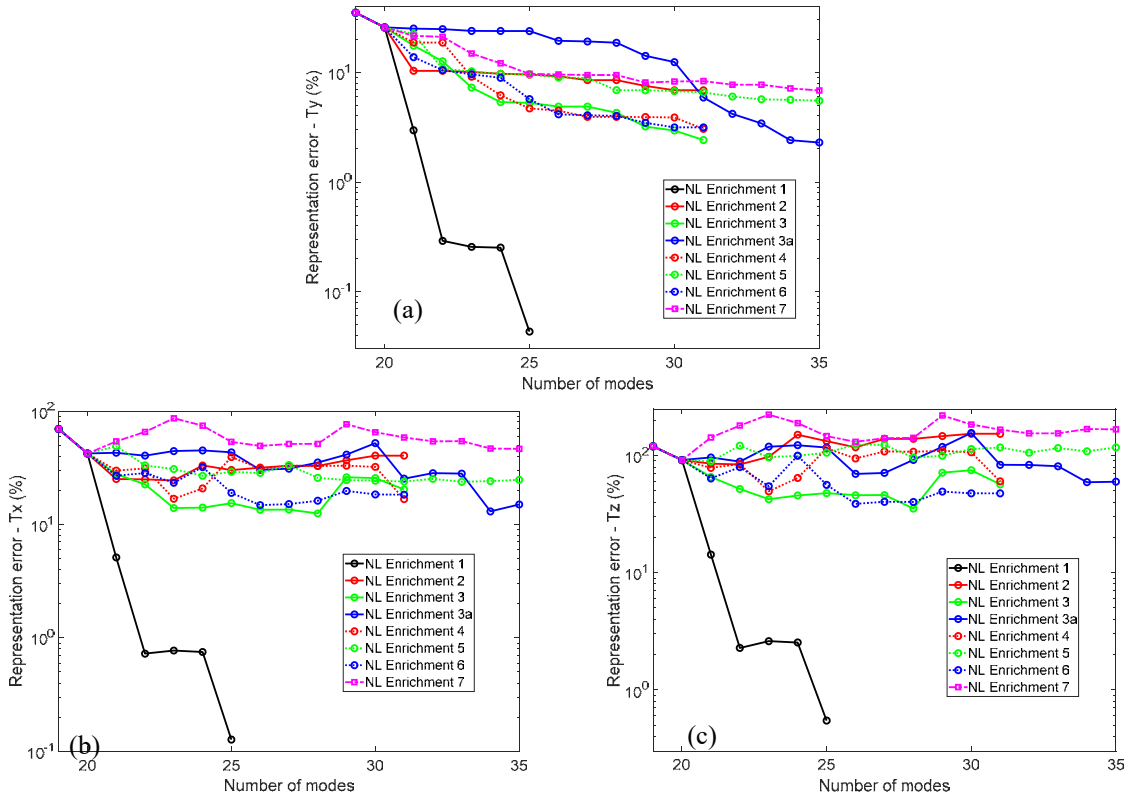

Figure 8. Representation error by various enriched structural bases of the nonlinear static response to the scaled temperature field of local heating. The maximum displacement level is about 4 thicknesses. (a) Transverse, Ty; (b) In-plane, Tx; and (c) In-plane, Tz.

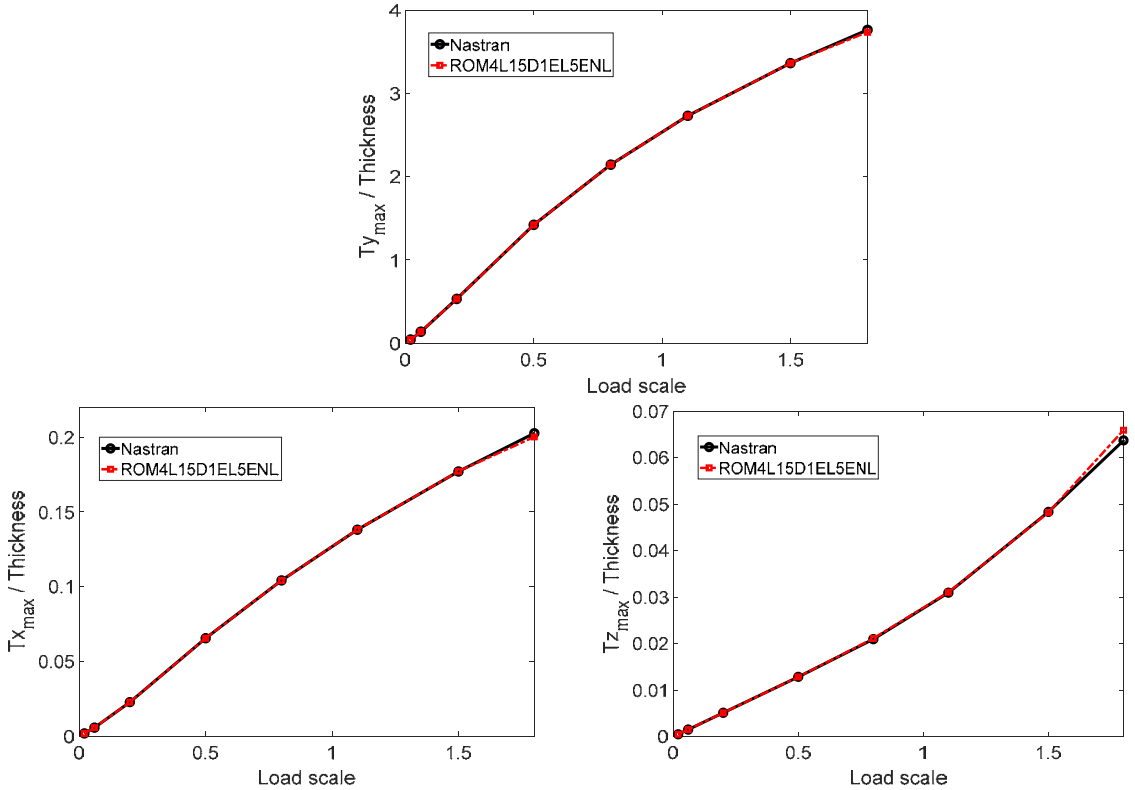

Figure 9. Validation of the 25-mode enriched ROM. (a) Transverse, Ty; (b) Inplane, Tx; and (c) Inplane, Tz.

CONCLUSION

A systematic investigation of nonlinear enrichment options for the construction of structural bases in coupled structural-thermal reduced order models is carried out. It is identified that three features are involved in the structural-thermal coupling, that is,

(i) the excitation force due to the thermal effect (the right-hand-side thermal effect),

(ii) the change in structural stiffness due to thermal stresses (the left-hand-side thermal effect), and

(iii) the large structural deformation (the nonlinear geometric effect)

Two example structures are studied: one is a piezoelectric beam with non-uniform asymmetric actuating load (akin to a temperature change) and the other is a curved panel subjected to local heating. It is found that the needed enrichments have to include all the three features, and the one derived from the nonlinear response data has optimal performance. The NLROM with such an enriched basis gives very good predictions as compared to the finite element (Nastran) results. The above discussion serves as foundation for the formulation of enrichments for heated structures in which the temperature is represented as a sum of thermal modes.

ACKNOWLEDGEMENTS

The authors gratefully acknowledge the support of this work by the AFRL-University Collaborative Center in Structural Sciences (Cooperative Agreement FA8650-13-2-2347), and the contract FA9550-16-1-0021 from the Air Force Office of Scientific Research with Dr. Ben Smarslok and Dr. Jaimie Tiley as program managers, respectively.

REFERENCES

[1] Perez, R., Wang, X.Q., and Mignolet, M.P., "Steady and Unsteady Nonlinear Thermoelastodynamic Response of Panels by Reduced Order Models," *Proceedings of the 51st Structures, Structural Dynamics, and Materials Conference*, Orlando, Florida, Apr. 12-15, 2010, Paper AIAA-2010-2724.

[2] Matney, A., Perez, R., and Mignolet, M.P., "Nonlinear Unsteady Thermoelastodynamic Response of a Panel Subjected to an Oscillating Flux by Reduced Order Models," *Proceedings of the 52nd Structures, Structural Dynamics and Materials Conference*, Apr. 4-7 2011, Denver, Colorado, AIAA 2011-2016.

[3] Gogulapati, A., Deshmukh, R., Crowell, A.R., McNamara, J.J., Vyas, V., Wang, X.Q., Mignolet, M., Beberniss, T., Spottswood, S.M., and Eason, T.G., "Response of a Panel to Shock Impingement: Modeling and Comparison with Experiments," *Proceedings of the AIAA Science and Technology Forum and Exposition (SciTech2014)*, National Harbor, Maryland, Jan. 13-17, 2014, AIAA Paper AIAA 2014-0148.

[4] Matney, A., Mignolet, M.P., Culler, A.J., McNamara, J.J., and Spottswood, S.M., "Panel Response Prediction through Reduced Order Models with Application to Hypersonic Aircraft," *Proceedings of the AIAA Science and Technology Forum and Exposition (SciTech2015)*, Orlando, Florida, Jan. 5-9, 2015, AIAA Paper AIAA 2015-1630.

[5] Gogulapati, A., Brouwer, K., Wang, X.Q., Murthy, R., McNamara, J.J., and Mignolet, M.P., "Full and Reduced Order Aerothermoelastic Modeling of Built-Up Aerospace Panels in High-Speed Flows," *Proceedings of the AIAA Science and Technology Forum and Exposition (SciTech2017)*, Dallas, Texas, Jan. 9-13, 2017, AIAA Paper AIAA 2017-0180.

[6] Vyas, V., Wang, X.Q., Jain, A., and Mignolet, M.P., "Nonlinear Geometric Reduced Order Model for the Response of a Beam with a Piezoelectric Actuator," *Proceedings of the AIAA Science and Technology Forum and Exposition (SciTech2015)*, Orlando, Florida, Jan. 5-9, 2015, AIAA Paper AIAA 2015-0692.

[7] Gordon, R.W., and Hollkamp, J.J., "Reduced-Order Models for Acoustic Response Prediction of a Curved Panel," Proceedings of the 52nd Structures, Structural Dynamics and Materials Conference, Apr. 4 – 7, 2011, Denver, Colorado, Paper AIAA 2011-2081.

APPENDIX D:

[C6]: Wang, X.Q., Lin, J., Wainwright, B.A., and Mignolet, M.P., "Multiple-Level Identification of Stiffness Coefficients in Nonlinear Reduced Order Modeling," *Proceedings of the International Modal Analysis Conference, IMAC XXXVII*, Orlando, Florida, Jan. 28-31, 2019.

Multiple-Level Identification of Stiffness Coefficients in Nonlinear Reduced Order Modeling

X.Q. Wang, Jinshan Lin, Bret A. Wainwright, and Marc P. Mignolet
SEMTE, Faculties of Mechanical and Aerospace Engineering,
Arizona State University, Tempe, AZ 85287-6106

ABSTRACT
One key issue in the reduced order modeling of geometric nonlinear vibration is the identification of stiffness coefficients of the reduced order model (ROM). For a non-intrusive ROM, the data of modal displacements and corresponding modal forces or modal tangent stiffness matrices are needed to identify the coefficients. The usual practice is using the data from commercial finite element software (e.g., Nastran) at an appropriate displacement level. According to the theoretical formulation of the ROM based on the general elasticity theory, the identified coefficients are independent of the level at which the data are obtained. In practice, however, this is not the case due to the inconsistence between the general elasticity formulation and the finite element formulation in the commercial software. The choice of an appropriate level for data acquisition is thus critical.

In the present study, a multiple-level (ML) identification strategy is proposed to reduce this inconsistence. The basic idea is to obtain the data at a series of displacement levels and identify each stiffness coefficient at this series of levels. For each coefficient, a local relative gradient metric is used to find the displacement level at which the coefficient has the least variation ("most constant"). The value at this level is taken as the identified coefficient.

The implementation procedure of the strategy is presented, and applied to a few structures with reasonable complexity, including a curved panel, a hat-stiffened panel, and a joined wing. As compared to the regular identification method, the improvements in the stability and/or the prediction capability and accuracy of the ROM are observed for each structure.

Keywords: reduced order modeling, geometric nonlinear vibration, multiple level identification of stiffness coefficients, non-intrusive identification, commercial FE software data

INTRODUCTION

Geometric nonlinear vibration of thin-walled structures has been an active research subject in many engineering disciplines. One example in the aerospace engineering discipline is the hypersonic aircraft structures in extreme aerodynamic-thermal environments, e.g., large aerodynamic, thermal, and mechanical loadings with nonlinear interactions [1-8]. Numerical methods, among which mainly the finite element method, have been developed for structural response and life predictions [9]. Meanwhile, the computational cost and complexity associated with numerical methods has motivated the study of reduced order modeling techniques for this subject, see a recent review [10].

The present study is concerned with one type of the reduced order models, that is, the non-intrusive ROM in which the nonlinear stiffness coefficients are identified indirectly from the data relating the loads and the nonlinear displacements. One advantage of the non-intrusive ROM is that these data can be obtained from commercial finite element software (e.g., Nastran) to address a broad set of complex geometries and boundary conditions experienced in practice. Such reduced order models have been constructed for a large number of structures, and their strong potentials have been demonstrated [11-25].

In a non-intrusive ROM, a modal basis is constructed to represent a given nonlinear displacement, $\underline{u}\left(\underline{X},t\right)$,

$$\underline{u}\left(\underline{X},t\right)=\sum_{n=1}^{N}q_n\left(t\right)\,\underline{\phi}^{(n)}(\underline{X}), \tag{1}$$

where $\underline{u}(\underline{X},t)$ denotes the vector of physical displacements defined on the finite element degrees of freedom. $\underline{\phi}^{(n)}$ are constant basis functions and $q_n(t)$ are the time dependent generalized coordinates.

The governing equation of the ROM can be obtained from the elasticity theory by the Galerkin approach [17], expressed as

$$M_{ij}\ddot{q}_j + D_{ij}\dot{q}_j + K_{ij}^{(1)} q_j + K_{ijl}^{(2)} q_j q_l + K_{ijlp}^{(3)} q_j q_l q_p = F_i \,, \tag{2}$$

where M_{ij} denotes the elements of the mass matrix, $K_{ij}^{(1)}$, $K_{ijl}^{(2)}$, $K_{ijlp}^{(3)}$ are the linear, quadratic, and cubic stiffness coefficients, and F_i are the modal forces. The viscous damping matrix $\{D_{ij}\}$ is added to collectively represent various dissipation mechanisms following standard practice.

It can be seen that two key issues need to be addressed for a non-intrusive ROM, i.e., the construction of the modal basis and the identification of nonlinear stiffness coefficients. The present study is concerned with the latter issue.
The nonlinear stiffness coefficients can be directly evaluated using their integral expressions as given in [17]. However, the ROM is usually constructed using the data from commercial finite element software (e.g., Nastran) for much broader applications, in which an indirect (non-intrusive) identification of these coefficients is desired.

One of such non-intrusive identification methods is the displacement-force method [16, 17], in which a set of designed static displacements are imposed to the structure and the corresponding nonlinear forces are obtained. They are then used to compute modal displacements and corresponding modal forces to identify the coefficients according to the static version of the governing equation, written as,

$$K_{ij}^{(1)} q_j + K_{ijl}^{(2)} q_j q_l + K_{ijlp}^{(3)} q_j q_l q_p = F_i \,, \tag{3}$$

where *N* denotes the number of modes in the ROM basis, and *p* is the number of displacement-force data required to identify the coefficients. A strategy has been developed so that these coefficients are separated into smaller groups of coefficients and identified independently. The details can be found in [16, 17].

When the basis of a ROM is large, this displacement-force method requires a huge number of data (order of N^3). A method using the tangent stiffness matrix ($K^{(T)}$) instead of the force in the identification has been developed [25]. This displacement-$K^{(T)}$ method replies on the availability of the tangent stiffness matrix for each imposed displacement. Its advantage is that an $N \times N$ matrix (the tangent stiffness matrix) is obtained for each solution, thus a reduction of the computational effort to $O(N^2)$ is achieved.

The *iu* element of the tangent stiffness matrix of a ROM can be derived from Eq. (3), expressed as

$$\begin{aligned} K_{iu}^{(T)} &= \frac{\partial}{\partial q_u}[K_{ij}^{(1)} q_j + K_{ijl}^{(2)} q_j q_l + K_{ijlp}^{(3)} q_j q_l q_p] \\ &= K_{iu}^{(1)} + [K_{iju}^{(2)} + K_{iuj}^{(2)}] q_j + [K_{ijlu}^{(3)} + K_{ijul}^{(3)} + K_{iujl}^{(3)}] q_j q_l \end{aligned} \tag{4}$$

Imposing a set of designed static displacements to the structure and obtaining the corresponding $K^{(T)}$ matrices, the coefficients can be identified according to Eq. (4). The details of the algorithm can be found in [25].

In the above methods, the data used in the identification are generated with a single generalized coordinate (q_j value) for each mode in the basis. In other words, each coefficient is basically identified at a single level of imposed displacement. Theoretically this is acceptable according to the formulation of the ROM, which shows that the identified coefficients are independent of the q_j value. However, when the data from commercial FE software are used, this is not the case due to the inconsistence between the general elasticity formulation and the finite element formulation in the commercial software. The choice of an appropriate displacement level (q_j value) for data

acquisition is thus critical. In the present paper, a multiple-level (ML) identification strategy is proposed to reduce this inconsistence with the objective to improve the prediction capability and/or accuracy of the ROM.

MULTIPLE-LEVEL IDNETIFICATION STRATEGY

The basic idea of the multiple-level identification strategy is described as follows. For a structure, assume a basis of *N* modes has been constructed, the multiple-level identification is carried out in three steps:

(1) A set of q_{jm} values is selected for each mode *j*, where $j = 1, 2, \ldots, N$, and $m = 1, 2, \ldots, M$ representing various q_j values giving rise to various maximum displacements covering the range of displacements to be captured by the ROM.

(2) For each set of q_{jm} values at the level *m*, the stiffness coefficients are identified by the regular identification method (e.g., the displacement-$K^{(T)}$ method) independently. The coefficient is not perfectly constant but a function of its corresponding q value, i.e., $K = K(q)$.

(3) It is expected that the value of a coefficient at a displacement level where it is closest to a constant would be the best one taken as the identified. To this end, a local relative gradient metric is proposed in the following to find such a displacement level (q_{jm} value): for a given q_{jm} value at $m = m_0$, the q_{jm} values in its vicinity can be expressed as $q_{jm_s}(\delta) = q_{jm_0}(1+\delta_s)$. The local relative gradient of a coefficient is thus given by $\frac{dK}{d\delta} = \frac{dK}{dq_{jm}} \cdot \frac{dq_{jm}}{d\delta} = \frac{dK}{dq_{jm}} q_{jm_0}$, where the local absolute gradient $\frac{dK}{dq_{jm}}$ can be computed by a numerical method, e.g., the central difference method. For each coefficient, the local relative gradient is computed, and the value corresponding to the displacement level at which it takes the minimum absolute value is taken as the identified value.

The multiple-level identification strategy can be implemented with any other regular identification method in the same fashion.

EXAMPLES

The multiple-level identification strategy has been applied to three structures with reasonable complexity: a curved panel, a hat-stiffened panel, and a joined wing.

Curved panel

The curved panel was originally studied by the AFRL researchers for geometric nonlinear response to large aero-acoustic loading with temperature [26], whose finite element model is shown in Fig.1. This curved panel is a part of a cylindrical shell with radius of curvature of 100 inch, curved along the *x*-axis while straight along the *z*-axis. When projected on the *x*-*z* plane, the dimension of the panel is 9.75 inch by 15.75 inch, and the thickness of the panel is 0.048 in. The panel material is stainless steel with elastic modulus of 2.85×10^6 psi, Poisson's ratio of 0.3, and density of 7.48×10^{-4} lb-sec^2/in^4. The panel is clamped along all the edges. The finite element model of the panel is constructed in MSC/Nastran, and the mesh has 39-by-63 CQUAD4 shell elements and 2560 nodes. A reduced order model of 17 modes (11 transverse and 7 dual, 11T7D) has been constructed (see the detail in [27]) and the nonlinear stiffness coefficients are identified using the regular displacement-$K^{(T)}$ method. In the present study, the same 17-mode basis is used in the multi-level identification.

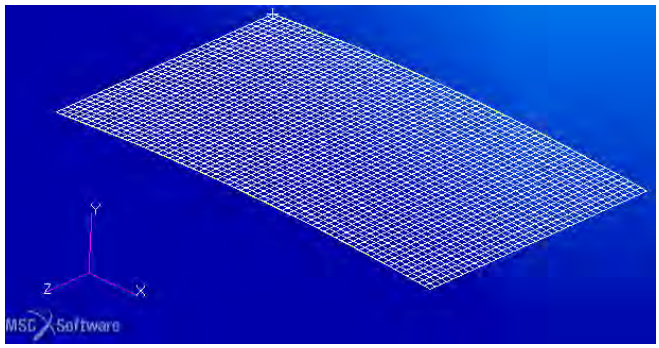

Figure 1. Finite element model of the curved panel.

A dynamic load case is considered to check the performance of the multi-level ROM and the regular ROM, as compared to the Nastran results. The loading is a spatially uniform pressure of 160 dB (OASPL) and temporally white noise with the cut-off frequency of 500 Hz. With this loading, the standard deviation of the center transverse displacement is about 0.24 thickness. In Fig.2 are shown the power spectral density (PSD) results of the displacements in the three directions at a quarter point of the panel. It can be seen that the multi-level ROM captures the first frequency peak of the PSD in the transverse (y) and the dominant inplane (x) directions very well. For the rest frequency peaks, the multi-level ROM also shows better matching with the Nastran results than the regular ROM.

It is worth noting that the regular ROM has a convergence issue when the pressure level is further increased to 170 dB, whereas the multi-level ROM converges at this increased load level. This suggests the multiple-level identification strategy also improve the prediction capability (stability) of the ROM.

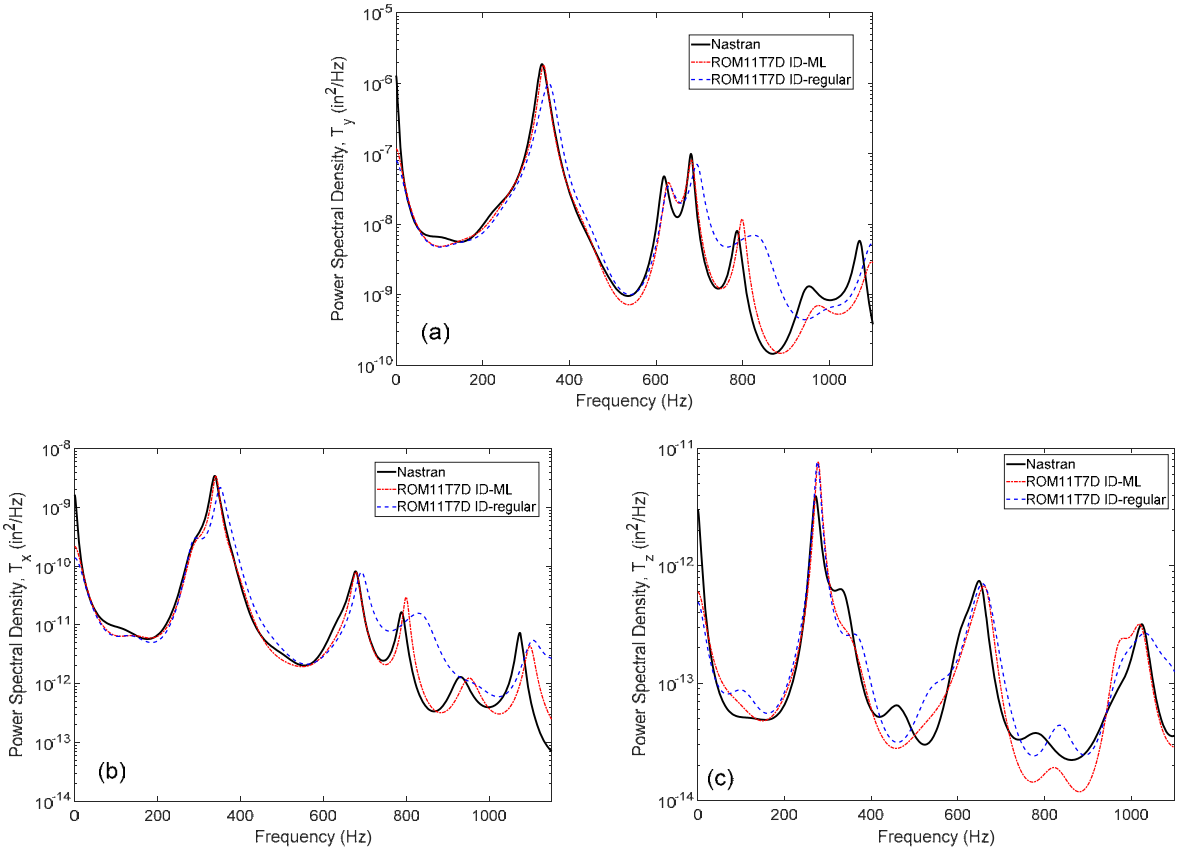

Figure 2. Comparison of ROM predictions of power spectral density at a quarter node. (a) Transverse displacement, Ty; (b) Inplane displacement, Tx; and (c) Inplane displacement, Tz.

Hat-stiffened panel

The hat-stiffened panel, whose finite element model is shown in Fig.3, is a highly asymmetric structure which composed of a flat symmetric rectangular plate (referred to as the skin) and a U open section rigidly connected along its entire length to the skin on only one side (referred to as the bottom). It is clamped at the two ends of the U section and free on the other two sides. Consistently with the hat stiffener, the skin is constrained at the ends only, with the U section remaining free. This panel is 25.4 cm long (in the *x* direction), 2.54 cm high (in the *z* direction), and 12.7 cm wide (in the *y* direction). The thickness of the panel skin is 6.35×10^{-4} m while the thickness of the hat section is 3.175×10^{-4} m. The material properties are selected as follows: Young's Modulus of 2×10^{11} Pa, shear modulus of 8×10^{10} Pa, and density of 7850 kg/m^3. The finite element model of the panel is constructed in MSC/Nastran, and the mesh has totally 360 CQUAD4 shell elements and 378 nodes. A reduced order model of 19 modes (11 transverse and 8 dual) has been constructed (see the detail in [28]) and the nonlinear stiffness coefficients are identified using the regular displacement- $K^{(T)}$ method. In the present study, the same 17-mode basis is used in the multi-level identification.

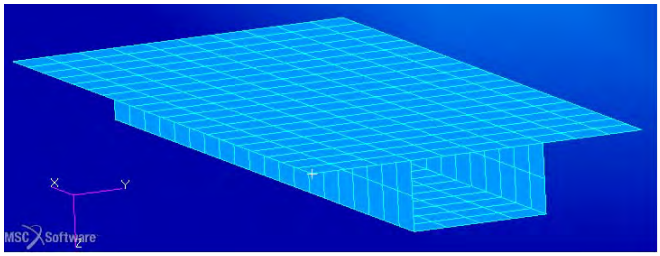

Figure 3. Finite element model of the hat stiffened panel.

The same dynamic load case as for the curved panel is considered here, and the spatially uniform pressure is applied at a level of 143.5dB, which induces the transverse displacement of a quarter node at a free edge to be about 0.16 thickness (standard deviation). In Fig.4 are shown the power spectral density (PSD) results of the displacements in the three directions at this free edge node. It can be seen that the multi-level ROM captures the two dominant frequency peaks of the PSD in the transverse (*z*) direction very well. For the two inplane directions (*x* and *y*), the multi-level ROM also shows better matching with the Nastran results than the regular ROM.

The regular ROM also has a convergence issue when the pressure level is further increased to a medium and a high nonlinear level of 150.9dB and 154.0dB, which give rise to the displacement levels of 0.35 and 0.50 thickness (standard deviation) respectively, whereas the multi-level ROM converges at these two increased load levels [28]. Again, the multiple-level identification improves the prediction capability (stability) of the ROM.

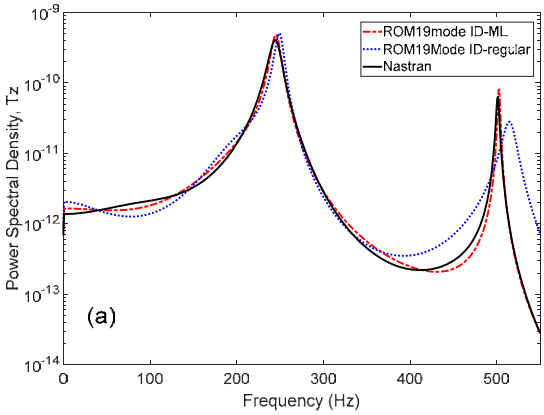

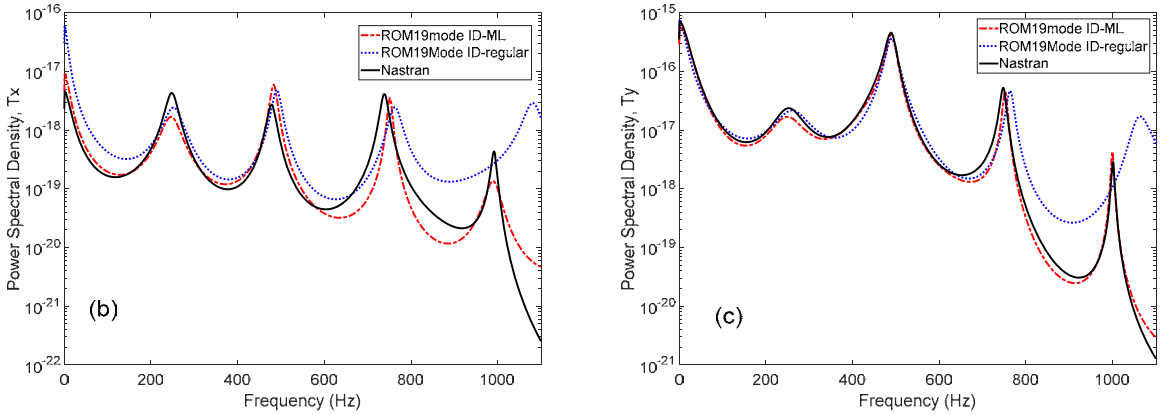

Figure 4. Comparison of ROM predictions of power spectral density at a free edge node. (a) Transverse displacement, Tz; (b) Inplane displacement, Tx; and (c) Inplane displacement, Ty.

Joined wing

The joined wing is in the PrandtlPlane-like concept (box wing), see its finite element model shown in Fig.5. This joined wing model is essentially two in parallel slender thin panels with their ends at one side joined by a vertical thin panel, while the ends at the other side (not joined) clamped. Each slender thin panel has a span of 500 mm and a width of 50 mm. The size of the vertical joining panel is 50 mm by 20 mm. The thickness of all the panels is 1 mm. The material properties are assumed to be those of aluminum, i.e. Young's modulus of 6.9×10^{10} Pa, Poisson's ratio of 0.33, and density of 2700 kg/m^3. The joined wing was modeled in MSC/Nastran with 704 CTRIA shell elements and 445 nodes. A reduced order model of 22 modes (4 transverse and 18 dual) has been constructed (see the detail in [29]) and the nonlinear stiffness coefficients are identified using the regular displacement- $K^{(T)}$ method. The same 22-mode basis is used in the multi-level identification.

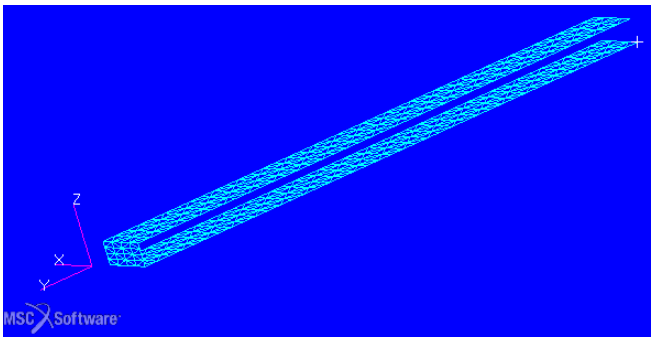

Figure 5. Finite element model of the joined wing.

A static load case is considered to check the performance of the multi-level ROM, as compared to the Nastran and the regular ROM results. The loading is a uniform pressure downward on the upper branch of the wing, varied from 0 to about 0.27 Pa. It should be noted (as seen in Fig.6) that the joined wing buckles when the pressure is increased to about 0.25 Pa, which induces significant increase of the displacement. Right before the buckling, the tip transverse displacement is already quite large, at about 13% of the span. When the buckling happens, the tip transverse displacement increases to about 27% of the span.

In Fig.6 are shown the tip displacements in the transverse (z) and the inplane (y) directions. The multi-level ROM has a much better prediction of the pre-buckling responses than the regular ROM, in both directions. Unfortunately, it is not able to predict the buckling behavior properly, and further refinement of the current strategy to capture such behavior is in progress.

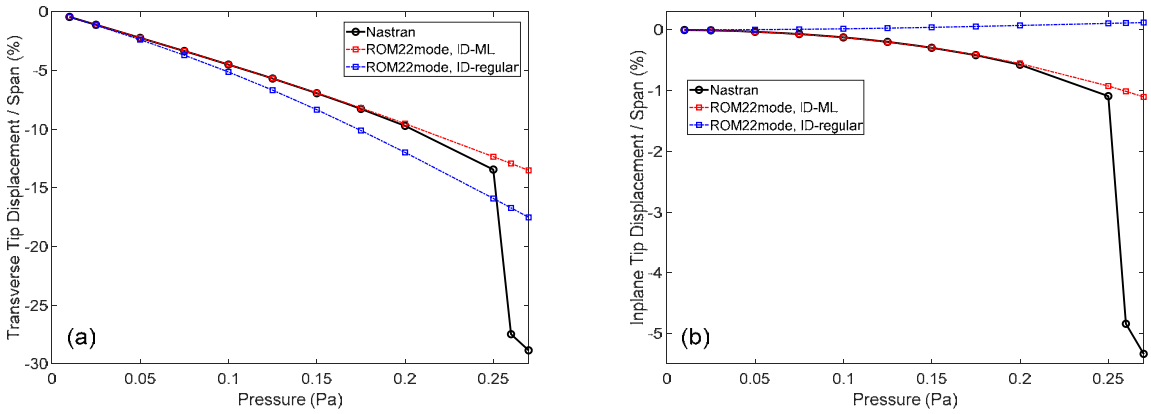

Figure 6. Comparison of ROM predictions. (a) Transverse displacement, Tz; and (b) Inplane displacement, Ty.

CONCLUSION

A multiple-level (ML) identification strategy is proposed to identify nonlinear stiffness coefficients of a non-intrusive type of reduced order model, when the data from a commercial finite element software (e.g. MSC/Nastran) are used, with the objective to improve the prediction capability and/or accuracy of the ROM. The basic idea is to find the displacement level for each coefficient, at which level the variation of this coefficient is the closest to constant, in order to be consistent with the formulation of the ROM from the elasticity theory. The strategy is applied to a few structures with reasonable complexity, including a curved panel, a hat-stiffened panel, and a joined wing. As compared to the ROM identified by the regular method, the improvements in both prediction capability (stability) and the accuracy of the ROM are achieved.

ACKNOWLEDGEMENTS

The authors gratefully acknowledge the financial support of this work by the contract FA9550-16-1-0021 from the Air Force Office of Scientific Research with Dr. Jaimie Tiley as program manager.

REFERENCES

[1] J.J. Bertin, R.M. Cummings, Fifty years of hypersonics: where we've been, where we're going, *Progress in Aerospace Structures*, 39, 511-536, 2003.

[2] McNamara, J.J., and Friedman, P.P., "Aeroelastic and aerothermoelastic analysis of hypersonic vehicles: current status and future trends," *Proceedings of the 48th Structures, Structural Dynamics, and Materials Conference*, Honolulu, Hawaii, April 23-26, 2007. Paper AIAA-2007-2013.

[3] R. D. Blevins, D. Bofilios, I. Holehouse, V. W. Hwa, M. D. Tratt, A. L. Laganelli, P. Pozefsky, and M. Pierucci, *Thermo-Vibro-Acoustic Loads and Fatigue of Hypersonic Flight Vehicle Structure*, Technical Report, AFRL-RB-WP-TR-2009-3139, 2009.

[4] G. Tzong, R. Jacobs, S. Liguore, *Predictive Capability for Hypersonic Structural Response and Life Prediction: Phase 1 – Identification of Knowledge Gaps*, Technical Report, AFRL-RB-WP-TR-2010-3068, V1, 2010.

[5] B. Zuchowski, *Predictive Capability for Hypersonic Structural Response and Life Prediction, Phase 1 – Identification of Knowledge Gaps*, Technical Report, AFRL-RB-WP-TR-2010-3069, 2010.

[6] R. Quiroz, J. Embler, R. Jacobs, G. Tzong, and S. Liguore, *Predictive Capability for Hypersonic Structural Response and Life Prediction: Phase II – Detailed Design of Hypersonic Cruise Vehicle Hot-Structure*, Technical Report, AFRL-RQ-WP-TR-2012-0265, 2012.

[7] B. Zuchowski, *Predictive Capability for Hypersonic Structural Response and Life Prediction: Phase II – Detailed Design of Hypersonic Cruise Vehicle Hot-Structure*, Technical Report, AFRL-RB-WP-TR-2012-0280, 2012.

[8] Eason, T., Spottswood, S., Chona, R., and Penmetsa, R., "A Structures Perspective on the Challenges Associated with Analyzing a Reusable Hypersonic Platform," *Proceedings of the 54th Structures, Structural Dynamics & Materials Conference*, Boston, Massachusetts, April 8-11, 2013. Paper AIAA-2013-1047.

[9] Mei, C., "Three Decades' Interesting Experience in Nonlinear Finite Element Formulation Development and Aerospace Applications", *Proceedings of Eighth International Conference on Recent Advances in Structural Dynamics*, Southampton, July 2003.
[10] Mignolet, M.P., Przekop, A., Rizzi, S.A., and Spottswood, S.M., "A Review of Indirect/Non-Intrusive Reduced Order Modeling of Nonlinear Geometric Structures," *Journal of Sound and Vibration*, Vol. 332, No. 10, pp. 2437-2460, 2013.
[11] McEwan, M.I., Wright, J.R., Cooper, J.E., and Leung, A.Y.T., "A combined Modal/Finite Element Analysis Technique for the Dynamic Response of a Nonlinear Beam to Harmonic Excitation," *Journal of Sound and Vibration*, Vol. 243, pp. 601-624, 2001.
[12] Hollkamp, J.J., Gordon, R.W., and Spottswood, S.M., "Nonlinear Modal Models for Sonic Fatigue Response Prediction: A Comparison of Methods," *Journal of Sound and Vibration*, Vol. 284, pp. 1145-1163, 2005.
[13] Mignolet, M.P., Radu, A.G., and Gao, X., "Validation of Reduced Order Modeling for the Prediction of the Response and Fatigue Life of Panels Subjected to Thermo-Acoustic Effects," *Proceedings of the 8th International Conference on Recent Advances in Structural Dynamics*, Southampton, United Kingdom, Jul. 14-16, 2003.
[14] Radu, A., Yang, B., Kim, K., and Mignolet, M.P., "Prediction of the Dynamic Response and Fatigue Life of Panels Subjected to Thermo-Acoustic Loading," *Proceedings of the 45th Structures, Structural Dynamics, and Materials Conference*, Palm Springs, California, Apr. 19-22, 2004. Paper AIAA-2004-1557.
[15] Hollkamp, J.J., and Gordon, R.W., 2008, "Reduced-Order Models for Nonlinear Response Prediction: Implicit Condensation and Expansion," *Journal of Sound and Vibration*, Vol. 318, pp. 1139–1153.
[16] Przekop, A., and Rizzi, S.A., "A Reduced Order Method for Predicting High Cycle Fatigue of Nonlinear Structures," *Computers and Structures*, Vol. 84, No. 24-25, pp. 1606-1618, 2006.
[17] Kim, K., Radu, A.G., Wang, X.Q., and Mignolet, M.P., "Nonlinear Reduced Order Modeling of Isotropic and Functionally Graded Plates," *International Journal of Non-Linear Mechanics*, Vol. 49, pp. 100-110, 2013.
[18] Kim, K., Khanna, V., Wang, X.Q., and Mignolet, M.P., "Nonlinear Reduced Order Modeling of Flat Cantilevered Structures," *Proceedings of the 50th Structures, Structural Dynamics, and Materials Conference*, Palm Springs, California, May 4-7, 2009. AIAA Paper AIAA-2009-2492.
[19] Przekop A., and Rizzi S.A., "Nonlinear Reduced Order Random Response Analysis of Structures with Shallow Curvature," *AIAA Journal*, Vol. 44 (8), pp. 1767-1778, 2006.
[20] Gordon R.W., and Hollkamp, J.J., "Reduced-Order Modeling of the Random Response of Curved Beams using Implicit Condensation," AIAA-2006-1926, 2006.
[21] Spottswood, S.M., Hollkamp, J.J., and Eason, T.G., "On the Use of Reduced-Order Models for a Shallow Curved Beam Under Combined Loading," *Proceedings of the 49th Structures, Structural Dynamics, and Materials Conference*, Schaumburg, Illinois, Apr. 7-10, 2008. AIAA Paper AIAA-2008-1873.
[22] Przekop, A., and Rizzi, S.A., "Dynamic Snap-Through of Thin-Walled Structures by a Reduced-Order Method," *AIAA Journal*, Vol. 45, No. 10, pp. 2510–2519, 2007.
[23] Spottswood, S.M., Eason, T.G., Wang, X.Q., and Mignolet, M.P., "Nonlinear Reduced Order Modeling of Curved Beams: A Comparison of Methods," *Proceedings of the 50th Structures, Structural Dynamics, and Materials Conference*, Palm Springs, California, May 4-7, 2009. AIAA Paper AIAA-2009-2433.
[24] Wang, X.Q., Perez, R., Mignolet, M.P., Capillon, R., and Soize, C., "Nonlinear Reduced Order Modeling of Complex Wing Models," *Proceedings of the 54th Structures, Structural Dynamics and Materials Conference*, Apr. 8-11, 2013, Boston, Massachusetts, AIAA Paper AIAA-2013-1520.
[25] Perez, R.A., Wang, X.Q., and Mignolet, M.P., "Non-Intrusive Structural Dynamic Reduced Order Modeling for Large Deformations: Enhancements for Complex Structures," *Journal of Computational and Nonlinear Dynamics*, Vol. 9, No. 3, pp. 031008-1 - 031008-12, 2014.
[26] Gordon, R.W., and Hollkamp, J.J., "Reduced-Order Models for Acoustic Response Prediction of a Curved Panel," Proceedings of the 52nd Structures, Structural Dynamics and Materials Conference, Apr. 4 – 7, 2011, Denver, Colorado, Paper AIAA 2011-2081.
[27] Jinshan Lin, X. Q. Wang, and M. P. Mignolet, "Nonlinear reduced order modeling of a cylindrical shell exhibiting mode veering and symmetry breaking', Proceedings of the 37th IMAC, A Conference and Exposition on Structural Dynamics, Orlando, Florida, USA, January 28-31, 2019.
[28] B. A. Wainwirght, X. Q. Wang, and M. P. Mignolet, "Nonlinear reduced order modeling for the dynamic repsonse of a built-up structure with strong asymmetry through thickness", Proceedings of the 37th IMAC, A Conference and Exposition on Structural Dynamics, Orlando, Florida, USA, January 28-31, 2019.
[29] G. Phlipot, X. Q. Wang, M. P. Mignolet, L. Demasi, and R. Cavallaro, "Nonintrusive reduced order modeling for the nonlinear geometric response of some joined wings", Proceedings of the 55th Structures, Structural

Dynamics, and Materials Conference (AIAA SciTech), National Harbor, Maryland, USA, January 13-17, 2014. Paper AIAA-2014-0151.

APPENDIX E:

[C1]: Wang, X.Q., and Mignolet, M.P., "Uncertainty Quantification of Nonlinear Stiffness Coefficients in Non-Intrusive Reduced Order Models," *Proceedings of the International Modal Analysis Conference, IMAC XXXVIII*, Houston, Texas, Feb. 10-13, 2020.

Uncertainty Quantification of Nonlinear Stiffness Coefficients in Non-Intrusive Reduced Order Models

X.Q. Wang, and Marc P. Mignolet

SEMTE, Faculties of Mechanical and Aerospace Engineering,
Arizona State University, Tempe, AZ 85287-6106

ABSTRACT

Reduced order modeling of structures for geometric nonlinear vibration has been an active research subject due to its advantage of reducing the computational cost associated with using traditional numerical methods. One type of reduced order models are the non-intrusive ones, for which the ROM is built from data obtained from commercial finite element software. Their advantage is the capability to handle a broad set of complex geometries and boundary conditions experienced in practice. Due to inconsistencies between the ROM and commercial software formulations, however, the constructed ROM cannot be an exact match of the finite element model. Accordingly, epistemic uncertainty exists in the ROM modeling beside issues of truncation of the number of modes.

In the present study, the epistemic uncertainty associated with nonlinear stiffness coefficients of the non-intrusive ROM is quantified using a clamped-clamped straight beam as a demonstration example. A Monte Carlo simulation strategy is used first. Random samples of the optimal displacement level at which the identification is performed are generated with their probability distribution consistent with those used in the construction of the deterministic ROM. Random ROM samples are then identified at these random optimal levels, and the corresponding predicted response for a particular dynamic excitation are computed. Uncertainty bands on these predictions are then calculated to quantify the uncertainty of the ROM predictions. Furthermore, the nonparametric stochastic approach is considered as an alternative strategy to generate these uncertainty bands. The mean ROM used is the one identified by the multiple-level identification method, and the dispersion parameter (a measure of uncertainty level in the approach) of the corresponding stochastic ROM is determined by the maximum likelihood principle. A number of random samples of the mean ROM are generated, and their predictions of the same dynamic validation cases are computed, from which the uncertainty bands of the predictions are obtained. The uncertainty band results are shown to match the Monte Carlo simulation results very well.

Keywords: uncertainty quantification, nonparametric stochastic approach, nonlinear stiffness coefficients, non-intrusive reduced order modeling

INTRODUCTION

Reduced order modeling of structures for geometric nonlinear vibration has been an active research subject due to its advantage of reducing the computational cost associated with using traditional numerical methods [1-14]. One particular class of applications are hypersonic aircraft structures in extreme aerodynamic-thermal environments, e.g., large aerodynamic, thermal, and mechanical loadings with nonlinear interactions [15-17].

One type of reduced order models are the non-intrusive ones, for which the ROM is built from data obtained from commercial finite element software (e.g., Nastran, Abaqus). Their advantage is the capability to handle a broad set of complex geometries and boundary conditions experienced in practice. Such reduced order models have been constructed for a large number of structures, and their strong potentials have been demonstrated. The details can be found in a recent review [18].

In a non-intrusive ROM [7], a modal basis is constructed to represent a given nonlinear displacement, $\underline{u}(\underline{X},t)$,

$$\underline{u}(\underline{X},t) = \sum_{n=1}^{N} q_n(t)\, \underline{\phi}^{(n)}(\underline{X}), \tag{1}$$

where $\underline{u}(\underline{X},t)$ denotes the vector of physical displacements defined on the finite element degrees of freedom. $\underline{\phi}^{(n)}$ are constant basis functions and $q_n(t)$ are the time dependent generalized coordinates.

The governing equation of the ROM is derived from the elasticity theory by the Galerkin approach, expressed as

$$M_{ij}\ddot{q}_j + D_{ij}\dot{q}_j + K_{ij}^{(1)} q_j + K_{ijl}^{(2)} q_j q_l + K_{ijlp}^{(3)} q_j q_l q_p = F_i, \tag{2}$$

where M_{ij} denotes the elements of the mass matrix, $K_{ij}^{(1)}$, $K_{ijl}^{(2)}$, $K_{ijlp}^{(3)}$ are the linear, quadratic, and cubic stiffness coefficients, and F_i are the modal forces. The viscous damping matrix $\{D_{ij}\}$ is added to collectively represent various dissipation mechanisms following standard practice.

The above formulation of the ROM is not necessarily the same as the commercial finite element software, hence the ROM built upon the data from the commercial software may show some variation from the finite element model even if a large number of modes are taken. One example is the nonlinear stiffness coefficients. In a non-intrusive ROM, they are identified from either nonlinear forces or tangent stiffness matrices corresponding to enforced displacements [19]. The stiffness coefficients are supposed to be independent of the displacement level enforced, but this is not the case, and a multi-level identification method has been developed to find the optimal displacement level for each nonlinear stiffness coefficient [20]. The optimal displacement levels show variability from one coefficient to another, thus the stiffness coefficients identified at these displacement levels. This variation can be considered as an epistemic uncertainty, that is, uncertainty due to the modeling.

In the present study, this epistemic uncertainty associated with the nonlinear stiffness coefficients is quantified. The Monte Carlo simulation is firstly carried out as follows. Random samples of optimal displacement levels will be generated, whose probability distribution is consistent with that observed in the multi-level identification. Random samples of nonlinear stiffness coefficients will be identified at these displacement-level samples, and structural responses to a dynamic load are computed. The uncertainty bands of the responses are then computed to give quantitative measure of the epistemic uncertainty. Afterwards, the nonparametric stochastic approach [21-24], which uses a dispersion parameter determined by a small number of samples from the Monte Carlo simulation to directly generate the large number of random samples, is employed to repeat the same uncertainty quantification and compared to the Monte Carlo simulation results.

QUANTIFICATION OF EPISTEMIC UNCERTAINTY: MONTE CARLO SIMULATION

As a demonstration example, a clamped-clamped straight beam is considered. The beam is of rectangular cross section and its geometric and material properties of the straight beam are given in Table 1. A finite element model of the beam was constructed with Nastran using 40 CBEAM elements.

Table 1. Beam Properties

Beam Length	0.2286 m
Cross-section Width	0.0127 m
Cross-section Thickness	$7.75\ 10^{-4}$ m
Mass per unit length	2763 kg/m^3
Young's Modulus	73,000 MPa
Shear Modulus	27,700 MPa

A nonlinear ROM of the beam has been constructed, including the first 4 symmetric linear modes and 4 associated duals (ROM4L4D). The stiffness coefficients were identified by the multi-level identification method [3]. Static and dynamic validations were carried out, and good matching between the ROM and the Nastran results is obtained (the results will be shown later along with the uncertainty quantification results).

Nevertheless, there is still some discrepancy, especially for the dynamic results at higher load levels. One observation from the multi-level identification results is that the optimal displacement level is not the same for all the coefficients. This is not consistent with the ROM formulation and suggests that epistemic uncertainty exist in the data used in the identification, which leads to the variation of the optimal displacement level. The uncertainty propagates further to affect the identified stiffness coefficients and eventually the ROM predictions.

This epistemic uncertainty can be seen from the distribution of the optimal displacement levels for the quadratic and the cubic coefficients, respectively, as shown in Fig.1. For the quadratic coefficients, the optimal displacement levels are concentrated at a low displacement level but there are a small number of coefficients whose optimal displacement levels distribute widely. For the cubic coefficients, the optimal displacement levels are concentrated at

a range of higher displacement level while there are a number of coefficients whose optimal displacement levels distribute widely.

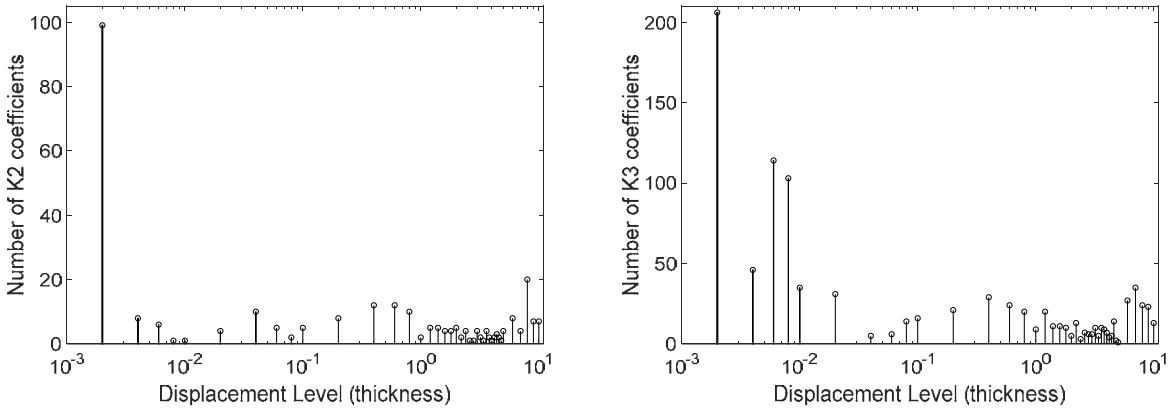

(a) (b)

Figure 1. Distribution of optimal displacement levels for the quadratic and the cubic coefficients. (a) Quadratic coefficients; (b) Cubic coefficients.

The cubic coefficients whose optimal displacement levels are at the highest displacement level are found to be the coefficients which are small and negligible thus difficult to be identified with high accuracy. This is indicated by the distribution of the optimal displacement levels for the remained cubic coefficients after "cleaning up" the ROM, that is, zeroing out those negligible coefficients, as shown in Fig.2. The distribution for the quadratic coefficients essentially does not change.

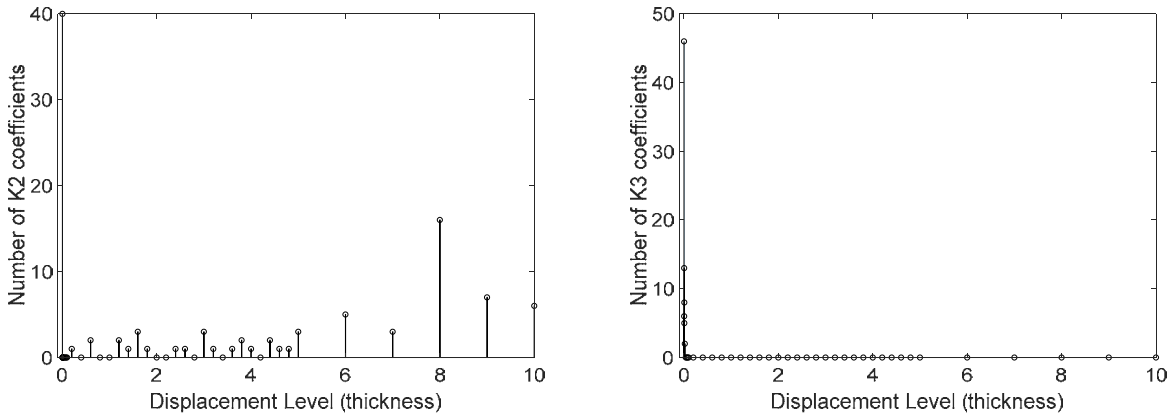

Figure 2. Distribution of optimal displacement levels for the remained quadratic and the cubic coefficients after "cleaning up" the ROM. (a) Quadratic coefficients; (b) Cubic coefficients.

In the present study, this epistemic uncertainty is firstly quantified using the Monte Carlo simulation:

(1) Two sets of random samples of optimal displacement levels are generated for the quadratic and the cubic coefficients, respectively, termed as quadratic and cubic random samples thereafter. The statistic distribution features of the two sets of random samples are made consistent with the cumulative distribution functions of the original data by using the inverse transform sampling method. The cumulative distribution functions of the original data and the generated random samples are shown in Fig.3, and it can be seen that the random samples represent the original data quite well.

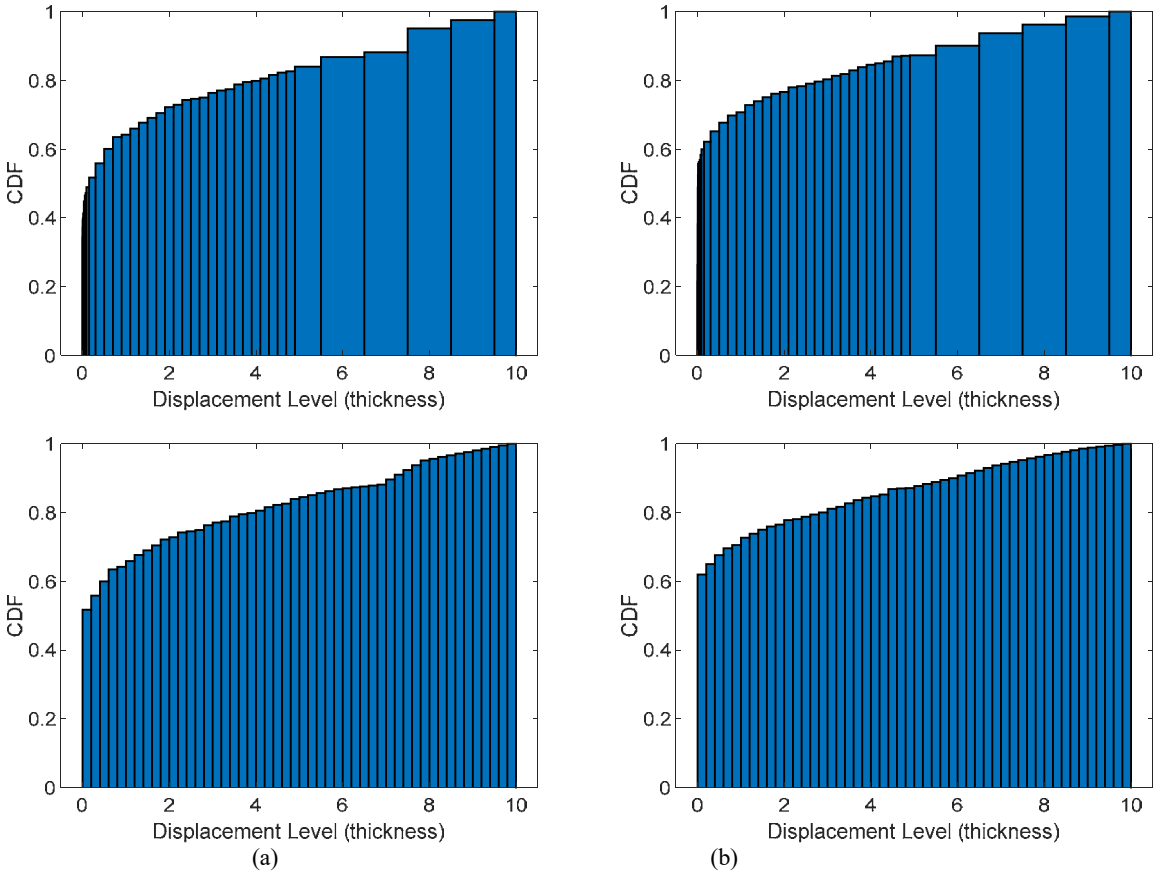

Figure 3. Cumulative distribution functions of optimal displacement levels for the quadratic and the cubic coefficients. Top: original data from multi-level identification. Bottom: random samples generated by the inverse transform sampling method. (a) Quadratic coefficients; (b) Cubic coefficients.

(2) 100 random samples are then taken. For each random sample (a displacement level) in the two sets, the stiffness coefficients are identified by the regular single-level identification method. The quadratic coefficients identified using a quadratic random sample and the cubic coefficients identified from a cubic random sample are combined and considered as a random sample of stiffness coefficients.

(3) Using the set of random samples of stiffness coefficients obtained in (2), a Monte Carlo simulation is carried out to compute the responses of the random samples to the static and dynamic loads used in the validation. The uncertainty bands are computed from the response data.

In Figs. 4 and 5 are shown the uncertainty band results, along with the validation results of ROM versus Nastran, for a dynamic load case at two load levels, respectively. The dynamic load case is a uniformly distributed force along the span, time-variant as modeled by a white noise with the cut-off frequency of 1000Hz. Firstly, the ROM predictions match Nastran results at dominant frequency peaks very well. Secondly, the uncertainty band encloses Nastran PSD curve in almost the whole range of frequency 0 to 1500 Hz, suggesting the epistemic uncertainty is properly quantified.

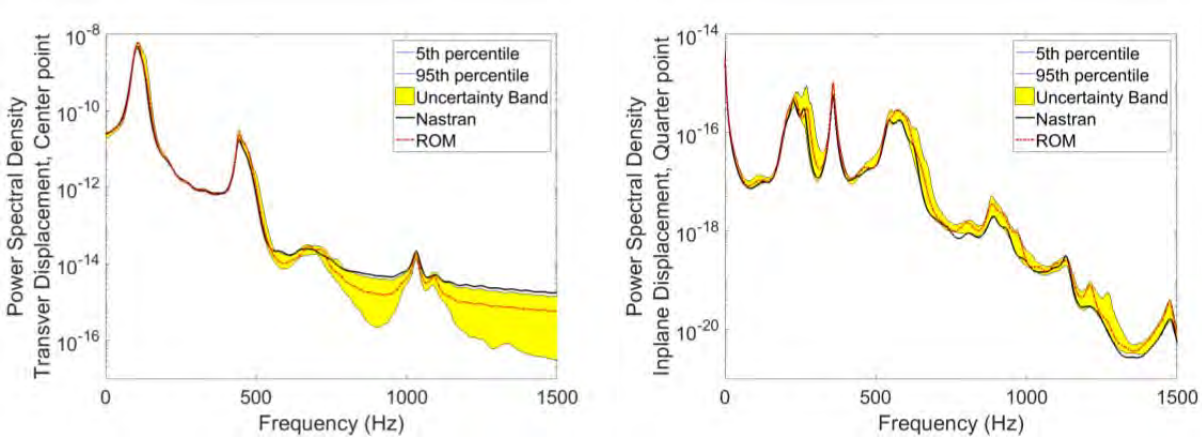

(a) (b)

Figure 4. Uncertainty band of the ROM predictions for the dynamic load case. Load level 130dB (OASPL) which gives standard deviation of center transverse displacement at about 0.75 thicknesses. (a) Transverse displacement, center point; (b) Inplane displacement, quarter point.

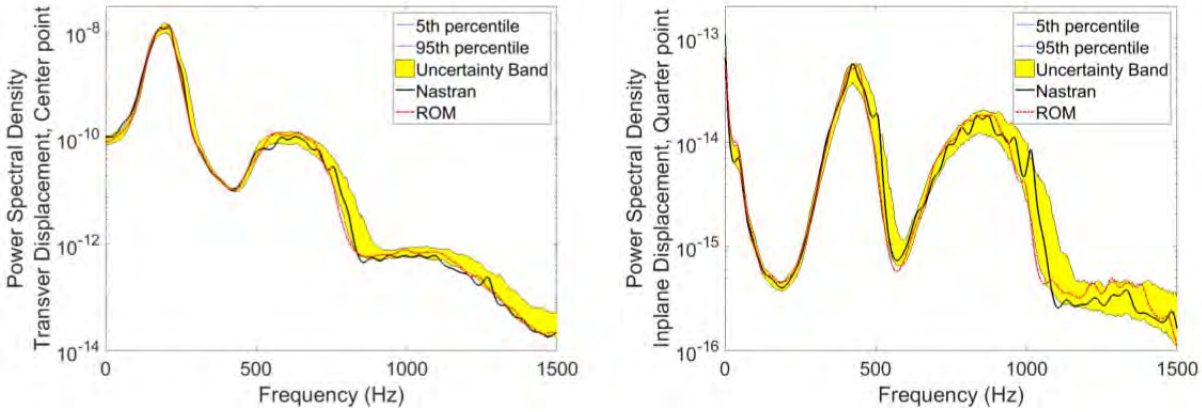

(a) (b)

Figure 5. Uncertainty band of the ROM predictions for the dynamic load case. Load level 145dB (OASPL) which gives standard deviation of center transverse displacement at about 1.9 thicknesses. (a) Transverse displacement, center point; (b) Inplane displacement, quarter point.

Uncertainty band of "cleaned" ROM

The above uncertainty quantification procedure is then applied to the cleaned ROM, to further understand the behavior of epistemic uncertainty.

The sets of quadratic and cubic random samples are generated according to the cumulative distribution functions of the data of the remained coefficients after cleaning up, using the inverse transform sampling method. The cumulative distribution functions of the cleaned data and the generated random samples are shown in Fig.6. A zoomed view is shown for the cubic coefficients since its CDF reaches 1 at a small value. It can be seen that the random samples represent the data quite well.

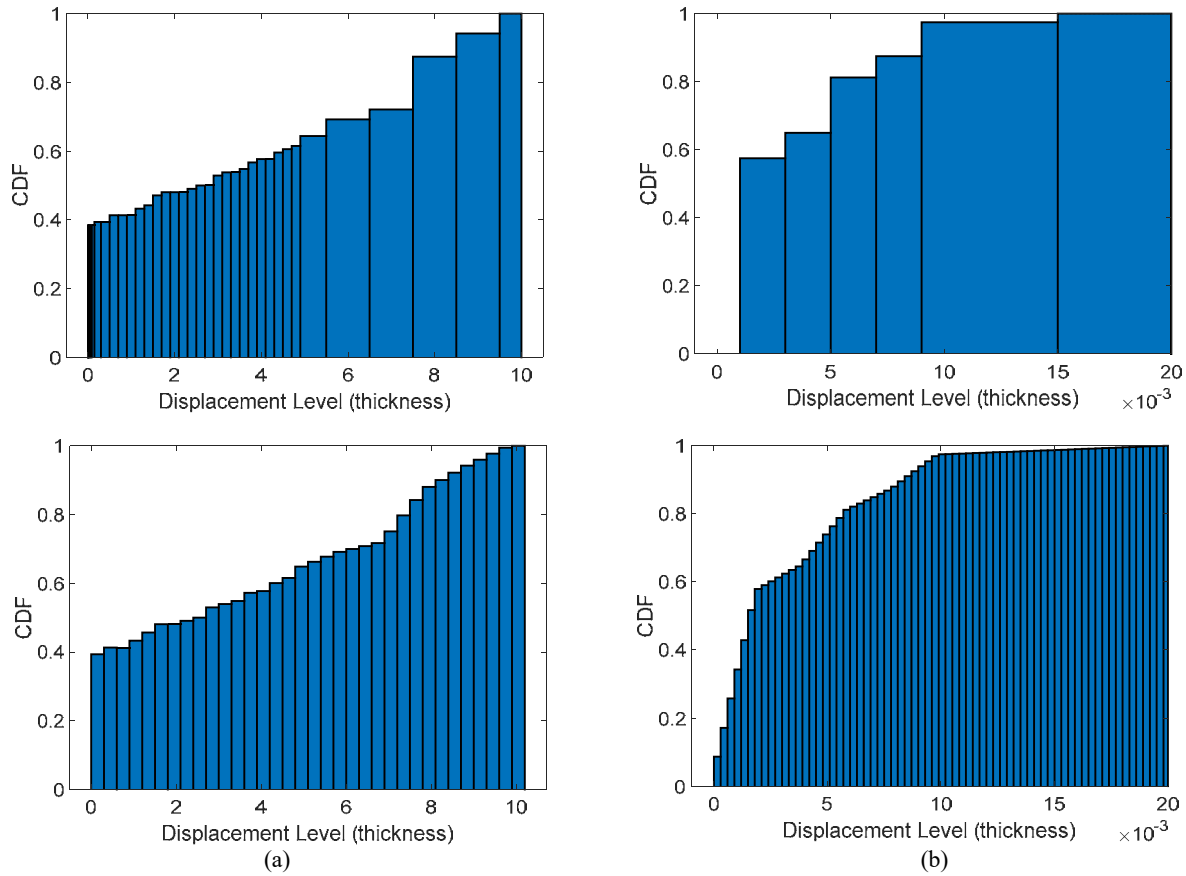

Figure 6. Cumulative distribution functions of optimal displacement levels for the quadratic and the cubic coefficients remained after cleaning up. Top: cleaned data from multi-level identification. Bottom: random samples generated by the inverse transform sampling method. (a) Quadratic coefficients; (b) Cubic coefficients, zoomed view.

Similar to the uncleaned ROM, random samples of stiffness coefficients are identified at displacement levels given by the above random samples. Again the quadratic coefficients identified using a quadratic random sample and the cubic coefficients identified from a cubic random sample are combined and considered as a random sample of stiffness coefficients. Using the set of random samples of stiffness coefficients obtained, a Monte Carlo simulation is carried out to compute the responses of the random samples to the dynamic loads used in the validation. The uncertainty bands are computed from the response data.

In Figs. 7 and 8 are shown the uncertainty band results for the save dynamic load case at two load levels, respectively. Compared to the uncleaned ROM, the uncertainty band of the cleaned ROM becomes broader. The coefficients remained after cleaning up are usually considered better identified, so the broader uncertainty band implies that the ROM has larger variation than what the uncleaned ROM has shown.

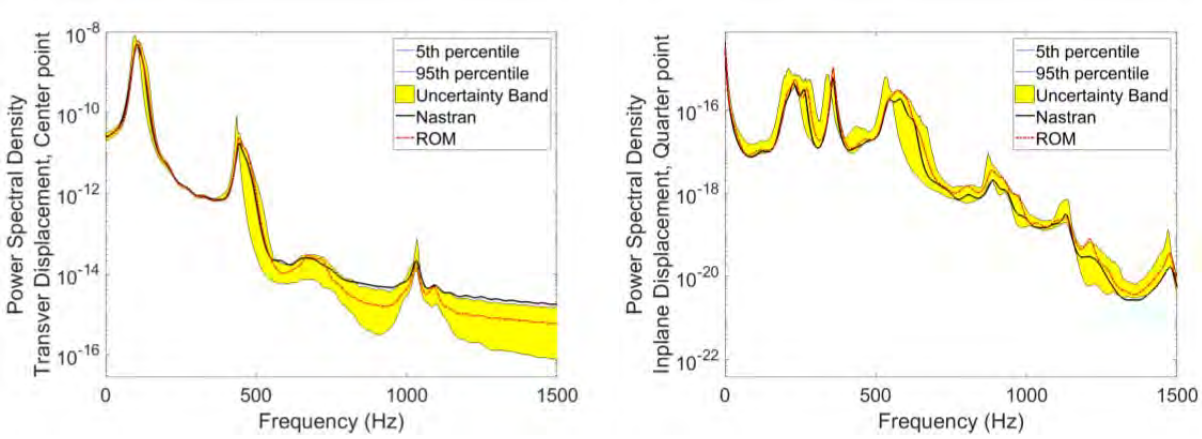

(a) (b)

Figure 7. Uncertainty band of the cleaned ROM predictions for the dynamic load case. Load level 130dB (OASPL) which gives standard deviation of center transverse displacement at about 0.75 thicknesses. (a) Transverse displacement, center point; (b) Inplane displacement, quarter point.

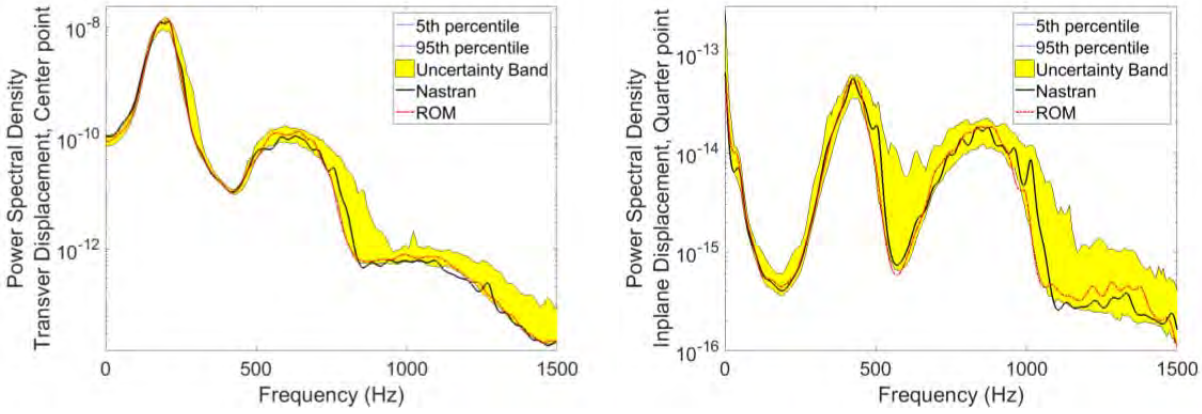

(a) (b)

Figure 8. Uncertainty band of the cleaned ROM predictions for the dynamic load case. Load level 145dB (OASPL) which gives standard deviation of center transverse displacement at about 1.9 thicknesses. (a) Transverse displacement, center point; (b) Inplane displacement, quarter point.

QUANTIFICATION OF EPISTEMIC UNCERTAINTY: NONPARAMETRIC APPROACH

As shown above, in order to evaluate the uncertainty band, a number of Monte Carlo simulations with the ROM have to be done. This requires the identification of random ROM samples, which could be time consuming when the number of samples is large.

The nonparametric approach [21-23] has been developed to directly generate random ROM samples. It can be accomplished using the maximum entropy approach as demonstrated in [24] for an elastic nonlinear ROM. A key observation is that the linear, quadratic, and cubic stiffnesses cannot be varied independently, rather a bigger matrix

$$\underline{\underline{K}}_B = \begin{bmatrix} \underline{\underline{K}}^{(1)} & \underline{\underline{\widetilde{K}}}^{(2)} \\ \underline{\underline{\widetilde{K}}}^{(2)T} & 2\underline{\underline{\widetilde{K}}}^{(3)} \end{bmatrix} \tag{3}$$

must remain positive definite for all realizations. In this equation, the matrices $\underline{\underline{\widetilde{K}}}^{(2)}$ and $\underline{\underline{\widetilde{K}}}^{(3)}$ are obtained by a reshaping of the quadratic and cubic stiffness tensors $K^{(2)}_{mnl}$ and $K^{(3)}_{mnlp}$, see [10]. This property was instrumental in

the uncertainty modeling which proceeds from the matrix $\underline{\underline{K}}_B$ of the mean model first decomposed as (e.g., Cholesky decomposition)

$$\underline{\underline{K}}_B = \underline{\underline{L}}_K \, \underline{\underline{L}}_K^T . \tag{4}$$

Next, lower triangular matrices $\breve{\underline{\underline{H}}}_K$ are generated according to the following, see Fig. 1:

(i) the elements $\breve{H}_{il}$, $i>l$, are all independent of each other and independent of the elements $\breve{H}_{ii}$. Further, they are normally distributed with mean 0 and standard deviation $\sigma_{il} = 1/\sqrt{2\mu_{ii}}$.

(ii) the elements $\breve{H}_{ii}$ are all independent of each other and can be expressed as

$$\breve{H}_{ii} = \sqrt{\frac{\breve{Y}_{ii}}{\mu_{ii}}} , \tag{5}$$

where $\breve{Y}_{ii}$ are Gamma random variables, and μ_{ii} is given by

$$\mu_{ii} = \frac{\bar{n} + 2\lambda - 1}{2} , \tag{6}$$

where $\bar{n}$ is the size of the matrix $\underline{\underline{K}}_B$ and λ is the free parameter of the distribution which can be used to specify a level of uncertainty on $\underline{\underline{K}}_B$. Finally, random $\underline{\underline{K}}_B$ matrices can be obtained as

$$\breve{\underline{\underline{K}}}_B = \underline{\underline{L}}_K \, \breve{\underline{\underline{H}}}_K \breve{\underline{\underline{H}}}_K^T \, \underline{\underline{L}}_K^T . \tag{7}$$

from which random linear, quadratic, and cubic stiffness parameters can be extracted given the form of $\underline{\underline{K}}_B$.

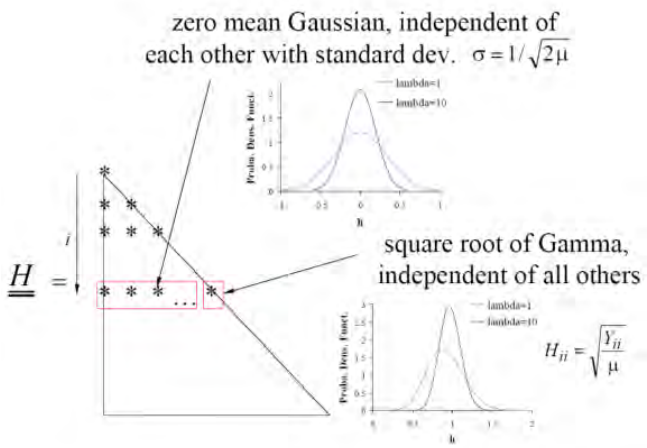

Figure 9. Structure of the random $\breve{\underline{\underline{H}}}_K$ matrices with $\bar{n}$ = 8, i =2, and λ_0=1 and 10.

In the nonparametric approach, the parameter λ needs to be determined. In practice, a dispersion parameter δ is usually used, and its relation to λ is given by

$$\delta^2 = \frac{\bar{n} + 1}{\bar{n} + 2\lambda - 1} . \tag{8}$$

The parameter δ can be determined using the maximum likelihood principle. To this end, a set of δ values are taken. For each of them, 100 $\underline{\underline{K}}_B$ samples are generated, and the PSD of the ROM responses to the dynamic load at 145dB are computed. For each δ value, the likelihood function of the PSD results from these $\underline{\underline{K}}_B$ samples is evaluated with respect to 10 samples from the Monte Carlo simulation as the true observations. The log of the likelihood function value as function of δ is shown in Fig. 10, from which δ = 0.04 is the optimal value for the nonparametric model.

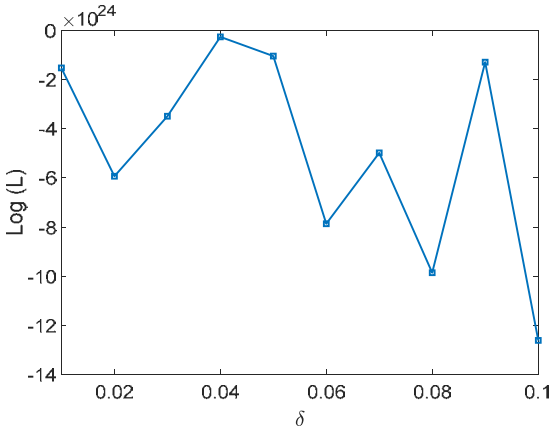

Figure 10. Log of likelihood function value as function of δ.

The 100 $\underline{\underline{K}}_B$ samples corresponding to δ = 0.04 are used to compute the responses to the dynamic load at 130dB and 145dB, then the uncertainty band of the PSD result is computed and shown in Figs. 10 and 11, respectively. The uncertainty band results from the nonparametric approach are almost the same as the results from the Monte Carlo simulation.

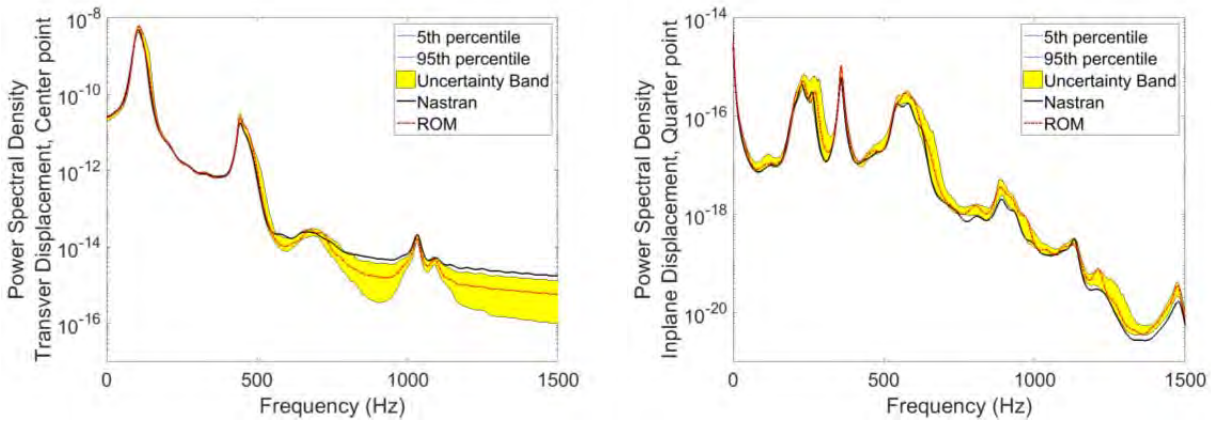

(b) (b)

Figure 10. Uncertainty band of the ROM predictions by the nonparametric approach. Dynamic load level 130dB (OASPL) which gives standard deviation of center transverse displacement at about 0.75 thicknesses. (a) Transverse displacement, center point; (b) Inplane displacement, quarter point.

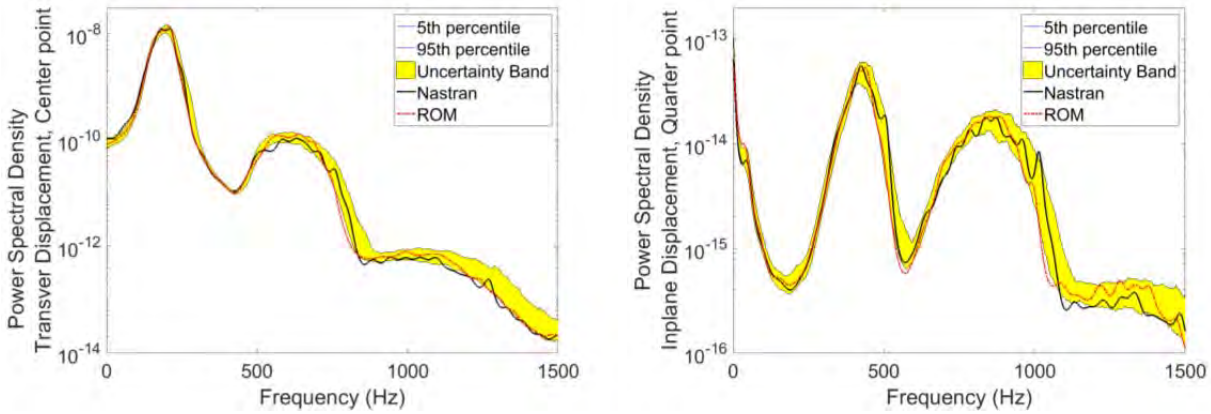

(a) (b)

Figure 11. Uncertainty band of the ROM predictions by the nonparametric approach. Dynamic load level 145dB (OASPL) which gives standard deviation of center transverse displacement at about 1.9 thicknesses. (a) Transverse displacement, center point; (b) Inplane displacement, quarter point.

CONCLUSION

The epistemic uncertainty associated with the nonlinear stiffness coefficients of the reduced order model (ROM) as evaluated by the multi-level identification method is quantified using both the Monte Carlo simulation and the nonparametric approach. A clamped-clamped straight beam is used as an example for demonstration. In the Monte Carlo simulation, random ROM samples are identified at random optimal displacement levels whose probability distribution is consistent with that observed in the multi-level identification. The responses of ROM samples to a dynamic load at two load levels are computed, and the uncertainty bands of the power spectral density (PSD) results are computed for uncertainty quantification. It is demonstrated that the uncertainty bands properly account for the uncertainty of the stiffness coefficients. For the nonparametric approach, the dispersion parameter is determined by using the maximum likelihood principle, then random ROM samples are directly generated. These ROM samples are used to obtain the uncertainty band results for the same dynamic load. The uncertainty bands from the nonparametric approach match the Monte Carlo simulation results very well.

ACKNOWLEDGEMENTS

The authors gratefully acknowledge the support of this work by the contract FA9550-16-1-0021 from the Air Force Office of Scientific Research with Dr. Jaimie Tiley as program manager.

REFERENCES

[1] McEwan, M.I., Wright, J.R., Cooper, J.E., and Leung, A.Y.T., "A combined Modal/Finite Element Analysis Technique for the Dynamic Response of a Nonlinear Beam to Harmonic Excitation," *Journal of Sound and Vibration*, Vol. 243, pp. 601-624, 2001.

[2] Hollkamp, J.J., Gordon, R.W., and Spottswood, S.M., "Nonlinear Modal Models for Sonic Fatigue Response Prediction: A Comparison of Methods," *Journal of Sound and Vibration*, Vol. 284, pp. 1145-1163, 2005.

[3] Mignolet, M.P., Radu, A.G., and Gao, X., "Validation of Reduced Order Modeling for the Prediction of the Response and Fatigue Life of Panels Subjected to Thermo-Acoustic Effects," *Proceedings of the 8th International Conference on Recent Advances in Structural Dynamics*, Southampton, United Kingdom, Jul. 14-16, 2003.

[4] Radu, A., Yang, B., Kim, K., and Mignolet, M.P., "Prediction of the Dynamic Response and Fatigue Life of Panels Subjected to Thermo-Acoustic Loading," *Proceedings of the 45th Structures, Structural Dynamics, and Materials Conference*, Palm Springs, California, Apr. 19-22, 2004. Paper AIAA-2004-1557.

[5] Hollkamp, J.J., and Gordon, R.W., 2008, "Reduced-Order Models for Nonlinear Response Prediction: Implicit Condensation and Expansion," *Journal of Sound and Vibration*, Vol. 318, pp. 1139–1153.

[6] Przekop, A., and Rizzi, S.A., "A Reduced Order Method for Predicting High Cycle Fatigue of Nonlinear Structures," *Computers and Structures*, Vol. 84, No. 24-25, pp. 1606-1618, 2006.

[7] Kim, K., Radu, A.G., Wang, X.Q., and Mignolet, M.P., "Nonlinear Reduced Order Modeling of Isotropic and Functionally Graded Plates," *International Journal of Non-Linear Mechanics*, Vol. 49, pp. 100-110, 2013.

[8] Przekop A., and Rizzi S.A., "Nonlinear Reduced Order Random Response Analysis of Structures with Shallow Curvature," *AIAA Journal*, Vol. 44 (8), pp. 1767-1778, 2006.

[9] Spottswood, S.M., Hollkamp, J.J., and Eason, T.G., "On the Use of Reduced-Order Models for a Shallow Curved Beam Under Combined Loading," *Proceedings of the 49th Structures, Structural Dynamics, and Materials Conference*, Schaumburg, Illinois, Apr. 7-10, 2008. AIAA Paper AIAA-2008-1873.

[10] Przekop, A., and Rizzi, S.A., "Dynamic Snap-Through of Thin-Walled Structures by a Reduced-Order Method," *AIAA Journal*, Vol. 45, No. 10, pp. 2510–2519, 2007.

[11] Spottswood, S.M., Eason, T.G., Wang, X.Q., and Mignolet, M.P., "Nonlinear Reduced Order Modeling of Curved Beams: A Comparison of Methods," *Proceedings of the 50th Structures, Structural Dynamics, and Materials Conference*, Palm Springs, California, May 4-7, 2009. AIAA Paper AIAA-2009-2433.
[12] Wang, X.Q., Perez, R., Mignolet, M.P., Capillon, R., and Soize, C., "Nonlinear Reduced Order Modeling of Complex Wing Models," *Proceedings of the 54th Structures, Structural Dynamics and Materials Conference*, Apr. 8-11, 2013, Boston, Massachusetts, AIAA Paper AIAA-2013-1520.
[13] Perez, R.A., Wang, X.Q., and Mignolet, M.P., "Non-Intrusive Structural Dynamic Reduced Order Modeling for Large Deformations: Enhancements for Complex Structures," *Journal of Computational and Nonlinear Dynamics*, Vol. 9, No. 3, pp. 031008-1 - 031008-12, 2014.
[14] Gordon, R.W., and Hollkamp, J.J., "Reduced-Order Models for Acoustic Response Prediction of a Curved Panel," Proceedings of the 52nd Structures, Structural Dynamics and Materials Conference, Apr. 4 – 7, 2011, Denver, Colorado, Paper AIAA 2011-2081.
[15] Gogulapati, A., Deshmukh, R., Crowell, A.R., McNamara, J.J., Vyas, V., Wang, X.Q., Mignolet, M., Beberniss, T., Spottswood, S.M., and Eason, T.G., "Response of a Panel to Shock Impingement: Modeling and Comparison with Experiments," *Proceedings of the AIAA Science and Technology Forum and Exposition (SciTech2014)*, National Harbor, Maryland, Jan. 13-17, 2014, AIAA Paper AIAA 2014-0148.
[16] Matney, A., Mignolet, M.P., Culler, A.J., McNamara, J.J., and Spottswood, S.M., "Panel Response Prediction through Reduced Order Models with Application to Hypersonic Aircraft," *Proceedings of the AIAA Science and Technology Forum and Exposition (SciTech2015)*, Orlando, Florida, Jan. 5-9, 2015, AIAA Paper AIAA 2015-1630.
[17] Gogulapati, A., Brouwer, K., Wang, X.Q., Murthy, R., McNamara, J.J., and Mignolet, M.P., "Full and Reduced Order Aerothermoelastic Modeling of Built-Up Aerospace Panels in High-Speed Flows," *Proceedings of the AIAA Science and Technology Forum and Exposition (SciTech2017)*, Dallas, Texas, Jan. 9-13, 2017, AIAA Paper AIAA 2017-0180.
[18] Mignolet, M.P., Przekop, A., Rizzi, S.A., and Spottswood, S.M., "A Review of Indirect/Non-Intrusive Reduced Order Modeling of Nonlinear Geometric Structures," *Journal of Sound and Vibration*, Vol. 332, No. 10, pp. 2437-2460, 2013.
[19] Perez, R.A., Wang, X.Q., and Mignolet, M.P., "Non-Intrusive Structural Dynamic Reduced Order Modeling for Large Deformations: Enhancements for Complex Structures," *Journal of Computational and Nonlinear Dynamics*, Vol. 9, No. 3, paper 031008, 2014.
[20] X.Q. Wang, Jinshan Lin, B.A. Wainwirght, and M.P. Mignolet, "Multiple-Level Identification of Stiffness Coefficients in Nonlinear Reduced Order Modeling," Proceedings of the 37th IMAC, Conference and Exposition on Structural Dynamics, Orlando, Florida, USA, January 28-31, 2019.
[21] Soize, C. "A Nonparametric Model of Random Uncertainties for Reduced Matrix Models in Structural Dynamics." *Probabilistic Engineering Mechanics*, Vol. 15, No. 3, 2000, pp. 277-294.
[22] Soize, C. *Stochastic Models of Uncertainties in Computational Mechanics*. American Society of Civil Engineers, Reston, VA, 2012.
[23] Soize, C., *Uncertainty Quantification: An Accelerated Course with Advanced Applications in Computational Engineering*, Springer-Verlag, 2017.
[24] Mignolet, M.P., and Soize, C., "Stochastic Reduced Order Models for Uncertain Geometrically Nonlinear Dynamical Systems," *Computer Methods in Applied Mechanics and Engineering*, Vol. 197, 2008, pp. 3951-3963.

APPENDIX F:

[J3]: Wang, X.Q., Liao, Y., and Mignolet, M.P., "Uncertainty Analysis of Piezoelectric Vibration Energy Harvesters Using a Finite Element Level-Based Maximum Entropy Approach," *ASCE-ASME Journal of Risk and Uncertainty in Engineering Systems Part B: Mechanical Engineering*, In Press.

Uncertainty analysis of piezoelectric vibration energy harvesters using a finite element level-based maximum entropy approach

X.Q. Wang[1], Yabin Liao[2]*, Marc P. Mignolet[1]

[1]SEMTE Faculties of Mechanical and Aerospace Engineering
Arizona State University, Tempe, AZ 85287
[2]Mechanical Engineering Technology
Penn State Erie, the Behrend College

* Corresponding author: Yabin.Liao@psu.edu

Abstract

Quantifying effects of system-wide uncertainties (i.e., affecting structural, piezoelectric, and/or electrical components) in the analysis and design of piezoelectric vibration energy harvesters has recently been emphasized. The present investigation proposes first a general methodology to model these uncertainties within a finite element model of the harvester obtained from an existing finite element software. Needed from this software are the matrices relating to the structural properties (mass, stiffness), the piezoelectric capacitance matrix, as well as the structural-piezoelectric coupling terms of the mean harvester. The thermal analogy linking piezoelectric and temperature effects is also extended to permit the use of finite element software that do not have piezoelectric elements but include thermal effects on structures. The approach is applied to a beam energy harvester. Both weak and strong coupling configurations are considered and various scenarios of load resistance tuning are considered, i.e., based on the mean model, for each harvester sample, or based on the entire set of harvesters. The uncertainty is shown to have significant effects in all cases even at a relatively low level and these effects are dominated by the uncertainty on the structure vs. the one on the piezoelectric component. The strongly coupled configuration is shown to be better as it is less sensitive to the uncertainty and its variability in power output can be significantly reduced by the adaptive optimization, and the harvested power can even be boosted if the target excitation frequency falls into the power saturation band of the system.

1 Introduction

Piezoelectric energy harvesting has received significant attention in recent years as a viable solution to self-powered wireless sensors for emerging applications including wearable electronics, structural health monitoring, Internet of Things (IoT) and robotics. Ambient vibrations are abundant in many applications, for example, industrial machines, moving vehicles and aircraft, building and bridges, and human motions, etc. Piezoelectric materials have a crystalline structure inside which the atoms are not symmetrically arranged. Deforming the structure modifies the balance of the electric charges and results in a net electric charge on the crystal surface, which is called the direct piezoelectric effect. This effect has typically been used for sensor devices such as accelerometers, microphones, load cells, etc., and also makes piezoelectrics a suitable material for vibration energy harvesting, where the piezoelectric material is strained as a result of vibration. In addition, piezoelectrics have attractive features such as high energy density and compact and simple architecture [1]. These all contributed to the growing interest in piezoelectric vibration energy harvesting for self-powered microsystems. A general overview of the research and development in piezoelectric vibration energy harvesting can be found in references [2-8].

Most of the analytical models of piezoelectric energy harvesters have been developed based on the assumption that the vibration excitation is harmonic. Also, it is desirable to make vibration energy harvesters lightly damped to utilize their large structural response for greater power output. As a result, the effective harvesting bandwidth is usually narrow and the power output is very sensitive to the "matching" between the excitation frequency and the natural frequency of the system. Though nonlinearity has been introduced to broaden the bandwidth and reduce this sensitivity [9,10] and was shown to overperform the linear configuration by an uncertainty propagation study [11], the uncertainty in the system

still has a significant influence on the power performance. Recognizing the uncertainty in most environmental vibration excitations, i.e., variation of amplitude and frequency, researcher have studied the effect of excitation randomness on harvested power and attempted to developed models in a stochastic manner. Lefeuvre et al [12] performed theoretical and experimental studies, and compared the power performance of the standard AC-DC and Synchronous Electric Charge Extraction (SECE) techniques in the case of broadband, random vibration. Halvorsen [13] developed a closed-form model of linear resonant energy harvesters driven by broadband vibrations, and obtained the Fokker-Planck equation describing the probability density function of the harvested power. Following a similar approach, Adhikari et al [14] derived expressions for the mean normalized power of system of stack configuration subjected to Gaussian white noise base acceleration. They studied the cases when the system was connected to a resistive load and connected to a resistive load and inductor in parallel. Seuaciuc-Osório and Daqaq [15] presented a theoretical analysis of the response of energy harvesters to excitations having a time-varying frequency. Yoon and Youn [16] applied a statistical time–frequency analysis to quantify the harvested power of a piezoelectric energy harvester under nonstationary random vibrations. Based on a distributed-parameter electroelastic formulation, Zhao and Erturk [17] presented analytical and numerical solutions, and experimental validations of piezoelectric energy harvesting from broadband random vibrations. Based on the Wiener path integral technique, a methodology was developed by Petromichelakis et al [18] to determine and optimize stochastic response of nonlinear electromechanical energy harvesters.

On the other hand, to enhance the power or energy conversion performance of the system and provide design guidance for energy harvesters, optimization studies have been conducted on the geometrical parameters [19-22] or the electrical parameters [23-26]. Additionally, topology optimization methods have also been applied [27-29]. However, as pointed out by Franco and Varoto [30], most of these optimization strategies usually seek for a single optimal parameter at a time. A piezoelectric energy harvester is an electromechanically coupled system whose performance is simultaneously affected by multiple parameters in the materials, mechanical, and electrical domain. Moreover, during the modeling and manufacturing processes, uncertainty is inevitably introduced into the mean model, for which the optimal parameters are obtained. As a result, the actual performance will deviate from predictions.

While some optimization methods have been coupled to stochastic response analysis tools for the response optimization of energy harvesters subjected to external random excitation, e.g., in [18], researchers have also recognized the importance of quantifying the uncertainties in the system parameters and further accounting for them in the analysis and design processes of harvesters, e.g., see [11,30-39]. These investigations have used parametric uncertainty, i.e., they have considered variations in some of the parameters of the system which they have modeled as random variables, independent of each other when multiple such parameters are varied. Geometrical dimensions, properties of the structural component and/or of the piezoelectric device, and characteristics of the electrical circuits have been treated as random. Moreover, the structural model of the harvester has typically been an equivalent SDOF although finite elements have also been used [36,39]. These investigations have yielded two key findings. First and foremost, they have demonstrated that a small level of uncertainty typically induces a dramatic change in power output. Relatedly they have also shown the interest of designing under uncertainty. That is, the performance of the harvester optimally designed based on the mean model is no longer optimum once uncertainty is introduced. These findings clearly demonstrate the need to include uncertainty in the analysis and design of piezoelectric energy harvesters and the focus of the present investigation is on developing a general framework to consider in such efforts the uncertainties on the geometry/material properties of the structural and piezoelectric components.

While the above investigations have focused on introducing uncertainty on certain parameters of simple structural models of the harvesters, the real-world uncertainty is expected to affect all components and parameters of the model in a coupled manner. For example, uncertainty in a natural frequency originates from uncertainty on the structural properties and/or geometry and thus also implies uncertainty in the mode shapes, in the coupling with the piezoelectric elements, as well as in other natural frequencies. To account for all these effects, it is necessary to have a global, or nonparametric, modeling of uncertainty and such a modeling is best performed on a finite element description of the harvester, i.e., structure and piezoelectric components, especially to enable the consideration of complex geometries. Such an uncertainty modeling is proposed here based on the very recent work in [40-42], where the developed nonparametric approach is nonintrusive to the finite element software, requiring only the capability to output finite element mass, stiffness, electromechanical coupling, and piezoelectric capacitance matrices for the mean harvester design. The approach in [40-42] follows the original work of Soize in [43], in which the maximum entropy principle is applied and

the uncertainty is modeled directly at the level of a reduced order model of the structure, not within the finite element formulation as is done with the stochastic finite element approach. In this nonparametric maximum entropy approach, the uncertainty is lumped into the mass and/or stiffness matrix of the structure corresponding to a specified, deterministic basis. The joint probability density function of the elements of these matrices is then selected to: (i) have means which equal the corresponding deterministic matrices of the mean structural model, (ii) satisfy the mathematical requirements existing for these matrices (symmetry, positive definiteness), (iii) satisfy an integrability condition which guarantees the existence of the response in mean square, and (iv) maximize the entropy. This maximum entropy approach has been applied to matrices and fields with a variety of properties for which the construction of realizations has been detailed and is often very straightforward permitting a broad set of applications, see [44,45] for extensive review. The specific formulation in [40-42], also used in the present study, is a modification of the original methodology of Soize, in which the elemental mass and stiffness matrices are recognized as reduced order model matrices of the structure within each of the finite elements with the interpolation functions serving as basis functions inside the elements. Once the mean model elemental matrices have been obtained, uncertainty is introduced element per element for each sample of the uncertain harvester, the structural-piezoelectric matrices are reassembled and the simulation, e.g., output power determination, can be carried out. Random elemental matrices are simulated in such a way that all sources of uncertainties, material properties and geometry, are accounted for as long as the components remain linear. The uncertainty modeling then becomes equivalent to the random field modeling of these elemental matrices, which is described in full in section 3 of the paper. For the broadest applicability, the use of finite element software that do not include an explicit piezoelectric element is also considered and it is shown by extending the thermal analogy, that the modeling of the complete system can still be accomplished if the finite element model includes thermal effects.

In the present study, the above approach is applied to a bimorph piezoelectric energy harvester (PEH), for which an analytical model and an optimization formula have been developed [24] to obtain the optimal load resistance for the specified maximum power output at a given excitation frequency. A finite element model of the energy harvester is first constructed with Nastran using the piezoelectric-thermal analogy and the uncertainty modeling is implemented to allow uncertainty in structural and/or piezoelectric properties. These capabilities are then utilized to study the effects of uncertainty on the power output of the energy harvester, both with weak and strong coupling and with different tuning scenarios of the resistive load to optimize the power output. Section 2 provides an overview of important power characteristics of piezoelectric vibration energy harvesters, along with their finite element modeling, including the thermal analogy necessary in Nastran, the finite element software chosen for this analysis. The uncertainty modeling is reviewed in Section 3 and the application to the bimorph PEH is detailed in Section 4.

2 Modeling of piezoelectric vibration energy harvesters

2.1 Electromechanical modeling and power behavior

Using a Rayleigh-Ritz formulation and a generalized form of Hamilton's Principle, Hagood, Chung and von Flotow [46] derived a set of equations to model the electromechanically coupled dynamics of an elastic structure with piezoelectric elements and passive electronics:

$$\mathbf{M}\ddot{\underline{\mathbf{w}}}(t)+\mathbf{C}\dot{\underline{\mathbf{w}}}(t)+\mathbf{K}\underline{\mathbf{w}}(t)-\boldsymbol{\Theta}\underline{\mathbf{v}}(t) = \mathbf{B}_f\underline{\mathbf{f}}(t), \tag{1}$$

$$\boldsymbol{\Theta}^T\underline{\mathbf{w}}(t)+\mathbf{C}_p\underline{\mathbf{v}}(t) = \mathbf{B}_q\underline{\mathbf{q}}(t), \tag{2}$$

which are called the actuator and sensor equations, respectively. There are n mechanical degrees of freedom (DOF), m electrical voltage DOF at the electrodes, nf forces, and nq applied electric charges. $\mathbf{M}$, $\mathbf{C}$, and $\mathbf{K}$ are the n-by-n mass, damping, and stiffness matrices, respectively. $\underline{\mathbf{w}}$ is the n-by-1 generalized mechanical (or displacement) coordinate vector, and $\underline{\mathbf{v}}$ is the m-by-1 generalized electrical (or voltage) coordinate vector. $\boldsymbol{\Theta}$ is the n-by-m electromechanical coupling matrix, and $\mathbf{C}_p$ the piezoelectric capacitance matrix. Finally, $\mathbf{B}_f$ is the n-by-nf force forcing matrix, $\mathbf{B}_q$ the m-by-nq charge forcing matrix, $\underline{\boldsymbol{f}}$ the nf-by-1 force vector, and $\underline{\boldsymbol{q}}$ is the nq-by-1 charge vector. The exact definitions of these quantities can be found in [46]. Beam harvesters subjected to base motion have received great interest because of their simplicity in implementation and large structural response, along with the fact that base motion excitations are abundant in environment. Following an approach similar to that of Hagood et. al, a single-mode (or equivalent SDOF) model for

beam harvesters operating near its resonance and subjected to base motion was developed by Liao and Sodano [24] as:

$$M\ddot{w}(t)+C\dot{w}(t)+Kw(t)-\theta v(t)=Da(t), \tag{3}$$

$$\theta w(t)+C_p v(t)=q(t), \tag{4}$$

where D is the equivalent input mass, a is the base motion acceleration selected here as $a(t)=A\cos\omega t$, and q is the total electric charge applied on the piezoelectric elements, v is the voltage across the elements. In the case of a fully-covered and symmetric bimorph beam configuration where the substrate layer is sandwiched between two piezoelectric layers, Liao and Sodano [24] derived the analytical expressions of the equivalent SDOF quantities in Eqs. (3) and (4) and they are given in the **Appendix**. In addition, if the energy harvesting interface circuit is simply resistive, i.e., connected to a resistor, the harvested power is given as

$$P=\frac{D^2A^2}{\sqrt{KM}}\frac{k^2r^2\rho}{\left[\left(1-r^2\right)-\left(2\zeta r^2\rho\right)\right]^2+\left[\left(2\zeta r\right)+\left(1-r^2+k^2\right)r\rho\right]^2}, \tag{5}$$

where the short-circuit natural frequency ω_n, damping factor ζ, frequency ratio r, and dimensionless resistance ρ are defined as

$$\omega_n^E=\sqrt{\frac{K}{M}},\ \zeta=\frac{C}{2\sqrt{KM}},\ r=\frac{\omega}{\omega_n^E},\ \rho=RC_p\omega_n \tag{6}$$

with ω and R being the excitation frequency and electrical load resistance, respectively. In addition, a very important parameter, the electromechanically coupling coefficient k^2 of the system, is defined as

$$k^2=\frac{\theta^2}{C_pK}. \tag{7}$$

The general power behavior of piezoelectric vibration energy harvesters is briefly reviewed here through an example of the energy harvester connected with a resistor. However, this behavior is also exhibited by energy harvesters with other types of interface circuits [47]. To facilitate the discussion, a numerical beam harvester has been created and the associated results are shown in Fig. 1. The properties of the simulated system are given in Table 1, where brass is used for the substrate and PSI-5H is for the PZT material. The mechanical damping ratio at the first mode of 0.02 is used. Generally, the harvested power depends on both the load resistance and excitation frequency [48]. Figure 1(a) plots the harvested power vs. the excitation frequency at different resistance values. Unsurprisingly, for each power curve, the peak power occurs near the structural natural frequency of the system where the structural response is large, resulting in more mechanical strain energy for energy conversion. It can be seen that the peak frequency increases (or moves from left to right, graphically) from the short-circuit to open-circuit frequency as the electrical load increases. This is due to the electromechanical coupling of the piezoelectric material, which changes the effective stiffness of the system. Furthermore, the energy harvesting process results in an additional damping effect as a part of the mechanical energy is "removed" from the system due to energy conversion. For a given frequency, the harvested power depends on the load resistance. This is illustrated in Fig. 2(b), where the harvested power at a given fixed frequency, i.e., 55 Hz, is plotted against the load resistance. There is an optimal resistance that maximizes the harvester power and its theoretical expression has been determined as [24]:

$$R_{opt}=\frac{1}{\omega C_p}\sqrt{\frac{\left(C\omega\right)^2+\left(K-M\omega^2\right)^2}{\left(C\omega\right)^2+\left(K+\theta^2/C_p-M\omega^2\right)^2}}, \tag{7}$$

which varies as the excitation frequency changes. If the load resistance is optimally tuned for all frequencies, this results in the *power envelope* of the system shown in Fig. 1(a), representing the maximum possible power through the tuning of load resistance. Graphically, this envelope is essentially the outer profile of the power curves if we plot them for a continuous and infinite range of load resistance instead of the five resistance values.

Table 1. Properties of the simulated bimorph beam harvester in Section 2

Property	Symbol	Value
Length	L	80 mm

Width	b	10 mm
Substrate thickness	t_s	0.25 mm
PZT thickness	t_p	0.25 mm
Substrate density	ρ_s	8740 kg/m^3
PZT density	ρ_p	7800 kg/m^3
Substrate modulus	Y_s	101 GPa
PZT modulus	Y_p	62 GPa
PZT dielectric constant	K^T_3	3800
PZT piezoelectric coefficient	d_{31}	-320×10^{-12} m/V
Damping ratio	ζ	0.02

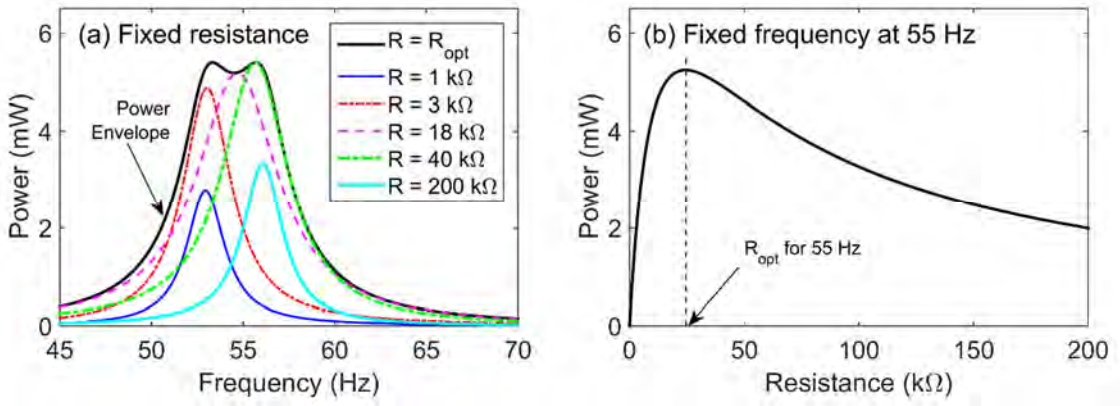

Figure 1. (a) Power vs. frequency at constant or optimal load resistance; (b) power vs. load resistance at a fixed excitation frequency.

In addition, the electromechanical coupling has a significant effect on the overall power behavior of the system. Figure 2 plots the power envelopes of the same system as given in Table 1 but at different levels of coupling by changing the piezoelectric coefficient d_{31}. Overall, initially the harvested power increases as the coupling increases as a result of a higher energy conversion efficiency. However, the electrically induced damping due to energy harvesting also increases, which leads to a reduced structural response. When the coupling coefficient reaches a critical value, a balance between the conversion efficiency and structural response is reached and the power saturates at a level called power limit, which has been determined [49] as

$$P_{\lim} = \frac{D^2 A^2}{\sqrt{MK}} \frac{1}{8\zeta}, \tag{8}$$

and represents the overall power ceiling of a harvester. Depending on the amount of coupling in the system, this limit may or may not be reached. The minimum coupling to reach the power limit, i.e., critical coupling, for energy harvesters of a resistive interface circuit is given [26,48] as

$$\left(k^2\right)_c = 4\zeta + 4\zeta^2, \tag{9}$$

which is a function of the mechanical damping ratio. A system of coupling higher than the critical coupling is defined as strongly coupled and it is weakly coupled if the coupling is lower than the critical coupling. For damping ratio 0.02, the critical coupling coefficient is 0.0816, and the curves for k^2 = 0.18 and 0.25 are of strongly coupled systems. There are two power limit peaks in the power envelope of a strongly-coupled resistive energy harvester: one near the short-circuit natural frequency and the other near the open-circuit natural frequency. Note that the critical coupling changes with the type of energy harvesting circuit interface [47], which has been utilized as a method for enhanced power performance through innovative circuit designs. However, the system is still subjected to the same power limit regardless of the interface circuit type [49].

Even though once the coupling reaches its critical value, the power saturates and further increasing of the coupling does not lead to enhanced power, a strongly coupled system still offers few benefits. For example, the higher coupling induces

more damping and further reduces the structural response and stress, which helps extend the fatigue life of the system. In addition, it can be seen from Fig. 2 that the frequency bandwidth, over which the harvested power is relatively large, is much wider at high coupling. This allows the system to be more robust as to the change in the excitation source frequency through a "correction" tuning of the electrical load to match the actual frequency.

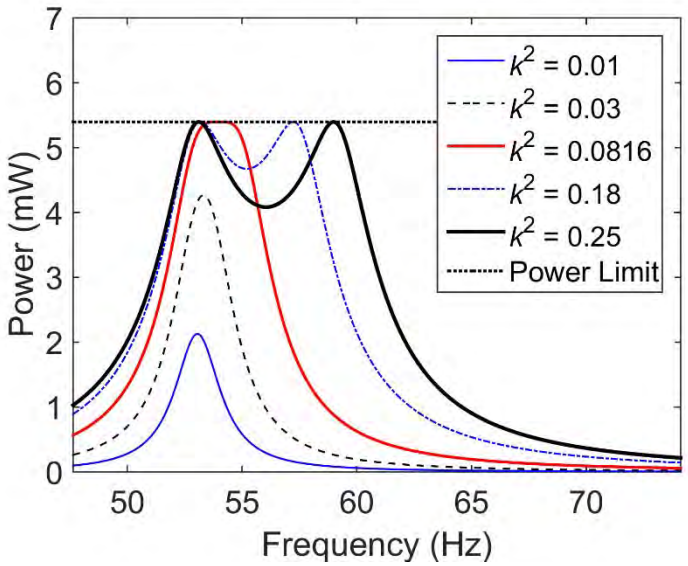

Figure 2. Power envelopes of the system given in Table 1 at various coupling. Base-motion acceleration is 1g and damping ratio is 0.02.

2.2 Finite element modeling of piezoelectric energy harvesters

2.2.1 Finite element formulation

The finite element formulation for the piezoelectric harvester can be rewritten as

$$\mathbf{M}^{(FE)}\underline{\ddot{\mathbf{u}}}^{(FE)}(t)+\mathbf{C}^{(FE)}\underline{\dot{\mathbf{u}}}^{(FE)}(t)+\mathbf{K}^{(FE)}\underline{\mathbf{u}}^{(FE)}(t)-\boldsymbol{\Theta}^{(FE)}\underline{\mathbf{v}}^{(FE)}(t)=\underline{\mathbf{f}}^{(FE)}(t), \tag{10a}$$

$$\boldsymbol{\Theta}^{(FE)T}\underline{\mathbf{u}}^{(FE)}(t)+\mathbf{C}_p^{(FE)}\underline{\mathbf{v}}^{(FE)}(t)=\underline{\mathbf{q}}^{(FE)}(t), \tag{10b}$$

where the actuator equation, Eq. (10a), is similar to the Rayleigh-Ritz formulation given by Eq. (1). However, it should be noted that Eq. (1) is a reduced-order formulation with system quantities obtained by using the assumed basis functions, e.g., mode shapes; while the quantities in Eqs. (10a) and (10b) are obtained at the element level. The superscript "(FE)" is used in Eqs. (10a,b) to emphasize this difference. Denoting by N_S and N_E as the numbers of the structural and the piezoelectric degrees of freedom (DOFs), respectively, $\mathbf{M}^{(FE)}$, $\mathbf{K}^{(FE)}$, and $\mathbf{C}^{(FE)}$ are N_S-by-N_S matrices, $\boldsymbol{\Theta}^{(FE)}$ is a N_S-by-N_E matrix, $\mathbf{C}_p^{(FE)}$ is a N_E-by-N_E matrix, $\underline{\mathbf{u}}^{(FE)}$ and $\underline{\mathbf{f}}^{(FE)}$ are N_S-by-1 vectors, and $\underline{\mathbf{v}}^{(FE)}$ and $\underline{\mathbf{q}}^{(FE)}$ are a N_E-by-1 vectors. Applying the electrical boundary condition that the electrodes on the PZT surfaces are connected, i.e., $v_i = v$, effectively reduces the number of DOFs for the voltage to be one and the actuator equation, Eq.(10a), can be rewritten as

$$\mathbf{M}^{(FE)}\underline{\ddot{\mathbf{u}}}^{(FE)}(t)+\mathbf{C}^{(FE)}\underline{\dot{\mathbf{u}}}^{(FE)}(t)+\mathbf{K}^{(FE)}\underline{\mathbf{u}}^{(FE)}(t)-\underline{\boldsymbol{\theta}}^{(FE)}v(t)=\underline{\mathbf{f}}^{(FE)}(t), \tag{11a}$$

where the coupling vector $\underline{\boldsymbol{\theta}}^{(FE)}$ is obtained by summing the columns of the coupling matrix $\boldsymbol{\Theta}^{(FE)}$ as a result of the electrical boundary condition. Accordingly, the sensor equation, Eq.(10b), becomes

$$\underline{\boldsymbol{\theta}}^{(FE)T}\underline{\mathbf{u}}^{(FE)}(t)+C_p v(t)=q(t), \tag{11b}$$

where C_p is the total piezoelectric capacitance of the PZT layer, obtained by the summation of all the elements of the

capacitance matrix, $\mathbf{C}_p^{(FE)}$, and q is the total electric charge induced on the layer, obtained by summing the columns of the charge vector, $\underline{\mathbf{q}}^{(FE)}$.

In the case of a resistive energy harvesting interface circuit, i.e., the harvester is connected to a resistor, one has

$$v = -R\dot{q}\,. \tag{12}$$

Substituting this relationship into Eqs. (11a,b) yields the governing equations

$$\mathbf{M}^{(FE)}\ddot{\underline{\mathbf{u}}}^{(FE)}(t)+\mathbf{C}^{(FE)}\dot{\underline{\mathbf{u}}}^{(FE)}(t)+\mathbf{K}^{(FE)}\underline{\mathbf{u}}^{(FE)}(t)+\underline{\boldsymbol{\theta}}^{(FE)}R\dot{q}(t) = \underline{\mathbf{f}}^{(FE)}(t), \tag{13a}$$

$$\left\{\underline{\boldsymbol{\theta}}^{(FE)}\right\}^T \underline{\mathbf{u}}^{(FE)}(t) - RC_p\dot{q}(t) - q(t) = 0\,. \tag{13b}$$

The set of equations can be rewritten in a state-space form as

$$\begin{bmatrix}\mathbf{M}^{(FE)} & 0\\ \mathbf{0} & 0\end{bmatrix}\begin{bmatrix}\ddot{\underline{\mathbf{u}}}^{(FE)}\\ \ddot{q}\end{bmatrix}+\begin{bmatrix}\mathbf{C}^{(FE)} & \underline{\boldsymbol{\theta}}^{(FE)}R\\ \mathbf{0} & -RC_p\end{bmatrix}\begin{bmatrix}\dot{\underline{\mathbf{u}}}^{(FE)}\\ \dot{q}\end{bmatrix}+\begin{bmatrix}\mathbf{K}^{(FE)} & 0\\ \left\{\underline{\boldsymbol{\theta}}^{(FE)}\right\}^T & -1\end{bmatrix}\begin{bmatrix}\underline{\mathbf{u}}^{(FE)}\\ q\end{bmatrix}=\begin{bmatrix}\underline{\mathbf{f}}^{(FE)}\\ 0\end{bmatrix}, \tag{14}$$

which serves as the governing FE equations to be solved.

2.2.2 Extraction of finite element matrices

To perform the uncertainty analysis at the finite element level, the FE matrices in Eqs. (10a,b) need to be obtained. A convenient way is to extract them from a commercial FE software. However, not all commercial finite element software allows directly modeling of piezoelectric element, which prevents piezoelectric matrices from direct extraction. This is the case for example of MSC Nastran which is a widely-used multidisciplinary finite element package that is capable of performing static, dynamic and thermal analysis of structures in both linear and nonlinear domains. Nevertheless, it is possible to resort to some analogy between piezoelectric and structural or thermal properties to extract these FE matrices. This is implemented in the present study, described as follows.

In general, the FE matrices to extract can be classified into three groups: (a) structural matrices; (b) piezoelectric-structural coupling matrix; and (c) piezoelectric matrix.

(a) The structural mass and stiffness matrices, $\mathbf{M}^{(FE)}$ and $\mathbf{K}^{(FE)}$, are output by using the Nastran DMAP alters, the high-level Nastran language commands. The damping matrix $\mathbf{C}^{(FE)}$ is then computed by using the Rayleigh damping model, i.e.,

$$\mathbf{C}^{(FE)} = \alpha\mathbf{M}^{(FE)} + \beta\mathbf{K}^{(FE)}, \tag{15}$$

where α and β are the Rayleigh damping coefficients, determined according to the damping ratio of the mode of interest. The Rayleigh damping model is a widely used viscous damping model where the damping is considered to be associated with mass and stiffness and expressed as a linear combination of the mass and the linear stiffness matrices, which is convenient to use with a finite element model or in the modal expansion approach.

(b) The electromechanical coupling matrix $\boldsymbol{\Theta}^{(FE)}$ is obtained by considering the following static actuation equation

$$\underline{\mathbf{f}}^{(FE)} = \boldsymbol{\Theta}^{(FE)}\underline{\mathbf{v}}^{(FE)}, \tag{16}$$

which shows that when a static distributed voltage $\underline{\mathbf{v}}^{(FE)}$ (a N_E-by-1 vector) is applied to the piezoelectric layer, it induces a static distributed force $\underline{\mathbf{f}}^{(FE)}$ (a N_S-by-1 vector) on the structure. From Eq. (16), one can imagine when the static voltage is such that its i_{th} element is one and the other elements are zeroes, the static structural force will be equivalent to the i_{th} column of the matrix $\boldsymbol{\Theta}^{(FE)}$. In this way, varying i from 1 to N_E one by one and collecting the corresponding structural force vectors, $\boldsymbol{\Theta}^{(FE)}$ can be obtained. With Nastran linear static solution (SOL101), the structural force vector can be obtained as the reaction force by applying the static voltage and fixing all the structural degrees of freedom, where the static voltage is applied by the equivalent distributed temperature using the piezoelectric-thermal analogy [50,51].

To clarify this analogy, consider a piezoelectric beam harvester with direction 1 defined along the length direction and direction 3 defined along the thickness direction (also the polarization direction). Due to the converse piezoelectric effect, the induced normal or bending strain in the 1-direction, i.e., ε_1, due to an applied electrical field in the 3-direction, E_3, is given as

$$\varepsilon_1 = d_{31} E_3 , \tag{17}$$

where d_{31} is the piezoelectric coefficient. Usually it is a negative number, meaning that application of a positive electric field in the polarization direction, i.e., direction 3, will generate a compressive strain in direction 1. Assume the electrical field within the PZT element is uniform and given as $E_3 = v/t_p$, where v is the voltage across the element (between the electrodes on the top and bottom surfaces) and t is the thickness of the PZT. Equation (17) can be rewritten as

$$\varepsilon_1 = \frac{d_{31}}{t_p} v . \tag{18}$$

On the other hand, the thermal strain induced by a temperature change is given as

$$\varepsilon_1 = \alpha_1 \left(T - T_{ref} \right), \tag{19}$$

where α is the coefficient of thermal expansion, T the current temperature, and T_{ref} is the reference temperature. Comparing Eqs. (17) and (18) and setting $T_{ref} = 0$ lead to the piezoelectric-thermal analogy:

$$v = T, \alpha_1 = \frac{d_{31}}{t_p} , \tag{20}$$

which means that the converse piezoelectric effect can be equivalently modeled by the thermoelastic effect of structures with the temperature corresponding to the applied voltage and the equivalent thermal expansion coefficient related to the piezoelectric properties as shown in Eq. (20).

(c) The piezoelectric-thermal analogy only models the converse piezoelectric effect only in the mechanical domain, i.e., Eq. (10a) or (13a), thus can only be used to extract the electromechanical coupling matrix $\boldsymbol{\Theta}^{(FE)}$. To model the direct effect on the circuit dynamics in the electrical domain and set up the other governing Eq. (10b) or (13b), the piezoelectric capacitance matrix needs to be extracted as well. This can be achieved by an analogy between the structural mass, M, and the total piezoelectric capacitance, C_p, expressed as, respectively,

$$M = \int_{V_S} \rho_S dv_S , \tag{21a}$$

$$C_p = \int_{V_S} \psi^T(z) \varepsilon^S \psi(z) dv_S , \tag{21b}$$

where ρ_S is the mass density, ε^S is the dielectric constant at constant strain, and $\psi(z)$ defines the distribution of the piezoelectric material across the thickness of the device domain, V_S. From Eqs. (21a,b), the capacitance matrix $\mathbf{C}_\mathbf{p}^{(FE)}$ can be obtained as the mass matrix of the structure, when the mass density is set to be

$$\rho_s^E = \psi^T(z) \varepsilon^S \psi(z) = \begin{cases} \varepsilon_0 (\varepsilon_{33} - \dfrac{d_{31}^2}{\varepsilon_{33} Y_{11}}) \cdot \dfrac{1}{t_p^2} & \text{piezoelectric layers} \\ 0 & \text{substrate} \end{cases} , \tag{22}$$

where ε_0 is the vacuum permittivity, ε_{33} is the relative permittivity in the 3-direction, Y_{11} is the Young's modulus in the 1-direction, and t_p is the thickness of the piezoelectric layer.

2.2.3 FE modeling validation

With the finite element modeling framework constructed above, fully coupled piezoelectric-structural simulations of piezoelectric energy harvesters can be performed. For validation, a finite element model of a bimorph harvester of properties given in Table 2 was constructed using Nastran, as shown in Fig. 3. The harvester is basically a cantilever beam type structure, and CQUAD4 shell elements were used for the structure FE model with 1760 elements and 1887

nodes. The composite property card (PCOMP) was used to define the substrate and the piezo layers structural properties.

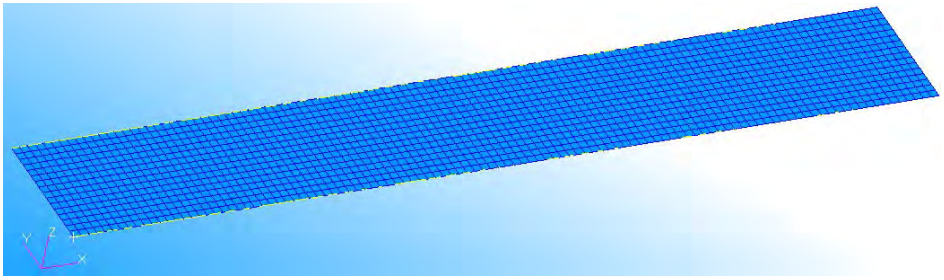

Figure 3. Finite element model in NASTRAN

The validation case is that the harvester is subject to base motion at the clamped end, of 1g acceleration at a single excitation frequency, the resultant force vector is constructed as

$$\underline{\mathbf{f}}^{(FE)}(t) = \underline{\mathbf{F}}^{(FE)} e^{i\omega t} = [\mathbf{M}^{(FE)} \underline{\mathbf{a}}^{(FE)} \cdot g] e^{i\omega t}, \tag{24}$$

where $\omega = 2\pi f$, f is the excitation frequency, and $\underline{\mathbf{a}}^{(FE)}$ is a N_S -by-1 acceleration vector. For a base acceleration excitation of 1g, the components of $\underline{\mathbf{a}}^{(FE)}$ are zero except those associated with the transverse translation which are all set to 1. The steady-state structural response and piezoelectric charge are computed by solving Eq. (14) using the method of frequency response function, i.e.,

$$\begin{bmatrix} \underline{\mathbf{u}}^{(FE)} \\ q \end{bmatrix} = \left\{ -\omega^2 \begin{bmatrix} \mathbf{M}^{(FE)} & 0 \\ \mathbf{0} & 0 \end{bmatrix} + i\omega \begin{bmatrix} \mathbf{C}^{(FE)} & \underline{\boldsymbol{\theta}}^{(FE)} R \\ \mathbf{0} & -RC_p \end{bmatrix} + \begin{bmatrix} \mathbf{K}^{(FE)} & 0 \\ \left\{ \underline{\boldsymbol{\theta}}^{(FE)} \right\}^T & -1 \end{bmatrix} \right\}^{-1} \cdot \begin{bmatrix} \underline{\mathbf{F}}^{(FE)} \\ 0 \end{bmatrix} \tag{25}$$

The solution is implemented outside of the Nastran environment. At each excitation frequency, the amplitude of harvested power output is computed from the solution as $P = (\omega q_0)^2 R$, where q_0 denotes the amplitude of the charge.

Table 2. Properties of the cantilever piezoelectric beam for validation [24]

Property	Symbol	Value
Length	L	66.62 mm
Width	b	9.72mm
Brass thickness	t_s	0.76mm
PSI-5H thickness	t_p	0.26 mm
Brass density	ρ_s	8740 kg/m^3
PSI-5H density	ρ_p	7800 kg/m^3
Brass modulus	Y_s	101 GPa
PSI-5H modulus	Y_p	62 GPa
PSI-5H dielectric constant	K^T_3	3800
PSI-5H piezoelectric coefficient	d_{31}	- 320×10^{-12} m/V

The harvested power vs. excitation frequency is plotted in Fig. 4(a) at different load resistances. It is the same configuration used by Liao and Sodano [24] in their experimental studies and the results are shown in Fig. 4(b). For further comparisons, its ANSYS and analytical results are shown in Figs. 4(c) and 4(d), respectively. The analytical results are obtained by using Eq. (5) with the effective system parameters evaluated by using the expression in the Appendix. Overall, it can be seen that the NASTRAN derived results are in excellent agreement with other results, which confirms the adequacy of the thermal analogy.

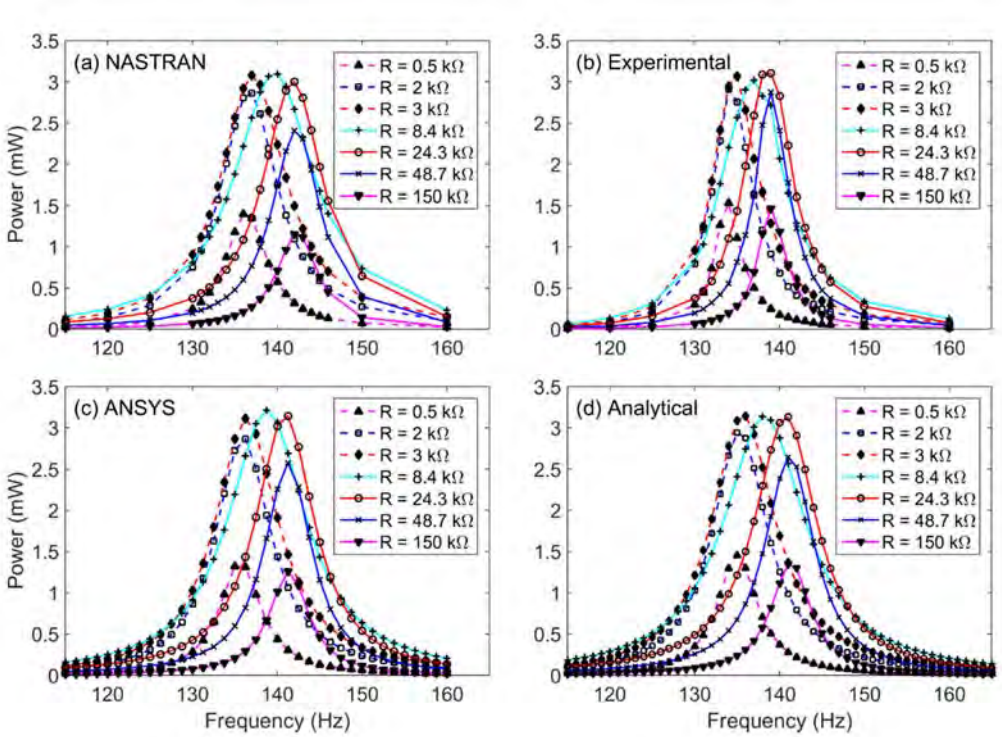

Figure 4. Harvested power vs. excitation frequency for the harvester given in Table 2. Base-motion acceleration is 1g and damping ratio is 0.019.

3. Nonparametric maximum entropy approach for uncertainty quantification at finite element level

In the present study, the finite-element-level nonparametric maximum entropy approach is used for uncertainty analysis of the bimorph piezoelectric energy harvester. Based on the piezoelectric-thermal analogy, the approach is implemented in a similar way to that in the uncertainty analysis of heated structures [42], where the details of the theoretical derivation can be found. The mass, stiffness, and the electromechanical coupling matrices of the FE model are randomized in the present uncertainty analysis to reflect the uncertainties of the parameters of the coupled system globally. Note that the ordering of the degrees of freedom in the matrices discussed below is degree of freedom 1 for all nodes, degree of freedom 2 for all nodes, etc.

For the mass matrix, the randomization is a single-physics one [41,42], i.e., it is performed with the matrix itself. For each elemental mass matrix of the mean FE model, denoted as $\bar{\boldsymbol{M}}^{(e)}$, its random sample is constructed as

$$\boldsymbol{M}^{(e)} = \bar{\boldsymbol{L}}_M^{(e)} \boldsymbol{H}_M^{(e)} \boldsymbol{H}_M^{(e)T} \bar{\boldsymbol{L}}_M^{(e)T}, \tag{26}$$

where $\bar{\boldsymbol{L}}_M^{(e)}$ is a decomposition of $\bar{\boldsymbol{M}}^{(e)}$ satisfying

$$\bar{\boldsymbol{M}}^{(e)} = \bar{\boldsymbol{L}}_M^{(e)} \bar{\boldsymbol{L}}_M^{(e)T}. \tag{27}$$

The random matrix $\boldsymbol{H}_M^{(e)}$ is obtained by

$$\boldsymbol{H}_M^{(e)} = \boldsymbol{H}^{(e)} \otimes \boldsymbol{I}_r, \tag{28}$$

where $\boldsymbol{H}^{(e)}$ is a m-by-m random matrix where m is the number of degrees of freedom per node and its structure is shown in Fig. 5, $\boldsymbol{I}_r$ is the r-by-r identity matrix where r is the number of nodes per element, and $\otimes$ denotes the Kronecker product operation.

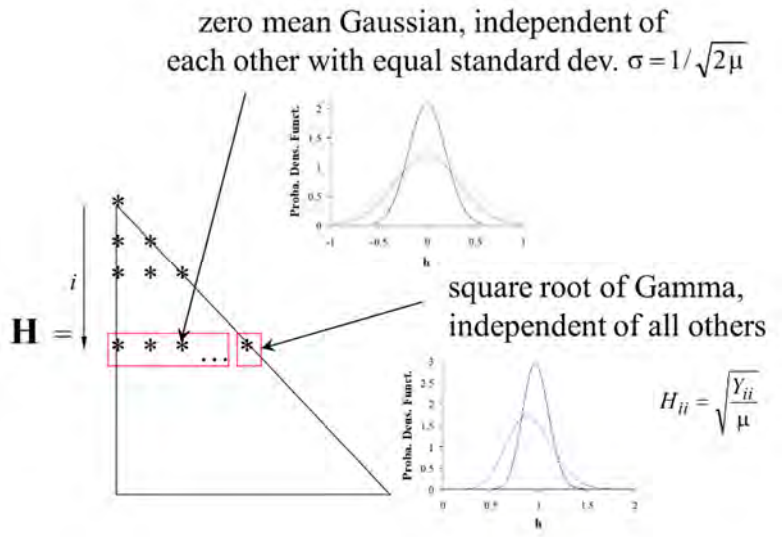

Figure 5. Structure of a random ***H*** matrix.

The randomization process is repeated for each element, but since these elements are connected to form the finite element mesh, the matrices $\boldsymbol{H}^{(e)}$ corresponding to different elements cannot be simulated independently of each other. Following the procedure proposed in [41,52,53], each element H_{ij} of the matrix $\boldsymbol{H}^{(e)}$ is treated as the transformation of a zero mean, unit variance Gaussian field P_{ij} with a specified stationary autocorrelation function

$$R(\underline{\boldsymbol{y}}) = E\left[P_{ij}(\underline{\boldsymbol{x}})P_{ij}(\underline{\boldsymbol{x}}')\right] \tag{29}$$

where $\underline{\boldsymbol{y}} = \underline{\boldsymbol{x}} - \underline{\boldsymbol{x}}'$, $\underline{\boldsymbol{x}}$ and $\underline{\boldsymbol{x}}'$ denote the coordinates of two elements (e.g., of their centers). Then,

$$H_{ij} = \begin{cases} \sigma P_{ij} & i \neq j \\ F_{H_{ii}}^{-1}[F(P_{ij})] & i = j \end{cases}, \tag{30}$$

where F is the cumulative distribution function of the standard Gaussian random variable, $F_{H_{ii}}^{-1}$ is the inverse of the cumulative distribution function of the Gamma random variable. As shown in Figure 5, $\sigma = 1/\sqrt{2\mu}$ where μ is the parameter controlling the uncertainty level. Usually an alternative dispersion parameter δ is used (as in the present study), which is related to μ as $\mu = (n+1)/(2\delta^2)$, where n is the dimension of the matrix. Once random samples of all elemental matrices are obtained, they are assembled to construct the random sample of the mass matrix of the whole FE model.

Different from the mass matrix, the randomization of the stiffness and the coupling matrices needs to be carried out together as a multiple-physics one due to the electromechanical coupling, similar to the heated structure case [40,42]. To this end, construct the matrix

$$\boldsymbol{K}_B^{(e)} = \begin{bmatrix} \boldsymbol{K}^{(e)} & \Theta^{(e)} \\ \Theta^{(e)T} & \boldsymbol{K}_{EE}^{(e)} \end{bmatrix}, \tag{31}$$

where $\boldsymbol{K}^{(e)}$ and $\Theta^{(e)}$ are the n_S -by- n_S structural stiffness and the n_S -by- n_Θ electromechanical coupling matrices of an element, respectively. Here, n_S and n_Θ are the numbers of degrees of freedom of structural displacement and electrical voltage per element, respectively. In the present application, $n_S = 6 \times r$ and $n_\Theta = 1 \times r$ where r = 4 as the

CQUAD4 elements have 4 nodes, with 6 structural degrees of freedom and 1 electrical degree of freedom each. Finally, $\boldsymbol{K}_{EE}^{(e)}$ denotes a n_Θ-by-n_Θ matrix relating to the strain energy induced by the electromechanical coupling, see [40] for discussion in the thermal case, and which will be discussed later in this section. The randomization of the elemental stiffness and the elemental electromechanical coupling matrices is carried out with the mean $\boldsymbol{K}_B^{(e)}$ matrix, denoted as $\bar{\boldsymbol{K}}_B^{(e)}$.

The randomization of the mean $\bar{\boldsymbol{K}}_B^{(e)}$ is given by

$$\boldsymbol{K}_B^{(e)} = \bar{\boldsymbol{L}}_B^{(e)} \boldsymbol{H}_B^{(e)} \boldsymbol{H}_B^{(e)T} \bar{\boldsymbol{L}}_B^{(e)T} . \tag{32}$$

In Eq.(32), the $\bar{\boldsymbol{L}}_B^{(e)}$ matrix is obtained from a decomposition of $\bar{\boldsymbol{K}}_B^{(e)}$,

$$\bar{\boldsymbol{K}}_B^{(e)} = \bar{\boldsymbol{L}}_B^{(e)} \, \bar{\boldsymbol{L}}_B^{(e)T} \quad , \tag{33}$$

in the block triangular form

$$\bar{\boldsymbol{L}}_B^{(e)} = \begin{bmatrix} \bar{\boldsymbol{L}}_{KK}^{(e)} & \boldsymbol{0}^{(e)} \\ \bar{\boldsymbol{L}}_{EK}^{(e)} & \bar{\boldsymbol{L}}_{EE}^{(e)} \end{bmatrix}. \tag{34}$$

The $\bar{\boldsymbol{L}}_B^{(e)}$ matrix includes three block matrices as shown in Eq.(34). The $\bar{\boldsymbol{L}}_{KK}^{(e)}$ matrix can be obtained by a decomposition of the mean elemental stiffness matrix $\bar{\boldsymbol{K}}^{(e)}$,

$$\bar{\boldsymbol{K}}^{(e)} = \bar{\boldsymbol{L}}_{KK}^{(e)} \bar{\boldsymbol{L}}_{KK}^{(e)T} . \tag{35}$$

Following the algorithm in [38], the $\bar{\boldsymbol{L}}_{EK}^{(e)}$ matrix is computed by

$$\bar{\boldsymbol{L}}_{EK}^{(e)} = \bar{\boldsymbol{q}}^T \bar{\boldsymbol{\Phi}}_D^{(e)T} , \tag{36}$$

where

$$\bar{\boldsymbol{q}} = [\bar{\boldsymbol{\Lambda}}_D^{(e)}]^{-1/2} \, \bar{\boldsymbol{p}} , \text{ and } \bar{\boldsymbol{p}} = \bar{\boldsymbol{\Phi}}_D^{(e)T} \bar{\Theta}^{(e)} , \tag{37}$$

that is, $\bar{\boldsymbol{\Phi}}_D^{(e)}$ and $\bar{\boldsymbol{\Lambda}}_D^{(e)}$ are the matrices of eigenvectors and eigenvalues (diagonal elements) of the matrix $\bar{\Theta}^{(e)}$.

The third matrix, $\bar{\boldsymbol{L}}_{EE}^{(e)}$, should be obtained from the matrix $\bar{\boldsymbol{K}}_{EE}^{(e)}$. The thermal counterpart of $\bar{\boldsymbol{K}}_{EE}^{(e)}$ has been shown [42,53] to be difficult to accurately estimate from a commercial finite element code non-intrusively. Hence, considering that it does not appear in the governing equation, it was proposed [42,53] that it be selected to maximize the entropy of the random samples, achieved by setting $\bar{\boldsymbol{L}}_{EE}^{(e)}$ to be the identity matrix.

The random part of $\boldsymbol{K}_B^{(e)}$ in Eq.(32) is represented by the lower triangular matrix $\boldsymbol{H}_B^{(e)}$, expressed as

$$\boldsymbol{H}_B^{(e)} = \begin{bmatrix} \boldsymbol{H}_{KK}^{(e)} & \boldsymbol{0}^{(e)} \\ \boldsymbol{H}_{EK}^{(e)} & \boldsymbol{H}_{EE}^{(e)} \end{bmatrix}, \tag{38}$$

where $\boldsymbol{H}_{EE}^{(e)}$ only affects the $\boldsymbol{K}_{EE}^{(e)}$ block. Since the $\boldsymbol{K}_{EE}^{(e)}$ matrix does not appear in the governing equation, its value is irrelevant and thus $\boldsymbol{H}_{EE}^{(e)}$ needs not be computed nor discussed. It is symbolically replaced by a * in the following.

Noting that the matrix $\boldsymbol{K}_B^{(e)}$ involves two quantities, the structural stiffness and the electromechanical coupling, and their uncertainty levels may be different, following the treatment in [42], $\boldsymbol{H}_B^{(e)}$ is expressed as the product of two lower

triangular matrices, one representing the uncertainty of the stiffness properties ($\boldsymbol{H}_S^{(e)}$) and the other of the piezoelectric properties ($\boldsymbol{H}_E^{(e)}$), i.e.,

$$\boldsymbol{H}_B^{(e)} = \boldsymbol{H}_E^{(e)}\, \boldsymbol{H}_S^{(e)}, \tag{39}$$

where

$$\boldsymbol{H}_E^{(e)} = \begin{pmatrix} \boldsymbol{I} & \boldsymbol{0} \\ \boldsymbol{H}_{EK}^{(e)} & * \end{pmatrix} \text{ and } \boldsymbol{H}_S^{(e)} = \begin{pmatrix} \boldsymbol{H}_{KK}^{(e)} & \boldsymbol{0} \\ \boldsymbol{0} & \boldsymbol{I} \end{pmatrix}. \tag{40),(41}$$

Two random matrices, $\boldsymbol{H}_{KK}^{(e)}$ and $\boldsymbol{H}_{EK}^{(e)}$, need to be realized. The matrix $\boldsymbol{H}_{KK}^{(e)}$ can be computed in the same way as $\boldsymbol{H}_M^{(e)}$ but with its own dispersion parameter δ_K. Finally, the random matrix $\boldsymbol{H}_{EK}^{(e)}$ is simulated row per row as

$$\boldsymbol{H}_{EK,i}^{(e)} = \bar{\boldsymbol{L}}_{EK,i}^{(e)}\, \boldsymbol{U}_i, \tag{42}$$

and

$$\boldsymbol{U}_i = \mathrm{diag}\left(\boldsymbol{h}_{EK,i}^{(e)} \otimes \boldsymbol{J}_r \right) \quad , \tag{43}$$

where the notation $\boldsymbol{A},i$ denotes the ith row of the matrix $\boldsymbol{A}$ and diag is the operation taking a vector and creating the diagonal matrix having these elements along the diagonal. Moreover in Eq. (43), $\boldsymbol{h}_{EK}^{(e)}$ is a matrix of n_Θ -by-6 components defined as independent Gaussian random fields with a specified autocorrelation function, e.g., Eq. (29), and $\boldsymbol{J}_r$ denotes the row vector of dimension r with all elements equal to one.

Finally, the random elemental stiffness and electromechanical coupling matrices are computed by

$$\boldsymbol{K}^{(e)} = \bar{\boldsymbol{L}}_{KK}^{(e)} \boldsymbol{H}_{KK}^{(e)} \boldsymbol{H}_{KK}^{(e)T} \bar{\boldsymbol{L}}_{KK}^{(e)T}, \tag{44}$$

$$\Theta^{(e)} = \bar{\boldsymbol{L}}_{KK}^{(e)} \boldsymbol{H}_{KK}^{(e)} \boldsymbol{H}_{EK}^{(e)T} + \bar{\boldsymbol{L}}_{KK}^{(e)} \boldsymbol{H}_{KK}^{(e)} \boldsymbol{H}_{KK}^{(e)T} \bar{\boldsymbol{L}}_{EK}^{(e)T}. \tag{45}$$

Once random samples of all elemental matrices are obtained, they are assembled to construct the random sample of the stiffness and the coupling matrices of the whole FE model. For each random sample, the damping matrix is computed by the Rayleigh damping model using the randomized mass and stiffness matrices and the same Rayleigh damping coefficients as in the nominal FE model. Therefore, the variation of the damping ratio is introduced through the variations of mass and stiffness.

In the present application, the autocorrelation functions of the independent Gaussian random fields P_{ij} for the simulation of the random elemental mass matrices, of their counterparts for the random elemental stiffnesses, and of the components of the random matrix $\boldsymbol{h}_{EK}^{(e)}$ were all selected as in [41,42,52] as

$$R(\boldsymbol{y}) = \left[\frac{4 L_{corr}^2}{\pi^2 |\boldsymbol{y}|^2} \right] \sin^2\left(\frac{\pi |\boldsymbol{y}|}{2 L_{corr}} \right), \tag{46}$$

where L_{corr} is the corresponding correlation length. While each random field can be described by its own correlation length, they were all taken equal here to 1/10 of the beam length to exemplify the methodology.

4 Uncertainty analysis of bimorph beam harvesters

4.1 Systems for analysis

To illustrate the uncertainty analysis process and investigate the effect of coupling and load tuning schemes on power uncertainty, two numerical beam configurations shown in Table 3 are studied. System 1 is weakly coupled with coupling coefficient $k^2 = 0.03$, and System 2 is strongly coupled with $k^2 = 0.15$. There are two sets of uncertainty studies performed for both systems: 1) uncertainty in the harvested power at a given excitation frequency, and 2) uncertainty in the power envelope. We also compare the situation when the electrical load remains fixed to its pre-tuned or preoptimized value to the situation when the load is "adaptively" re-tuned to the modified system parameters due to the introduced uncertainty. As a comparison baseline, the two systems harvest the same amount of power at a target excitation frequency, i.e., 3 mW at 135 Hz. The analytical model discussed in Section 2.1 has been used to guide the selection of these system properties in Table 3. The associated power behavior of the systems is shown in Fig. 6, which shows that the analytical model predicts that the two systems will harvest 3 mW at 135 Hz with an electrical load of 6001 Ω and 2806 Ω, respectively. To provide a "nominal" model for the uncertainty analysis, the two systems are also analyzed by NASTRAN using the approach outlined in Section 2.2 and the results are shown in Fig. 6 as well. Overall, the NASTRAN results match the analytical results quite well, except for a slightly frequency shift (about 2 Hz or 1.5% w.r.t 135 Hz) between the results.

For these two configurations, the mass, stiffness, and the electromechanical coupling matrices of the FE model are randomized to globally reflect the uncertainties of the parameters of the coupled system. Since no detailed uncertainty information is available for the system parameters, the uncertainty levels of the three matrices, denoted as δ_M, δ_K, and δ_Θ, respectively, are selected to yield specified values of the coefficient of variation of three quantities, selected here to be the total mass, the natural frequency of the first mode, and the modal coupling coefficient of the first mode, i.e., $\theta_1 = \underline{\phi}_1^{(FE)T} \cdot \underline{\boldsymbol{\theta}}^{(FE)T}$ where $\underline{\phi}_1^{(FE)}$ is the first mode. A population of 100 random samples was generated with coefficients of variation of the above three quantities set to 1.0%, 1.0%, and 1.5%, respectively following the discussion of Section 3.

Table 3. Properties of the cantilever piezoelectric beams for uncertainty analysis

Property	Symbol	System 1	System 2
Length	L	66.86 mm	66.81 mm
Width	b	12.12 mm	9.60 mm
Substrate thickness	t_s	0.76 mm	0.76 mm
PZT thickness	t_p	0.26 mm	0.26 mm
Substrate density	ρ_s	8740 kg/m^3	8740 kg/m^3
PZT density	ρ_p	7800 kg/m^3	7800 kg/m^3
Substrate modulus	Y_s	101 GPa	101 GPa
PZT modulus	Y_p	62 GPa	62 GPa
PZT dielectric constant	K^T_3	3800	3800
PZT piezoelectric coefficient	d_{31}	-320×10^{-12} m/V	-378.1×10^{-12} m/V

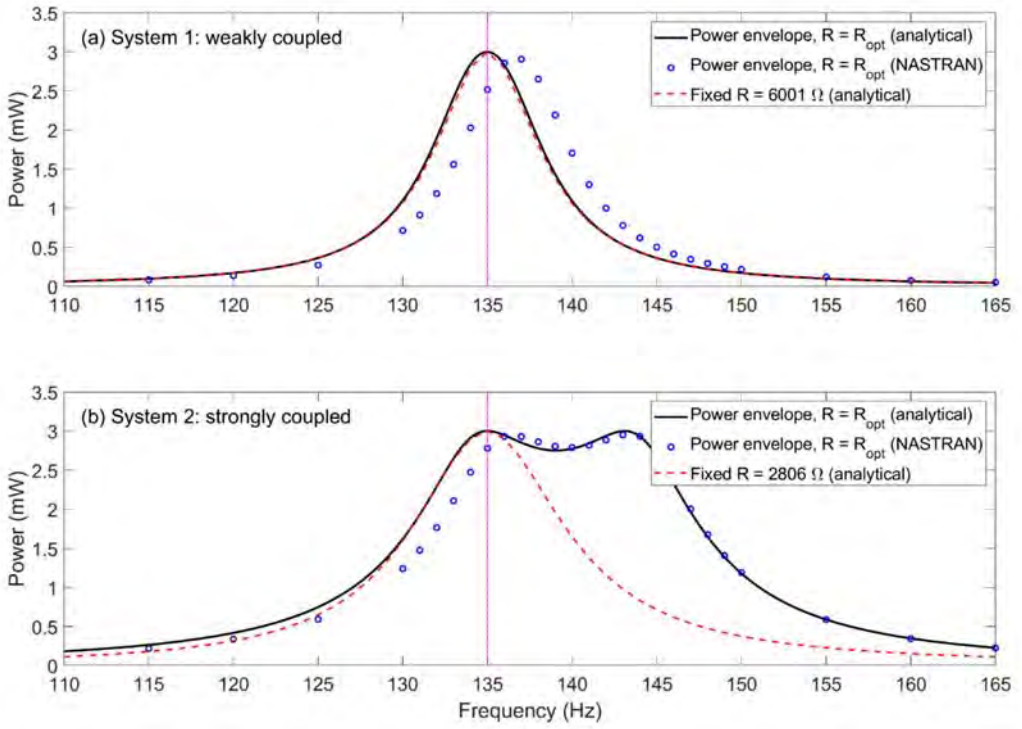

Figure 6. Analytical and NASTRAN power envelopes of the weakly and strongly coupled systems for uncertainty analysis.

If some detailed information about the uncertainty in the parameters of the energy harvester is known, it can be used to determine the above uncertainty levels. For example, if the variation of the mass density is known, a number of samples of the total structural mass can be generated by a traditional stochastic approach, e.g., the Monte Carlo method, from which the true variation of the total mass is computed. Then, for each of a set of uncertainty levels δ_M, a number of random samples are generated by the nonparametric approach, and the corresponding variation of total mass is computed. The uncertainty level at which the variation of total mass matches the true variation is taken. Alternatively, a more rigorous approach is to evaluate the likelihood function using the sample data for each uncertainty level, with respect to the true sample data, then the uncertainty level is determined as the one corresponding to the maximum likelihood [54,55]. The above procedure can be applied to δ_K if the variation of the Young's modulus is known thus the variation of the natural frequency of the first mode can be computed, and to δ_Θ if the variation of the piezoelectric coefficient is known thus the variation of the modal coupling coefficient of the first mode can be computed.

4.2 Results and discussions

4.2.1 Effect of mass, stiffness and coupling uncertainties and load resistance tuning

The uncertainty analysis results are presented in Fig. 7 in the form of uncertainty bands spanning the 5th to 95th percentile interval. For both beam configurations (weakly and strongly coupled), there are 100 random samples at each nominal point, i.e., for each particular frequency of excitation in the band 115 Hz to 160 Hz. For each of the 100 samples, the response to the base excitation of 1g acceleration at the nominal point is computed and the harvested power is determined. These computations are performed for two situations: 1) the load resistance is fixed to its pre-optimized (*pre-tuned*) value of the nominal model for all 100 samples, and 2) the load resistance is "adaptively" optimized (*adaptively re-tuned*) for each sample individually to account for the system change due to uncertainty using based on Eq. (7). The first scenario corresponds to a harvester produced as a black box ready to be installed for a particular application. The second scenario would correspond to a critical use of a harvester where availability of maximum power is more important than the additional cost associated with the tuning of the load.

In the case of pre-optimized resistance, as seen from Figs. 7(a) and 7(b), the uncertainty effect on the power envelope is

significant. For both configurations, the uncertainty band is quite broad with the relatively small uncertainty level, and the effect on the weakly-coupled configuration appears to be larger than that of the strongly coupled one. The uncertainty does not appear to affect the overall maximum value of the harvested power as much, which is consistent with the piezoelectric energy harvesting theory that the overall maximum power of an energy harvester is "capped" by its system properties, for example, Eq. (8). The change in system properties due to uncertainty is not significant enough to result in a large change in the overall maximum power. On the other hand, the uncertainty analysis shows that there could be a large probability that an energy harvester sample does not yield this maximum power. This means that a factor of safety on power needs to be considered in the design process, and the uncertainty analysis serves as an effective tool to quantify it.

In the case of adaptively re-optimized resistance, as seen from Figs. 7(c) and 7(d), the uncertainty band of the weakly coupling configuration does not change as much; while that of the strongly coupling configuration is reduced by almost half in the frequency range between the two power limit frequencies, over which the power level is high. This is consistent with the piezoelectric energy harvesting theory that higher coupling leads to a broader harvesting bandwidth. The uncertainty in the system changes the system parameters and graphically moves the power envelope left and right (with small change in power). For a weakly coupled system, this movement could lead to a significant power drop at a particular frequency because of its narrow power envelope; while the effect is not as significant for a strongly coupled system because of the wider frequency range of high power. In all, the uncertainty results and observations suggest that the configuration of strong coupling be preferred in the design, since it is less sensitive to the uncertainty as shown in Figs. 7(a) and 7(b); and when the uncertainty is present, its performance can be improved, e.g., by the adaptive optimization, as shown in Figs. 7(c) and 7(d).

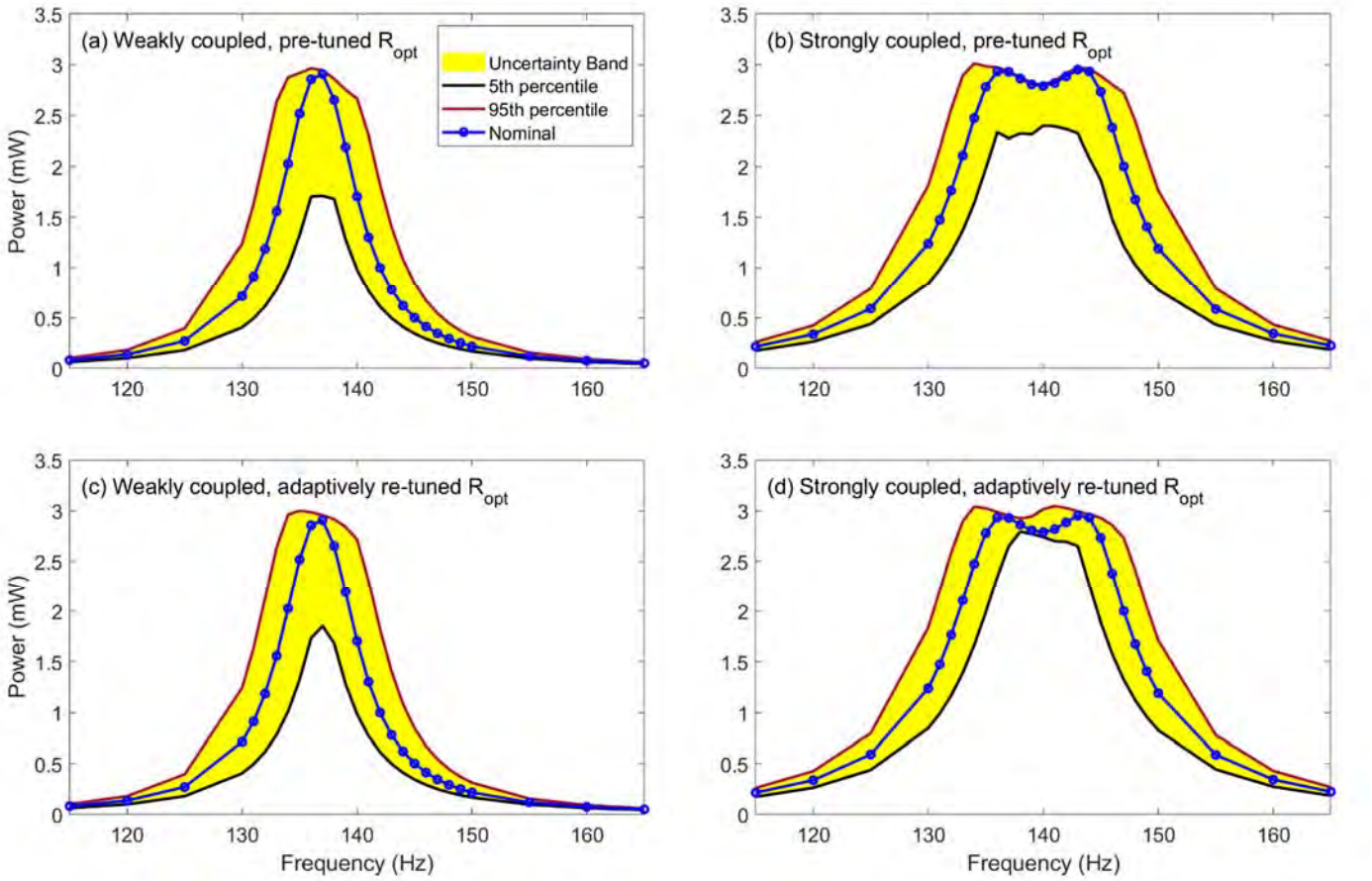

Figure 7. Uncertainty band of the power envelope of the energy harvester with weak or strong coupling for two situations of optimal load resistance, R_{opt}. (a) weakly coupled, nominal optimized R_{opt}; (b) strongly coupled, nominal optimized R_{opt}; (c) weakly coupling, adaptively optimized R_{opt}; and (d) strongly coupling, adaptively optimized R_{opt}.

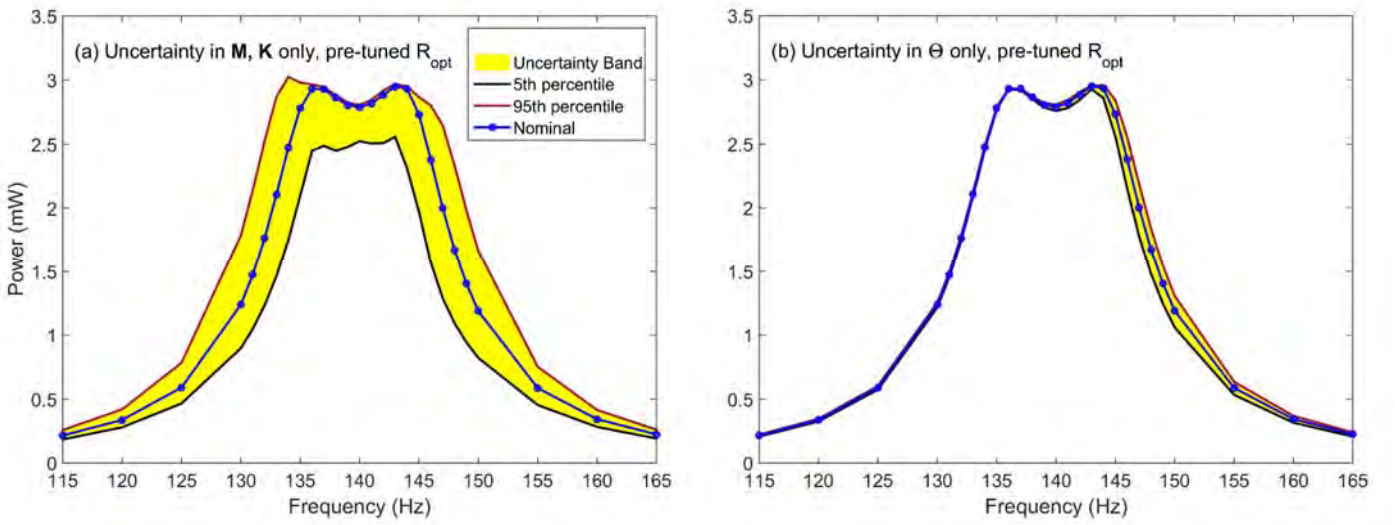

Figure 8. Uncertainty band of the power envelope of a strongly coupled energy harvester with the pre-tuned load resistance, R_{opt}, in the presence of (a) uncertainty in mass and stiffness only, and (b) uncertainty in coupling only.

In the above study, the uncertainties in mass, stiffness and coupling are all included. To examine their effects separately, the configuration in Fig. 7(b) was used as an example and analyzed in two scenarios: presence of uncertainty in mass and stiffness only, and presence of uncertainty in coupling only. The results for the two scenarios are presented in Figs. 8(a) and 8(b), respectively. For the system and under the uncertainty settings, it can be seen that the overall uncertainty of power shown in Fig. 7(b) is mostly due to the uncertainty in mass and stiffness. In addition, the effect from the mass and stiffness uncertainty appears to be "centered" about the nominal power envelope through most of the frequency range; while the effect from the coupling uncertainty alone is almost unnoticeable on the left side of the power envelope and becomes much more visible on the right side. These observations are consistent with the analytical PEH power characteristics discussed in Section 2.1. For Fig. 8(a), the uncertainty in mass and stiffness changes the natural frequency of the system, effectively moving the power envelope left and right about the original power envelope. In the middle frequency range between the two power limit peaks, the maximum power is still subjected to the power limit, and the pre-tuned load resistance becomes "mistuned" to the "new" system in the presence of uncertainty. As a result, almost all the power points fall below the nominal power envelope curve over the middle frequency range. On the other hand, the change in the coupling of a strongly coupled system does not change its short-circuit natural frequency but open-circuit natural frequency. As illustrated in Fig. 2, when the coupling increases, the left side of the power envelope (near the short-circuit natural frequency) remains almost "fixed" while the right side extends to the right as a result of increased open-circuit natural frequency. Therefore, the effect of uncertainty in coupling causes the power envelope to extends and contracts mostly on the right side. This is in agreement with the results shown in Fig. 8(b), where the uncertainty band is very noticeable on the right side but not on the left side of the power envelope.

4.2.2 Further discussion on the effect of load resistance tuning schemes

To investigate further the role of adaptive optimization in handling the uncertainty effect, the distribution of the harvested power (samples) at a few selected excitation frequencies by the systems shown in Fig. 7 are presented in Fig. 9. The adaptive optimization does not offer much power improvement as to uncertainty for the weakly coupled system throughout the frequencies, e.g. Figs. 9(c), and 9(e), except some slight enhancement near the peak frequency, e.g., Fig. 9(a). This can be also stated about the strongly coupled system for frequencies outside the frequency band between the two power limit frequencies, e.g., Figs. 9(d) and 9(f). There are only a very small number of samples whose harvested power is increased by the adaptive optimization. However, as shown in Fig. 9(b), for frequencies that fall into the band, the adaptive optimization is able to not only reduce the size of the uncertainty band (or scattering), but also boost the harvested power for most of the samples. In addition, the distribution of the optimized values of the load resistance are shown in Fig. 10. It can be seen that the enhanced power in Figs. 9(a) and 9(b) is connected to a more centered distribution of the adaptively re-tuned optimized resistance about its associated pre-tuned optimal value.

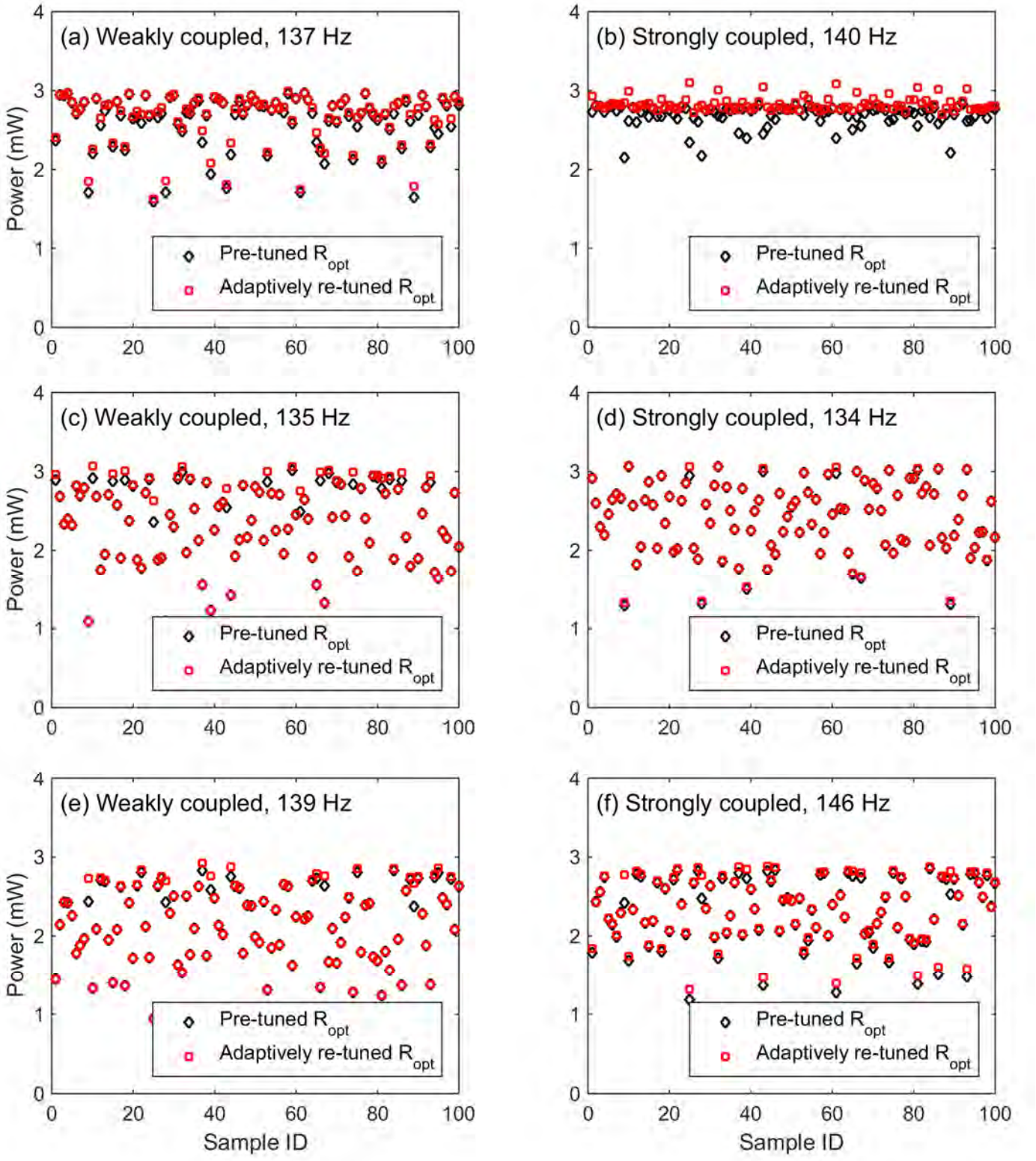

Figure 9. Distribution of harvested power at selected excitation frequencies for the weakly and strongly coupled configurations. Weakly coupled: (a) 137 Hz; (c) 135 Hz; and (e) 139 Hz. Strongly coupled: (b) 140 Hz; (d) 134 Hz; and (f) 146 Hz.

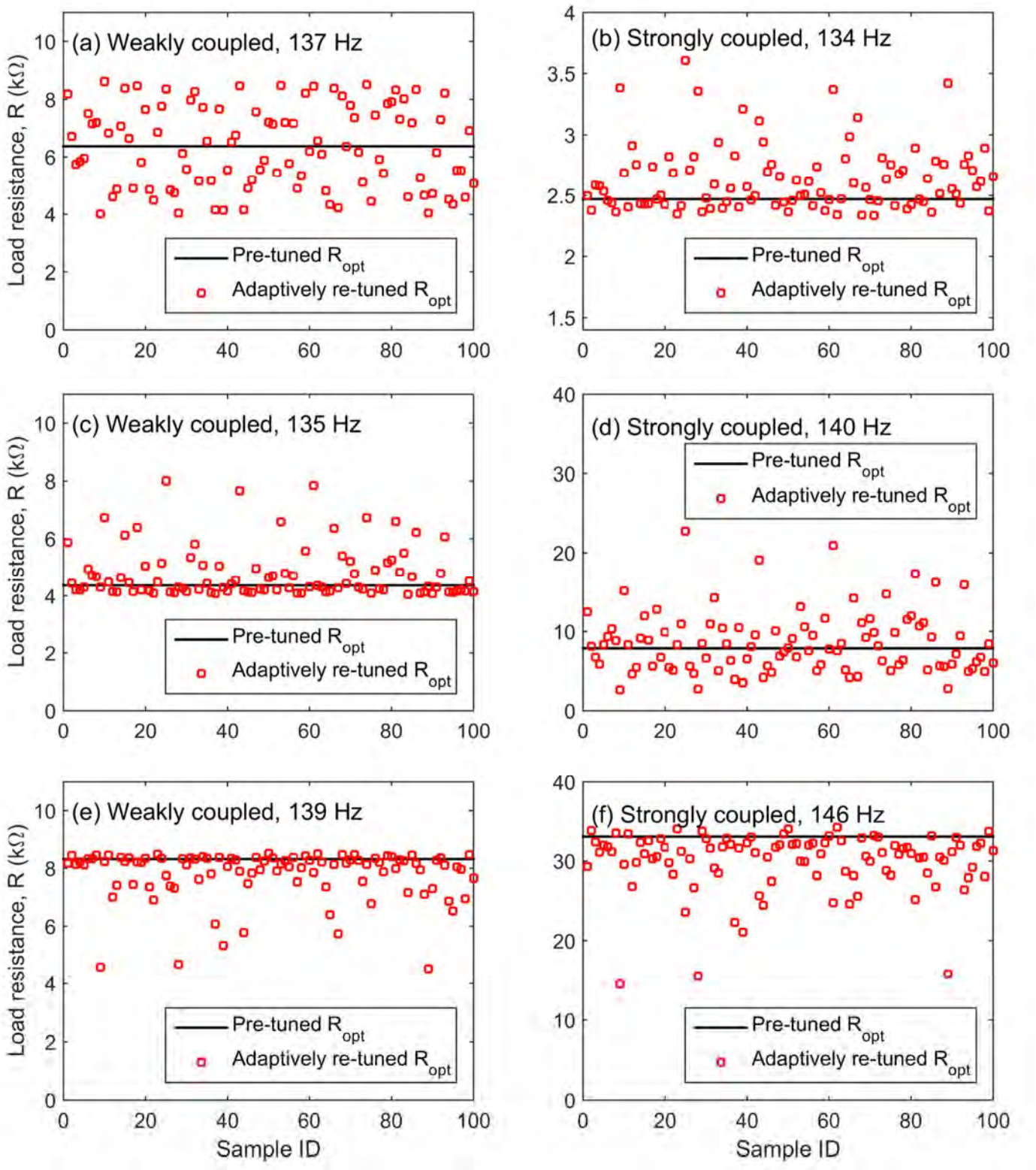

Figure 10. Distribution of optimized load resistance at selected excitation frequencies for the weakly and strongly coupled configurations. Weakly coupled: (a) 137 Hz; (c) 135 Hz; and (e) 139 Hz. Strongly coupled: (b) 140 Hz; (d) 134 Hz; and (f) 146 Hz.

The adaptive re-tuning of the load resistance has been shown to be an effective method for power enhancement and uncertainty reduction of strongly coupled systems. However, compared to the pre-tuned method, it requires an additional tuning step and its implementation increases the complexity of the system because the load needs to be adjustable. As another effort to find a pre-tuned and fixed load resistance for power enhancement, a new tuning scheme was investigated. Instead of using the analytical optimization Eq. (7) to determine the pre-tuned optimal resistance, uncertainty analysis was performed to find an optimal resistance that maximizes the mean power of the samples [24]. As an example, the harvested power of the strongly coupled system at excitation frequency 140 Hz was studied. Uncertainty was introduced into 100 samples. For a fixed pre-tuned resistance, the harvested power was obtained for all the samples. The results are presented in Fig. 11, where the harvested power is plotted against the pre-tuned resistance. The plot clearly demonstrates the load dependence of power, a characteristic of PEHs. The pre-tuned R_{opt} given analytically by Eq. (7) based on the nominal model is 7863 Ω, and the numerical study finds the load resistance maximizing the mean power (of the 100 samples) is 8200 Ω. Table 3 summarizes and compare the power characteristics of the three load-resistance tuning schemes. The pre-tuned R_{opt} scheme determines a fixed load resistance analytically from Eq. (7) based on the nominal model; the adaptive re-tuned R_{opt} scheme adjusts the load resistance still analytically from Eq. (7) but based on the updated model due to the presence of uncertainty; and the pre-tuned-for-the-mean method finds the optimal load resistance through the uncertainty analysis of the nominal model. It can be seen from the table that the two pre-tuned methods perform about the same. However, the pre-tuned-for-the-mean method could be a more practical approach as the pre-tuned R_{opt} scheme relies on the analytical theory, i.e., Eq. (7), which might not be available or accurate due to the modeling complexity of energy harvesters. The adaptive tuning scheme outperforms the other two. However, as mentioned above, the load needs be adjustable and adjusted individually to account for different uncertainty effects in the samples.

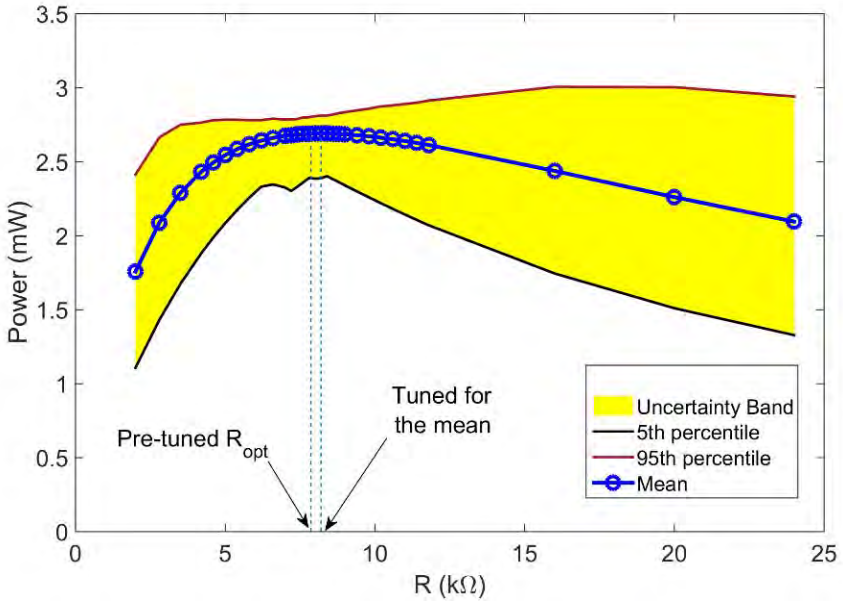

Figure 11. Mean and uncertainty band of harvested power vs. pre-tuned resistance of the strongly coupled system at 140 Hz

Table 3. Power statistics of load-resistance tuning schemes

Power statistics	Pre-tuned R_{opt}	Adaptively re-tuned R_{opt}	Tuned for the mean
Mean (mW)	2.6895	2.8297	2.6907
Standard deviation (mW)	0.1331	0.0819	0.1415
95th percentile (mW)	2.8036	3.0211	2.8132
75th percentile (mW)	2.7728	2.8502	2.7807
25th percentile (mW)	2.6511	2.7739	2.6440
5th percentile (mW)	2.4004	2.7423	2.4060

4. Conclusions

A general nonparametric uncertainty analysis methodology is presented for uncertainty quantifications of piezoelectric energy harvesters at the finite element level. First, a finite element modeling framework is developed which utilizes the matrices relating to the structural properties (mass, stiffness), the piezoelectric capacitance matrix, as well as the structural-piezoelectric coupling terms of the mean harvester. For finite element software that do not have piezoelectric elements but include thermal effects on structures, the thermal analogy linking piezoelectric and temperature effects can be applied. Fully coupled piezoelectric-structural simulations can be performed using the constructed finite element modeling framework. This framework was applied to a bimorph energy harvester in Nastran and validated by the excellent agreement between its results and those obtained experimentally, analytically and from Ansys.

To better account for the coupled manner that the real world uncertainty is expected to affect all components and parameters of the model, a global, nonparametric uncertainty modeling approach based on the maximum entropy principle is adopted with the constructed finite element model, and applied to two configurations of the energy harvester, one of weak and the other of strong piezoelectric-structural coupling. For a fair comparison, they are designed for the same excitation frequency at the same power level. Random samples of mass, stiffness, and electromechanical coupling matrices are generated to represent the global effects of the uncertainties of the system parameters. The uncertainty analysis is performed to study the uncertainty effect on the power output of the energy harvester with three load resistance tuning schemes: First scheme is when a fixed load resistance is given by an optimization method applied to the nominal model without considering the system changes due to uncertainty; second scheme is when the effect of uncertainty is considered and the load resistance of each random sample is adaptively optimized to the changed system parameters; third scheme is when a fixed load resistance is designed to maximum the mean power of the entire sample set. The uncertainty effect is shown to be significant even at a relatively low uncertainty level, and more pronounced for the weakly coupled configuration than the strongly coupled one. The uncertainty analysis demonstrates the advantages of a strongly coupled harvester over a weakly coupled harvester. Firstly, its harvested power is less sensitive to uncertainty with either pre-optimized or adaptively optimized load resistance. Secondly, with the application of the adaptive optimization, its uncertainty effect can be significantly reduced and the harvested power can even be boosted if the target excitation frequency falls within the "harvesting bandwidth" between the two power limit frequencies. On the other hand, the application of the adaptive optimization method does not affect the uncertainty characteristic of the weakly coupled harvester as much.

Appendix: Analytical expressions of system parameters in Eqs. (3) and (4)

For a fully-covered and symmetric bimorph beam harvester, its equivalent parameters in the single-mode model have been obtained as [24]:

$$M = \left(\rho_s t_s + 2\rho_p t_p\right) b \tag{46}$$

$$K = \left[1.0302 Y_s \left(\frac{t_s^3}{L^4}\right) + 2.0604 Y_p \left(\frac{3t_s^2 t_p + 6t_s t_p^2 + 4t_p^3}{L^4}\right)\right] b \tag{47}$$

$$\theta = -2.753 d_{31} Y_p b \left(\frac{t_s + t_p}{\sqrt{L^3}}\right) \tag{48}$$

$$C_p = 2K_3^S \varepsilon_0 b \left(\frac{L}{t_p}\right) \tag{49}$$

$$D = -0.783 b \left(2\rho_p t_p + \rho_s t_s\right) \sqrt{L} \tag{50}$$

where the subscripts s and p denote the substrate and piezoelectric materials, respectively. The length, width and thickness are denoted by L, b and t, respectively. In addition, ρ is the density, Y the Young's modulus in the 1-direction, K_3^S the relative dielectric constant measured at constant strain, and d_{31} is the piezoelectric coefficient.

Acknowledgements
The financial support of this work to the first (XQW) and third (MPM) authors by the Air Force Multi University Research Initiative contract FA9550-15-1-0038 with Dr. Jean-Luc Cambier as Technical Monitor and the Air Force Office of Scientific Research grant FA9550-16-1-0021 with Dr. Jaimie Tiley as Technical Monitor are gratefully acknowledged.

References:

[1] Todaro, M. T., Guido, F., Mastronardi, V., Desmaele, De., Epifani, G., Algieri, L., and Vittorio, M. D., 2017, "Piezoelectric MEMS vibration energy harvesters: Advances and outlook," Microelectronic Engineering, 183-184, pp. 23-36.
[2] Priya, S., and Inman, D. J., 2009, Energy Harvesting Technologies, Springer, NY.
[3] Beeby, S. P., Tudor, M. J., and White, N. M., 2006, "Energy harvesting vibration sources for microsystems applications," Meas. Sci.Technol., 17, pp. R175-R195.
[4] Sodano, H. A., Inman, D. J., and Park, G., 2004. "A review of power harvesting from vibration using piezoelectric materials," The Shock and Vibration Digest, 36, pp. 197-205
[5] Priya, S., 2007 "Advances in energy harvesting using low profile piezoelectric transducers," J. Electroceram, 19, pp. 165-182
[6] Anton, S. R., and Sodano, H. A, 2007, "A review of power harvesting using piezoelectric materials (2003-2006)," Smart Materials and Structures, 16, pp. R1-R21.
[7] Cook-Chennault, K. A., Thambi, N., and Satry, A. M., 2008, "Powering MEMS portable devices-a review of non-regenerative and regenerative power supply systems with special emphasis on piezoelectric energy harvesting systems," Smart Materials and Structures, 17, 043001.
[8] Calio, R., Rongala, U. B., Camboni, D., Milazzo, M., Stefanini, C., Petris, G., and Oddo, C. M., 2014, "Piezoelectric energy harvesting solutions," Sensors, 14, pp. 4755-4790
[9] Tang, L., and Yang, Y., and Soh, C. K., 2010, "Toward broadband vibration-based energy harvesting," Journal of Intelligent Material Systems and Structures, 21, pp. 1867-1897.
[10] Harne, R. L., and Wang, K. W., 2013, "A review of the recent research on vibration energy harvesting via bistable systems," Smart Materials and Structures, 22, 023001
[11] Mann, B. P., Barton, D. A. W., and Owens, B. A. M., 2012, "Uncertainty in performance for linear and nonlinear energy harvesting strategies," Journal of Intelligent Material Systems and Structures, 23, pp. 1451-1460.
[12] Lefeuvre, E., Badel, A., Richard, C., and Guyomar, D., 2007, "Energy harvesting using piezoelectric materials: Case of random vibrations," Journal of Electroceramics, 19, 349–355.
[13] Halvorsen, E., 2008, "Energy harvesters driven by broadband random vibrations," J. Microelectromech. Syst., 17, 1061–71
[14] Adhikari, S., Friswell, M., and Inman, D. J., 2009, "Piezoelectric energy harvesting from broadband random vibrations," Smart Mater. Struct., 18, 115005
[15] Seuaciuc-Osório, T., and Daqaq, M. F., 2010, "Energy harvesting under excitations of time-varying frequency," J. Sound Vib., 329, 2497–515
[16] Yoon, H., and Youn, B. D., 2014, "Stochastic quantification of the electric power generated by a piezoelectric energy harvester using a time–frequency analysis under non-stationary random vibrations," Smart Materials and Structures, 23, 045035
[17] Zhao, S., and Erturk, A., 2012, "Electroelastic modeling and experimental validations of piezoelectric energy harvesting from broadband random vibrations of cantilevered bimorphs," Smart Mater. Struct., 22, 015002
[18] Petromichelakis, I., Psaros, A. F., and Kougioumtzoglou, I. A., 2018, "Stochastic response determination and optimization of a class of nonlinear electromechanical energy harvesters: A Wiener path integral approach," Probabilistic Engineering Mechanics, 53, 116-125
[19] Li, Y., Li, W., Guo, T., Yan, Z., Fu, X., and Hu, X., 2009, "Study on structure optimization of a piezoelectric cantilever with a proof mass for vibration-powered energy harvesting system," J. Vac. Sci. Technol. B, 27, pp. 1288–1290.
[20] Bourisli, R. I., and Al-Ajmi, M. A., 2010, "Optimization of smart beams for maximum modal electromechanical coupling using genetic algorithms," J. Intell. Mater. Syst. Struct., 21, pp. 907–914.
[21] Dietl, J. M., and Garcia, E., 2010, "Beam shape optimization for power Harvesting," J. Intell. Mater. Syst. Struct., 21, pp. 633–646.

[22] Paquin, S., and St-Amant, Y., 2010, “Improving the performance of a piezoelectric energy harvester using a variable thickness beam,” Smart Mater. Struct., 19, 105020.
[23] Lefeuvre, E., Badel, A., Richard, C., and Guyomar, D., 2005, “Piezoelectric energy harvesting device optimization by synchronous electric charge extraction,” Journal of Intelligent Material Systems and Structures, 16, pp. 865-876
[24] Liao, Y., and Sodano, H. A., 2008, “Model of a single mode energy harvester and properties for optimal power generation,” Smart Materials and Structures, 17, 065026
[25] Wickenheiser, A. M., and Garcia, E., 2010, “Power optimization of vibration energy harvesters utilizing passive and active circuits,” J. Intell. Mater. Syst. Struct., 21, pp. 1343–1361.
[26] Liao, Y., and Sodano, H. A., 2018, “Optimal power, power limit, and damping of vibration based power harvesters,” Smart Materials and Structures, 27, 075057
[27] Zheng, B., Chang, C. J., and Gea, H. C., 2009, “Topology optimization of energy harvesting devices using piezoelectric materials,” Structural and Multidisciplinary Optimization, 38, pp. 17-23
[28] Rupp, C. J., Evgrafov, A., Maute, K., and Dunn, M. L., 2009, “Design of piezoelectric energy harvesting systems: a topology optimization approach based on multilayer plates and shells,” J. Intell. Mater. Syst. Struct., 20, pp. 1923–1939.
[29] Nakasone, P. H., Silva, E. C. N., 2010, “Dynamic design of piezoelectric laminated sensors and actuators using topology optimization,” J. Intell. Mater. Syst. Struct., 21, pp. 1627–1652.
[30] Franco, V. R., and Varoto, P. S., 2017, “Parameter uncertainties in the design and optimization of cantilever piezoelectric energy harvesters,” Mechanical Systems and Signal Processing, 93, pp. 593–609.
[31] Ali, S. F., Friswell, M. I., and Adhikari, S., 2010, “Piezoelectric energy harvesting with parametric uncertainty,” Smart Materials and Structures, 19, 105010
[32] Li, Y., and Zhou, S., 2018, “Probability analysis of asymmetric tristable energy harvesters,” AIP Advances, 8, 075221
[33] Abdelkefi, A., Hajj, M. R., and Nayfeh, A. H., 2012, “Uncertainty quantification of piezoelectric energy harvesters from aeroelastic vibrations,” MATEC Web of conferences, 1, 03007
[34] Nanda, A., Singla, P., and Karami, M. A., “Uncertainty quantification of energy harvesting systems using method of quadratures and maximum entropy principle,” Proceedings of the ASME 2015 Conference on Smart materials, Adaptive Structures and Intelligent Systems (SMASIS2015), Denver, Colorado, September 21-23, 2015. V002T07A016. ASME.
[35] Hosseinloo, A. H., and Turitsyn, K., 2016, “Design of vibratory energy harvesters under stochastic parametric uncertainty: a new optimization philosophy,” Smart Materials and Structures, 25, 055023
[36] Kim, J., Lee, T. H., Song, Y., and Sung, T. H., 2017, “Robust design optimization of fixed-fixed beam piezoelectric energy harvester considering manufacturing uncertainties,” Sensors and Actuators A, 260, pp. 236-246
[37] Seong, S., Hu, C., and Lee, S., 2017, “Design under uncertainty for reliable power generation of piezoelectric energy harvester,” Journal of Intelligent Material Systems and Structures, 28, pp. 2437-2449.
[38] Peralta, P., Ruiz, R. O., and Taflanidis, A. A., 2020, “Bayesian identification of electromechanical properties in piezoelectric energy harvesters,” Mechanical Systems and Signal Processing, article in press
[39] de Godoy, T. C., and Trindade, M. A., 2012, “Effect of parametric uncertainties on the performance of a piezoelectric energy harvesting device,” Journal of Brazilian Society of Mechanical Sciences and Engineering, 34, pp. 552-560
[40] Song, P., Wang, X. Q., Matney, A., Murthy, R., and Mignolet, M. P., “Nonlinear Geometric Thermoelastic Response of Structures with Uncertain Thermal and Structural Properties,” Proceedings of the AIAA Science and Technology Forum and Exposition (SciTech2017), Dallas, Texas, Jan. 9-13, 2017, AIAA Paper AIAA 2017-0181.
[41] Song, P., and Mignolet, M. P., 2019, “Maximum entropy-based uncertainty modeling at the elemental level in linear structural and thermal problems,” Computational Mechanics, 64, pp. 1557-1566.
[42] Song, P., Wang, X. Q., and Mignolet, M. P., "Maximum entropy structural-thermal uncertainty modeling at the finite element level,” Proceedings of the AIAA Science and Technology Forum and Exposition (SciTech2019), San Diego, California, USA, January 7-11, 2019, AIAA Paper AIAA 2019-0443.
[43] Soize, C., 2000, “A Nonparametric Model of Random Uncertainties for Reduced Matrix Models in Structural Dynamics,” Probabilistic Engineering Mechanics 15, pp. 277-294.
[44] Soize, C., 2012, Stochastic Models of Uncertainties in Computational Mechanics, American Society of Civil Engineers (ASCE).
[45] Soize, C., 2017, Uncertainty Quantification: An Accelerated Course in Advanced Applications in Computational Engineering, Springer
[46] Hagood, N. W., Chung, W. H., von Flotow, A., 1990, “Modeling of piezoelectric actuator dynamics for active structural control,” Journal of Intelligent Material Systems and Structures, 1:3, pp. 327-354.
[47] Liao, Y., and Liang, J., 2019, “Unified modeling, analysis and comparison of piezoelectric vibration energy harvesters,” Mechanical Systems and Signal Processing, 123, pp. 403-425.
[48] Liao, Y., 2019, “Analysis of power and efficiency of piezoelectric vibration energy harvesters through an impedance plot,” Journal of Intelligent Material Systems and Structures, 30, pp. 3036-3055.

[49] Liao, Y., and Liang, J., 2018, “Maximum power, optimal load, and impedance analysis of piezoelectric vibration energy harvesters,” Smart Materials and Structures, 27, 075053
[50] Staworko, M., and Uhl, T., 2008, “Modeling and simulation of piezoelectric elements-comparison of available methods and tools,” Mechanics, 27, pp. 161-171.
[51] Vyas, V., Wang, X. Q., Jain, A., and Mignolet M. P., 2015 “Nonlinear geometric reduced order model for the response of a beam with a piezoelectric actuator,” Proceedings of the 56th Structures, Structural Dynamics, and Materials Conference (AIAA SciTech), Kissimmee, Florida, USA, January 5-9, 2015. AIAA Paper AIAA-2015-0692.
[52] Soize, C., 2005, “Random matrix theory for modeling uncertainties in computational mechanics,” Computer Methods in Applied Mechanics and Engineering, 194, pp. 1333–1366.
[53] Song, P., 2019, “Response of Heated Structures: Reduced Order Models and Uncertainty Modeling,” Ph.D. Dissertation, Arizona State University, Tempe, AZ.
[54] Perez, R. A., Smarslok, B. P., and Mignolet, M. P., “Deterministic and stochastic partial linearization approach for nonlinear reduced order models of structures,” Proceedings of the 56th Structures, Structural Dynamics, and Materials Conference (AIAA SciTech), Kissimmee, Florida, USA, January 5-9, 2015. AIAA Paper AIAA-2015-2052.
[55] Wang, X. Q., and Mignolet, M. P., “Uncertainty quantification of nonlinear stiffness coefficients in non-intrusive reduced order models”, Proceedings of the 38th IMAC, Conference and Exposition on Structural Dynamics, Houston, Texas, USA, February 10-13, 2020. Paper 8474.

APPENDIX G:

[A1]: Extension of the concepts of [C3](Appendix I) to include the epistemic uncertainty associated with incomplete bases

MODELING OF EPISTEMIC UNCERTAINTY DUE TO INCOMPLETE BASES

The work carried out in the previous section focused on epistemic uncertainty induced by an imposed sparsity of the parameters of the reduced order model. Another source of epistemic uncertainty relates to the basis of the ROM, i.e., that it is not complete enough to represent the response within the desired accuracy. This realistic situation reflects the current methodology used to construct a priori the basis in structural-thermal ROMs. For example, the structural basis is composed of (i) linear modes of the structure, (ii) dual modes, and (iii) enrichments.

The purpose of the dual modes is to capture the nonlinear effects present when the response along the linear modes becomes "large" due to the mechanical loading which is primarily transverse in thin shell structures, see [13]. The enrichments are basis functions introduced to widen the basis to allow the capture of the displacements fields induced by a temperature distribution. These displacements are often very different from those induced by mechanical loads and further depend strongly on the applied temperature, see [32] for discussion. One challenge of the dual modes and enrichment construction processes is that they do not guarantee completeness and thus it may not be possible to reduce the error to be small enough. A corollary of this issue is that the low error level may be reach but requires a very large number of either dual modes or enrichments.

A similar situation in encountered for the thermal basis which has been proposed [26] to be constructed from the eigenvectors of the steady heat conduction problem. While its first eigenvalues are well separated, their spacing decreases with eigenvalue number and the number of eigenvectors needed increases very rapidly as the error is decreased. This situation reflects the physics that the heat conduction problem may be very localized to different areas of the structure. A different construction strategy of the thermal bases has recently been proposed [33] which is structure-centric, i.e., aims to reduce the basis by capturing primarily the temperature distributions that affect the structural response. As for the dual modes and enrichments, no completeness property has been derived for such a thermal basis.

Based on the above discussion, it is of interest here to investigate how to model the epistemic uncertainty associated with an incomplete set of:

(i) thermal basis functions,
(ii) enrichments, or
(iii) dual modes.

This modeling is achieved for these three conditions in the ensuing sections. The basic perspective is to recognize the incomplete basis as a complete one from which a set of basis function has been removed. Then, the group of components of the matrix $\overline{\boldsymbol{K}}_D$ that are affected by the removal of these basis functions is randomized to reflect the induced uncertainty. This strategy will be demonstrated on the heated beam introduced in [27], see also [29], which is briefly reviewed in next section.

BEAM SUBJECTED TO AN OSCILLATING FLUX

The panel was modeled as an isotropic clamped-clamped beam with temperature independent properties given in Table 1 and was modeled by finite elements in Nastran. Structurally, the beam was considered as one-dimensional and was discretized using 40 beam elements ("CBEAM" within Nastran). Thermally, the structure was considered as a two-dimensional object discretized with 40 4-node elements ("CQUAD4" within Nastran) along its length and 6 through the thickness thereby allowing the capture of the temperature distribution along the beam and across its thickness.

Table 1. Clamped-Clamped Beam Mean Properties

Beam Length (L)	0.2286 m
Cross-section Width (w)	0.0127 m
Cross-section Thickness (h)	7.88 10^{-4} m
Density	2700 kg/m^3
Young's Modulus	73,000 MPa
Shear Modulus	27,730 MPa
Coeff. Thermal Expansion	2.5 10^{-5} /°C
Mesh (CBEAM)	40

The beam was subjected to a triangular flux of width 2Δ=0.4 L, see Fig. 18, oscillating about the middle of the beam ($a_0 = L/2$) with a frequency Ω and an amplitude $\bar{\delta}$=0.075 L. The peak heat flux was selected so that the peak temperature on the upper surface of the beam would be 10°C for the steady problem ($\Omega = 0$) while the bottom surface was maintained at 0°C. The ends of the beam were also maintained at 0°C. This thermal loading led to a tip static deflection of 0.65 thickness and thus to a nonlinear geometric behavior.

An initial ROM of the panel was constructed using 17 structural modes and 12 thermal basis functions, see [27] for details, which led to an excellent prediction of the full Nastran results. A Reduced ROM (RROM), see [34], was also constructed that includes 12 structural modes and 5 thermal basis functions. The RROM predictions are essentially identical to those of the original ROM.

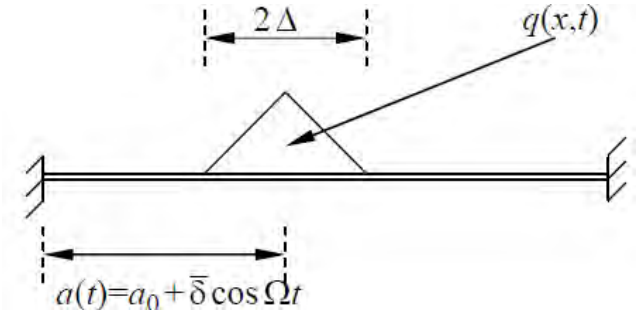

Figure 18. Beam panel subjected to an oscillating flux.

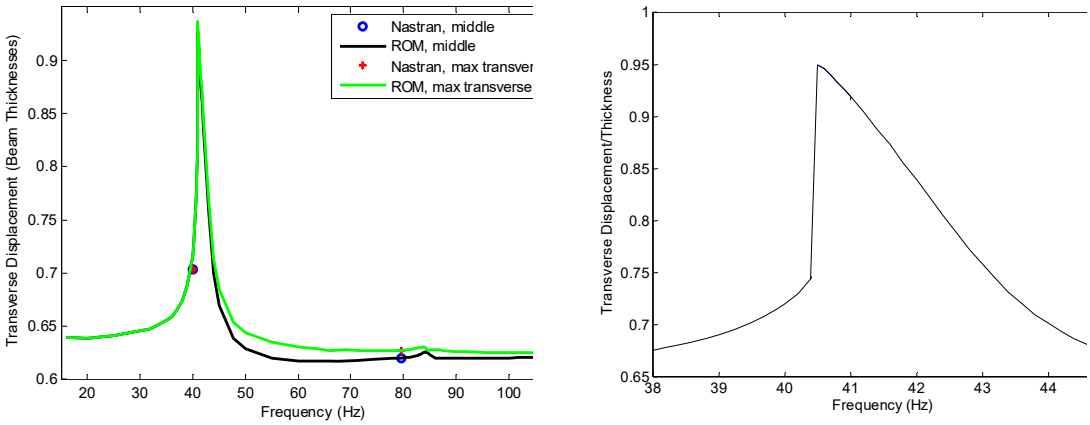

Figure 19. Maximum transverse deflection on the beam and at the beam middle vs. flux oscillation frequency Ω as determined from the ROM and Nastran computations.

Of particular interest here is the peak response vs. frequency Ω which displays a peak for Ω approximately equal to 1/2 of the first linear natural frequency of the beam, see Fig. 19.

Focusing next on the uncertainty modeling, note that since the properties of the beam are temperature independent, the matrix $\overline{\boldsymbol{K}}_D$ is reduced in size to the following matrix

$$\overline{\boldsymbol{K}}_C = \begin{bmatrix} \boldsymbol{K}^{(1)} & \tilde{\boldsymbol{K}}^{(2)} & \boldsymbol{F}^{(th)} \\ \tilde{\boldsymbol{K}}^{(2)T} & 2\tilde{\boldsymbol{K}}^{(3)} & \tilde{\boldsymbol{K}}^{(th)} \\ \boldsymbol{F}^{(th)T} & \tilde{\boldsymbol{K}}^{(th)T} & \boldsymbol{K}^{(tt)} \end{bmatrix}. \tag{28}$$

INCOMPLETE THERMAL BASIS

The absence of thermal basis functions is reflected by the absence of terms in the blocks $\boldsymbol{F}^{(th)}$, $\tilde{\boldsymbol{K}}^{(th)}$, and $\boldsymbol{K}^{(tt)}$ of the matrix $\overline{\boldsymbol{K}}_C$ as shown in Fig. 20. Accordingly, the uncertainty should be introduced on those terms through the random matrix $\boldsymbol{H}_D$ of Eq. (25) with $\boldsymbol{H}_T$ random and $\boldsymbol{H}_S$ identity.

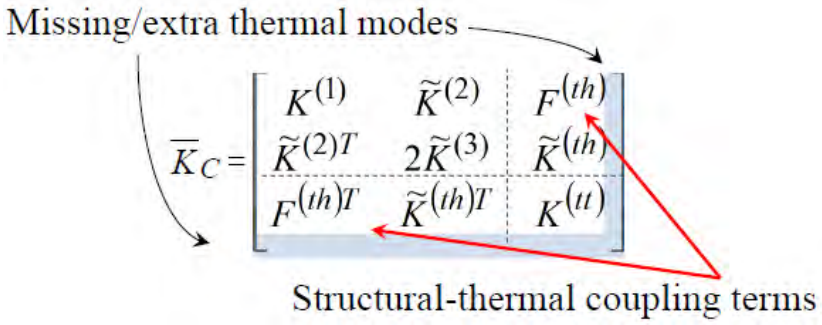

Figure 20. Effect of incomplete thermal basis on the matrix $\overline{\boldsymbol{K}}_C$.

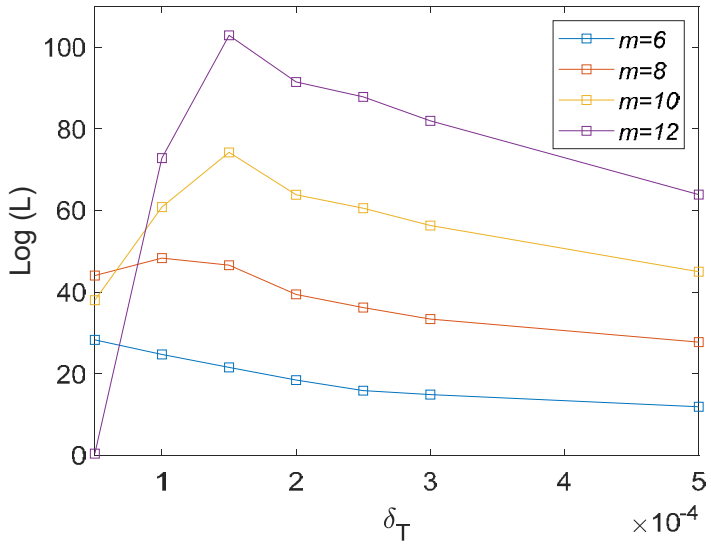

Figure 21. Log likelihood function as a function of the uncertainty level δ_T for several numbers (m) of eigenvectors retained. Incomplete thermal basis.

The validation of this strategy was accomplished on the heated beam by decreasing the number of thermal modes in the RROM from 5 to 3 keeping the 3 most dominant. The value of the parameter δ_T was identified by the maximum likelihood strategy as in the earlier part of this investigation using the response of the maximum transverse displacements of the mean model with 5 thermal basis functions at the various frequencies. This process, see Fig. 21, led to the value δ_T =1.5 10^{-4} and shown in Fig. 22 are the uncertainty bands on the maximum transverse displacement of the beam. It is seen as expected that the mean model response with the 5 thermal basis functions is within the uncertainty band of the small model with only 3 thermal basis functions. This result validates the concept that the epistemic uncertainty associated with an incomplete thermal basis can indeed be introduced directly in the matrix $\overline{\boldsymbol{K}}_C$.

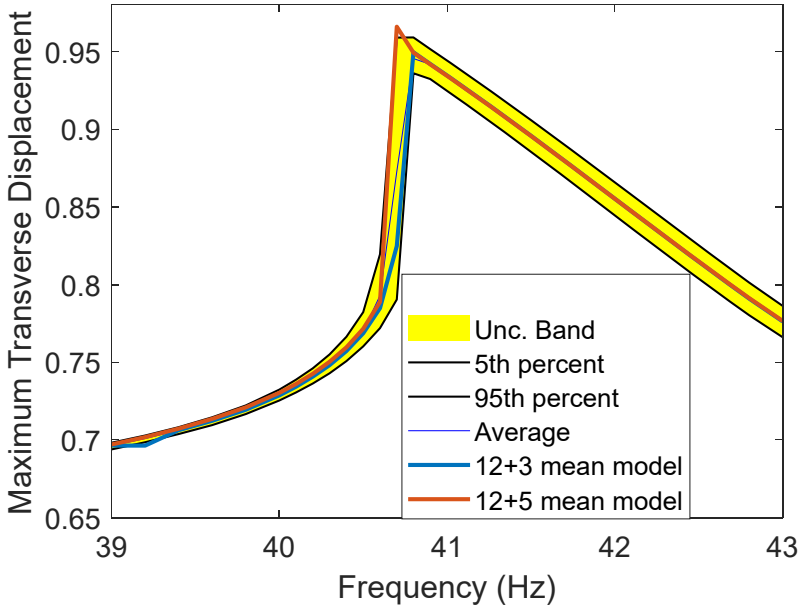

Figure 22. Uncertainty band on peak transverse response as a function of the flux oscillating frequency. Displacement expressed as fraction of thickness. Incomplete thermal basis.

INCOMPLETE SET OF ENRICHMENTS

A similar process to the one above was followed for an incomplete set of enrichments. The absence of some of those is reflected by the absence of terms in the blocks $\boldsymbol{K}^{(1)}$, $\tilde{\boldsymbol{K}}^{(2)}$, $\tilde{\boldsymbol{K}}^{(3)}$, $\boldsymbol{F}^{(th)}$, and $\tilde{\boldsymbol{K}}^{(th)}$ of the matrix $\overline{\boldsymbol{K}}_C$ as shown in Fig. 23(a). Accordingly, the uncertainty should be introduced on the structural terms only in $\boldsymbol{H}_D$, i.e., with $\boldsymbol{H}_T$ identify and $\boldsymbol{H}_S$ an appropriate random matrix. To proceed further, it is worthwhile to carry out a series of permutations of the rows and columns of $\overline{\boldsymbol{K}}_C$ so that the linear, quadratic, and cubic stiffness coefficients involving only the linear modes and dual modes, collectively referred to as "O" basis functions below, are regrouped in the top left block. Similarly, those same stiffness coefficients involving only the enrichments, collectively referred to as "E", will be positioned along the second diagonal block, leaving the thermal modes related terms at their original

locations. After those permutations, the structure of the matrix $\overline{\boldsymbol{K}}_C$ is as shown in Fig. 23(b). Accordingly, it is proposed here to randomize the block K_{EE} which can be achieved with the $\boldsymbol{H}_S$ matrix of the form of Eq. (29) in the permuted form.

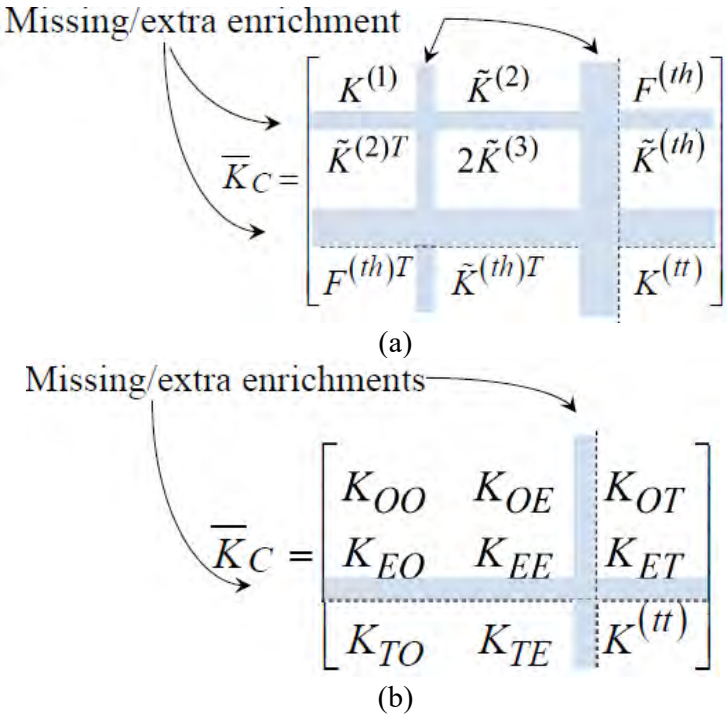

Figure 23. Effect of incomplete set of enrichments on the matrix $\overline{\boldsymbol{K}}_C$.

$$\boldsymbol{H_S} = \begin{bmatrix} \boldsymbol{I} & 0 & 0 \\ 0 & \boldsymbol{H_{EE}} & 0 \\ 0 & 0 & \boldsymbol{I} \end{bmatrix}. \tag{29}$$

The selection of the parameter δ_E of the random matrix $\boldsymbol{H_{EE}}$ was performed once again using the maximum likelihood identification approach with the data from the mean model with the 3 enrichments but the incomplete model only included the first two of these enrichments. This process, see Fig. 24, led to the value δ_E=0.1 and shown in Fig. 25 are the uncertainty bands on the maximum transverse displacement of the beam. It is seen as expected that the mean model response with the 3 enrichments is within the uncertainty band of the small model with only 2 of them.

A final validation of this uncertainty modeling was achieved by determining the band of uncertainty induced on a purely structural loading, i.e., a uniform pressure. Since the purpose of the enrichments is to capture the effects of thermal loading, not mechanical ones, it would be expected that the uncertainty bands on the response to the pressure are very small. This is indeed the case as seen in Fig. 26, the bands are so small that they are not visible.

This result validates the concept that the epistemic uncertainty associated with an incomplete set of enrichments can indeed be introduced directly in the matrix $\overline{\boldsymbol{K}}_C$.

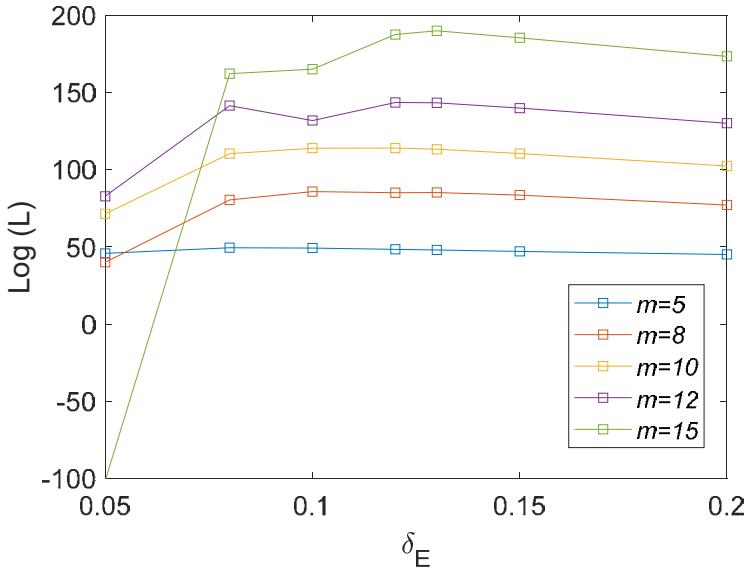

Figure 24. Log likelihood function as a function of the uncertainty level δ_E for several numbers (m) of eigenvectors retained. Incomplete set of enrichments.

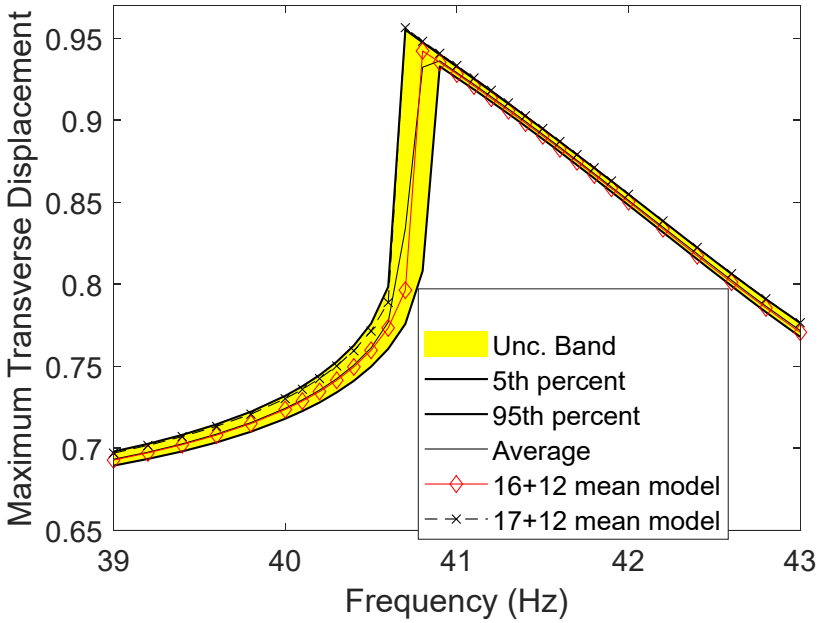

Figure 25. Uncertainty band on peak transverse response as a function of the flux oscillating frequency. Displacement expressed as fraction of thickness. Incomplete set of enrichments.

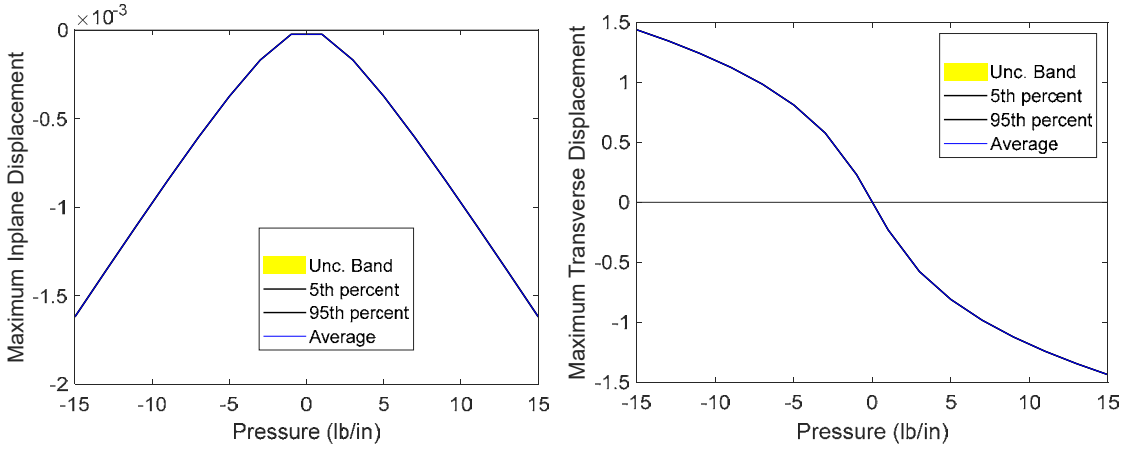

(a) (b)

Figure 26. Maximum (a) inplane and (b) transverse displacement of the beam subjected to a uniform pressure. Displacements expressed as fraction of thickness.

INCOMPLETE SET OF DUAL MODES

A final analysis is currently being carried out which investigates the epistemic uncertainty induced by an incomplete set of dual modes. In the absence of temperature, the matrices $\overline{\boldsymbol{K}}_D$ and $\overline{\boldsymbol{K}}_C$ both reduce to

$$\overline{\boldsymbol{K}}_B = \begin{bmatrix} \boldsymbol{K}^{(1)} & \tilde{\boldsymbol{K}}^{(2)} \\ \tilde{\boldsymbol{K}}^{(2)T} & 2\tilde{\boldsymbol{K}}^{(3)} \end{bmatrix}. \tag{30}$$

As done for the enrichments, it is desirable to separate the terms (linear, quadratic, and cubic stiffnesses) that involve only the linear modes (referred to "L" below) and only the dual modes (referred to as "D"). Then, through a series of permutations, the above matrix can be rewritten as

$$\overline{\boldsymbol{K}}_B = \begin{bmatrix} \boldsymbol{K}_{LL} & \boldsymbol{K}_{LD} \\ \boldsymbol{K}_{DL} & \boldsymbol{K}_{DD} \end{bmatrix}. \tag{31}$$

Accordingly, missing dual modes are reflected on the $\boldsymbol{K}_{LD}$, $\boldsymbol{K}_{DL}$, and $\boldsymbol{K}_{DD}$ blocks of the matrix $\overline{\boldsymbol{K}}_B$. Then, uncertainty can be introduced as in Eqs (23) and (24) with the random matrix $\boldsymbol{H}$ of the form of Eq. (32) in the permuted configuration

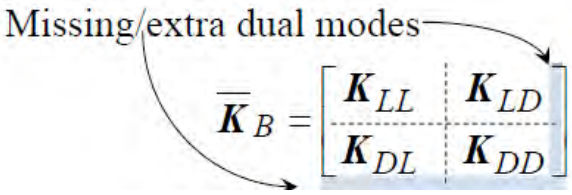

Figure 23. Effect of incomplete set of dual modes on the matrix $\overline{\boldsymbol{K}}_B$.

$$\boldsymbol{H} = \begin{bmatrix} \boldsymbol{I} & 0 \\ 0 & \boldsymbol{H}_{DD} \end{bmatrix}. \tag{32}$$

ADDITIONAL REFERENCES:

[32] Wang, X.Q., and Mignolet, M.P., "Enrichments of Structural Bases for the Reduced Order Modeling of Heated Structures Undergoing Nonlinear Geometric Response," *Proceedings of the International Modal Analysis Conference, IMAC XXXVIII*, Houston, Texas, Feb. 10-13, 2020.

[33] Murthy, R., Wang, X.Q., Matney, A., and Mignolet, M.P., "Optimum Thermal Modes for Coupled Structural - Thermal Reduced Order Models," *Proceedings of the AIAA Science and Technology Forum and Exposition (SciTech2016)*, San Diego, California, Jan. 4-8, 2016, AIAA Paper AIAA 2016-1709.

APPENDIX H:

[C5]: Lin, J., Wang, X.Q., and Mignolet, M.P., "Nonlinear Reduced Order Modeling of a Cylindrical Shell Exhibiting Mode Veering and Symmetry Breaking," *Proceedings of the International Modal Analysis Conference, IMAC XXXVII*, Orlando, Florida, Jan. 28-31, 2019.
[C7]: Lin, J., Wang, X.Q., and Mignolet, M.P., "Nonlinear Reduced Order Modeling of Strongly Nonlinear Behavior: A Revisit of a Curved Beam Example," *Proceedings of the International Modal Analysis Conference, IMAC XXXVI*, Orlando, Florida, Feb. 12- 15, 2018.
[T2]: Lin, J., "Nonlinear Reduced Order Modeling of Structures Exhibiting a Strong Nonlinearity, Ph.D., May 2020 (Chapters 4 and 6).

Nonlinear Reduced Order Modeling of a Cylindrical Shell Exhibiting Mode Veering and Symmetry Breaking

Jinshan Lin, X.Q. Wang, and Marc P. Mignolet

SEMTE, Faculties of Mechanical and Aerospace Engineering, Arizona State University, Tempe, AZ 85287-6106

Key words : reduced order modeling, nonlinear geometric, structural modeling, curved shell, asymmetric structure.

This paper is the continuation of an investigation on the application of nonlinear reduced order models (ROMs) for the large deformation analysis of structures, curved ones especially, exhibiting strongly nonlinear behavior, see [1] for an earlier study of a curved beam. The present efforts are focused on a fully clamped cylindrical shell successfully modeled by nonlinear reduced order models in [2]. This panel has a footprint of 9.75in by 15.75in by 0.048in thick and a radius of curvature of 100in. The panel material had an elastic modulus of 2.85x106 psi, Poisson's ratio of 0.3, density of 7.48x10-4 lb-sec2/in4, and coefficient of thermal expansion of 10.5x10-6 in/in/°F. Mass proportional damping was selected with coefficient $\alpha = 39.93$ which leads to a damping ratio of 1% on the first symmetric mode. The shell was discretized within Nastran with a mesh of 39x63 square CQUAD4 elements (40x64 nodes), see Fig. 1.

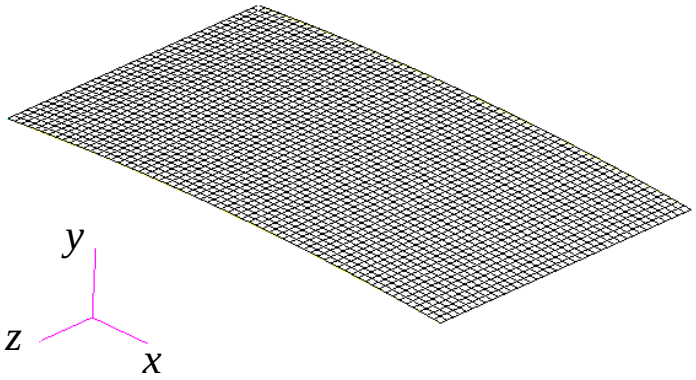

Figure 1. Finite element model of the curved shell of [2].

A first challenge encountered in the construction of a nonlinear reduced order model for the shell of Fig. 1 was the determination of a set of dual modes leading to a good representation of the response in the *x* and *z* directions. Following our earlier work on a clamped-clamped curved beam [1], the first part of the basis was constructed by a proper orthogonal decomposition of the projection of a series (11) of nonlinear Nastran static solutions (SOL 106) on the first 8 symmetric linear modes of the undeformed panel. The 6 POD modes with the largest eigenvalues, see Fig. 2, were retained in this computation. Duals were then constructed with the first 2 POD modes as dominant leading to 7 duals orthogonal to the first 27 symmetric linear modes. This 13-mode 6POD7D model performed very well in predicting the static response vs. load over a broad range of pressures including the occurrence of a mode switching event, see Figs 3 and 4.

Also investigated, see Fig. 5, are the first two eigenvalues of the tangent stiffness matrix as a function of the applied pressure. Shown on this figure are the Nastran eigenvalues, those of the Nastran tangent stiffness projected on the basis, and those predicted from the ROM generalized coordinates obtained for the various loading conditions. Note that the Nastran eigenvalues clearly show the veering that is the origin of the mode switching. Moreover, the eigenvalues of the projected tangent stiffness matrix match very well those predicted from the ROM suggesting that the identified model is accurate but the difference between these two curves and the Nastran one for the second eigenvalue suggests that the basis is not quite appropriate for large enough load levels.

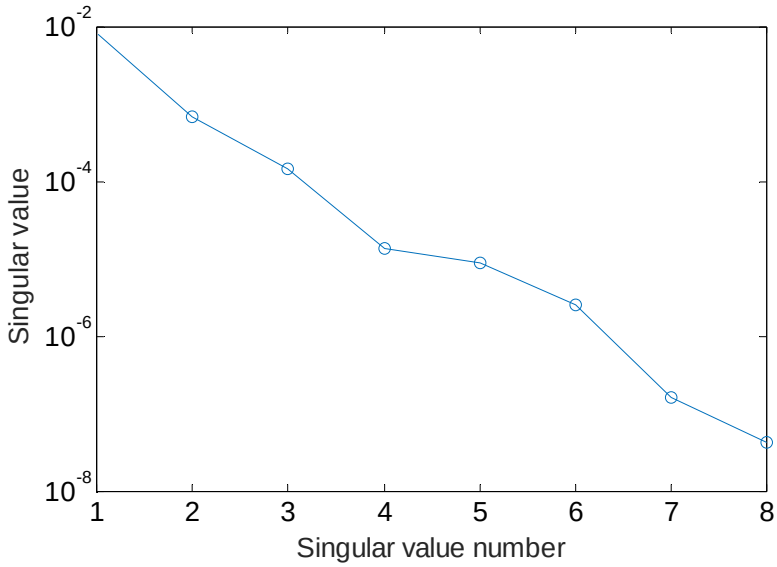

Figure 2. Singular values of the POD of the projections on the first 8 symmetric linear modes

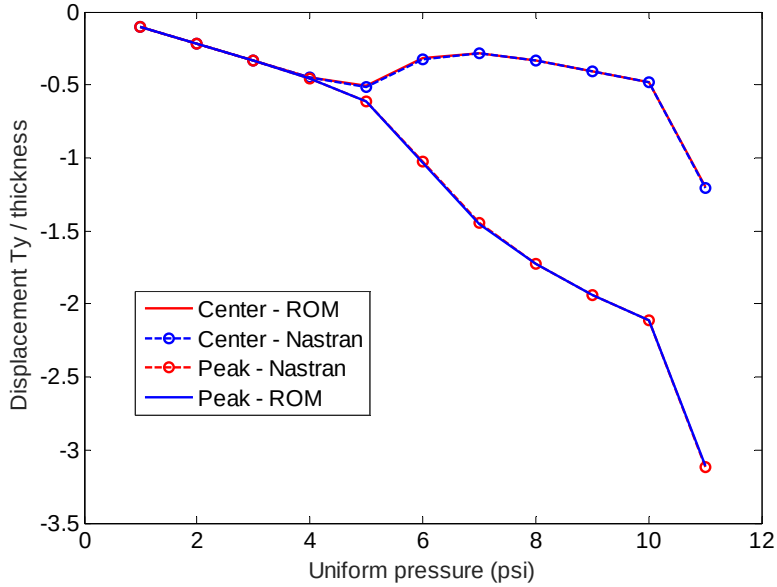

Figure 3. Center and peak displacement along the *y* (transverse) direction vs. applied uniform pressure. Nastran SOL 106 and ROM predictions

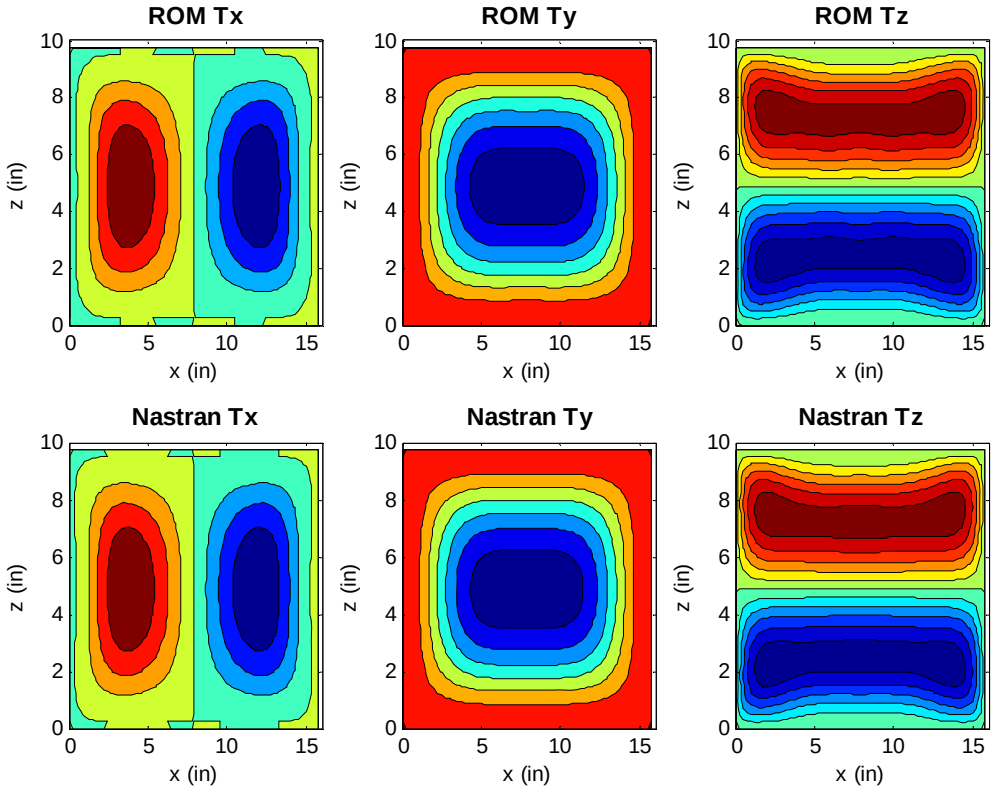

(a)

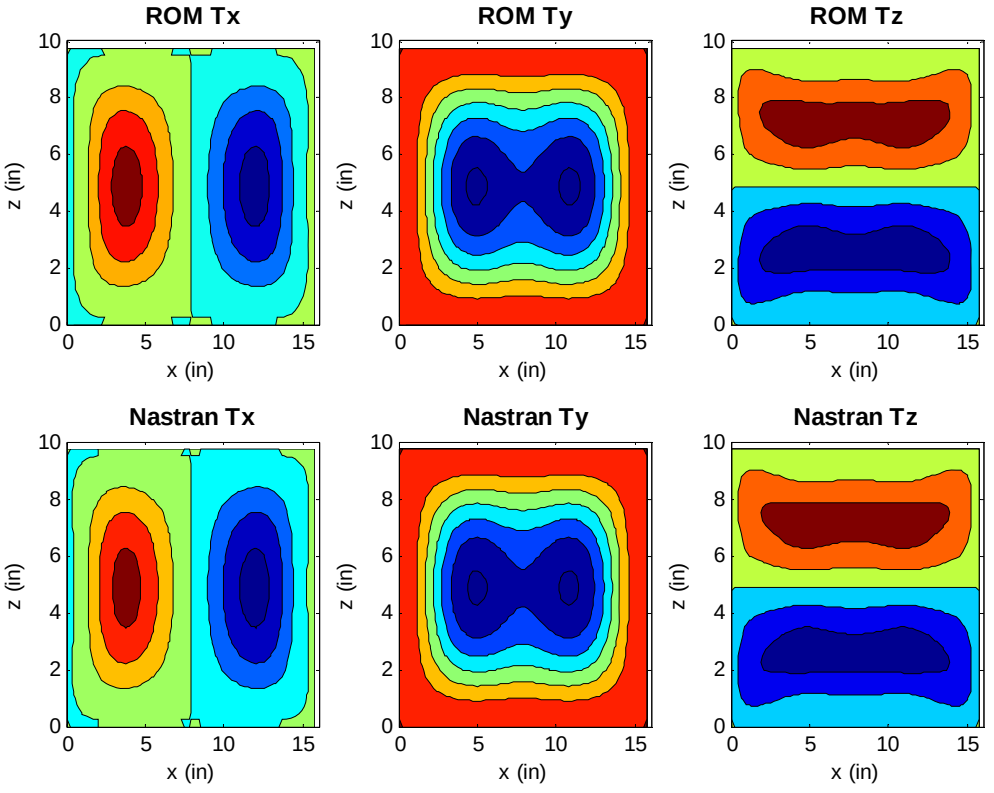

(b)

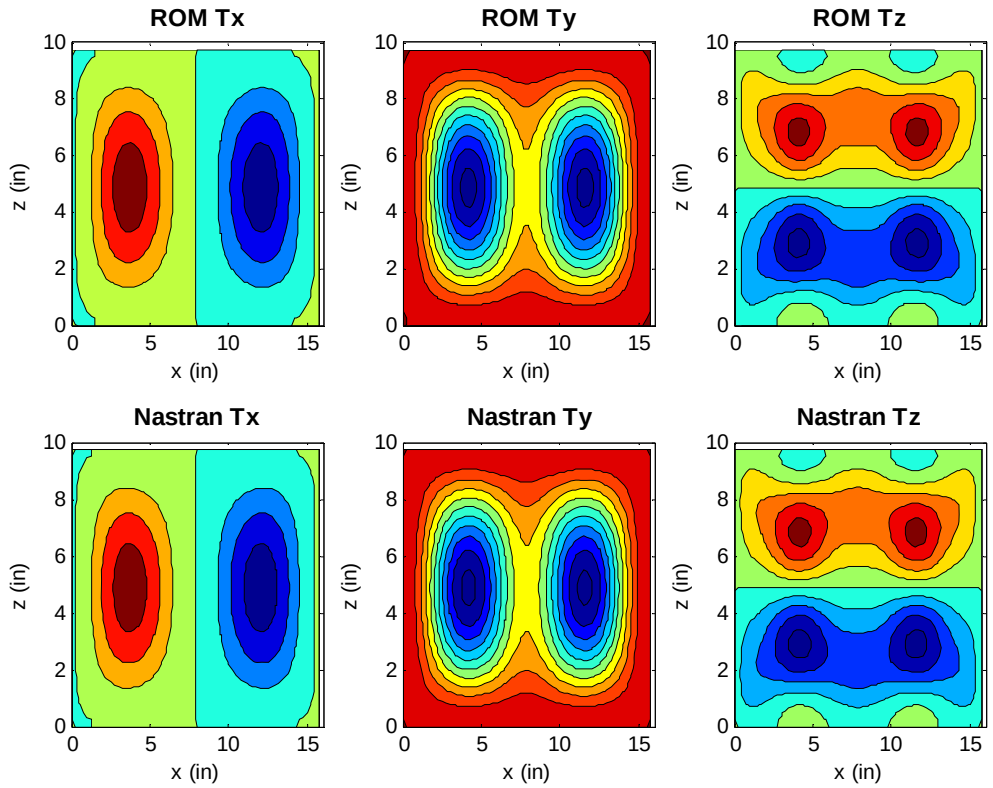

(c)

Figure 4. Contour plots of displacements along *x*, *y*, *z* as predicted by Nastran SOL106 and the ROM for uniform pressures of (a) 1.5 psi, (b) 2.5 psi, and (c) 3.0 psi.

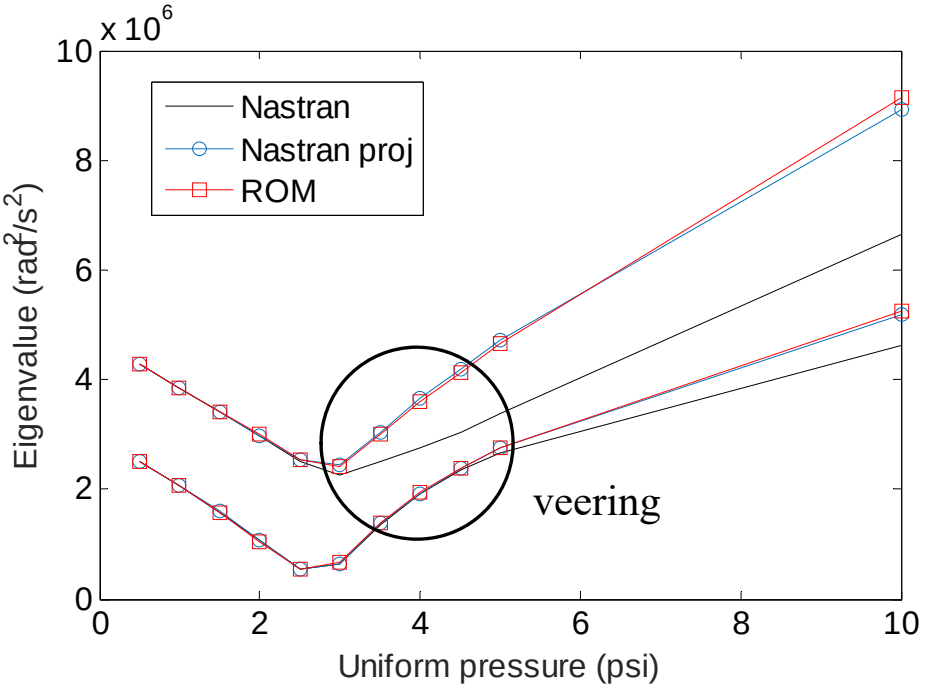

Figure 5. Eigenvalues of the tangent stiffness matrix from Nastran, projected Nastran tangent stiffness matrix on the basis, and from the ROM.

Having successfully predicted the static response of the shell, the ROM construction focused next on dynamic comparisons under a uniform pressure varying in time as a white noise in the frequency range of [0,500]Hz with variable overall sound pressure levels. It was first recognized that the dynamic response is dominated in the linear case by the first two symmetric modes (of frequencies 272Hz and 346Hz) which are not exactly represented by the 6 POD modes. This issue was resolved by appending to the 6 POD modes, the first 11 linear modes from which they were extracted, then proceeding with a Gram-Schmidt orthogonalization (with respect to the mass matrix) limited to the first 11 modes. These modes are *not* the linear modes but a rotation of them. While it would seem that these modes span a much larger frequency band than necessary, dynamic computations have shown that there is significant out-of-band response, especially at the higher load levels, which warrant the use of that number of modes.

The first dynamic model considered was obtained by appending the 7 dual modes derived from the 6 POD modes only and this 18-mode model provided an excellent prediction of the Nastran results at low (140dB and 150dB) levels but it did not capture well the high frequency component of the power spectral density at the 160dB. The issue was eventually found to be rooted in a poor identification of some of the nonlinear stiffness coefficients using the tangent stiffness approach of [3], even though it has been very successful in many prior applications.

To resolve this issue, the multilevel identification method developed recently, see [4], was used. In this process, it was found that the difficulties encountered at the 160dB level were resolved and that the 18-mode ROM does indeed provide a very good match of the Nastran predictions at that level, see Fig. 6.

Based on the very good results obtained in Fig. 6, the analysis proceeded to the higher level of 170dB excitation, see Fig. 7. While the ROM predictions are still very good in the band, there is a clear worsening of the matching with Nastran in the band [500,1000]Hz. To understand the source of this degradation, a short time history of the full Nastran displacement field was computed and outputted. The representation error of this data with the existing basis and the remaining 18 symmetric linear modes in the range of 1-100 is shown in Fig. 8(a). It is seen on this figure that with the 11L7D basis, the representation error is 16% which is certainly too large to have a good match as observed in Fig. 7. Moreover, the addition of a series of symmetric linear modes does not lead to a significant reduction of the error, only by about 2.5%!

This observation suggests that the response of the panel may be exhibiting an antisymmetric component. To confirm this assumption, the 18-mode basis was complemented with the 71 antisymmetric modes in the range 1-100 and shown in Fig. 8(b) is the corresponding representation error vs. mode number. It is clearly seen that the addition of antisymmetric modes reduces the error significantly, by approximately 13% from 16% to 2.5%. Moreover, much of this drop is generated by the antisymmetric modes 1, 3, and 9 (i.e., linear modes 1, 5, and 14). The inclusion of these 3 modes would lead to a representation error of approximately 6% which is still reasonably large and with no obvious strong contributor, either symmetric or antisymmetric, see Figs 8 (a) and (b).

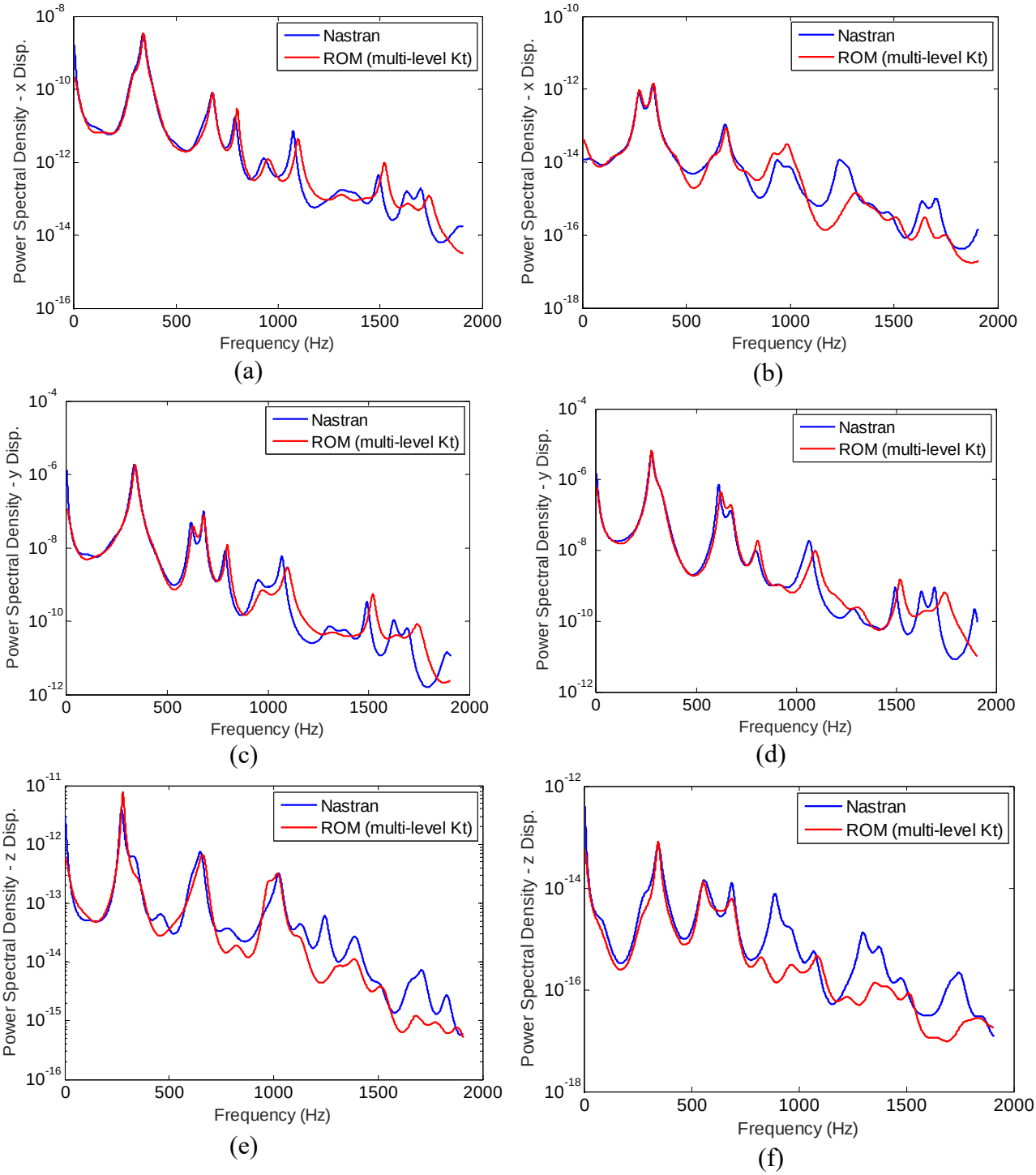

Figure 6. Power spectral densities of the response corresponding to 160dB excitation, Nastran and ROM. (a), (c), (e) node 657 of coordinates (0.25,0.25), (b),(d),(f) node 1248 near middle. Displacements along the (a),(b) x, (c),(d) y, and (e), (f) z directions.

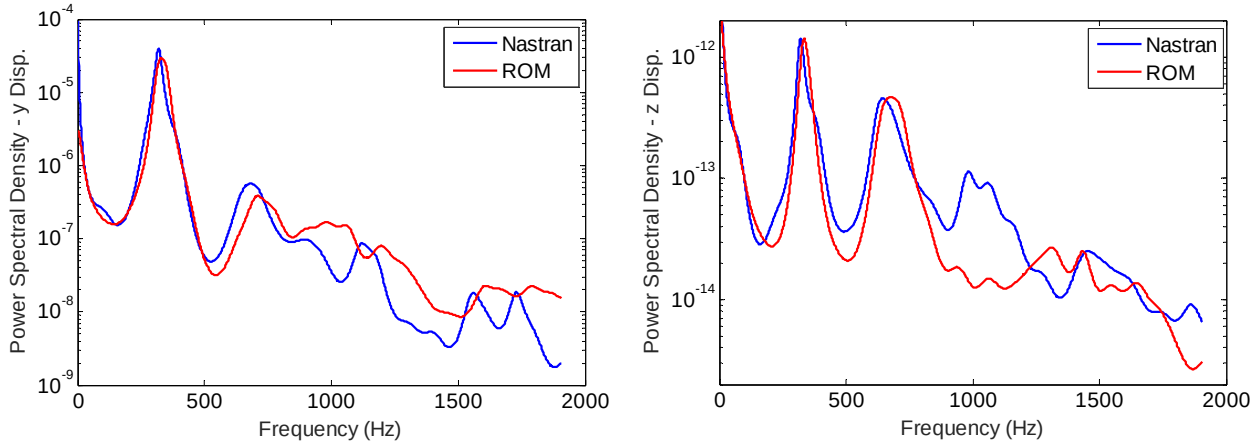

(a) (b)

Figure 7. Power spectral densities of the response corresponding to 170dB excitation, Nastran and ROM at node 1248 near panel middle. Displacements along the (a) y, and (b) z directions.

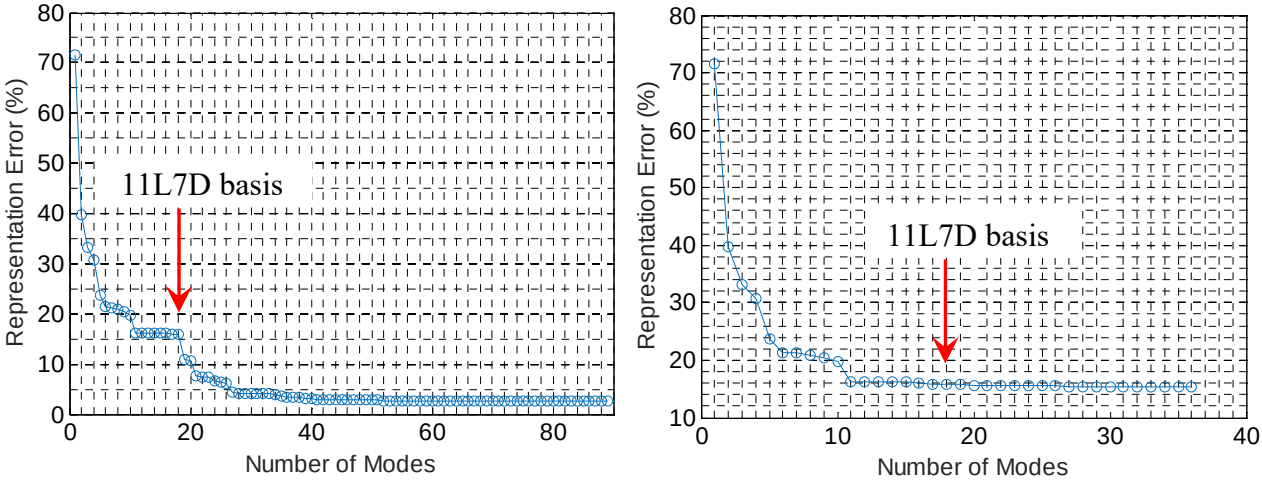

(a) (b)

Figure 8. Representation errors of a short time Nastran displacement field corresponding to a 170dB excitation with the 18 mode basis and additional (a) symmetric, (b) antisymmetric modes.

To confirm the presence of antisymmetric components in the Nastran response, segments of the transverse (in the *y* direction) displacements of the nodes 657, 688, 1873, and 1904 are shown on Figs 9(a)-(c). These nodes are located symmetrically with respect to the panel center at (*x*, *z*) coordinates (0.25,0.25), (0.25,0.75), (0.75,0.25), and (0.75,0.75). In Fig. 9(a), the displacements are all the same and the response is symmetric. In Fig. 9(b), the displacements of nodes 657 and 1873 and 688 and 1904 are equal but not altogether. The response is thus, rather significantly, asymmetric including an antisymmetric component around the parallel to the *z* axis passing by the panel middle, as in linear modes 1, 5, and 14 of the panel. Finally, in Fig. 9(c), the pairs of nodes with equal (or nearly equal) displacements are 657-1904 and 688-1803 so that the antisymmetric component present is antisymmetric with respect to the parallels of both the *x* and *z* axes as in linear mode 6 of the panel.

The results of Figs 8 and 9 confirm that a symmetry breaking occurs in the response at an excitation level between 160dB and 170dB. Future efforts in this investigation will focus on

extending the current 18-mode ROM to include antisymmetric modes to capture the symmetry breaking of the dynamic response.

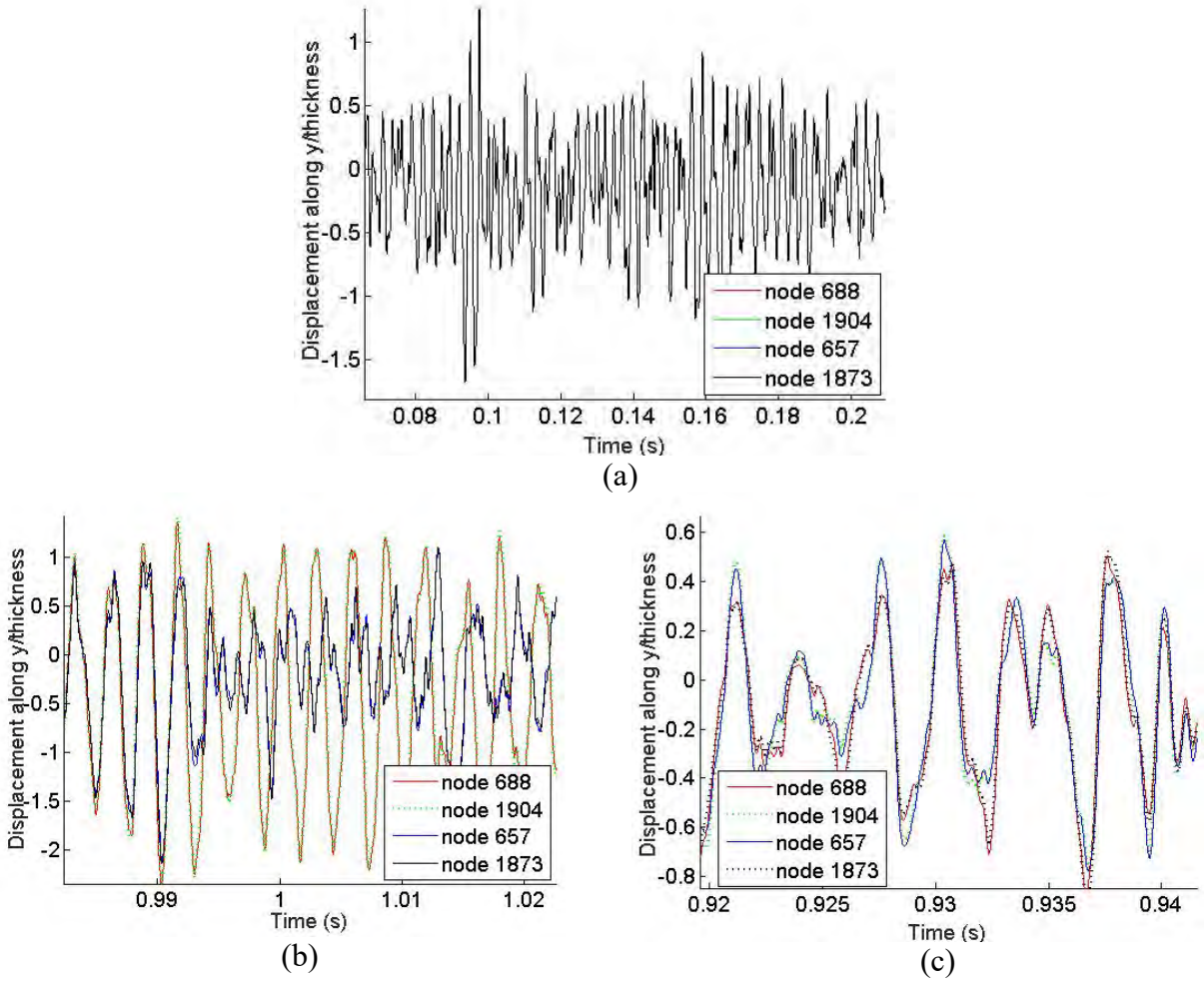

Figure 9. Segments of time history of the Nastran displacement along the *y* direction at the nodes 657, 688, 1873, and 1904. 170dB excitation.

Acknowledgements

The authors gratefully acknowledge the support of this work by the AFRL-University Collaborative Center in Structural Sciences (Cooperative Agreement FA8650-13-2-2347) with Dr. Ben Smarslok as program manager and by the contract FA9550-16-1-0021 from the Air Force Office of Scientific Research with Dr. Jaimie Tiley as program manager.

References

[1] Lin, J., Wang, X.Q., and Mignolet, M.P., "Nonlinear Reduced Order Modeling of Strongly Nonlinear Behavior: A Revisit of a Curved Beam Example," *Proceedings of the International Modal Analysis Conference, IMAC XXXVI*, Orlando, Florida, Feb. 12- 15, 2018.

[2] Gordon, R.W., and Hollkamp, J.J., "Reduced-Order Models for Acoustic Response Prediction of a Curved Panel," *Proceedings of the 52nd AIAA/ASME/ASCE/AHS/ASC Structures, Structural Dynamics and Materials Conference*, Denver, Colorado, April 4-7 2011, AIAA Paper AIAA 2011-2081.
[3] Perez, R.A., Wang, X.Q., and Mignolet, M.P., "Non-Intrusive Structural Dynamic Reduced Order Modeling for Large Deformations: Enhancements for Complex Structures," *Journal of Computational and Nonlinear Dynamics*, Vol. 9, No. 3, pp. 031008-1 - 031008-12, 2014.
[4] Wang, X.Q., Lin, J., Wainwright, B.A., and Mignolet, M.P., "Multiple Level Identification of Stiffness Coefficients in Nonlinear Reduced Order Modeling," *Proceedings of the International Modal Analysis Conference, IMAC XXXVII*, Orlando, Florida, Jan. 28-31, 2019.

Nonlinear Reduced Order Modeling of Strongly Nonlinear Behavior: A Revisit of a Curved Beam Example

Jinshan Lin, X.Q. Wang, and Marc P. Mignolet

SEMTE, Faculties of Mechanical and Aerospace Engineering, Arizona State University, Tempe, AZ 85287-6106

Key words : reduced order modeling, nonlinear geometric, structural modeling, snap-through, curved beam.

The construction of nonlinear reduced order models (ROMs) for the large deformation analysis of structures, e.g., see [1,2], has been successfully applied to many structures of broadly varying complexity, from simple flat beam/plate models to complex multi-bay panels, see [2] and references therein. A particularly interesting example within this list is the curved beam considered in [3-6], see Fig. 1, for which very good match of full finite element data with ROM predictions were obtained by all three of the approaches reviewed in [1], even in the highly nonlinear regime of snap-through responses, see [4-6].

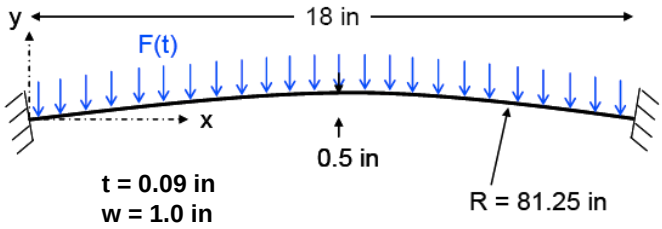

Figure 1. Curved beam geometry.

While carrying out the work reported in [5,6], the authors observed a strong sensitivity of the nonlinear response to small variations of some of the nonlinear stiffness coefficients of the reduced order model. This sensitivity motivated the revisit in [6] of the identification of these coefficients, carried in [5] by the imposed displacement method of [7]. This approach proceeds first with the imposition of a well chosen set of displacements fields to the finite element model from which the required forces are extracted. Then, requiring that these displacements and forces are consistent with the nonlinear ROM leads to a series of small size linear systems of equations for the unknown nonlinear stiffnesses. The displacements selected in this process are proportional to each mode alone and each combination of 2 and of 3 modes. Note that the magnitudes of these displacement fields have typically been taken "small" to avoid any potential effect of differences in the nonlinear formulations of the finite element code (e.g., updated Lagrangian) vs. the full Lagrangian assumptions underlying the reduced order model. A variant of this approach which utilizes the tangent stiffness matrix of the finite element and ROM models has also been developed [2].

Due to the curvature of the beam, the quadratic stiffness coefficients of its ROM are significant and play a dominant role in the response until snap-through. Past snap-through however, the response is dominated by the cubic stiffness coefficients. An accurate prediction of the response through the entire range of motions thus requires an accurate identification of all nonlinear

stiffness coefficients. When proceeding with small imposed displacements, it was noted that the values of the identified cubic coefficients were notably more sensitive than the quadratic ones to small changes in the levels of these displacements. This finding suggested in [6] a revisit of the identification strategy to include not only imposed displacement fields around the undeformed configuration (as described above) but also around specific deformed states. For example, utilizing data around the beam deformed beyond snap-through naturally highlights the cubic coefficients. Moreover, proceeding around a deformed state right before snap-through permits a good identification of the quadratic terms, etc. While this approach performed well and an accurate ROM was indeed obtained, see [6], it requires a first hand knowledge of the behavior of the structure, i.e., the presence and location of the snap-through, and leads to systems of equations for the coefficients which are full vs. the almost decoupled equations obtained with the original imposed displacements strategy of [7] or [2].

An alternative approach, referred to as the multi point identification (MTP) approach, is developed here as a variant of the above methods. It involves carrying out the original imposed displacement identification approach of [2,7] but at a variety of displacement levels. The linear, quadratic, and cubic stiffness coefficients of the model are identified at each of these "low", "medium", and "high" levels, and the final values of the coefficients are taken as the ones having minimum variations with respect to the displacement level. This is consistent with a basic property of the ROM that the stiffness coefficients are independent of the displacement levels.

Besides the identification of the coefficients, the selection of the basis functions also plays a key role in the quality of the ROM predictions. Clearly, this basis must represent well the finite element displacements but, in the presence of a structure with ROM parameters and predictions that are sensitive, it is additionally desired that the response be dominated by the smallest possible number of basis functions. The number of ROM parameters strongly affecting the response is then minimized and the propagation of the sensitivity to the predicted response may be limited. For the curved beam of Fig. 1, this strategy suggests to *not* use its linear modes as they are very different from the static deformations induced by the beam, see Fig. 2.

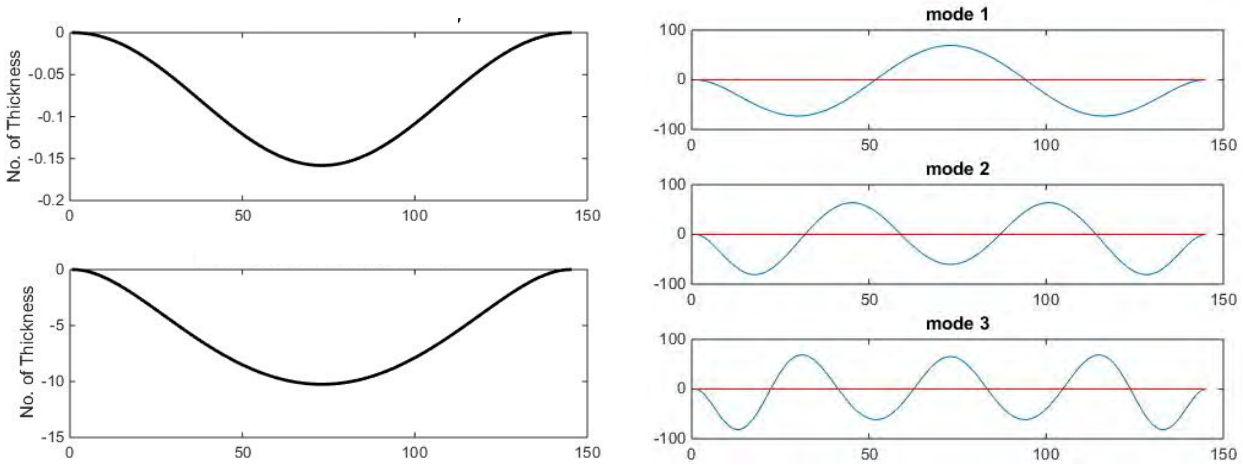

Figure 2. (a) Static nonlinear transverse displacement of the beam normalized by beam thickness below (top) and above (bottom) snap-through. (b) First three linear modes of the beam. Both plotted vs. node number.

Rather, a different selection was performed. Specifically, a set of static nonlinear displacements of the beam were generated (as shown in Fig. 2(a)) under a broad set of uniform loads. These displacement fields were then projected on the first 6 linear modes of the beam and a POD analysis of these projections was then carried out. As may be construed from Fig. 2(a), the eigenvector with the largest eigenvalue is strongly dominant and it was retained as the first basis functions. The linear modes 1 and 2 of the beam (see Fig. 2(b)) were then added after being rendered orthogonal to the first basis functions. This process is effectively equivalent to a rotation and down select of the linear modes vs. adopting them as is. To complete the basis, four dual modes were determined based on these 3 linear modes as described in [1] resulting in 7 basis functions.

The identification of the ROM stiffness parameters of this 7-mode model was carried out by both the original imposed displacement approach and its MPT variant, both using tangent stiffness data. The displacements predicted from the MPT-identified model, see Fig. 3 were found to be notably closer to the Nastran data than those resulting from the original identification scheme (not shown here from brevity), especially for the inplane displacements. Yet, it may be seen from Fig. 3 that there is still a large discrepancy between Nastran and MPT-identified ROM predictions.

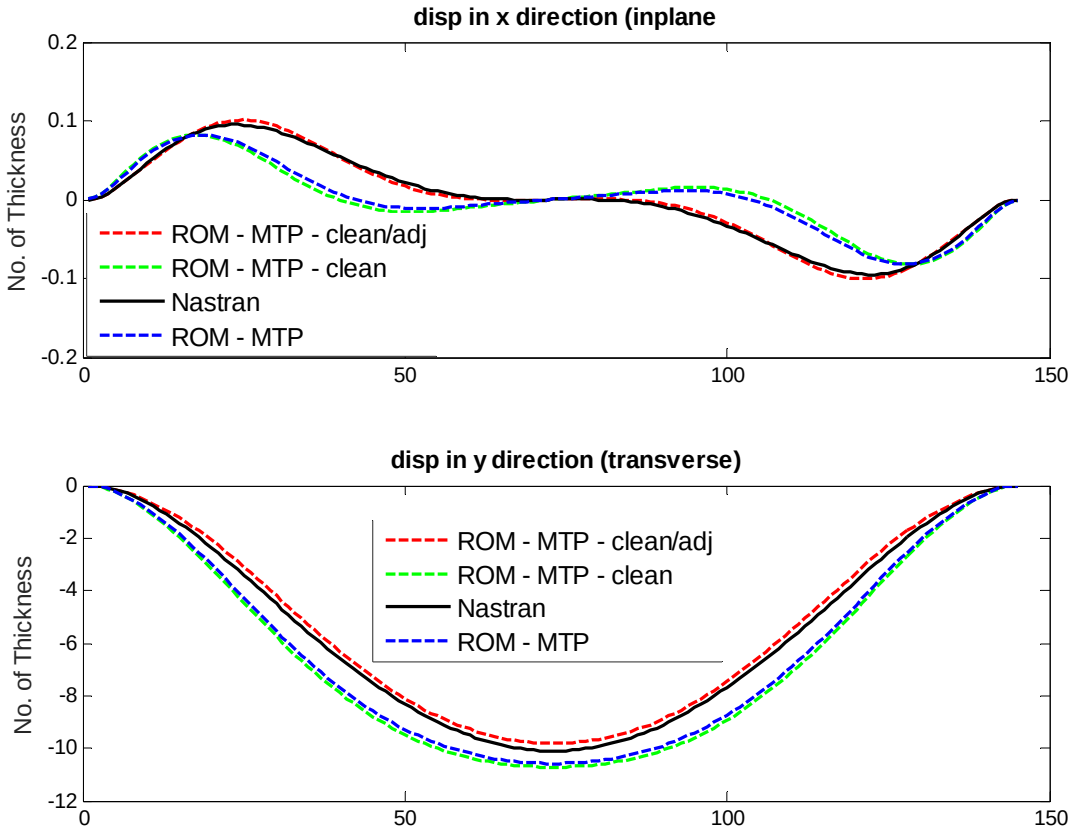

Figure 3. Static nonlinear transverse and inplane displacements of the beam normalized by beam thickness for a loading above snap-through. Finite element (Nastran) and ROM predictions identified by the MTP algorithm.

Given past history, it was wondered whether this relatively poor matching could be attributed to just small inaccuracies of the identified coefficients. To this end, a sensitivity analysis was next

carried out in which each ROM coefficient was varied by 5% and the prediction of the model at a post snap-through level recomputed. This effort demonstrated that:

(i) the cubic stiffness coefficient of the first basis function, i.e., the term $K_{1111}^{(3)}$ has by far the strongest effect on the response, especially on its inplane component, and

(ii) that there are many coefficients which have no significant effect on the response.

In this light, the model was first "cleaned" by eliminating the coefficients having no effect on the response. While a significant fraction of the stiffness coefficients were thus eliminated, the response is almost unaffected as seen in Fig. 3. In a second step, a manual adjustment of the coefficient $K_{1111}^{(3)}$ was attempted and it was found that increasing it by 1% led to a dramatically improved prediction, matching the Nastran results almost perfectly, see Fig. 3.

In summary, this investigation has confirmed the past observation that the nonlinear ROM response of the curved beam is very sensitive to small changes in some of its coefficients. This sensitivity was reduced here by (i) the development of a novel variant of the imposed displacements identification approach and (ii) optimally selecting the basis so that it contains a limited number of dominant modes. While the sensitivity is not eliminated, it appears to be limited to a very small number of parameters which can then be carefully tuned as necessary. Excellent predictions were thus obtained with a 7-mode ROM.

Acknowledgements

The financial support of this work by the Air Force Office of Scientific Research contract FA9550-16-1-0021 with Dr. Jaimie Tiley as technical monitor is gratefully acknowledged.

References

[1] Mignolet, M.P., Przekop, A., Rizzi, S.A, and Spottswood, S.M., "A Review of Indirect/Non-Intrusive Reduced Order Modeling of Nonlinear Geometric Structures," Invited Paper, *Journal of Sound and Vibration*, Vol. 332, No. 10, pp. 2437-2460, 2013.

[2] Perez, R.A., Wang, X.Q., and Mignolet, M.P., "Non-Intrusive Structural Dynamic Reduced Order Modeling for Large Deformations: Enhancements for Complex Structures," *Journal of Computational and Nonlinear Dynamics*, Vol. 9, No. 3, pp. 031008-1 - 031008-12, 2014.

[3] Przekop A., and Rizzi S.A., "Nonlinear Reduced Order Random Response Analysis of Structures with Shallow Curvature," *AIAA Journal*, Vol. 44, No. 8, pp. 1767-1778, 2006.

[4] Przekop, A., and Rizzi, S.A., "Dynamic snap-through of thin-walled structures by a reduced-order method," *AIAA Journal*, Vol. 45, No. 10, pp. 2510–2519, 2007.

[5] Spottswood, S.M., Eason, T.G., Wang, X.Q., and Mignolet, M.P., "Nonlinear Reduced Order Modeling of Curved Beams: A Comparison of Methods", *Proceedings of the 50th Structures, Structural Dynamics, and Materials Conference*, Palm Springs, May 2009. Paper AIAA-2009-2433.

[6] Chang, Y.-W., Wang, X.Q., Capiez-Lernout, E., Mignolet, M.P., and Soize, C., "Reduced order modeling for the nonlinear geometric response of some curved structures," *Proceedings of the 2011 International Forum of Aeroelasticity and Structural Dynamics*, June 2011, Paris, France, IFASD-2011-185.

[7] Muravyov, A.A., Rizzi, S.A., "Determination of Nonlinear Stiffness with Application to Random Vibration of Geometrically Nonlinear Structures," *Computers and Structures*, Vol. 81 pp. 1513-1523, 2003.

Nonlinear Reduced Order Modeling of Structures Exhibiting a Strong Nonlinearity

by

Jinshan Lin

A Dissertation Presented in Partial Fulfillment
of the requirements for the Degree of
Doctor of Philosophy

Approved March 2020 by the
Graduate Supervisory Committee:

Marc Mignolet, Chair
Hanqing Jiang
Jay Oswald
Stephen Spottswood
Subramaniam Rajan

ARIZONA STATE UNIVERSITY

May 2020

ABSTRACT

The focus of this dissertation is first on understanding the difficulties involved in constructing reduced order models of structures that exhibit a strong nonlinearity/strongly nonlinear events such as snap-through, buckling (local or global), mode switching, symmetry breaking. Next, based on this understanding, it is desired to modify/extend the current Nonlinear Reduced Order Modeling (NLROM) methodology, basis selection and/or identification methodology, to obtain reliable reduced order models of these structures. Focusing on these goals, the work carried out addressed more specifically the following issues:

i) optimization of the basis to capture at best the response in the smallest number of modes,

ii) improved identification of the reduced order model stiffness coefficients,

iii) detection of strongly nonlinear events using NLROM.

For the first issue, an approach was proposed to rotate a limited number of linear modes to become more dominant in the response of the structure. This step was achieved through a proper orthogonal decomposition of the projection on these linear modes of a series of representative nonlinear displacements. This rotation does not expand the modal space but renders that part of the basis more efficient, the identification of stiffness coefficients more reliable, and the selection of dual modes more compact. In fact, a separate approach was also proposed for an independent optimization of the duals. Regarding the second issue, two tuning approaches of the stiffness coefficients were proposed to improve the identification of a limited set of

critical coefficients based on independent response data of the structure. Both approaches led to a significant improvement of the static prediction for the clamped-clamped curved beam model. Extensive validations of the NLROMs based on the above novel approaches was carried out by comparisons with full finite element response data. The third issue, the detection of nonlinear events, was finally addressed by building connections between the eigenvalues of the finite element software (Nastran here) and NLROM tangent stiffness matrices and the occurrence of the 'events' which is further extended to the assessment of the accuracy with which the NLROM captures the full finite element behavior after the event has occurred.

ACKNOWLEDGEMENTS

Firstly, I would like to express my very great appreciation to my advisor Dr. Mignolet for his valuable and constructive suggestions during the planning and development of this research work. Without his guidance the work would not have been finished. His willingness to give his time so generously has been very much appreciated. Besides, I would like to offer my special thanks to Dr. Julian Wang for his patient instructions whenever I met problem and technical support during the research. My grateful thanks are also extended to Dr. Murthy, Dr. Song, Bret Wainwright and Dr. Yuting Wang for nice discussions when I met problem in research. Additionally, my sincere thank also goes to Dr. Jiang who provided me lab support in my first year of PhD study. I would like to thank Dr. Oswald, Dr. Rajan and Dr. Spottswood for serving on my committee. Last but not the least, I gratefully acknowledge the support of this work by the AFRL-University Collaborative Center in Structural Sciences (Cooperative Agreement FA8650-13-2-2347), and the contract FA9550-16-1-0021 from the Air Force Office of Scientific Research with Dr. Ben Smarslok and Dr. Jaimie Tiley as program managers, respectively.

TABLE OF CONTENTS

Page

CHAPTER Page

CHAPTER 4 BASIS OPTIMIZATION

4.1 Optimization of the Transverse Basis $\hat{\varphi}_l$

A standard observation made in regards to modal expansion of the form of Eq. (1) is that replacing the basis function $\psi^{(n)}$ by linear combinations of themselves does not change the capability of the sum to represent any particular function. It may thus be concluded that there is no value in performing a rotation of the linear modes to form the first, transverse part of the basis.

This conclusion is correct for the transverse basis alone, but it must be remembered that these transverse modes are the source of the dual modes. So, a transformation of the transverse modes will give rise to new dual modes which are not simple rotations of the prior duals because the duals are derived from a nonlinear problem. Accordingly, it is meaningful to investigate the role of a rotation of the transverse mode on the appropriateness of the duals and, more globally of the corresponding basis, in representing the response.

In this regard, it has long been noted that the duals are particularly efficient when there is only one mode that dominates the response. In fact, in most of the successful NLROMs, there is a strongly dominant single mode – typically the lowest frequency mode excited. Accordingly, it is proposed here to induce a rotation of the linear modes to capture, at best with one mode, the response of the structure in some typical nonlinear responses computed in advance for that purpose.

Emphasizing one mode vs. multiple ones has also some potential stability benefit. Indeed, it has often been observed that the cubic coefficients $K_{iujl}^{(3)}$ with $u \neq j \neq l$ are more sensitive to the conditions of the identification than their counterparts where $u = j = l$. When the response is primarily split between two or more modes, many more cubic coefficients are strongly involved in the equations than when there is a single mode. So, a single dominant mode response is likely to provide an increase accuracy/stability by reducing the number of terms on which the identification may be inaccurate (this issue results from the nonlinear geometric model of the finite element being different from the one assumed from the NLROM, see [13,14]).

Consider the curved beam of section 2.3.1 and shown in Figure 8 are its first 6 linear modes. Shown in Figure 9 are the displacement of the beam under downward pressures, one below the snap-through level and the other above it.

At first glance, the curves of Figure 8 and Figure 9 are quite different. There are a few nodal points on linear modes but not on the displacements. Using that linear basis to represent well the deformations is possible but this approximation will heavily involve several of the linear modes.

Based on the above discussion, a process was established to create a rotation of the basis (the 6 linear modes) so that one of them provides the best possible approximation of the observed (reference) static deformations. This process is as follows.

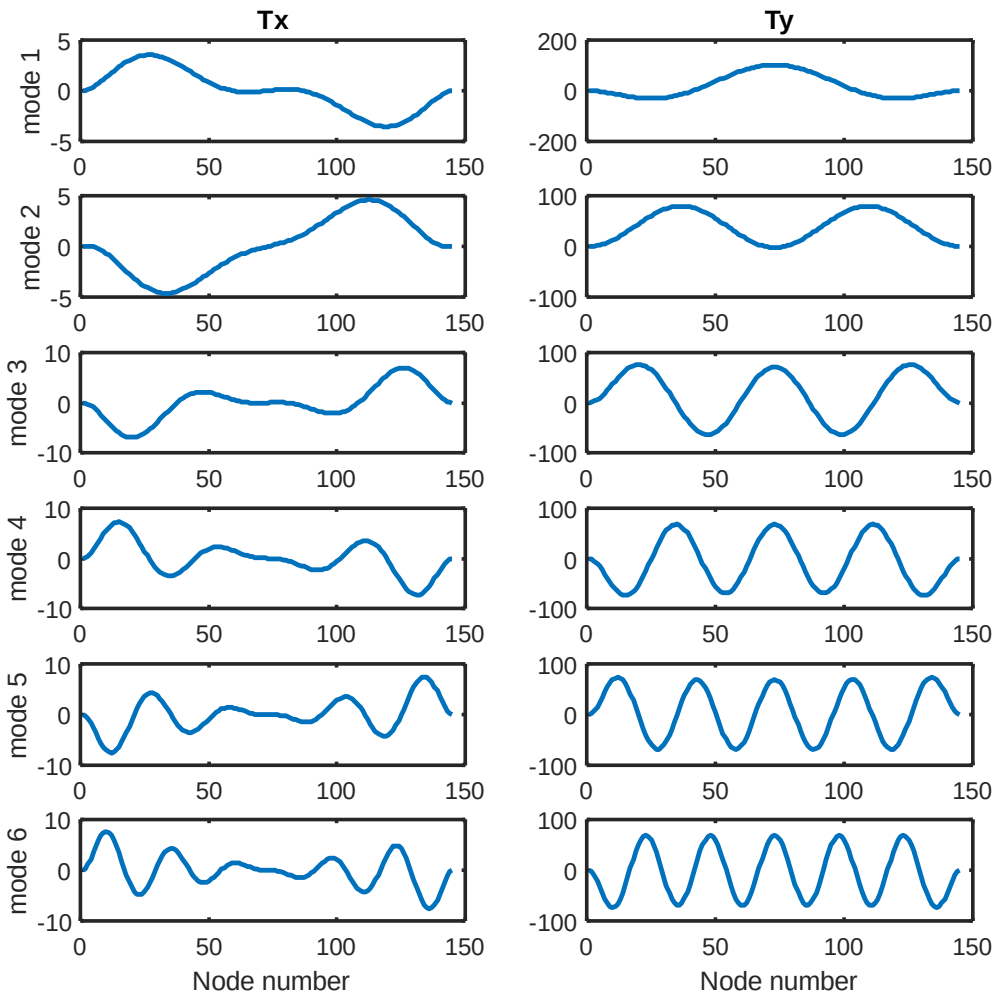

Figure 8. Mode Shape of the First 6 Linear Modes. In-plane (T_x, Left Column) and Transverse (T_y, Right Column) Deflections.

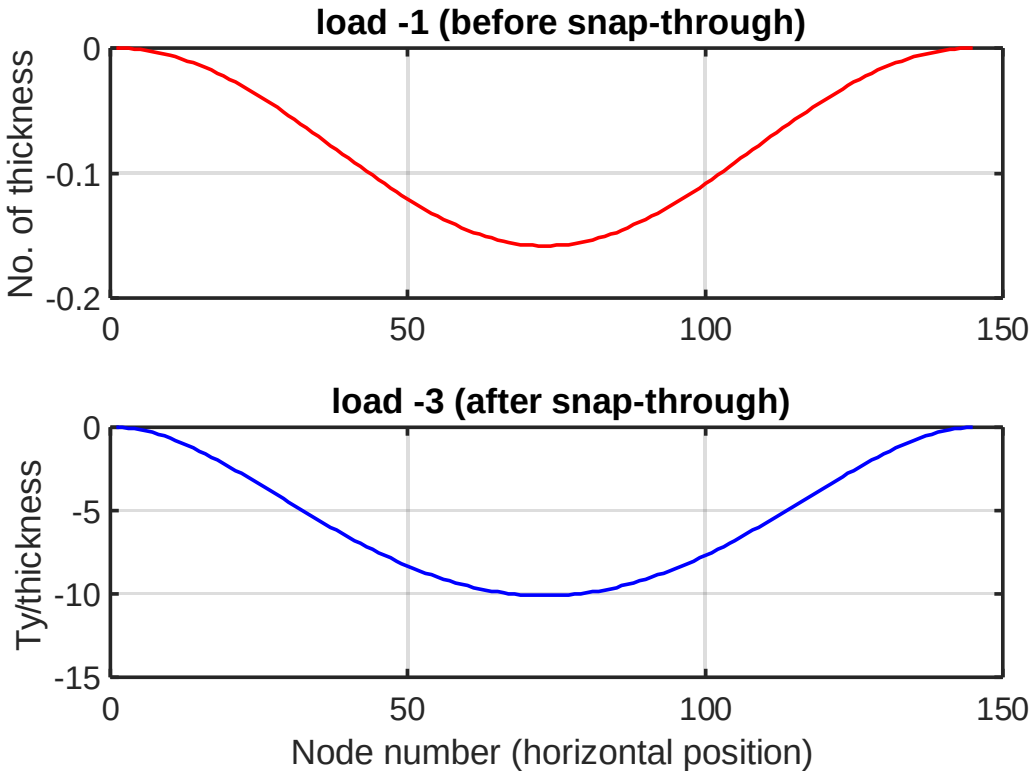

Figure 9. Deformation of the Curved Beam under Uniform Downward Loadings of 1 lb/in (Top) and 3 lbs/in (Bottom).

(1) Generate a series of nonlinear displacements from the finite element under loading that are relevant to the structure and its expected excitation. These nonlinear displacements are typically static ones, which are faster to determine, but dynamic ones are also applicable. These nonlinear displacements should span the range of expected deformations of the structure.

(2) Project the nonlinear displacements on the selected normal modes.

(3) Perform a POD analysis of the projection coefficients, selecting the eigenvectors corresponding to the largest eigenvalues.

(4) Using the eigenvectors, transform the original modes into modes that span the structure.

The application of this process to the curved beam using displacements under uniform pressures from -0.1 lb/in to -4.5 lbs/in led to the mode shown on Figure 10 (from the eigenvector with largest eigenvalue). Clearly, this new mode is much closer to the reference static displacements implying that it will be dominant in the response of the curved beam.

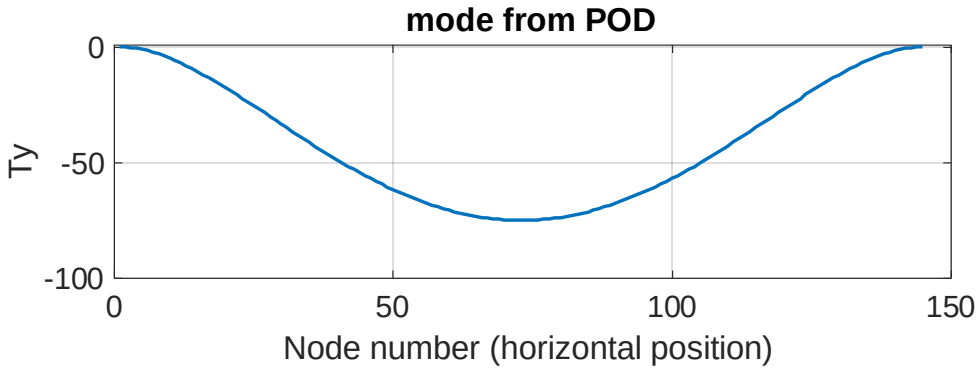

Figure 10. Mode Shape of the POD Mode.

It is not enough to consider only one mode and thus others must be appended. They could be chosen either as originating from additional eigenvectors of the POD analysis, especially those with eigenvalues larger than the floor, or from linear modes.

4.2 Optimization of the Dual Basis $\hat{\varphi}_d$

Past efforts have shown that the dual modes are often very efficient in complementing the transverse modes, i.e., that they represent well reference nonlinear responses with only a few modes. In some cases, a slow convergence of the representation with respect to the number of dual modes has been observed thereby penalizing the computational benefits of the NLROM but also, as pointed out above, potentially leading to stability problems of this model.

On that basis, it was questioned whether it would be possible to rotate a given basis of dual modes into one in which the number of dominant duals is reduced. This effort could be accomplished as done with the transverse basis by performing a POD of the projections of the reference deflections, but this strategy may lead to a set of dual modes too biased toward the reference data.

A different approach was adopted here that is similar in spirit to some aspects of the construction of the optimum thermal modes [46]. Specifically, recognize first that the dominant stiffness coefficient $K_{ijl}^{(2)}$ where '*i*' and '*j*' refer to linear (transverse) modes and '*l*' is associated with a dual. These terms are the most significant ones (besides the linear) because (i) they are the main coupling mechanism between the linear and the dual modes and thus induce the membrane softening effects and (ii) because they are multiplied by a first power of the dual modes generalized coordinates which are typically much smaller than their linear modes counterparts. So, quadratic terms involving two or more dual modes coordinates have typically small effects and are often neglected (as proposed in [47]). Cubic terms involving the dual modes are also known to be very small.

Given the linearity of the coefficients $K_{ijl}^{(2)}$ with respect to the dual mode l, see Eqs (17)-(18), it is concluded that the coefficient $\tilde{K}_{ijl}^{(2)}$ corresponding to a linear combination of dual modes

$$\tilde{\boldsymbol{\psi}}^{(l)} = \sum_n \gamma_n \boldsymbol{\psi}^{(n)} \tag{42}$$

where the summation extend over the dual mode indices, would be given by

$$\tilde{K}_{ijl}^{(2)} = \sum_n \gamma_n K_{ijn}^{(2)} \qquad (43)$$

On this basis, one can define an optimization of the dual mode basis seeking to maximize, with respect to the parameters γ_n, one or a particular set of coefficients $\tilde{K}_{ijl}^{(2)}$ for specific values of *i* and *j*. Of particular interest would be the optimization of the dual associated with transverse mode 1, i.e., $\tilde{K}_{11l}^{(2)}$. Note in this effort that a normalization constraint should be imposed on the parameters γ_n to avoid an unbounded solution.

Define here $K_{ttd}^{(2)} = \left[K_{ttd_1}^{(2)}, K_{ttd_2}^{(2)}, ..., K_{ttd_n}^{(2)} \right]$ the vector of quadratic coefficients of interest where the first two indices could be any pair of transverse mode numbers but remain the same for all terms. Introduce similarly $\gamma = \left[\gamma_1, \gamma_2, ..., \gamma_n \right]^T$. The problem is then to maximize $\left| K_{ttd}^{(2)} \gamma \right|^2$ given $\gamma^T \gamma = 1$ (the constraint could be changed to be adapted to different problem) where

$$\left| K_{ttd}^{(2)} \gamma \right|^2 = \left(K_{ttd}^{(2)} \gamma \right)^T \left(K_{ttd}^{(2)} \gamma \right) = \gamma^T K_{ttd}^{(2)T} K_{ttd}^{(2)} \gamma \qquad (44)$$

Adding the constraint through a Lagrange multiplier, the objective function becomes

$$f = \gamma^T K_{ttd}^{(2)T} K_{ttd}^{(2)} \gamma + \lambda \left(\gamma^T \gamma - 1 \right) \qquad (45)$$

Rewriting in index format and differentiating yields

$$f = \gamma_i V_{ij} \gamma_j + \lambda \left(\gamma_i \gamma_i - 1 \right) \qquad (46)$$

$$\frac{\partial f}{\partial \gamma_k} = V_{kj}\gamma_j + V_{ik}\gamma_i + 2\lambda\gamma_k \qquad (47)$$

where $V = K_{ttd}^{(2)T} K_{ttd}^{(2)}$ and thus is symmetric so that

$$\frac{\partial f}{\partial \gamma_k} = 2V_{kj}\gamma_j + 2\lambda\gamma_k \qquad (48)$$

Setting the above derivative to zero to achieve the optimum leads to

$$V_{kj}\gamma_j = -\lambda\gamma_k \qquad (49)$$

Rewriting this equation in matrix form yields the eigenvalue problem

$$\mathbf{V}\,\boldsymbol{\gamma} = \lambda\,\boldsymbol{\gamma} \qquad (50)$$

The corresponding eigenvector(s) $\boldsymbol{\gamma}$ with largest eigenvalue(s) λ could then be used to rotate the dual modes as in Eq. (42).

Another strategy for the dual modes optimization is based on performing their modal analysis, i.e., solving the eigenvalue problem

$$K_{dd}\boldsymbol{\gamma} = \bar{\lambda}\, M_{dd}\boldsymbol{\gamma} \qquad (51)$$

where K_{dd}, M_{dd} are the dual blocks of the linear stiffness and mass matrices. Eigenvectors in Eq (51) associated with eigenvalues $\bar{\lambda}$ that are in the range of those of the linear modes should likely be eliminated as duplicating the role of the linear modes. Moreover, the eigenvectors with very large eigenvalues would lead to dual modes that are

extremely stiff and thus not likely to contribute significantly to the response. It is thus suggested that the eigenvectors with low eigenvalues but larger than those of the linear modes be kept and that the rotation be carried out as in Eq. (42)

CHAPTER 6 VALIDATION RESULTS

6.1 Validation Plan

The focus of this chapter is on validating the concepts developed in previous sections, in particular the optimization of the linear modes, of the duals, as well as the stiffness coefficients tuning. The three structures discussed in section 2.3 will be considered for this validation effort. More specifically, the optimization of the linear modes of section 4.1 will be carried for all three structures, either as a strategy to reduce the number of linear modes and/or to improve the construction of the duals by creating more distinct dominant modes. The optimization of the duals, as discussed in section 4.2, will be applied solely to the clamped-clamped curved beam. This structure will also be the primary testbed for the stiffness coefficients tuning strategies of Chapter 5 because capturing its snap throughs in either static or dynamic conditions has been shown to require a particular good reduced order model which is difficult to achieve directly using the existing methods of section 3.3. The stiffness coefficients tuning approach will also be performed on the hypersonic panel in an unsuccessful attempt to better capture the occurrence of local buckling. The lack of success in this effort is not due to the tuning strategy but rather to the inadequacy of the basis which it cannot overcome. The validations of the NLROM will be performed on static loading, assessing displacements and eigenvalues of tangent stiffness matrix, as well as on dynamic conditions, and, for a small set of NLROMs, on the response due to a constant applied temperature.

6.2 Application to the Curved Beam

The strategies developed in the last two sections were first applied to the clamped-clamped curved beam shown in Figure 1 under symmetry constraints, i.e., the finite element model was forced to only exhibit symmetric deformations using multi point constraints. This constraint was imposed to reduce the complexity of the problem since the snap-through may occur under both symmetric and antisymmetric motions with the latter occurring at a slight lower load level than the former. The validation results presented below are split into 4 separate efforts/sections:

i) Optimization of the basis.

ii) Results with optimized basis before tuning.

iii) Results after tuning based on modal force.

iv) Results after tuning based on generalized displacements.

6.2.1 Optimization of the Basis

As mentioned in Chapter 4, see Figure 8, the mode shapes of the linear modes of the curved beam are not very similar to the actual deformation induced by a uniform load. Accordingly, the first task focused on the optimization of the linear basis. Specifically, the Nastran static nonlinear displacements induced by the uniform pressures of -0.1, -0.2, -0.3, ..., -4.5 lbs/in were used as reference data and were projected on the first 15 linear modes of the beam. The set of projection coefficients were then processed by a POD and the first eigenvector was retained to construct the first transverse mode. The linear (normal) modes 1, 2, 3, 5, 6 from Nastran SOL103 were added to this first transverse mode and made orthogonal to it. leading finally to 6 transverse modes (denoted as transverse 1 to 6).

Next, 8 dual modes were determined from these 6 transverse modes considering combinations (1-1), (1-2), (1-3), (1-4), (1-5), (1-6), and are shown in Figure 20-Figure 21. While the predictions of this 6T8D NLROM were very close to those of Nastran prior to the snap-through, the model is unstable post snap-through even though the truncation error is quite small. A possible reason for this behavior is an inaccurate identification of some of stiffness coefficients as discussed in Chapter 5. To circumvent this issue, it was desired here to proceed with an optimization of the dual modes to reduce the size of the basis and hopefully improved the predictive capabilities of the NLROM.

Before performing this optimization, it is useful to investigate the relative magnitudes of the transverse (*T*y) and in-plane (*Tx*) of the linear (see Figure 8) and dual (see Figure 20-Figure 21) modes, see Table 3. Note on this table that the ratio is inverted for the linear and dual modes. It is seen that the (original) linear modes are strongly transverse dominant while the reverse typically holds for the duals, although the ratio of magnitudes is smaller, i.e., there is a large contribution of transverse motions in the duals than in-plane in the linear modes. Moreover, the third dual is clearly transverse dominant.

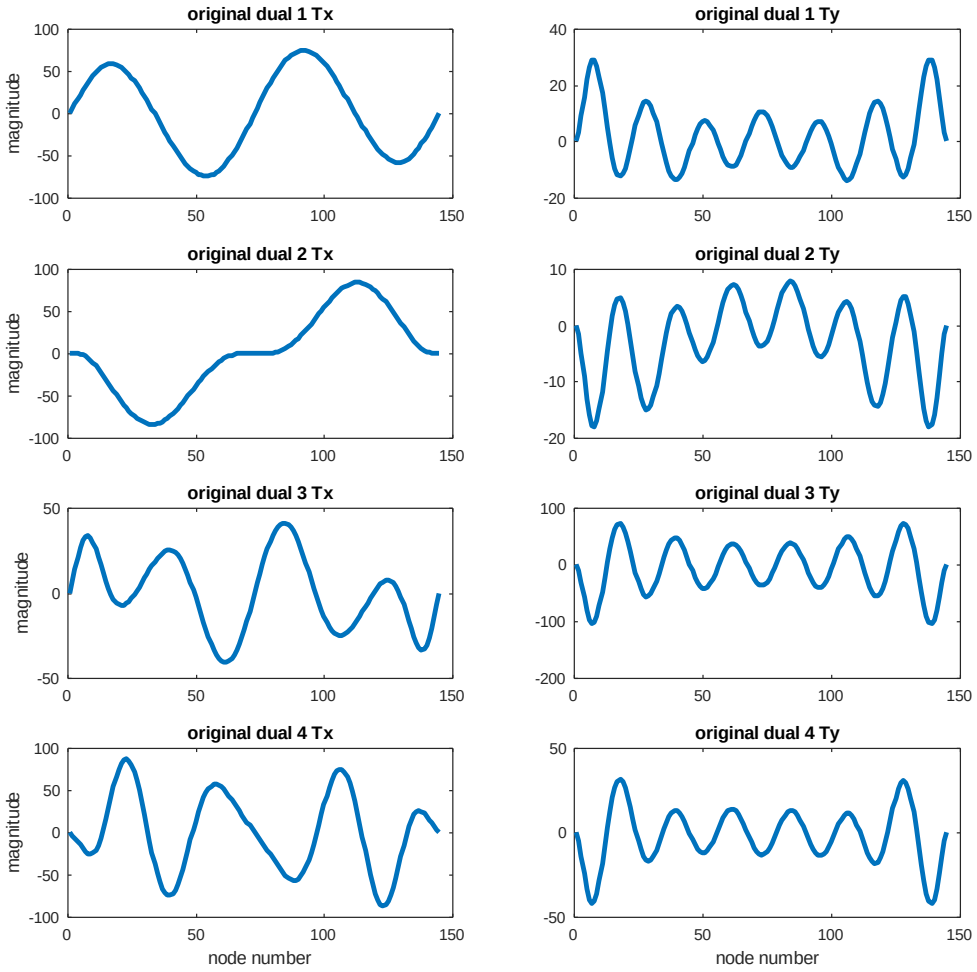

Figure 20. In-plane (Left Column) and Transverse (Right Column) Displacements of the Original Duals 1-4. Curved Beam.

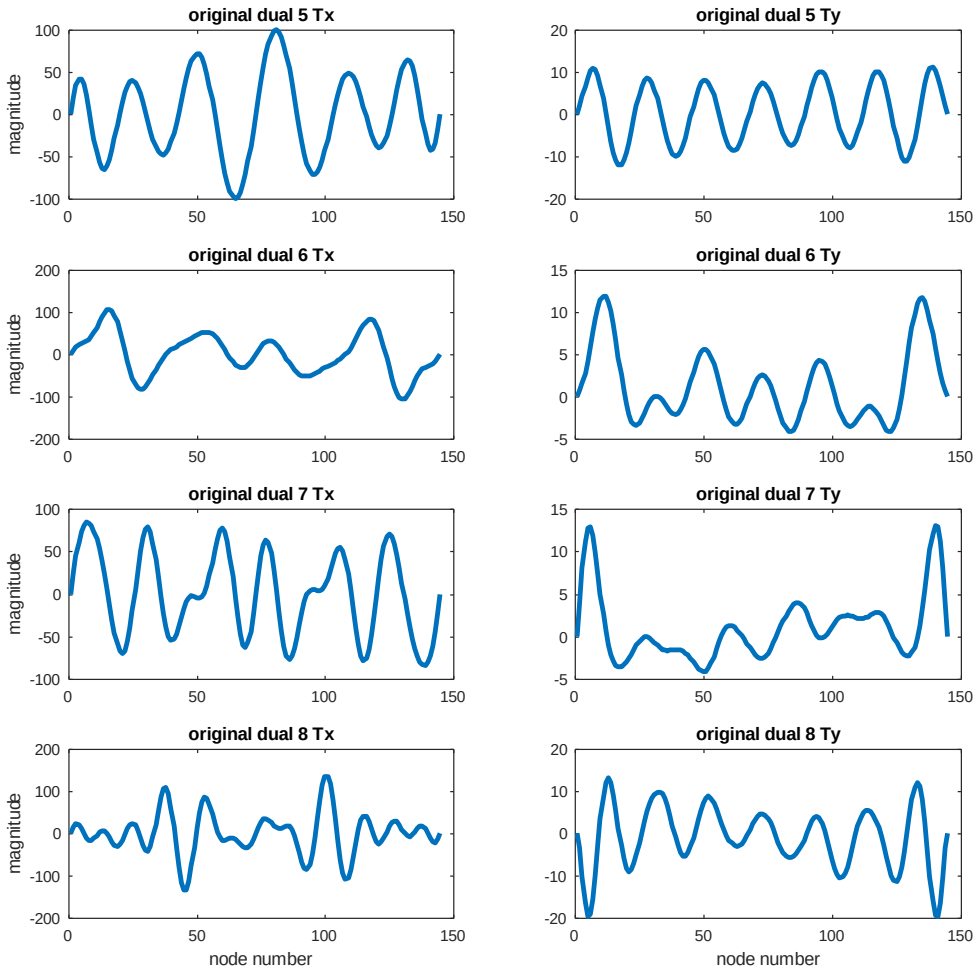

Figure 21. In-plane (Left Column) and Transverse (Right Column) Displacements of the Original Duals 5-8. Curved Beam.

Table 3. Ratios of Transverse and In-plane Displacements NORMs, Linear, Transverse and Dual Modes, Curved Beam.

Norm(Ty)/Norm(Tx)	Lin. 1	Lin. 2	Lin. 3	Lin. 4	Lin. 5	Lin. 6		
	24.04	17.57	14.50	14.97	15.17	15.27		
Norm(Ty)/Norm(Tx)	Tran. 1	Tran. 2	Tran. 3	Tran. 4	Tran. 5	Tran. 6		
	61.26	13.97	13.51	14.08	18.96	15.58		
Norm(Tx)/Norm(Ty)	Dual 1	Dual 2	Dual 3	Dual 4	Dual 5	Dual 6	Dual 7	Dual 8
	4.26	6.28	0.50	2.77	7.16	10.81	12.21	6.70

The first effort to optimize the duals proceeded as in Eq. (49) and (50) focusing on the quadratic stiffness term $K_{ttd}^{(2)}$. Since there is only one combination of transverse modes, only one optimum dual can be generated in this process and it is shown in Figure 22. This basis function is fairly similar to the first dual of Figure 20 but the first and last peaks have been reduced. Note that the ratio of the norms of the in-plane and transverse displacement is rather small, 2.57, confirming the visual expectation from Figure 22 that the transverse component is still rather large. Nevertheless, this mode seems very efficient in reducing the representation error of the uniform response post snap-through as shown in Figure 23 (curve "Opti 1") for the loadings of 2.5, 3, 3.5, 4, and 4.5 lbf/inch. More specifically, this error drops from 164% to 32% with that single dual. For comparison, the first original dual only reduces it to 95%. Enriching further the model would require the consideration of other combinations of the transverse modes beside the 1-1.

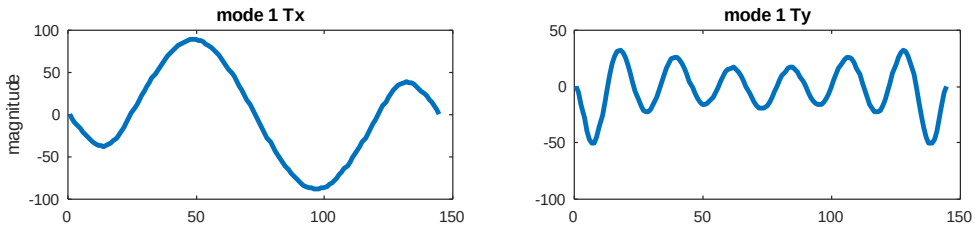

Figure 22. In-plane and Transverse Components of the Dual Mode Optimized According to Eqs (49) and (50). Curved Beam.

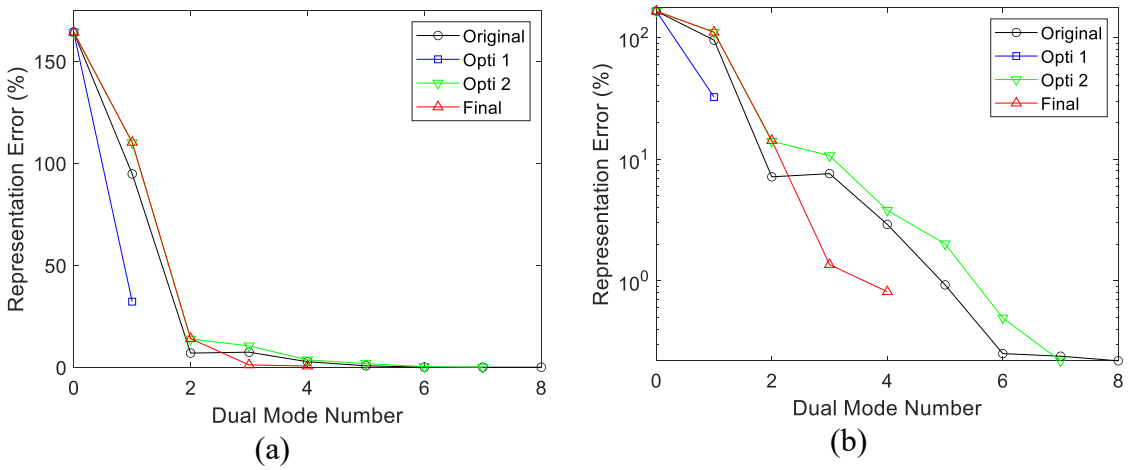

Figure 23. Average Representation Error, in %, of the In-plane Displacements corresponding to Loadings of 2.5, 3, 3.5, 4, and 4.5 lbf/inch (i.e., Post Snap Through) vs. Number of Various Types of Dual Modes. (a) Linear, (b) Log Scale.

It was next desired to assess the benefits of the second dual optimization, i.e., based on the modal analysis of the corresponding blocks of the mass and linear stiffness matrices, see Eq. (51). That computation was performed with the 8 original duals and given in Table 4 are the corresponding eigenvalues while the new duals associated with the corresponding eigenvectors are shown in Figure 24-Figure 25

Table 4. Eigenvalues Associated with the Original Dual Mass and Linear Stiffness Matrices.

1	2	3	4	5	6	7	8
$4.24\ 10^{11}$	$2.05\ 10^{11}$	$1.55\ 10^{11}$	$9.58\ 10^{10}$	$6.34\ 10^{10}$	$1.99\ 10^{10}$	$6.78\ 10^{9}$	$1.33\ 10^{9}$

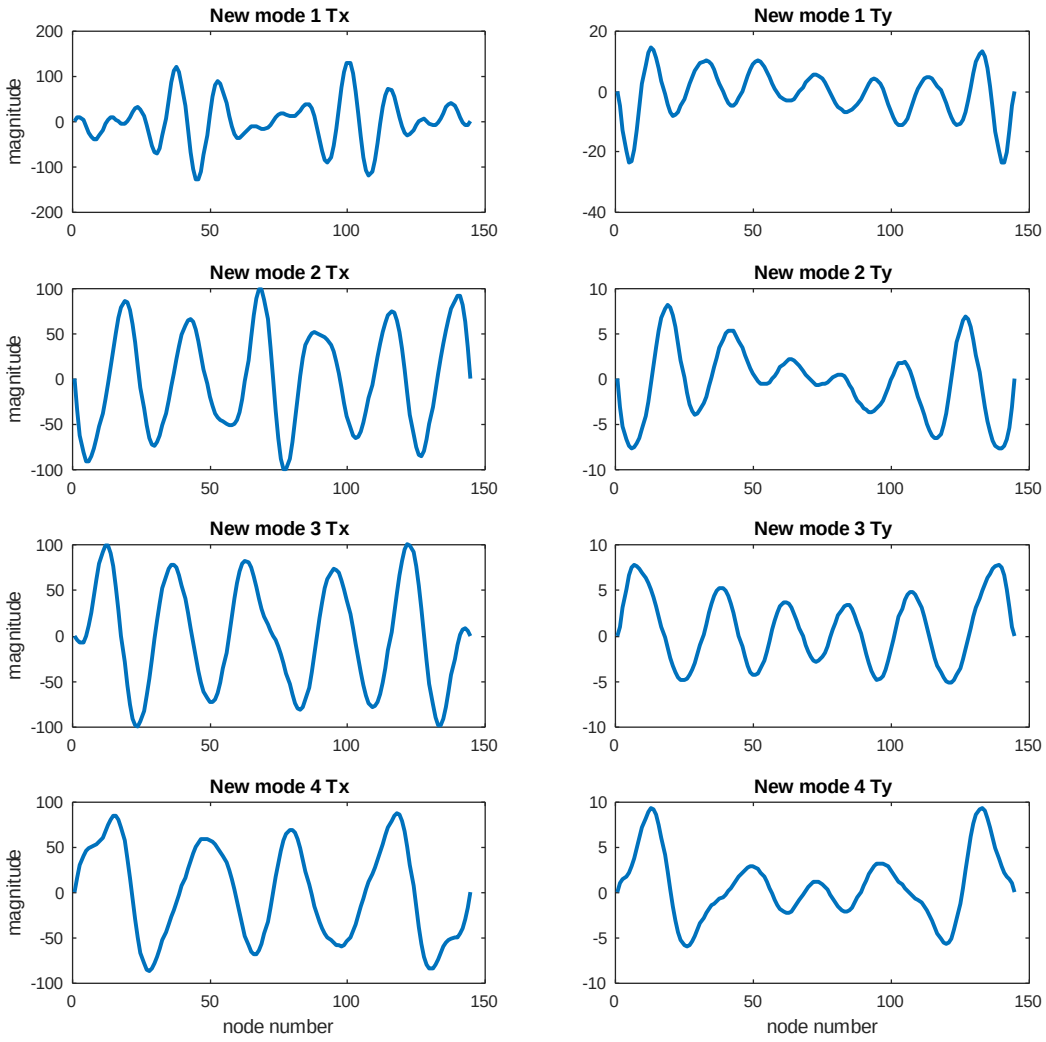

Figure 24. In-plane (Left Column) and Transverse (Right Column) Displacements of the New Duals 1-4 Following the Modal Analysis of Eq. (51). Curved Beam.

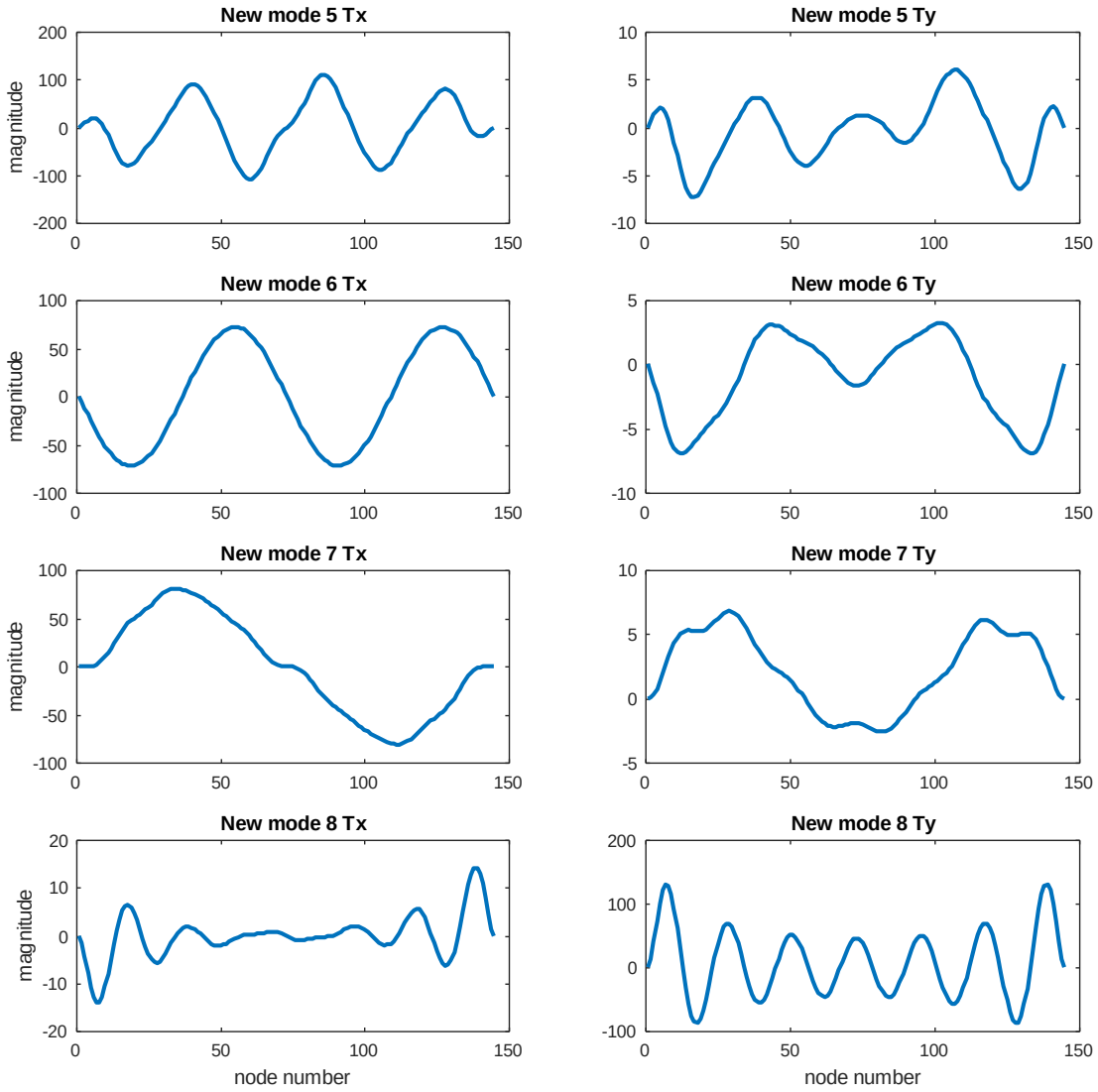

Figure 25. In-plane (Left Column) and Transverse (Right Column) Displacements of the New Duals 5-8 Following the Modal Analysis of Eq. (51). Curved Beam.

Two key observations can be drawn from Figure 24-Figure 25. First, it is seen that the new dual with the lowest eigenvalue (number 8) is primarily transverse while all others are primarily in-plane. In fact, comparing Figure 24-Figure 25 and Figure 20-Figure 21, it appears that the new duals are significantly more in-plane dominant than the original ones. This finding, which is confirmed by the norm ratios shown in Table 5, is actually expected

as the transverse motions are much softer than the in-plane ones and thus the eigenvalue problem splits these motions into separate eigenvectors/new duals.

Table 5. Ratio of Transverse and In-plane Displacements Norms, New Dual Modes, Curved Beam.

	Dual 1	Dual 2	Dual 3	Dual 4	Dual 5	Dual 6	Dual 7	Dual 8
Norm(*Tx*)/Norm(*Ty*)	6.23	14.18	15.21	14.01	18.01	14.72	13.40	0.08

The assessment of these new duals for the representation of the uniform displacement data was carried out as before by evaluating the average in-plane representation error corresponding to the loadings of 2.5, 3, 3.5, 4, and 4.5 lbf/inch, see Figure 23. Note in this figure that the new duals were considered in order of increasing eigenvalue and that the transverse dominant one was not included. That is, the error is presented for new duals in order 7, 6, 5, ..., 1. It is seen that the two in-plane duals with lowest eigenvalues (i.e., 6 and 7 in Figure 25) provide a significant drop in the representation error, yet, not quite as large as the original duals. However, the representation error drops consistently with these new duals at the contrary of the original ones. In this regard, note that the increase in representation error for the original duals associated with dual #3 results from this dual being primarily transverse. Thus, it leads to a decrease of the representation error in the transverse error but at the cost of an increase in the in-plane one. In this light, the continuous decrease of the representation error for the new duals is effectively associated with the decoupling induced by the eigenvalue problem.

It is concluded from the above discussion that the two dual optimization strategies of section 4.2 are both beneficial but in different ways. Then, it was questioned whether they could be combined to achieve an even better selection of duals. To this end, the two duals 7 and 6 were first retained and an optimization as in Eqs (49)-(50) was performed with transverse mode 1 (the POD mode) and the remaining 5 new duals (1 to 5) in Figure 24-Figure 25. Shown in Table 6 are the corresponding quadratic coefficients $K_{11d}^{(2)}$ for d =7 to 11 (new dual modes 1 to 5) after separate identification. Also shown on this table, on the left most column, is the optimum value corresponding to the optimum new dual shown as final dual 3 on Table 7.

The inclusion of this 3rd final dual led to a significant drop in the representation error which still was slightly larger than the 1% usually desired. Accordingly, other combinations of linear modes were considered in the quadratic stiffness coefficients-based optimization and it was found that the 1-3 transverse mode combination led to the largest drop in representation error. Shown in Table 7 and Figure 26 (final dual 4) are the result of this optimization which does lead to yet another notable drop in the representation error, see Figure 23, well below 1%. Note that this 4th new dual appears very similar to the new dual 5 (flipped sign) which is consistent with the very close values of the quadratic stiffness coefficient of mode 11 (new dual 5). Given the low representation error, no further duals were considered leading to a 4 dual mode basis, shown in Figure 26, vs. the original 8.

Table 6. Data and Result of Optimization of New Duals 1-5 Using Eqs (49)-(50) for the 1-1 Combination.

	Index and values of $K_{ijl}^{(2)}$ for the 5 new dual modes before optimization				
$\tilde{K}_{ijl}^{(2)}$	(1,1,7)	(1,1,8)	(1,1,9)	(1,1,10)	(1,1,11)
2.1679e+10	3.7415e+09	6.7323e+09	-5.6926e+09	-1.0910e+10	8.0979e+09

Table 7. Data and Result of Optimization of New Duals 1-5 Using Eqs (49)-(50) for the 1-3 Combination.

	Index and values of $K_{ijl}^{(2)}$ for the 5 new dual modes before optimization				
$\tilde{K}_{ijl}^{(2)}$	(1,3,7)	(1,3,8)	(1,3,9)	(1,3,10)	(1,3,11)
-3.7078e+11	-1.8903e+10	-1.2731e+11	5.0843e+10	4.6443e+10	3.4567e+11

In a final attempt to reduce the basis size, the role of each of the 6 transverse modes was analyzed and it was found that the last 3 transverse modes contributed only little to the reduction of the transverse representation error. Accordingly, they were removed yielding a 3 transverse – 4 dual (3T4D) basis which will be validated in the next section.

It was of interest to assess this basis in comparison to a 3T4D one which would be built following the standard dual construction process. Specifically, 2 duals were taken from each of the 1-1 and 1-2 combinations. Then, the in-plane representation error of the 2 3T4D bases are compared on Figure 27 on the same data as Figure 23. As would be expected, the 4 optimized duals decrease the representation error faster than the one constructed by the regular process. The gain is minimal for the first dual but is much larger for the next two. Eventually, on dual 4, the optimum approach cannot reduce the error

much more but the regular process still can and yields to a final representation error that is very similar to that of the optimized process. This comparison confirms that the benefit of the dual optimization process is primarily in potentially reducing the number of duals necessary.

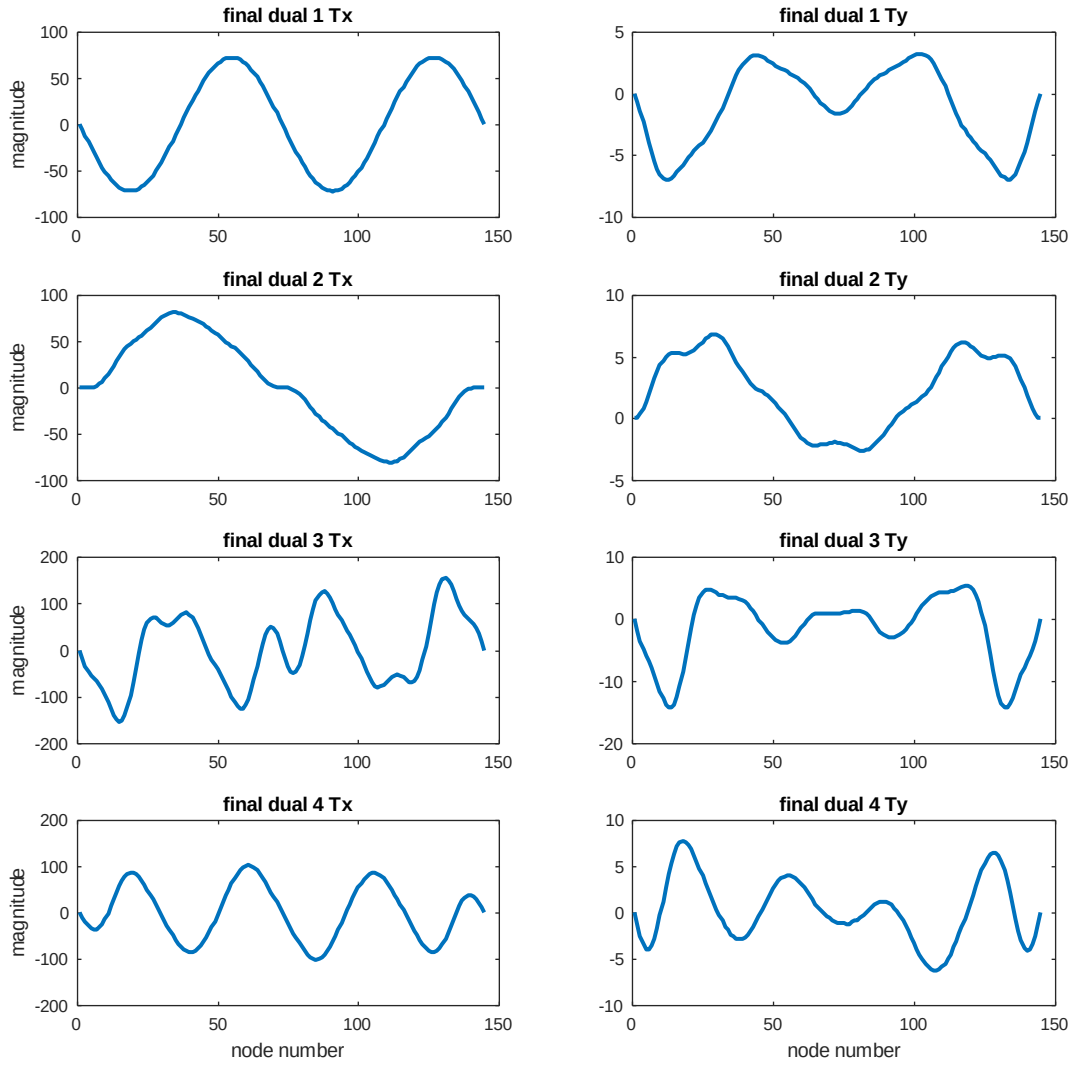

Figure 26. In-plane (Left Column) and Transverse (Right Column) Displacements of the 4 Final Duals Following from the Two Optimizations. Curved Beam.

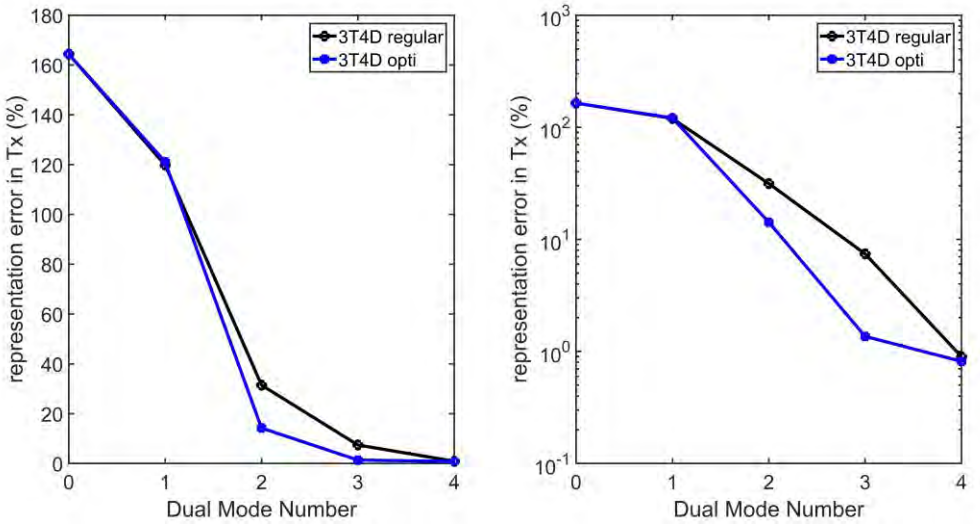

Figure 27. Average Representation Error for the Two 3T4D Models, in %, of the In-plane Displacements corresponding to Loadings of 2.5, 3, 3.5, 4, and 4.5 lbf/inch (i.e., Post Snap Through) vs. Number of Various Types of Dual Modes. (a) Linear, (b) Log Scale.

6.2.2 Results with Optimized Basis before Tuning

The identification of the stiffness coefficients of the 3T4D NLROM were determined using the single-level tangent stiffness approach and the model was cleaned. Then, the assessment of this NLROM started with the comparison of static predictions. The static displacements before snap-through and the location of that event are well captured by the ROM, see Figure 28 and Figure 29, but not as well after snap-through (which occurs for a load of 2.4 lbf/inch). Similar observations can be drawn from the prediction of the lowest eigenvalue of the tangent stiffness matrix, see Figure 30. Note on this figure that the lowest eigenvalues obtained by projecting the Nastran tangent stiffness matrix on the NLROM basis ("Nastran proj.") are also shown and are much closer to those of the full Nastran model than its NLROM counterpart. This observation suggests that the largest

source of the discrepancy between NLROM and Nastran above the snap-through load originates from the coefficients of the model, not from the basis selection.

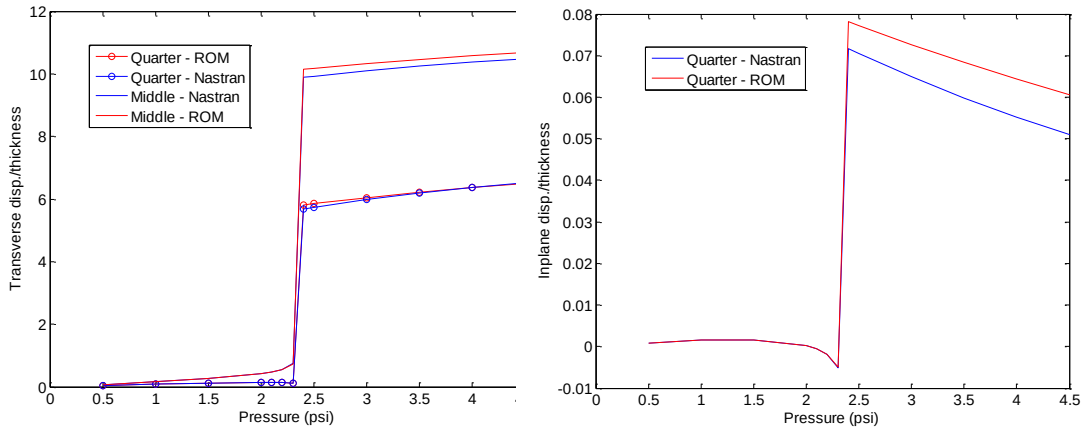

(a) (b)

Figure 28. Displacements vs. Uniform Load, Clamped-Clamped Cantilevered Beam. (a) Transverse Displacement at Beam Middle and Quarter Point, (b) In-Plane Displacement at Quarter Point.

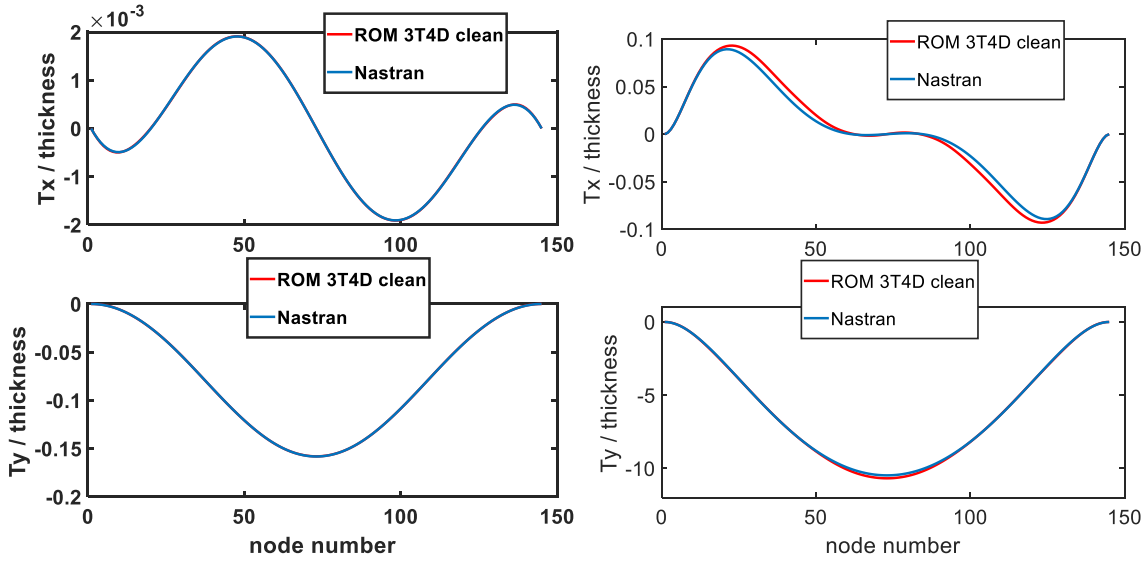

(a) (b)

Figure 29. In-Plane (Top) and Transverse (Bottom) Deformations of the Clamped-Clamped Curved Beam under a Uniform Load of (a) 1 lbs/in, (b) 4.5 lbs/in.

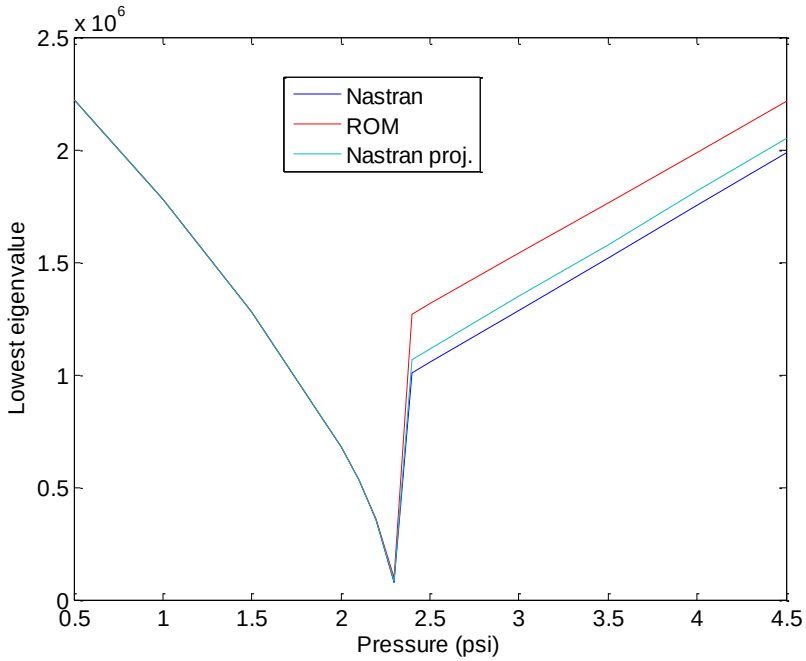

Figure 30. Lowest Eigenvalue of the Tangent Stiffness Matrix Corresponding to a Symmetric Eigenvector vs. Uniform Load Magnitude. Clamped-Clamped Curved Beam

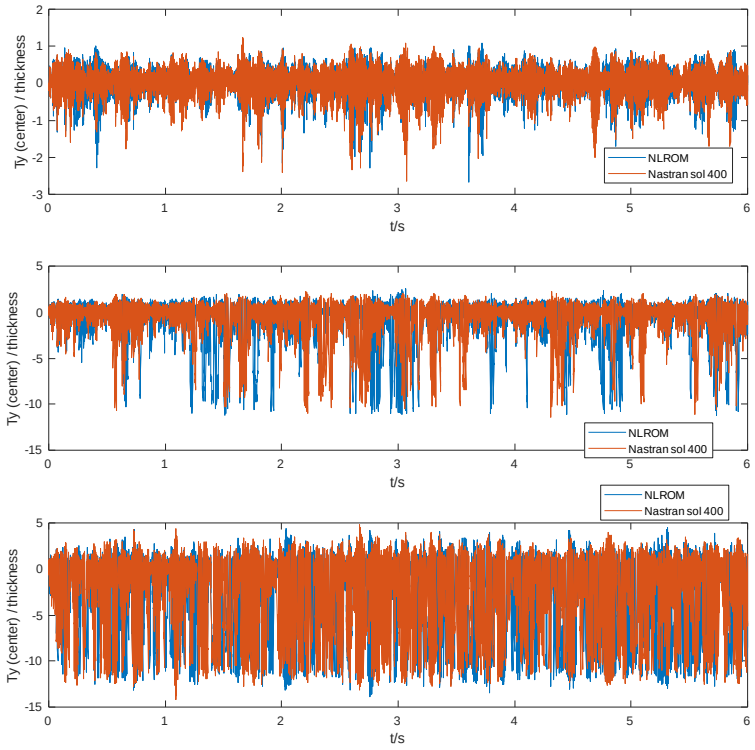

Figure 31. Time Histories of the Transverse Displacement of the Center of the Clamped-Clamped Beam under Low (Top), Medium (Middle), and High (Bottom) Acoustic Loadings.

A dynamic validation of this NLROM was also carried out, see Figure 31 and Figure 32 for time histories and power spectra density, under acoustic loads bandlimited in the [0,500]Hz frequency and of level ranging from low to medium to high for which the beam vibrates around the undeformed position, exhibits occasional snap-throughs, and regularly snap-through, respectively, see Figure 31. As shown in Figure 32, a good to very good match of the Nastran and NLROM power spectra was observed.

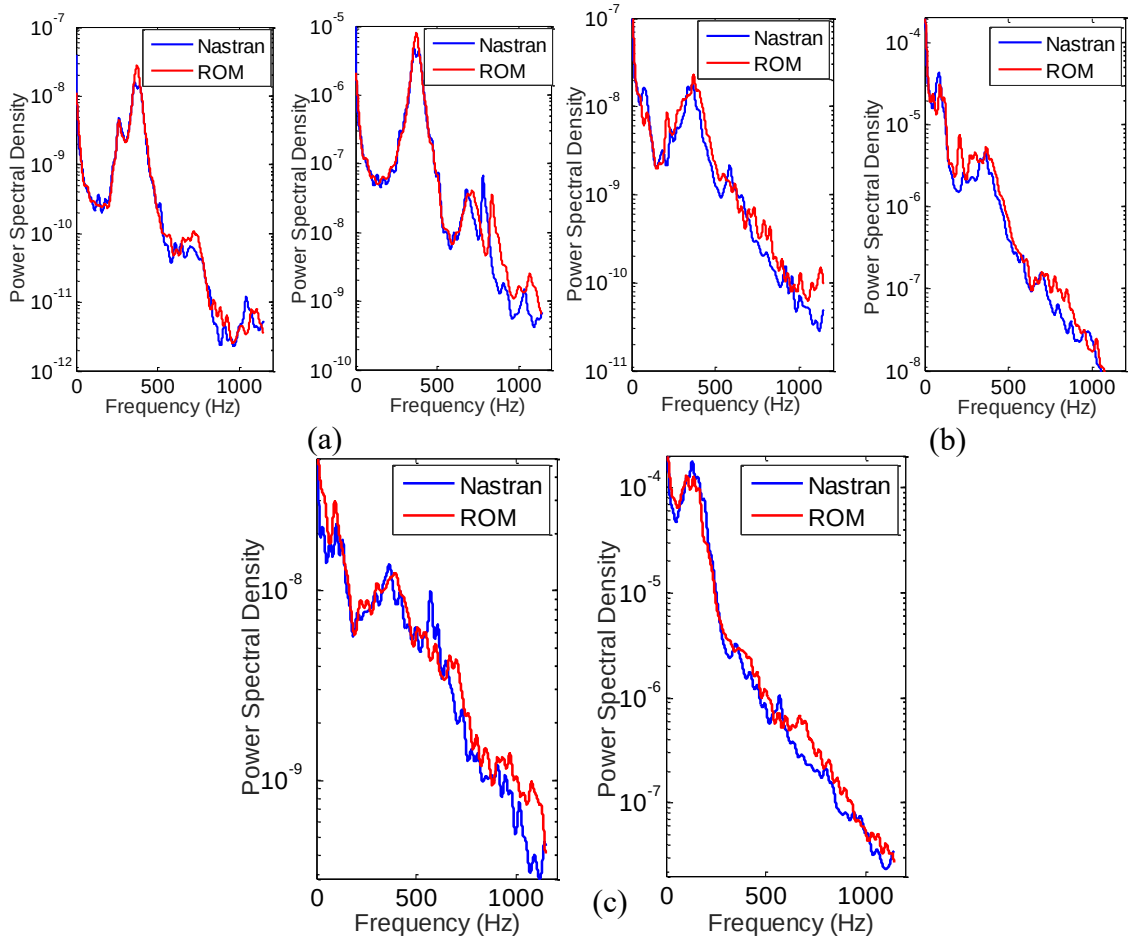

Figure 32. Power Spectral Densities of the In-Plane (Left) and Transverse (Right) Displacements at the Quarter Point of the Clamped-Clamped Beam under (a) Low, (b) Medium, and (c) High Loading.

6.3 Application to the Shallow Cylindrical Shell

The shallow cylindrical shell shown in Figure 4 has been found in this investigation to exhibit two strong nonlinear features, i.e., of mode switching and symmetry breaking. A first challenge of this model construction was the determination of a set of dual modes leading to a good representation of the response in the x and z directions. Following the work on the clamped-clamped curved beam, the first part of the basis was constructed by a proper orthogonal decomposition of the projection of a series (11) of nonlinear Nastran static solutions (SOL 106) corresponding to uniform pressures of different magnitudes with peak transverse displacement extending up to 3.1 thicknesses on the first 8 symmetric linear modes of the undeformed panel. The 6 POD modes with the largest eigenvalues, see Figure 57, were retained as the transverse modes in this computation. Duals were then constructed with the first 2 POD modes as dominant leading to 7 dual modes orthogonal to the first 27 symmetric linear modes. This extended orthogonalization was carried out to eliminate more significantly the transverse components present in the data and thereby generate dual modes with stronger in-plane components that rapidly reduce the in-plane representation error. The identification of the stiffness coefficients was initially done with the single level approach.

6.3.1 Validation Results under Static Load

This 13-mode 6T7D model performed very well in predicting the static response vs. load over a broad range of pressures including the occurrence of a mode switching event. see Figure 58 and Figure 59. A deviation between the maximum displacement and displacement at the center of the panel in transverse direction arises as the load increases.

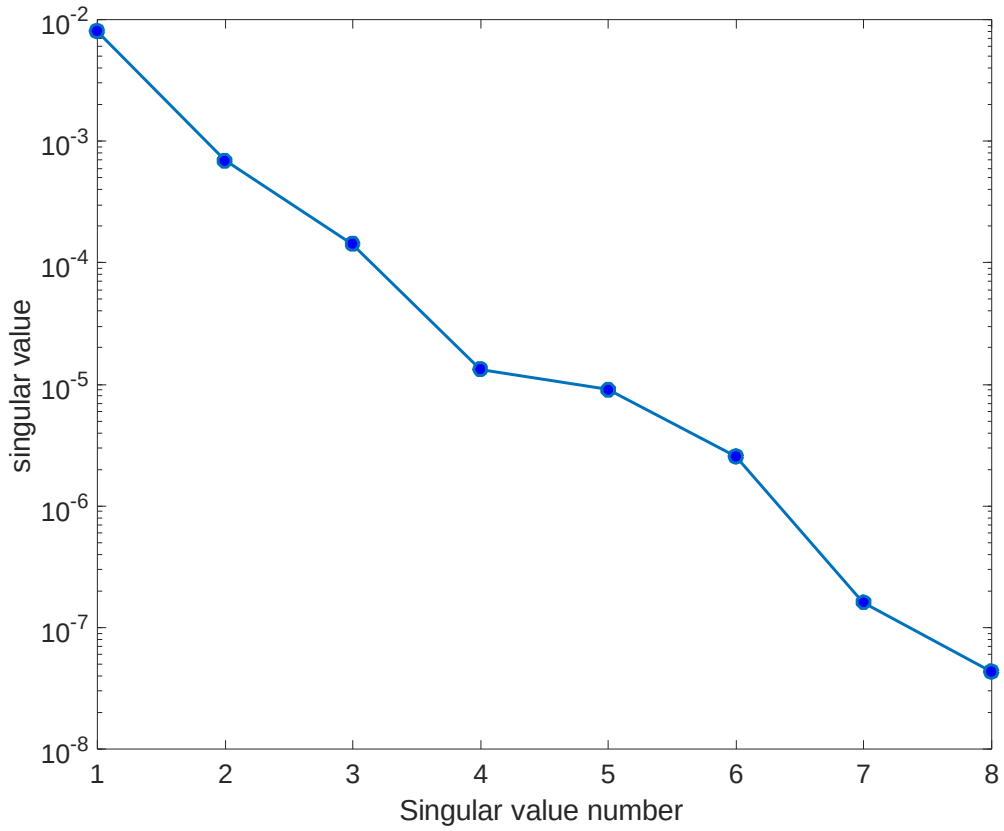

Figure 57. Singular Values of the POD of the Projections on the First 8 Symmetric Linear Modes

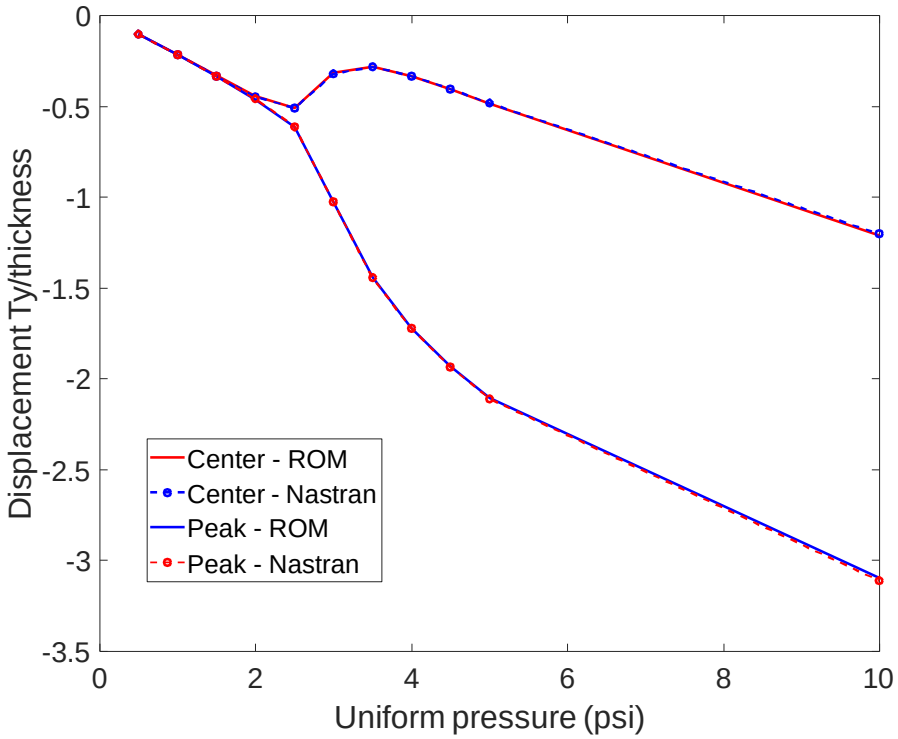

Figure 58. Center and Peak Displacements along the Y (Transverse) Direction vs. Applied Uniform Pressure. Nastran and NLROM Predictions.

Also investigated, see Figure 60, are the first two eigenvalues of the tangent stiffness matrix as a function of the applied pressure. Shown on this figure are the first two Nastran eigenvalues corresponding to symmetric eigenvectors, those of the Nastran tangent stiffness projected on the basis, and those predicted from the NLROM generalized coordinates obtained for the various loading conditions. Note that the Nastran eigenvalues clearly show the veering that is the origin of the mode switching. Moreover, the eigenvalues of the projected tangent stiffness matrix match very well those predicted from the NLROM suggesting that the identified model is accurate but the difference between these two curves and the Nastran one for the second eigenvalue suggests that the basis is not quite appropriate for large enough load levels.

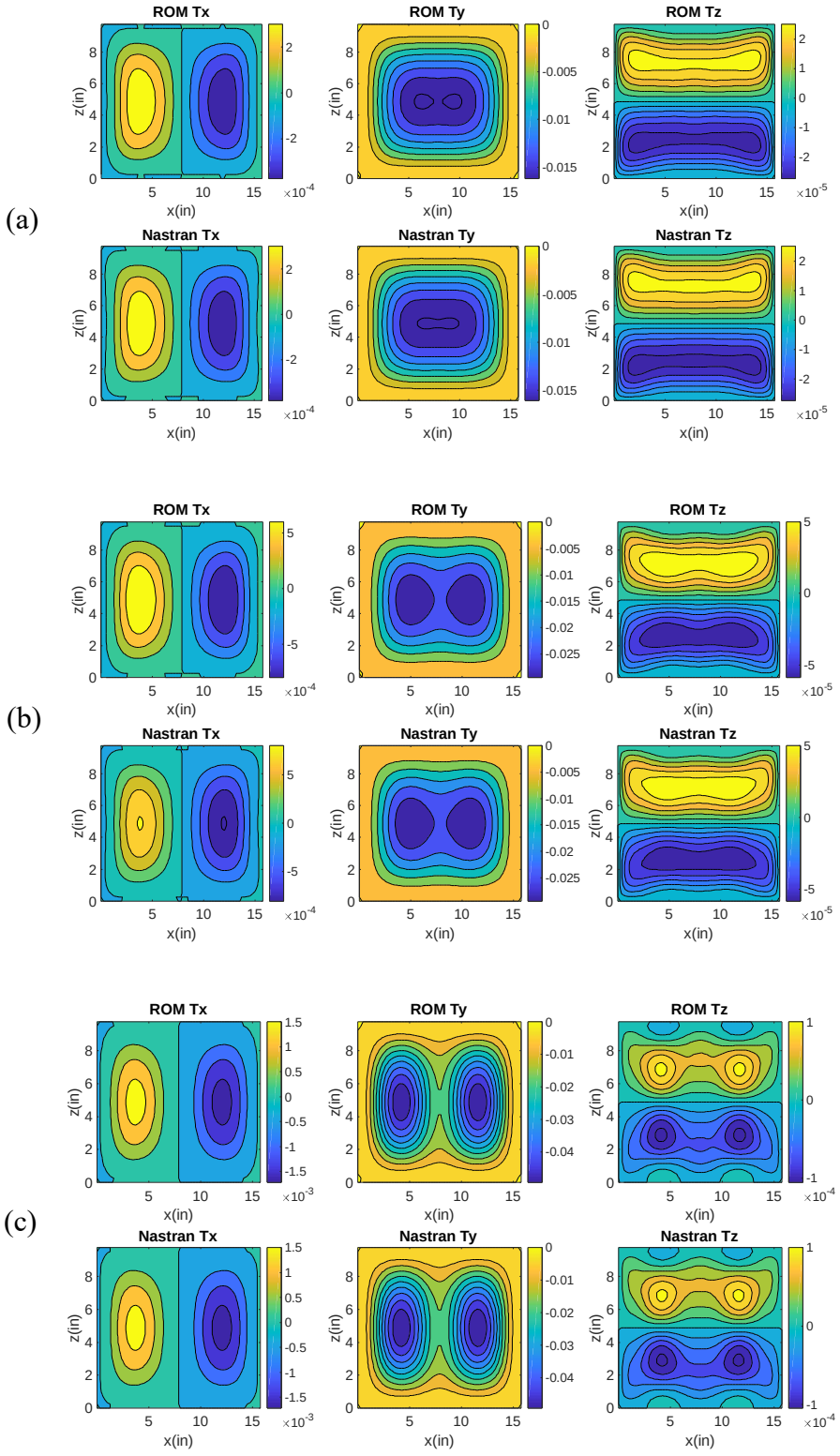

Figure 59. Contour Plots of Displacements along X, Y, Z as Predicted by Nastran and the NLROM for Uniform Pressures of (a) 1.5 psi, (b) 2.5 psi, and (c) 3.0 psi.

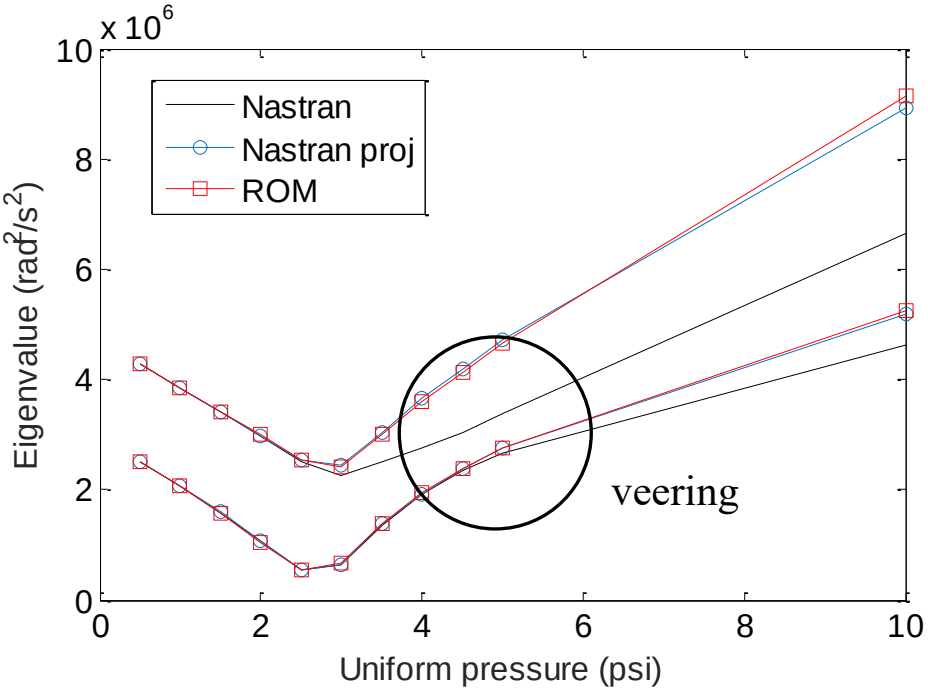

Figure 60. Eigenvalues of the Tangent Stiffness Matrix from Nastran (Corresponding to Symmetric Eigenvectors), Projected Nastran Tangent Stiffness Matrix on the Basis, and from the ROM.

6.3.2 Validation Results under Dynamic Load

6.3.2.1 140dB, 150dB, 160dB

Having successfully predicted the static response of the shell, the NLROM construction focused next on dynamic comparisons under a uniform pressure varying in time as a white noise in the frequency range of [0,500] Hz with variable overall sound pressure levels. It was first recognized that the dynamic response is dominated in the linear case by the first two symmetric modes (of frequencies 272Hz and 346Hz) which are not exactly represented by the 6 POD modes. This issue was resolved by appending to the 6 POD modes, the first 11 linear modes from which they were extracted, then proceeding with a Gram-Schmidt orthogonalization (with respect to the mass matrix) limited to the first 11 modes. These modes are not the linear modes but a rotation of them. They span a

APPENDIX I:

[C3]: Song, P., Wang, X.Q., and Mignolet, M.P., "Uncertainty Management for the Stochastic Response of Uncertain Structures," *Proceedings of the AIAA Science and Technology Forum and Exposition (SciTech2020)*, Orlando, Florida, Jan.6-10, 2020. AIAA Paper AIAA-2020-1419.

AIAA SciTech Forum
6-10 January 2020, Orlando, FL
AIAA Scitech 2020 Forum

10.2514/6.2020-1419

UNCERTAINTY MANAGEMENT FOR THE STOCHASTIC RESPONSE OF UNCERTAIN STRUCTURES

P. Song, X.Q. Wang, and M.P. Mignolet

SEMTE, Faculties of Mechanical and Aerospace Engineering,
Arizona State University, Tempe, AZ 85287-6106

ABSTRACT

The present investigation hinges on the perspective that using the most detailed computational models (e.g., very refined meshes) and/or the most complete physical models to evaluate each sample of the response is not an efficient use of computational or time resources in the presence of aleatoric uncertainty. Rather, the fidelity of the models can be degraded as long as the induced epistemic uncertainty remains small in comparison of the aleatoric uncertainty present. This perspective is here referred to as uncertainty management and the focus of the present effort is to validate this concept to two very different structures: the first is linear modeled in finite elements while the second behaves nonlinearly, is part of a multiphysics problem and is represented as a reduced order model (ROM). The reduction of fidelity and increase in computational speed is achieved in the first problem by relying on a coarse model while in the second sparsity is introduced in a large group of ROM coefficients. For these model downgrades which induce only small changes in the response, it is indeed shown that a well identified/calibrated lower fidelity model provides indeed a close fit of the random response of the higher order one. The maximum entropy nonparametric approach to uncertainty modeling is a convenient framework for this uncertainty management strategy given its capability to represent both aleatoric and some epistemic uncertainties.

INTRODUCTION

The present effort is concerned with the computationally efficient prediction of the uncertainty on the response of a system/structure induced by a combination of epistemic and aleatoric uncertainties in the system properties. It is assumed here that different models of the system are available, e.g., finite element models with different mesh densities or reduced order models with different number of basis functions. Then, to each of these models may be associated a level of epistemic uncertainty with respect to the "truth" or to each other.

The central point of the present effort is that *using the most detailed computational models (e.g., very refined meshes) and/or the most complete physical models to evaluate each sample of the response is not an efficient use of computational or time resources in the presence of aleatoric uncertainty*. Rather, an optimum resource management strategy would be to relax the computational and modeling accuracies to a level such that the resulting (epistemic) uncertainty does not lead to a significant increase in the uncertainty band on the prediction as compared to the one obtained with the inherent uncertainty in the system/its excitation.

This strategy, referred to here as uncertainty management, thus focuses on the balancing of epistemic and aleatoric uncertainties, i.e., the joint selection of a fidelity level and a global uncertainty level, to achieve the required prediction accurately with a low computational cost.

It is assumed here that the epistemic and aleatoric uncertainties are modeled stochastically within a single framework. For example, if considering reduced order models within matrix coefficients, such a single framework could conveniently be taken as the maximum entropy-based approach of Soize [1,2]. Within the context of linear finite element models, the single framework could be chosen as the maximum entropy modeling at the elemental level recently introduced by the authors [3,4]. Then, epistemic and aleatoric uncertainty are characterized by similar metrics which allows for their comparison and their interchange.

In this light, the specific objectives of the present effort are to exemplify the above uncertainty management process which involves:

(1) the quantification of the level of epistemic uncertainty associated with a lower fidelity model in comparison to a higher fidelity one,

(2) the comparison of the levels of epistemic and aleatoric uncertainties. One would expect similar predictions from a lower fidelity model and a higher fidelity one when the level of epistemic uncertainty of the former is lower/much lower than its aleatoric counterpart. This requirement is the basis of the selection of an appropriate lower fidelity model.

(3) the "training" of the lower fidelity model to emulate the uncertain high fidelity model, e.g., identify the uncertainty level of the low fidelity model given samples of the response of the high fidelity one, thereby decreasing the computational cost of the prediction effort.

The two examples given below demonstrate that the uncertainty management can be carried out on either full finite element models or reduced order models thereof.

The above focus has overlap with the recent innovative work of [5,6] in which a multi-fidelity prediction strategy is developed and validated, combining the predictions from multiple models of different fidelity to yield high fidelity equivalent predictions. The present approach proceeds differently with all computations originating from a single model but this model is required to have sufficient fidelity so that the aleatoric uncertainty is larger/much larger than the epistemic one.

Before describing in details the two examples, their mean and uncertain models, a brief review of the maximum likelihood identification approach is presented below as it represents the strategy used here for the estimation of the level of uncertainty.

MAXIMUM LIKELIHOOD IDENTIFICATION OF PARAMETERS

It is proposed here to identify the deterministic parameter(s) of the uncertainty model through the maximum likelihood strategy. This approach proceeds as follows.

Denote by $\boldsymbol{x}_i^{(obs)}$, i =1, ..., R, a series of R observations/samples of the random vector $\boldsymbol{X}$, i.e., the response of the uncertain system considered. The model of this system is characterized by a set of deterministic parameters $\boldsymbol{\theta}$ which are to be identified from the given observations. Then, according to the maximum likelihood approach, the most appropriate values of $\boldsymbol{\theta}$ are those which maximize the likelihood function

$$L = \prod_{i=1}^{R} p_{\boldsymbol{X}}\left(\boldsymbol{x}_i^{(obs)};\boldsymbol{\theta}\right) \tag{1}$$

where $p_{\boldsymbol{X}}\left(\boldsymbol{x}_i^{(obs)};\boldsymbol{\theta}\right)$ denotes the probability density function of the random vector $\boldsymbol{X}$ corresponding to the values $\boldsymbol{\theta}$ of the parameters of the model. This probability density function is in general estimated statistically from a number of samples produced in a Monte Carlo analysis, e.g., by using the kernel density estimation method [7-9]. This approach may be expensive when

the vector $\boldsymbol{X}$ has many components in which case one can resort (e.g., see [10]) to a Gaussian approximation of it for which the probability density function is readily expressed as

$$p_{\boldsymbol{X}}^{G}\left(\boldsymbol{x};\boldsymbol{\theta}\right)=\frac{1}{\left(2\pi\right)^{p/2}\sqrt{\det\left(\boldsymbol{K}_{\boldsymbol{XX}}\right)}}\exp\left[-\frac{1}{2}\left(\boldsymbol{x}-\boldsymbol{\mu}_{\boldsymbol{X}}\right)^{T}\boldsymbol{K}_{\boldsymbol{XX}}^{-1}\left(\boldsymbol{x}-\boldsymbol{\mu}_{\boldsymbol{X}}\right)\right] \tag{2}$$

where ^{T} denotes the operation of matrix/vector transposition. Note in Eq. (2) that $\boldsymbol{\mu}_{\boldsymbol{X}}\left(\boldsymbol{\theta}\right)$ and $\boldsymbol{K}_{\boldsymbol{XX}}\left(\boldsymbol{\theta}\right)$ denote the mean vector and covariance matrix of the random vector $\boldsymbol{X}$ determined for particular values $\boldsymbol{\theta}$ of the parameters of the uncertain model. The Gaussian assumption of Eq. (2) leads to significant computational savings as it requires only the estimation of the mean and covariance matrix.

In computational problems that lead to a "large" vector $\boldsymbol{X}$, e.g., response over a fine finite element mesh or time dependent response computed at a small time step, it is quite typical that the covariance matrix $\boldsymbol{K}_{\boldsymbol{XX}}$ of the ensemble of components is nearly singular. This finding is not surprising as, for example, the responses at neighboring nodes of a fine mesh are expected to be closely correlated to each other. Then, a preliminary step in the maximum likelihood construction is to proceed with a Principal Component Analysis (PCA) to reduce the random vector $\boldsymbol{X}$ to another, $\boldsymbol{Y}$, of typically much smaller size which corresponds to the projection of $\boldsymbol{X}$ on the set of m eigenvectors of $\boldsymbol{K}_{\boldsymbol{XX}}$ with largest eigenvalues λ_i.

This approach is effectively equivalent as approximating in Eq. (2) the covariance matrix $\boldsymbol{K}_{\boldsymbol{XX}}$ by its approximation $\boldsymbol{K}_{\boldsymbol{XX}}^{(m)}$ based on the m largest eigenvalues and associated eigenvectors. That is,

$$\boldsymbol{K}_{\boldsymbol{XX}}^{(m)}=\boldsymbol{\Phi}^{(m)}\boldsymbol{\Lambda}^{(m)}\boldsymbol{\Phi}^{(m)T} \tag{3}$$

where $\boldsymbol{\Phi}^{(m)}$ denotes the matrix with the orthonormal eigenvectors in columns, $\boldsymbol{\Lambda}^{(m)}$ is the $m\times m$ diagonal matrix of the largest eigenvalues.

Combining Eqs (2) and (3) yields

$$p_{\boldsymbol{X}}^{G}\left(\boldsymbol{x};\boldsymbol{\theta}\right)=\frac{1}{\left(2\pi\right)^{p/2}\sqrt{\det\left(\boldsymbol{\Lambda}^{(m)}\right)}}\exp\left[-\frac{1}{2}\boldsymbol{z}^{T}\left[\boldsymbol{\Lambda}^{(m)}\right]^{-1}\boldsymbol{z}\right] \tag{4}$$

where

$$\boldsymbol{z}=\boldsymbol{\Phi}^{(m)T}\left(\boldsymbol{x}-\boldsymbol{\mu}_{\boldsymbol{X}}\right). \tag{5}$$

Owing to the diagonal nature of $\boldsymbol{\Lambda}^{(m)}$, Eq. (4) can be rewritten as

$$p_{\boldsymbol{X}}^{G}\left(\boldsymbol{x};\boldsymbol{\theta}\right)=\prod_{i=1}^{m}\frac{1}{\sqrt{2\pi\lambda_i}}\exp\left[-\frac{z_i^2}{2\lambda_i}\right] \tag{6}$$

where z_i denotes the ith component of the vector $\mathbf{z}$.

FIRST SAMPLE PROBLEM: FINITE ELEMENT MODELS

Physical System and Model

The first sample problem considered here is the response of the uncertain plate of mean model shown in Fig. 1(a). It is an annulus of inner radius 0.8m, outer radius 1m, thickness 0.002m clamped on its inner radius and free on the outer one. The material, aluminum, is

assumed to be homogenous and isotropic with Young's modulus E = 7.3 10^{10} Pa and Poisson's ratio ν= 0.316. This mean structure and all uncertain ones are subjected to a static uniform unit (1 Pa) pressure in the quadrant θ∈[180,270] degrees highlighted in yellow in Fig. 1(a).

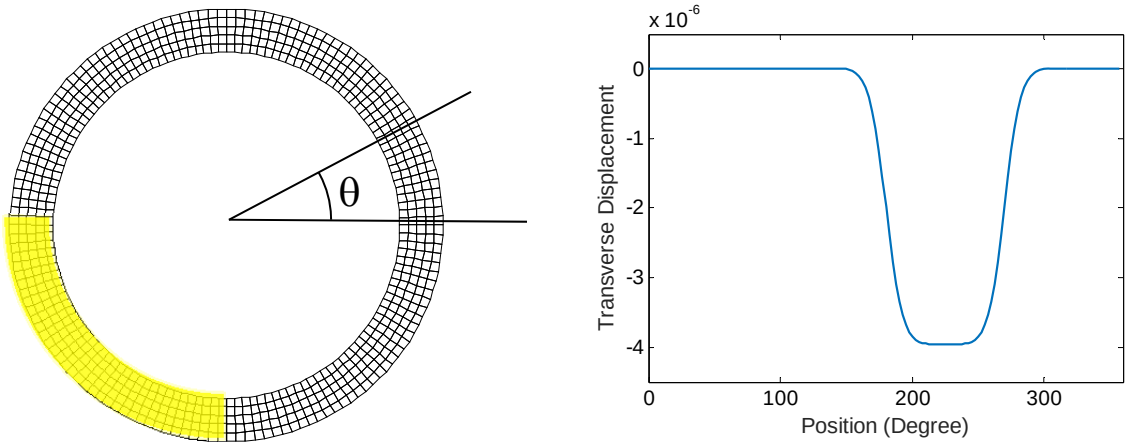

(a) (b)

Figure 1. (a) The annulus and its "truth" finite element model with the loading domain highlighted in yellow. (b) Static transverse displacement at the periphery.

The "truth" model considered here is a finite element model of the annulus using 4-node shell finite elements within Nastran (CQUAD4 elements with 6 degrees of freedom per node) with a mesh of 144 nodes around the periphery and 6 in the radial direction. Then, shown in Fig. 1(b) is the transverse displacement of the periphery which is clearly localized near the excitation, i.e., in the band θ∈[150,300] degrees.

Stochastic Model of Uncertainties at the Finite Element Level

The modeling of uncertainties for this problem will be accomplished at the level of each element using the recently proposed application of the maximum entropy at the finite element level [3,4]. In this approach, the uncertainty is accounted for by randomizing the elemental (stiffness here) matrices of each element with the maximum entropy construct.

Specifically, denote by $\overline{\boldsymbol{K}}$ the elemental stiffness matrix of a typical element of the mean model finite element. Then, following the maximum entropy strategy, one can express the uncertain stiffness matrix of that element as

$$\boldsymbol{K} = \overline{\boldsymbol{L}}_{\boldsymbol{K}}\, \boldsymbol{H}_{\boldsymbol{K}}\, \boldsymbol{H}_{\boldsymbol{K}}^{T}\, \overline{\boldsymbol{L}}_{\boldsymbol{K}}^{T} \tag{7}$$

where $\overline{\boldsymbol{L}}_{\boldsymbol{K}}$ is a decomposition of $\overline{\boldsymbol{K}}$ satisfying

$$\overline{\boldsymbol{K}} = \overline{\boldsymbol{L}}_{\boldsymbol{K}}\, \overline{\boldsymbol{L}}_{\boldsymbol{K}}^{T} \tag{8}$$

and $\boldsymbol{H}_{\boldsymbol{K}}$ is a random matrix. The above process is carried out for each element and the resulting samples of the elemental matrices are assembled to form one realization of the global stiffness matrix characterizing the uncertain structure.

In applying the above concepts, there are two key issues which must be carefully addressed. The first one is that (R.1) *the matrices* $\boldsymbol{H}_{\boldsymbol{K}}$ *corresponding to different elements cannot be simulated independently of each other*. Doing so would induce very high spatial frequency variations which are unphysical. The second is that (R.2) *each simulated sample of the random*

global matrix must be independent of the ordering of the nodes and degrees of freedom in each element to represent a physical realization of the uncertain structure, see [3,4] for discussion.

To satisfy the second requirement, the matrices $\boldsymbol{H_K}$ are simulated as [3,4]

$$\boldsymbol{H_K} = \boldsymbol{H} \otimes \boldsymbol{I_r} \tag{9}$$

where $\boldsymbol{H}$ is a *m*x*m* lower triangular random matrix with *m* the number of degrees of freedom per node and $\boldsymbol{I_r}$ denotes the *r*x*r* identity matrix where *r* is the number of nodes per element. Finally, $\otimes$ denotes the Kronecker product operation.

The above expression is appropriate when the degrees of freedom of the element follow the "degree of freedom – node" ordering, i.e., ordered as degree of freedom 1 for all nodes, degree of freedom 2 for all nodes, etc. If they are ordered along "node - degree of freedom", i.e., all degrees of freedom of the first node, then all of the second node, etc., Eq. (9) should be replaced by

$$\boldsymbol{H_K} = \boldsymbol{R}\left(\boldsymbol{H} \otimes \boldsymbol{I}_r\right) \tag{10}$$

where the matrix $\boldsymbol{R}$ corresponds to the permutation of the degrees of freedom. It contains all zeros except the *IJ* elements which equal 1 when $I = (j - 1)\, m + i$ and $J = (i - 1)\, r + j$, $i = 1, 2, ..., m$ and $j = 1, ..., r$.

To satisfy the requirement (R.1), it is necessary that a correlation exist between the matrices $\boldsymbol{H}$ corresponding to different elements. This is accomplished following the matrix field modeling proposed in [5] which views each element H_{ij} as the transformation of a zero mean, unit variance Gaussian field S_{ij} with a specified stationary autocorrelation function

$$R_{SS}^{ij}\left(\boldsymbol{y}\right) = E\left[S_{ij}\left(\boldsymbol{x}\right) S_{ij}\left(\boldsymbol{x}'\right)\right] \qquad \boldsymbol{y} = \boldsymbol{x}' - \boldsymbol{x} \tag{11}$$

where $\boldsymbol{x}$ and $\boldsymbol{x}'$ denote the coordinates of two elements (e.g., of their center).

Specifically, for $i \neq j$

$$H_{ij} = \sigma S_{ij} \tag{12}$$

while for $i = j$

$$H_{ii} = F_{H_{ii}}^{-1}\left[F\left(S_{ii}\right)\right] \tag{13}$$

where F is the cumulative distribution function of the standard Gaussian random variable and $F_{H_{ii}}^{-1}$ is the inverse of the cumulative distribution function of the Gamma random variable $H_{ii} = \sqrt{Y_{ii} / \mu}$. In the above equations, the parameters μ and σ are related to the uncertainty level δ through

$$\sigma = 1/\sqrt{2\mu} \qquad \text{and} \qquad \mu = \left(m+1\right)/2/\delta^2 . \tag{14}$$

In this paper, the autocorrelation functions $R_{SS}^{ij}\left(\boldsymbol{y}\right)$ will be selected the same for all *i* and *j* and defined as

$$R_{SS}^{ij}\left(\boldsymbol{y}\right) = \left[\frac{4\, L_{corr}^2}{\pi^2 \left|y\right|^2}\right] \sin^2\left(\frac{\pi \left|y\right|}{2\, L_{corr}}\right) \tag{15}$$

where L_{corr} is its single parameter, quantifying the correlation length of the Gaussian processes S_{ij} . The stochastic model presented above thus involves two parameters δ and L_{corr} that fully

define the stochastic representation of the elemental (and thus the global) stiffness matrices.

Results

To assess the proposed uncertainty management approach, a coarse mesh was defined which exhibits 1/2 the number of nodes along the periphery as well as radially, so 1/4 of the total nodes of the truth model. Then, shown in Fig. 2 are the mean model predictions of the transverse response (the in plane ones are zero) from the coarse and truth models which are seen to be different, notably by a shift of the response.

Next, the coarse model was randomized according to the elemental approach described in the previous section with a correlation length selected as $L_{corr} = \pi/3$ and with varying values of the uncertainty level δ_c. It was then desired to estimate this level for which the mean response of the fine mesh could be considered as a realization of the uncertain coarse mesh model. This estimation was carried out using the maximum likelihood approach for which the first step is to determine the number m of eigenvectors to retain. To this end, shown in Fig. 3(a) is a typical plot of the eigenvalues λ_i vs. the index i (for δ=0.06 of the uncertain coarse model) which suggests to retain approximately m = 10 eigenvectors. This data was obtained by stacking in the vector $\boldsymbol{X}$ the values of the 6 degrees of freedom at each of the nodes of the coarse model. The evolution of the maximum likelihood function vs. δ was then carried for several numbers of m as shown in Fig. 3(b). It is observed from these plots that the value of δ_c for which the maximum of the likelihood is achieved varies little with m in the range and occurs for δ_c =0.05. To support this finding, shown in Fig. 4 are the 5th-95th bands of uncertainties corresponding to this level and which clearly enclose the fine mesh model predictions which can thus be viewed as a realization of the uncertain coarse model. Note that uncertain bands exist on the in plane (radial and tangential) directions as the elemental uncertainty modeling produces samples of the elemental stiffness matrices that do not preserve the flatness of the annulus.

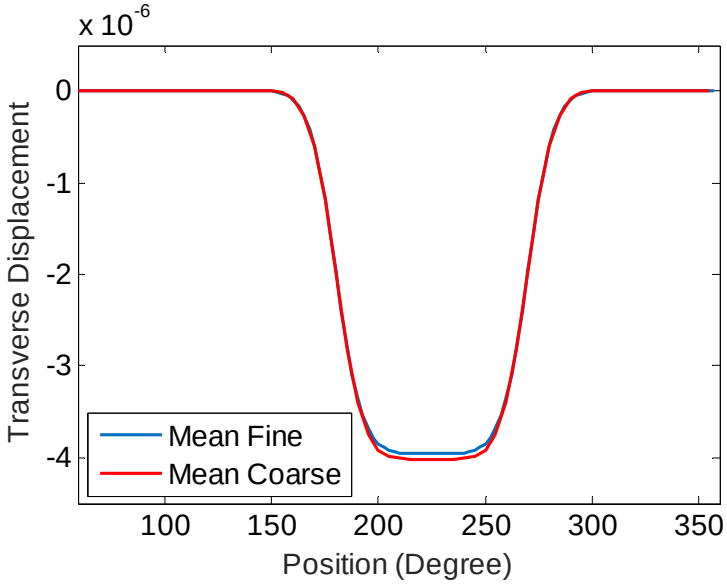

Figure 2. Static transverse displacement at the periphery of the mean annulus. Mean fine model (in blue), mean coarse model (in red).

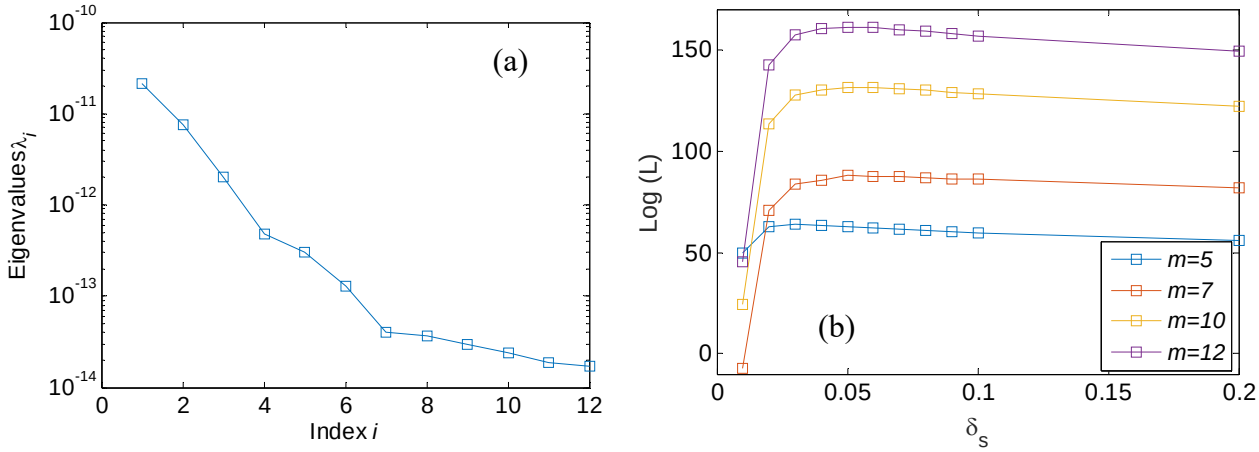

Figure 3. (a) Eigenvalues λ_i of the covariance matrix vs. index i for δ_c=0.06. (b) Log likelihood function as a function of the uncertainty level δ_c for several numbers (m) of eigenvectors retained. Mean model/epistemic uncertainty only.

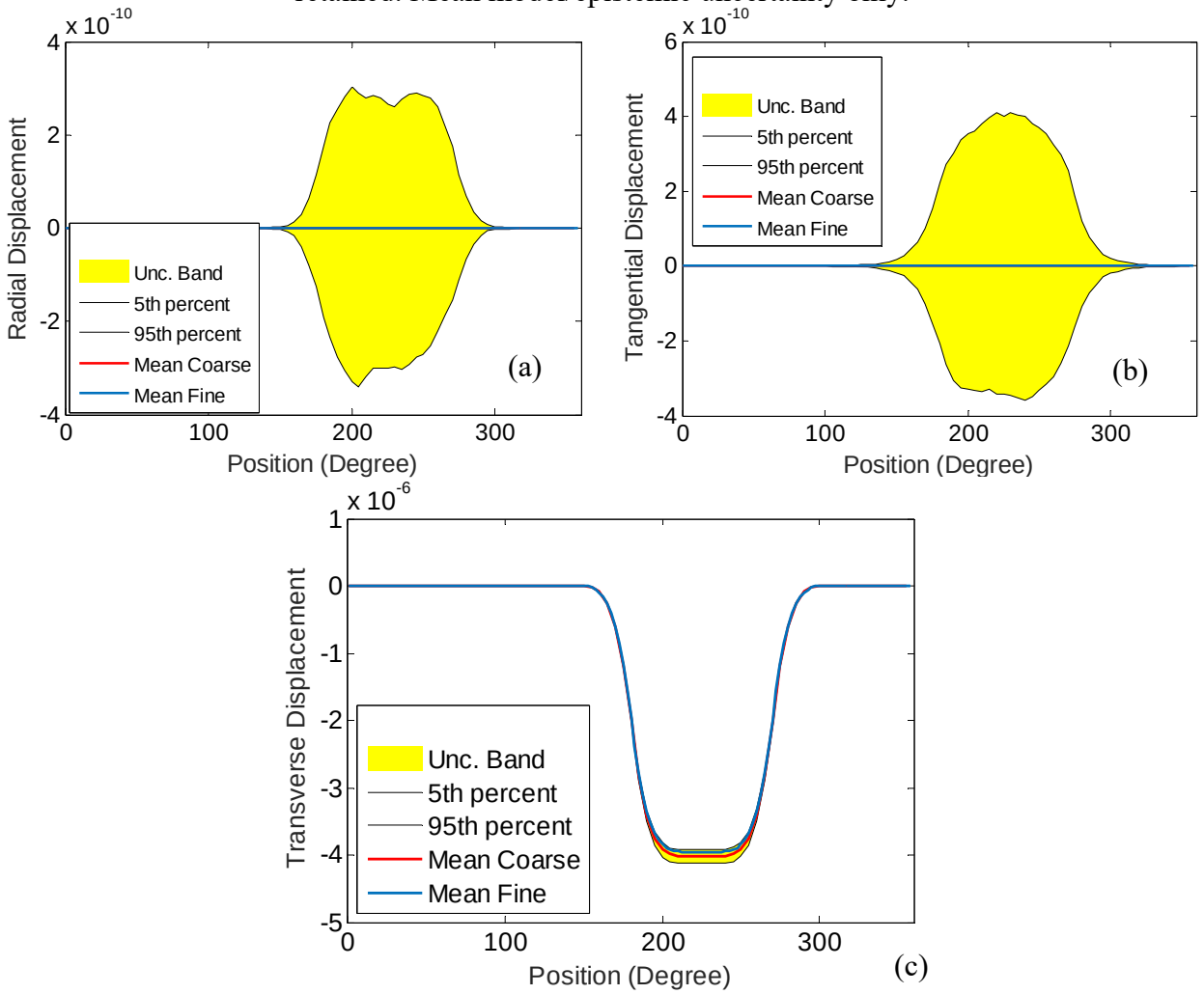

Figure 4. Static displacement at the periphery of the mean annulii. (a) radial, (b) tangential, (c) transverse. Mean fine model (in blue), mean coarse model (in red), and 5th-95th percentile uncertainty band (in yellow). δ_c=0.05, L_{corr} =π/3.

It was next desired to introduce aleatoric uncertainty in the models. In this regard, it was recognized that the elemental uncertainty modeling introduced above does not alter notably the mean of the responses. Thus, the difference between coarse and fine mesh, see Fig. 2, which appears as a shift, effectively induces a difference in the mean responses obtained with aleatoric uncertainty. This shift pushes to higher values the uncertainty level δ_c of the coarse model that is required by the maximum likelihood approach so that the nearly symmetric uncertainty band of the coarse model essentially includes the shifted symmetric uncertainty band of the fine model, see Fig. 5.

This issue can be resolved by a change in either the mean coarse model or by the introduction of a variable mean (not identity) in the random matrices $\boldsymbol{H}$. In the former case, what is desired is modifying the coarse model so that the average of the quantities of interest, i.e., here the responses of the fine and coarse model over the periphery, equals nearly zero. This option was adopted here and the modification to the model was a slight reduction, by 1.5%, of the applied load achieving the nearly zero average difference between fine and coarse model predictions. In this particular case, this resulting difference was nearly zero everywhere.

Five samples of the response of the uncertain (aleatoric) fine model, with $\delta_f = 0.1$, were generated and used in the maximum likelihood approach to identify the necessary uncertainty level of the coarse model. As seen in Fig. 6, the maximum likelihood estimate is also $\delta_c = 0.1$ which is consistent with the observation that the epistemic uncertainty level of the modified coarse model to simulate the response of the mean fine model is very small. Note that the correlation length was maintained for both models at $L_{corr} = \pi/3$ but it could also have been identified for the coarse model as a second parameter in the likelihood function optimization. As shown in Fig. 7, the uncertainty band of the resulting coarse model matches extremely well its counterpart for the fine model at a significant computation savings.

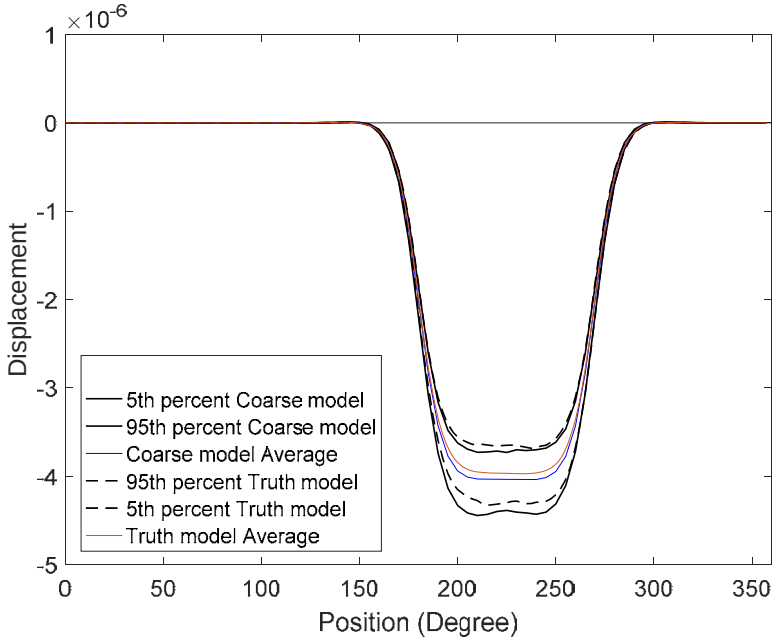

Figure 5. Uncertainty bands of the fine and coarse models resulting from maximum likelihood identification showing the effect of the difference in mean.

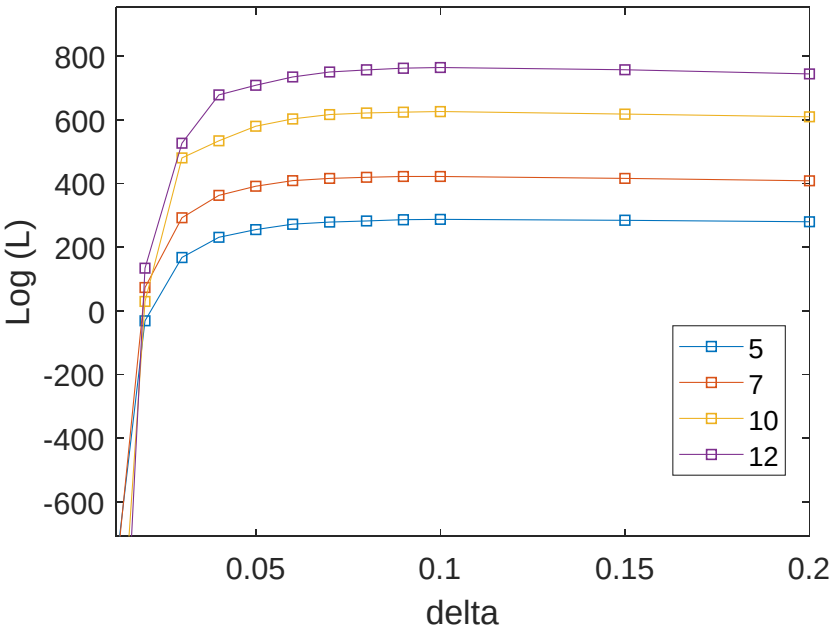

Figure 6. Log likelihood function as a function of the uncertainty level δ_c for several numbers (m) of eigenvectors retained. Aleatoric and epistemic uncertainty.

SECOND SAMPLE PROBLEM: REDUCED ORDER MODELS

In the context of reduced order models (ROMs), a lower fidelity model could be obtained as resulting from selecting a smaller basis or by eliminating some of the coefficients of the ROM. It is the latter perspective that will be emphasized here by considering nonlinear reduced order models that account for the nonlinear geometric behavior of the structure undergoing large deformation. Lower fidelity then results from an imposed "sparsity" of the ROM coefficients, see [11] for an earlier example.

Physical System and Model

The physical system of interest is the panel with stiffeners as shown in Fig. 8 which was originally considered in [12] and is subjected to a trajectory spanning Mach 2 to Mach 12 in 300 seconds with fully coupled structural/thermal/aerodynamic computations. Full details of the panel properties are in [12] but some key features are:

(i) nonlinear geometric structural effects are considered,

(ii) the coefficient of thermal expansion is linearly dependent on temperature but the tensor of elasticity is not,

(iii) the heat conduction problem is solved on the undeformed configuration with capacitance and conductance properties varying with temperature,

(iv) the aerodynamic forces are determined from piston theory while the aerodynamic heat flux is estimated from Eckert reference enthalpy method,

(v) the structural problem is solved quasi statically while the heat conduction is marched through a time step;

(vi) the computations of the thermal problem and the structural one are staggered, marched with time step of 0.5s. The thermal solution at one time step is obtained first, from the thermal and structural fields at the previous time step. Then, the structural problem is solved using the current temperature distribution.

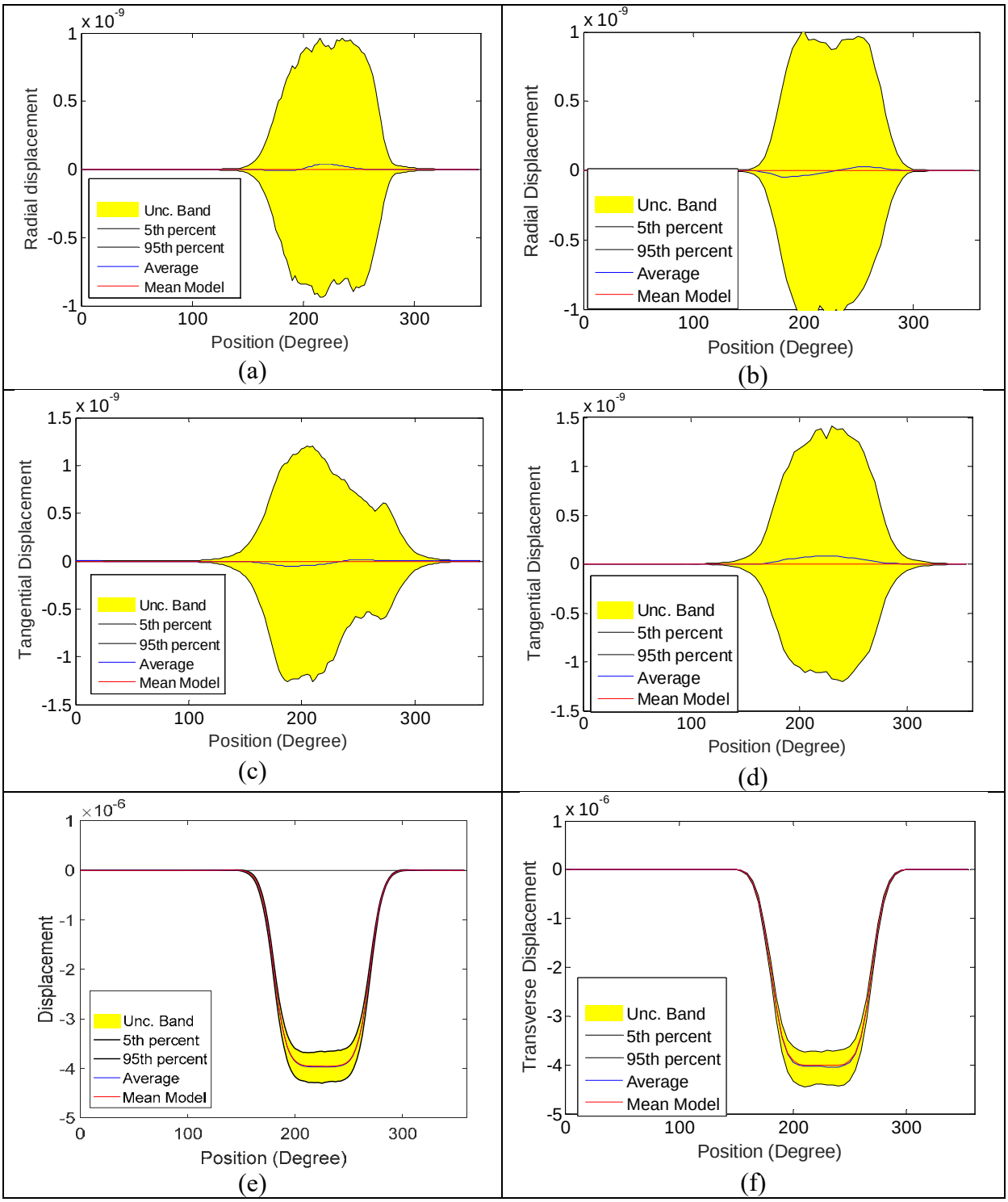

Figure 7. Static displacement at the periphery of the mean annulii. Respective mean models, and 5th-95th percentile uncertainty band. (a),(b) radial, (c),(d) tangential, (e),(f) transverse. (a),(c),(e) from fine model, $\delta_f = 0.1$, (b),(d),(f) from coarse model. $\delta_c = 0.1$, $L_{corr} = \pi/3$.

Based on the above assumptions, shown in Fig. 9 and 10 are the maximum transverse displacements and the temperature at the center of the panel over the 300 seconds of the trajectory. The computation of this response by structural and thermal finite element models and their coupling is an extensive process and reduced order modeling techniques have been devised for problems such as this one to dramatically speed up the computations. A brief review of these methods (see also [13-28]) is provided below followed by the uncertainty modeling that has been proposed for these ROMs.

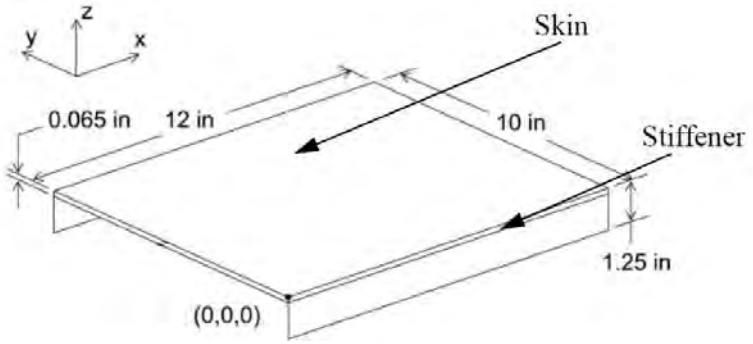

Figure 8. Hypersonic panel with stiffener [12].

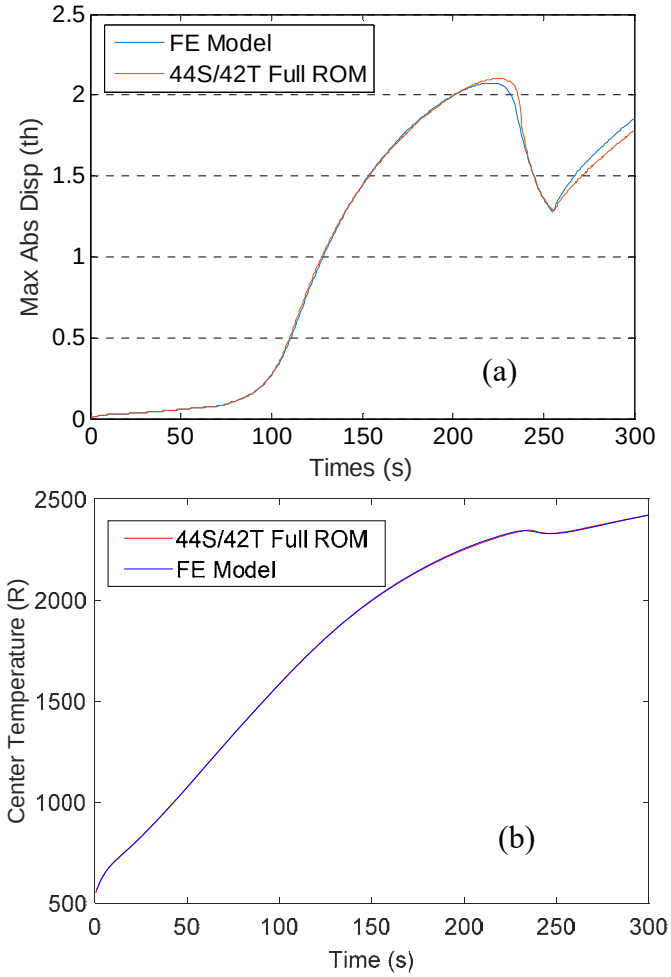

Figure 9. (a) Maximum transverse displacement and (b) temperature of the panel center over the trajectory. Predictions by finite element models [12] and structural-thermal full ROM [28].

Nonlinear Structural-Thermal Reduced Order Models

The reduced order models considered here are based on a representation of the temperature and displacement fields in the continuum structure in a "modal expansion" form, i.e. as

$$T(\boldsymbol{X},t)=\sum_{n=1}^{\mu}\tau_n(t)\,T^{(n)}(\boldsymbol{X}) \tag{16}$$

for the temperature, and

$$u_i(\boldsymbol{X},t)=\sum_{n=1}^{M}q_n(t)\,U_i^{(n)}(\boldsymbol{X}) \tag{17}$$

for the displacement. Note that $U_i^{(m)}$ and $T^{(m)}$ are specified functions of the position vector $\boldsymbol{X}$ in the *undeformed* configuration of the structure, chosen to satisfy the necessary boundary conditions. In the context of finite elements, the analogous representations of the displacement and temperature vectors, $\boldsymbol{w}$ and $\boldsymbol{T}$, are

$$\boldsymbol{T}(t)=\sum_{n=1}^{\mu}\tau_n(t)\,\boldsymbol{T}^{(n)} \tag{18}$$

and

$$\boldsymbol{w}(t)=\sum_{n=1}^{M}q_n(t)\,\boldsymbol{\Psi}_i^{(n)}\ . \tag{19}$$

A set of nonlinear ordinary differential equations governing the evolution of the generalized coordinates $q_n(t)$ and $\tau_n(t)$ can be obtained in a Galerkin format from the governing field equations for the displacements $u_i(\boldsymbol{X},t)$ and temperature $T(\boldsymbol{X},t)$ in the undeformed configuration. Specifically, assuming a Duhamel-Neumann form of the Helmholtz free energy in terms of the temperature and Green strain tensors, it is found that (summation implied over repeated indices)

$$\begin{aligned} M_{ij}\ddot{q}_j+D_{ij}\dot{q}_j+\left[K_{ij}^{(1)}+K_{ijl}^{(th)}\tau_l+K_{ijlp}^{(th)}\tau_l\tau_p\right]q_j+K_{ijl}^{(2)}q_jq_l+K_{ijlp}^{(3)}q_jq_lq_p \\ =F_i+F_{il}^{(th)}\tau_l+F_{ilp}^{(th)}\tau_l\tau_p \end{aligned} \tag{20}$$

and

$$B_{ij}\,\dot{\tau}_j+\tilde{K}_{ij}\tau_j+K_{ijl}^{(st)}\,\dot{q}_j\,\tau_l=P_i \tag{21}$$

where the terms $K_{ijlp}^{(th)}$ and $F_{ilp}^{(th)}$ are induced by a coefficient of thermal expansion dependent linearly on the local temperature while the elasticity tensor is assumed independent of it. Note that B_{ij} and $\tilde{K}_{ij}$ denote the components of the capacitance and conductance matrices, $K_{ijl}^{(st)}$ is a coefficient that models the latency effect (neglected here), and P_i denotes the various applies fluxes.

A structural-thermal ROM of this panel providing a close match of finite element results was developed in [28]. Shown in Fig. 9 is a comparison of the maximum transverse displacement and the temperature of the center of the panel predicted by the finite element model [12] and by the ROM [28] both of which match very well. In this ROM, the structural model included 44 structural basis functions, and the thermal model included 42 basis functions.

One notable drawback of these large bases is a large number of ROM coefficients, of the order of $M^4/6 + \mu^2 M^2/4$ in the above example, which will in turn lead to a large computational cost undercutting the benefits of using ROMs. A similar observation drawn for structural ROMs only [18] motivated there the introduction of a computational cost cutting strategy in which nonlinear stiffness terms (which constitute the vast majority of ROM coefficients) were retained only for the dominant structural modes creating a sparse ROM from a full one. Of course, associated with the sparsity is an error which unfortunately may not be easy to quantify ahead of time. Thus, the second stage of the sparsity modeling of [18] was the introduction of the induced modeling error as an epistemic uncertainty in the linear stiffness coefficients of the modes of which the nonlinear terms were discarded consistently with the uncertainty management strategy proposed here.

The present effort focuses on complementing the work of [18] by performing a similar reduction of coefficients but focusing on those modeling the temperature dependent stiffness terms, coupling the structural and thermal problems, as well as considering aleatoric uncertainty not investigated in [18].

Uncertainty Modeling for Nonlinear ROMs

Following [29,30], it is possible to introduce uncertainty on the structural and structural-thermal properties of the structure directly at the level of the reduced order model using an extended version of the maximum entropy nonparametric approach developed in [1,2] in the linear case and in [31] for nonlinear structural only applications. This methodology is based on the regrouping of the various ROM coefficients of Eq. (20) in a single matrix

$$\overline{\boldsymbol{K}}_D = \begin{bmatrix} \boldsymbol{K}^{(1)} & \tilde{\boldsymbol{K}}^{(2)} & \boldsymbol{F}^{(th)} & \boldsymbol{F}_2^{(th)} \\ \tilde{\boldsymbol{K}}^{(2)T} & 2\tilde{\boldsymbol{K}}^{(3)} & \tilde{\boldsymbol{K}}^{(th)} & \tilde{\boldsymbol{K}}_2^{(th)} \\ \boldsymbol{F}^{(th)T} & \tilde{\boldsymbol{K}}^{(th)T} & * & * \\ \boldsymbol{F}_2^{(th)T} & \tilde{\boldsymbol{K}}_2^{(th)T} & * & * \end{bmatrix} \tag{22}$$

where $\boldsymbol{K}^{(1)}$ denotes the linear stiffness matrix without temperature, the arrays $\tilde{\boldsymbol{K}}^{(2)}$ and $\tilde{\boldsymbol{K}}^{(3)}$ involve the quadratic and cubic stiffness coefficients $K_{ijl}^{(2)}$ and $K_{ijlp}^{(3)}$. Further, $\tilde{\boldsymbol{K}}^{(th)}$ and $\tilde{\boldsymbol{K}}_2^{(th)}$ contain the coefficients of the components of the linear stiffness matrix that are proportional and quadratic, respectively, to the thermal generalized coordinates, that is $K_{ijl}^{(th)}$ and $K_{ijlp}^{(th)}$. Finally, the arrays $\boldsymbol{F}^{(th)}$ and $\boldsymbol{F}_2^{(th)}$ are similarly constructed from $F_{il}^{(th)}$ and $F_{ilp}^{(th)}$. Note that the * denote blocks of coefficients that are mathematically defined in [29,30] in terms of the tensors of elasticity and thermal expansion but do not appear in the ROM governing equation (20). Accordingly, see [29,30], the evaluation of these blocks of terms can be sidestepped.

It is shown in [29,30] that the mean matrix $\overline{\boldsymbol{K}}_D$ is theoretically positive definite and thus the maximum entropy nonparametric approach can be applied to it. That is, random matrices $\boldsymbol{K}_D$ can be generated as

$$\boldsymbol{K}_D = \overline{\boldsymbol{L}}_D \, \boldsymbol{H}_D \, \boldsymbol{H}_D^T \, \overline{\boldsymbol{L}}_D^T \tag{23}$$

where

$$\overline{\boldsymbol{K}}_D = \overline{\boldsymbol{L}}_D \, \overline{\boldsymbol{L}}_D^T \tag{24}$$

$\overline{\boldsymbol{L}}_D$ being a lower triangular matrix of the block form (see [29,30])

$$\overline{\boldsymbol{L}}_D = \begin{bmatrix} \boldsymbol{L}_{11} & \boldsymbol{0} & \boldsymbol{0} & \boldsymbol{0} \\ \boldsymbol{L}_{21} & \boldsymbol{L}_{22} & \boldsymbol{0} & \boldsymbol{0} \\ \boldsymbol{L}_{31} & \boldsymbol{L}_{32} & \boldsymbol{I} & \boldsymbol{0} \\ \boldsymbol{L}_{41} & \boldsymbol{L}_{42} & \boldsymbol{0} & \boldsymbol{I} \end{bmatrix} \tag{25}$$

where $\boldsymbol{I}$ denotes the identity matrix of appropriate dimensions. Note that the 2×2 block identity matrix on the lower right corner of $\overline{\boldsymbol{L}}_D$ fully defines the * blocks in Eq. (22). Moreover, the lower triangular matrix $\boldsymbol{H}_D$ can be expressed as the product of 2 matrices of similar shape, i.e.,

$$\boldsymbol{H}_D = \boldsymbol{H}_T \, \boldsymbol{H}_S \tag{25}$$

where $\boldsymbol{H}_T$ and $\boldsymbol{H}_S$ induce uncertainty in the structural-thermal coupling terms and the structural terms. That is, these matrices are of the form

$$\boldsymbol{H}_T = \begin{bmatrix} \boldsymbol{I} & \boldsymbol{0} & \boldsymbol{0} & \boldsymbol{0} \\ \boldsymbol{0} & \boldsymbol{I} & \boldsymbol{0} & \boldsymbol{0} \\ \boldsymbol{H}_{T,31} & \boldsymbol{H}_{T,32} & * & * \\ \boldsymbol{H}_{T,41} & \boldsymbol{H}_{T,42} & * & * \end{bmatrix} \quad \text{and} \quad \boldsymbol{H}_S = \begin{bmatrix} \boldsymbol{H}_{S,11} & \boldsymbol{0} & \boldsymbol{0} & \boldsymbol{0} \\ \boldsymbol{H}_{S,21} & \boldsymbol{H}_{S,22} & \boldsymbol{0} & \boldsymbol{0} \\ \boldsymbol{0} & \boldsymbol{0} & \boldsymbol{I} & \boldsymbol{0} \\ \boldsymbol{0} & \boldsymbol{0} & \boldsymbol{0} & \boldsymbol{I} \end{bmatrix}. \tag{26}$$

Following [29,30], the elements of the full matrices $\boldsymbol{H}_{T,31}$, $\boldsymbol{H}_{T,32}$, $\boldsymbol{H}_{T,41}$, and $\boldsymbol{H}_{T,42}$ are selected as independent identically distributed zero mean Gaussian random variables. Moreover, the nonzero off-diagonal elements of $\boldsymbol{H}_{S,11}$, $\boldsymbol{H}_{S,21}$, and $\boldsymbol{H}_{S,22}$ are also independent identically distributed zero mean Gaussian random variables while the diagonal terms of $\boldsymbol{H}_{S,11}$ and $\boldsymbol{H}_{S,22}$ are independent Gamma random variables.

Results

As stated above, the focus of this second validation is on inducing sparsity in the structural-thermal coupling terms $K_{ijlp}^{(th)}$ and $F_{ilp}^{(th)}$ to reduce the number of coefficients to involve at each step of the computations and thus speed up the determination of the response. A first step is thus to decide for which *thermal* modes l and p, these coefficients must be kept and for which combinations of these indices the coefficients can be eliminated.

Observing the thermal response in the whole trajectory, the thermal modes were found to be divided into three groups. The first group S1 contains thermal modes [1, 3, 4], which are dominant modes; the second group S2 contains modes [5, 10, 13, 15, 17, 25, 26, 28, 30] whose general coordinates τ_n are relatively smaller in magnitude; and the remaining 30 out of the 42 thermal modes were chosen to be group S3 because their responses are the smallest in magnitude. Correspondingly, the $K_{ijlp}^{(th)}$ and $F_{ilp}^{(th)}$ are retained only when the l and p terms are (i) both in S1 and (ii) one in S1 one in S2. This process gives the simplified model, where the maximum transverse displacements only changed moderately after about 230s comparing to the response of the original model, see Fig. 10. Accordingly, this model will serve as the lower fidelity one vs. the original, full ROM being the higher fidelity one.

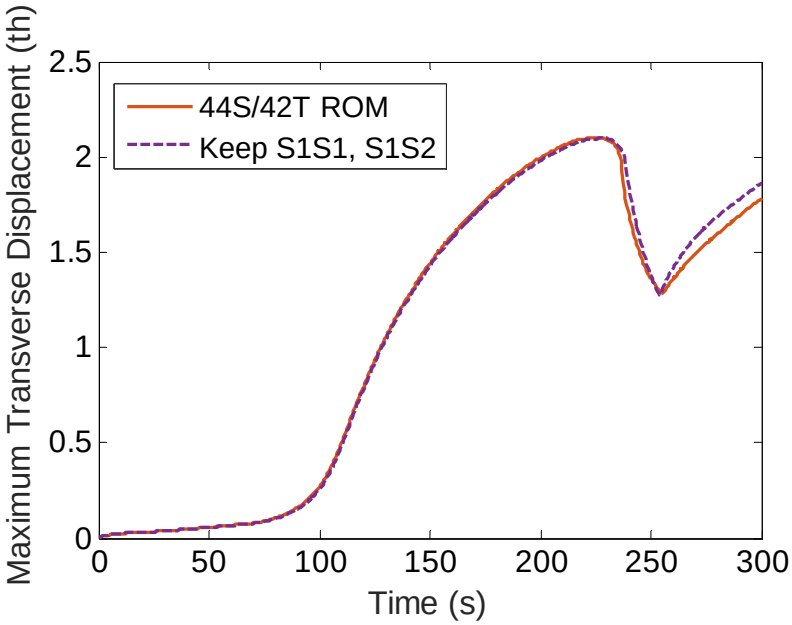

Figure 10. Maximum transverse displacement (in thickness), full ROM and ROM with eliminated thermal structural coupling terms.

Considering first the epistemic uncertainty modeling of the mean full ROM, two options have been investigated. The first, consistent with the approach of [18], introduced the uncertainty only on the terms $K_{ijl}^{(th)}$ and $F_{il}^{(th)}$ for the thermal modes indices l corresponding to the sets S2 and S3 only. This perspective stems from rewriting $K_{ijl}^{(th)}\tau_l + K_{ijlp}^{(th)}\tau_l\tau_p$ as $\left[K_{ijl}^{(th)} + K_{ijlp}^{(th)}\tau_p\right]\tau_l$. Then, eliminating the terms $K_{ijlp}^{(th)}$ could be balanced by variations of the other term in bracket, i.e., $K_{ijl}^{(th)}$. A similar argument also holds for $F_{ilp}^{(th)}$ and $F_{il}^{(th)}$.

For this first alternative, shown in Fig. 11 is the evolution of the log likelihood function as a function of the uncertainty level δ_s of the simplified/sparse model for various values of m, the number of eigenvectors of $\boldsymbol{K_{XX}}$ retained. For this plot, the entire time histories of the structural response, i.e., all 600 time steps and 44 structural generalized coordinates, were used to form the vector $\boldsymbol{X}$. This figure shows a peak at δ_s = 0.008 for most values of m which was accordingly selected as measure of the epistemic uncertainty. The band of uncertainty on the predictions of the sparse ROM corresponding to this value of δ_s is shown in Fig. 12 and it encloses most of the mean response of the full ROM.

Another option to account for the epistemic uncertainty is to introduce the uncertainty on all kept structural-thermal coefficients. From the plot of the log likelihood function, see Fig. 13, it is seen that δ_s=1.0 10^{-4} which is significantly smaller than the value of 0.008 obtained in the first case. The reduction may be understood by recognizing that this second option induces also variations of the most significant coupling terms and thus smaller changes of them are warranted. The resulting band of uncertainty, see Fig. 14, is in fact wider than the one shown in Fig. 12 and does also mostly enclose the response of the full ROM.

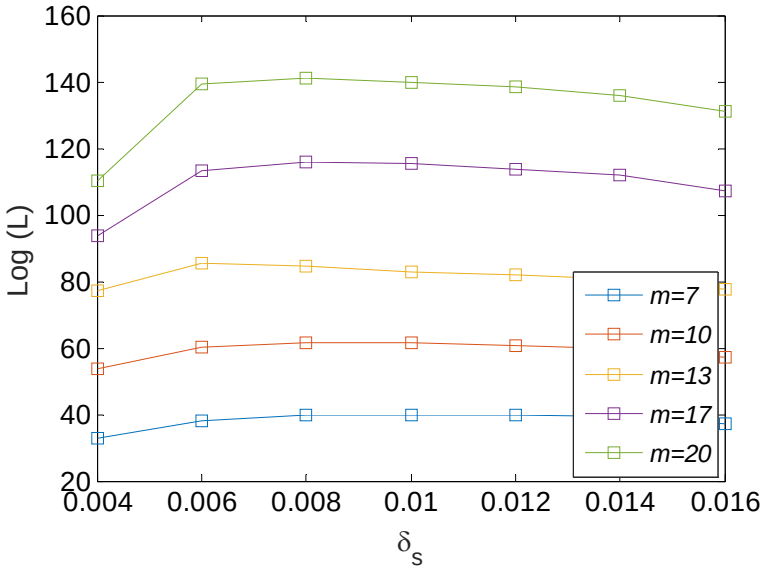

Figure 11. Log likelihood function as a function of the uncertainty level δ_s for several numbers (m) of eigenvectors retained. Mean model/epistemic uncertainty only. First uncertain modeling.

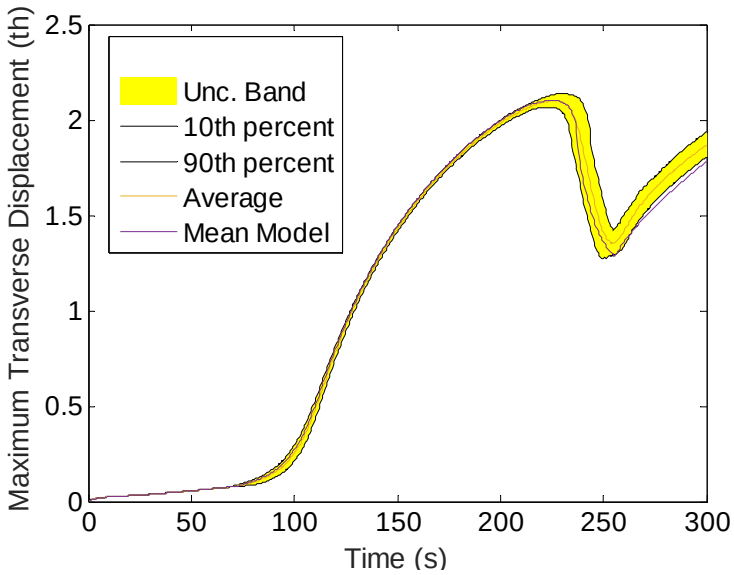

Figure 12. Maximum transverse displacement (in thickness) vs. time, full ROM (in blue) and 5th-95th percentile uncertainty band (in yellow) of the sparse ROM, δ_s=0.008. First uncertain modeling.

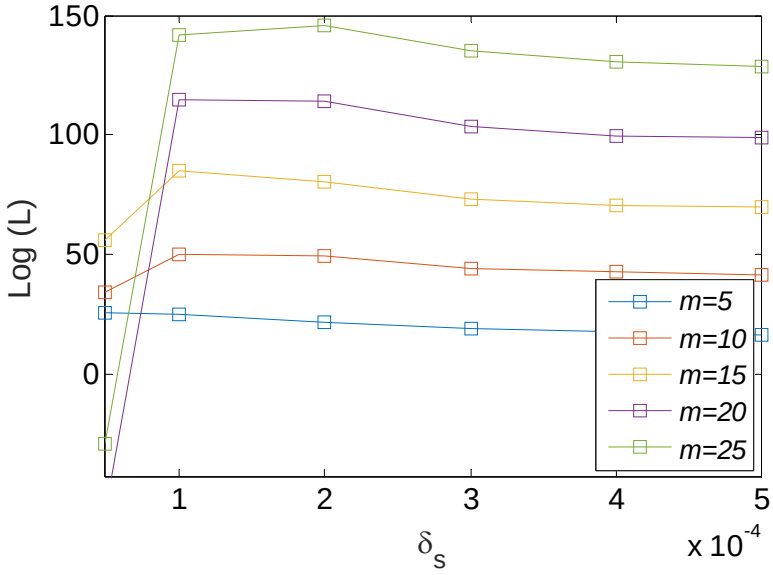

Figure 13. Log likelihood function as a function of the uncertainty level δ_s for several numbers (m) of eigenvectors retained. Mean model/epistemic uncertainty only. Second uncertain modeling.

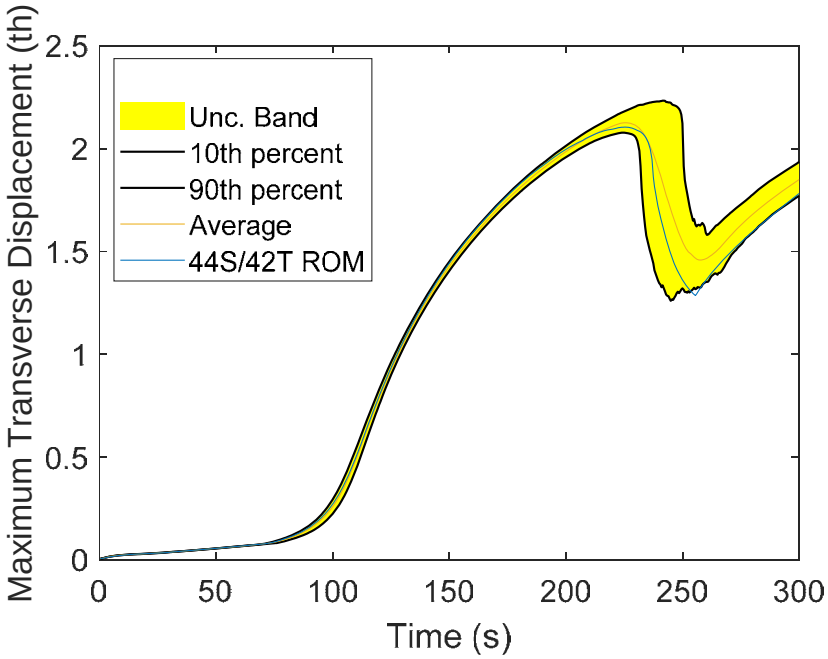

Figure 14. Maximum transverse displacement (in thickness) vs. time, full ROM (in blue) and 5th-95th percentile uncertainty band (in yellow) of the sparse ROM, δ_s=1.0 10^{-4}. Second uncertain modeling.

The above computations were next repeated in the presence of aleatoric uncertainty which was introduced only on the structural-thermal part of the model, i.e., with the matrix $\boldsymbol{H}_T$ keeping $\boldsymbol{H}_S$ to be the identity matrix. In this case, uncertainty on the sparse ROM is introduced on all coefficients and thus only the second modeling option above was considered. The aleatoric uncertainty level on the full ROM was selected to be $\delta_T = 5.0\ 10^{-4}$. Using 15 samples of the full ROM as data, the maximum likelihood identification led to the higher $3\ 10^{-4}$ value for the corresponding uncertainty level δ_s, see Figure 15, which leads to the uncertainty bands shown in Fig. 16 in which the 5 samples of the full ROM shown do fit in. Shown in Fig. 17 is the uncertainty band for the full model for $\delta_T = 5.0\ 10^{-4}$. Comparing Figs 16 and 17, it is seen that they match fairly well with the largest difference being the 95th percentile for $t > 250$ s which is higher for the full ROM than for the sparse one. This finding results from the lower identified δ_s which itself is due to the 15 samples selected that did not emphasize the high values of the response in that time segment. Since this issue is about identification not about the sparsity of the model, it is concluded that the sparse model appropriately calibrated would indeed capture well the band of uncertainty of the response in the presence of aleatoric uncertainty.

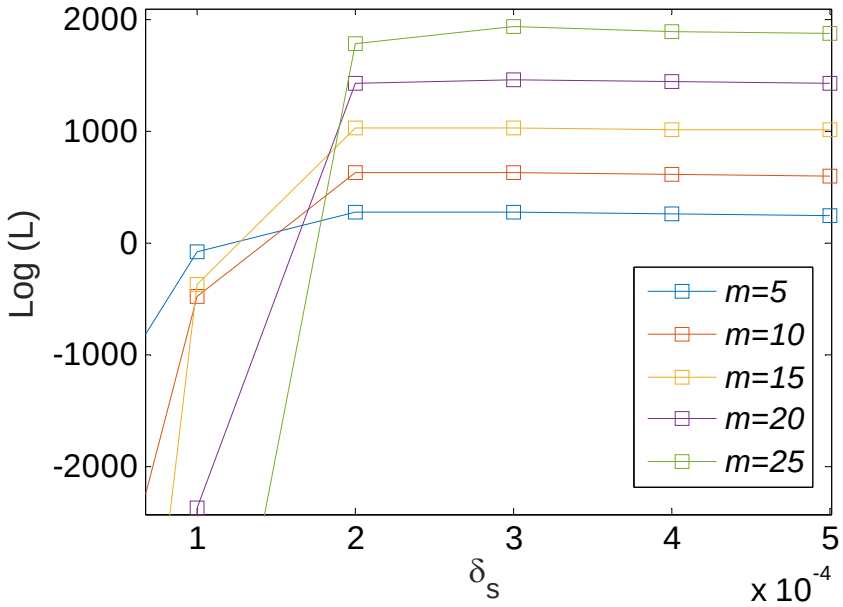

Figure 15. Log likelihood function as a function of the uncertainty level δ_s for several numbers (m) of eigenvectors retained. Aleatoric and epistemic uncertainty only. Second uncertain modeling.

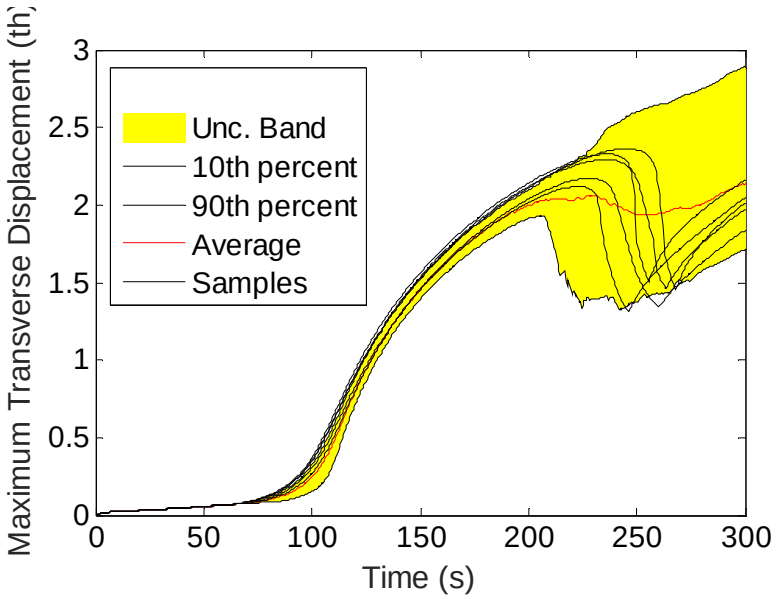

Figure 16. Maximum transverse displacement (in thickness) vs. time, 5 samples of the full ROM, $\delta_T = 5.0\ 10^{-4}$, and 5th-95th percentile uncertainty band (in yellow) of the sparse ROM, $\delta_s = 3.0\ 10^{-4}$. Second uncertain modeling.

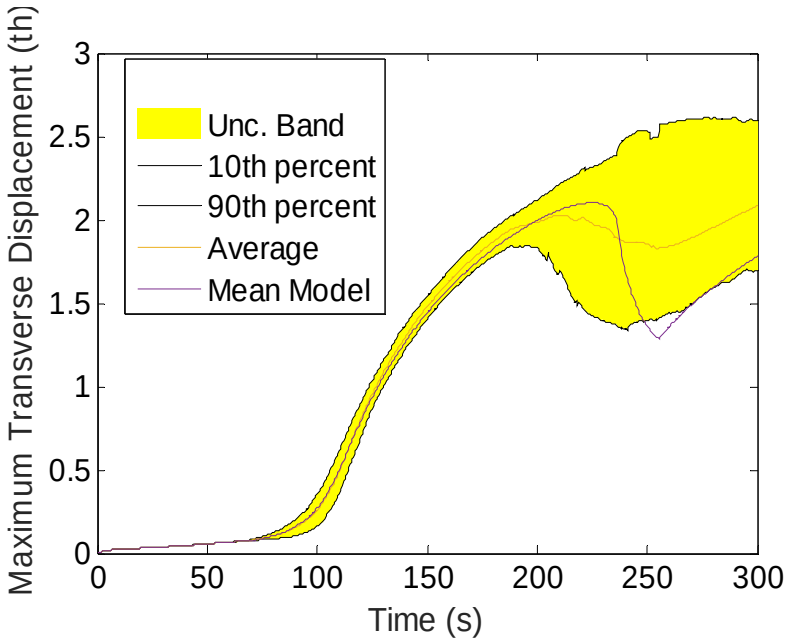

Figure 17. Maximum transverse displacement (in thickness) vs. time, 5th-95th percentile uncertainty band (in yellow) of the full ROM, $\delta_T = 5.0\ 10^{-4}$.

SUMMARY

The focus of the present investigation has been on assessing whether a well identified/calibrated lower fidelity model can provide a close fit of the response of the higher order one when both are subjected to uncertainty. This perspective has been validated on two very different structures: the first is linear modeled in finite elements while the second behaves

nonlinearly, is part of a multiphysics problem and is represented as a reduced order model (ROM). The reduction of fidelity and increase in computational speed was achieved in the first problem by relying on a coarse model while in the second sparsity was introduced in a large group of ROM coefficients. For these model downgrades which induced only small changes in the response, it was indeed shown that a well identified/calibrated uncertain lower fidelity model provides a close fit of the random response of the higher order one. Globally, it is suggested that the fidelity of the models can be degraded as long as the induced epistemic uncertainty remains small in comparison of the aleatoric uncertainty present. This perspective is here referred to as uncertainty management. Finally, it was noted that the maximum entropy nonparametric modeling approach to uncertainty is particularly convenient in the present context as it permits the quantification of the epistemic uncertainty with the same metric than used for the aleatoric one, thereby allowing a straightforward comparison.

ACKNOWLEDGEMENTS

The authors gratefully acknowledge the financial support of this work by the contract FA9550-16-1-0021 from the Air Force Office of Scientific Research with Dr. Jaimie Tiley as program manager.

REFERENCES

[1] C. Soize, A nonparametric model of random uncertainties for reduced matrix models in structural dynamics. *Probabilistic Engineering Mechanics*, Vol. **15**, pp. 277-294, 2000.

[2] C. Soize, *Stochastic Models of Uncertainties in Computational Mechanics.* American Society of Civil Engineers (ASCE). 2012.

[3] Song, P., and Mignolet, M.P., "Maximum Entropy-Based Uncertainty Modeling at the Elemental Level in Linear Structural and Thermal Problems," *Computational Mechanics*, Vol 64, No. 6, pp 1557–1566, 2019.

[4] Song, P., Wang, X.Q., and Mignolet, M.P., "Maximum Entropy Structural-Thermal Uncertainty Modeling at the Finite Element Level," *Proceedings of the AIAA Science and Technology Forum and Exposition (SciTech2019)*, San Diego, California, Jan.7-11, 2019.

[5] Ng, L.W., and Willcox, K.E., "Multifidelity approaches for optimization under uncertainty," *International Journal for Numerical Methods in Engineering*, Vol. 100, No. 10, 2014, pp. 746–772.

[6] Chaudhuri, A., Jasa, J., Martins, J.R.R.A., and Willcox, K.E., "Multifidelity Optimization Under Uncertainty for a Tailless Aircraft, *Proceedings of the AIAA Science and Technology Forum and Exposition (SciTech2018)*, Kissimmee, Florida, Jan. 8-12, 2018, AIAA Paper AIAA-1658.

[7] Bowman, A.W., and Azzalini, A., *Applied Smoothing Techniques for Data Analysis*, Oxford University Press, 1997.

[8] Terrell, G.R., and Scott, D.W., "Variable kernel density estimation," *The Annals of Statistics*, Vol. 20, No. 3, pp. 1236-1265, 1992.

[9] Soize, C., "A computational inverse method for identification of non-Gaussian random fields using the Bayesian approach in very high dimension," *Computer Methods in Applied Mechanics and Engineering*, Vol. 200, No. 45-46, pp. 3083-3099, 2011.

[10] Avalos, J., Swenson, E.D., Mignolet, M.P., and Lindsley, N.J., "Stochastic Modeling of Structural Uncertainty/Variability from GVT Test Data," *Journal of Aircraft*, Vol. 49, No. 3, pp. 870-884, 2012.

[11] Perez, R.A., Smarslok, B.P., and Mignolet, M.P., "Deterministic and Stochastic Partial Linearization Approach for Nonlinear Reduced Order Models of Structures," *Proceedings of the AIAA Science and Technology Forum and Exposition (SciTech2015)*, Orlando, Florida, Jan. 5-9, 2015, AIAA Paper AIAA 2015-2052.
[12] Culler, A.J., and McNamara, J.J. 2011. Impact of fluid-thermal-structural coupling on response prediction of hypersonic skin panels. AIAA Journal Vol. 49: 2393-2406.
[13] Mignolet, M.P., Przekop, A., Rizzi, S.A., and Spottswood, S.M., "A Review of Indirect/Non-Intrusive Reduced Order Modeling of Nonlinear Geometric Structures," *Journal of Sound and Vibration*, Vol. 332, No. 10, pp. 2437-2460, 2013.
[14] McEwan, M.I., Wright, J.R., Cooper, J.E., and Leung, A.Y.T., "A combined Modal/Finite Element Analysis Technique for the Dynamic Response of a Nonlinear Beam to Harmonic Excitation," *Journal of Sound and Vibration*, Vol. 243, pp. 601-624, 2001.
[15] Hollkamp, J.J., Gordon, R.W., and Spottswood, S.M., "Nonlinear Modal Models for Sonic Fatigue Response Prediction: A Comparison of Methods," *Journal of Sound and Vibration*, Vol. 284, pp. 1145-1163, 2005.
[16] Przekop A., and Rizzi S.A., "Nonlinear Reduced Order Random Response Analysis of Structures with Shallow Curvature," *AIAA Journal*, Vol. 44 (8), pp. 1767-1778, 2006.
[17] Przekop, A., and Rizzi, S.A., "Dynamic Snap-Through of Thin-Walled Structures by a Reduced-Order Method," *AIAA Journal*, Vol. 45, No. 10, pp. 2510–2519, 2007.
[18] Hollkamp, J.J., and Gordon, R.W., 2008, "Reduced-Order Models for Nonlinear Response Prediction: Implicit Condensation and Expansion," *Journal of Sound and Vibration*, Vol. 318, pp. 1139–1153.
[19] Spottswood, S.M., Hollkamp, J.J., and Eason, T.G., "On the Use of Reduced-Order Models for a Shallow Curved Beam Under Combined Loading," Proceedings of the 49th Structures, Structural Dynamics, and Materials Conference, Schaumburg, Illinois, Apr. 7-10, 2008. AIAA Paper AIAA-2008-1873.
[20] Kim, K., Radu, A.G., Wang, X.Q., and Mignolet, M.P., "Nonlinear Reduced Order Modeling of Isotropic and Functionally Graded Plates," *International Journal of Non-Linear Mechanics*, Vol. 49, pp. 100-110, 2013.
[21] Perez, R.A., Wang, X.Q., and Mignolet, M.P., "Non-Intrusive Structural Dynamic Reduced Order Modeling for Large Deformations: Enhancements for Complex Structures," *Journal of Computational and Nonlinear Dynamics*, Vol. 9, No. 3, pp. 031008-1 - 031008-12, 2014.
[22] Kuether, R.J., Allen, M.S., and Hollkamp, J.J., "Modal Substructuring for Geometrically Nonlinear Finite Element Models," *AIAA Journal*, Vol. 54, pp. 691-702, 2016.
[23] Kuether, R.J., Deaner, B., Allen, M.S., and Hollkamp, J.J., "An Evaluation of Nonlinear Reduced Order Models used to Compute Nonlinear Normal Modes of Geometrically Nonlinear Structures," *AIAA Journal*, vol. 53, pp. 3273-3285, 2015.
[24] Wang, X.Q., Perez, R., Mignolet, M.P., Capillon, R., and Soize, C., "Nonlinear Reduced Order Modeling of Complex Wing Models," *Proceedings of the 54th Structures, Structural Dynamics and Materials Conference*, Apr. 8-11, 2013, Boston, Massachusetts, AIAA Paper AIAA-2013-1520.
[25] Gogulapati, A., Brouwer, K., Wang, X.Q., Murthy, R., McNamara, J.J., and Mignolet, M.P., "Full and Reduced Order Aerothermoelastic Modeling of Built-Up Aerospace Panels in High-Speed Flows," *Proceedings of the AIAA Science and Technology Forum and Exposition (SciTech2017)*, Dallas, Texas, Jan. 9-13, 2017, AIAA Paper AIAA 2017-0180.

[26] Perez, R., Wang, X.Q., and Mignolet, M.P., "Nonlinear Reduced Order Models for Thermoelastodynamic Response of Isotropic and FGM Panels," *AIAA Journal*, Vol. 49, No. 3, pp. 630-641, 2011.

[27] Matney, A.K., Perez, R.A., and Mignolet, M.P., "Nonlinear Unsteady Thermoelastodynamic Response of a Panel Subjected to an Oscillating Flux by Reduced Order Models, *Proceedings of the 52nd Structures, Structural Dynamics and Materials Conference*, Denver, Colorado, Apr. 4-7, AIAA 2011-2016, 2011.

[28] Matney, A., Mignolet, M.P., Culler, A.J., McNamara, J.J., and Spottswood, S.M. 2015. Panel response prediction through reduced order models with application to hypersonic aircraft. *Proceedings of the AIAA Science and Technology Forum and Exposition (SciTech2015). Orlando, Florida. Jan. 5-9*. AIAA 2015-1630.

[29] Song, P., Wang, X.Q., Matney, A., Murthy, R., Mignolet, M.P., "Nonlinear Geometric Thermoelastic Response of Structures with Uncertain Thermal and Structural Properties," *Proceedings of the AIAA Science and Technology Forum and Exposition (SciTech2017)*, Dallas, Texas, Jan. 9-13, 2017, AIAA Paper AIAA 2017-0181.

[30] Song, P., "Uncertainty Modeling for Nonlinear and Linear Heated Structures," Ph.D., May 2019.

[31] Mignolet, M.P., and Soize, C. "Stochastic reduced order models for uncertain geometrically nonlinear dynamical systems." *Computer Methods in Applied Mechanics and Engineering*, Vol. 197, No. 45, 2008, pp. 3951-3963.

APPENDIX J:

[C4]: Sharma, P., Wang, X.Q., and Mignolet, M.P., "Toward an Uncertain Modeling of Hypersonic Aerodynamic Forces," *Proceedings of the AIAA Science and Technology Forum and Exposition (SciTech2020)*, Orlando, Florida, Jan.6-10, 2020. AIAA-2020-1878.
[T1] : Sharma, P., "Toward an Uncertain Modeling of Hypersonic Aerodynamic Forces," M.S., May 2017.

AIAA SciTech Forum
6-10 January 2020, Orlando, FL
AIAA Scitech 2020 Forum

10.2514/6.2020-1878

TOWARD AN UNCERTAIN MODELING OF HYPERSONIC AERODYNAMIC FORCES

P. Sharma, X.Q. Wang, and M.P. Mignolet

SEMTE, Faculties of Mechanical and Aerospace Engineering,
Arizona State University, Tempe, AZ 85287-6106

ABSTRACT

This investigation lies within the focus of aeroelastic analyses of uncertain structures in hypersonic flow conditions. Given the uncertainty, aleatoric or epistemic, on the structure, it is computationally advantageous to reduce the aerodynamic model complexity as long as the induced epistemic uncertainty is "small" enough not to affect the band of predictions of the response. Within this perspective of uncertainty management, it is desirable to have computationally very efficient, physically-based, surrogates of the fluid forces that provide approximate fluid forces with tunable accuracy. Moreover, such surrogates should be stochastic in that the aerodynamic epistemic uncertainty should be included and modeled. The present investigation provides some recent efforts toward the constructions of such stochastic surrogates in which the pressure is expressed as a sum of a local component, modeled with piston theory, and a global one.

INTRODUCTION

The fielding of hypersonic vehicles has long been a goal of the U.S. Air Force to increase its operational envelope. The design of such vehicles is however a new paradigm owing first to the strong multi-physics interactions between structural response, aerodynamic forces and heating, and heat conduction and to the severity of the aerodynamic and thermal loading which will result in large deformations and strong nonlinearities in the structural response. Further, uncertainties resulting from vehicle-to-vehicle variability (aleatoric uncertainty) and from modeling assumptions (epistemic uncertainty) are expected to be important and to affect significantly the vehicle response. The use of safety factors to address these uncertainties has been shown to be inappropriate, it would lead to overweight vehicles unable to carry out the planned missions.

Thus, the successful design of hypersonic vehicles will require the modeling of all aleatoric and epistemic uncertainties and their propagation to the structural response in a computationally viable framework. A key observation in this regard is that it is not efficient to use the most accurate computational models when aleatoric uncertainty is present. Rather, *it is computationally advantageous to reduce somewhat the model complexity, i.e., allow epistemic uncertainty to increase until it becomes measurable with respect to its aleatoric counterpart.* The process of balancing computational efficiency versus overall uncertainty is referred to here as uncertainty management.

The accurate determination of the fluid forces on a vibrating vehicle represents a very significant effort typically involving unsteady computational fluid dynamics (CFD) runs over a very large grid. Such computations include all effects such as the viscosity of the fluid and are applicable to any level of deformation of the structure. This generality is in contrast with the limited applicability of historical simple (closed form) models, the best known of which is the piston theory (see [1] for discussion of the various piston theory formulations) which *models* the

inviscid fluid forces in a particular set of conditions (see [1]). Notwithstanding its simplicity, the piston theory formulation has been shown [2] to provide an appropriate framework for connecting unsteady forces on a vibrating structure to their quasi-steady equivalent on the statically deformed structure. This finding has then permitted the construction of surrogate models of the unsteady fluid forces, see [3] for a recent application and references. While the reduction of computational effort is very significant, the construction of the surrogate still requires a large number of steady computations which may have be repeated, e.g., on slightly different geometries, when uncertainty in the structural properties/geometry is introduced.

Within the above perspective of uncertainty management, the objective of this paper is to develop computationally very efficient, physically-based, *stochastic* surrogates of the fluid forces that are applicable to *uncertain* structures (with uncertainty in material properties/geometry). For the ensemble of structural samples considered, these surrogates should lead to an uncertainty band on the fluid forces that is the same as the one obtained by using full CFD computations on every sample. Yet, for a particular structure, the surrogate will not necessarily provide a close match of those CFD computations but rather a band around them. The present effort thus focuses first on understanding which physically-based models could be used and how uncertainty could be introduced for a particular, simple structure.

AEROELASTIC SYSTEM

Given the existing discussions of [2,3], the present effort focuses on a simple aeroelastic system as a first validation case, i.e., the hypersonic flow over a flexible straight clamped-clamped beam. The beam of length 1.5m and thickness (th.) 5 mm is part of a wedge of angle 5 degree in a uniform upstream flow of Mach equal to 5, 7, 8, 10, or 12 at an altitude of 30km. The beam was discretized by finite elements using a uniform mesh of 1001 nodes. It was then deformed along each of its first four normal modes at various amplitudes, see Table 1 for details, with positive amplitudes corresponding to beam displacements into the fluid flow. The corresponding steady pressure distributions were computed using CFL3D with the Menter k-ω SST turbulence model and for each of the upstream Mach numbers. From the perspective of generating mode independent models later, note that the range of amplitudes for modes 1 and 2 is larger than for modes 3 and 4, hence a wider distribution of data is used for the former modes but that there is an increasing complexity of the pressure with mode number that counterbalance the lower amplitudes at higher modes.

Table 1. System steady configurations for surrogate generation and validation

mode	Amplitudes (thickness)	upstream Mach
1	±8, ±6, ±4, ±3, ±2, ±1	12, 10, 8, 7, 5
2	±7, ±6, ±4, ±3, ±2, ±1	12, 10, 8, 7, 5
3	±3, ±2.5, ±2, ±1.5, ±1, ±0.5	12, 10, 8, 7, 5
4	±1.5, ±1, ±0.5	12, 10, 8, 7, 5

Unsteady computations were also carried for 2.25 cycles of harmonic motions of the beam along each of its first four modes with amplitudes and frequencies shown in Table 2 to provide an additional validation of the steady-based surrogates.

Table 2. System unsteady configurations for surrogate validation

mode	Amplitudes (thickness)	Frequency (Hz)	upstream Mach
1	1, 2, 3, 4, 6	100, 140, 160	12, 10, 8, 5
2	1, 2, 3, 4	100, 140, 160	12, 10, 8, 5
3	0.5, 1, 1.5, 2, 3	100, 140, 160	12, 10, 8, 5
4	0.5, 1, 1.5	100, 140, 160	12, 10, 8, 5

DETERMINISTIC MODELING EFFORT SUMMARY

Local Modeling – Piston Theory

The first physically-based model considered was piston theory which relates the pressure at one point to only the material derivative of the beam displacement *at that point* and *at that time*. Accordingly, such models will here be referred to as *local* as they would predict the pressure using only local information on the structural deformations. Such local models with powers 0, 1, 2, and 3 (as is usual) of the material derivative and coefficients dependent on the Mach number but not the mode considered were found to be insufficient to accurately represent the pressure field from the available, viscous CFD data, see Fig. 1 for an example. Rather, it was found that the approximation should also involve powers and combinations of the displacement and its integral, see [4] for details. Such approximations are succinctly written as

$$C_p(x,t) = C_p^L\left(s, s^2, s^3, w, i, s\,w, \ldots\right) \tag{1}$$

where $w(x,t)$ is the displacement at position x on the beam at time t. Moreover,

$$s(x,t) = \frac{Dw}{Dt} = \frac{\partial w}{\partial t} + U_\infty \frac{\partial w}{\partial x} \qquad \text{and} \qquad i(x,t) = \int_0^x w(z,t)\,dz \tag{2}$$

are the material derivative and integral of the displacement.

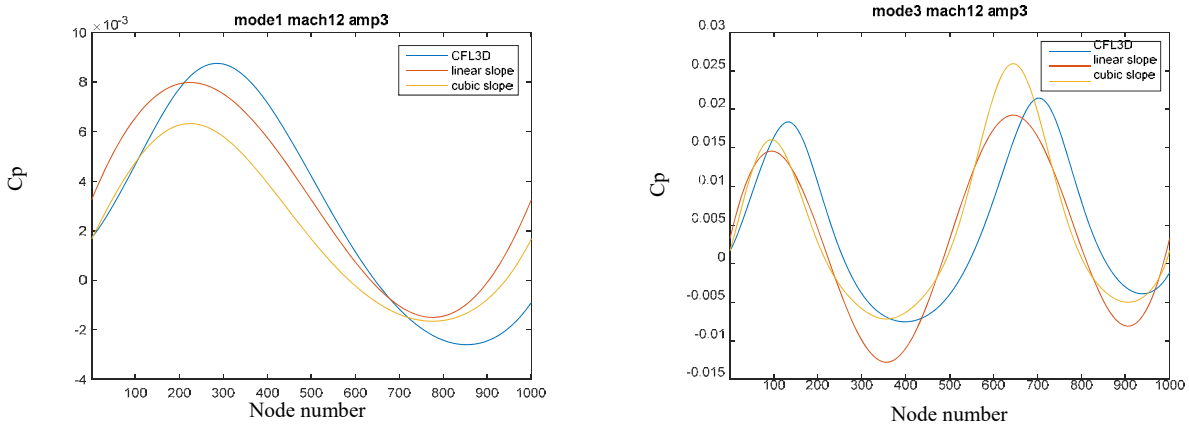

(a) (b)

Figure 1. Comparison of steady C_p from CFL3D (blue) and piston theory with linear (red) and cubic (yellow) slope terms for Mach 12, amplitude +3 th. and (a) mode 1, (b) mode 3.

Local – Global Modeling

The need to include notably more variables than the material derivative in Eq. (1) to obtain an appropriate matching of the CFD data prompted an investigation of other physically-based

models. Of particular interest was the unified hypersonic model of [1] in which the introduction of a limited spatial (downstream) coupling between pressure at neighboring locations was shown to provide significant improvements over the piston theory predictions. Based on that finding, the approximation of the pressure field was written as the sum of a local (as in Eq. (1)) and a "global" component C_p^G, i.e.,

$$C_p(x,t) = C_p^L\left(s, s^2, s^3\right) + C_p^G = \alpha_0 + \alpha_1 s + \alpha_2 s^2 + \alpha_3 s^3 + C_p^G \tag{3}$$

where the local term was assumed to be a linear combination of a constant and the first three powers of *s* only with α_i dependent on the Mach number but not the mode of deformation. Two different construction of the global components C_p^G are described below.

ARMA-Based Global Modeling

To induce a coupling between pressure values at neighboring locations, the global component C_p^G was modeled through an Autoregressive Moving Average (ARMA) difference equation, i.e.,

$$C_p^G(x_n,t) = -\sum_{j=1}^{m} a_j\ C_p^G\left(x_{n-j},t\right) + \sum_{l=1}^{r}\sum_{k=0}^{p} b_k^{(l)}\ Z_l\left(x_{n-k},t\right) \tag{4}$$

where $x_n = (n-1)\Delta x$ is the *n*th (equidistant) location on the beam and a_j and $b_k^{(l)}$ are parameters of the model. Further, the variables $Z_l(x,t)$ potentially include $s, s^2, s^3, w, i, s\,w$, etc.

Two different types of models were considered. The first one is applicable for the prediction of the pressure distribution induced by motions of the structure along a particular mode and at a particular Mach number. This model is appropriate if it is further assumed/demonstrated that superposition applies and that the pressure distribution induced by a linear combination of modal deflections is the sum of the pressures obtained by considering one mode at a time. The second model is applicable to the entire set of modes at a particular Mach number and thus would be applicable even if superposition cannot be assumed.

The identification of these models was carried out in a least squares manner from the CFD data with the determination of the parameters α_i performed first. The ensuing determination of the ARMA parameters a_j and $b_k^{(l)}$ was carried out using the residual of the pressure distribution through a separate least squares process. In those computations, the variable $Z_l(x,t)$ retained were s, s^2, s^3, and *s i*. Then, shown in Fig. 2 is a typical comparison of the steady pressure distributions obtained by the above approximations with the original CFD data showing the improvements obtained by the addition of the global term.

Next, it was proposed to apply the above two-level composite model, with the same coefficients, to the unsteady situation based on the material derivative, i.e., $\frac{1}{U_\infty}\frac{Dw}{Dt}\left(=\frac{\partial w}{\partial x}+\frac{1}{U_\infty}\frac{\partial w}{\partial t}\right)$ instead of $\frac{dw}{dx}$. The approximate C_p distributions exhibit an offset and a phase difference for smaller displacement (see Fig. 3 (a),(c)) but as the displacement level increases the fitting improves. In contrast to the steady case where the fitting error increased with increasing amplitude, it appears here that the error decreases (see Fig. 3(b),(d)). Since the same

coefficients are utilized to generate the unsteady C_p this is due to the nature of $\frac{Dw}{Dt}$ over time. Similar observations can also be drawn from Fig. 4 corresponding to mode 3 displacement. The improvement at higher negative displacements, Fig. 4(c), (d) is more pronounced than on the positive, Fig. 4(a), (b).

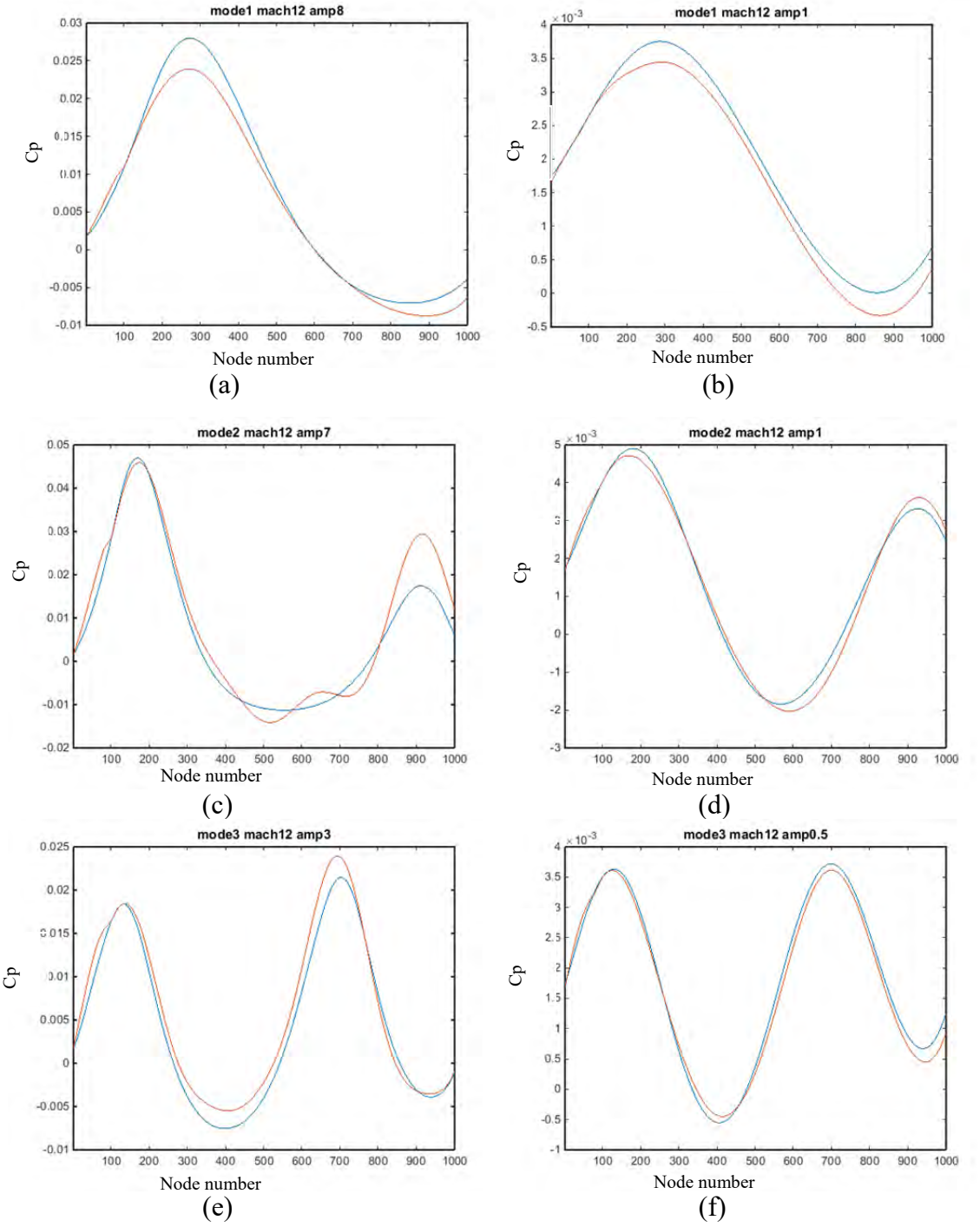

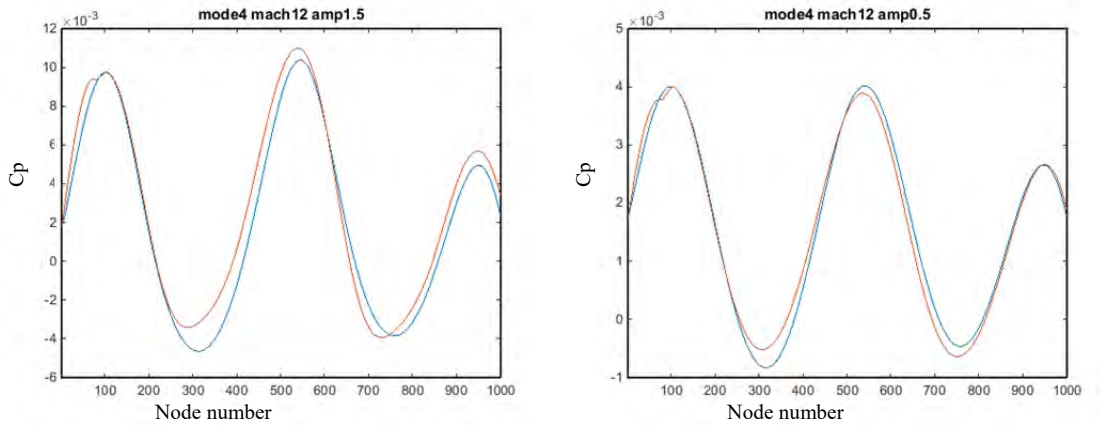

(g) (h)

Figure 2. Comparison of steady C_p from CFL3D (blue) and approximate C_p with composite model of Eqs (3)-(4) (red) for mode 1, Mach 12, (a) amplitude +8th., (b) amplitude +1th.; mode 2, Mach 12, (c) amplitude +7th., (d) amplitude +1th.; mode 3, Mach 12, (e) amplitude +3th., (f) amplitude +0.5th.; mode 4, Mach 12, (g) amplitude +1.5th., (h) amplitude +0.5th.

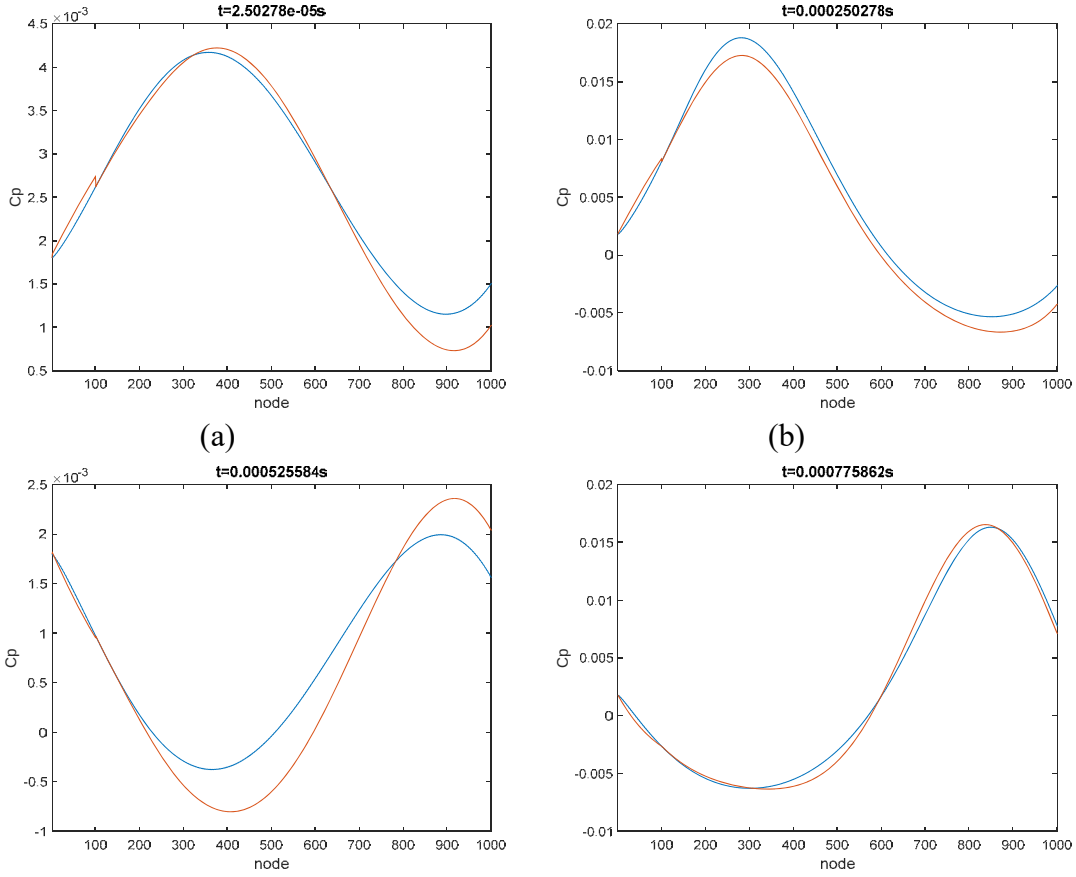

(a) (b) (c) (d)

Figure 3. Comparison of unsteady C_p from CFL3D (blue) and approximate C_p with composite model of Eqs (3)-(4) (red) for mode1 Mach 12 amplitude 6th., frequency 160Hz (a) t = 2.5e-05 s (b) t = 0.00025 s (c) t = 0.00052 s (d) t = 0.00077 s

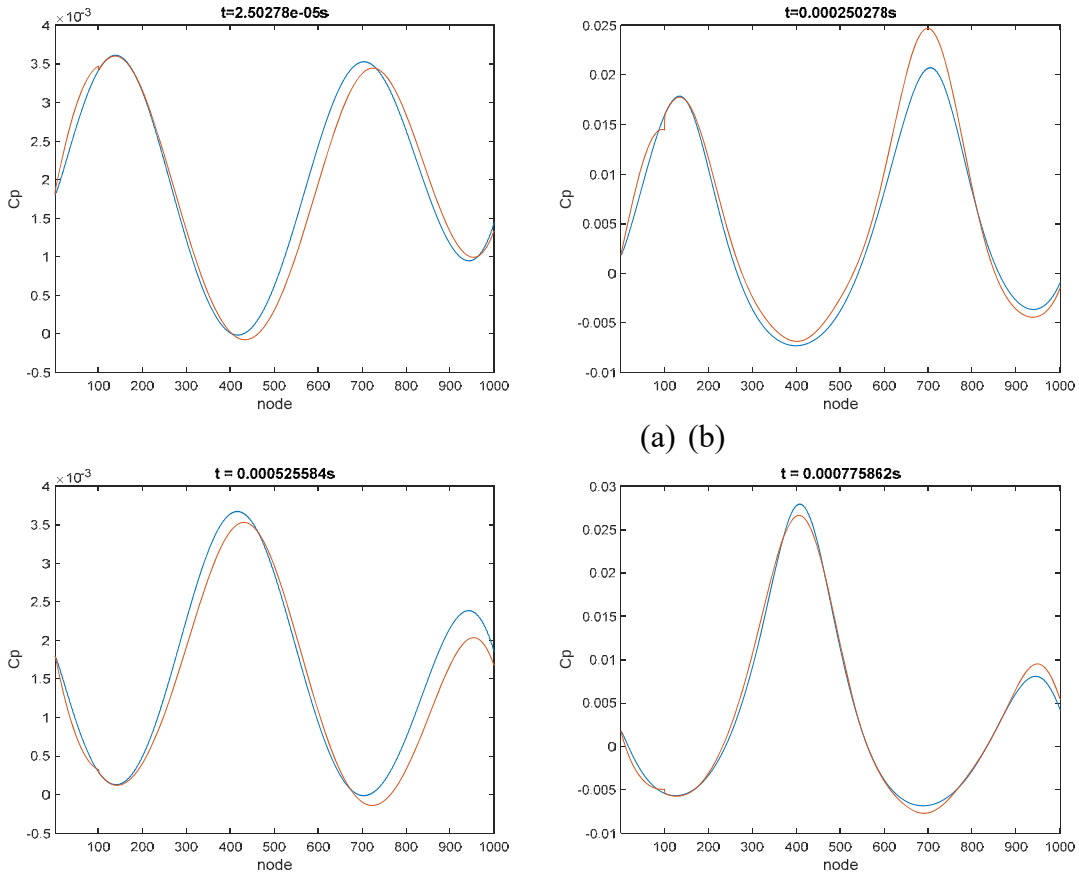

Figure 4. Comparison of unsteady C_p from CFL3D (blue) and approximate C_p with composite model of Eqs (3)-(4) (red) for mode 3, Mach 12, amplitude 3th., frequency 160Hz (a) t = 2.5e-05 s (b) t = 0.00025 s (c) t = 0.00052 s (d) t = 0.00077 s

Modal Amplitude-Based Global Modeling

The pressure component given by Eq. (4) is global because the deformations of the beam at a particular location is propagated in the flow direction through the ARMA model but it is still constructed, as the piston theory term, from local information. Another perspective is to correlate the difference in pressure $C_p - C_p^L$ to the amplitudes q_i, i = 1, 2, 3, 4, of the four structural modes that created the deformations, see Table 1. That is, the global component C_p^G will be expressed as

$$C_p^G(x,t) = \sum_{i=1}^{4} q_i(t) U_i(x) + \sum_{i=1}^{4} q_i^2(t) V_i(x) + \ldots \tag{5}$$

where $U_i(x)$ and $V_i(x)$ are unknown functions dependent on the Mach number. They were estimated here through a least squares of the difference $C_p - C_p^L$ once the piston theory coefficients α_i were determined as in the ARMA-based approach. Note in Eq. (5) that no quadratic term involving two different modal amplitudes q_i and q_j, $i \neq j$, is included here as

that pressure data does not include any such cases. Figures 5 and 6 provide an overall perspective on the accuracy of the composite model of Eqs (3) and (5) and include linear, quadratic, but also cubic approximations of the form of Eq. (5). Both of these figures clearly indicate that the approximation improves significantly by the addition of the linear terms in Eq. (5) but also of the quadratic ones. However, using a cubic model only provides a slight improvement, typically for higher Mach numbers.

For the quadratic and cubic models, the largest relative error norms occur typically (and for all modes) for the lower modal amplitudes. This property results from the least squares process that has more emphasis on the higher modal amplitudes thereby leading to a better fit of those conditions.

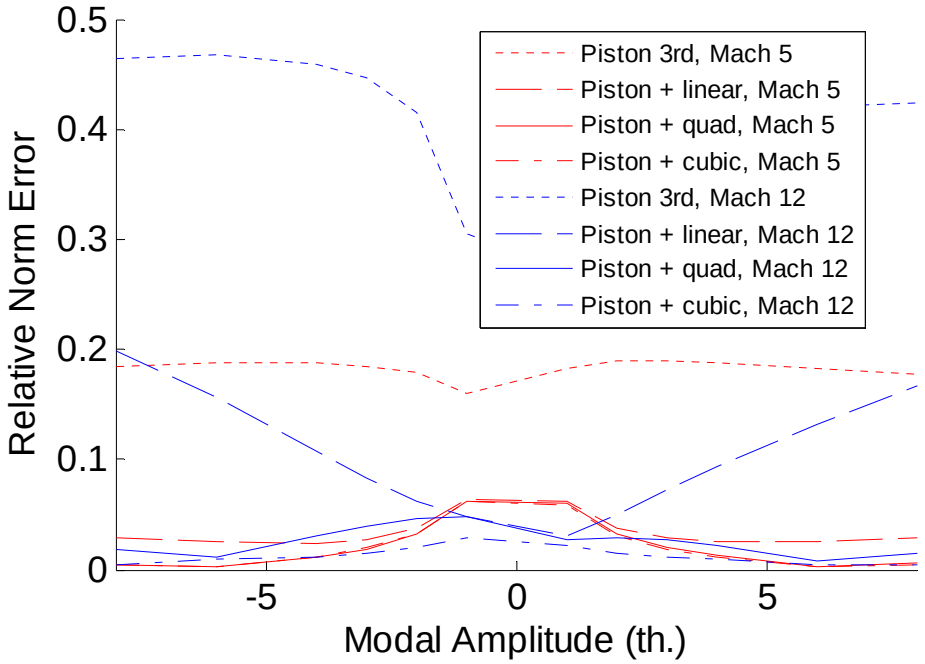

Figure 5. Relative norm of error between the CFL3D C_p distribution and its approximation by the composite model of Eqs (3),(5). Mode 1 deformations.

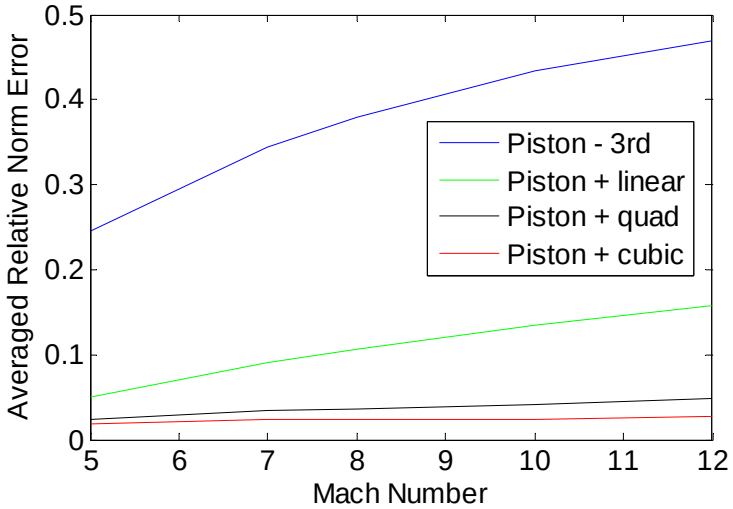

Figure 6. Relative norm error averaged over all deformations vs. Mach number, local and composite models of Eq. (3),(5).

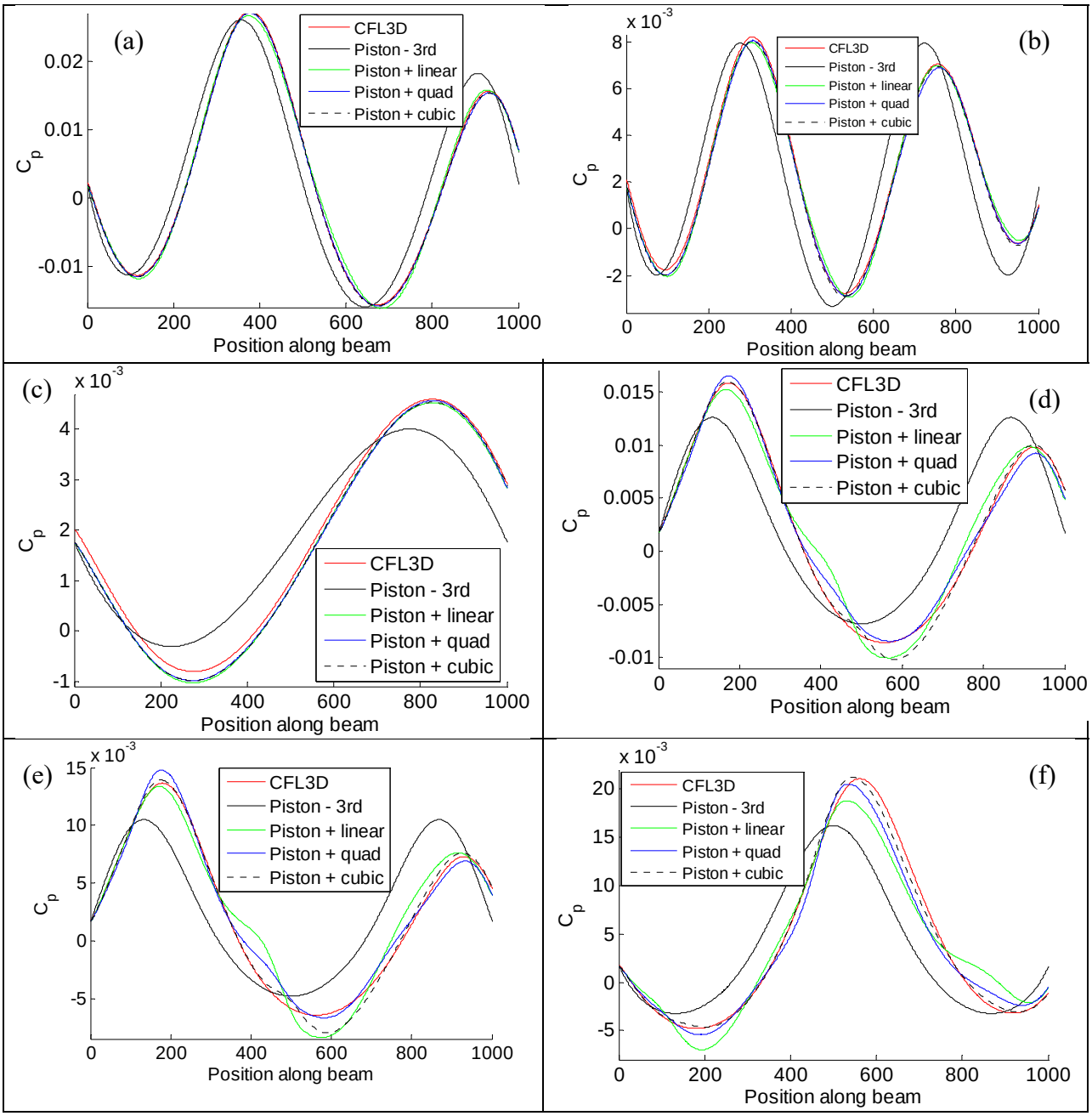

Figure 7. Comparison of steady C_p from CFL3D and approximate C_p with local and composite model of Eqs (3),(5). (a) Mode 3, amplitude -1.5th, Mach 5 (1.8% error), (b) Mode 4, amplitude -0.5th.; Mach 7 (4.48% error), (c) Mode 1, amplitude -1th., Mach 8 (5.56% error), (d) Mode 2, amplitude +3th., Mach 10, (8.33% error), (e) Mode 2, amplitude +3th., Mach 12, (10.31% error), (f) Mode 2, amplitude -3th, Mach 12 (12.7% error).

When considering the Mach dependence, it is seen that the norm error typically increases with this parameter, increasing on average over all amplitudes and mode numbers from 2.4% to 4.8% between Mach 5 and 12 for the quadratic model. The maximum relative error norm with this model is 12.7% observed for deformations of amplitude of -3 thicknesses along mode 2 at Mach 12. As seen in Fig. 7(f), this error originates mostly from a slight shift in the pressure

distributions. Other comparisons leading to approximately 2%, 4%, 6%, 8%, and 10% relative norm errors are also shown in Fig. 7(a)-(e). As can be noted, several of the higher error cases are obtained for mode 2 deformations of which the induced pressure distribution seems harder to model. Based on these results and those shown in Fig. 2, it is suggested that the composite approximation of Eqs (3) and (5) is better than its counterpart from Eqs (3)-(4).

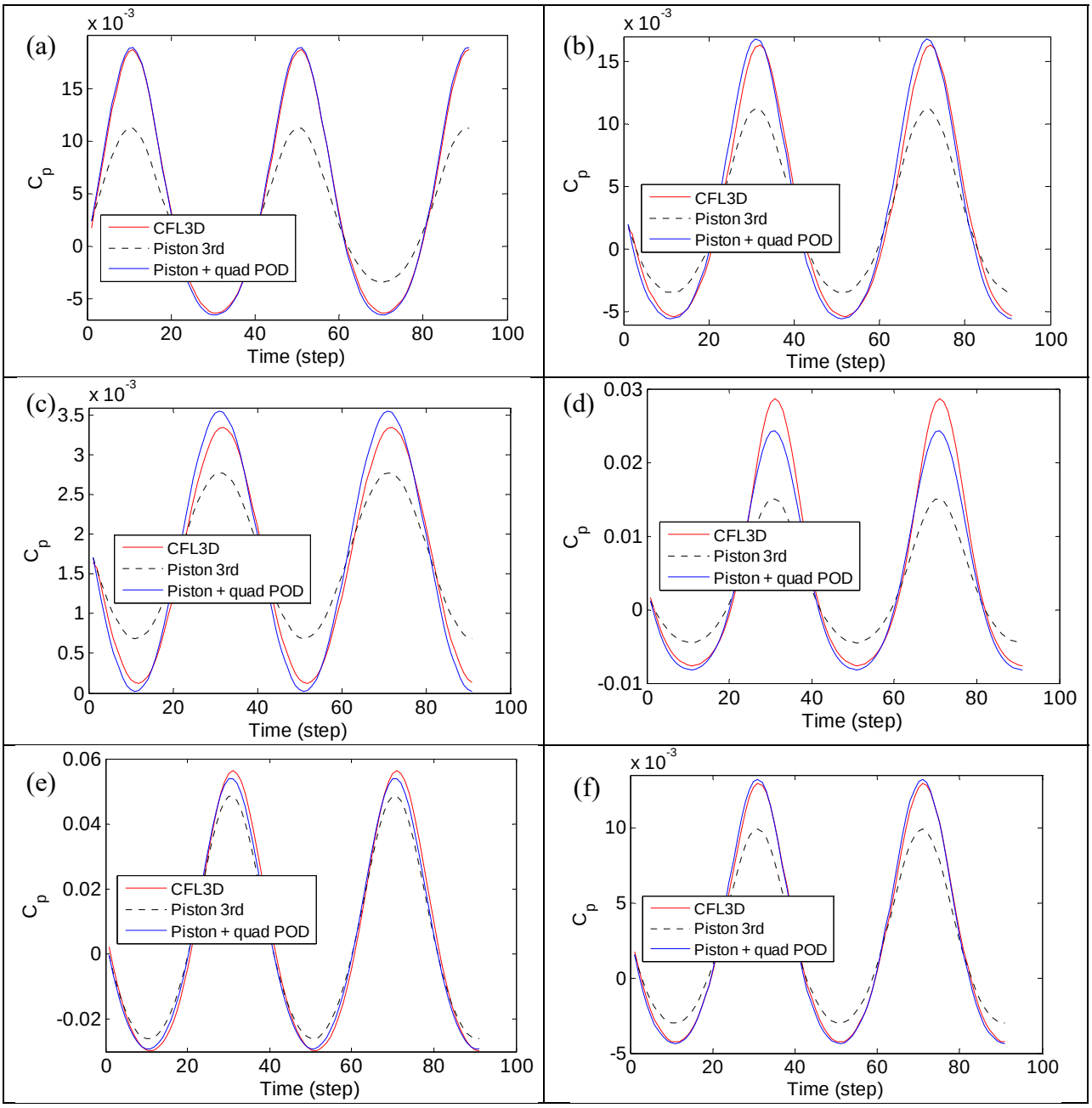

Figure 8. Comparison of unsteady C_p from CFL3D and approximate C_p with local and composite model of Eqs (3),(5). Frequency 160Hz. (a),(b) Mode 1, amplitude 6th, Mach 12. Location: (a) node 300, (b) worst node (846), (c) Mode 1, amplitude 1th, Mach 12, (d) Mode 2, amplitude 4th., Mach 12, (e) Mode 2, amplitude 4th., Mach 5, (f) Mode 4, amplitude 1.5th, Mach 12. Figures (b)-(f) correspond to location with largest error for each case.

As done for the ARMA-based modeling, the composite model of Eqs (3) and (5) was also validated to unsteady cases by using time independent piston theory coefficients α_i and the material derivative instead of the slope. With regard to the global component, the time dependent modal amplitudes were used directly in Eq. (5) so that both local and global components are position and time dependent. The unsteady comparison focused most specifically on evolution with time of the pressure and shown in Fig. 8 are typical examples over the 2.25 cycles with 40 time steps per cycle at the frequency of 160Hz obtained with the quadratic model of Eq. (5).

Figures 8(a) and (b) correspond to the same conditions (mode, amplitude, and Mach) but to different locations along the beam, a generic point for Fig. 8(a) but the location with the worst match between CFL3D and the composite model of Eqs (3), (5) for Fig. 8(b). A slight phase difference between the two curves is seen on the latter that induces a larger difference at certain time steps. The remaining figures, i.e., Figs 8(c)-(f), all correspond to the worst location and show similar trends to those observed in the steady case. Specifically, the smaller modal amplitudes show larger errors than the larger ones, compare Figs 8(b) and (c). Moreover, the pressure distribution induced by mode 2 motions are not as well captured as those of any other mode, compare Figs 8(b) and (d) and Figs 8(d) and (f). Finally, the pressure distribution is more accurately predicted at lower Mach numbers than higher ones, compare Figs 8(d) and (e).

STOCHASTIC MODELING

As expected, the models of Eqs (3)-(4) and (3),(5) do not always provides a close approximation of the CFD results, i.e., they exhibit epistemic uncertainty. The next phase of the modeling effort was then the incorporation of this uncertainty in Eqs (3)-(5) to obtain a stochastic/uncertain aerodynamic model such that the CFD results fit within the band of uncertainty of the model predictions. The uncertainty was introduced in both the local and global component of the model. For the former, each coefficient α_i was considered as independent Gaussian random variable with mean equal to the value identified in the previous section and of equal coefficient of variation, δ. This modeling is consistent with the maximum entropy principle.

ARMA-Based Global Modeling

The introduction of uncertainty in the global component of Eq. (4) was achieved through the randomization of the autoregressive coefficients following the maximum entropy based method proposed by Wang et al. [5].

As shown in Figs 9-12, the combination of the uncertainties on the local and autoregressive components for an equal uncertainty level $\delta = 0.1$ leads to the desired results, i.e., the CFD results are contained within the band of uncertainty and we have constructed a simple approximation of the CFD data that carries/quantifies its epistemic uncertainty.

Modal Amplitude-Based Global Modeling

The introduction of uncertainty in the global component of Eq. (5) was performed by randomizing each of the terms in the sum as

$$C_p^G(x,t) = \sum_{i=1}^{4} \xi_i \, q_i(t) U_i(x) + \sum_{i=1}^{4} \eta_i \, q_i^2(t) V_i(x) + \ldots \tag{6}$$

where ξ_i and η_i, i = 1, 2, 3, 4, are independent Gaussian random variables with unit mean and standard deviation equal to δ, the same standard deviation as that of the local model coefficients.

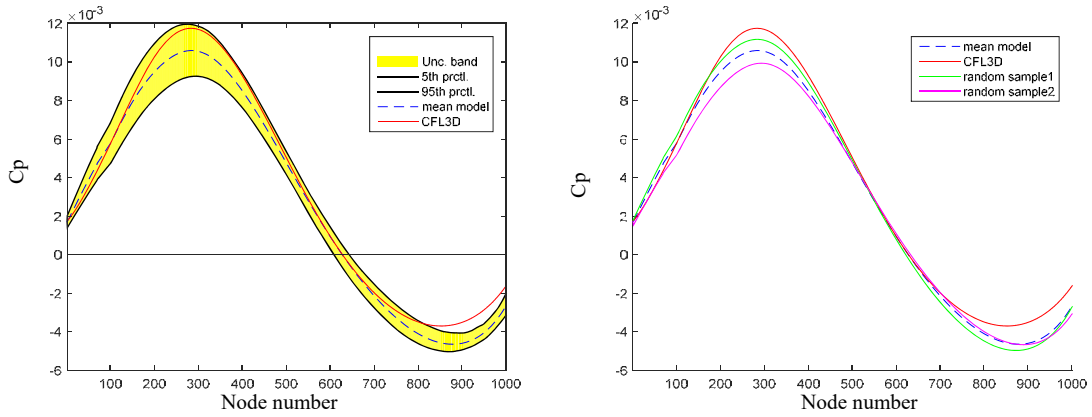

(a) (b)

Figure 9. (a) Uncertainty band on the C_p for the composite model of Eqs (3)-(4). (b) Random samples with CFL3D C_p. Mode 1, Mach 12, amplitude +4th.

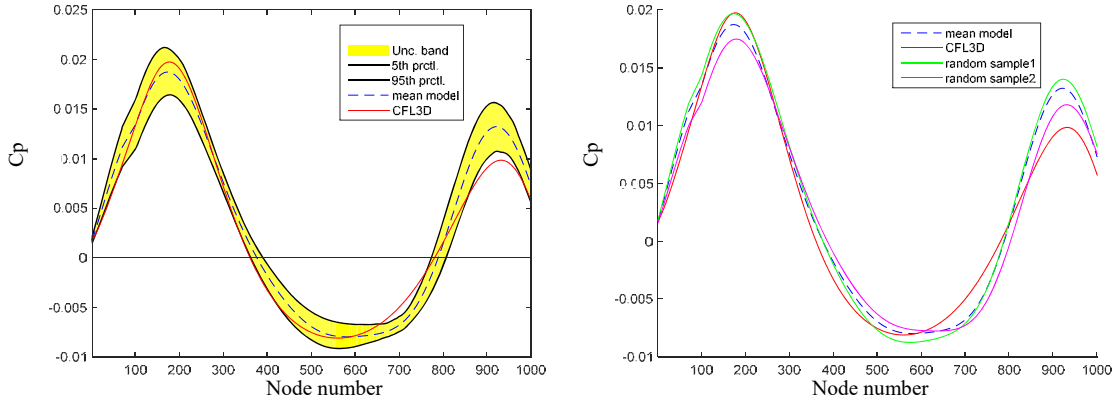

(a) (b)

Figure 10. (a) Uncertainty band on the C_p for the composite model of Eqs (3)-(4). (b) Random samples with CFL3D C_p. mode 2, Mach 12, amplitude +6th.

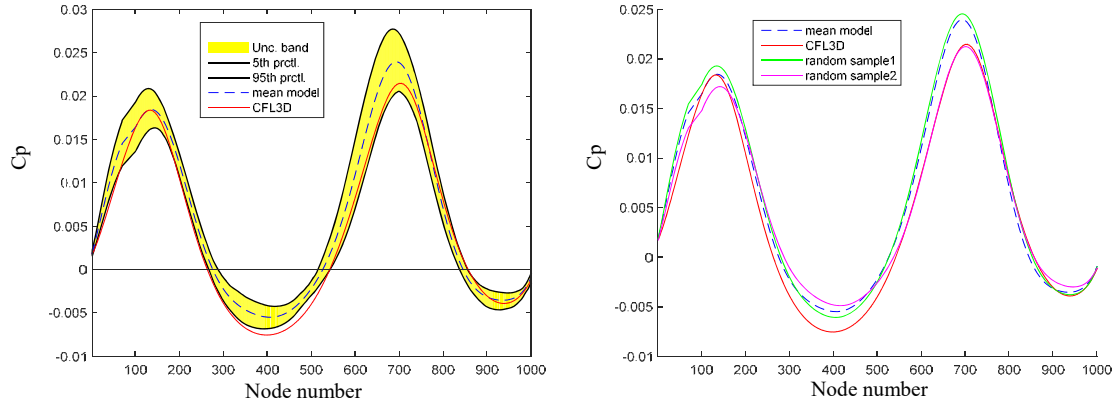

(a) (b)

Figure 11. (a) Uncertainty band on the C_p for the composite model of Eqs (3)-(4). (b) Random samples with CFL3D C_p. mode 3, Mach 12, amplitude +3th.

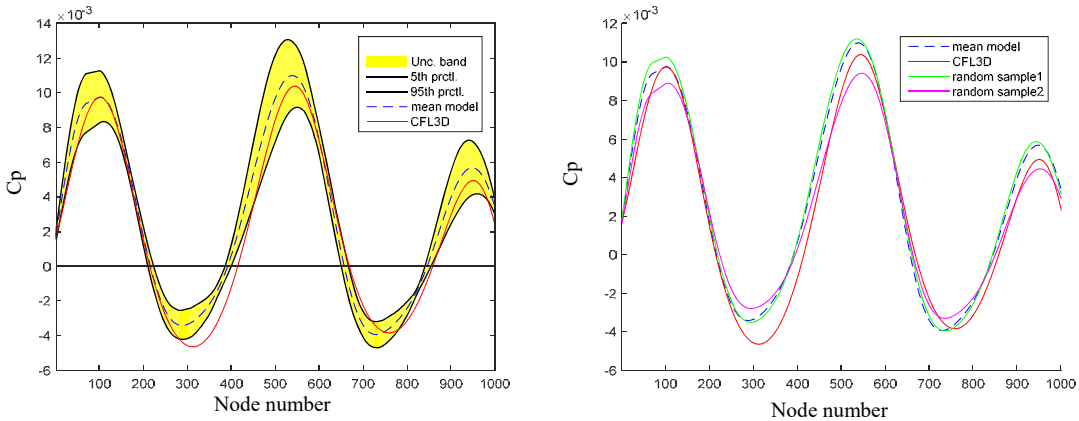

Figure 12. (a) Uncertainty band on the C_p for the composite model of Eqs (3)-(4). (b) Random samples with CFL3D C_p. Mode 4, Mach 12, amplitude +1.5th.

The value of this standard deviation was estimated using the maximum likelihood approach from the steady data at each Mach number. It is found that δ decreases quite linearly as the Mach number is increased, see Fig. 13.

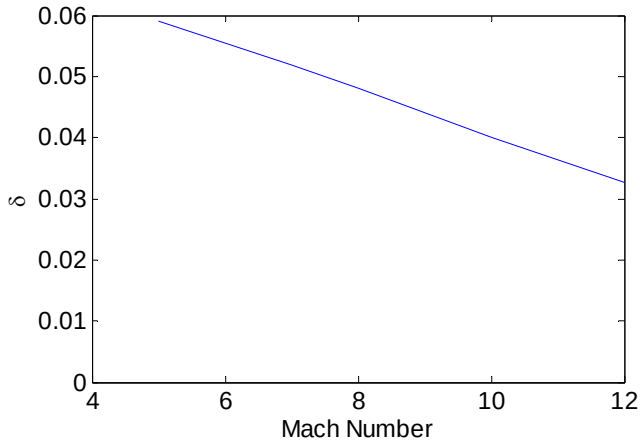

Figure 13. Common standard deviation δ vs. Mach number estimated from maximum likelihood.

To evaluate the effects of this uncertainty on the predicted pressure distributions, the cases of Fig. 7(c)-(f) were considered again and shown in Fig. 14 are the mean predictions as well as the associated uncertainty bands corresponding to the 5th and 95th percentiles with the quadratic model in Eqs (5)-(6). As expected, it is seen that the differences between the pressure distributions predicted by CFL3D and the composite model fit within the uncertainty band with the exception of the largest deviations in the worst cases, see Figs 14(c),(d). On that basis, the proposed uncertainty modeling appears appropriate.

The final validation was carried out on unsteady data, more specifically on the cases of Fig. 8(b)-(e), see Fig. 15. It is seen that the uncertainty band on the time evolution of the response is broad near the peak values but thin otherwise. Accordingly, the uncertainty accounts well for reasonable differences in the peak, as in Figs 15(b),(d), not the worst cases, as in Fig. 15(c), but not well for small phase differences, see Fig. 15(a).

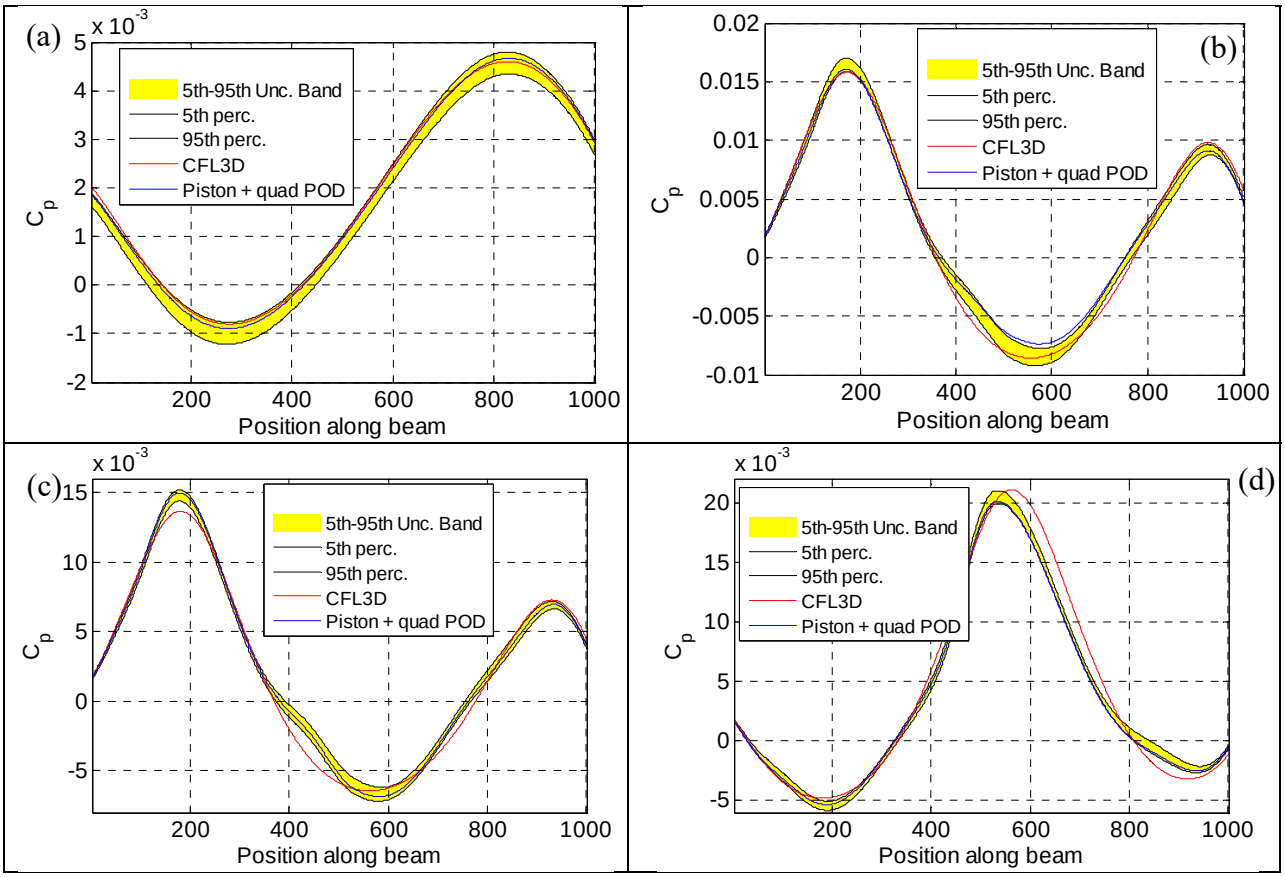

Figure 14. Uncertainty band on steady C_p from composite model of Eqs (3),(5) and CFL3D predictions. (a) Mode 1, amplitude -1th., Mach 8 (5.56% error), (b) Mode 2, amplitude +3th., Mach 10, (8.33% error), (c) Mode 2, amplitude +3th., Mach 12, (10.31% error), (d) Mode 2, amplitude -3th, Mach 12 (12.7% error).

CONCLUSIONS

The present investigation focused on the development of stochastic surrogates of the aerodynamic pressure induced by displacements of the structure in hypersonic flow conditions. The randomness in the surrogate is of epistemic origin to account for the lack of accuracy of the otherwise deterministic surrogate which is constructed first.

In constructing these surrogates, it was first confirmed that a model involving only the local slope, e.g., as in piston theory, does not predict well the viscous pressures. While improvements of this model can be obtained by including additional quantities such as displacement and integral thereof, it was concluded that a global component of the pressure must be included as well. Two such global components were proposed and analyzed. The first is based on an autoregressive moving average model which propagates the set of local displacements and slopes along the flow direction thereby inducing a global effects. The second global component is based on a correlation between the differences in steady pressure obtained from viscous CFD and from the local model and the amplitudes of the modal deformations to which they correspond. As such, this surrogate is only applicable as long as the structure deforms along the modes considered in the database while the ARMA-based one may be used with other deformations as it only involves the set of displacements and slopes. Both surrogates were built using steady data

but were shown to be applicable as is to unsteady pressures induced by time varying displacements. Globally, it was found that the deterministic modal amplitude-based surrogate provided a closer fit of the viscous CFD data than the ARMA-based one.

Epistemic uncertainty was introduced in both composite models, i.e., combinations of local and global components, by randomizing the coefficients of the local model and the coefficients of the autoregressive model, for the ARMA-based surrogate, or the modal amplitudes, for the modal amplitude-based surrogate. This modeling of uncertainty produces samples of the pressure which are smooth and thus physically admissible. Moreover, calibrating the uncertainty level permits to obtain uncertainty bands on the pressure prediction that include the viscous CFD data so that this data can be considered as a sample of the stochastic surrogates as was desired.

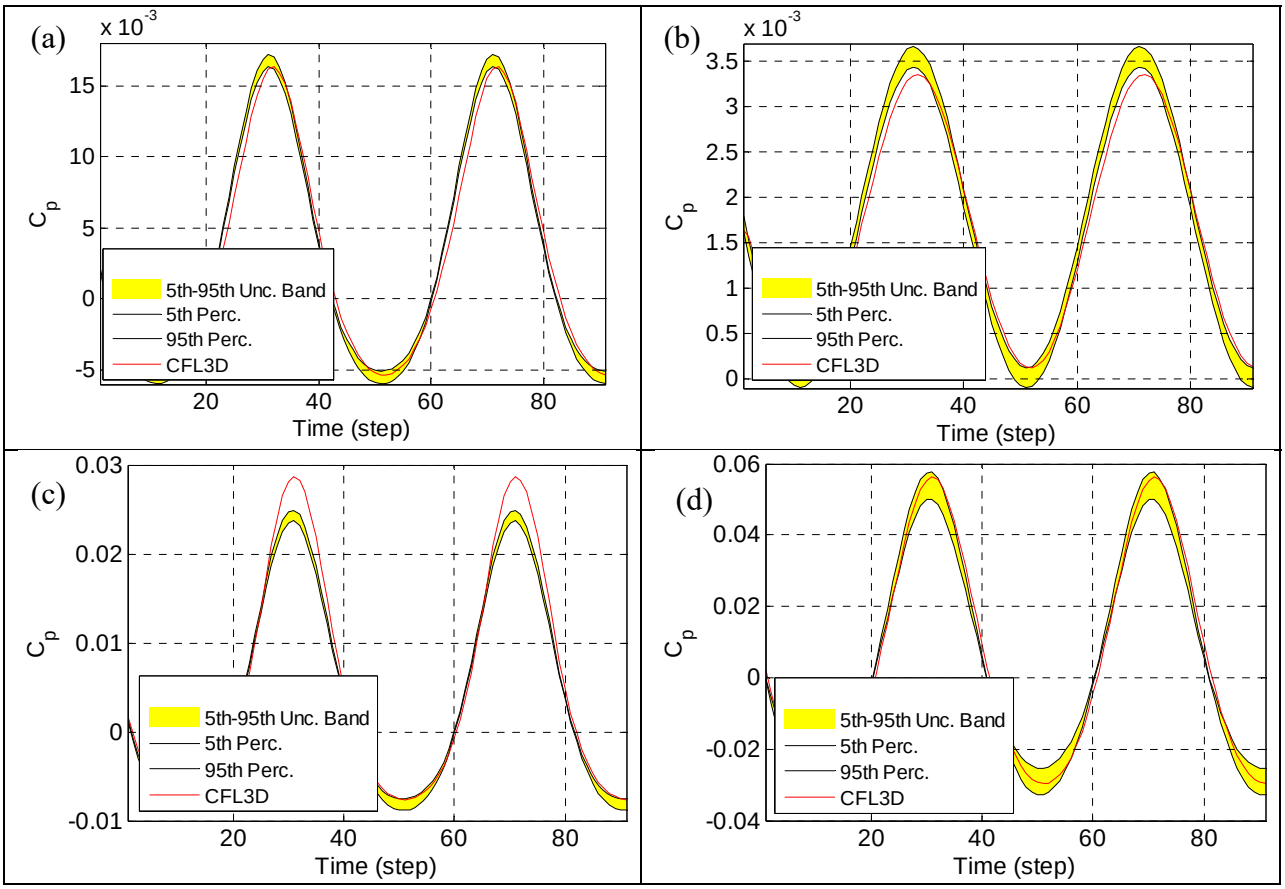

Figure 15. Uncertainty band on unsteady C_p from composite model of Eqs (3),(5) and CFL3D predictions. Frequency 160Hz. (a) Mode 1, amplitude 6th, Mach 12, (b) Mode 1, amplitude 1th, Mach 12, (c) Mode 2, amplitude 4th., Mach 12, (d) Mode 2, amplitude 4th., Mach 5. All figures correspond to location with largest error in the mean prediction for each case.

ACKNOWLEDGEMENTS

The authors gratefully acknowledge the financial support of this work by the contract FA9550-16-1-0021 from the Air Force Office of Scientific Research with Dr. Jaimie Tiley as program manager. The authors are greatly appreciative of Prof. J.J. McNamara and his group for sharing the CFD data.

REFERENCES

[1] Liu, D.D., Yao, Z.X., Sarhaddi, D., and Chavez, F., "From Piston Theory to a Unified Hypersonic – Supersonic Lifting Surface Method", *Journal of Aircraft*, Vol. 34, No. 3, 1997, 304-312.

[2] Crowell, A.R., McNamara, J.J., and Miller, B.A., "Hypersonic Aerothermoelastic Response Prediction of Skin Panels Using Computational Fluid Dynamic Surrogates," *ASD Journal*, Vol. 2, No. 2, pp. 3-30, 2011.

[3] Gogulapati, A., Brouwer, K., Wang, X.Q., Murthy, R., McNamara, J.J., and Mignolet, M.P., Full and Reduced Order Aerothermoelastic Modeling of Built-Up Aerospace Panels in High-Speed Flows, *Proceedings of the AIAA Science and Technology Forum and Exposition (SciTech2017)*, Dallas, Texas, Jan. 9-13, 2017.

[4] Sharma, P., *Toward an Uncertain Modeling of Hypersonic Aerodynamic Forces*, M.S. Thesis, Arizona State University, May 2017.

[5] Wang, Y., Wang, X.Q., Mignolet, M.P., Yang, S., Chen, P.C., "Modeling of Uncertain Spectra Through Stochastic Autoregressive Systems," Mechanical Systems and Signal Processing, Vol. 70-71, pp. 506-526, 2016.

Assessment and Application of

Maximum Entropy Based Stochastic Modelling

by

Pulkit Sharma

A Thesis Presented in Partial Fulfillment
of the Requirements for the Degree
Masters of Science

To be reviewed April 2017 by the
Graduate Supervisory Committee:

Marc Mignolet, Chair
Yongming Liu
Jack McNamara

ARIZONA STATE UNIVERSITY
May 2017

ABSTRACT

Analysis of structure under Hypersonic flow is computationally intensive due to complex coupled behavior between fluid dynamics, structural dynamics, control and material properties. Current investigation focusses on analysis and calibration of Stochastic Piston Theory based surrogate model for reconstructing steady and unsteady pressure coefficient under inviscid hypersonic flow over clamp-clamp beam. Mean model based on local linear and cubic downwash are analyzed. The model is enriched with contributing local linear and quadratic displacement, curvature and displacement integral terms to capture the phase difference in downwash constructed Cp. At second stage, model is further enriched with global terms (upstream properties) of the beam which leads to ill conditioned matrices due to fine mesh. Conditioning is improved by considering only discrete global terms. Third stage is enrichment of global formulation with Cp for upstream nodes leading to an ARMA model with moving average of nonlinear dsci or cubic slope. Finally, a two-level composite model where initial modelling with local cubic slope and modelling of residual with cubic slope ARMA provide the most efficient and simplest mean model. This model is applicable to reconstructing steady Cp (downwash = $\frac{\partial w}{\partial x}$) and unsteady Cp (downwash = $\frac{\partial w}{\partial x} + \frac{1}{U_\infty}\frac{\partial w}{\partial t}$). For generation of stochastic samples auto-regressive coefficients are randomized with maximum entropy approach. The uncertainty band constructed doesn't have desired features to capture all the peaks in the data. Local model is randomized with maximum entropy approach in two ways – (i) randomizing model coefficients and (ii) randomizing diagonal, positive definite and symmetric matrix of coefficients. Former approach leads to uncertainty band

characteristic proportional to local component of the reconstruction. A composite technique is presented with random local and auto-regressive coefficients capturing the validation data with smooth reconstruction. Later approach leads to globalization of the construction due to non-zero elements at non-diagonal locations of random coefficients. The feature of globalization of the random local model generated by maximum entropy approach is studied for simple system of 1D beam with winkler foundation. This is established by inability to optimally reconstruct corresponding full tridiagonal stiffness matrix from reduced random stiffness matrices. Random stiffness matrices lead to global response to a local force.

ACKNOWLEDGMENTS

I would like to thank my committee members, Dr. Mignolet for advisement and guidance through the project, Dr. McNamara for the CFL3D simulation data, and Dr. Liu for his participation in the committee. I would also like to acknowledge Dr. Ricardo Perez for continuous support and clarifications on the test cases for the data and the financial support of this work by the contract FA9550-16-1-0021 from the Air Force Office of Scientific Research with Dr. Dr. Jaimie Tiley as program manager.

TABLE OF CONTENTS

Page

1. Introduction

Deterministic response and characterization have been a norm for solving the engineering problems but in real world scenarios these deterministic results form a subset of all possible results. For instance, deterministic dynamic response of a structure mathematically depends on physical properties and loading conditions and to be calculated for design specification but deviation in manufacturing processes and operating load in service are inevitable. To accommodate deviation in physical parameter (dimensions, stiffness etc.) or loading conditions stochastic outcomes can be developed through Monte Carlo simulation. Joint Probability Density Function for each parameter must be postulated to generate stochastic outcomes from the model. A Parametric approach require exhaustive experimental/physical samples to proceed which in most practical cases are not available. In most cases, only marginal probability density function can be formulated. Unlike deterministic analysis, here a band of response is obtained and the width depends on magnitude of uncertainty and model characteristics. To tackle the unavailability of data, Soize [1] introduced a Non-Parametric Uncertainty Quantification methodology initially for applications in matrix based structural dynamics system.

Non-Parametric methodology mandates that (i) Matrices are positive definite (ii) Mean for matrices are prescribed ($\overline{A} = E[A]$) and (iii) Overall variance for matrices are prescribed. Elements (A_{ij}) can have broad set of distribution and the one selected should put large emphasis on deviation from mean which ensures robustness of design under limited Monte Carlo Simulations. [7], [8] discusses that these properties can be achieved by selecting distribution maximizing the statistical entropy given above constraints. To

satisfy the conditions, A is generated as $A = \bar{L} H H^T \bar{L}^T$, where $\bar{L}$ is Cholesky Decomposition of $\bar{A}$ and H is lower triangular matrix for which all elements are statistically independent. Probability density functions for diagonal (H_{ii}) and non-diagonal (H_{il}) elements of $H H^T$ are given by

$p_{H_{ii}}(h) = C_{ii}\, h^{p(i)} \exp[-\mu h^2], h \geq 0$

$p_{H_{il}}(h) = C_{il} \exp[-\mu h^2], i \neq j$

where,

$$p(i) = N - i + 2\lambda - 1$$

$$\mu = \frac{N + 2\lambda - 1}{2}$$

$$C_{ii} = \frac{2\mu^{\frac{p(i)+1}{2}}}{\Gamma((p(i)+1)/2)}$$

$$C_{il} = \sqrt{\frac{\mu}{\Pi}}$$

With the above distribution, diagonal elements H_{ii} are obtained as $\sqrt{\frac{Y_{ii}}{\mu}}$ where Y_{ii} is gamma distributed with parameter (p(i) - 1)/2. Non-diagonal elements H_{il} ($i \neq l$) are obtained as normal distributed variables with standard deviation $\sigma = \frac{1}{\sqrt{2\mu}}$. λ is an independent variable for statistical distribution of random matrices H and A. The correlation to the variability in the experimental/physical data is obtained by defining an overall measure of variability given by

$$\delta^2 = \frac{1}{N} E\left[\left\| HH^T - I_N \right\|_F^2\right] = \frac{N+1}{N + 2\lambda - 1}$$

where $\| \ \|_F$ is frobenius norm. The generation process starting with calibration of δ with given data will give matrices with desired features. This approach was introduced for application to matrix based systems in structural dynamics but has been since suitably modified and applied to other applications. Since parameterization is not essential for maximum entropy approach, so aleatory (variability of parameters) and epistemic (variability due to model deficiency) can be modelled using the same approach.

Design and application of projectiles with hypersonic velocity is an important ongoing research in aerodynamics. Due to complex nature of the coupling of structural, fluid, material and control phenomenon involved, the orthodox CFD computation are expensive and leads to requirement of computational surrogate. McNamara et. al. [1] have been successful in modelling time dependent component of pressure by piston theory surrogate hence removing the need to compute time series for unsteady pressure. The model demands to calculate steady Cp through CFD solution and further use the surrogate to calculate unsteady pressure. In the current work piston theory based surrogate model is calibrated to model Steady Cp. In the process, steady Cp is modelled by local slope from classical piston theory, effect of global parameters is studied with direct and Auto-Regressive Moving-Average (ARMA) modelling approaches. The peculiar feature of high speed flow, that it causes complex and nonlinear loading conditions under service. The uncertainty in the environment of flight coupled with deviation in manufacturing process and material properties from the design specification (in this context, mean values) requires an aleatory uncertainty modelling with the model. Using non-parametric methodology uncertainty can be modelled without having to differentiate between aleatory and epistemic. Hence this gives us an opportunity to model pressure under

hypersonic flow with simplistic classical theories (piston theory) and epistemic uncertainty to cover the deficiencies.

Application is divided in two sections; Chapter 2 discusses calibration of mean piston theory based surrogate model for modelling of coefficient of pressure for hypersonic flow over clamp-clamp beam. The models evaluated are local linear and cubic slope, global linear and cubic slope, local linear and nonlinear dsci (displacement, slope, curvature, displacement integral), global linear and nonlinear dsci, Auto-regressive Moving-average (various configurations). Secondly, Chapter 3 discusses performance of uncertainty propagation in the global, ARMA and composite models by randomizing the coefficients through Non-Parametric approach and by direct marching of noise. In Chapter 4, stochastic reduced order stiffness matrices generated by the non-parametric approach for their feasibility to physically feasible system (i.e. tridiagonal matrix). The correlation will be achieved by generating banded matrices of full order corresponding to reduced order stochastic matrices. For the reverse optimization, we will be looking at performance of Lagrange multipliers and MATLAB TOOLBOX (fmincon & fminsearch). Scope of the analysis is reduced model of order 2 to 20 for a simply supported beam with 1001 nodes.

Chapter 2. Piston Theory based surrogate for hypersonic flow: Mean Model

Under an inviscid flow and away from shock Piston Theory introduced by Lighthill [2] claims that gradient in the direction of flow is small as compared to gradient in perpendicular direction of flow. As velocity of flow increases within supersonic range this relation become prominent and local pressure coefficient is a function of local linear gradient.

$$v_n = \frac{\partial Z(x,y,t)}{\partial t} + V_\infty \left[\frac{\partial Z(x,y,t)}{\partial x} + \alpha_s \right]$$
$$\text{where, } Z(x,y,t) = \omega_d(x,y,z,t) + Z_{str}(x,y)$$

Piston Theory was further improved by Rodden et. al. [10] by including cubic terms in addition to linear terms.

$$Cp = \frac{2}{M^2}\left[c_1\left(\frac{w}{a_0}\right) + c_2\left(\frac{w}{a_0}\right)^2 + c_3\left(\frac{w}{a_0}\right)^3 \right]$$

where, w is upwash

$c_1 = 1, c_2 = (\gamma+1)/4, c_3 = (\gamma+1)/12$ for piston theory

As we move into hypersonic range of flow Piston Theory approximation becomes inaccurate. In this chapter, modelling of Piston Theory based surrogate is explored to represent Steady and Unsteady Cp with hypersonic flow over clamp-clamp beam. Table 1 gives detail of the CFD solutions of steady pressure coefficients for creating and validating the model. Each beam loading test case is under single normal mode with various amplitudes for different mach number of inviscid fluid flow over the beam. Positive amplitude refers to beam displacement into the fluid flow and negative refers to

away from fluid flow. From the perspective of generating mode independent model, range of amplitudes for mode 1 and mode2 of nonlinear Cp is larger than mode 3 and mode 4 hence a wider distribution of data is used for those modes and on the other hand factor of increasing complexity with mode counter balance it.

Table 1

CFD solution (steady Cp) data for model generation and validation

mode	Amplitude	Mach
1	+ and - 8, 6, 4, 3, 2, 1	12, 10, 8, 7, 5
2	+ and - 7, 6, 4, 3, 2, 1	12, 10, 8, 7, 5
3	+ and - 3, 2.5, 2, 1.5, 1, 0.5	12, 10, 8, 7, 5
4	+ and - 1.5, 1, 0.5	12, 10, 8, 7, 5

Steady data can be categorized in four overlapping bins to visualize the effect of each parameter (mode, magnitude of amplitude, polarity of amplitude and mach number). Figure 1 shows the variation for mode 1, coefficient of pressure increases non-linearly with amplitude and decreases with a phase generation with mach number

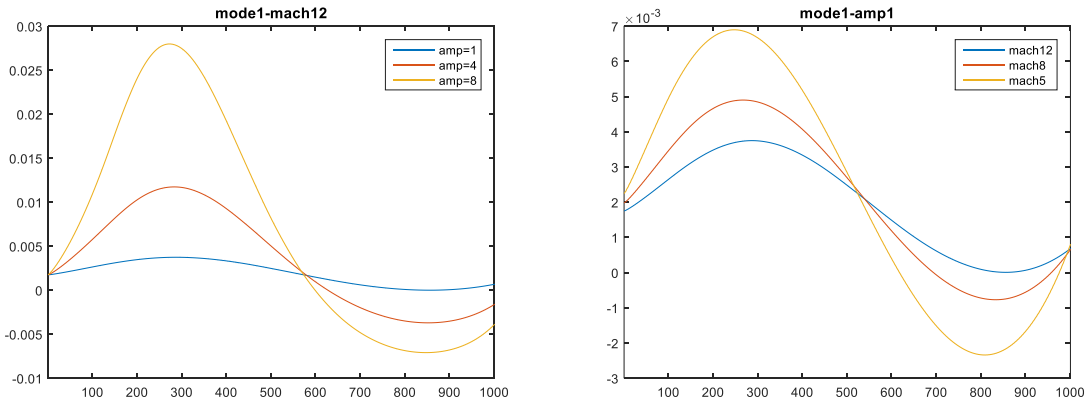

(a) (b)

Figure 1. Variation of steady Cp for mode 1 with (a) amplitude for mach 12 (b) mach number for amplitude =1

Figure 2 shows the variation for mode 3, coefficient of pressure increases linearly with amplitude (unlike mode 1 because of smaller range of amplitude compared to mode 1) and decreases and generating phase difference with mach number.

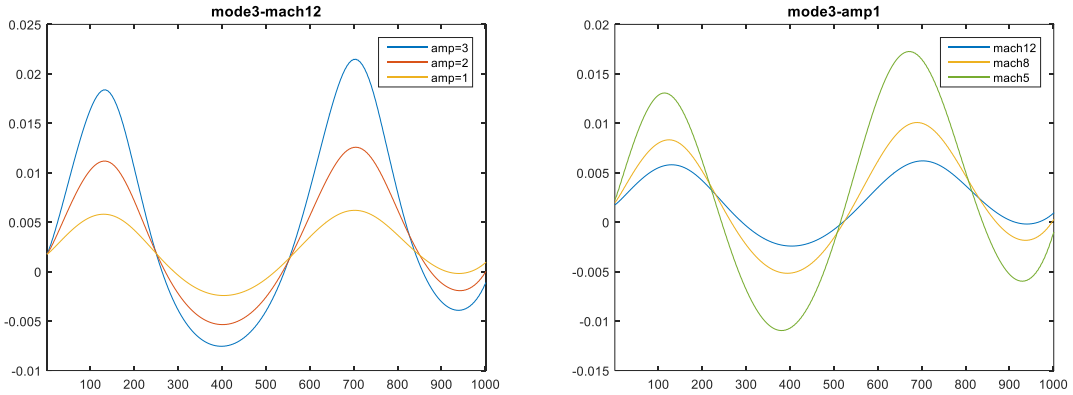

(a) (b)

Figure 2. Variation of steady Cp for mode 3 with (a) amplitude for mach 12 (b) mach number for amplitude =1

Like mode 3, in case of mode 4 Cp increases linearly with amplitude and decreases (with smaller phase difference) with mach number.

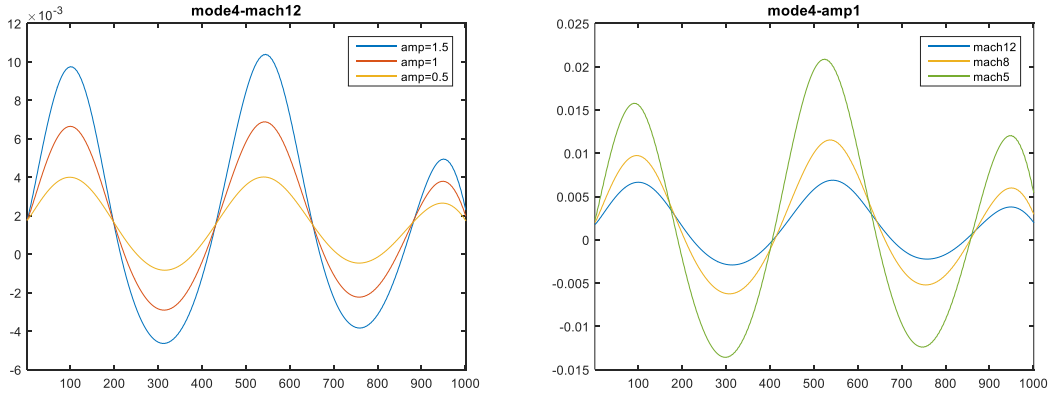

(a) (b)

Figure 3. Variation of steady Cp for mode 4 with (a) amplitude for mach 12 (b) mach number for amplitude =1

Due to non-linearity in the data Cp corresponding to negative amplitude have different features from positive counter parts. As the amplitude or mach number is increased asymmetry increases. For smaller amplitude Cp is closely symmetric for with respect to polarity of amplitude. Figure 4 shows the comparison of large and small amplitude.

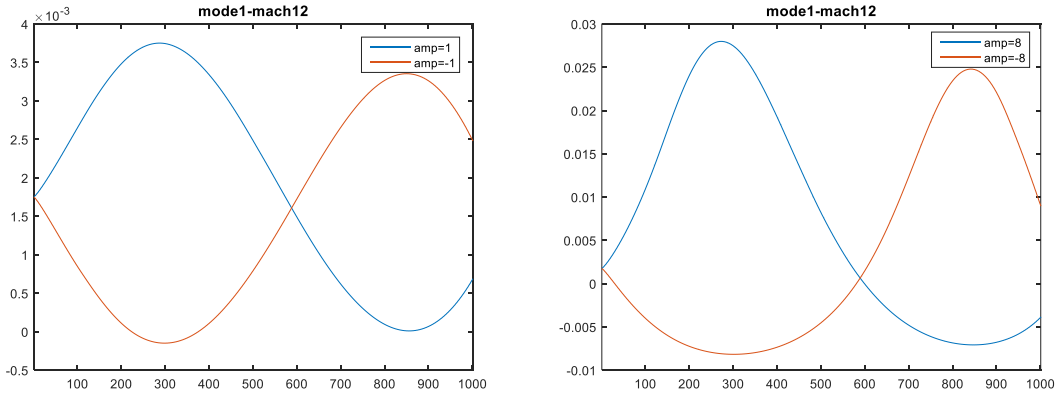

(a) (b)

Figure 4. Variation of Cp for mode 1 and mach 12 (a) amplitude = -/+ 1 (b) amplitude = -/+ 8

Unsteady data is generated for 2.25 cycles of amplitudes and frequencies as mentioned in Table 2 with 400 time steps per cycle. Figure 5. shows Cp for various time steps. These time step data can be directly compared to steady Cp of different amplitudes. In

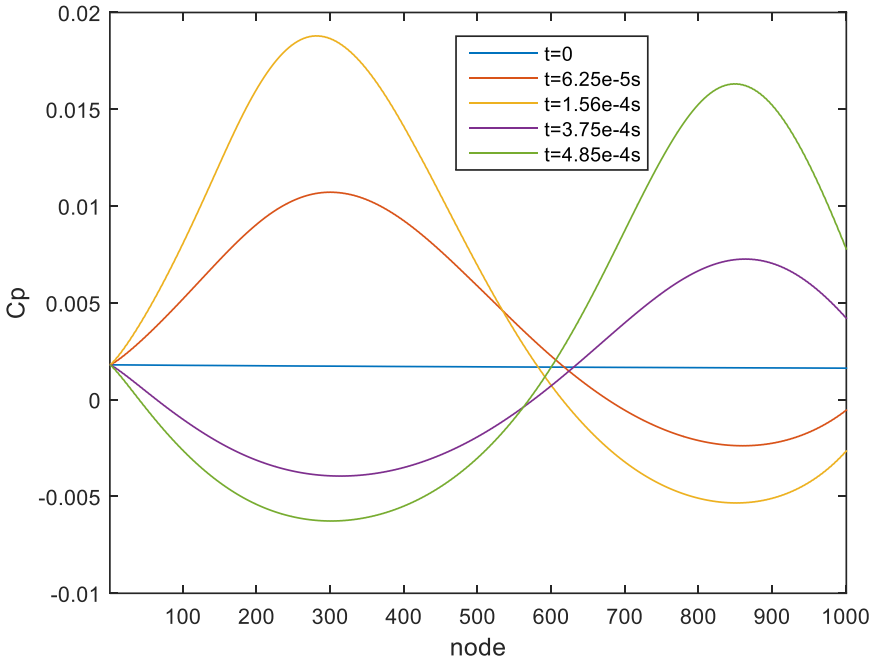

Figure 5. Unsteady Cp for mode1 mach12 freq160 amp6 for different time steps during first cycle

comparison to steady Cp of increasing amplitudes (both polarity) there is a phase difference in time step data. Cp is periodic through the excitation cycles, Figure 6 compares various corresponding time steps in during cycle 1 and 2. As already mentioned these have similar shapes as steady Cp, Figure 7 confirms the similarity of maximum unsteady Cp with steady Cp of same amplitude. The model will not be frequency dependent as the three frequencies considered have mainly offsetting effect on Cp for smaller displacement at later nodes. As the displacement of the beam increases role of frequencies reduces to convergence of the Cp data (as shown in Figure 8).

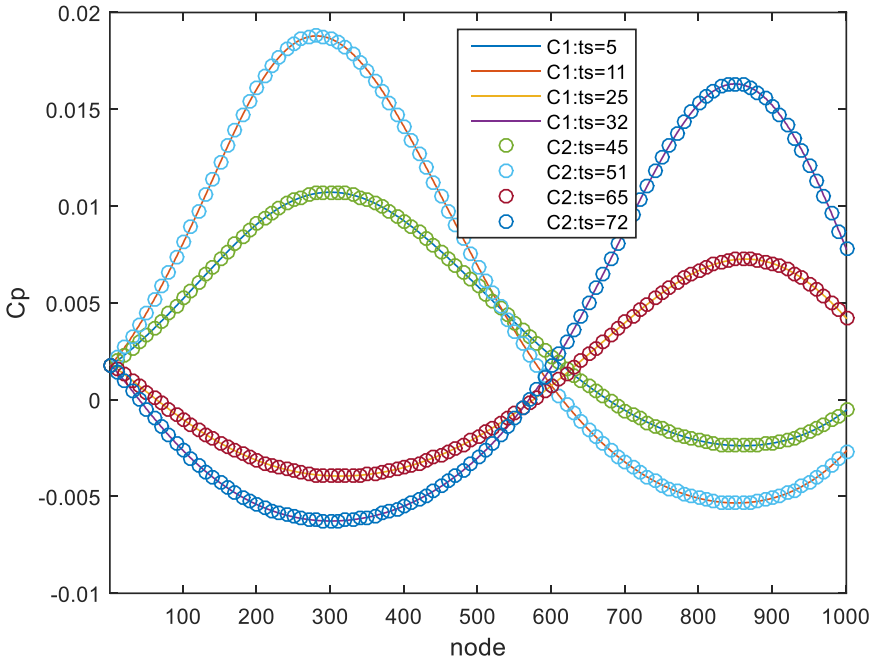

Figure 6. Comparison of Unsteady Cp for mode1 mach12 freq160 amp6 for corresponding time steps during first (C1) and second (C2) cycle

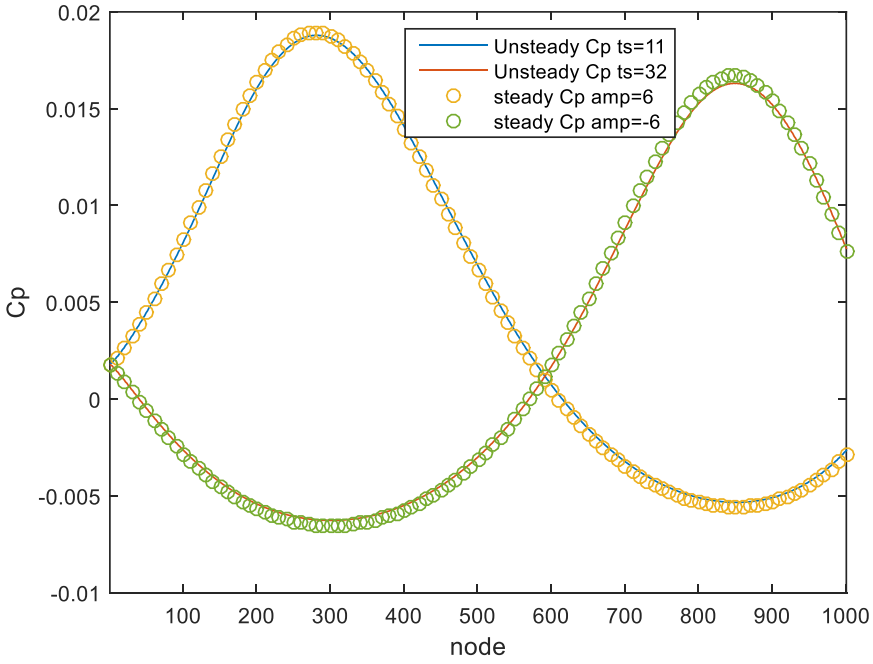

Figure 7. Comparison of max. Unsteady Cp for mode1 mach12 freq160 amp6 and Steady Cp for mode1 mach12 amp6

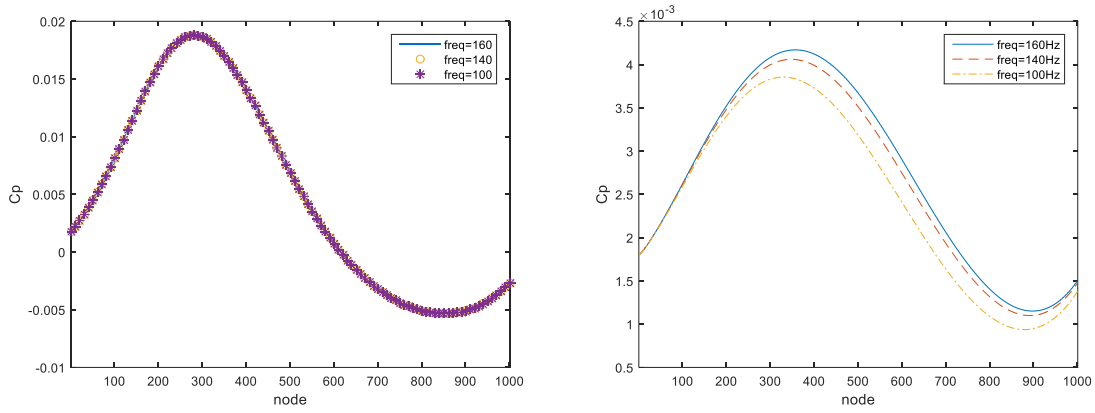

(a) (b)

Figure 8. Comparison of Unsteady Cp for mode1 mach12 amp6 (a) maximum displacement of beam (b) small displacement of beam for various excitation frequencies

Table 2

CFD solution (unsteady Cp) data for model generation and validation

mode	Amplitude	Frequency (Hz)	Mach number
1	6, 4, 3, 2, 1	160, 140, 100	12, 10, 8, 5
2	4, 3, 2, 1	160, 140, 100	12, 10, 8, 5
3	3, 2.5, 2, 1.5, 1, 0.5	160, 140, 100	12, 10, 8, 5
4	1.5, 1, 0.5	160, 140, 100	12, 10, 8, 5

Model calibration is sub-divided into two categories – mode dependent and mode independent. Mode dependent is applicable when loading comprised of only 1 normal mode (as in the current case) or modal superposition is applicable. For modal superposition to be valid, model should be linear. Mode independent is a general model applicable irrespective of the loading condition as it depends only on physical parameters. Following sections define the various models and discusses characteristics of reconstructed Cp.

2.1 Local Linear and Cubic Piston Theory

Linear piston theory model, $Cp = (aM + bM^2 + c)(dw/dx) + (a_2M + b_2M^2 + c_2)$

Cubic piston theory model, $Cp = (aM + bM^2 + c)(dw/dx) + (a_2M + b_2M^2 + c_2)(dw/dx)^2 + (a_3M + b_3M^2 + c_3)(dw/dx)^3 + (a_4M + b_4M^2 + c_4)$

2.1.1 Mode independent model

As mach number increases in hypersonic range linear Piston Theory becomes increasing inaccurate in modelling pressure coefficient. As can be seen from Figure 1, reconstruction for all the mach number for mode 1 are similar in nature (peaking error for small amplitude is discussed below) but error increases. The behavior of fitting error with respect to mach number is true for all the models so for analysis and reporting hereon only mach 12 will be considered.

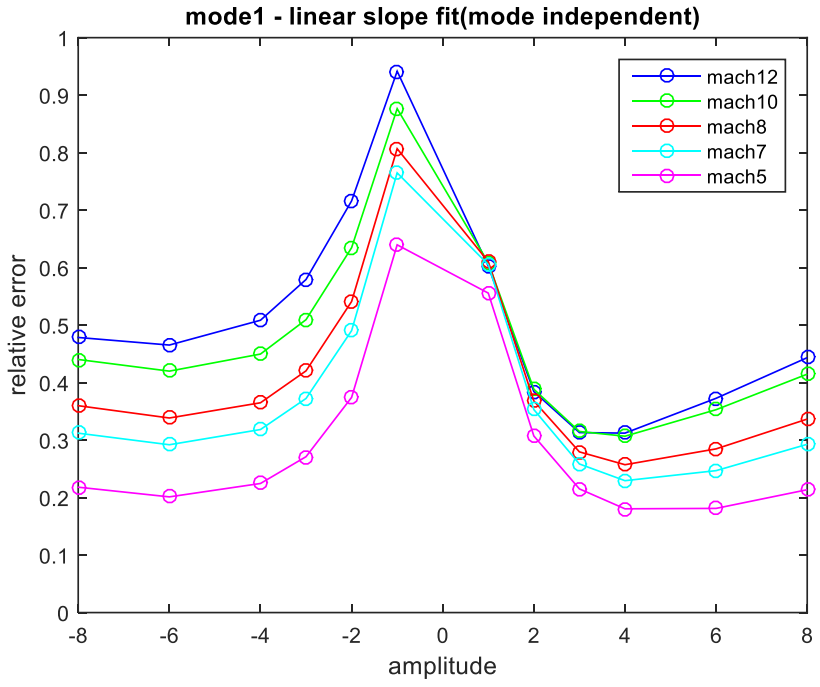

Figure 9. Fitting error comparison for all mach nos. with local linear slope mode independent model

The peak values for both polarities is at the smallest amplitude (1 and -1) due to offsetting of reconstructed Cp in y-axis from the CFL3D Cp (refer figure 3(a)). This characteristic of offset is mitigated by introducing higher order factors of slope as can be seen in Figure 1 and Figure 3(a). Solving the offset issue reduces the fitting error sharply and cubic slope model have a more predictable performance i.e. error is proportional to amplitude due to magnitude of Cp values.

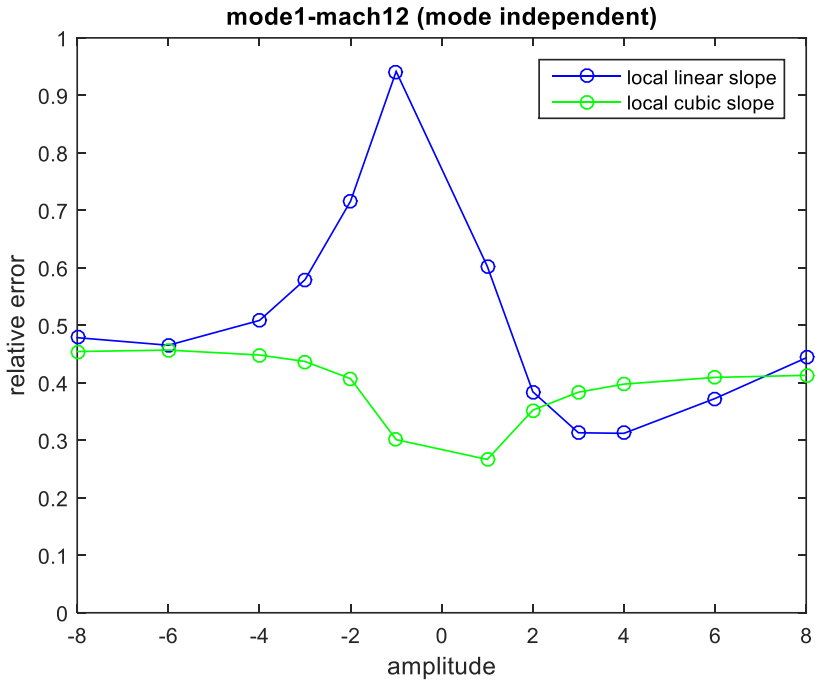

Figure 10. Fitting error (%) comparison for mode1-mach12 with local linear and cubic slope mode independent model

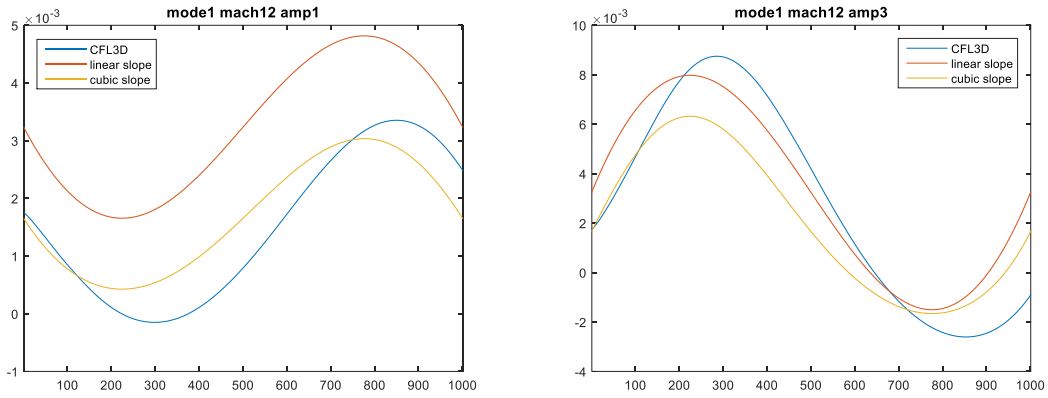

(a) (b)

Figure 11. Comparison of CFL3D Cp and reconstructed Cp with local linear slope and local cubic slope mode independent model (a) mode1 mach12 amp1 (b) mode1 mach12 amp3

Second prominent feature of local linear slope fit is the phase difference in the reconstructed Cp with respect to CFL3D Cp. This issue is not mitigated by adding higher order terms of slope. These two features are so prominent that nothing else can be concluded about the fit removing these anomalies. Similar feature is observed for all the modes.

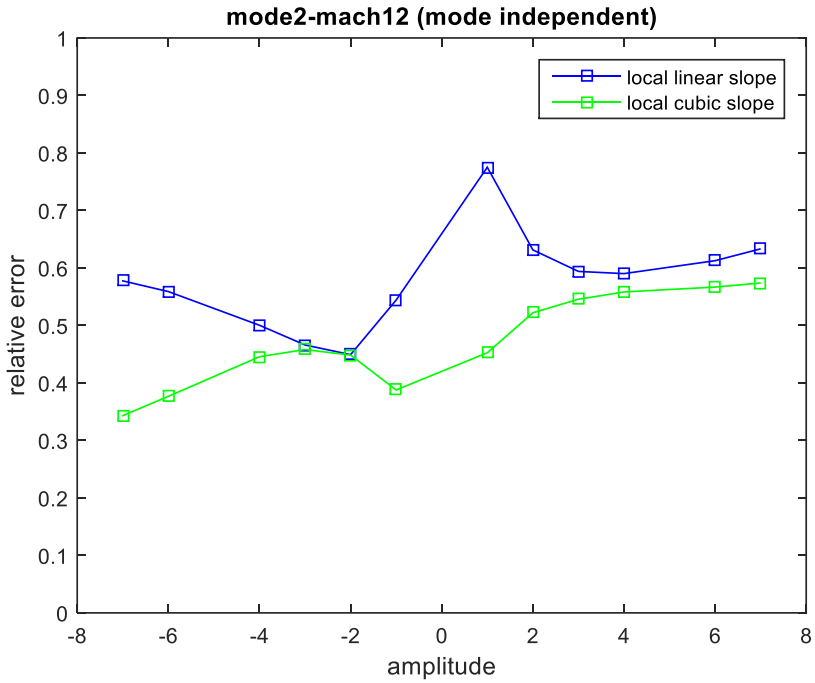

Figure 12. Fitting error comparison for mode2-mach12 with local linear and cubic slope mode independent model

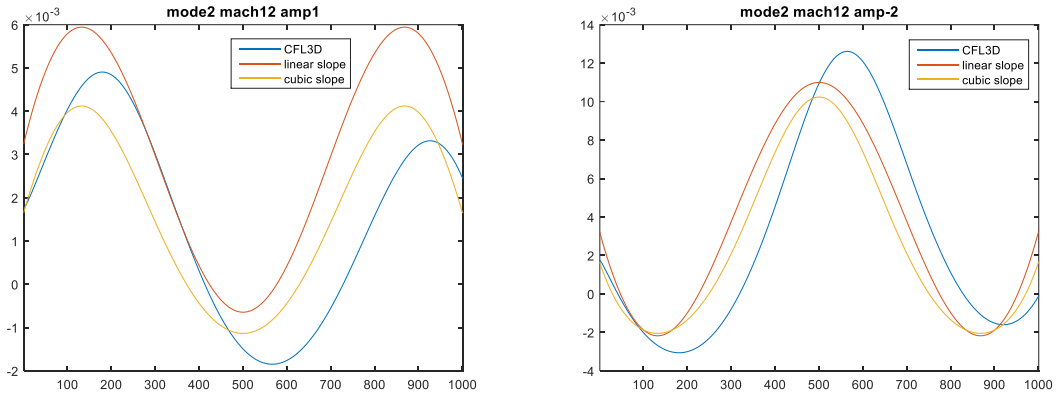

(a) (b)

Figure 13. Comparison of CFL3D Cp and reconstructed Cp with local linear slope and local cubic slope mode independent model (a) mode2 mach12 amp1 (b) mode2 mach12 amp-2

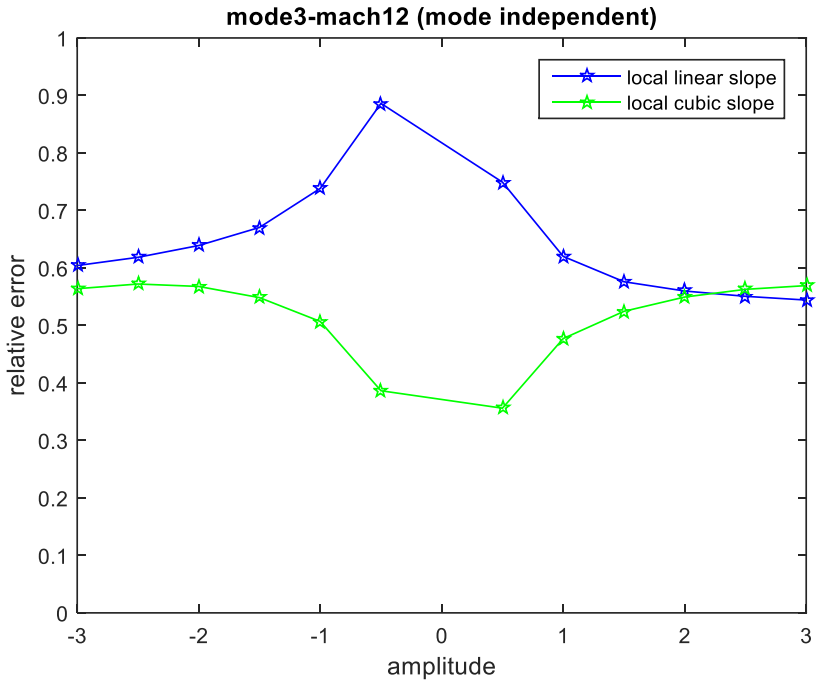

Figure 14. Fitting error comparison for mode3-mach12 with local linear and cubic slope mode independent model

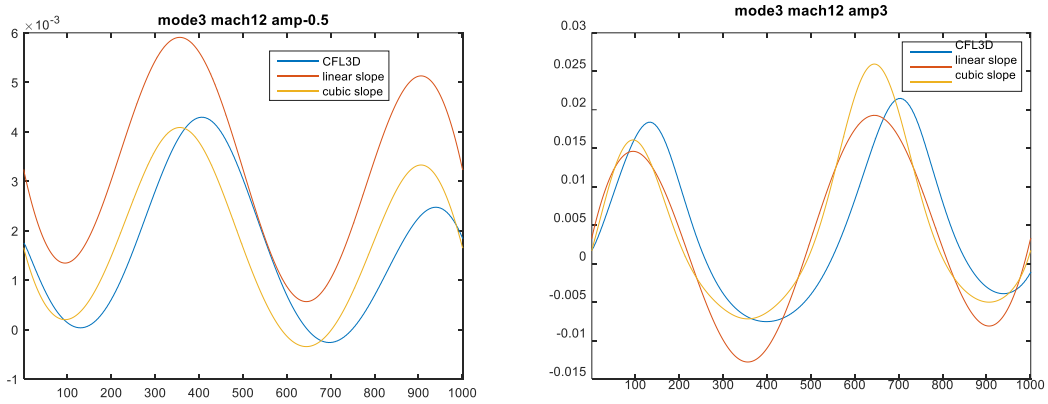

(a) (b)

Figure 15. Comparison of CFL3D Cp and reconstructed Cp with local linear slope and local cubic slope mode independent model (a) mode3 mach12 amp-0.5 (b) mode3 mach12 amp3

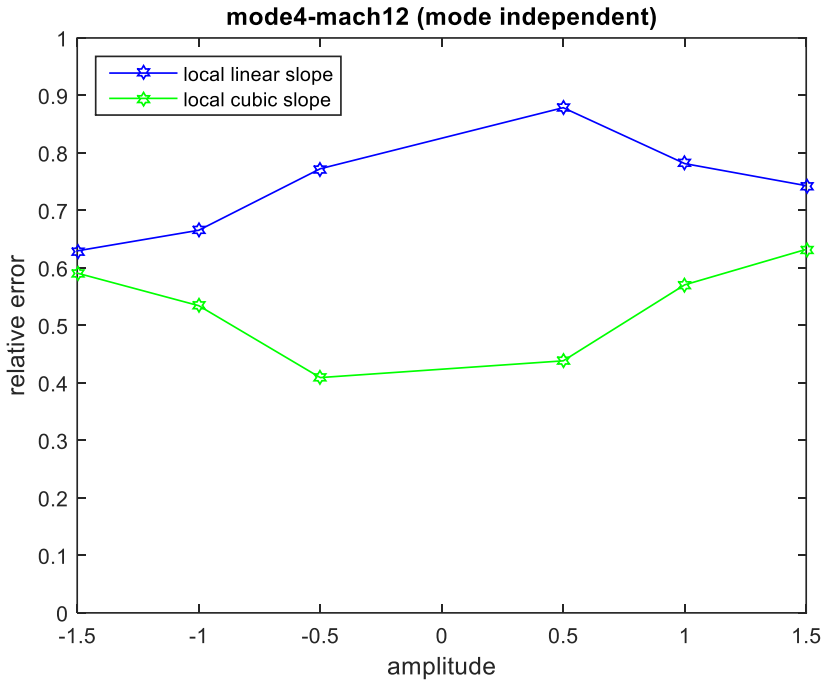

Figure 16. Fitting error comparison for mode4-mach12 with local linear and cubic slope mode independent model

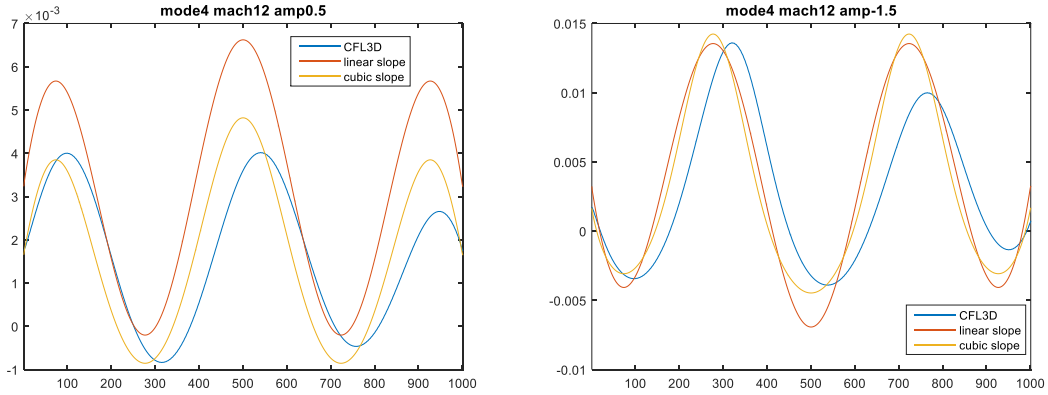

(a) (b)

Figure 17. Comparison of CFL3D Cp and reconstructed Cp with local linear slope and local cubic slope mode independent model (a) mode4 mach12 amp0.5 (b) mode4 mach12 amp-1.5

2.1.2 Mode dependent model

Although the aim of current work is to generate a model which only depend on physical parameters of the beam under investigation and the spectrum of data is based on realistic chances of occurrence (for example, considering data with amplitude 8 for mode 4 deformation would not be physically feasible but is feasible for mode 1). Given this constraint, the fitting error with mode independent model for higher modes is partly due to higher complexity associated and non-linearity associated with higher amplitude for lower modes. Cp corresponding to higher amplitude have larger magnitude hence a higher weightage in fitting the data with least square methodology by default. The contribution of complexity associated with mode number can be dissected by generating a mode dependent model also this can be applicable if either the loading is comprised of one mode only or modal superposition is applicable. Applicability of modal superposition is out of the scope of current work.

Reconstruction using mode dependent model for mode 1 improves the fit reducing the error (refer Figure 13). But the prominent features of phase difference and offset reconstruction of lower amplitude Cp still exists (refer Figure 14).

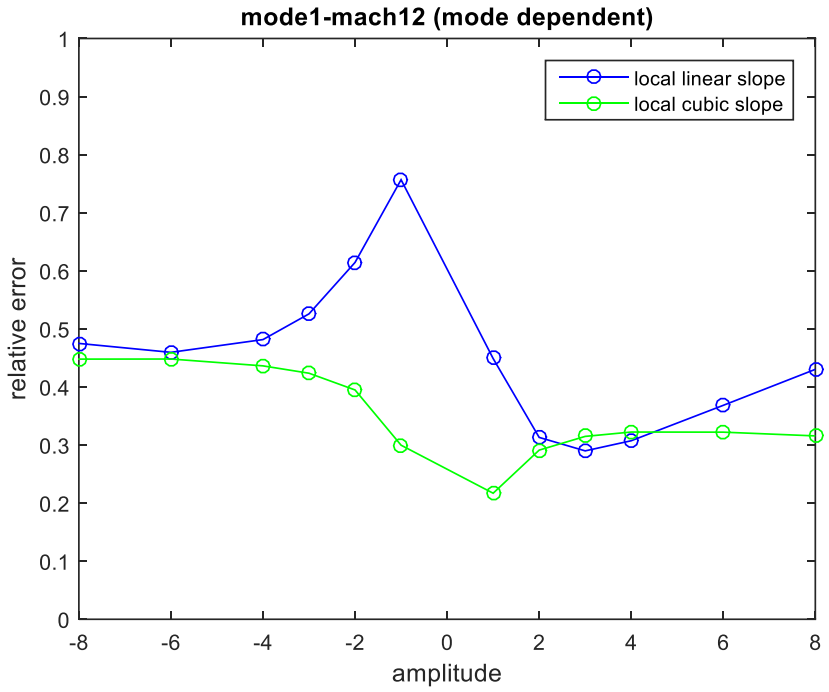

Figure 18. Fitting error comparison for mode1-mach12 with local linear and cubic slope mode independent model

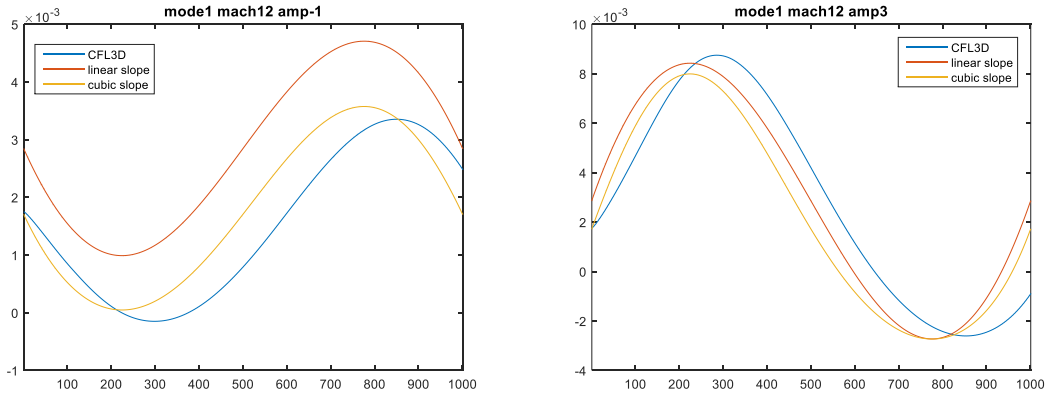

(a) (b)

Figure 19. Comparison of CFL3D Cp and reconstructed Cp with local linear slope and local cubic slope mode independent model (a) mode1 mach12 amp-1 (b) mode1 mach12 amp3

Mode 2 data has a unique feature that it has higher complexity as compared mode 1 but the amplitude are similar (for mode 3 and mode 4 amplitude reduces). Hence the mode

dependent modelling error increases for mode 2 in addition to the previous mentioned features for local linear slope model.

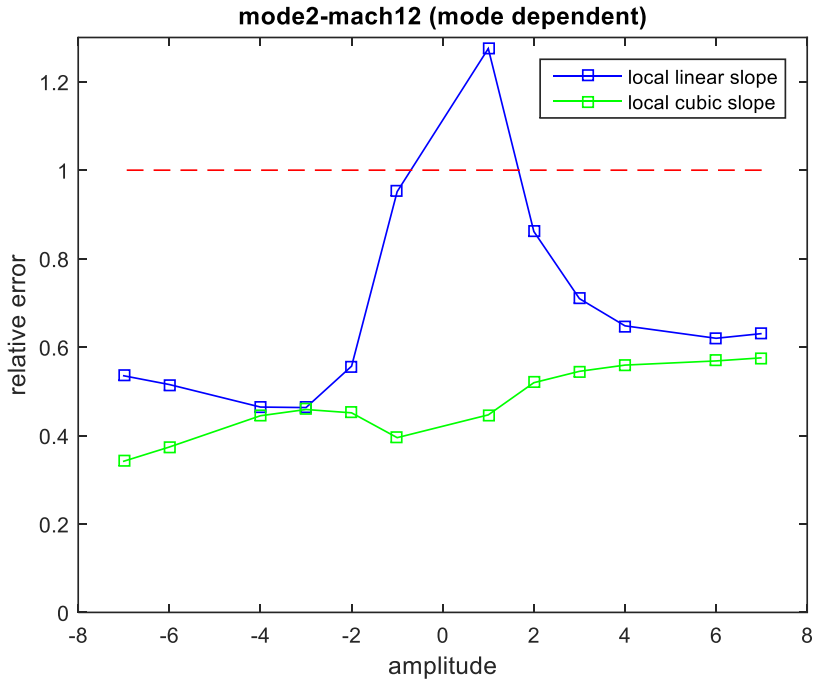

Figure 20. Fitting error comparison for mode2-mach12 with local linear and cubic slope mode independent model

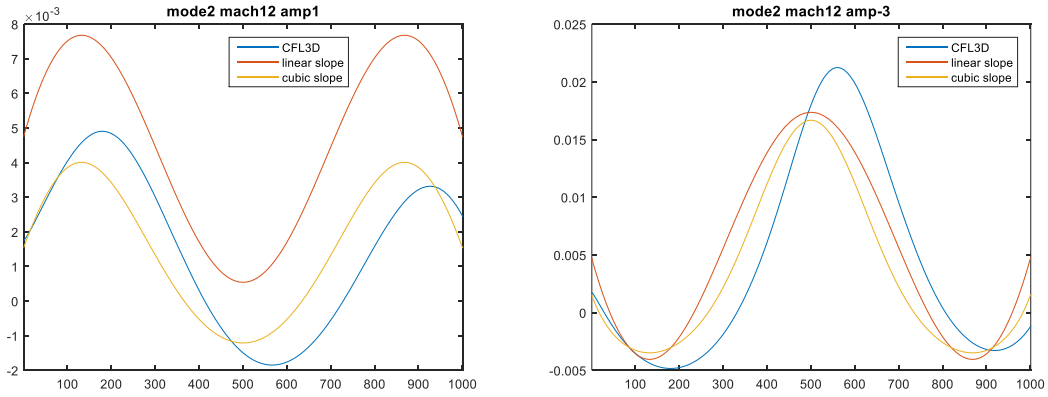

(a) (b)

Figure 21. Comparison of CFL3D Cp and reconstructed Cp with local linear slope and local cubic slope mode independent model (a) mode2 mach12 amp1 (b) mode2 mach12 amp-3

In contrast to mode 2, for mode 3 peak error for lower amplitude doesn't increase drastically due to low amplitude of overall data. But similar issues persist with these results as before (refer Figure 17 and 18). The reconstruction for mode 4 also give similar observations (Figure 19 and 20).

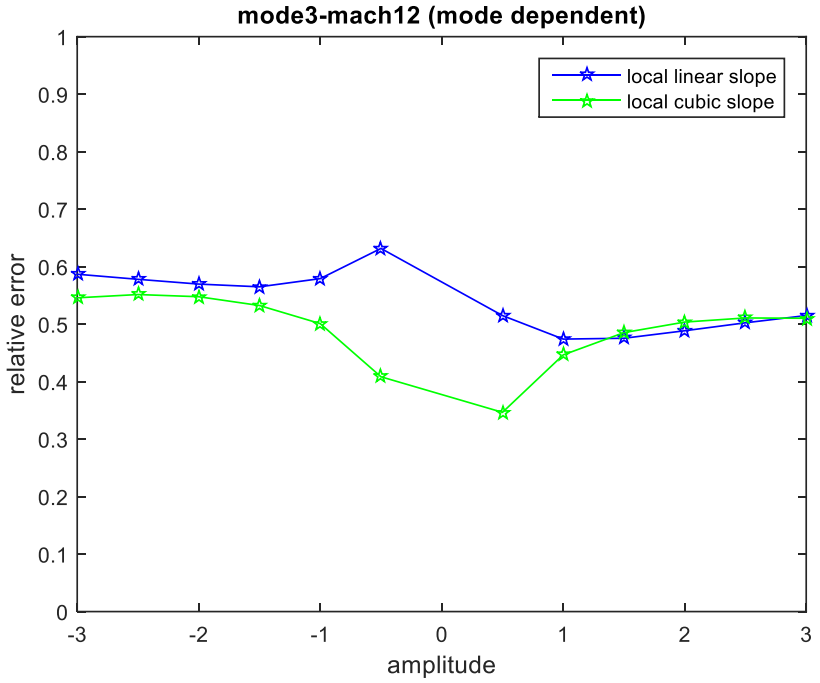

Figure 22. Fitting error comparison for mode3-mach12 with local linear and cubic slope mode independent model

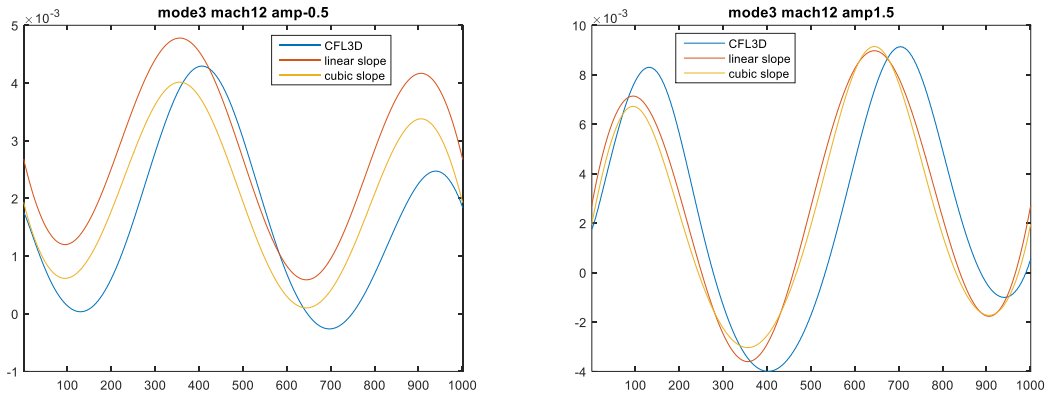

(a) (b)

Figure 23. Comparison of CFL3D Cp and reconstructed Cp with local linear slope and local cubic slope mode independent model (a) mode3 mach12 amp-0.5 (b) mode3 mach12 amp1.5

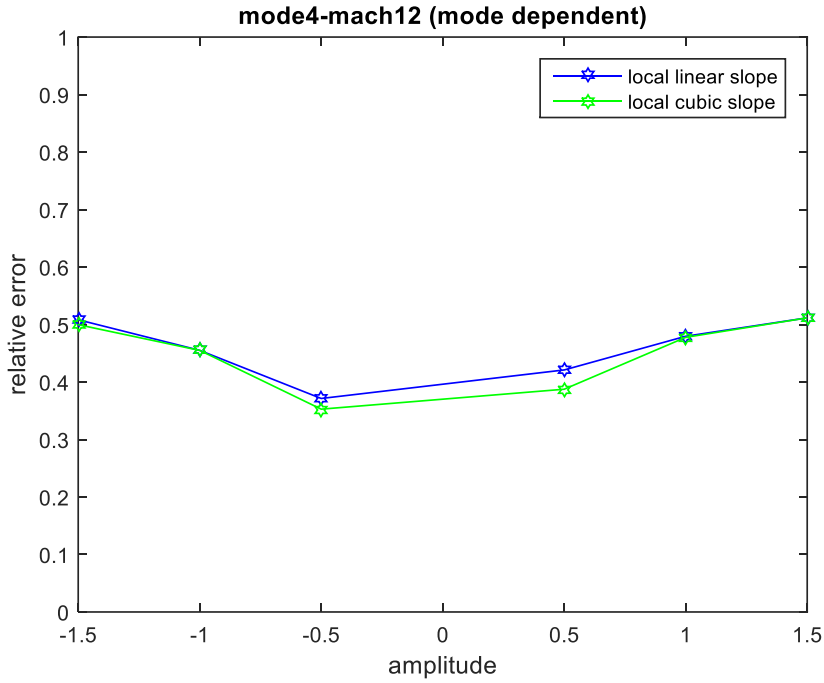

Figure 24. Fitting error comparison for mode4-mach12 with local linear and cubic slope mode independent model

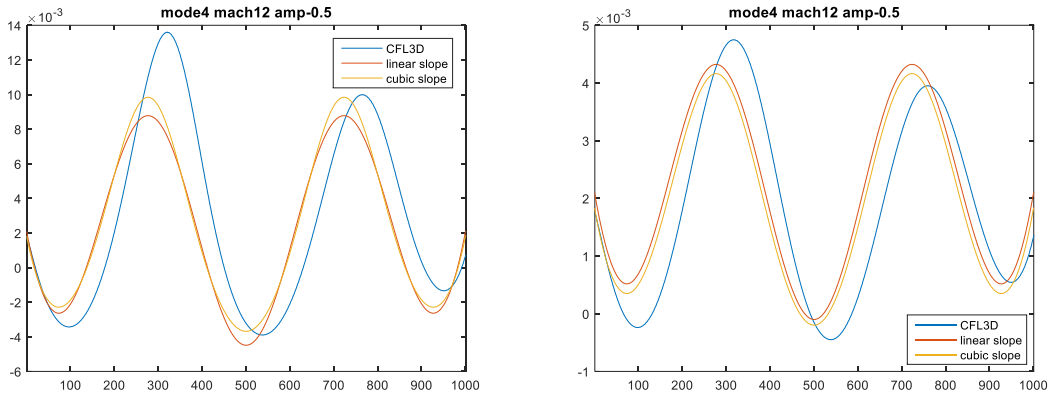

(a) (b)

Figure 25. Comparison of CFL3D Cp and reconstructed Cp with local linear slope and local cubic slope mode independent model (a) mode4 mach12 amp-1.5 (b) mode4 mach12 amp-0.5

2.2 Global Linear and Cubic Slope model

2.2.1 Mode independent model

The critical feature of phase difference between CFD solution and local Piston Theory reconstruction in section 3.1 leads to the thought that the upstream parameters can have impact on pressure developed downstream. In the current section contribution of global terms (upstream) are studied. Important thing is to keep an optimal number of nodes in the equation corresponding to the correlation length of the system of equation. Considering higher number of nodes may lead to nonphysical solution (for example, nodes at the beginning of the beam may not have a considerable impact on solution of end nodes) and on the other hand smaller number of nodes may not lead required fitting.

Global linear slope, Cp (ii) = $(a_{11}M + b_{11}M^2 + c_{11})$ (dw(ii)/dx) + …. + $(a_{1n}M + b_{1n}M^2 + c_{1n})$ (dw (ii - n)/dx) + $(a_2M + b_2M^2 + c_2)$

Global cubic slope, Cp (ii) = $(a_{11}M + b_{11}M^2 + c_{11})$ (dw(ii)/dx) + …. + $(a_{1n}M + b_{1n}M^2 + c_{1n})$ (dw (ii - n)/dx) + $(a_{21}M + b_{21}M^2 + c_{21})$ * $(dw(ii)/dx)^2$ + …. + $(a_{2n}M + b_{2n}M^2 + c_{2n})$

$(dw(ii-n)/dx)^2 + (a_{31}M + b_{31}M^2 + c_{31}) * (dw(ii)/dx)^3 + \ldots + (a_{3n}M + b_{3n}M^2 + c_{3n}) (dw(ii-n)/dx)^3 + (a_3M + b_3M^2 + c_3)$

Global formulation for linear and cubic piston theory leads to ill-conditioned matrices of parameter hence the effect of global terms cannot be studied. The issue is due to the fine mesh which leads to almost equal values on adjacent nodes. The component of global terms can now be inspected by examining (i) Reconstruction error v/s distance of global node (only 1 global node considered) and (ii) Reconstruction error v/s number of global nodes.

The error and reconstruction is compared for node 101 to 1001 (highest global term is 100 so the reconstruction can only start from node101 onwards). Referring to the error plot for mode1 (Figure 21.), introducing global term in linear slope formulation doesn't mitigate the issue of offset reconstruction as seen in previous section.

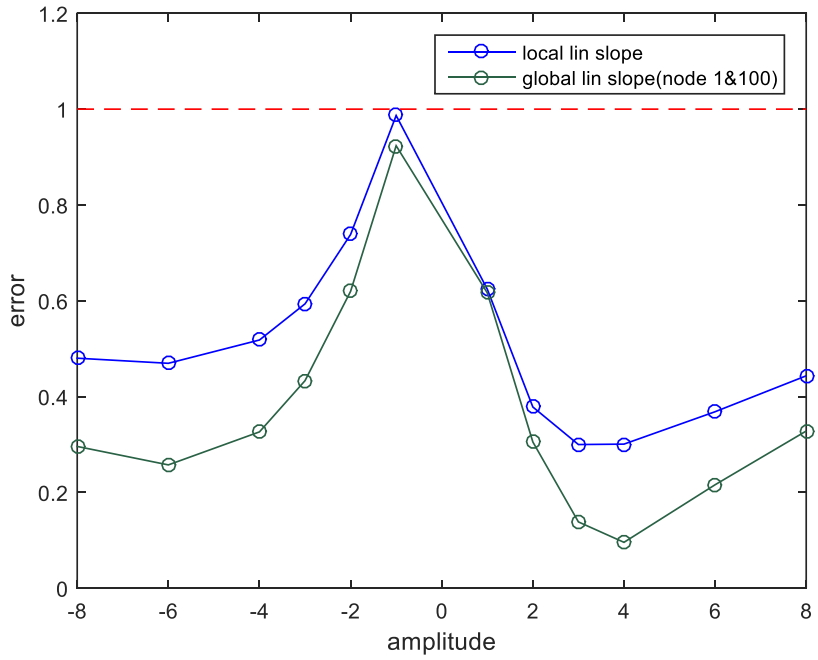

Figure 26. Fitting error comparison for mode1-mach12 with local linear and global linear slope mode independent model

On the other hand, reconstructed result with local cubic formulation has phase difference with CFD Cp. By using a global term the phase difference is improved (not completely corrected) and because this formulation has an extra variable the fitting improves. As the distance of global node is increased, fitting further improves but this change is minimal (refer Figure 22). In case of mode 2, Cp for large positive amplitude is highly nonlinear hence the reconstruction worsens as amplitude increases. Observations and characteristics for mode 3 and mode 4 are like mode 1. As observed with local model, the error increases with mode number. For the ongoing section, global term will be analyzed for cubic slope model only.

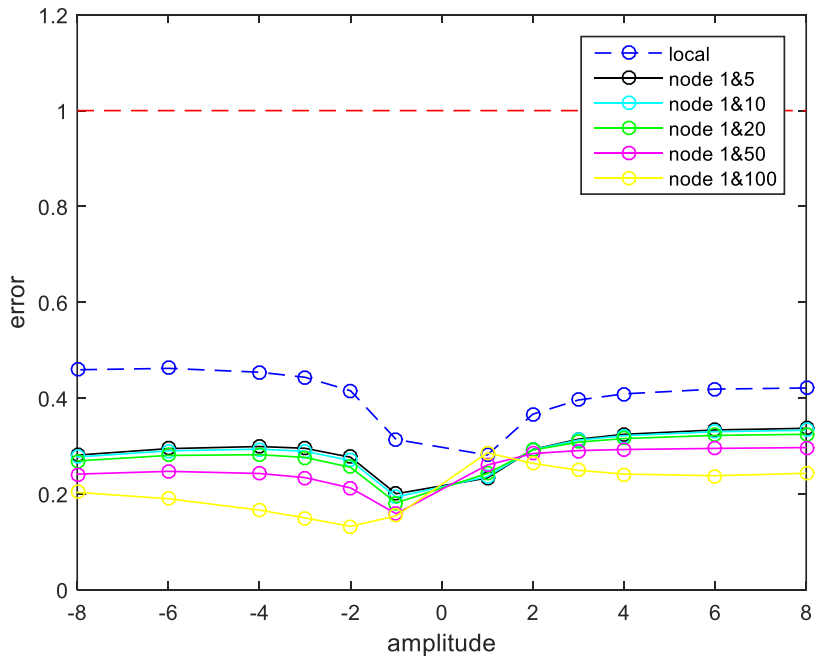

Figure 27. Fitting error comparison for mode1-mach12 with local cubic slope and global cubic slope (various configuration) mode independent model

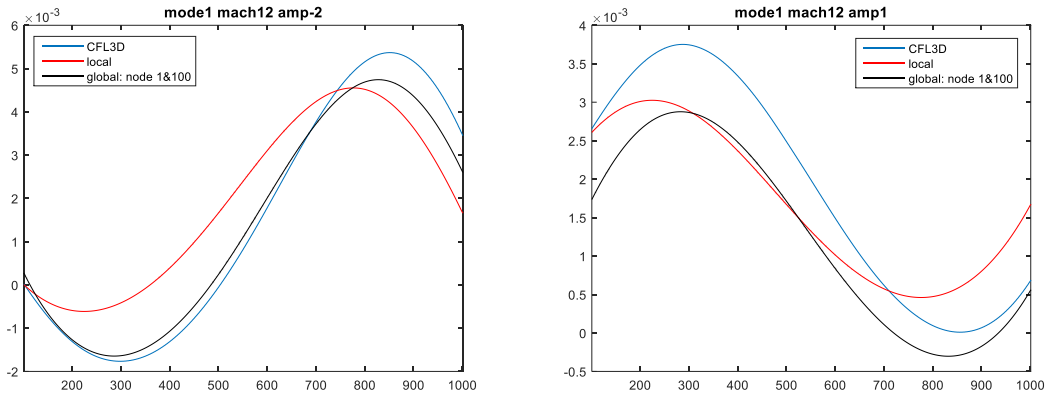

(a) (b)

Figure 28. Comparison of CFL3D Cp and reconstructed Cp with local cubic slope and global cubic slope mode independent model (a) mode1 mach12 amp-2 (b) mode1 mach12 amp1

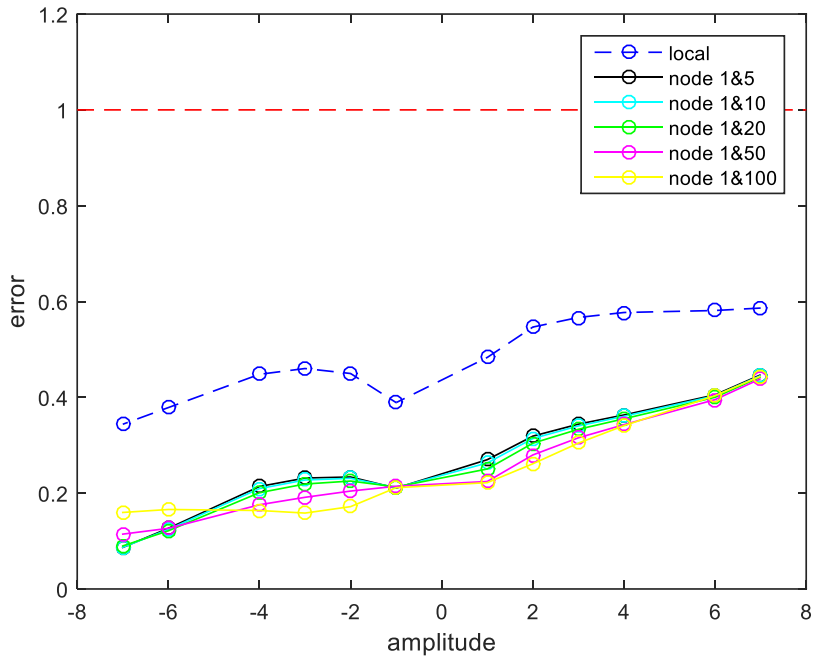

Figure 29. Fitting error comparison for mode2-mach12 with local cubic slope and global cubic slope (various configuration) mode independent model

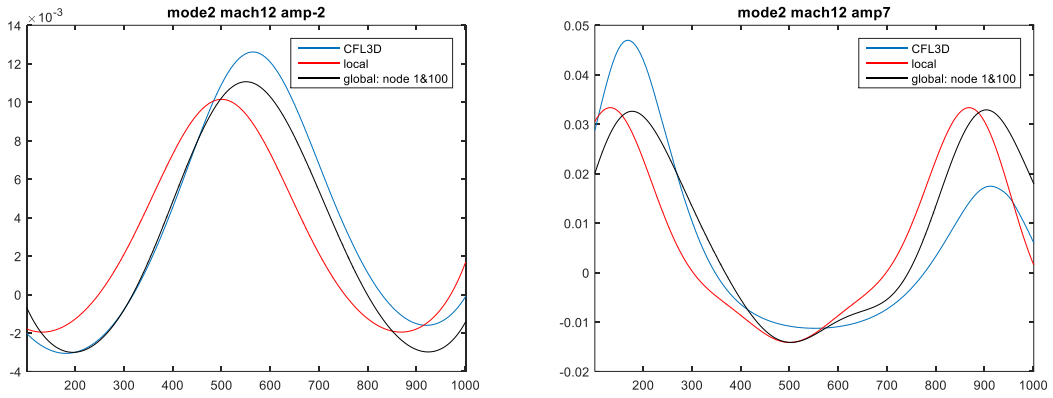

(a) (b)

Figure 30. Comparison of CFL3D Cp and reconstructed Cp with local cubic slope and global cubic slope mode independent model (a) mode2 mach12 amp-2 (b) mode1 mach12 amp7

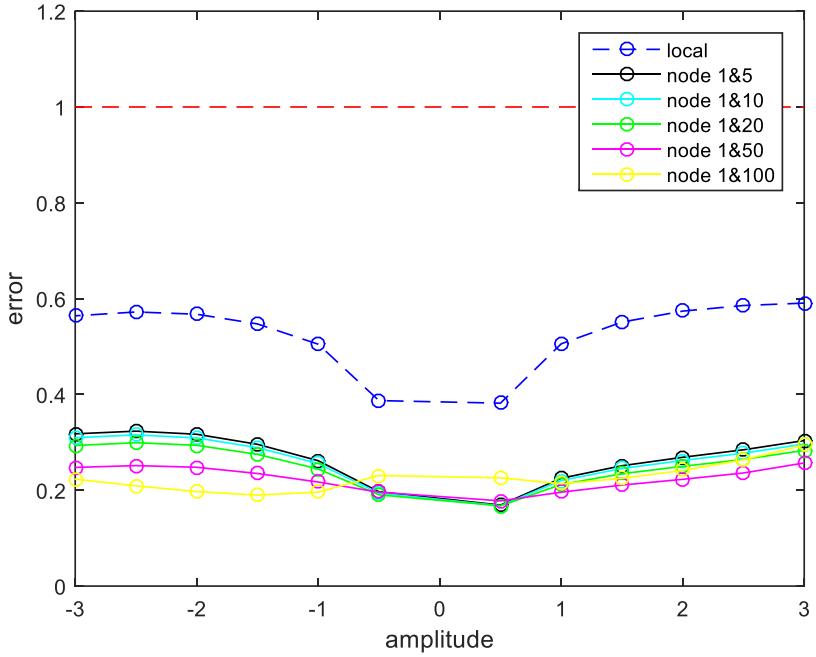

Figure 31. Fitting error comparison for mode3-mach12 with local cubic slope and global cubic slope (various configuration) mode independent model

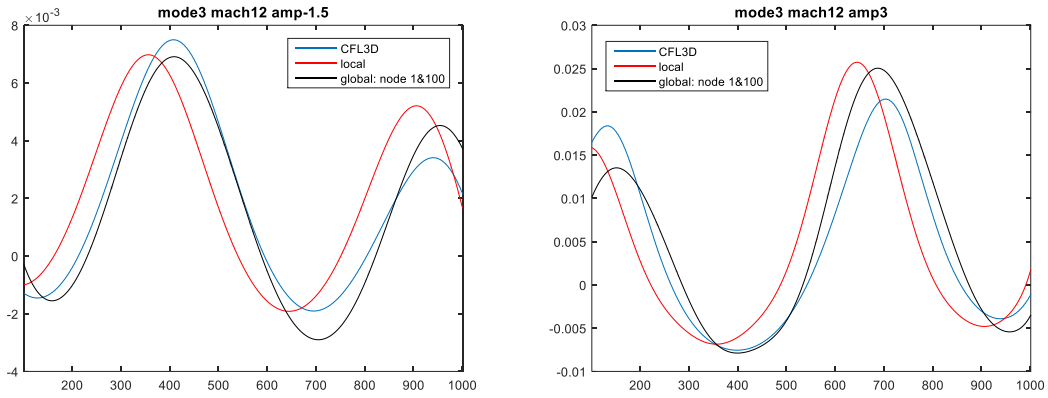

(a) (b)

Figure 32. Comparison of CFL3D Cp and reconstructed Cp with local cubic slope and global cubic slope mode independent model (a) mode3 mach12 amp-1.5 (b) mode3 mach12 amp3

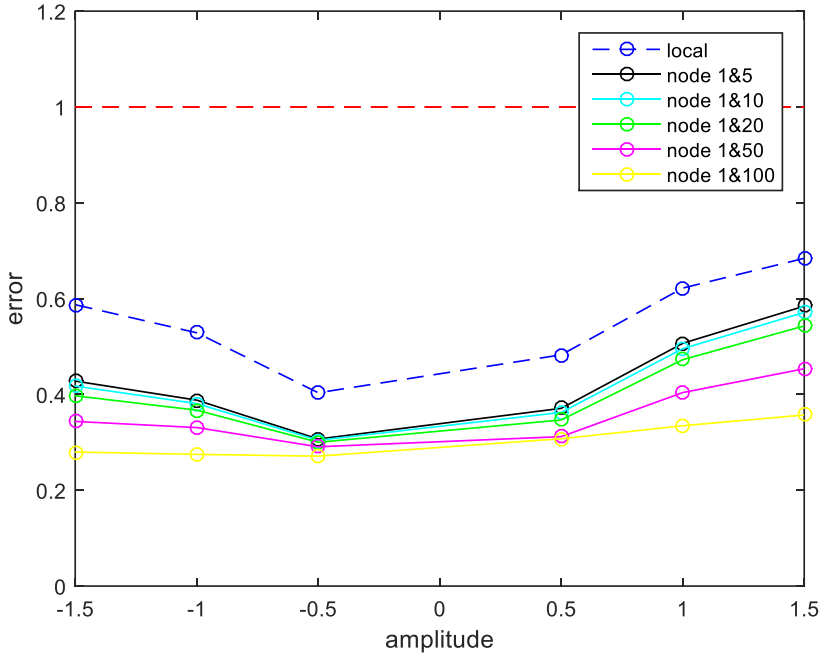

Figure 33. Fitting error comparison for mode4-mach12 with local cubic slope and global cubic slope (various configuration) mode independent model

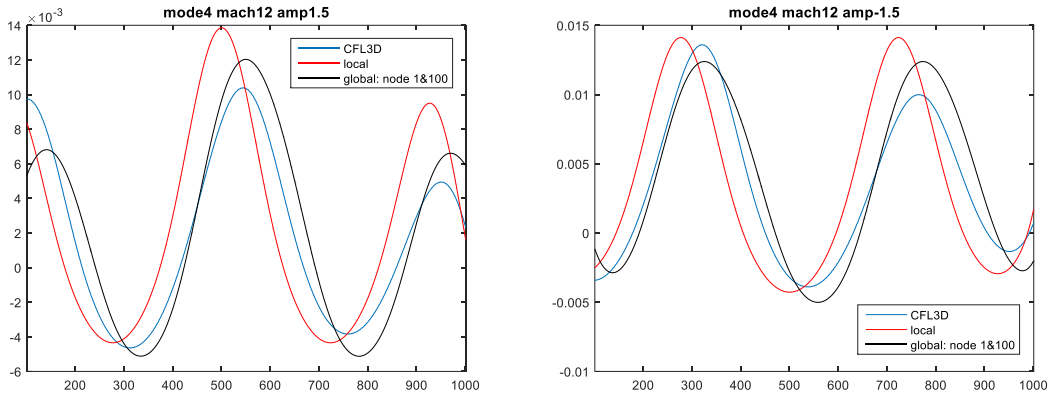

(a) (b)

Figure 34. Comparison of CFL3D Cp and reconstructed Cp with local cubic slope and global cubic slope mode independent model (a) mode4 mach12 amp1.5 (b) mode4 mach12 amp-1.5

2.2.1.1 Reconstruction with added global nodes

For this subsection, 100th node global model will be further analyzed as it gives most accurate prediction of pressure coefficient. To analyze effect of number of global terms 25th, 50th and 75th will be considered in addition to 1st and 100th term. In general, referring to Figure 30., 32, 33, 34 reconstruction error decreases with number of global terms involved in formulation due to increased number of variables except for mode 4 where best fit is attained by only adding 50th term to default global model. Reconstructed Cp are compared in figure 37 for mode4 which shows that final configuration is distorted (but the computation it is still conditioned).

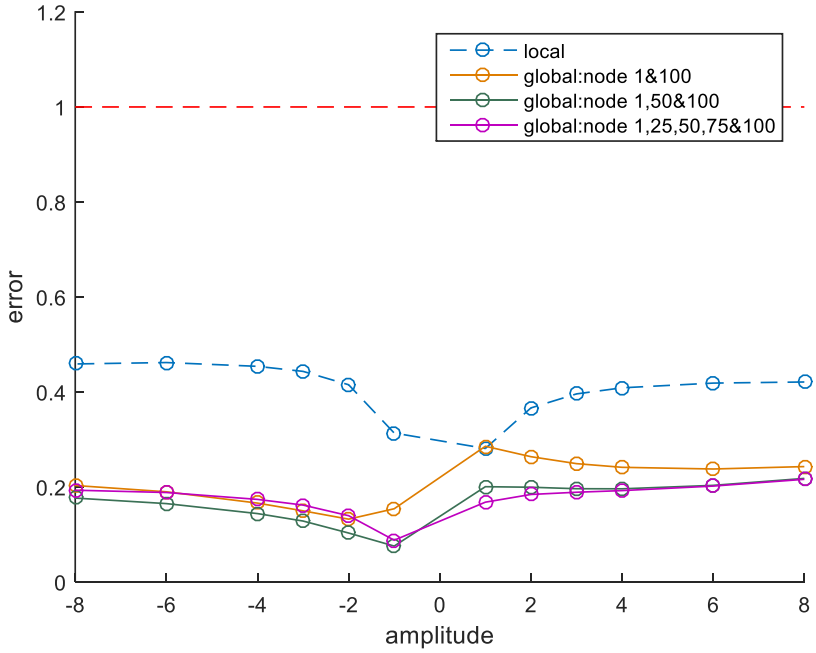

Figure 35. Fitting error comparison for mode1-mach12 with local cubic slope and global cubic slope (various configuration) mode independent model

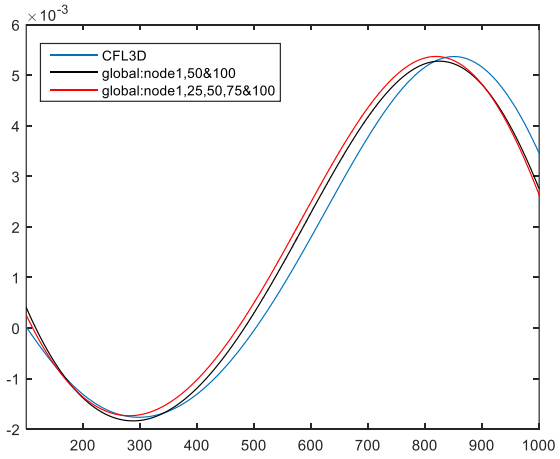

Figure 36. Comparison of CFL3D Cp and reconstructed Cp with global cubic slope (node 1, 50 & 100) and global cubic slope (node 1, 25, 50, 75 & 100) mode independent model for mode1 mach12 amp-1

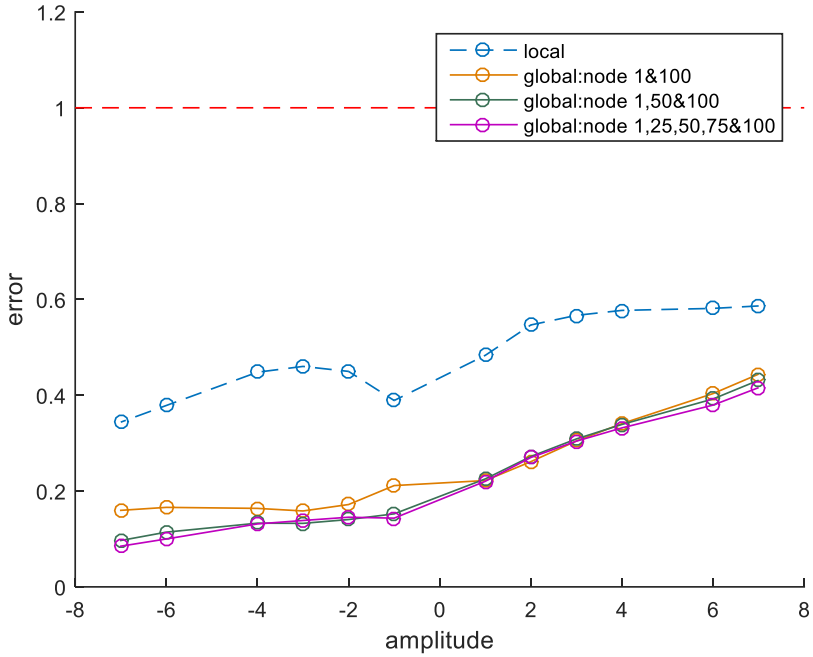

Figure 37. Fitting error comparison for mode2-mach12 with local cubic slope and global cubic slope (various configuration) mode independent model

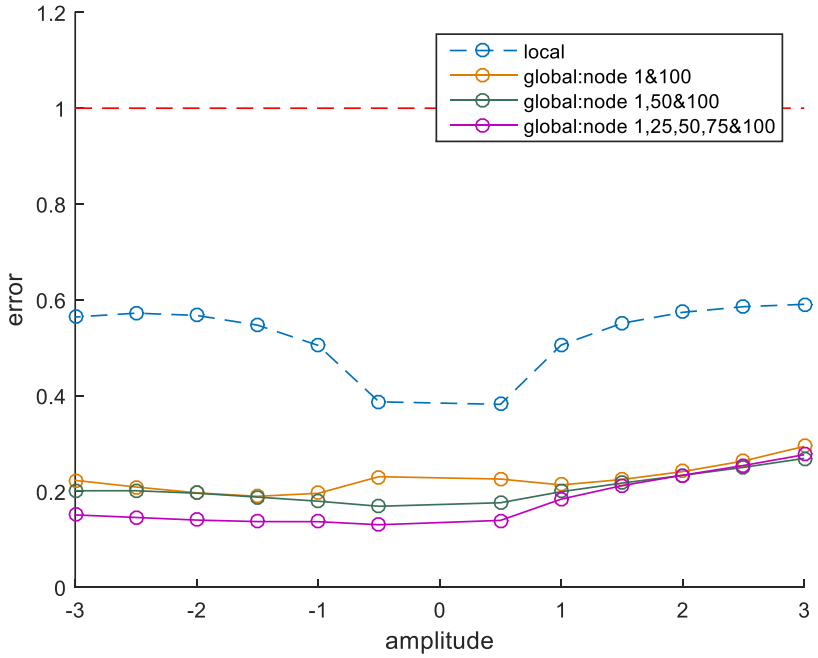

Figure 38. Fitting error comparison for mode3-mach12 with local cubic slope and global cubic slope (various configuration) mode independent model

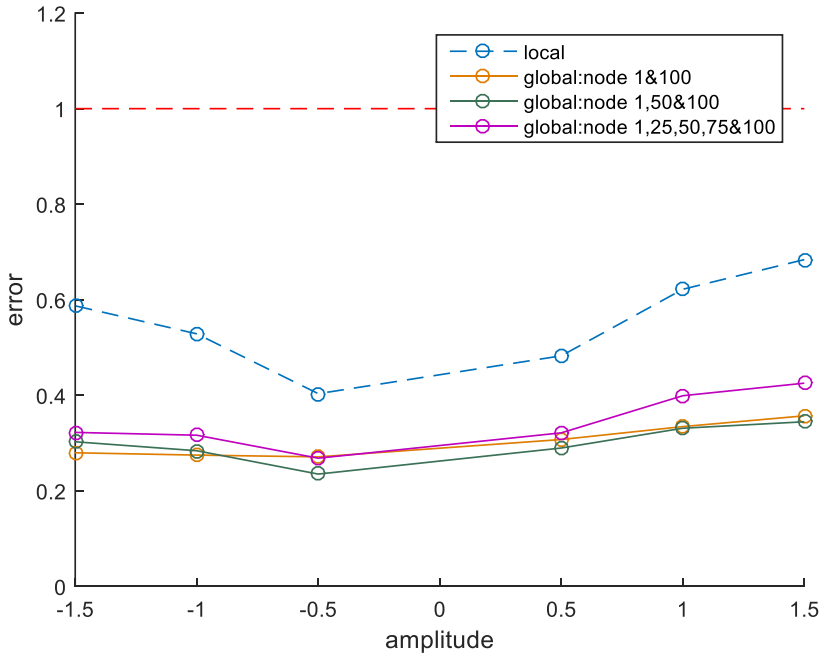

Figure 39. Fitting error comparison for mode4-mach12 with local cubic slope and global cubic slope (various configuration) mode independent model

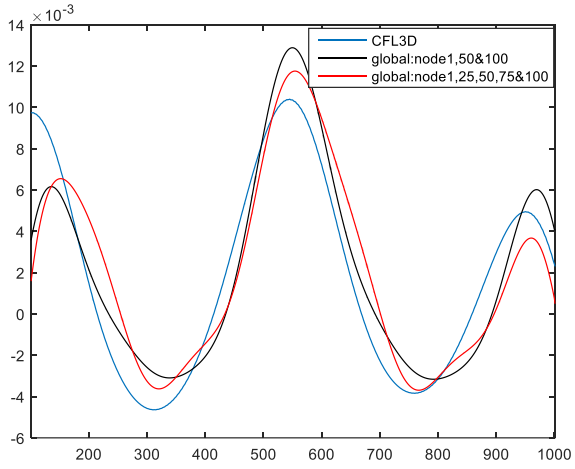

Figure 40. Comparison of CFL3D Cp and reconstructed Cp with global cubic slope (node 1, 50 & 100) and global cubic slope (node 1, 25, 50, 75 & 100) mode independent model for mode4 mach12 amp-0.5

2.3 Local and global linear dsci model

Considering the limitation of previous model of cubic slope if a linear model is used then modal superposition can applied. Introducing displacement, curvature and displacement-integral with linear slope in the model.

Local linear dsci, $Cp = (a_1M + b_1M^2 + c_1)\, w + (a_2M + b_2M^2 + c_2)\, (dw/dx) + (a_3M + b_3M^2 + c_3)\, (d^2w/dx^2) + (a_4M + b_4M^2 + c_4)\, (\int_0^x w dx) + (a_5M + b_5M^2 + c_5)$

3.3.1 Mode independent

Local and global linear dsci model has similar characteristic as linear slope model of offsetting of reconstructed result for smaller amplitude. But it improves the phase difference observed in linear slope model.

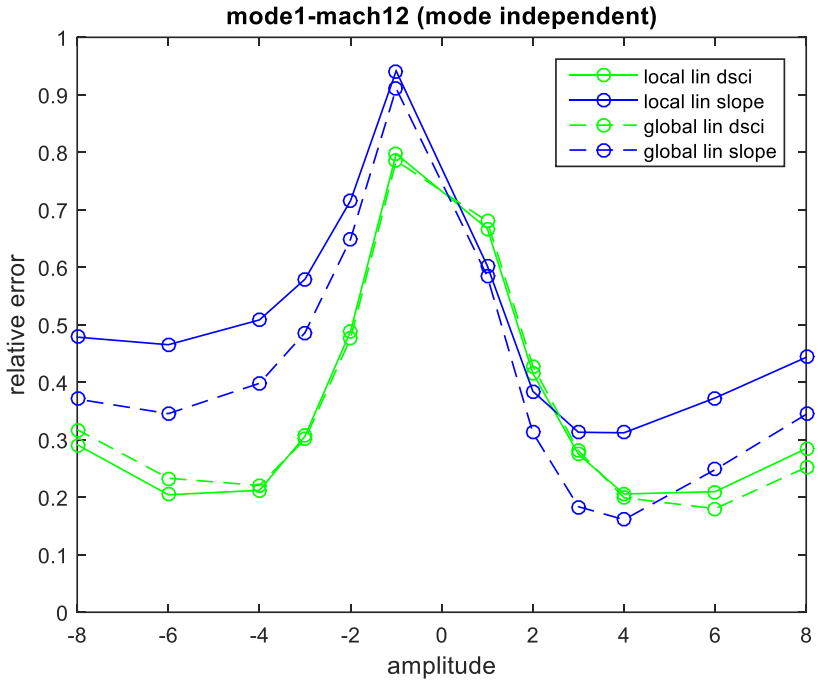

Figure 41. Fitting error comparison for mode1-mach12 with local linear slope, local linear dsci and global linear dsci (1 & 100 node) mode independent model

Referring to Figure 36, the decrease in fitting error is accounted to increase in parameters involved.

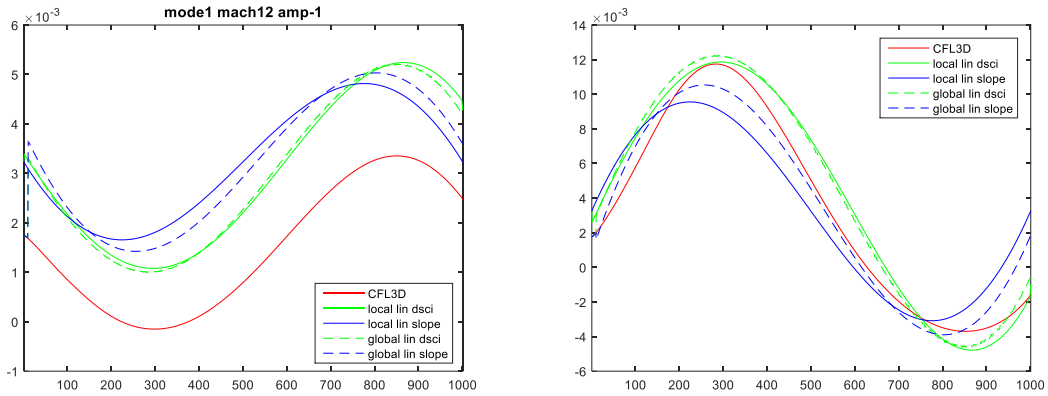

Figure 42. Comparison of CFL3D Cp and reconstructed Cp with local linear dsci, global linear dsci (node 1& 100), local linear slope and global linear slope (node 1 & 100) mode independent model (a) mode1 mach12 amp-1 and (b) mode1 mach12 amp6

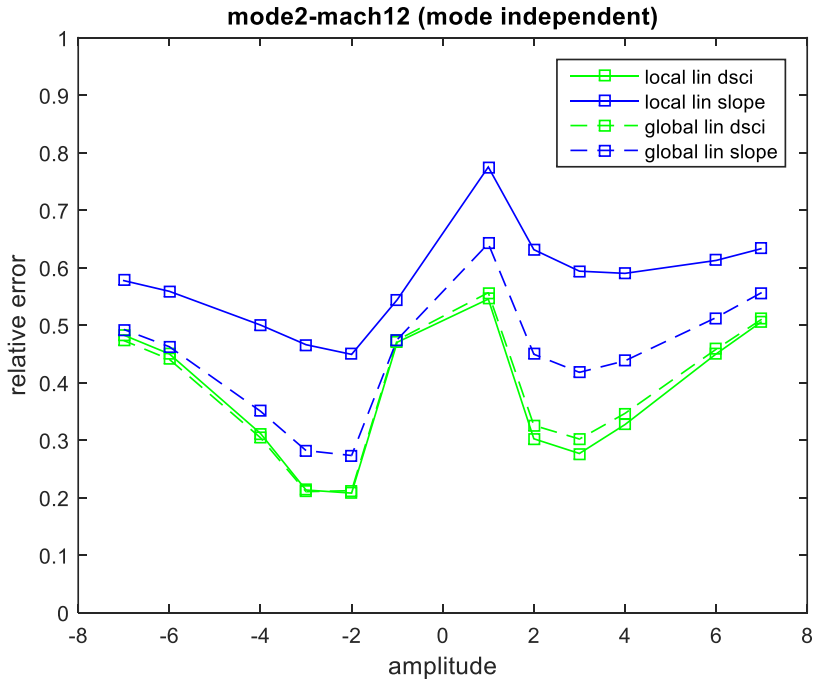

Figure 43. Fitting error comparison for mode2-mach12 with local linear slope, local linear dsci and global linear dsci (1 & 100 node) mode independent model

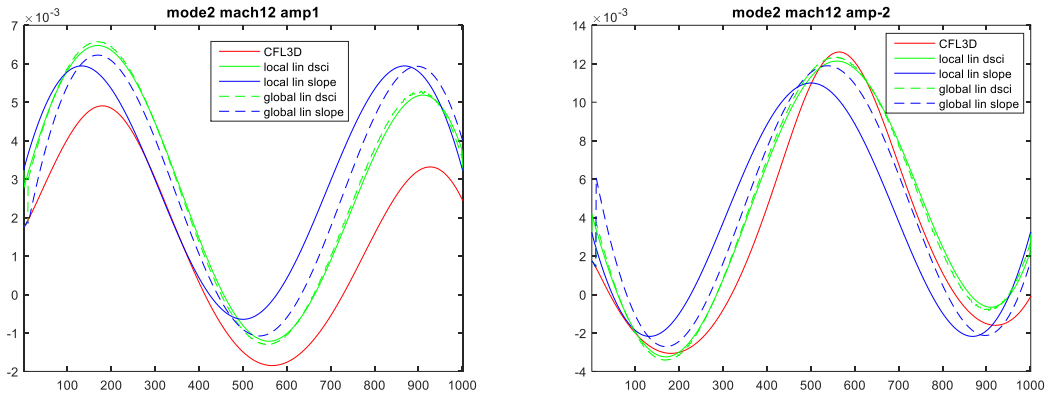

(a) (b)

Figure 44. Comparison of CFL3D Cp and reconstructed Cp with local linear dsci, global linear dsci (node 1& 100), local linear slope and global linear slope (node 1 & 100) mode independent model (a) mode2 mach12 amp1 and (b) mode2 mach12 amp-2

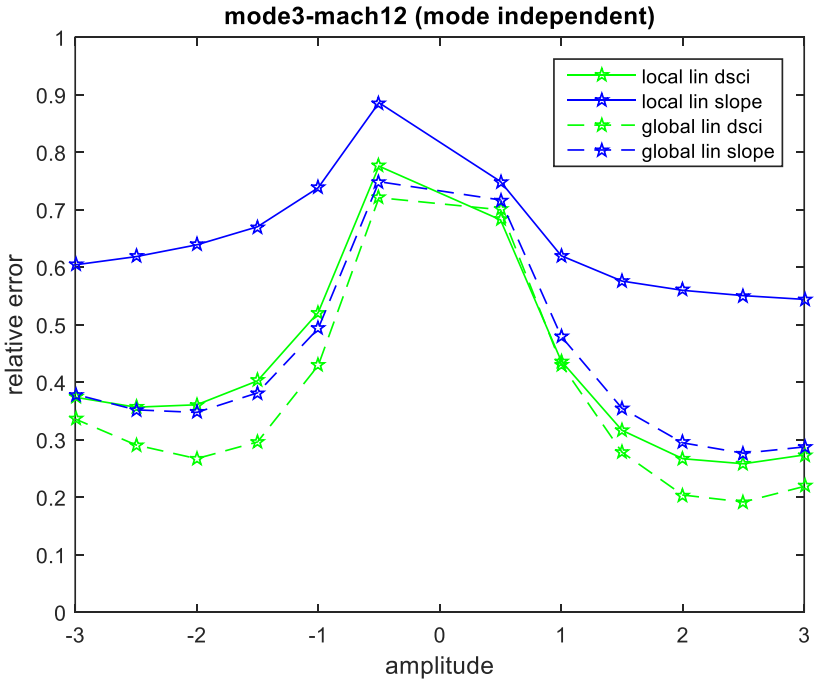

Figure 45. Fitting error comparison for mode3-mach12 with local linear slope, local linear dsci and global linear dsci (1 & 100 node) mode independent model

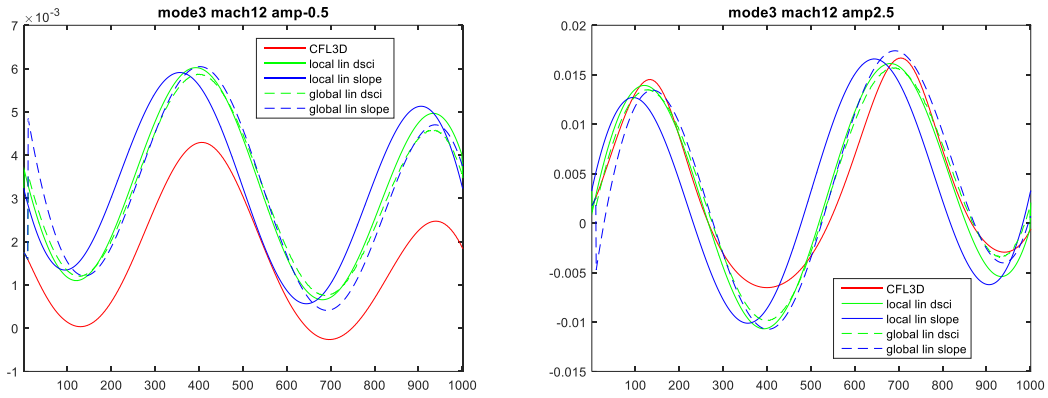

(a) (b)

Figure 46. Comparison of CFL3D Cp and reconstructed Cp with local linear dsci, global linear dsci (node 1& 100), local linear slope and global linear slope (node 1 & 100) mode independent model (a) mode3 mach12 amp-0.5 and (b) mode3 mach12 amp2.5

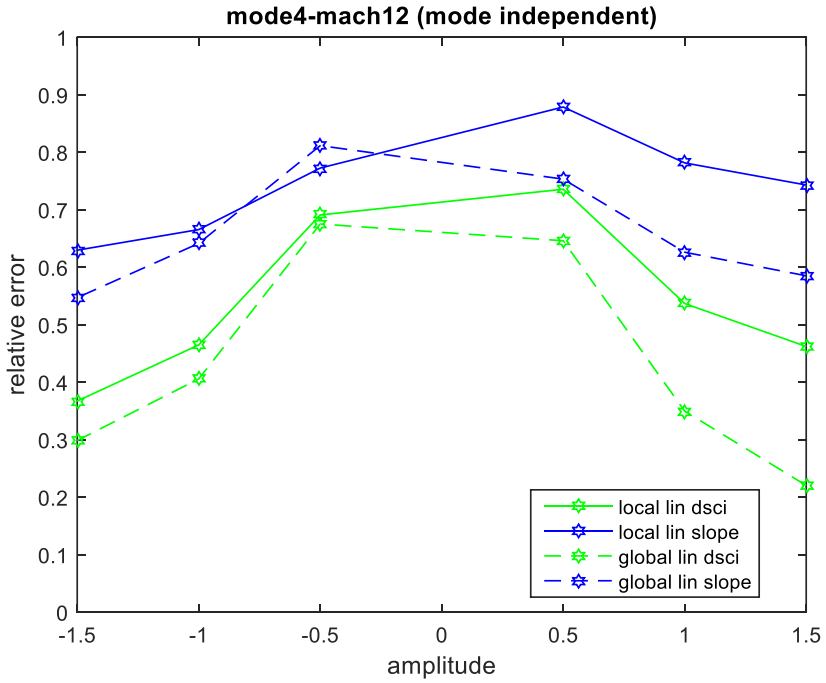

Figure 47. Fitting error comparison for mode4-mach12 with local linear slope, local linear dsci and global linear dsci (1 & 100 node) mode independent model

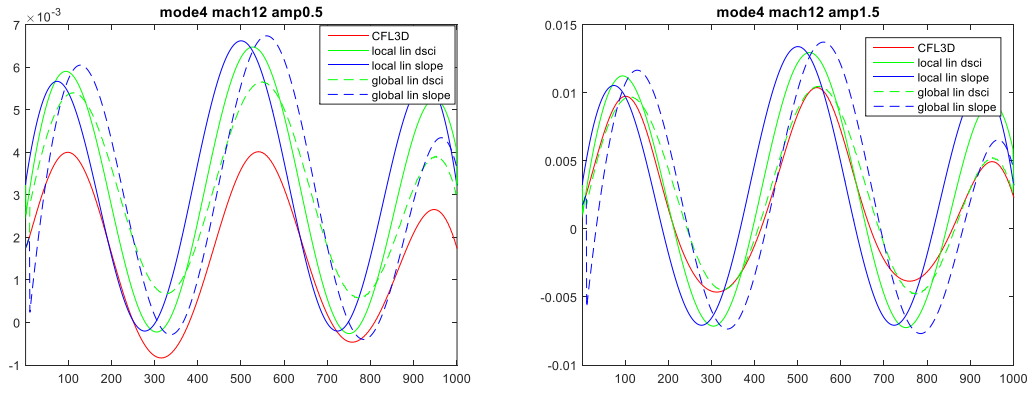

(a) (b)

Figure 48. Comparison of CFL3D Cp and reconstructed Cp with local linear dsci, global linear dsci (node 1& 100), local linear slope and global linear slope (node 1 & 100) mode independent model (a) mode1 mach12 amp-1 and (b) mode1 mach12 amp6

2.4 Local and Global Non-linear dsci model

The issue of phase difference can be solved either by using global model or adding linear d, c & i to slope in the model. And issue of offsetting can be solved only by including nonlinear terms in the model. In this section, we will look at reconstruction with local and global nonlinear dsci formulation.

Local non-linear dsci model, $Cp = (a_1M + b_1M^2 + c_1)\, w + (a_2M + b_2M^2 + c_2)\, (dw/dx) + (a_3M + b_3M^2 + c_3)\, (d^2w/dx^2) + (a_4M + b_4M^2 + c_4)\, (\int_0^x w dx) + (a_5M + b_5M^2 + c_5)\, w^2 + (a_6M + b_6M^2 + c_6)\, w\, (dw/dx) + (a_7M + b_7M^2 + c_7)\, w\, (d^2w/dx^2) + (a_8M + b_8M^2 + c_8)\, w\, (\int_0^x w dx) + (a_9M + b_9M^2 + c_9)\, (dw/dx)^2 + (a_{10}M + b_{10}M^2 + c_{10})\, (dw/dx)\, (d^2w/dx^2) + (a_{11}M + b_{11}M^2 + c_{11})\, (dw/dx)\, (\int_0^x w dx) + (a_{12}M + b_{12}M^2 + c_{12})\, (d^2w/dx^2)^2 + (a_{13}M + b_{13}M^2 + c_{13})\, (d^2w/dx^2)\, (\int_0^x w dx) + (a_{14}M + b_{14}M^2 + c_{14})\, (\int_0^x w dx)^2 + (a_{15}M + b_{15}M^2 + c_{15})$

There are 14 factors to be considered, not all the parameters contribute to the reconstruction. To make decision on elimination of non-contributing factor out of the above formulation weightage of each factor in reconstruction must be calculated. Individual factor is removed and error in reconstruction is compared to full configuration.

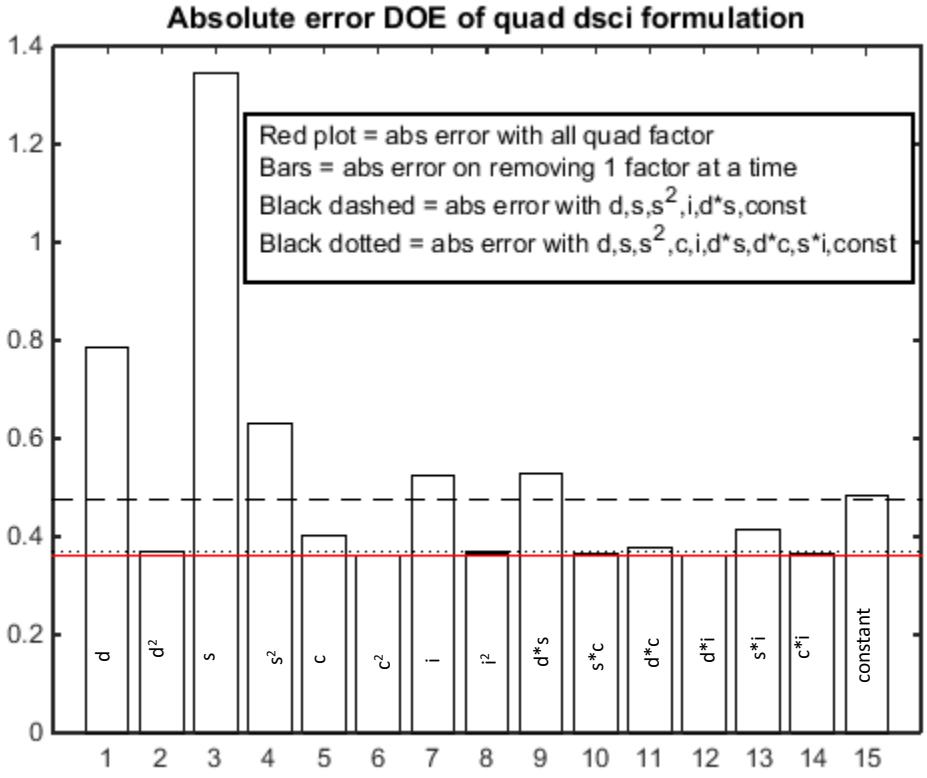

Figure 49. Comparison of contribution of each term of Non-linear dsci formulation to reconstruction error

Based on Figure 44., the dominating factors are d, s, s^2, c, i, d*s, d*c, s*I and constant. Further analysis is conducted on this formulation only. Like linear dsci analysis, not all nodes can be used for global formulation so contribution of global terms is studied keeping constraint on conditioning of the matrix. As expected the offsetting of reconstructed Cp for small amplitude is eradicated by introduction of non-linear terms.

For mode 1 (Figure 45) and mode 2 (Figure 46) global terms do not contribute largely to the efficient construction. As distance between nodes increases reconstruction error reduces but the improvement is not significant because the error for local formulation is already small reducing priority in mode independent least square solution.

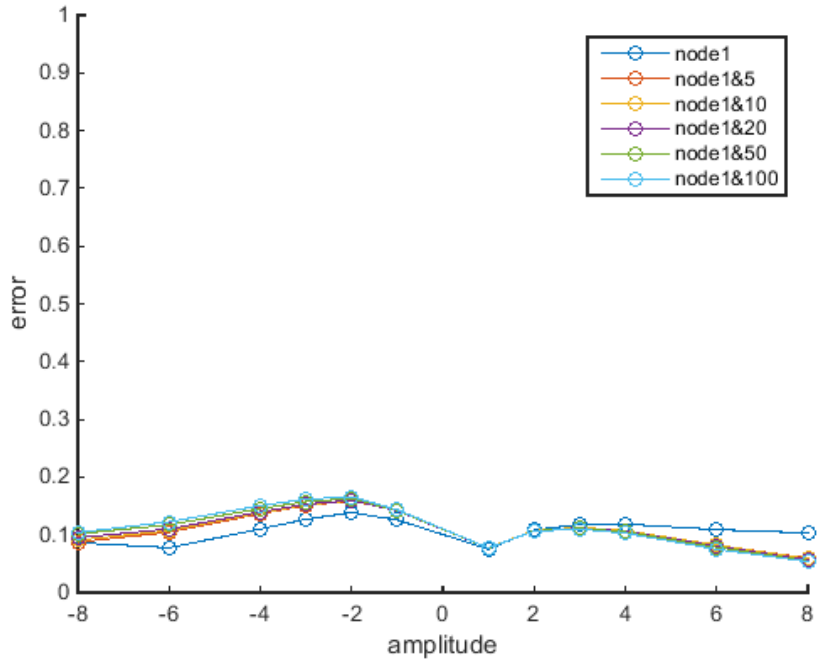

Figure 50. Fitting error comparison for mode1-mach12 with local non-linear dsci and global non-linear dsci (only 1 global term - various configurations of distance) mode independent model

In contrary to mode 1 and 2, for mode 3 (Figure 47) and mode 4 (Figure 48) reconstruction improves with addition of global nodes. And further fitting improves with increasing distance of global node. This indicates that using 100^{th} global nodal parameter with local parameter would give the best fit across the modes.

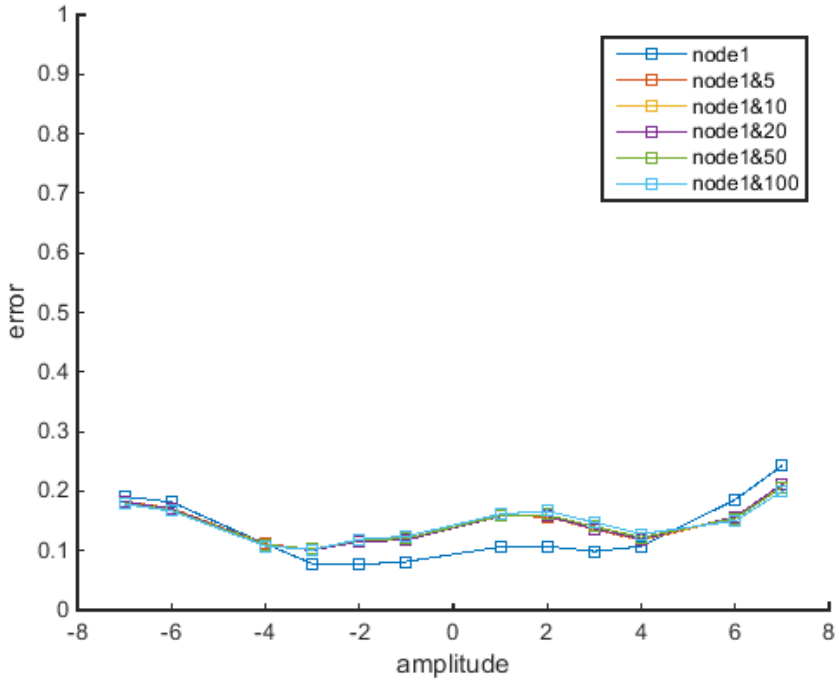

Figure 51. Fitting error comparison for mode2-mach12 with local non-linear dsci and global non-linear dsci (only 1 global term - various configurations of distance) mode independent model

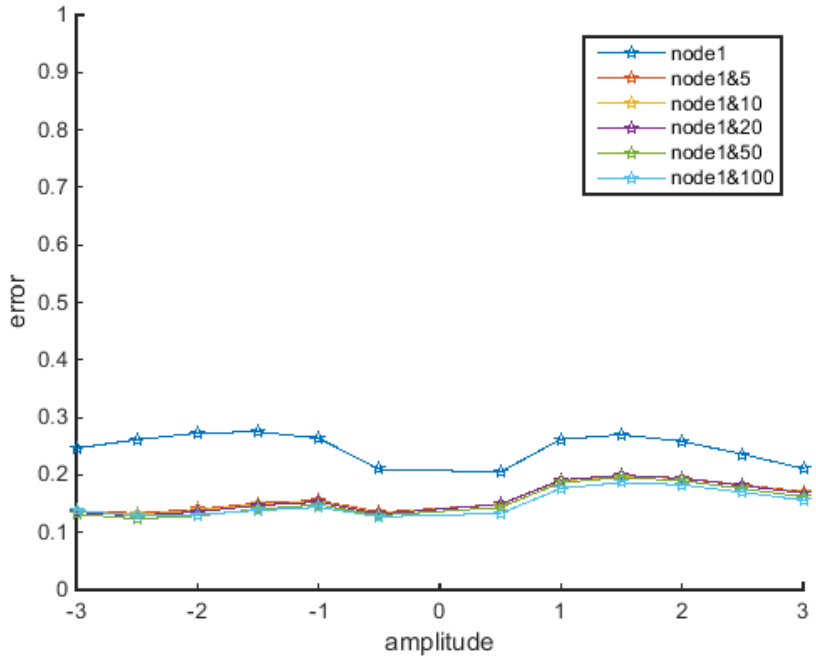

Figure 52. Fitting error comparison for mode3-mach12 with local non-linear dsci and global non-linear dsci (only 1 global term - various configurations of distance) mode independent model

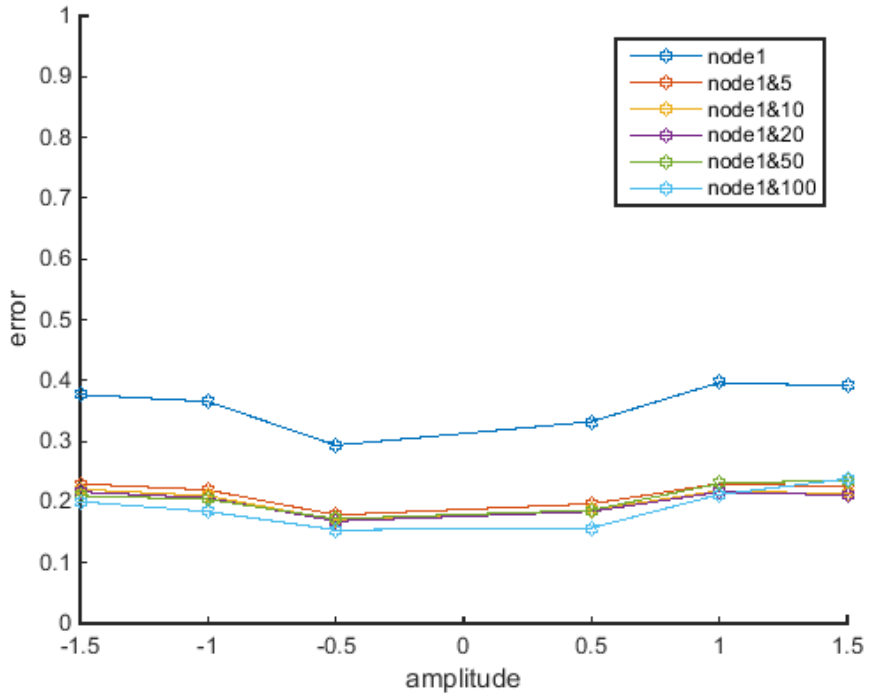

Figure 53. Fitting error comparison for mode4-mach12 with local non-linear dsci and global non-linear dsci (only 1 global term - various configurations of distance) mode independent model

2.4.1.1 Reconstruction with multiple global nodes

Continuing from the conclusion of previous section, more global nodes are added to 100th node keeping constraint of conditioning of the system. For other configurations, similar fit is achieved for mode 1 (Figure 49) and mode 2 (Figure 50). But for mode 3 (Figure 51) and mode 4 (Figure 52) improvement is achieved due to higher base error compared to lower modes.

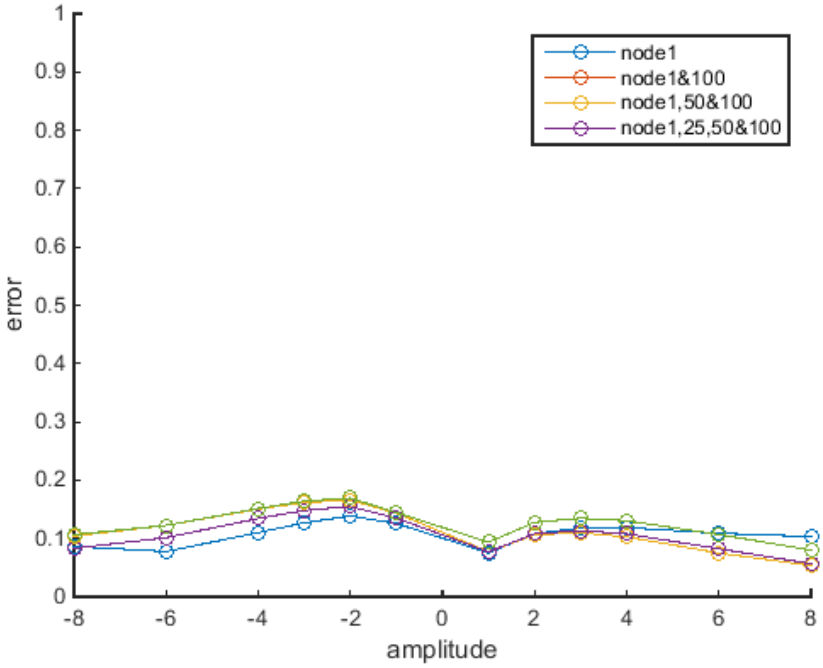

Figure 54. Fitting error comparison for mode1-mach12 with local non-linear dsci and global non-linear dsci (various configurations of number of nodes) mode independent model

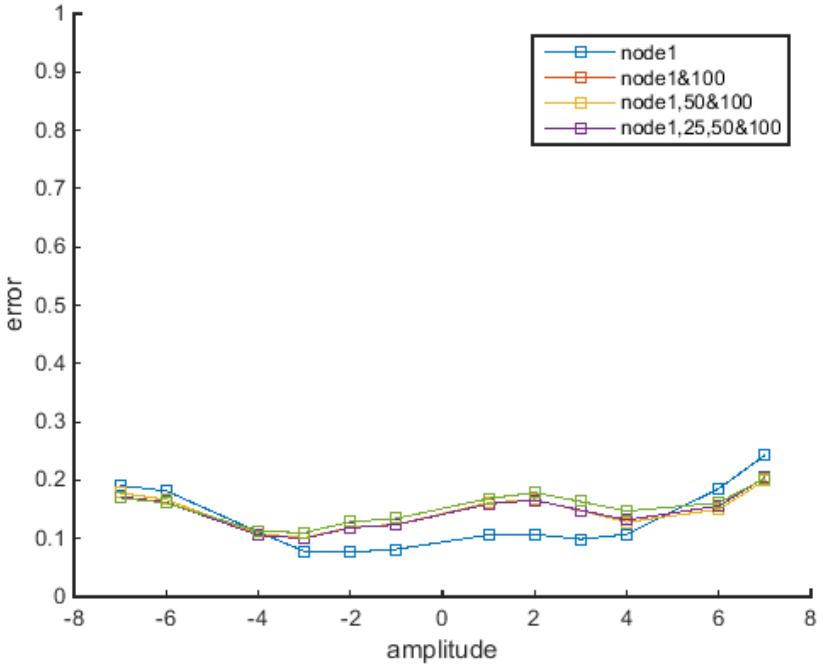

Figure 55. Fitting error comparison for mode2-mach12 with local non-linear dsci and global non-linear dsci (various configurations of number of nodes) mode independent model

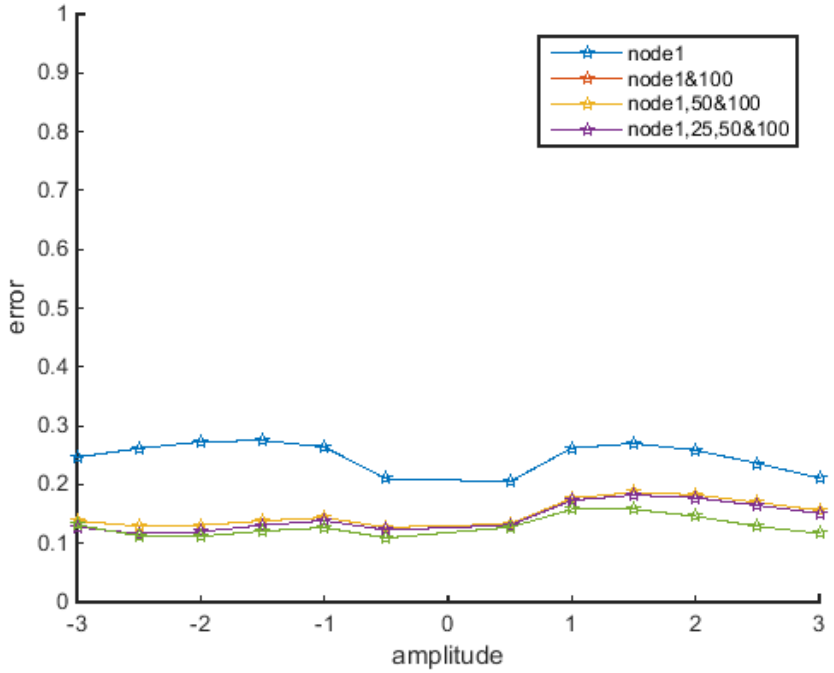

Figure 56. Fitting error comparison for mode3-mach12 with local non-linear dsci and global non-linear dsci (various configurations of number of nodes) mode independent model

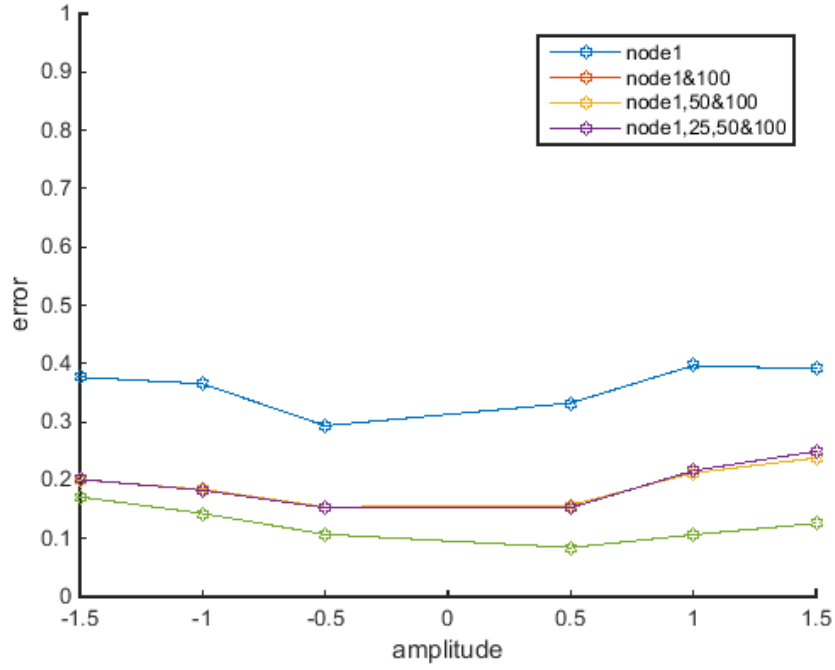

Figure 57. Fitting error comparison for mode4-mach12 with local non-linear dsci and global non-linear dsci (various configurations of number of nodes) mode independent model

With global nodes (25, 50, 100) in addition to local node the error across the modes are reduced considerably. Average error across the modes with global non-linear dsci is 16%.

2.5 Auto -regressive Moving-average (Nonlinear dsci) model

Liu [4] relates pressure coefficient under supersonic flow to classical piston theory which is formulated with previous Cp values as well. Taking inspiration from that formulation, in this section Cp for each node is reconstructed with moving average of global nonlinear dsci and Cp for upstream nodes. The matrix system in this case is also ill-conditioned (RCOND=5e-26) but like global model with 10 previous nodes here as well the coefficients are realistic and the results match. But this doesn't guarantee that this methodology will be stable for any system. So, it is important to study if we need all the nodes in the problem because spacing the nodes would make the system conditioned. Using the similar strategy as in previous section of using only 1 global node for both auto regressive and moving average term, iterations are conducted with 5^{th}, 10^{th}, 20^{th}, 50^{th} and 100^{th} in addition to 1^{st} (local) node. Impact of global terms is seen clearly as higher modes are reconstructed (Figure 52-55) and reconstruction error reduces as distance of global node increases. Additionally, if only local values are used either for regressive term or moving average reconstruction worsens.

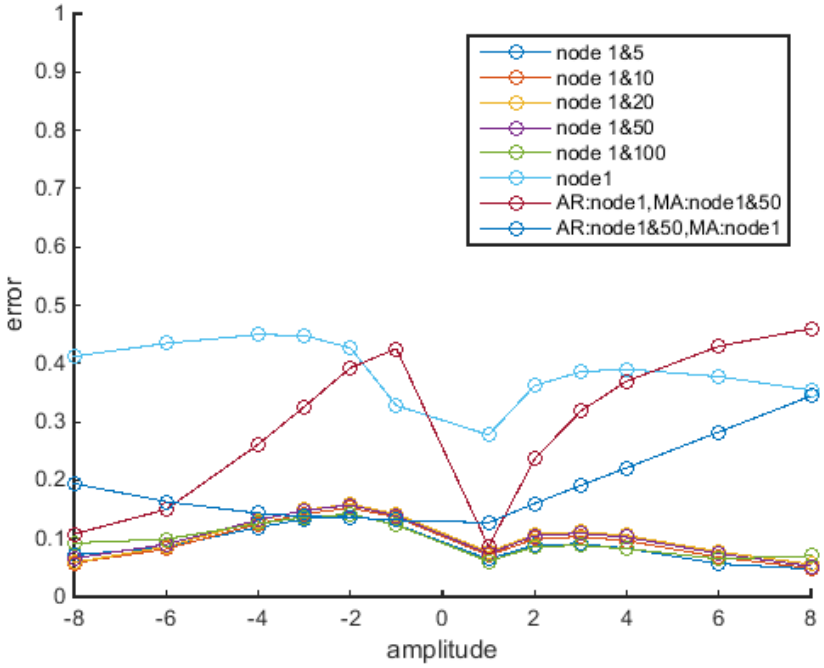

Figure 58. Fitting error comparison for different configuration of mode independent ARMA model with moving average of nonlinear dsci for mode 1 mach12

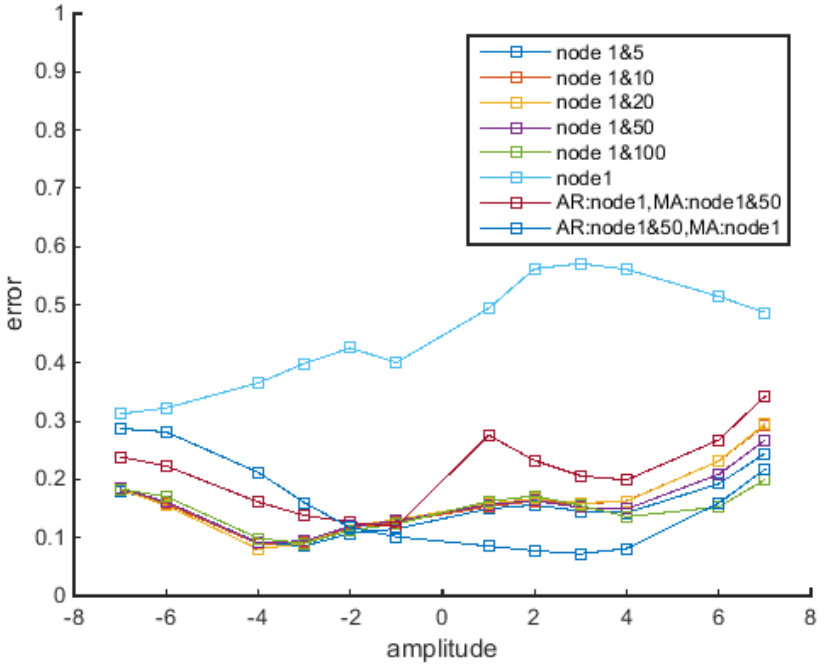

Figure 59. Fitting error comparison for different configuration of mode independent ARMA model with moving average of nonlinear dsci for mode 2 mach12

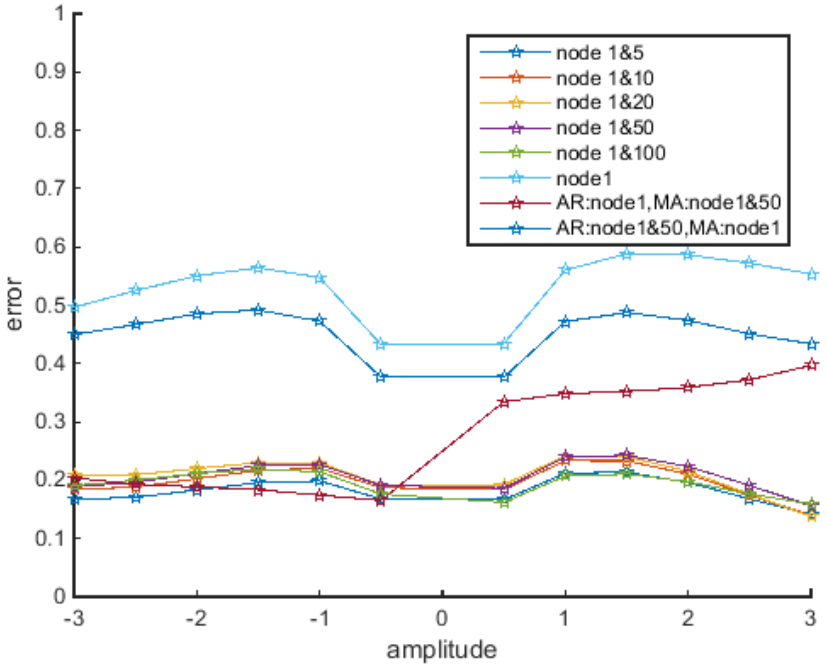

Figure 60. Fitting error comparison for different configuration of mode independent ARMA model with moving average of nonlinear dsci for mode 3 mach12

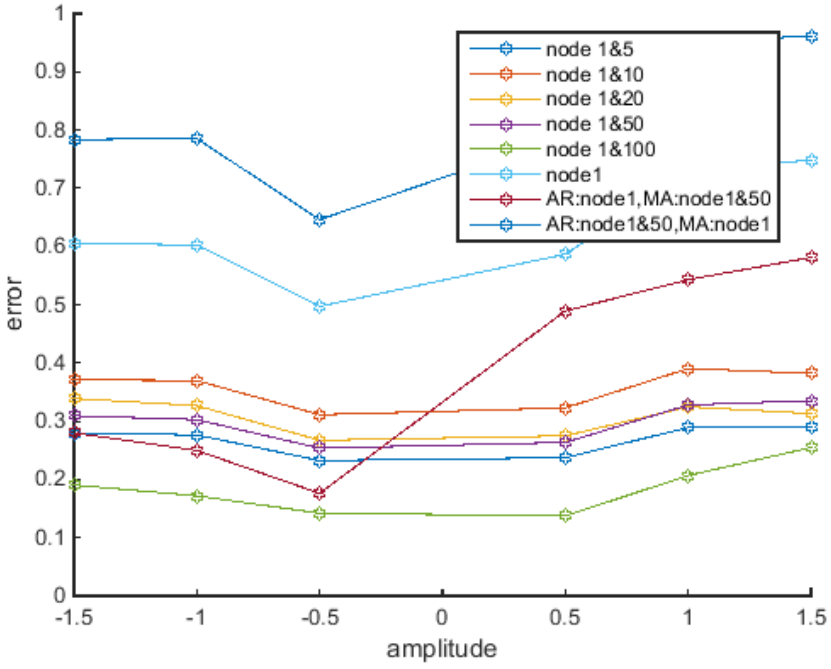

Figure 61. Fitting error comparison for different configuration of mode independent ARMA model with moving average of nonlinear dsci for mode 4 mach12

2.6 Auto -regressive Moving-average (Cubic Slope) model

Taking inspiration from the nonlinear term based ARMA model in previous section, it is important if similar formulation can be achieved with cubic piston theory also. The disadvantage of a nonlinear dsci model is that it would be cumbersome to create the formulation for higher dimensions and strategy regarding integration of displacement. Another advantage of global cubic slope model over global nonlinear dsci model is that more closely spaced global terms can be used which improves the fit. Figure 57-60 shows the fitting error for each mode with mode independent ARMA (global cubic slope) model having 20^{th}, 50^{th}, 100^{th} node in addition to local slope. The fit is further enhanced with addition of closely spaced global node keeping the system well-conditioned.

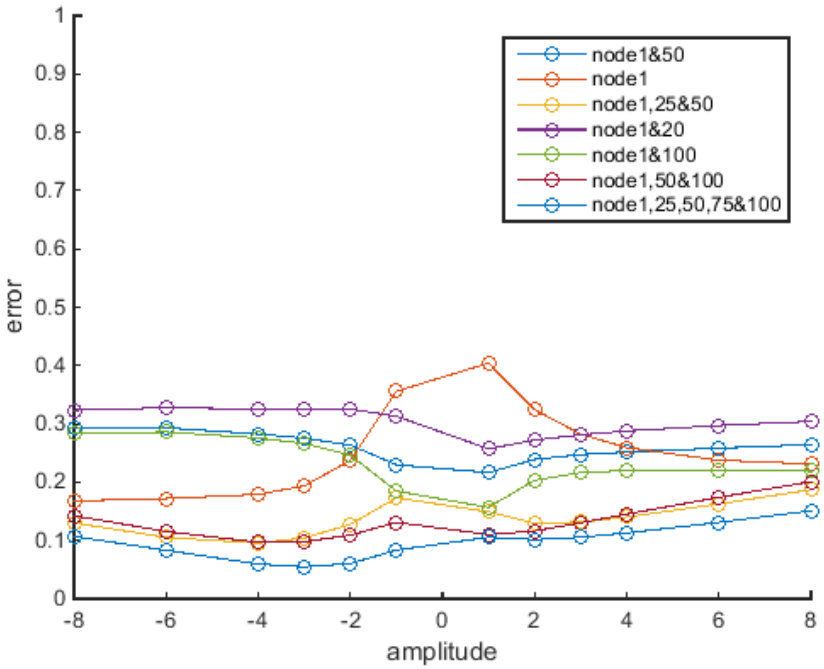

Figure 62. Fitting error comparison for different configuration of mode independent ARMA model with moving average of cubic slope for mode 1 mach12

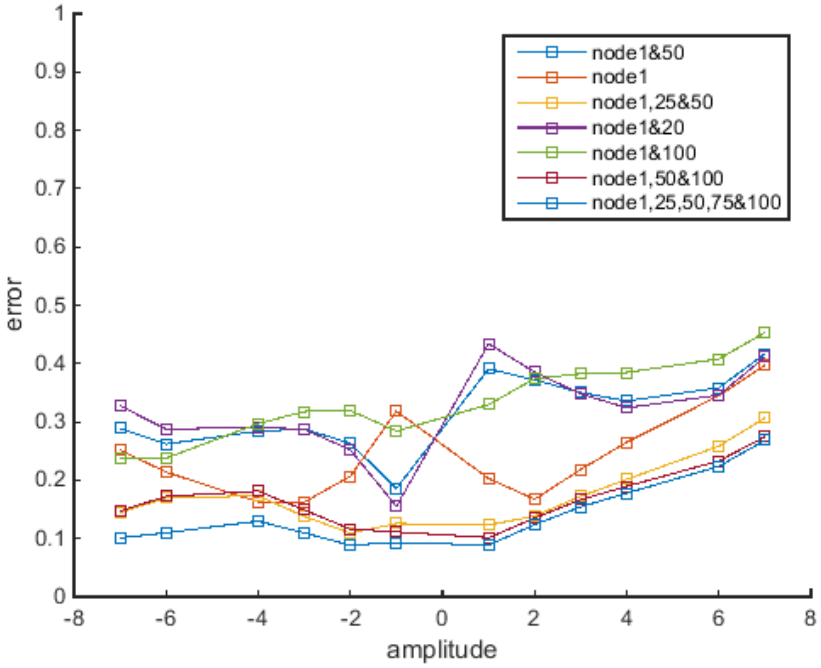

Figure 63. Fitting error comparison for different configuration of mode independent ARMA model with moving average of cubic slope for mode 2 mach12

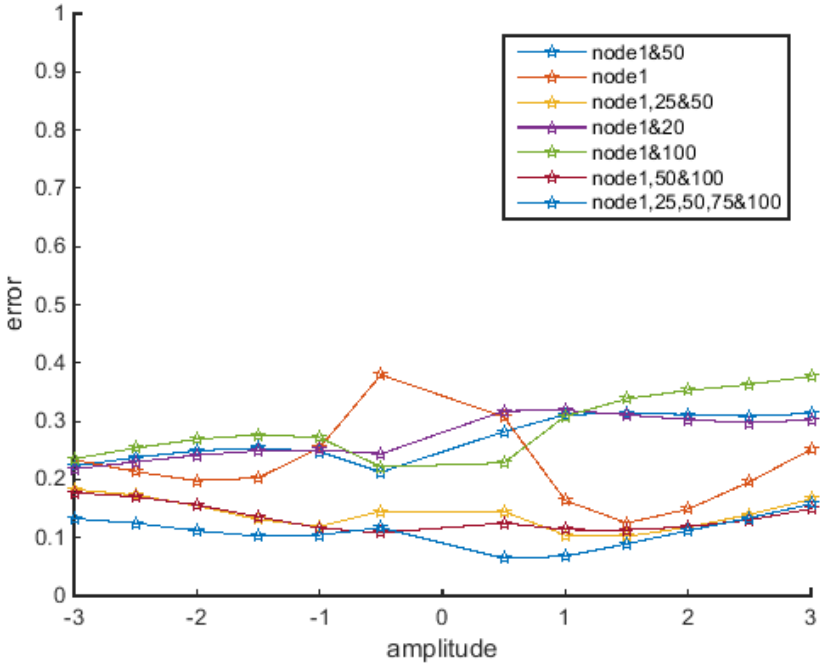

Figure 64. Fitting error comparison for different configuration of mode independent ARMA model with moving average of cubic slope for mode 3 mach12

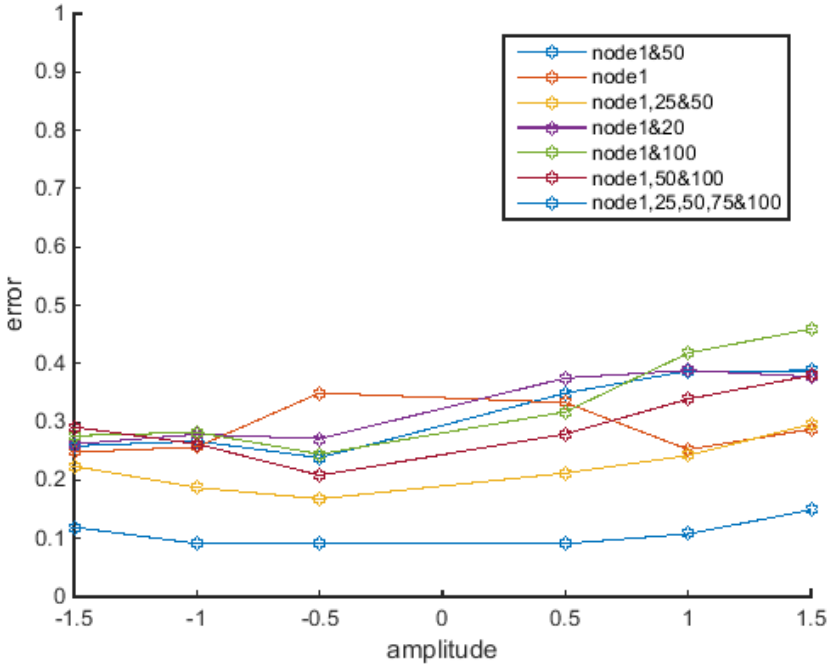

Figure 65. Fitting error comparison for different configuration of mode independent ARMA model with moving average of cubic slope for mode 4 mach12

Conclusively a cubic slope based ARMA model with 1st, 25th, 50th, 75th and 100th node for regressive and moving average terms can give comparable results to nonlinear dsci based ARMA formulation with significantly lower computation effort.

Section 3.5 and 3.6 have been reconstruction for node 101 to 1001, which leads to next obvious thought about the reconstruction of node 1 to 100 and the addition to the reconstruction error for node 101 to 1001 due to prediction of those nodes. The simplest models of local cubic slope and local nonlinear dsci provide decent fit for initial nodes of the beam with small phase difference until the first peak.

2.7 Composite modelling with local nonlinear dsci and ARMA cubic slope

In this section node 1 to 100 will be first modelled with local nonlinear dsci formulation from Section 3.4 and then further used to propagate with cubic slope based ARMA model (discussed in section 3.6) to reconstruct Cp for the beam. Figure 62 shows that except for larger amplitudes for mode2 all the data can be reconstructed within acceptable error range.

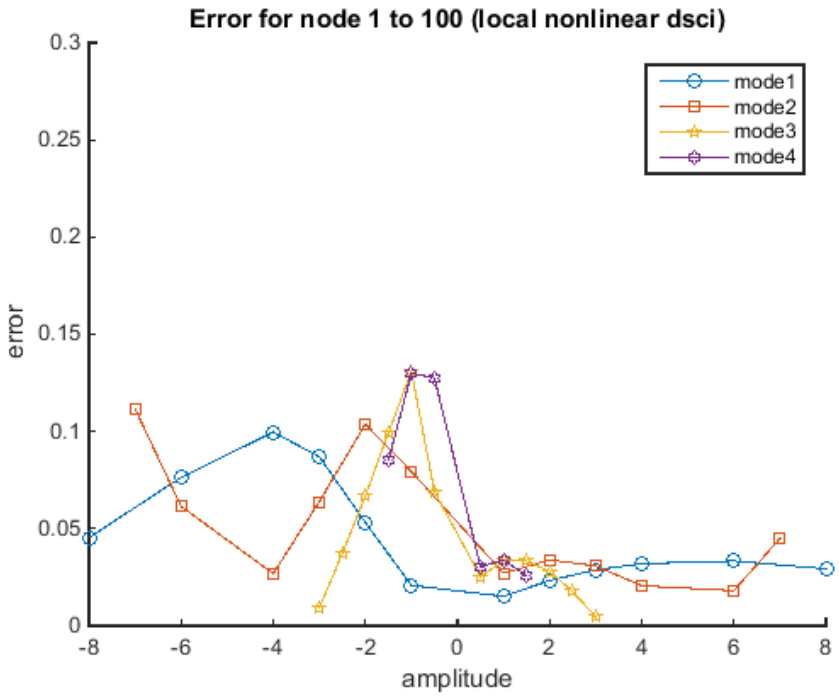

Figure 70. Fitting error comparison for node 1 to 100 reconstructed with mode independent local nonlinear dsci model

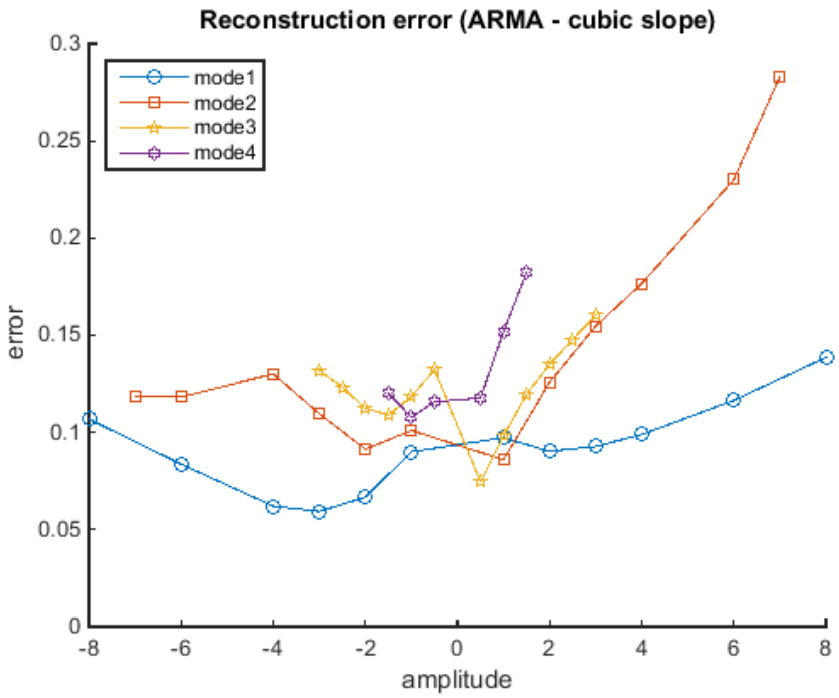

Figure 71. Fitting error comparison for reconstructed with mode independent local nonlinear dsci model (1 to 100 node) and cubic slope based ARMA model (101 to 1001 node)

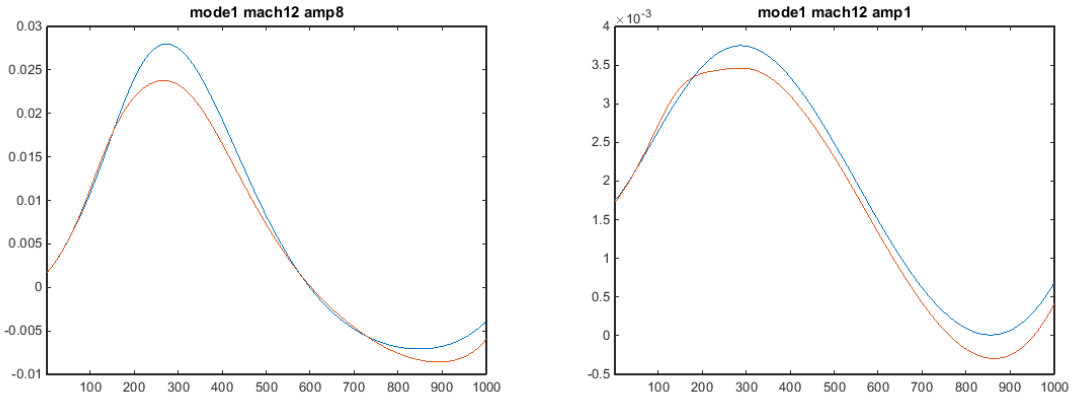

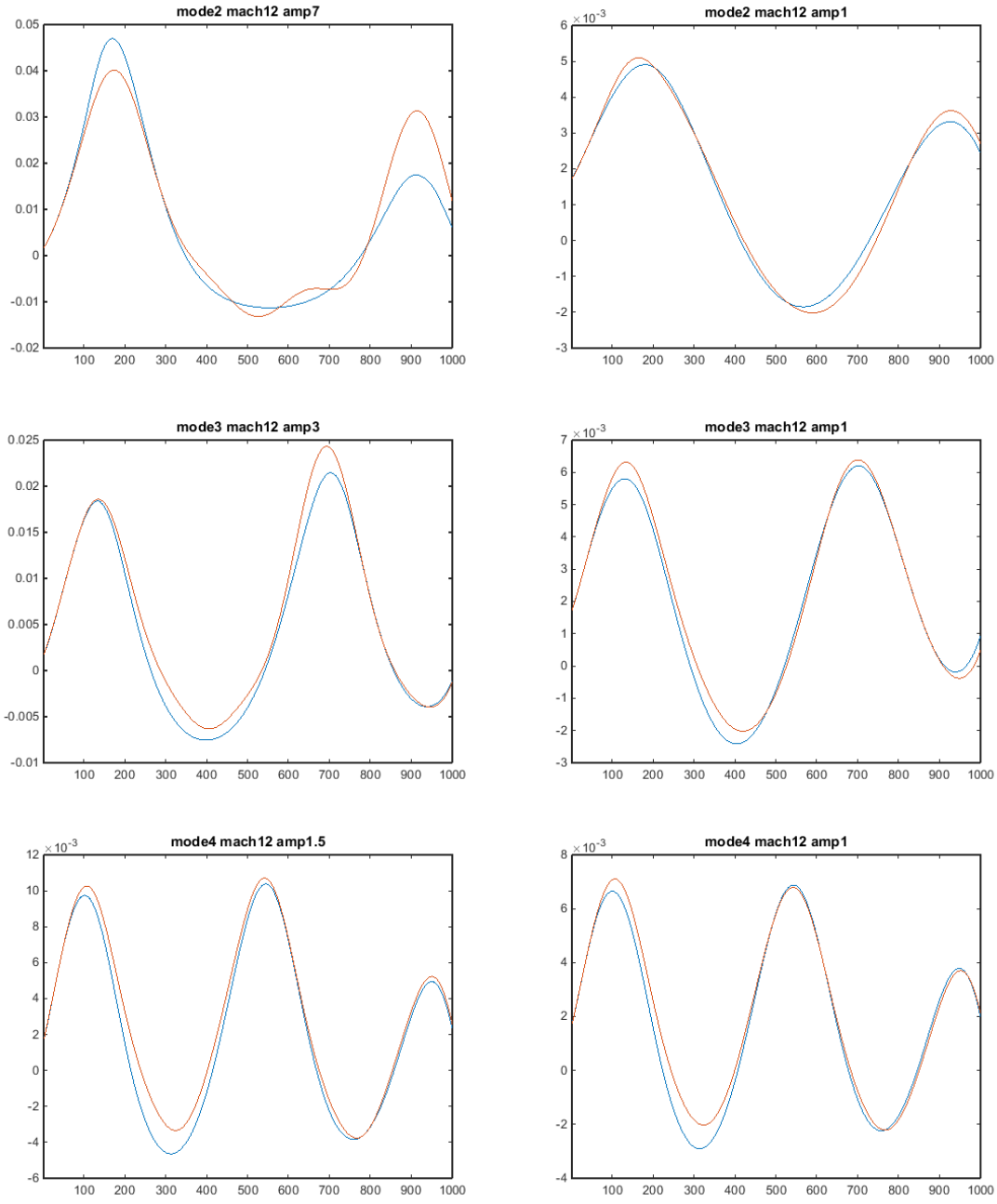

Figure 72. Comparison of Cp from CFL3D (blue) and reconstructed Cp with composite model (red) for mode1 mach12 amp8, amp1; mode2 mach12 amp7, amp1; mode3 mach12 amp3, amp0.5; mode4 mach12 amp1.5, amp0.5

2.8 Two-level composite model

Based on the above iterations, increasing nonlinearity in the data causes increased error in reconstruction. Eyeballing on the residual of the mode independent local cubic slope model gives an increasing linear behavior with respect to polarity of amplitude. Utilizing this behavior, model can be further trimmed down from composite model in Section 3.7. Figure 64-67 shows the residual after fitting mode independent local cubic slope model. The residual become increasing linear with respect to polarity of the amplitude as higher modes are considered. This feature negates the increasing complexity of the higher order mode data. These residuals will now be fitted with mode independent global cubic slope based ARMA model. Hence Cp for node 1 to 100 are fitted with local cubic slope model and the residual for node 101 to 1001 are fitted with global cubic slope ARMA model (node 1st, 25th, 50th, 75th, 100th).

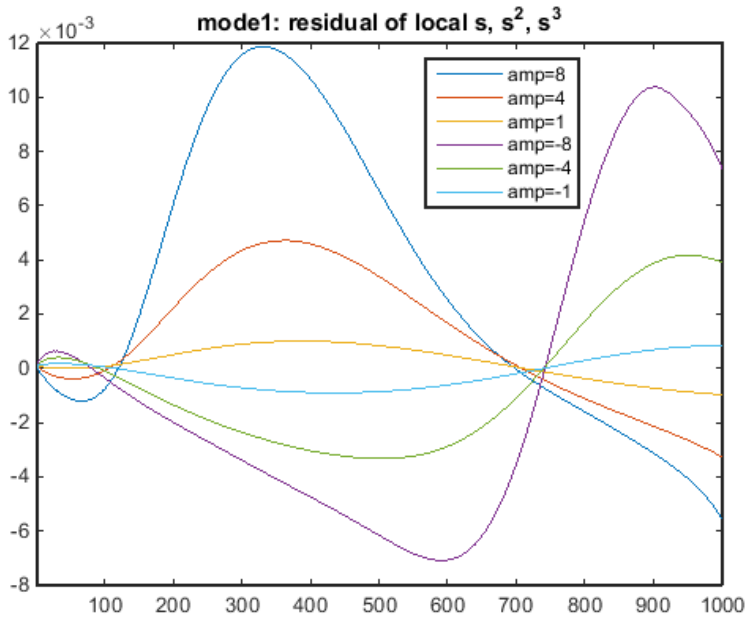

Figure 73. Residual of Cp from fitting mode independent local cubic slope model for mode1 mach12

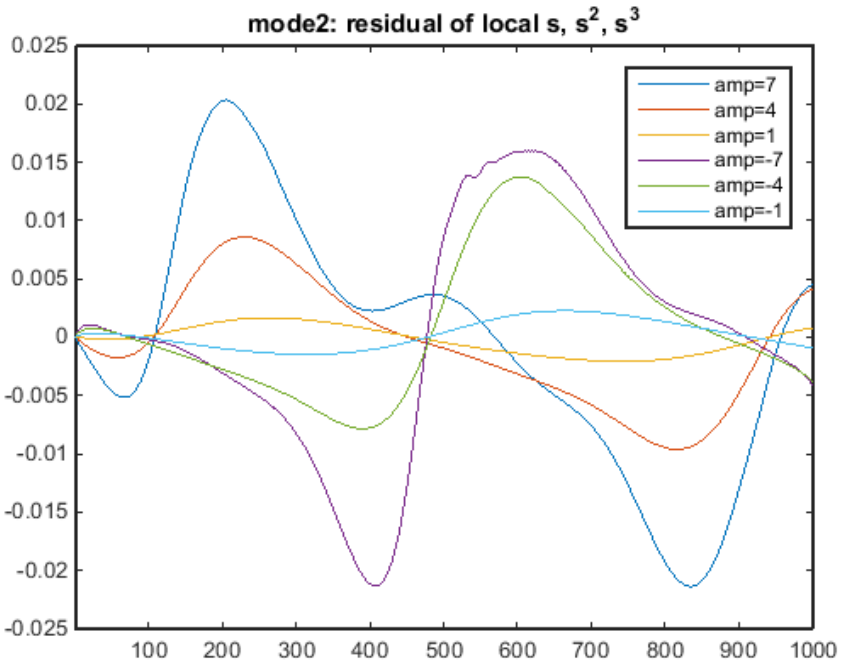

Figure 74. Residual of Cp from fitting mode independent local cubic slope model for mode2 mach12

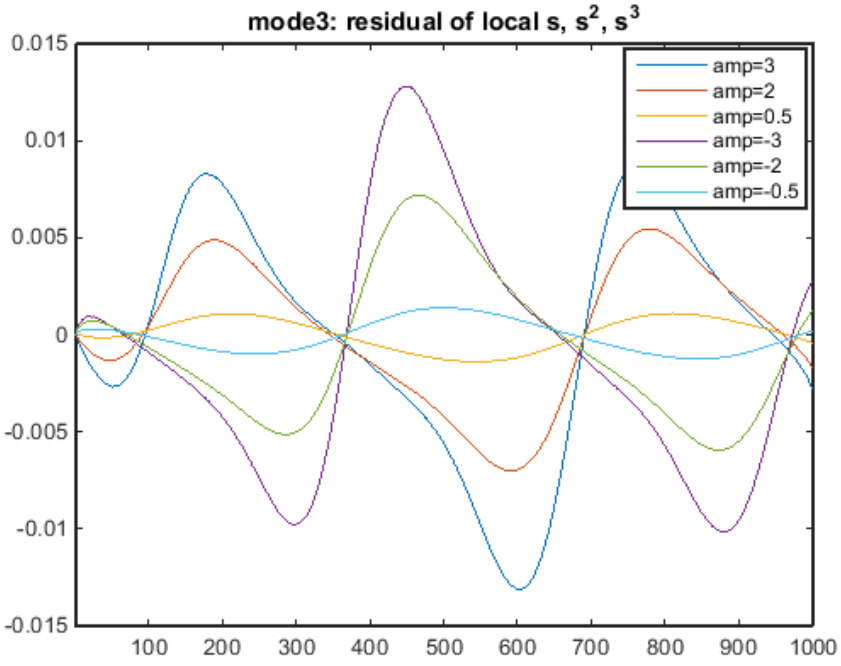

Figure 75. Residual of Cp from fitting mode independent local cubic slope model for mode3 mach12

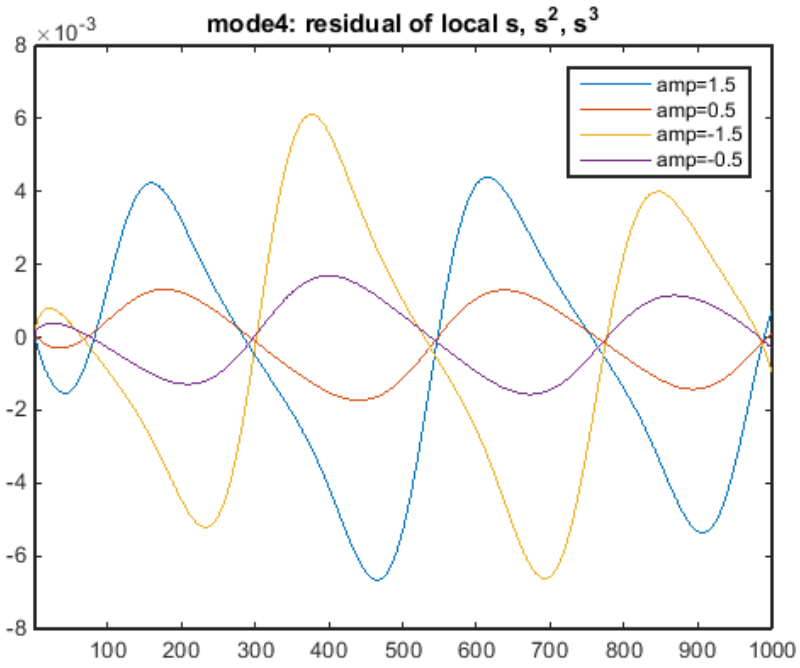

Figure 76. Residual of Cp from fitting mode independent local cubic slope model for mode4 mach12

Compared to previous composite model, error reduces for large amplitudes of mode2 and others remains in the acceptable range.

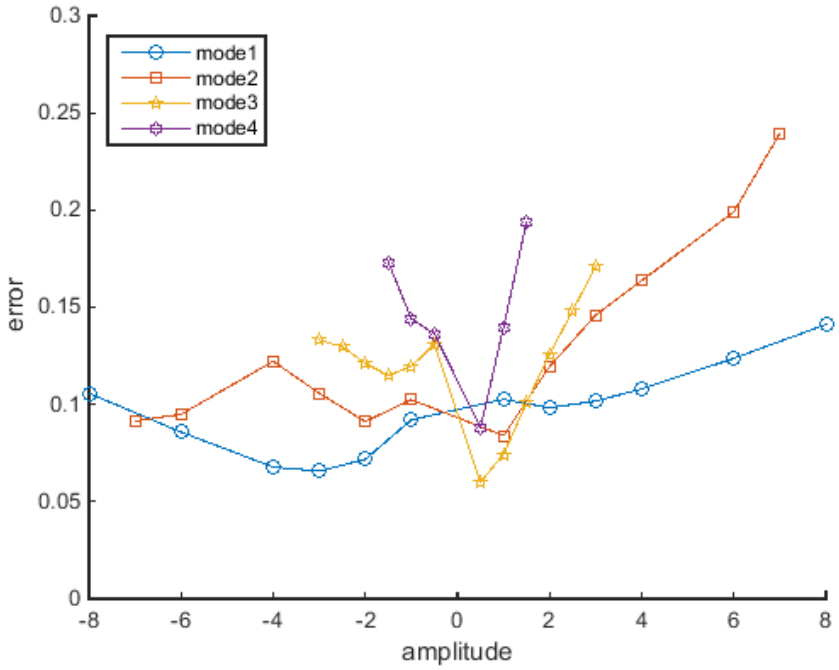

Figure 77. Fitting error comparison for reconstructed with mode independent local cubic slope model (1 to 1001 node) and residual with cubic slope based ARMA model (101 to 1001 node)

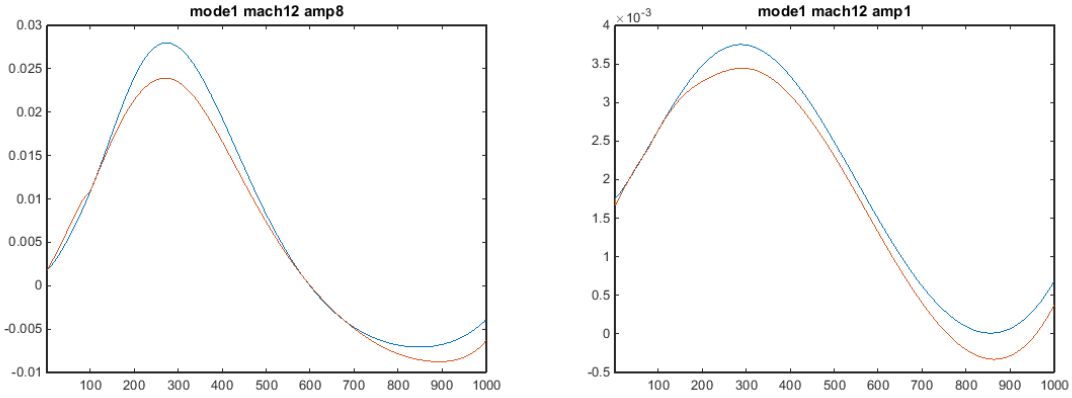

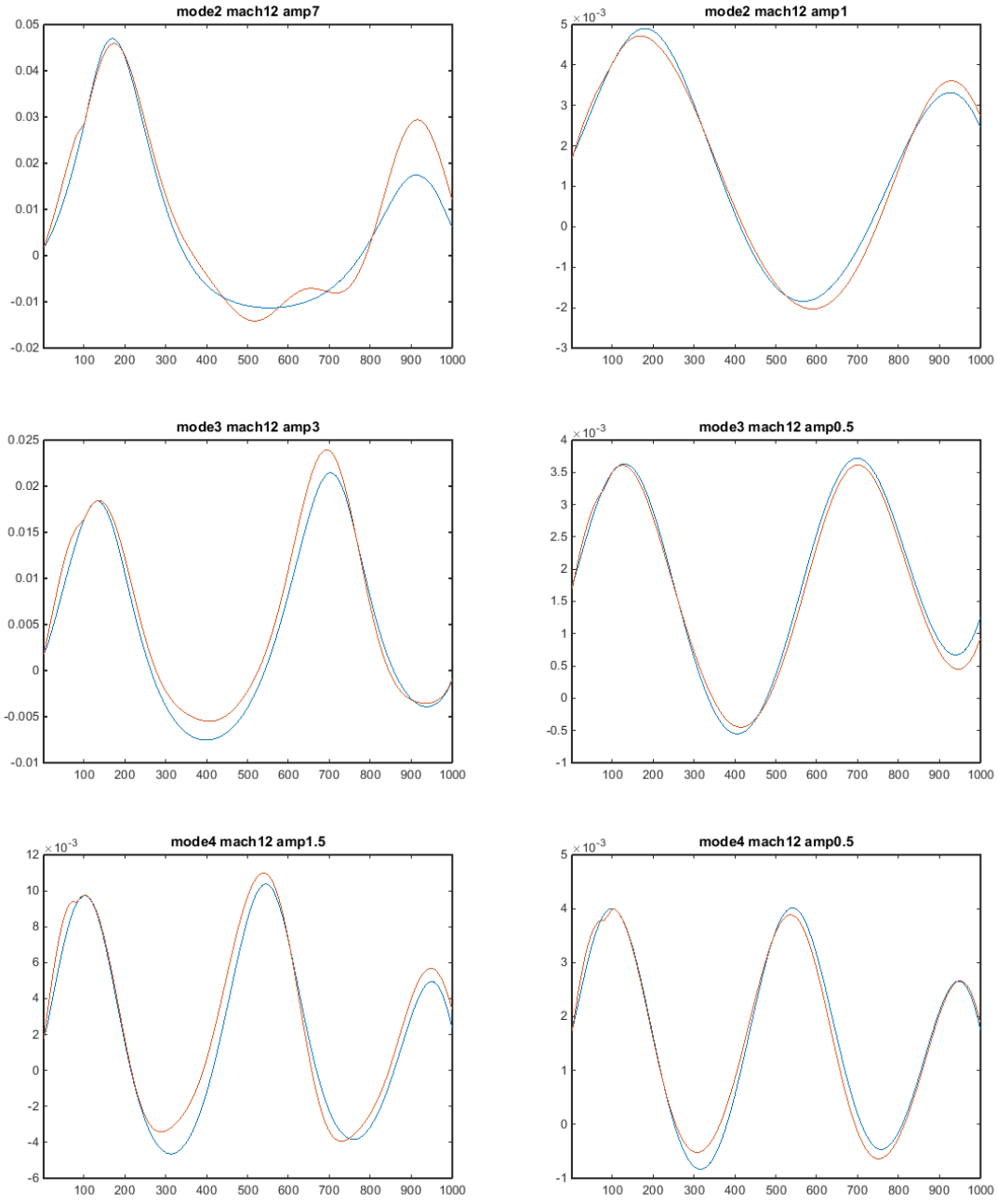

Figure 78. Comparison of Cp from CFL3D (blue) and reconstructed Cp with composite model (red) for mode1 mach12 amp8, amp1; mode2 mach12 amp7, amp1; mode3 mach12 amp3, amp0.5; mode4 mach12 amp1.5, amp0.5

2.9 Modelling Unsteady Cp with two-level composite model

Considering the similarities of Steady and Unsteady Cp, in this section Cp is reconstructed with the same model based on $\frac{Dw}{Dt}(=\frac{\partial w}{\partial x}+\frac{1}{U_\infty}\frac{\partial w}{\partial t})$ instead of $\frac{dw}{dx}$. $\frac{Dw}{Dt}$ has time dependent component which helps in modelling phase difference between time steps of increasing displacements. Note that coefficients of steady model with the same amplitudes as unsteady data are considered which is a subset of all the steady data.

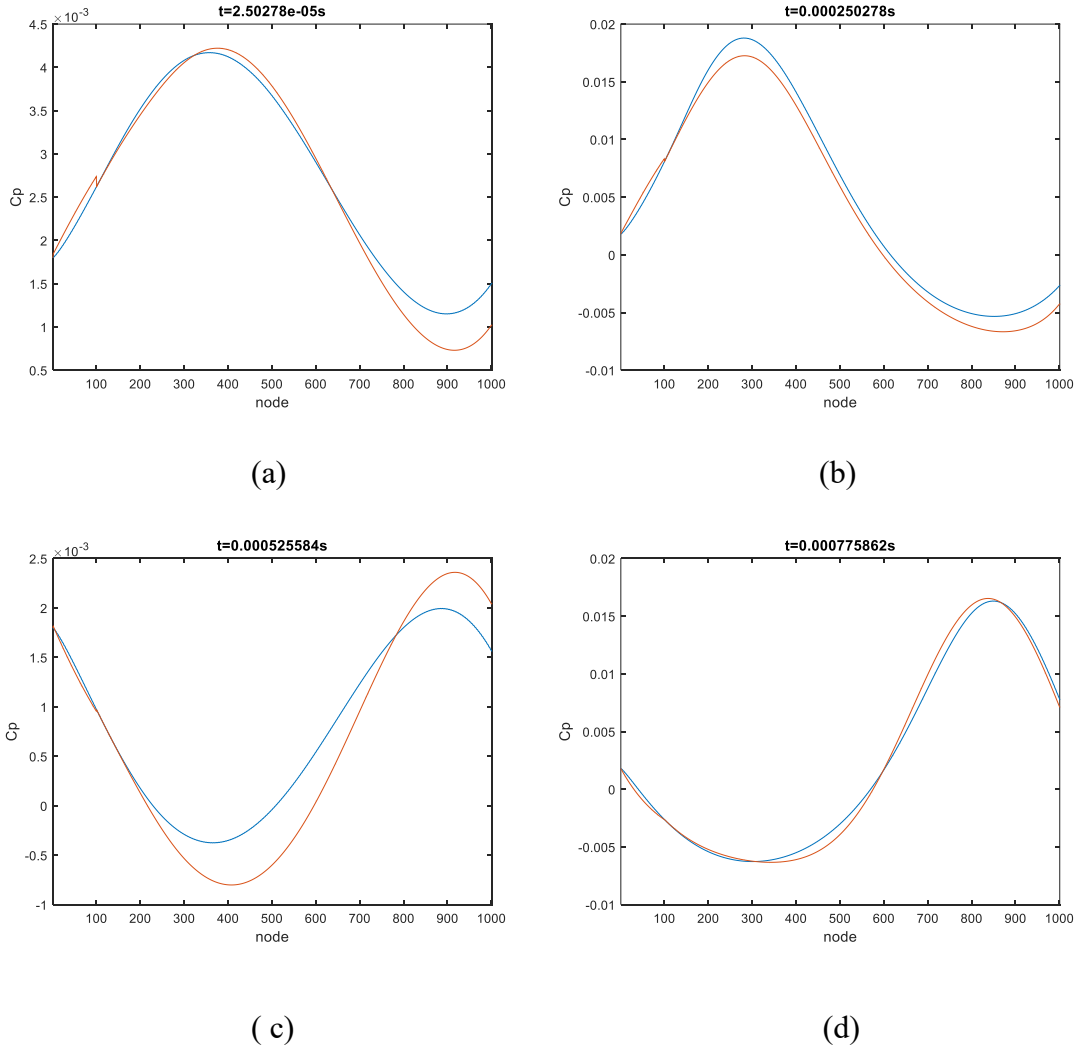

Figure 79. Comparison of CFD unsteady Cp (blue) and reconstructed with two-level model (red) for mode1 mach12 amp6 freq160 (a) t = 2.5e-05 s (b) t = 0.00025 s (c) t = 0.00052 s (d) t = 0.00077 s

The reconstructed Cp have a offset and phase difference for smaller displacement (Figure 70 (a)(c)) but as the displacement increases fitting improves. In comparison to steady Cp where error increases with amplitude here the error decreases. Since the same coefficients are utilized to generate unsteady Cp this is due to nature of $\frac{Dw}{Dt}$ over time. This is further proved by reconstruction for lower amplitudes which similar pattern as steady Cp. For example, Figure 71 shows reconstruction of mode3 amp3 where the fitting is substantially better.

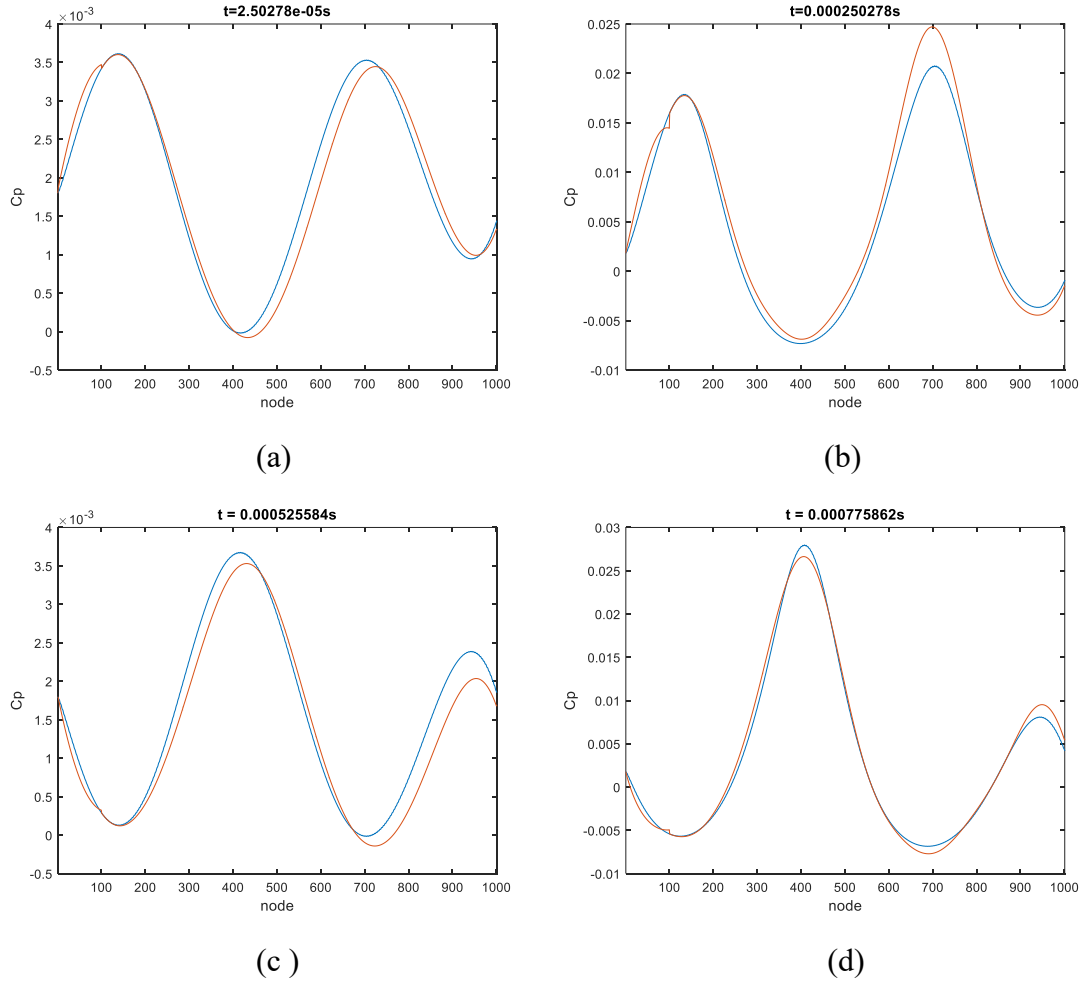

Figure 80. Comparison of CFD unsteady Cp (blue) and reconstructed with two-level model (red) for mode3 mach12 amp3 freq160 (a) t = 2.5e-05 s (b) t = 0.00025 s (c) t = 0.00052 s (d) t = 0.00077 s

3 Piston Theory based surrogate model for Hypersonic flow: Stochastic model

From Chapter 2, Cp can be modelled closely with a two-level model where ARMA (1st, 25th, 50th, 75th and 100th node cubic slope) model reconstructs residual after fitting local cubic slope model. This model is the simplest model among the tested options. This model also gives the flexibility of modelling uncertainty with either local, ARMA or both models. In ensuing section analysis on component of each layer in the reconstruction is conducted. Section 3.2 discusses randomizing Auto regressive coefficients of the mean model with the Non-Parametric method defined by Mignolet et. al. [5]. Further on same principle, Section 3.3 discusses randomizing coefficients of moving average of slope and reconstruction achieved. Modelling model uncertainty through the local model is described in Section 3.4 where randomization is also achieved by Non-Parametric method and ensuing issue.

3.1 Contribution of Local and Global component of the model

In the reconstructed result, local component is the major contributor and global component provides corrections to the phase difference and peak. Figure 63-66 shows the comparative plots of local and ARMA component for a mode independent model.

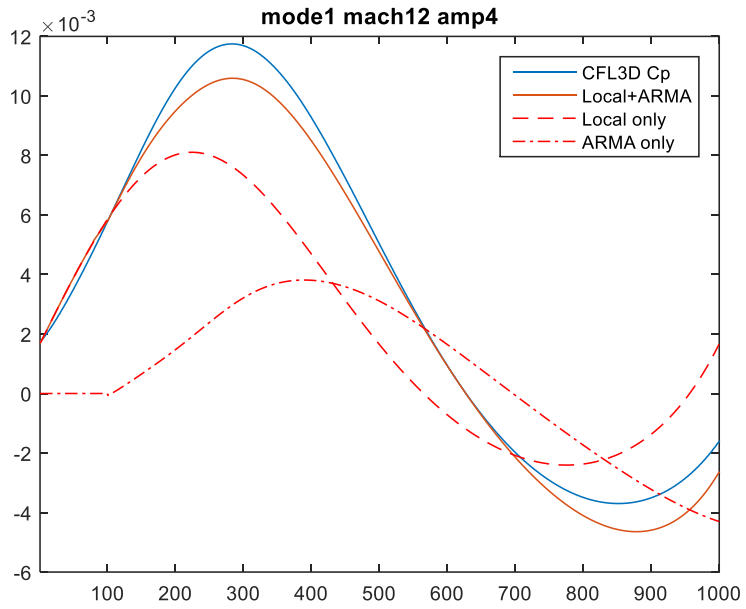

Figure 81. Comparative plot of local and global component of the reconstruction for mode1 mach12 amp4 Cp in two-layer mode independent model

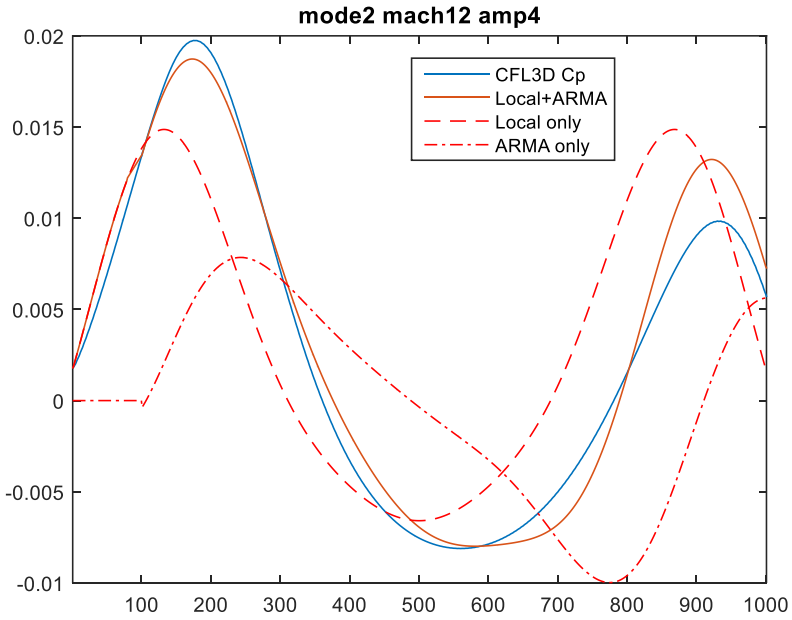

Figure 82. Comparative plot of local and global component of the reconstruction for mode2 mach12 amp4 Cp in two-layer mode independent model

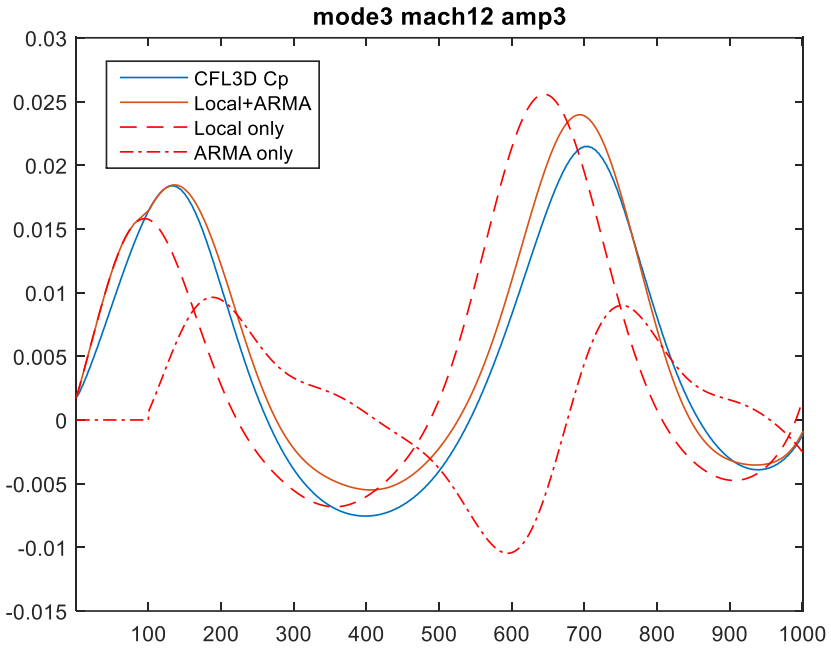

Figure 83. Comparative plot of local and global component of the reconstruction for mode3 mach12 amp3 Cp in two-layer mode independent model

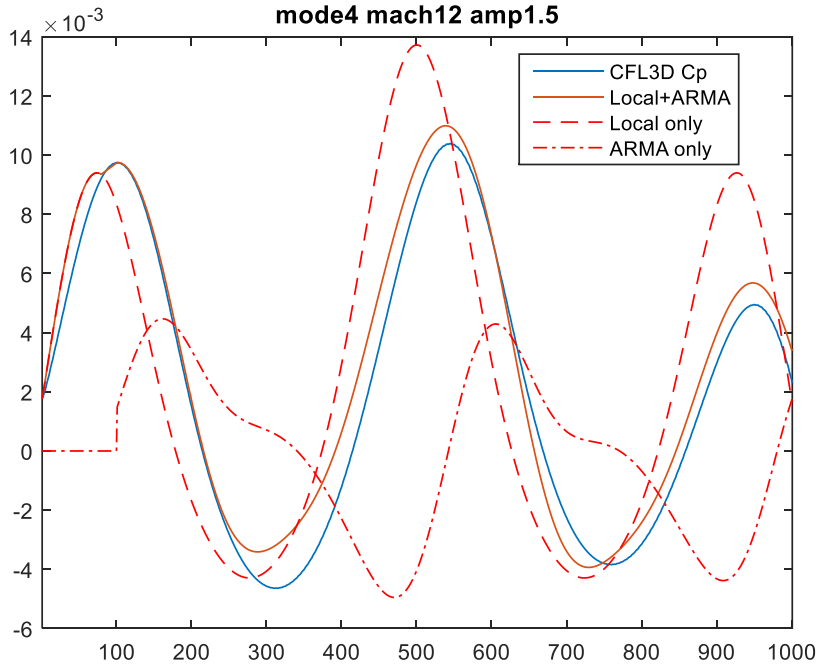

Figure 84. Comparative plot of local and global component of the reconstruction for mode4 mach12 amp1.5 Cp in two-layer mode independent model

3.2 Random AR coefficients

Reflection coefficients are derived from autoregressive coefficients for the mean model and are randomized with maximum entropy approach [5]. Figure 67 shows the roots of 100 samples of random ARMA model (delta = 0.1). Both mean and stochastic ARMA formulation are stable with roots less than 1.

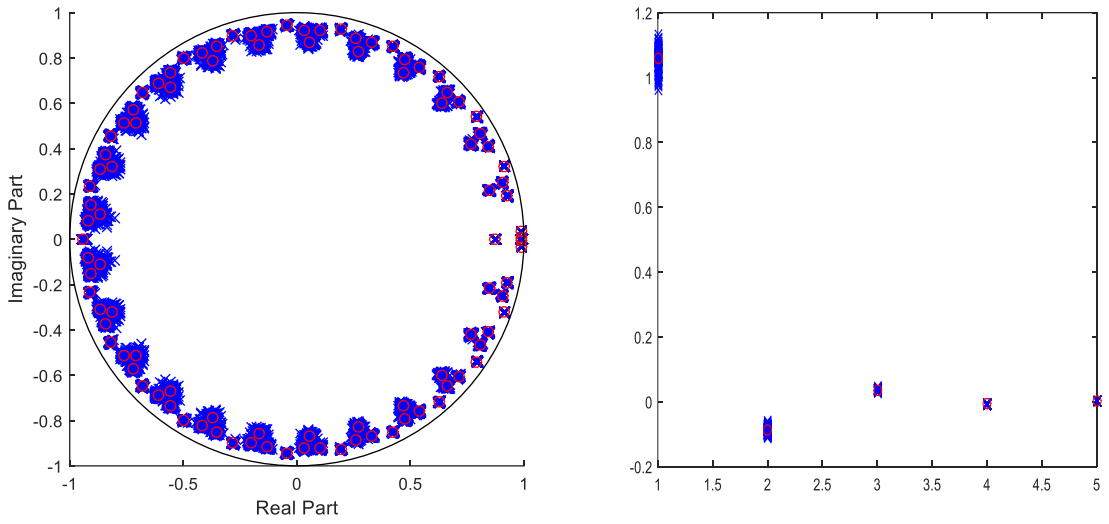

(a) (b)

Figure 85. (a) Roots of mean (red) and stochastic (blue) ARMA model (b) Autoregressive coefficients of mean (red) and stochastic (blue) ARMA model

In terms of autoregressive coefficients, all the coefficients are zero except 1, 25, 50, 75 and 100 for mean model. But for stochastic model, all the coefficients are non-zero. Figure 68 shows the random auto regressive coefficient corresponding to non-zero mean coefficients. The random samples of Cp are reconstructed with the random AR coefficients are smooth. Figure 69 – 72 shows the 5^{th} and 95^{th} percentile band of 100 random Cp. For node 1 to 100, there is no band as it is constructed solely with local component. Uncertainty band grows slowly from node 101 onwards and remains constant

throughout the length of beam indicating the stability of formulation and poles close to 1. This feature of the band does not help in the current situation, ideally we would want band to be proportional to the magnitude of Cp so that the peaks are captured well.

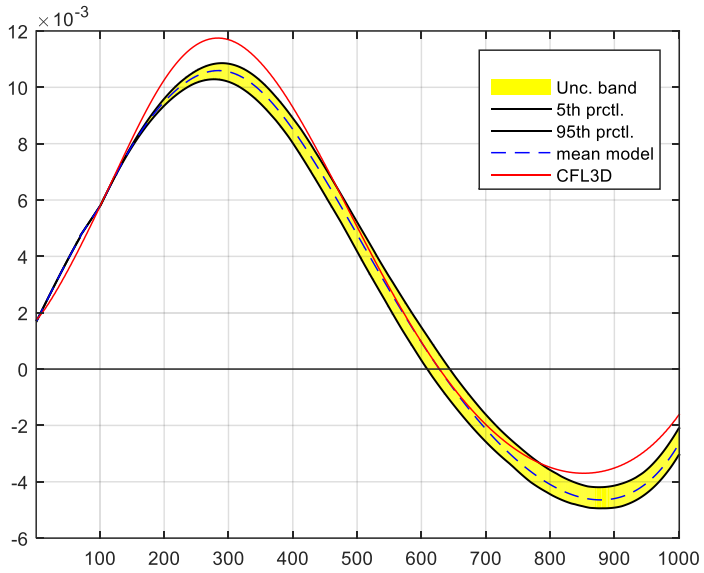

Figure 86. Uncertainty band obtained with random autoregressive coefficients for reconstructed Cp for mode1 mach12 amp4

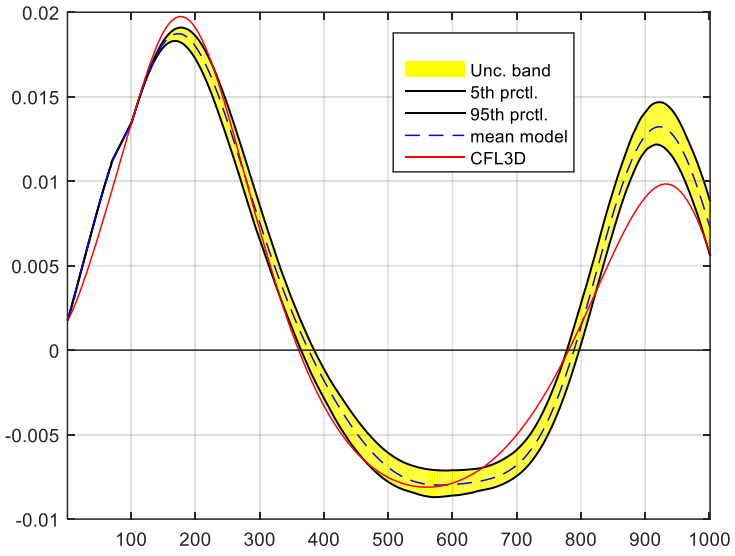

Figure 87. Uncertainty band for reconstructed Cp with random autoregressive coefficients for mode2 mach12 amp4

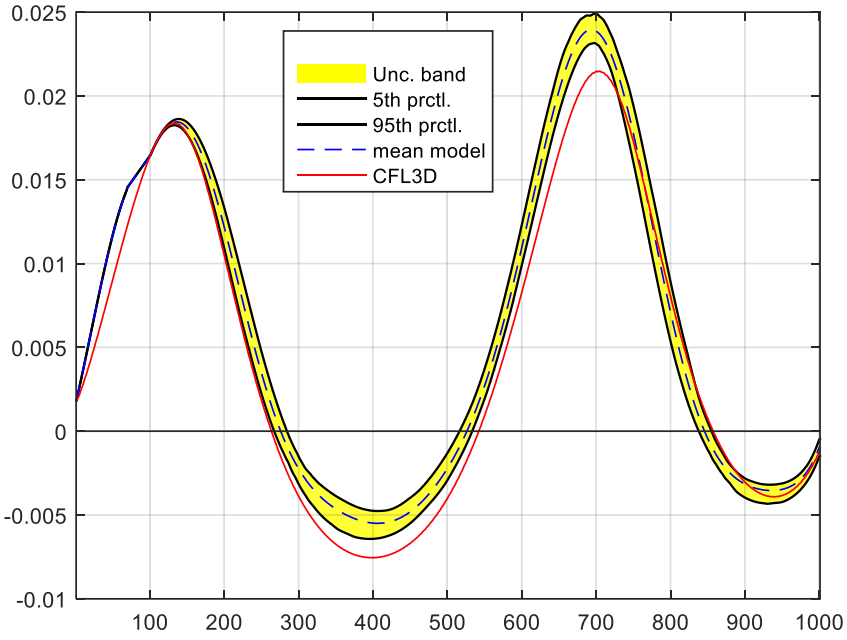

Figure 88. Uncertainty band for reconstructed Cp with random autoregressive coefficients for mode3 mach12 amp3

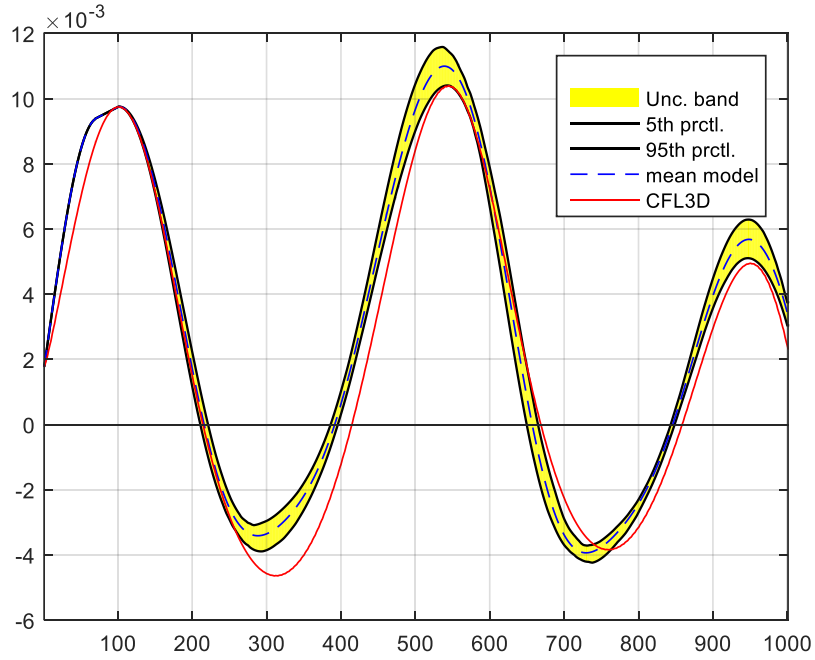

Figure 89. Uncertainty band for reconstructed Cp with random autoregressive coefficients for mode4 mach12 amp1.5

3.3 Random local coefficient

The uncertainty band in previous section is stable but it is inefficient in capturing the peaks of the Cp. This leads us to thought of modelling uncertainty on local component. There are couple of reasons, (i) Local component resembles the shape of given Cp and hence would be more effective in capturing peak and (ii) Local component solely constructs node 1 to 100, unlike random AR coefficients uncertainty band can be constructed for the complete beam. The approach is like randomizing AR coefficients; each local coefficient is randomized with max entropy approach to generate 100 samples and hence random local component is constructed. Figure 73-76 shows the uncertainty band constructed for each mode.

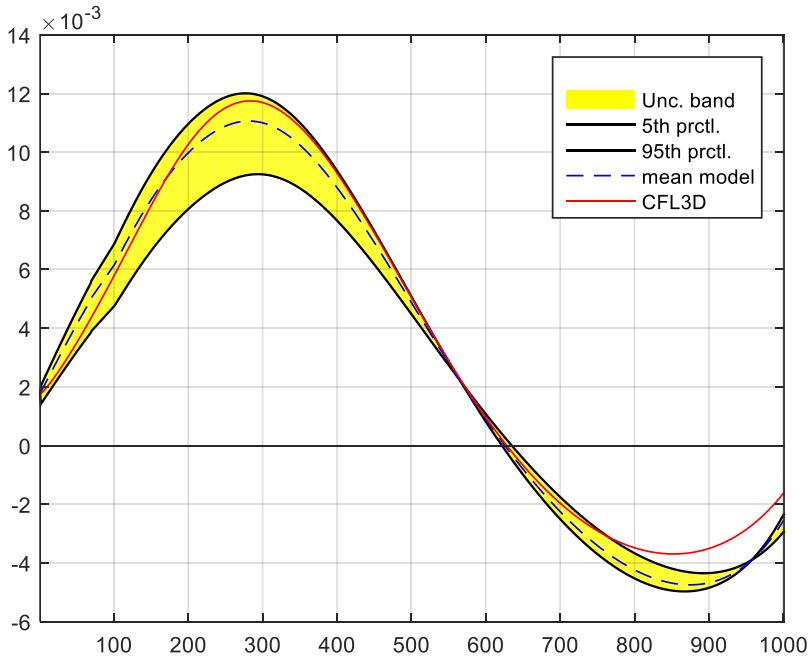

Figure 90. Uncertainty band for reconstructed Cp with random local coefficients for mode1 mach12 amp4

The constructed band width is proportional to magnitude of mean local reconstruction. As result of this correlation, the band width is high close to peak of CFL3D Cp (not matching exactly due to phase difference of local component). Further this also leads to narrow or zero width at the nodes with small or zero local component (for example, mid node of the beam for mode 1 in Figure 73). Significant effect can be seen on higher modes, where there are multiple nodes of zero width of band.

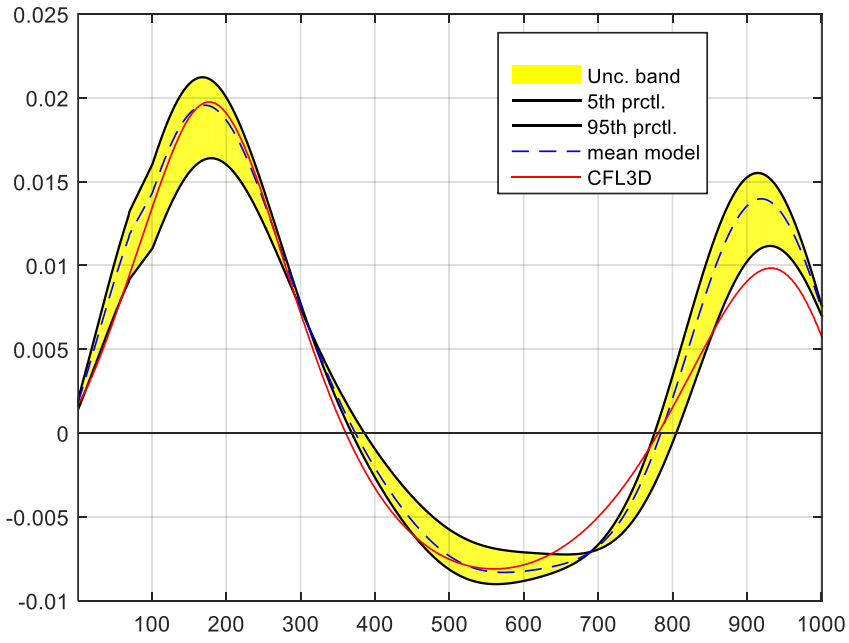

Figure 91. Uncertainty band for reconstructed Cp with random local coefficients for mode2 mach12 amp4

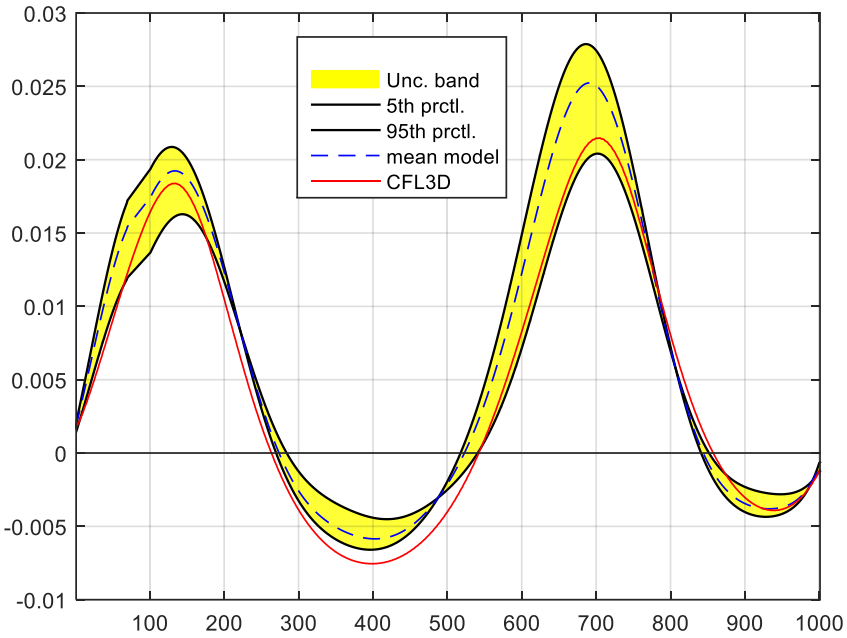

Figure 92. Uncertainty band for reconstructed Cp with random local coefficients for mode3 mach12 amp3

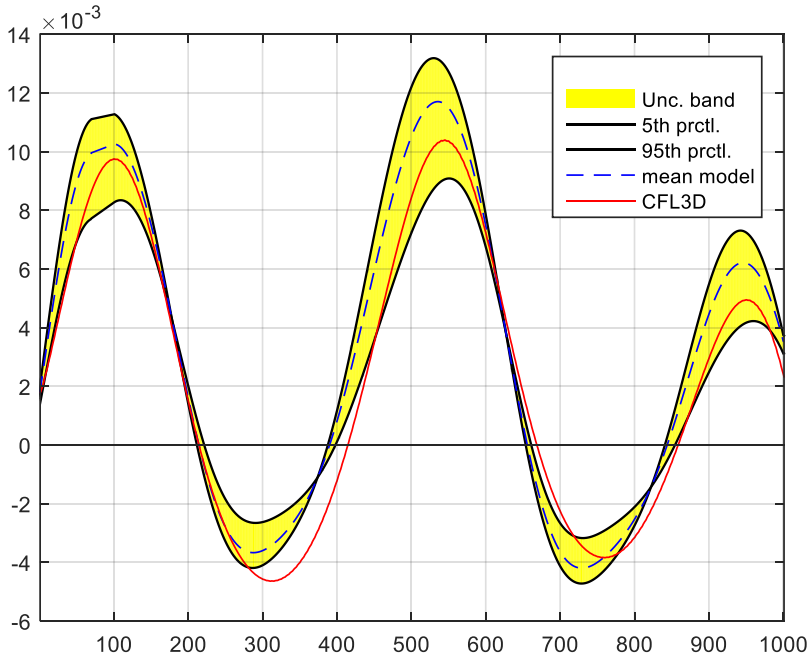

Figure 93. Uncertainty band for reconstructed Cp with random local coefficients for mode4 mach12 amp1.5

Local component of the construction is a direct product of slope and coefficients, it can be given by the equation below

$$\begin{bmatrix} Cp\_local(1) \\ . \\ . \\ . \\ Cp\_local(1001) \end{bmatrix} = \begin{bmatrix} a_1 & 0 & 0 & 0 \\ 0 & . & 0 & 0 \\ 0 & 0 & . & 0 \\ 0 & 0 & 0 & a_1 \end{bmatrix} \begin{bmatrix} \frac{dw}{dx} \end{bmatrix} + \begin{bmatrix} a_2 & 0 & 0 & 0 \\ 0 & . & 0 & 0 \\ 0 & 0 & . & 0 \\ 0 & 0 & 0 & a_2 \end{bmatrix} \begin{bmatrix} \left(\frac{dw}{dx}\right)^2 \end{bmatrix} + \begin{bmatrix} a_3 & 0 & 0 & 0 \\ 0 & . & 0 & 0 \\ 0 & 0 & . & 0 \\ 0 & 0 & 0 & a_3 \end{bmatrix} \begin{bmatrix} \left(\frac{dw}{dx}\right)^3 \end{bmatrix} + \begin{bmatrix} a_4 \\ . \\ . \\ a_4 \end{bmatrix}$$

The coefficient matrices are positive definite, symmetric and mean is prescribed which maximum entropy to be applicable to it. Randomization of individual coefficients and coefficient matrix form two alternative technique to obtain randomized local system. Figure 76 shows the 5th and 95th percentile uncertainty band for the later approach for mode1 mach12 amp8. Using the former approach results in band proportional to the magnitude of local component. But unlike former approach, if matrices are randomized then the band is uniform across the length of the beam. This is a globalization behavior (like band characteristics of random ARMA model) which is due to global coupling caused by non-zero non-diagonal elements in random matrices. The global coupling in a local problem is further investigated in Chapter 4. Further samples constructed are erratic making this approach unrealistic.

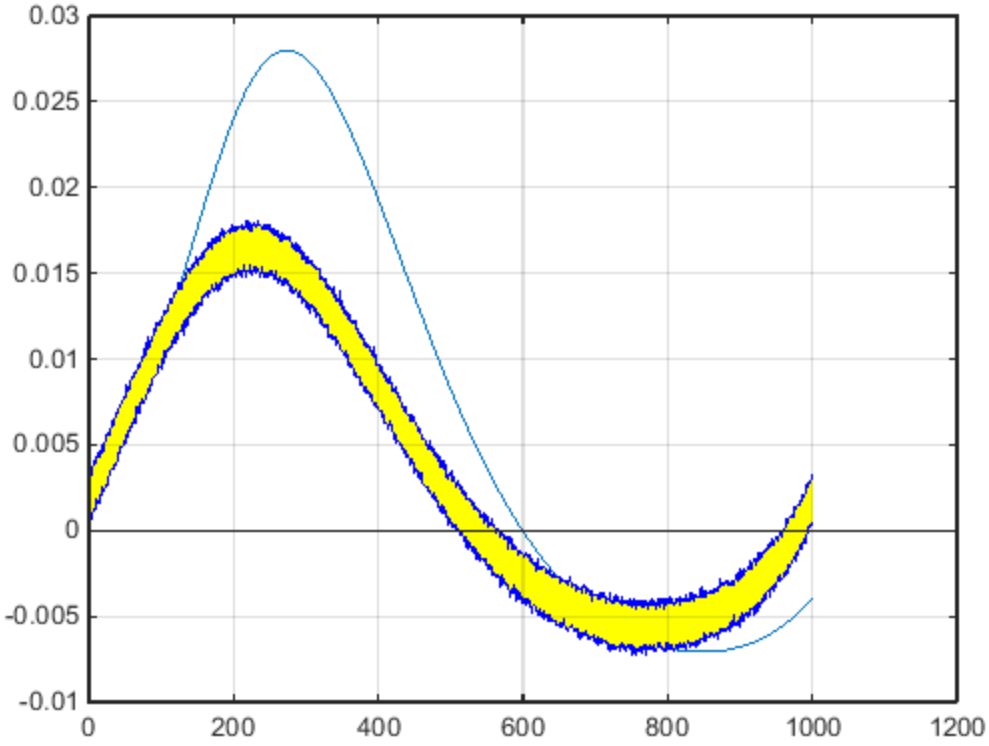

Figure 94. 5th and 95th percentile uncertainty band with random local coefficient matrix

3.4 Random local and ARMA coefficients

Due to the shortcomings explained in Section 3.2 and 3.3, In this section both autoregressive and local coefficients are randomized with delta = 0.1 and random samples of total solutions are constructed.

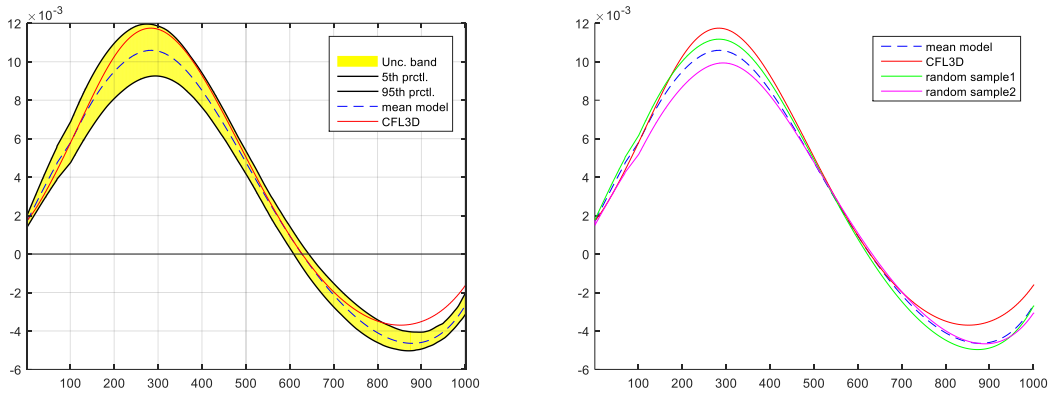

(a) (b)

Figure 95. (a) Uncertainty band for reconstructed Cp with random local and AR coefficients (b) Comparison of random samples with CFL3D Cp for mode1 mach12 amp4

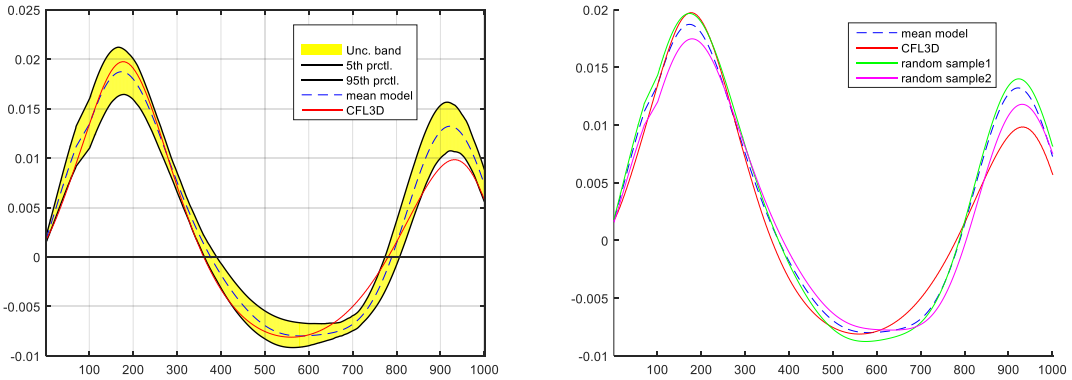

(a) (b)

Figure 96. (a) Uncertainty band for reconstructed Cp with random local and AR coefficients (b) Comparison of random samples with CFL3D Cp for mode2 mach12 amp6

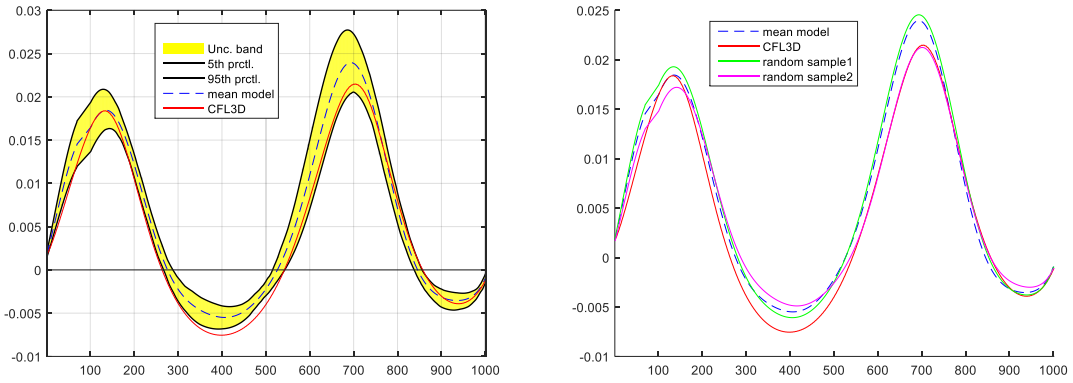

(a) (b)

Figure 97. (a) Uncertainty band for reconstructed Cp with random local and AR coefficients (b) Comparison of random samples with CFL3D Cp for mode3 mach12 amp3

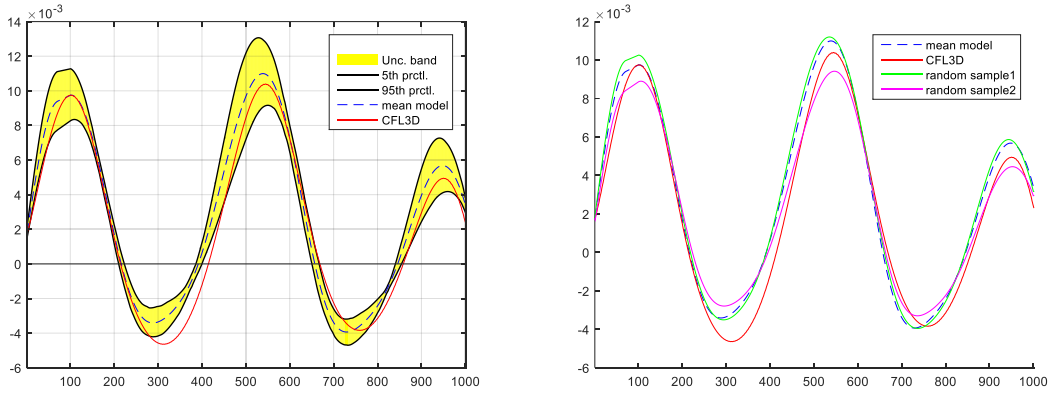

(a) (b)

Figure 98. (a) Uncertainty band for reconstructed Cp with random local and AR coefficients (b) Comparison of random samples with CFL3D Cp for mode4 mach12 amp1.5

4 Assessment of Non-Parametric Approach on local system

In the previous chapter, local model randomized with Non-Parametric method in addition to global ARMA model but there are global effects for the reconstructed results of the beam. The local model can be written as equation (3) where coefficient matrices are diagonal. To analyze this feature of Non-Parametric approach a one dimensional beam discretized with 39 nodes is considered. The Stiffness matrix is tri-diagonal like the local component of mean model. To study the effect of maximum entropy approach, the random stiffness matrices generated from mean matrix would be correlated to equivalent tridiagonal matrices. The analysis is extended to reduced order matrix which reduces the number of constraints in the optimization problem and establishes relation of reconstruction with number of terms. Further the response to a localized force (point load) on the configuration for full and reduced order random stiffness matrix with Winkler foundation boundary condition for uniformity of response.

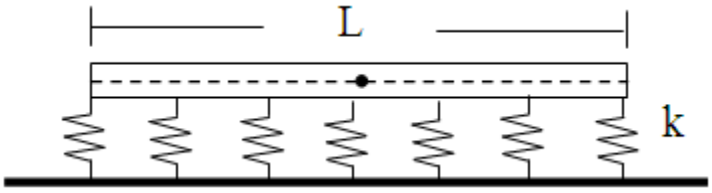

Figure 99. Beam under consideration (L = 1m, k = kg = 10 N/m) (Image Credits: Mohammad A. R. et. al [6])

Reconstruction cannot be directly carried out because modal matrix for order reduction are not square matrices hence not invertible. Following is the procedure employed for constructing best mean model -

- Calculate reduce order mean stiffness matrix ($\overline{K}_{ROM}$) to desired order using

  modal vector matrix

  $\overline{K}_{ROM} = \phi' \overline{K} \phi$

  Where ϕ is matrix of eigenvectors of $\overline{K}$

- Randomize the reduced order matrix through non-parametric approach

  $K_{ROM} = \overline{H}_{ROM} G \overline{H}_{ROM}^{T}$

  $where, \overline{K}_{ROM} = \overline{H}_{ROM} \overline{H}_{ROM}^{T}$ is Cholesky decomposition

  G is random matrix with independent element (generated with Maximum entropy principle defined in Chapter 1)

  The aim is to reconstruct $\overline{K}$ from given samples of K_{ROM} , this cannot be derived directly as matrix of modal vectors is rectangular

- Convert LHS in A * x for only lower triangular + diagonal elements

  where, x = [kg; kc] (77X1 array)

  A = matrix of coefficients

  kg = element stiffness of winkler foundation element

  kc = element stiffness of beam

  Write RHS in b so that it only has lower triangular + diagonal elements (since

  K_{ROM} is symmetric)

- Apply optimization techniques with xmean as starting value to get x
- Generate Kfull from x
- Find Error_constr = norm(A*x-b) and Error_stiffness = norm(|x-xmean|)

4.1 Comparison of methods of optimization

In this section, optimization through Lagrange Multiplier, MATLAB OPTIMIZATION TOOLBOX (fminsearch and fmincon) and composite methodology are evaluated for performance. Optimization results are iterated for various starting values; the best results are obtained with mean values of kg and kc as the start point. 100 samples of K_{ROM} are generated and optimized to obtain coefficients of full deterministic stiffness matrix by Lagrange multiplier, Lagrange multiplier + fmincon, fmincon only and fminsearch only. Figure 80 gives the 5^{th} and 95^{th} percentile band of respective norm error in reconstruction of stiffness. The constraint violation error for each method is comparable with Lagrange multiplier constructing better for lower order. Exact stiffness matrix is not constructed because applying maximum entropy principle induce non-zero independent elements at non-diagonal locations in the matrix. Disadvantage with Lagrange multiplier method being that constraint cannot be applied on physical feasibility on values of parameters, i.e. kg and kc must be positive or zero values, but in below results Lagrange gives few negative values of nodal stiffness yielding lower error. Comparing fmincon and fminsearch yields positive elemental stiffness with fminsearch being computationally inexpensive.

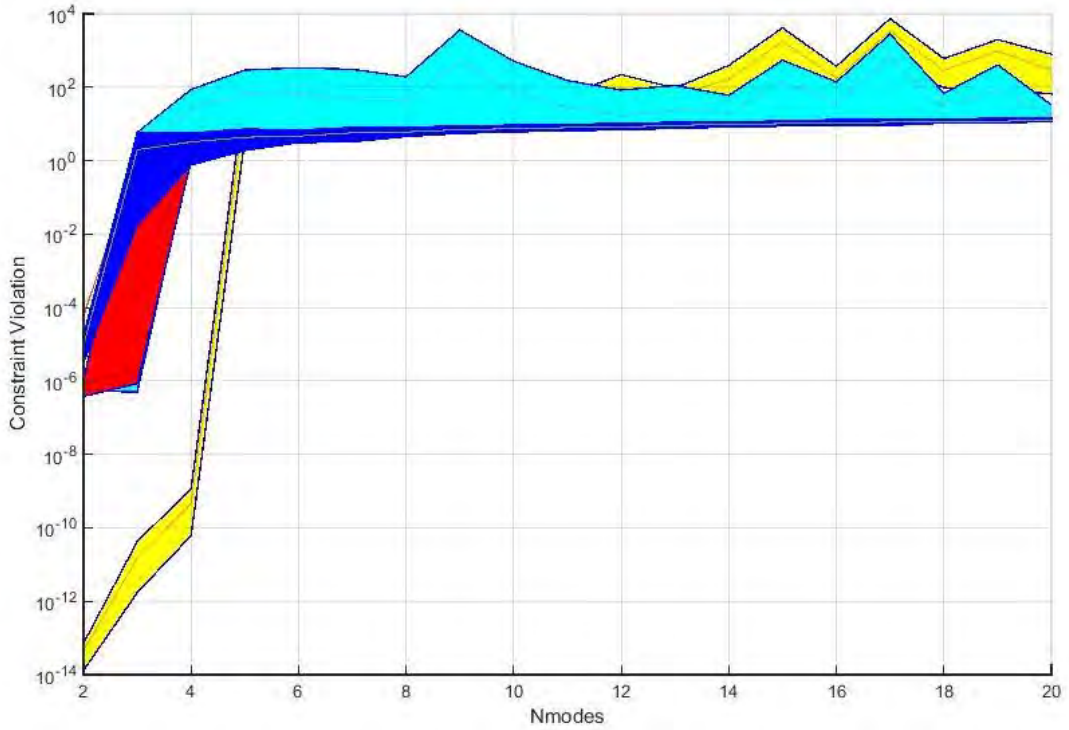

Figure 100. Comparison of constraint violation 5th and 95th percentile band (log-log scale) with Lagrange multiplier (yellow), Lagrange + fmincon (cyan), fmincon (red) and fminsearch (blue)

Similarly, lagrange multiplier gives better overall proximity of stiffness coefficients to the mean values but with the above stated disadvantage of converging to negative (unfeasible) values (Figure 81). Further analysis will be conducted with results of fminsearch optimization.

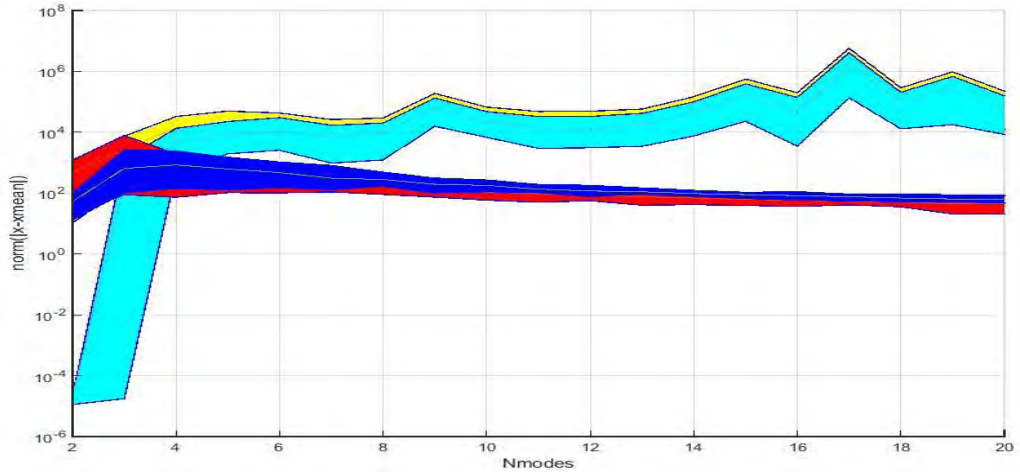

Figure 101. Comparison of deviation of elemental stiffness 5th and 95th percentile band (log-log scale) with Lagrange multiplier (yellow), Lagrange + fmincon (cyan), fmincon (red) and fminsearch (blue)

4.2 Analysis of Error in reconstruction

The mean stiffness coefficients are not recoverable from the random stiffness matrix generated with maximum entropy principle because of global coupling established by introducing non-diagonal elements into tridiagonal mean matrix. This correlation depends on the magnitude of non-diagonal elements, to analyze this behavior delta (magnitude of uncertainty) is varied to get range of randomness in the mode. The reconstruction is compared for delta = 1e-1, 1e-3 and 1e-5. Figure 82-84 shows the absolute reconstruction error with decreasing magnitude of uncertainty (delta). With less constraints on lower order matrices, it can reconstruct the equivalent mean reduced order matrix but as constraints increases the error climbs steeply. For delta = 0.1, only matrix of order 2 can be reconstructed completely indicating the magnitude of global coupling in the matrix. As delta is reduced, global coupling gets weaker and reconstruction error reduces significantly. But even for delta as small as 1e-5 exact reconstruction is not possible indicating even small global coupling would give global components in the response of the beam if analyzed with these random stiffness matrices.

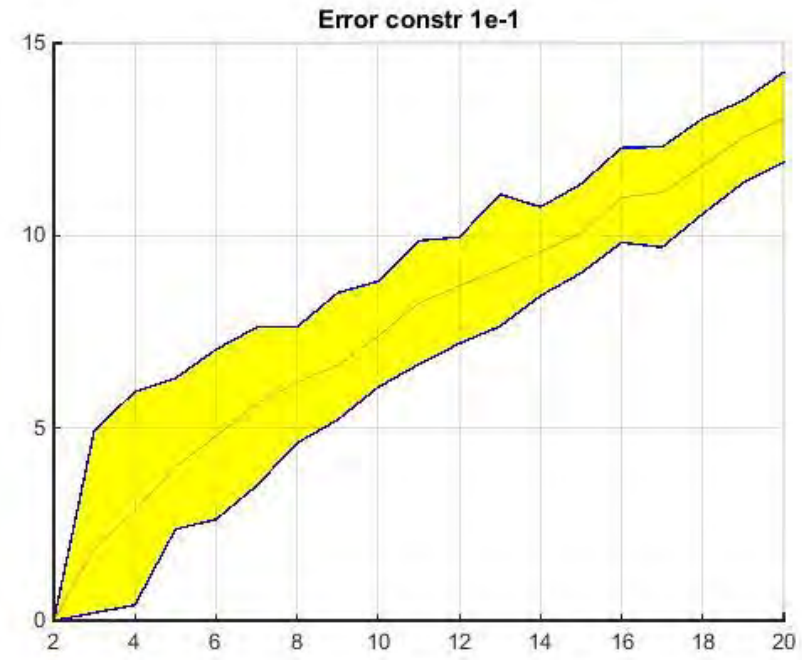

Figure 102. Variation of Absolute reconstruction error 5th and 95th percentile band with order of reduction for delta = 0.1

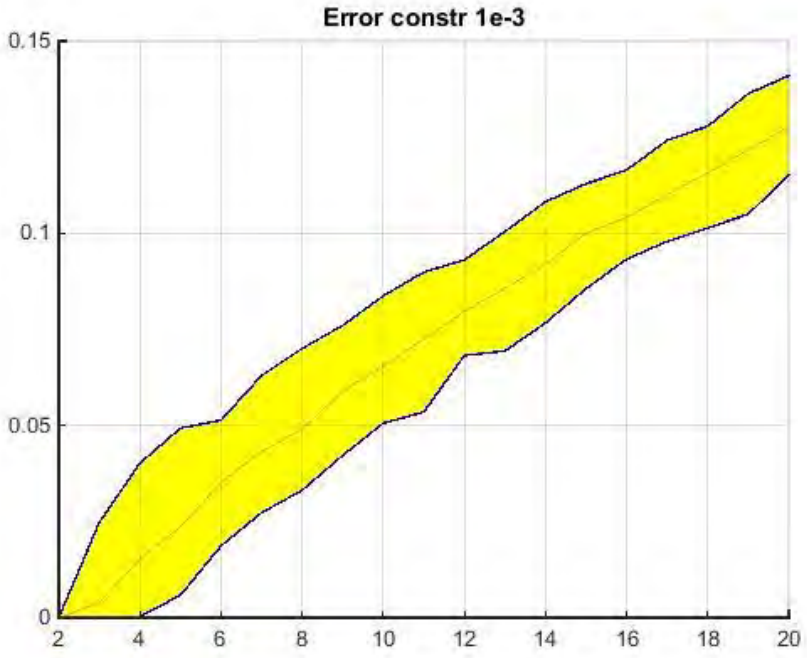

Figure 103. Variation of absolute reconstruction error 5th and 95th percentile band with order of reduction for delta = 0.001

Figure 104. Variation of absolute reconstruction error 5th and 95th percentile band with order of reduction for delta = 0.00001

4.3 Error in response to localized forces

Since the random matrices have global coupling unlike mean full matrix, the response of localized force on these random matrices must produce response on global nodes proportional to the non-diagonal terms. Figure 83-85 shows the error on static response obtained with random reduced stiffness matrices with respect to mean reduced stiffness matrix. Agreeing to results of previous section, here as well error increases with increasing reduction order and uncertainty level.

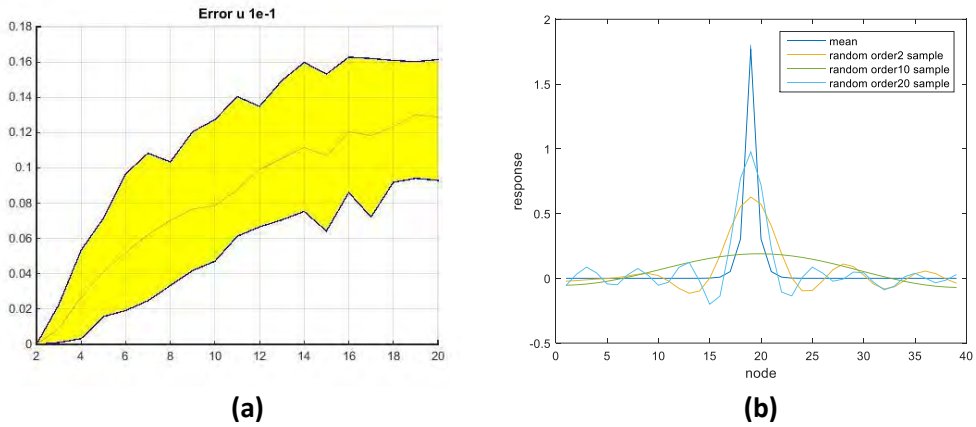

Figure 105. (a) Variation of absolute response error 5th and 95th percentile band with order of reduction for delta = 0.1 for localized force (point load at mid node) (b) samples of response with random reduced order stiffness matrix

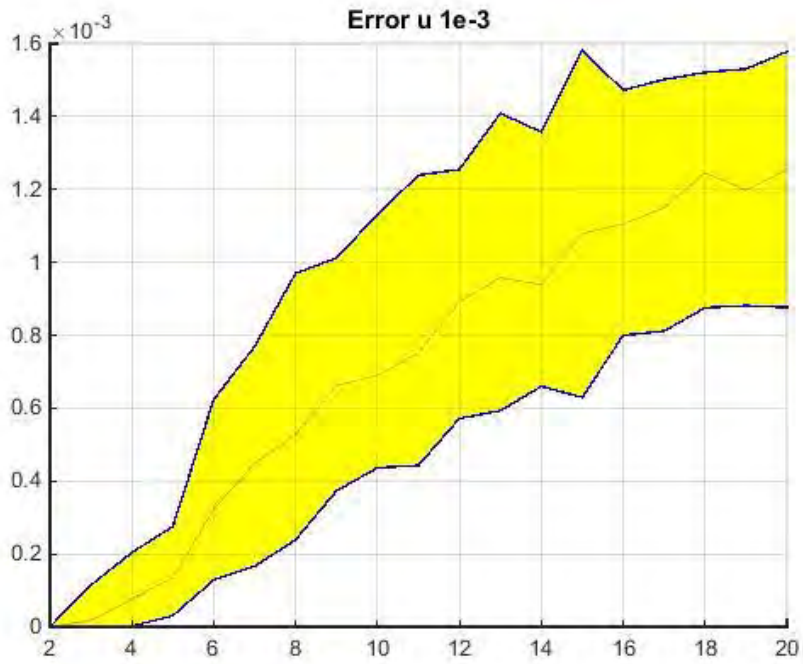

Figure 106. Variation of absolute response error 5th and 95th percentile band with order of reduction for delta = 0.001 for localized force (point load at mid node)

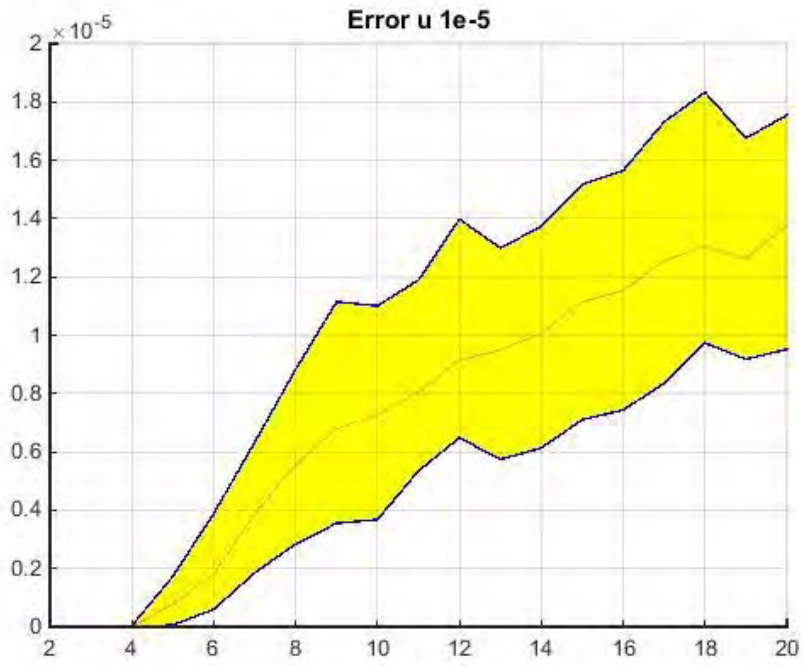

Figure 107. Variation of absolute response error 5th and 95th percentile band with order of reduction for delta = 0.00001 for localized force (point load at mid node)

REFERENCES

[1] C. Soize, A nonparametric model of random uncertainties on reduced matrix models in structural dynamics, Probab. Eng. Mech. 15(3)(2000)277–294.

[2] C. Soize, Stochastic Models of Uncertainties in Computational Mechanics, American Society of Civil Engineers (ASCE), Reston, 2012.

[3] Crowell A. R., McNamara J.J., Miller B.A., Hypersonic Aerothermoelastic Response Prediction of Skin Panels Using Computational Fluid Dynamic Surrogates, ASDJournal (2011), Vol. 2, No. 2, pp. 3-30

[4] D. D. Liu, Z. X. Yao, D. Sarhaddi, F. Chavez, From Piston Theory to a Unified Hypersonic – Supersonic Lifting Surface Method, JOURNAL OF AIRCRAFT Vol. 34, No. 3, May – June 1997

[5] Y. Wang, X.Q. Wang, M. Mignolet, S.Yang, P.C. Chen, Modeling of uncertain spectra through stochastic autoregressive systems, Mechanical Systems and Signal Processing 70-71 (2016) 506–526